Spectroscopic Identification of Fractional Rydberg States of Atomic Hydrogen

Randell L. Mills,* Paresh C. Ray, Bala Dhandapani, Jiliang He

ABSTRACT

Extreme ultraviolet (EUV) spectroscopy was recorded on microwave discharges of helium with 2% hydrogen. Novel emission lines were observed with energies of $q \cdot 13.6\,eV$ where $q = 1,2,3,4,6,7,8,9,11,12$ or these lines inelastically scattered by helium atoms wherein $21.2\,eV$ was absorbed in the excitation of $He\,(1s^2)$ to $He\,(1s^1 2p^1)$. These lines can be explained as fractional Rydberg states of atomic hydrogen. Novel emission lines were also observed at $44.2\,nm$ and $40.5\,nm$ with energies of

$$q \cdot 13.6 + \left(\frac{1}{n_f^2} - \frac{1}{n_i^2} \right) X 13.6\,eV$$ where $q = 2$ and $n_f = 2,4$ $n_i = \infty$ that corresponded

to multipole coupling to give two photon emission from a continuum excited state atom and an atom undergoing a fractional Rydberg state transition. Such transitions would be extremely energetic; so, the width of the 656.2 nm Balmer α line emitted from the plasmas was measured, and the electron temperature T_e was measured from the ratio of the intensity of the He 501.6 nm line to that of the He 492.2 line. Significant line broadening corresponding to an average hydrogen atom temperature of $180\text{-}210\,eV$ was observed for helium-hydrogen microwave plasmas; whereas, pure hydrogen showed no excessive broadening corresponding to an average hydrogen atom temperature of $\approx 3\,eV$. Similarly, the average electron temperature for helium-hydrogen plasma was 28,000 K; whereas, the corresponding temperature of helium alone was only 6800 K.

*Randell L. Mills, BlackLight Power, Inc., 493 Old Trenton Road, Cranbury, NJ 08512, USA, 609-490-1090, 609-490-1066 (fax), rmills@blacklightpower.com

I. INTRODUCTION

J. J. Balmer showed in 1885 that the frequencies for some of the lines observed in the emission spectrum of atomic hydrogen could be expressed with a completely empirical relationship. This approach was later extended by J. R. Rydberg, who showed that all of the spectral lines of atomic hydrogen were given by the equation:

$$\bar{v} = R\left(\frac{1}{n_f^2} - \frac{1}{n_i^2}\right) \tag{1}$$

where $R = 109{,}677\ cm^{-1}$, $n_f = 1,2,3,...$, $n_i = 2,3,4,...$, and $n_i > n_f$.

Niels Bohr, in 1913, developed a theory for atomic hydrogen that gave the energy levels in agreement with Rydberg's equation. An identical equation, based on a totally different theory for the hydrogen atom, was developed by E. Schrödinger, and independently by W. Heisenberg, in 1926.

$$E_n = -\frac{e^2}{n^2 8\pi\varepsilon_o a_H} = -\frac{13.598\ eV}{n^2} \tag{2a}$$

$$n = 1,2,3,... \tag{2b}$$

where a_H is the Bohr radius for the hydrogen atom ($52.947\ pm$), e is the magnitude of the charge of the electron, and ε_o is the vacuum permittivity.

The excited energy states of atomic hydrogen are given by Eq. (2a) for $n > 1$ in Eq. (2b). The $n = 1$ state is the "ground" state for "pure" photon transitions (the $n = 1$ state can absorb a photon and go to an excited electronic state, but it cannot release a photon and go to a lower-energy electronic state). However, an electron transition from the ground state to a lower-energy state may be possible by a nonradiative energy transfer such as multipole coupling or a resonant collision mechanism. Processes such as hydrogen molecular bond formation that occur without photons and that require collisions are common [1]. Also, some commercial phosphors are based on resonant nonradiative energy transfer involving multipole coupling [2].

We propose that atomic hydrogen may undergo a catalytic reaction with certain atomized elements and ions which singly or multiply ionize

2

at integer multiples of the potential energy of atomic hydrogen, $m \cdot 27.2 \, eV$ wherein m is an integer. The theory was given previously [3-5]. The reaction involves a nonradiative energy transfer to form a hydrogen atom that is lower in energy than unreacted atomic hydrogen that corresponds to a fractional principal quantum number. That is

$$n = \frac{1}{2}, \frac{1}{3}, \frac{1}{4}, ..., \frac{1}{p}; \quad p \text{ is an integer} \tag{2c}$$

replaces the well known parameter $n = \text{integer}$ in the Rydberg equation for hydrogen excited states. The $n = 1$ state of hydrogen and the $n = \dfrac{1}{\text{integer}}$ states of hydrogen are nonradiative, but a transition between two nonradiative states is possible via a nonradiative energy transfer, say $n = 1$ to $n = 1/2$. In these cases, during the transition the electron couples to another electron transition, electron transfer reaction, or inelastic scattering reaction which can absorb the exact amount of energy that must be removed from the hydrogen atom to cause the transition. Thus, a catalyst provides a net positive enthalpy of reaction of $m \cdot 27.2 \, eV$ (i.e. it absorbs $m \cdot 27.2 \, eV$ where m is an integer). Certain atoms or ions serve as catalysts which resonantly accept the nonradiative energy transfer from hydrogen atoms and release the energy to the surroundings to affect electronic transitions to fractional quantum energy levels. As a consequence of the nonradiative energy transfer, the hydrogen atom becomes unstable and emits further energy until it achieves a lower-energy nonradiative state having a principal energy level given by Eqs. (2a) and (2c).

A number of independent experimental observations lead to the conclusion that atomic hydrogen can exist in fractional quantum states that are at lower energies than the traditional "ground" ($n = 1$) state. Prior related studies that support the possibility of a novel reaction of atomic hydrogen which produces a chemically generated or assisted plasma and produces novel hydride compounds include extreme ultraviolet (EUV) spectroscopy [6-8, 11-13], characteristic emission from catalysis and the hydride ion products [8], lower-energy hydrogen emission [6-8], plasma formation [8, 11-13], Balmer α line broadening [9], anomalous plasma afterglow duration [13], power generation [9-11], and analysis of chemical compounds [14]. Since the second ionization energy of He^+ is an

3

exact multiple of the potential energy of atomic hydrogen and microwave plasmas may have significant concentrations of He^+ as well as atomic hydrogen, microwave discharges of helium-hydrogen mixtures were studied by extreme ultraviolet (EUV) spectroscopy to search for line emission from transitions to fractional Rydberg states of atomic hydrogen. Since the electronic transitions are very energetic, Balmer α line broadening and an elevated electron temperature were anticipated and was measured.

II. EXPERIMENTAL

A. EUV Spectroscopy

EUV spectroscopy was recorded on hydrogen, helium, and helium-hydrogen (98/2%) microwave discharge plasmas according to the methods given previously [6]. Hydrogen alone, helium alone, and helium-hydrogen (98/2%) gas mixture was flowed through a half inch diameter quartz tube at 20 torr, 1 torr, or 0.1 torr. The gas pressure inside the cell was maintained by flowing the mixture while monitoring the pressure with a 10 torr and 1000 torr MKS Baratron absolute pressure gauge. The tube was fitted with an Opthos coaxial microwave cavity (Evenson cavity). The microwave generator was a Opthos model MPG-4M generator (Frequency: 2450 MHz). The input power to the plasma was set at 85 watts with forced air cooling of the cell. The spectrometer was a normal incidence McPherson 0.2 meter monochromator (Model 302, Seya-Namioka type) equipped with a 1200 lines/mm holographic grating with a platinum coating or a MgF_2 coating in the case of the spectra recorded at 0.1 torr. The wavelength region covered by the monochromator was $2-560\,nm$. The EUV spectrum was recorded with a channel electron multiplier (CEM) at $2500-3000\,V$. The wavelength resolution was about $0.02\,nm$ (FWHM) with an entrance and exit slit width of $50\,\mu m$. The increment was $0.2\,nm$ and the dwell time was $500\,ms$. Novel peak positions were based on a calibration against the known He I and He II lines.

To achieve higher sensitivity at the shorter EUV wavelengths, the light emission from plasmas of helium alone was recorded with a

4

McPherson 4° grazing incidence EUV spectrometer (Model 248/310G) equipped with a grating having 600 G/mm with a radius of curvature of $\approx 1\,m$. The angle of incidence was 87°. The wavelength region covered by the monochromator was $5-65\,nm$. The wavelength resolution was about $0.04\,nm$ (FWHM) with an entrance and exit slit width of $300\,\mu m$. A channel electron multiplier (CEM) at $2400\,V$ was used to detect the EUV light. The increment was $0.1\,nm$ and the dwell time was $1\,s$.

B. Line broadening and T_e measurements

The width of the 656.2 nm Balmer α line emitted from hydrogen or helium-hydrogen mixture (90/10)% microwave discharge plasmas was measured. The plasma conditions was as described in section A except that the total pressure was 1 torr, and the input power to the plasma was set at 40 W. The plasma emission was fiber-optically coupled through a 220F matching fiber adapter positioned 2 cm from the cell wall to a high resolution visible spectrometer with a resolution of $\pm 0.006\,nm$ over the spectral range $190-860\,nm$. The spectrometer was a Jobin Yvon Horiba 1250 M with 2400 groves/mm ion-etched holographic diffraction grating. The entrance and exit slits were set to $20\,\mu m$. The spectrometer was scanned between $655.5-657\,nm$ using a $0.005\,nm$ step size. The signal was recorded by a PMT with a stand alone high voltage power supply (950 V) and an acquisition controller. The data was obtained in a single accumulation with a 1 second integration time.

T_e was measured on microwave plasmas of helium alone and helium-hydrogen mixtures (90/10%) from the ratio of the intensity of the He 501.6 nm (upper quantum level n=3) line to that of the He 492.2 nm (n=4) line as described by Griem [15]. In each case, the microwave plasma cell was run under the conditions given in section A, except that the total pressure was 0.1 torr. The visible spectrum was recorded with the normal incidence EUV spectrometer as described section A except that visible spectrum ($400-560\,nm$) of the cell emission was recorded with a photomultiplier tube (PMT) and a sodium salicylate scintillator. The PMT (Model R1527P, Hamamatsu) used has a spectral response in the range of $185-680\,nm$ with a peak efficiency at about $400\,nm$. The scan interval was $0.4\,nm$. The inlet and outlet slit were $300\,\mu m$ with a

5

corresponding wavelength resolution of 2 nm. The spectra were repeated five times per experiment and were found to be reproducible within less than 5%.

III. RESULTS AND DISCUSSION

A. EUV Spectroscopy

The EUV emission was recorded at pressures of 20, 1, and 0.1 torr from microwave plasmas of hydrogen, helium, and helium with 2% hydrogen over the wavelength range 2-125 nm. In the case of hydrogen, no peaks were observed below 78 nm, and no spurious peaks or artifacts due to the grating or the spectrometer were observed. Only known He I and He II peaks were observed in the EUV spectrum of the control helium microwave discharge cell emission.

The EUV spectra (17.5-50 nm) of the microwave cell emission of the helium-hydrogen mixture (98/2%) (top curve) and the helium control (bottom curve) are shown in Figure 1. Ordinary hydrogen has no emission in these regions. Novel peaks were observed at 45.6 nm, 37.4 nm, and 20.5 nm which do not correspond to helium.

The effect of decreasing the pressure from 20 torr to 1 torr was studied. At the 1 torr condition, additional novel peaks were observed in the short wavelength region. The short wavelength EUV spectrum (5-65 nm) of the control hydrogen microwave cell emission (bottom curve) is shown in Figure 2. No spectrometer artifacts were observed at the short wavelengths. The short wavelength EUV spectrum (5-65 nm) of the helium-hydrogen mixture (98/2%) microwave cell emission with a pressure of 1 torr (top curve) is also shown in Figure 2. Novel peaks were observed at 14.15 nm, 13.03 nm, 10.13 nm, and 8.29 nm which do not correspond to helium. Known He I lines which were used for calibration of the novel peak positions were observed at 58.4 nm, 53.7 nm, and 52.4 nm.

A broad continuum shoulder on the sharp 45.6 nm peak was observed at 20 torr as shown in Figure 1. A 44.2 nm peak could be resolved at 1 torr as shown in Figure 2. The effect of further decreasing the pressure from 1 torr to 0.1 torr and was studied using the MgF_2 coated grating. At the 0.1 torr condition, additional novel peaks were
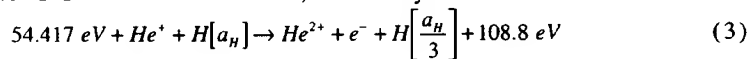
6

observed. The short wavelength EUV spectrum ($2-50\,nm$) of the control hydrogen microwave cell emission (bottom curve) is shown in Figure 3. No spectrometer artifacts were observed at the short wavelengths. The short wavelength EUV spectrum ($2-50\,nm$) of the helium-hydrogen mixture (98/2%) microwave cell emission (top curve) is also shown in Figure 3. Novel peaks were observed at $45.6\,nm$, $13.03\,nm$, $10.13\,nm$, and $7.60\,nm$ which do not correspond to helium, and novel peaks at $44.2\,nm$ and $40.5\,nm$ could be resolved on the sharp $45.6\,nm$ peak. It is also proposed that the $30.4\,nm$ peak shown in Figures 1-3 was not entirely due to the He II transition. In the case of helium-hydrogen mixture, conspicuously absent was the $25.6\,nm$ ($48.3\,eV$) line of He II shown in Figure 1 which implies only a minor He II transition contribution to the $30.4\,nm$ peak.

At 20 torr, the ratio of the $L\beta$ peak to the $91.2\,nm$ peak of the helium-hydrogen plasma was 2; whereas, the ratio of the $L\beta$ peak to the $91.2\,nm$ peak of the control hydrogen plasma was 8 which indicates that the majority of the $91.2\,nm$ peak was due to a transition other than the binding of an electron by a proton. Based on the intensity, it is proposed that the majority of the $91.2\,nm$ peak was due to a novel peak.

The novel peaks fit three empirical relationships. In order of energy, the set comprising the peaks at $91.2\,nm$, $45.6\,nm$, $30.4\,nm$, $13.03\,nm$, $10.13\,nm$, $8.29\,nm$, and $7.60\,nm$ correspond to energies of $q \cdot 13.6\,eV$ where $q = 1,2,3,7,9,11,12$. In order of energy, the set comprising the peaks at $37.4\,nm$, $20.5\,nm$, and $14.15\,nm$ correspond to energies of $q \cdot 13.6 - 21.21\,eV$ where $q = 4, 6,\ or\ 8$. In order of energy, the set comprising the peaks at $44.2\,nm$ and $40.5\,nm$ correspond to energies of $q \cdot 13.6 + \left(\dfrac{1}{n_f^2} - \dfrac{1}{n_i^2} \right) X 13.6\,eV$ where $q = 2$ and $n_f = 2,4\ \ n_i = \infty$. These lines can be explained as electronic transitions to fractional Rydberg states of atomic hydrogen given by Eqs. (2a) and (2c) wherein the catalytic system involves helium ions because the second ionization energy of helium is $54.417\,eV$, which is equivalent to $2 \cdot 27.2\,eV$. In this case, the catalysis reaction is

$$54.417\,eV + He^+ + H[a_H] \rightarrow He^{2+} + e^- + H\left[\frac{a_H}{3}\right] + 108.8\,eV \qquad (3)$$

$$He^{2+} + e^- \rightarrow He^+ + 54.417\,eV \qquad (4)$$

And, the overall reaction is

$$H[a_H] \rightarrow H\left[\frac{a_H}{3}\right] + 54.4 \ eV + 54.4 \ eV \tag{5}$$

Since the products of the catalysis reaction have binding energies of $m \cdot 27.2 \ eV$, they may further serve as catalysts. Thus, further catalytic transitions may occur: $n = \frac{1}{3} \rightarrow \frac{1}{4}, \ \frac{1}{4} \rightarrow \frac{1}{5}$, and so on.

Electronic transitions to Rydberg states given by Eqs. (2a) and (2c) catalyzed by the resonant nonradiative transfer of $m \cdot 27.2 \ eV$ would give rise to a series of emission lines of energies $q \cdot 13.6 \ eV$ where q is an integer. It is further proposed that the photons that arise from hydrogen transitions may undergo inelastic helium scattering. That is, the catalytic reaction

$$H[a_H] \xrightarrow{He^*} H\left[\frac{a_H}{3}\right] + 54.4 \ eV + 54.4 \ eV \tag{6}$$

yields two $54.4 \ eV$ photons $(22.8 \ nm)$. When each of these photons strikes $He \ (1s^2)$, $21.2 \ eV$ is absorbed in the excitation to $He \ (1s^1 2p^1)$. This leaves a $33.19 \ eV$ $(37.4 \ nm)$ photon peak and a $21.2 \ eV$ $(58.4 \ nm)$ photon from $He \ (1s^1 2p^1)$. Thus, for helium the inelastic scattered peak of $54.4 \ eV$ photons from Eq. (3) is given by

$$E = 54.4 \ eV - 21.21 \ eV = 33.19 \ eV \ (37.4 \ nm) \tag{7}$$

A novel peak shown in Figures 1 and 2 was observed at $37.4 \ nm$. Furthermore, the corresponding intensity of the $58.4 \ nm$ shown in Figure 2 was off-scale with 60,000 photons/sec. Thus, the transition $He \ (1s^2) \rightarrow He \ (1s^1 2p^1)$ dominated the inelastic scattering of EUV peaks. The general reaction is

$$photon \ (h\nu) + He \ (1s^2) \rightarrow He \ (1s^1 2p^1) + photon \ (h\nu - 21.21 \ eV) \tag{8}$$

Helium ion catalyzes $H[a_H]$ to $H\left[\frac{a_H}{3}\right]$ as shown in Eqs. (3-5). Further reactions may then proceed:

$$H\left[\frac{a_H}{3}\right] + H\left[\frac{a_H}{3}\right] \rightarrow H\left[\frac{a_H}{4}\right] + H\left[\frac{a_H}{2}\right] + 27.2 \ eV \tag{9}$$

It is further proposed that hydrogen transitions from continuum excited states may couple to fractional Rydberg transitions of the same multipolarity. The novel emission lines observed at $44.2 \ nm$ and $40.5 \ nm$ with energies of $q \cdot 13.6 + \left(\frac{1}{n_f^2} - \frac{1}{n_i^2}\right) X 13.6 \ eV$ where $q = 2$ and $n_f = 2,4 \ \ n_i = \infty$ can be explained by multipole coupling of the

8

transitions to $n = 1/4$ and $n = 1/2$ with the transition from continuum states to $n = 4$ and $n = 2$, respectively, to give two photon emission.

With inelastic helium scattering and multipole coupling, the three empirical series may be combined. The energies for the novel lines in order of energy are $13.6\ eV$, $27.2\ eV$, $40.8\ eV$, $54.4\ eV$, $81.6\ eV$, $95.2\ eV$, $108.8\ eV$, $122.4\ eV$, $149.6\ eV$, and $163.2\ eV$. The corresponding peaks are $91.2\ nm$, $45.6\ nm$ with $44.2\ nm$ and $40.5\ nm$, $30.4\ nm$, $37.4\ nm$, $20.5\ nm$, $13.03\ nm$, $14.15\ nm$, $10.13\ nm$, $8.29\ nm$, and $7.60\ nm$ respectively. Thus, the identified novel lines correspond to energies of $q \cdot 13.6\ eV$ where $q = 1,2,3,4,6,7,8,9,11,12$, these lines inelastically scattered by helium atoms wherein $21.2\ eV$ was absorbed in the excitation of $He\,(1s^2)$ to $He\,(1s^1 2p^1)$, or the two photon emission from a continuum excited state atom and an atom undergoing a fractional Rydberg state transition. There is remarkable agreement between the data and the proposed transitions. All other peaks could be assigned to He I, He II, second order lines, or atomic or molecular hydrogen emission. No known lines of helium or hydrogen explain the $q \cdot 13.6\ eV$ related set of peaks. Given that these spectra are readily repeatable, these peaks may have been overlooked in the past without considering the role of the helium scattering. It is also remarkable that the novel lines are moderately intense based on the low grating efficiency at these short wavelengths.

B. Line broadening and T_e measurements

The method of Videnocic et al. [16] was used to calculate the energetic hydrogen atom densities and energies from the width of the 656.2 nm Balmer α line emitted from the hydrogen and helium-hydrogen mixture (90/10%) microwave plasmas. It was found that helium-hydrogen showed significant broadening corresponding to an average hydrogen atom temperature of $180 - 210\ eV$ and an atom density of $5 \times 10^{14}\ atoms/cm^3$; whereas, pure hydrogen showed no excessive broadening corresponding to an average hydrogen atom temperature of $\approx 3\ eV$ and an atom density of only $7 \times 10^{13}\ atoms/cm^3$ even though 10 times more hydrogen was present. Similarly, the average electron temperature for helium-hydrogen plasma was 28,000 K; whereas, the corresponding temperature of helium alone was only 6800 K.

9

IV. CONCLUSION

We report that extreme ultraviolet (EUV) spectroscopy was recorded on microwave discharges of helium with 2% hydrogen. Novel emission lines were observed with energies of $q \cdot 13.6 \, eV$ where $q = 1,2,3,4,6,7,8,9,11,12$ or these lines inelastically scattered by helium atoms wherein $21.2 \, eV$ was absorbed in the excitation of $He \, (1s^2)$ to $He \, (1s^1 2p^1)$. These lines were identified as transitions to fractional Rydberg states of atomic hydrogen ($n = \dfrac{1}{p} = \dfrac{1}{\text{integer}}$ replaces the well known parameter $n = \text{integer}$ in the Rydberg equation for hydrogen excited states). Novel emission lines were also observed at $44.2 \, nm$ and $40.5 \, nm$ with energies of $q \cdot 13.6 + \left(\dfrac{1}{n_f^2} - \dfrac{1}{n_i^2} \right) X 13.6 \, eV$ where $q = 2$ and $n_f = 2,4$ $n_i = \infty$ that corresponded to multipole coupling to give two photon emission from a continuum excited state atom and an atom undergoing a fractional Rydberg state transition.

An average hydrogen atom temperature of 180-$210 \, eV$ was observed by line broadening with the presence of helium ions with hydrogen; whereas, pure hydrogen plasmas showed no excessive broadening corresponding to an average hydrogen atom temperature of $\approx 3 \, eV$. Similarly, the average electron temperature for helium-hydrogen plasma was 28,000 K; whereas, the corresponding temperature of helium alone was only 6800 K. No electric field was present in our experiments. Thus, the results can not be explained by Stark broadening or acceleration of charged species due to high fields of over $10 \, kV/cm$ as proposed by Videnocic et al. [16] to explain excessive broadening observed in glow discharges.

The novel emission lines and extraordinarily elevated temperatures may be explained by a highly energetic catalytic reaction involving a resonant nonradiative energy transfer of $m \cdot 27.2 \, eV$ from atomic hydrogen to a catalyst wherein m is an integer. One such atomic catalytic system involves helium ions. The second ionization energy of helium is $54.4 \, eV$; thus, the ionization reaction of He^+ to He^{2+} has a net enthalpy of reaction of $54.4 \, eV$ which is equivalent to $2 \cdot 27.2 \, eV$. Since the products of the

catalysis reaction have binding energies of $m \cdot 27.2\ eV$, they may further serve as catalysts.

ACKNOWLEDGMENT

Special thanks to Y. Lu and T. Onuma for recording some spectra.

REFERENCES

1. N. V. Sidgwick, *The Chemical Elements and Their Compounds*, Volume I, Oxford, Clarendon Press, (1950), p.17.
2. M. D. Lamb, *Luminescence Spectroscopy*, Academic Press, London, (1978), p. 68.
3. R. Mills, *The Grand Unified Theory of Classical Quantum Mechanics*, January 2000 Edition, BlackLight Power, Inc., Cranbury, New Jersey, Distributed by Amazon.com; posted at www.blacklightpower.com.
4. R. Mills, "The Grand Unified Theory of Classical Quantum Mechanics", Int. J. Hydrogen Energy, in press.
5. R. Mills, The Nature of Free Electrons in Superfluid Helium--a Test of Quantum Mechanics and a Basis to Review its Foundations and Make a Comparison to Classical Theory, Int. J. Hydrogen Energy, Vol. 26, No. 10, (2001), pp. 1059-1096.
6. R. Mills, P. Ray, "Spectral Emission of Fractional Quantum Energy Levels of Atomic Hydrogen from a Helium-Hydrogen Plasma and the Implications for Dark Matter", Int. J. Hydrogen Energy, in press.
7. R. Mills, P. Ray, "Vibrational Spectral Emission of Fractional-Principal-Quantum-Energy-Level Hydrogen Molecular Ion", Int. J. Hydrogen Energy, in press.
8. R. Mills, "Spectroscopic Identification of a Novel Catalytic Reaction of Atomic Hydrogen and the Hydride Ion Product", Int. J. Hydrogen Energy, Vol. 26, No. 10, (2001), pp. 1041-1058.
9. R. Mills, A. Voigt, P. Ray, M. Nanstell, "Measurement of Hydrogen Balmer Line Broadening and Thermal Power Balances of Noble Gas-Hydrogen Discharge Plasmas", Int. J. Hydrogen Energy, submitted.
10. R. Mills, N. Greenig, S. Hicks, "Optically Measured Power Balances of Anomalous Discharges of Mixtures of Argon, Hydrogen, and Potassium,
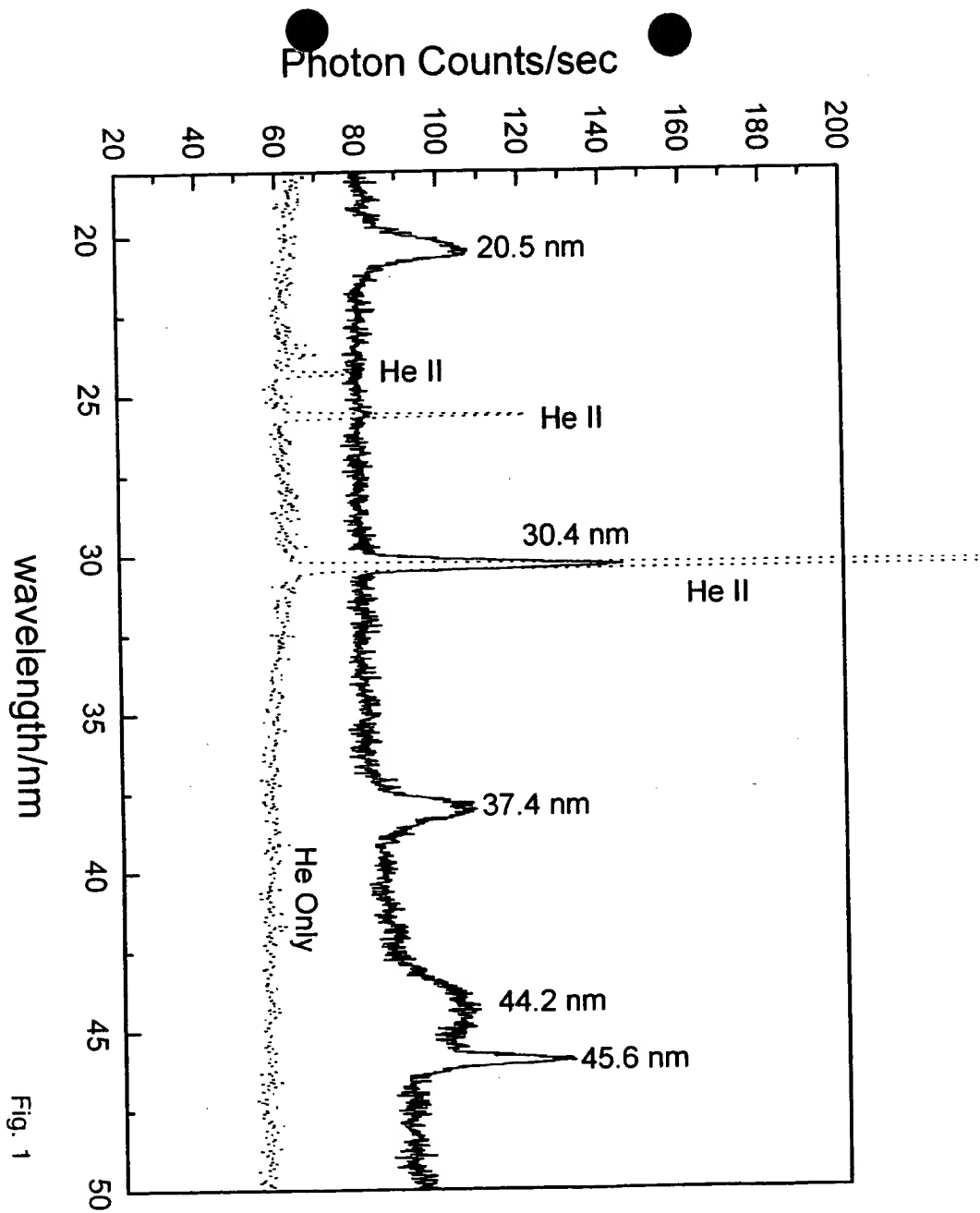
Rubidium, Cesium, or Strontium Vapor", Int. J. Hydrogen Energy, submitted.

11. R. Mills, M. Nansteel, and Y. Lu, "Observation of Extreme Ultraviolet Hydrogen Emission from Incandescently Heated Hydrogen Gas with Strontium that Produced an Anomalous Optically Measured Power Balance", Int. J. Hydrogen Energy, Vol. 26, No. 4, (2001), pp. 309-326.

12. R. Mills, J. Dong, Y. Lu, "Observation of Extreme Ultraviolet Hydrogen Emission from Incandescently Heated Hydrogen Gas with Certain Catalysts", Int. J. Hydrogen Energy, Vol. 25, (2000), pp. 919-943.

13. R. Mills, T. Onuma, and Y. Lu, "Formation of a Hydrogen Plasma from an Incandescently Heated Hydrogen-Catalyst Gas Mixture with an Anomalous Afterglow Duration", Int. J. Hydrogen Energy, Vol. 26, No. 7, July, (2001), pp. 749-762.

14. R. Mills, B. Dhandapani, M. Nansteel, J. He, T. Shannon, A. Echezuria, "Synthesis and Characterization of Novel Hydride Compounds", Int. J. of Hydrogen Energy, Vol. 26, No. 4, (2001), pp. 339-367.

15. Griem, *Principle of Plasma Spectroscopy*, Cambridge University Press, (1987).

16. I. R. Videnocic, N. Konjevic, M. M. Kuraica, "Spectroscopic investigations of a cathode fall region of the Grimm-type glow discharge", Spectrochimica Acta, Part B, Vol. 51, (1996), pp. 1707-1731.

Figure Captions

Figure 1. The EUV spectra ($17.5-50\,nm$) of the microwave cell emission of the helium-hydrogen mixture (98/2%) (top curve) recorded at 20 torr with a normal incidence EUV spectrometer and a CEM, and control helium (bottom curve) recorded at 20 torr with a $4°$ grazing incidence EUV spectrometer and a CEM. Only known He I and He II peaks were observed with the helium control. Reproducible novel emission lines were observed at $45.6\,nm$ and $30.4\,nm$ with energies of $q \cdot 13.6\,eV$ where $q = 2\,or\,3$ and at $37.4\,nm$ and $20.5\,nm$ with energies of $q \cdot 13.6\,eV$ where $q = 4\,or\,6$ that were inelastically scattered by helium atoms wherein $21.2\,eV$ ($58.4\,nm$) was absorbed in the excitation of $He\,(1s^2)$.

Figure 2. The short wavelength EUV spectra ($5-65\,nm$) of the microwave cell emission of the helium-hydrogen mixture (98/2%) (top curve) and control hydrogen (bottom curve) recorded at 1 torr with a normal incidence EUV spectrometer and a CEM. No hydrogen emission was observed in this region, and no instrument artifacts were observed. Reproducible novel emission lines were observed at $45.6\,nm$, $30.4\,nm$, $13.03\,nm$, $10.13\,nm$, and $8.29\,nm$ with energies of $q \cdot 13.6\,eV$ where $q = 2,3,7,9,\,or\,11$ and at $37.4\,nm$, $20.5\,nm$, and $14.15\,nm$ with energies of $q \cdot 13.6\,eV$ where $q = 4,6,\,or\,8$ that were inelastically scattered by helium atoms wherein $21.2\,eV$ ($58.4\,nm$) was absorbed in the excitation of $He\,(1s^2)$.

Figure 3. The short wavelength EUV spectra ($2-50\,nm$) of the microwave cell emission of the helium-hydrogen mixture (98/2%) (top curve) and control hydrogen (bottom curve) recorded at 0.1 torr with a normal incidence EUV spectrometer, a MgF_2 coated grating, and a CEM. No hydrogen emission was observed in this region, and no instrument artifacts were observed. Reproducible novel emission lines were observed at $45.6\,nm$, $30.4\,nm$, $13.03\,nm$, $10.13\,nm$, and $7.60\,nm$ with energies of $q \cdot 13.6\,eV$ where $q = 2,3,7,9,12$. Novel emission lines were also observed at $44.2\,nm$ and $40.5\,nm$ with energies of $q \cdot 13.6 + \left(\dfrac{1}{n_f^2} - \dfrac{1}{n_i^2} \right) X 13.6\,eV$ where $q = 2$ and $n_f = 2,4$ $n_i = \infty$ that corresponded to multipole coupling to give two photon emission from a continuum excited state atom and an atom undergoing a fractional Rydberg state transition.
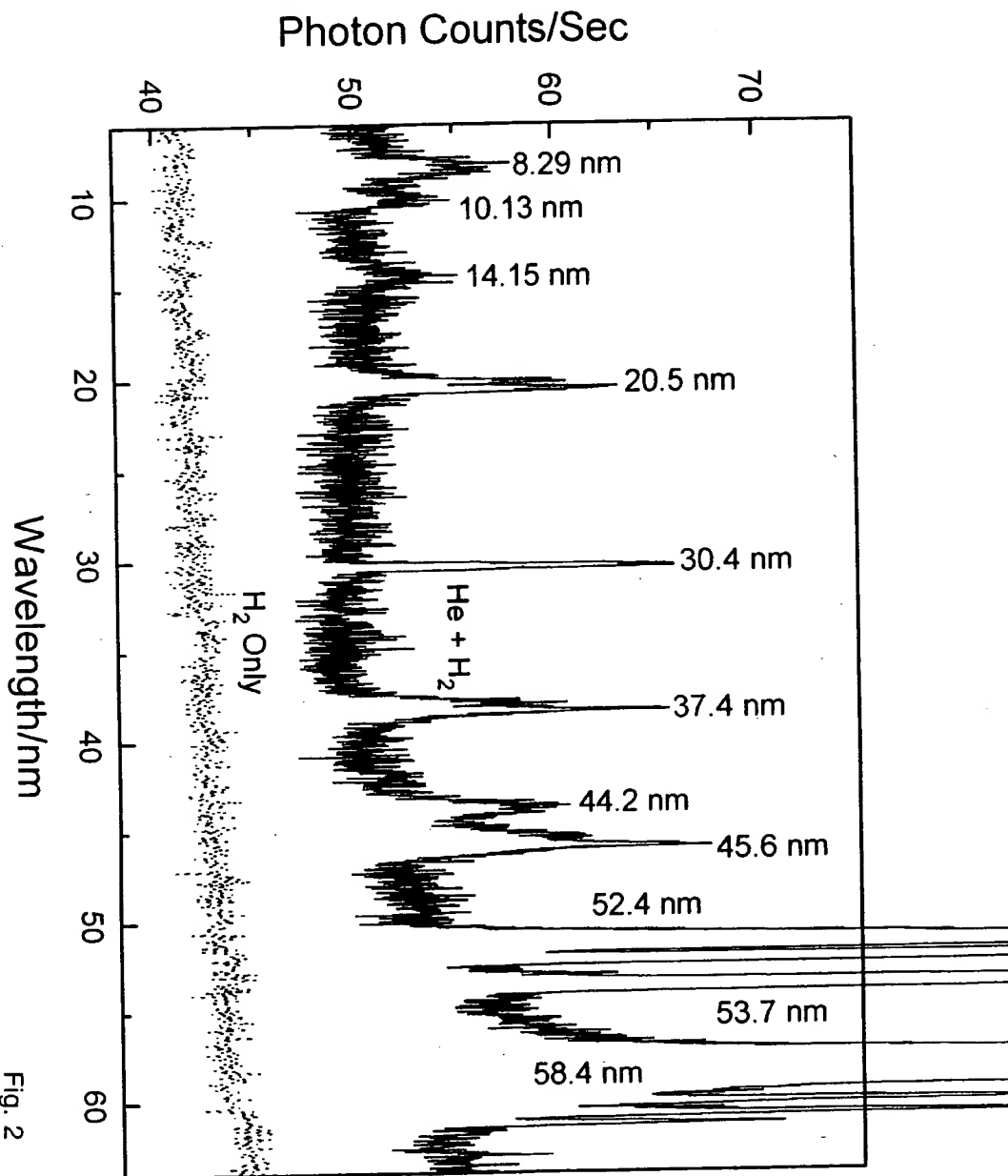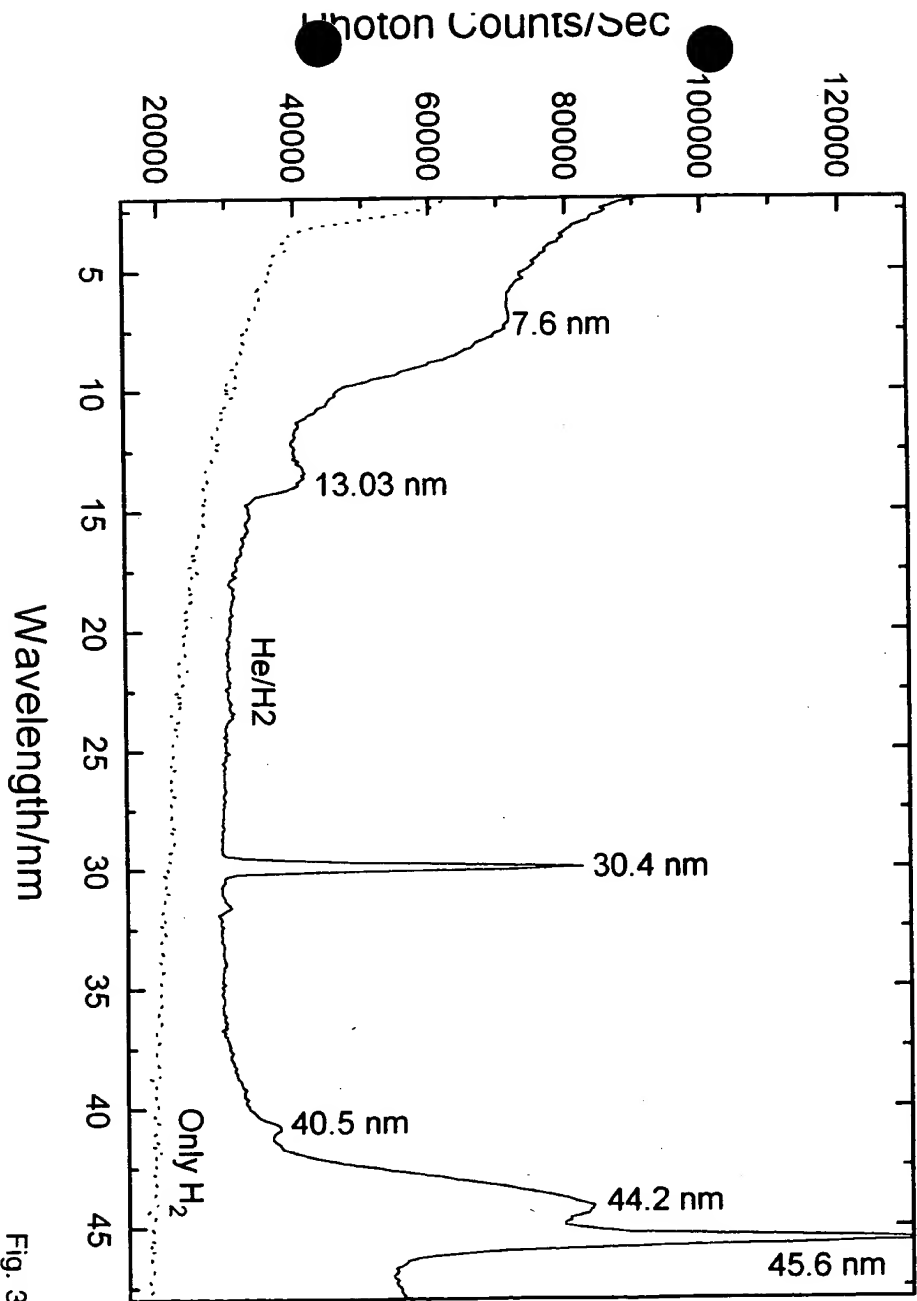
Fig. 1

Fig. 2

Photon Counts/Sec

Wavelength/nm

H₂ Only

He + H₂

8.29 nm
10.13 nm
14.15 nm
20.5 nm
30.4 nm
37.4 nm
44.2 nm
45.6 nm
52.4 nm
53.7 nm
58.4 nm

Fig. 3

New Power Source from Fractional Rydberg States of Atomic Hydrogen

R. L. Mills, P. Ray, B. Dhandapani, M. Nansteel, X. Chen, J. He

BlackLight Power, Inc.

493 Old Trenton Road

Cranbury, NJ 08512

ABSTRACT

Extreme ultraviolet (EUV) spectroscopy was recorded on microwave discharges of helium with 2% hydrogen. Novel emission lines were observed with energies of $q \cdot 13.6\ eV$ where $q = 1,2,3,4,6,7,8,9,11$ or these lines inelastically scattered by helium wherein 21.2 eV was absorbed in the excitation of $He\,(1s^2)$ to $He\,(1s^1 2p^1)$. The average hydrogen atom temperature was measured to be 180-$210\ eV$ versus $\approx 3\ eV$ for pure hydrogen. The electron temperature T_e for helium-hydrogen was 28,000 K compared to 6800 K for pure helium. With a microwave input power of 40 W, the gas temperature of the plasma was measured to be 1200°C after 150 s compared to 185°C for helium alone.

1. Introduction

J. R. Rydberg showed that all of the spectral lines of atomic hydrogen were given by a completely empirical relationship:

$$\bar{v} = R\left(\frac{1}{n_f^2} - \frac{1}{n_i^2}\right) \tag{1}$$

where $R = 109,677 \ cm^{-1}$, $n_f = 1,2,3,...$, $n_i = 2,3,4,...$ and $n_i > n_f$. Bohr, Schrödinger, and Heisenberg each developed a theory for atomic hydrogen that gave the energy levels in agreement with Rydberg's equation.

$$E_n = -\frac{e^2}{n^2 8\pi\varepsilon_o a_H} = -\frac{13.598 \ eV}{n^2} \tag{2a}$$

$$n = 1,2,3,... \tag{2b}$$

The excited energy states of atomic hydrogen are given by Eq. (2a) for $n > 1$ in Eq. (2b). The $n = 1$ state is the "ground" state for "pure" photon transitions (i.e. the $n = 1$ state can absorb a photon and go to an excited electronic state, but it cannot release a photon and go to a lower-energy electronic state). However, an electron transition from the ground state to a lower-energy state may be possible by a resonant nonradiative energy transfer such as multipole coupling or a resonant collision mechanism. Processes such as hydrogen molecular bond formation that occur without photons and that require collisions are common [1]. Also, some commercial phosphors are based on resonant nonradiative energy transfer involving multipole coupling [2].

We propose that atomic hydrogen may undergo a catalytic reaction with certain atoms and ions such as He^+ which singly or multiply ionize at integer multiples of the potential energy of atomic hydrogen, $m \cdot 27.2 \ eV$ wherein m is an integer. The theory was given previously [3-5]. The reaction involves a nonradiative energy transfer to form a hydrogen atom that is lower in energy than unreacted atomic hydrogen that corresponds to a fractional principal quantum number. That is

$$n = \frac{1}{2}, \frac{1}{3}, \frac{1}{4},..., \frac{1}{p}; \quad p \text{ is an integer} \tag{2c}$$

replaces the well known parameter $n = $ integer in the Rydberg equation for hydrogen excited states. The $n = 1$ state of hydrogen and the $n = \frac{1}{\text{integer}}$

2

states of hydrogen are nonradiative, but a transition between two nonradiative states is possible via a nonradiative energy transfer, say $n = 1$ to $n = 1/2$. Thus, a catalyst provides a net positive enthalpy of reaction of $m \cdot 27.2 \, eV$ (i.e. it resonantly accepts the nonradiative energy transfer from hydrogen atoms and releases the energy to the surroundings to affect electronic transitions to fractional quantum energy levels). As a consequence of the nonradiative energy transfer, the hydrogen atom becomes unstable and emits further energy until it achieves a lower-energy nonradiative state having a principal energy level given by Eqs. (2a) and (2c).

Prior related studies that support the possibility of a novel reaction of atomic hydrogen which produces hydrogen in fractional quantum states that are at lower energies than the traditional "ground" ($n = 1$) state include EUV spectroscopy [6-12], characteristic emission from catalysts and the hydride ion products [8], lower-energy hydrogen emission [6-8, 12], chemically formed plasmas [8-11], Balmer α line broadening [12-13], anomalous plasma afterglow duration [11], power generation [9, 13-14], and analysis of novel chemical compounds [15]. We report that microwave discharges of helium-hydrogen mixtures were studied by EUV spectroscopy to search for line emission from transitions to fractional Rydberg states of atomic hydrogen. Since the electronic transitions are very energetic, Balmer α line broadening, electron temperature, and the gas temperature were measured.

2. Experimental

EUV spectroscopy was recorded on hydrogen, xenon, helium, xenon-hydrogen (98/2%), and helium-hydrogen (98/2%) microwave discharge plasmas (Frequency: 2450 MHz) according to the methods given previously [6]. A xenon-hydrogen (98/2%) or helium-hydrogen (98/2%) gas mixture was flowed at 1 Torr or 20 Torr through a half inch diameter quartz tube fitted with an Evenson cavity, and each plasma of hydrogen, xenon, and helium alone was run at 20 Torr. The input power to the plasma was set at 85 W with forced air cooling of the cell. The spectrometer was a normal incidence 0.2 m monochromator equipped with a 1200 lines/mm holographic grating with a platinum coating that

3

covered the region $2-560\,nm$. The EUV spectrum was recorded with a CEM. The wavelength resolution was about $0.02\,nm$ (FWHM) with slit widths of $50\,\mu m$. The increment was $0.2\,nm$ and the dwell time was $500\,ms$. Peak assignments were based on a calibration against the known He I and He II lines.

To achieve higher sensitivity at the shorter EUV wavelengths, the light emission from plasmas of helium alone was recorded with a 4° grazing incidence EUV spectrometer equipped with a grating having 600 G/mm with a radius of curvature of $\approx 1\,m$ that covered the region $5-65\,nm$. The angle of incidence was 87°. The resolution was about $0.04\,nm$ (FWHM) with slit widths of $300\,\mu m$. A CEM was used to detect the EUV light. The increment was $0.1\,nm$ and the dwell time was $1\,s$.

The width of the 656.2 nm Balmer α line emitted from hydrogen alone, xenon-hydrogen mixture (90/10)%, and helium-hydrogen mixture (90/10)% microwave discharge plasmas was measured with a high resolution visible spectrometer capable of a resolution of $\pm 0.006\,nm$ [16]. In this case, the total pressure was 1 Torr, and the input power to the plasma was set at 40 W.

T_e was measured on 0.1 Torr microwave plasmas of helium alone and helium-hydrogen mixtures (90/10%) from the ratio of the intensity of the He 501.6 nm (upper quantum level n=3) line to that of the He 492.2 nm (n=4) line as described by Griem [17]. T_e was measured on hydrogen alone plasmas from their Balmer line intensities. The visible spectrum $400-560\,nm$ was recorded with the normal incidence EUV spectrometer using a PMT and a sodium salicylate scintillator.

In order to estimate the power of the cell as described previously [18], the gas temperature of microwave plasmas of helium and xenon alone and each noble gas with 10% hydrogen was recorded using a K-type thermocouple ($\pm 0.1\,°C$) housed in a stainless steel tube that was placed axially inside the center of the 10 cm^3 plasma volume of the quartz microwave cell. At 40 W input with forced air cooling, the temperature rise was measured for 150 s then stopped, and the cooling curve was measured. The pressure of the ultrahigh pure gas inside the cell was maintained at about 300 mTorr with a noble gas flow rate of 9.3 sccm or a noble gas flow rate of 8.3 sccm and a hydrogen flow rate of 1 sccm controlled by a mass flow controller.

3. Results and discussion
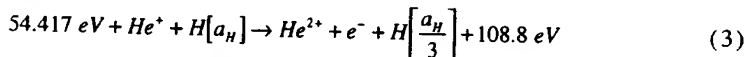
A. EUV Spectroscopy

In the case of the EUV spectrum of hydrogen, xenon, or xenon-hydrogen (98/2%), no peaks were observed below 78 nm, and no spurious peaks or artifacts due to the grating or the spectrometer were observed. Only known He I and He II peaks were observed in the EUV spectrum of the control helium microwave discharge cell emission.

The EUV spectra (17.5 – 50 nm) of the microwave cell emission of the helium-hydrogen mixture (98/2%) (top curve) and the helium control (bottom curve) are shown in Figure 1. Ordinary hydrogen has no emission in these regions. Novel peaks were observed at 45.6 nm, 37.4 nm, and 20.5 nm which do not correspond to helium. At the 1 Torr condition, additional novel peaks were observed in the short wavelength region (5 – 65 nm) at 14.15 nm, 13.03 nm, 10.13 nm, and 8.29 nm which do not correspond to helium as shown in Figure 1. Known He I lines which were used for calibration of the novel peak positions were observed at 58.4 nm, 53.7 nm, and 52.4 nm. It is proposed that the 30.4 nm peak shown in Figures 1 and 2 was not entirely due to the He II transition. In the case of the helium-hydrogen mixture, the ratio of 30.4 nm (40.8 eV) peak to the 25.6 nm (48.3 eV) was 10 compared to 5.4 for helium alone as shown in Figure 1 which implies only a minor He II transition contribution to the 30.4 nm peak.

It is proposed that the majority of the 91.2 nm peak was also due to a novel transition. At 20 Torr, the ratio of the Lyman β peak to the 91.2 nm peak of the helium-hydrogen plasma was 2 compared to 8 for each control hydrogen and xenon-hydrogen plasma which indicates that the majority of the 91.2 nm peak was due to a transition other than the binding of an electron by a proton.

The novel peaks fit two empirical relationships. In order of energy, the set comprising the peaks at 91.2 nm, 45.6 nm, 30.4 nm, 13.03 nm, 10.13 nm, and 8.29 nm correspond to energies of $q \cdot 13.6 \, eV$ where $q = 1,2,3,7,9,11$. In order of energy, the set comprising the peaks at 37.4 nm, 20.5 nm, and 14.15 nm correspond to energies of $q \cdot 13.6 - 21.21 \, eV$ where $q = 4,6,8$. These

lines can be explained as electronic transitions to fractional Rydberg states of atomic hydrogen given by Eqs. (2a) and (2c) wherein the catalytic system involves helium ions because the second ionization energy of helium is $54.417\,eV$, which is equivalent to $2 \cdot 27.2\,eV$. In this case, $54.417\,eV$ is transferred nonradiatively from atomic hydrogen to He^+ which is resonantly ionized. The electron decays to the $n = 1/3$ state with the further release of $54.417\,eV$ which may be emitted as a photon. The catalysis reaction is
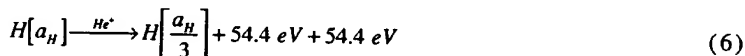
$$54.417\,eV + He^+ + H[a_H] \rightarrow He^{2+} + e^- + H\left[\frac{a_H}{3}\right] + 108.8\,eV \tag{3}$$

$$He^{2+} + e^- \rightarrow He^+ + 54.417\,eV \tag{4}$$

And, the overall reaction is

$$H[a_H] \rightarrow H\left[\frac{a_H}{3}\right] + 54.4\,eV + 54.4\,eV \tag{5}$$

Since the products of the catalysis reaction have binding energies of $m \cdot 27.2\,eV$, they may further serve as catalysts. Thus, further catalytic transitions may occur: $n = \frac{1}{3} \rightarrow \frac{1}{4}, \frac{1}{4} \rightarrow \frac{1}{5}$, and so on.

Electronic transitions to Rydberg states given by Eqs. (2a) and (2c) catalyzed by the resonant nonradiative transfer of $m \cdot 27.2\,eV$ would give rise to a series of emission lines of energies $q \cdot 13.6\,eV$ where q is an integer. It is further proposed that the photons that arise from hydrogen transitions may undergo inelastic helium scattering. That is, the catalytic reaction

$$H[a_H] \xrightarrow{\;He^+\;} H\left[\frac{a_H}{3}\right] + 54.4\,eV + 54.4\,eV \tag{6}$$

yields $54.4\,eV$ by Eq. (4) and a photon of $54.4\,eV$ ($22.8\,nm$). Once emitted, the photon may be absorbed or scattered. When this photon strikes $He\,(1s^2)$, $21.2\,eV$ may be absorbed in the excitation to $He\,(1s^1 2p^1)$. This leaves a $33.19\,eV$ ($37.4\,nm$) photon peak and a $21.2\,eV$ ($58.4\,nm$) photon from $He\,(1s^1 2p^1)$. Thus, for helium the inelastic scattered peak of $54.4\,eV$ photons from Eq. (3) is given by

$$E = 54.4\,eV - 21.21\,eV = 33.19\,eV \; (37.4\,nm) \tag{7}$$

A novel peak shown in Figures 1 and 2 was observed at $37.4\,nm$. Furthermore, the intensity of the $58.4\,nm$ peak corresponding to the spectra shown in Figure 2 was about 60,000 photons/sec. Thus, the transition $He\,(1s^2) \rightarrow He\,(1s^1 2p^1)$ dominated the inelastic scattering of EUV

6

peaks. The general reaction is

$$photon\ (h\nu) + He\ (1s^2) \rightarrow He\ (1s^1 2p^1) + photon\ (h\nu - 21.21\ eV) \tag{8}$$
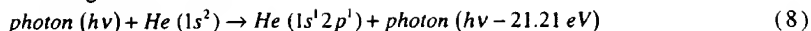
The two empirical series may be combined—one directly from Eqs. (2a, 2c) and the other indirectly with Eq. (8). The energies for the novel lines in order of energy are $13.6\ eV$, $27.2\ eV$, $40.8\ eV$, $54.4\ eV$, $81.6\ eV$, $95.2\ eV$, $108.8\ eV$, $122.4\ eV$ and $149.6\ eV$. The corresponding peaks are $91.2\ nm$, $45.6\ nm$, $30.4\ nm$, $37.4\ nm$, $20.5\ nm$, $13.03\ nm$, $14.15\ nm$, $10.13\ nm$, and $8.29\ nm$, respectively. Thus, the identified novel lines correspond to energies of $q \cdot 13.6\ eV$ where $q = 1,2,3,4,6,7,8,9,11$ or these lines inelastically scattered by helium atoms wherein $21.2\ eV$ was absorbed in the excitation of $He\ (1s^2)$ to $He\ (1s^1 2p^1)$. The values of q observed are consistent with those excepted based on Eq. (5) and the subsequent autocatalyzed reactions as discussed previously [6]. The satellite peak at $44.2\ nm$ show in Figure 1 and 2 may be due to multipole coupling as discussed elsewhere [12]. There is remarkable agreement between the data and the proposed transitions to fractional Rydberg states and these lines inelastically scattered by helium according to Eq. (8). All other peaks could be assigned to He I, He II, second order lines, or atomic or molecular hydrogen emission. No known lines of helium or hydrogen explain the $q \cdot 13.6\ eV$ related set of peaks.

Since its ionization energy is $27.63\ eV$, Ar^+ may also serve as a catalyst by providing a net enthalpy of an integer multiple of the potential energy of atomic hydrogen. In recent argon-hydrogen plasma experiments, to be reported, lines with energies of $q \cdot 13.6\ eV$ where $q = 7,9,11$ were observed without the lines assigned in Figures 1-2 to helium inelastic scattering. This supports the present assignment of the helium scattered lines. Furthermore, hydrogen scattered lines were not expected since the gas was helium-hydrogen (98/2%).

B. Line broadening and T_e measurements

The Doppler-broadened line shape for atomic hydrogen has been studied on many sources such as hollow cathode [19-20] and rf [21-22] discharges. The method of Videnocic et al. [19] was used to calculate the energetic hydrogen atom densities and energies from the width of the $656.2\ nm$ Balmer α line emitted from the hydrogen and helium-hydrogen mixture (90/10%) microwave plasmas shown in Figure 3.

7

Gigosos et al. [23] have reviewed the literature and have discussed the limitations of this method. The average helium-hydrogen Doppler half-width of $0.52 \pm 5\%\,nm$ was not appreciably changed with pressure. The corresponding energy of $180-210\,eV$ and the number densities of $5 \times 10^{14} \pm 20\%\,atoms/cm^3$, depending on the pressure, were significant compared to only $\approx 3\,eV$ and $7 \times 10^{13}\,atoms/cm^3$ for pure hydrogen even though 10 times more hydrogen was present. Only $\approx 3\,eV$ broadening was observed with xenon-hydrogen (98/2%) ruling out collisional broadening.

Similarly, the average electron temperature for helium-hydrogen plasma was $28,000 \pm 5\%\,K$. Whereas, the corresponding temperature of helium alone was only $6800 \pm 5\%\,K$, and hydrogen alone was $5500 \pm 5\%\,K$. No high electric field was present in our experiments. Thus, the results can not be explained by Stark broadening or acceleration of charged species due to high fields of over $10\,kV/cm$ as proposed by Videnocic et al. [19] to explain excessive broadening observed in glow discharges.

C. Gas temperature measurements

No increase in temperature was observed with the addition of hydrogen to xenon control. In contrast, the plasma gas temperature increased from room temperature to 1200°C within 150 seconds for helium-hydrogen compared to only 185°C for helium alone as shown in Figure 4.

A conservative estimate of the total output power was determined by taking the ratio of the areas of the helium-hydrogen temperature-rise-above-ambient-versus-time curve compared to that of helium only, 10, multiplied by the common input. Thus, with a microwave input power of $40\,W$, the thermal output power was estimated to be $400\,W$. A second estimate of the power from the $10\,cm^3$ plasma volume based on the Stefan-Boltzmann equation using an emissivity of 0.5 and a measured wall temperature of 1200°C was at least $400\,W$. Since the hydrogen flow rate was 1 sccm, an estimate of the corresponding energy balance was over $-5 \times 10^5\,kJ/mole\,H_2$ compared to the enthalpy of combustion of hydrogen of $-241.8\,kJ/mole\,H_2$.

8

4. Conclusion

We report that novel emission lines were observed with energies of $q \cdot 13.6 \, eV$ where $q = 1,2,3,4,6,7,8,9,11$ or these lines inelastically scattered by helium atoms wherein $21.2 \, eV$ was absorbed in the excitation of $He \, (1s^2)$ to $He \, (1s^1 2p^1)$. These lines were identified as transitions to fractional Rydberg states of atomic hydrogen. An extremely high hydrogen-atom temperature of $180 - 210 \, eV$ was observed with the presence of helium ion catalyst only with hydrogen also present. Similarly, the average electron temperature for helium-hydrogen plasma was high, 28,000 K, compared to 6800 K for helium alone. An estimate of the thermal power was $400 \, W$ in $10 \, cm^3$.

References

[1] N. V. Sidgwick, *The Chemical Elements and Their Compounds*, Volume I, Oxford, Clarendon Press, (1950), p.17.

[2] M. D. Lamb, *Luminescence Spectroscopy*, Academic Press, London, (1978), p. 68.

[3] R. Mills, *The Grand Unified Theory of Classical Quantum Mechanics*, September 2001 Edition, BlackLight Power, Inc., Cranbury, New Jersey, Distributed by Amazon.com; posted at www.blacklightpower.com.

[4] R. Mills, Int. J. Hydrogen Energy, in press.

[5] R. Mills, Int. J. Hydrogen Energy, Vol. 26, No. 10, (2001), pp. 1059-1096.

[6] R. Mills, P. Ray, Int. J. Hydrogen Energy, in press.

[7] R. Mills, P. Ray, Int. J. Hydrogen Energy, in press.

[8] R. Mills, Int. J. Hydrogen Energy, Vol. 26, No. 10, (2001), pp. 1041-1058.

[9] R. Mills, M. Nansteel, and Y. Lu, Int. J. Hydrogen Energy, Vol. 26, No. 4, (2001), pp. 309-326.

[10] R. Mills, J. Dong, Y. Lu, Int. J. Hydrogen Energy, Vol. 25, (2000), pp. 919-943.

[11] R. Mills, T. Onuma, and Y. Lu, Int. J. Hydrogen Energy, Vol. 26, No. 7, July, (2001), pp. 749-762.

[12] R. L. Mills, P. Ray, B. Dhandapani, J. He, J. of Phys. Chem., submitted.

[13] R. Mills, A. Voigt, P. Ray, M. Nanstell, Int. J. Hydrogen Energy, in press.

[14] R. Mills, N. Greenig, S. Hicks, Int. J. Hydrogen Energy, in press.

[15] R. Mills, B. Dhandapani, M. Nansteel, J. He, T. Shannon, A. Echezuria, Int. J. of Hydrogen Energy, Vol. 26, No. 4, (2001), pp. 339-367.

[16] R. L. Mills, P. Ray, B. Dhandapani, J. He, Chem. Phys., submitted.

[17] H. R. Griem, *Principle of Plasma Spectroscopy*, Cambridge University Press, (1987).

[18] C. Chen, T. Wei, L. R. Collins, J. Phillips, J. Phys. D: Appl. Phys., Vol. 32, (1999), pp. 688-698.

[19] I. R. Videnocic, N. Konjevic, M. M. Kuraica, Spectrochimica Acta, Part B, Vol. 51, (1996), pp. 1707-1731.

[20] S. Alexiou, E. Leboucher-Dalimier, Phys, Rev. E, Vol. 60, No. 3, (1999), pp. 3436-3438.

[21] S. Djurovic, J. R. Roberts, J. Appl. Phys., Vol. 74, No. 11, (1993), pp. 6558-6565.

[22] S. B. Radovanov, K. Dzierzega, J. R. Roberts, J. K. Olthoff, Appl. Phys. Lett., Vol. 66, No. 20, (1995), pp. 2637-2639.

[23] M. A. Gigosos, V. Cardenoso, J. Phys. B: At. Mol. Opt. Phys., Vol. 29, (1996), pp. 4795-4838.

Figure Captions

Figure 1. The EUV spectra ($17.5 - 50\,nm$) of the microwave cell emission of the helium-hydrogen mixture (98/2%) (top curve) recorded at 20 Torr with a normal incidence EUV spectrometer and a CEM, and control helium (bottom curve) recorded at 20 Torr with a 4° grazing incidence EUV spectrometer and a CEM. Only known He I and He II peaks were observed with the helium control. Reproducible novel emission lines were observed at $45.6\,nm$ and $30.4\,nm$ with energies of $q \cdot 13.6\,eV$ where $q = 2\ or\ 3$ (Eqs. (2a, 2c)) and at $37.4\,nm$ and $20.5\,nm$ with energies of $q \cdot 13.6\,eV$ where $q = 4\ or\ 6$ that were inelastically scattered by helium atoms wherein $21.2\,eV$ was absorbed in the excitation of $He\,(1s^2)$ to $He\,(1s^1 2p^1)$ as proposed in Eq. (8).

Figure 2. The short wavelength EUV spectra ($5 - 65\,nm$) of the microwave cell emission of the helium-hydrogen mixture (98/2%) (top curve) and control hydrogen (bottom curve) recorded at 1 Torr with a normal incidence EUV spectrometer and a CEM. No hydrogen emission was observed in this region, and no instrument artifacts were observed. Reproducible novel emission lines were observed at $45.6\,nm$, $30.4\,nm$, $13.03\,nm$, $10.13\,nm$, and $8.29\,nm$ with energies of $q \cdot 13.6\,eV$ where $q = 2,3,7,9,\ or\ 11$ and at $37.4\,nm$, $20.5\,nm$, and $14.15\,nm$ with energies of $q \cdot 13.6\,eV$ where $q = 4,6,\ or\ 8$ that were inelastically scattered by helium atoms wherein $21.2\,eV$ was absorbed in the excitation of $He\,(1s^2)$ to $He\,(1s^1 2p^1)$ as proposed in Eq. (8).

Figure 3. The 656.2 nm Balmer α line width recorded with a high resolution ($\pm 0.006\,nm$) visible spectrometer on a helium-hydrogen (90/10%) and a hydrogen microwave discharge plasma. Significant broadening was observed corresponding to an average hydrogen atom temperature of $180 - 210\,eV$.

Figure 4. The plasma gas temperature rise as a function of time for helium alone and the helium-hydrogen mixture (90/10%) with microwave input power set at 40 W. The maximum temperature of the helium-hydrogen mixture and the helium alone plasma was 1200°C and 185°C, respectively. The thermal output power of the helium-hydrogen plasma was estimated to be $400\,W$.
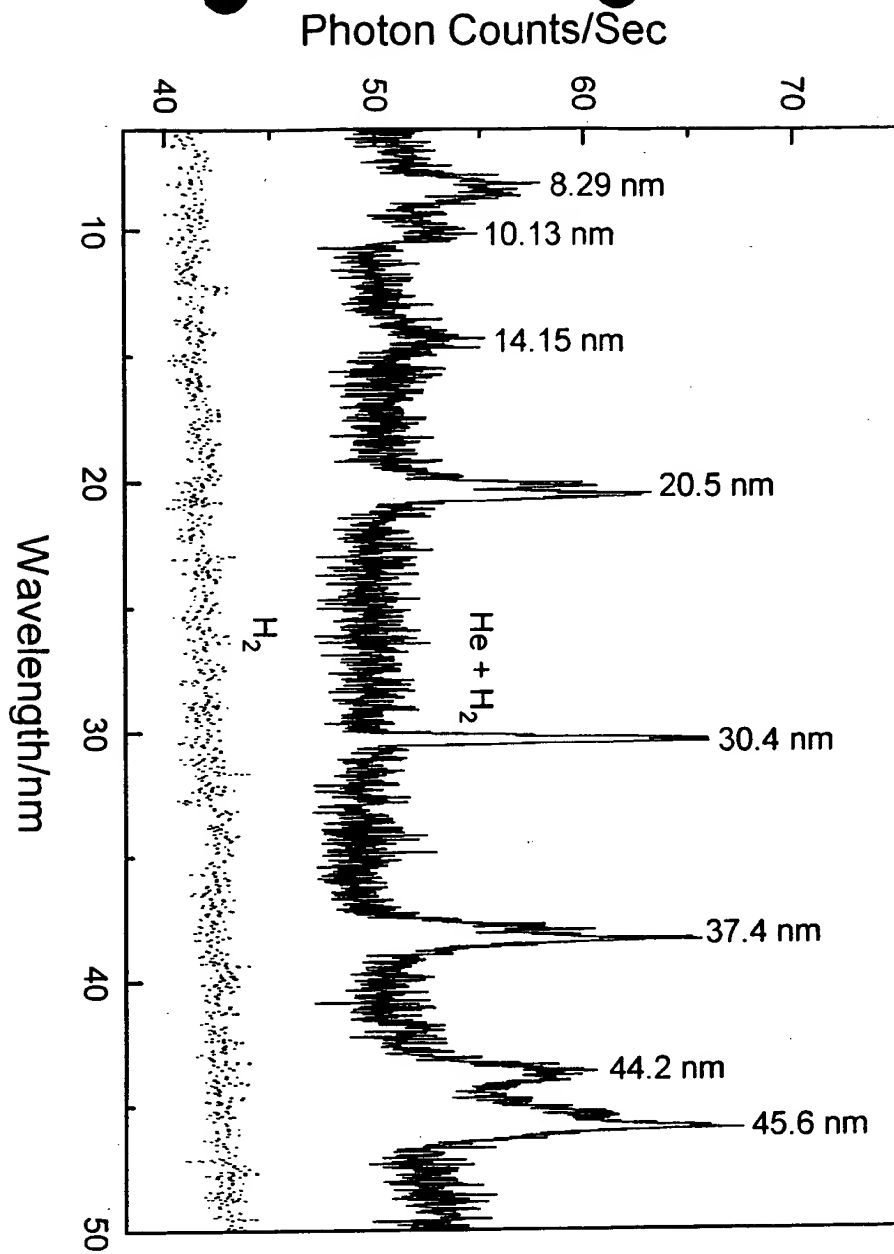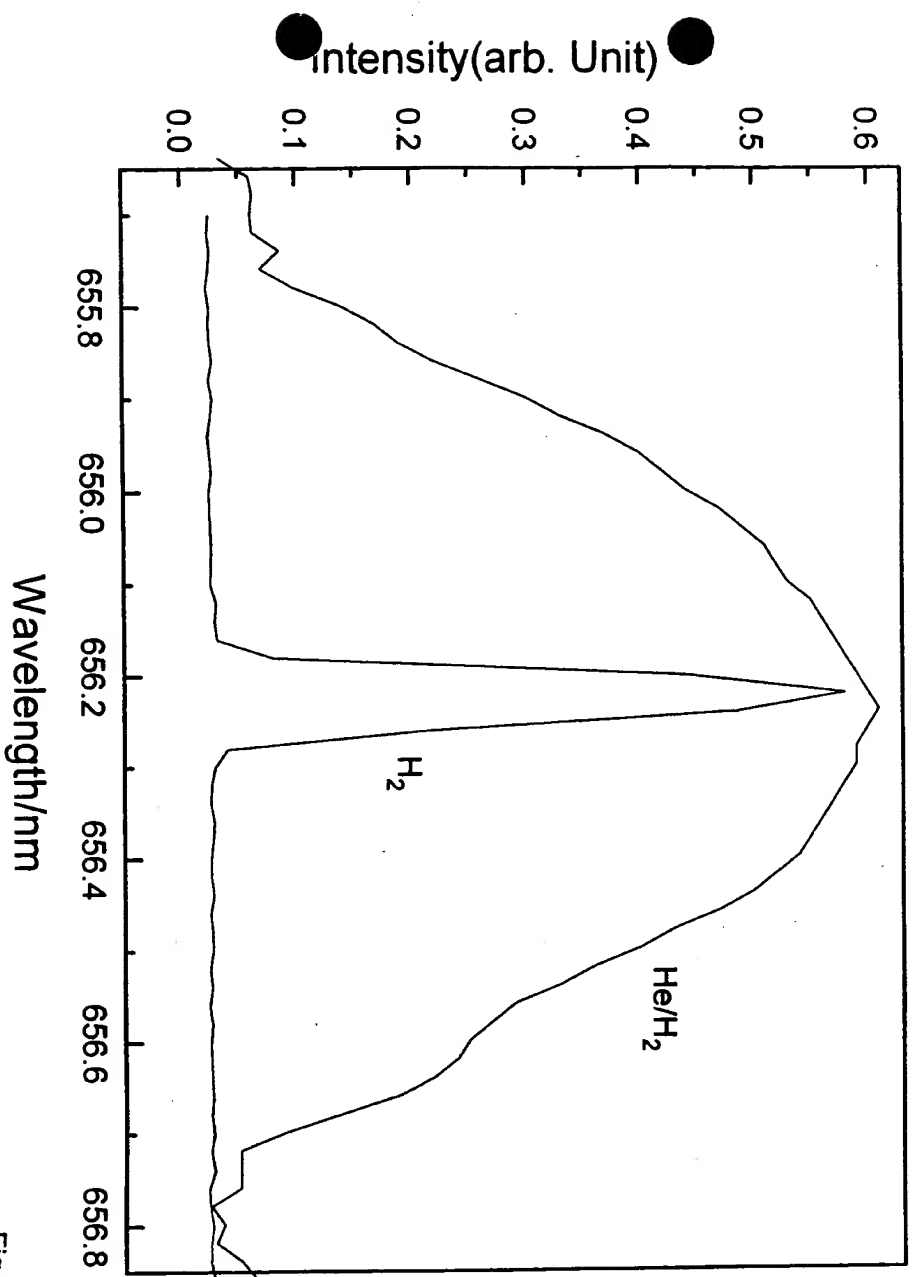
Fig. 1

Fig. 2

Fig. 3

Fig. 4

Temperature/ ^{0}C
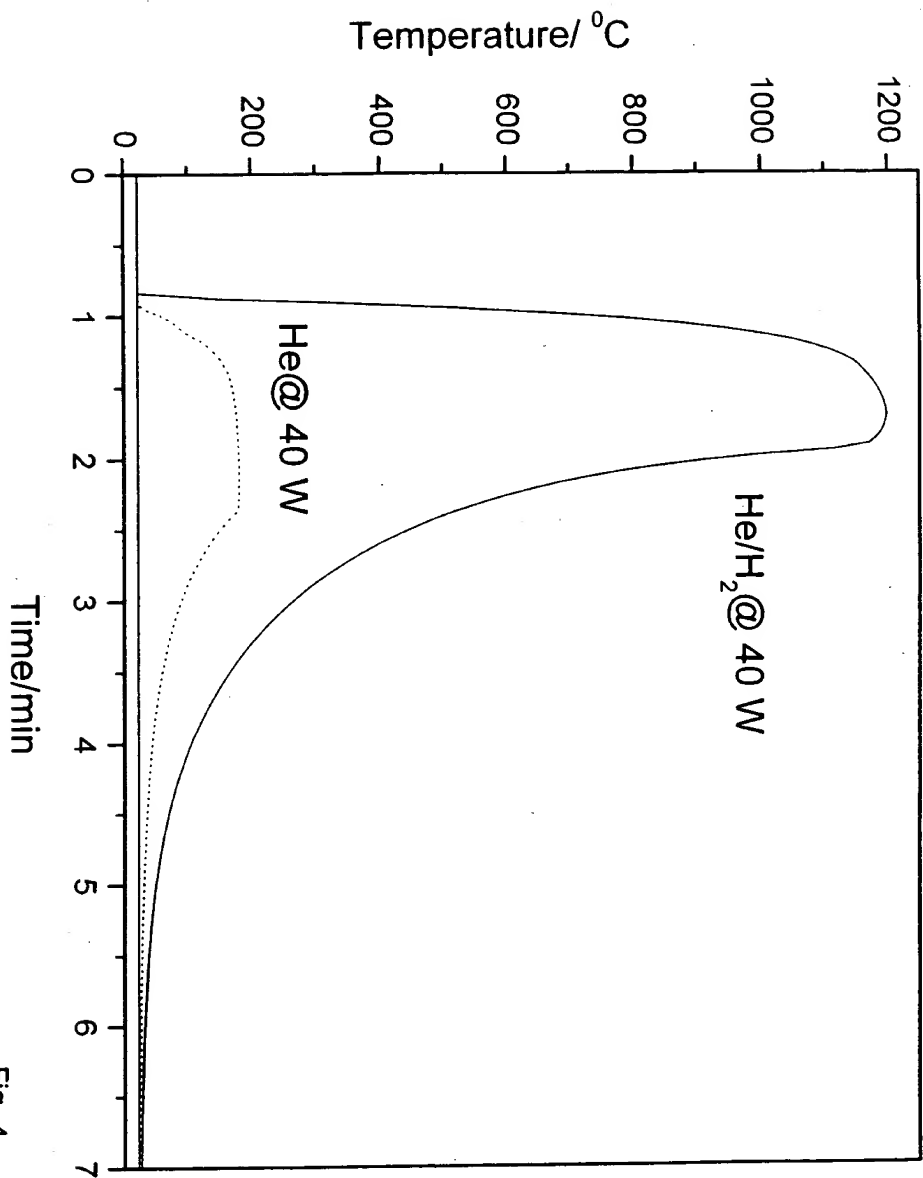
He@ 40 W

He/H$_2$ @ 40 W

Time/min
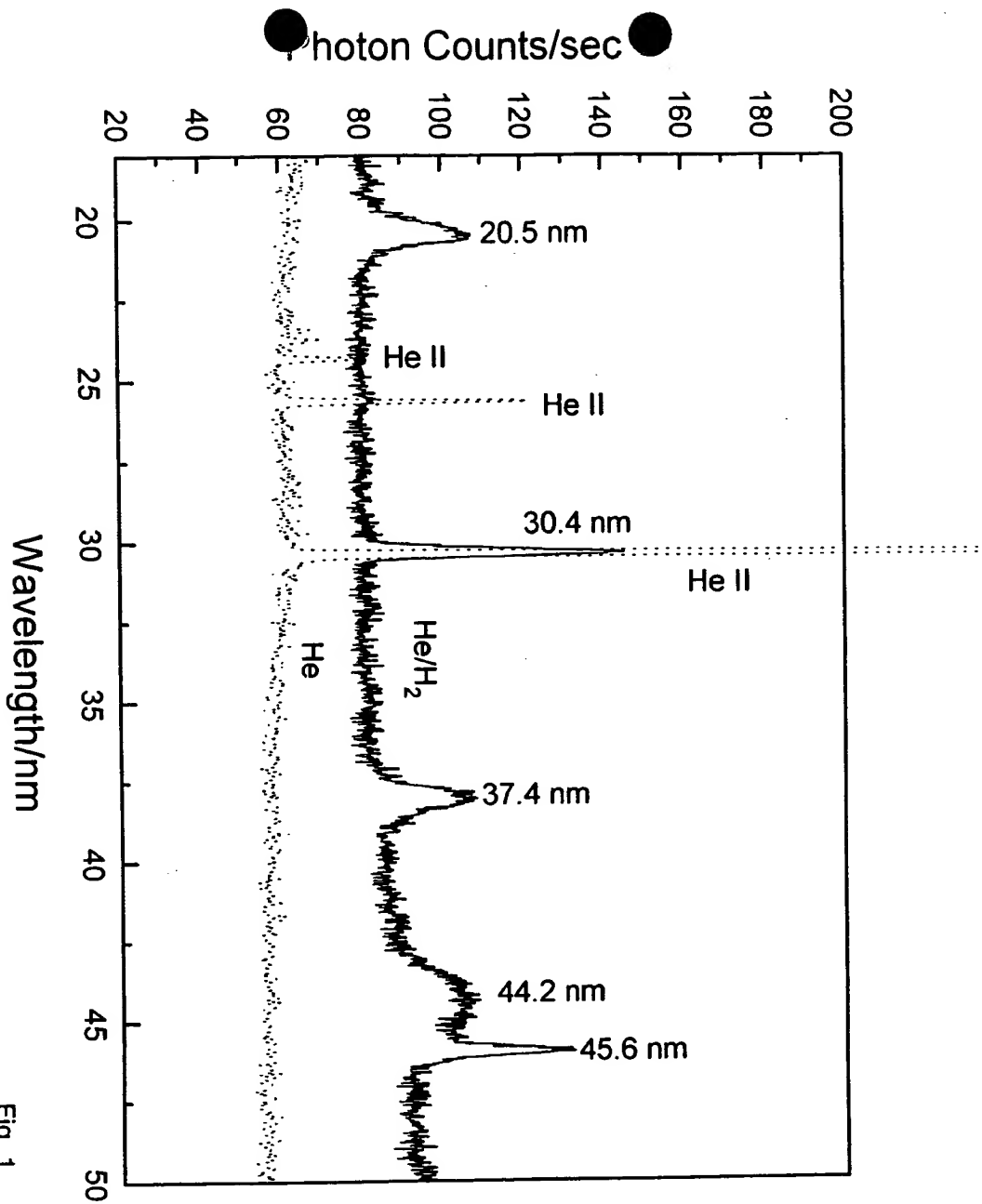
THIS PAGE BLANK (USPTO)

Spectroscopic Identification of Transitions of Fractional Rydberg States of Atomic Hydrogen

R. L. Mills,[*] P. Ray, B. Dhandapani, M. Nansteel, X. Chen, J. He

BlackLight Power, Inc.
493 Old Trenton Road
Cranbury, NJ 08512

ABSTRACT

Extreme ultraviolet (EUV) spectroscopy was recorded on microwave discharges of helium with 2% hydrogen. Novel emission lines were observed with energies of $q \cdot 13.6 \, eV$ where $q = 1, 2, 3, 4, 6, 7, 8, 9,$ or 11 or these lines inelastically scattered by helium atoms wherein $21.2 \, eV$ was absorbed in the excitation of $He \, (1s^2)$ to $He \, (1s^1 2p^1)$. These lines can be explained as fractional Rydberg states of atomic hydrogen. Such transitions would be extremely energetic; so, the width of the 656.2 nm Balmer α line emitted from glow discharge plasmas and the electron temperature T_e and the gas temperature of microwave plasmas were measured. The average hydrogen atom temperature of the helium-hydrogen plasma was $33 - 38 \, eV$ versus $\approx 3 \, eV$ for pure hydrogen. Similarly, T_e for helium-hydrogen was 28,000 K compared to 6800 K for pure helium. With a microwave input power of 40 W, the thermal output power was estimated to be $238 \pm 8 \, W$ based the rise of the plasma gas temperature from room temperature to 1240 °C within 60 seconds compared to 186°C for helium alone. The corresponding power density was $24 \, MW/m^3$, and the energy balance of at least $-3 \, X \, 10^5 \, kJ/mole \, H_2$ was high compared to the enthalpy of combustion of hydrogen of $-241.8 \, kJ/mole \, H_2$.

Key Words: hydrogen catalysis, fractional hydrogen Rydberg states, Balmer α line broadening, electron temperature

[*] Fax: 609-490-1066; e-mail: rmills@blacklightpower.com

I. INTRODUCTION

J. J. Balmer showed in 1885 that the frequencies for some of the lines observed in the emission spectrum of atomic hydrogen could be expressed with a completely empirical relationship. This approach was later extended by J. R. Rydberg, who showed that all of the spectral lines of atomic hydrogen were given by the equation:

$$\bar{v} = R\left(\frac{1}{n_f^2} - \frac{1}{n_i^2}\right) \tag{1}$$

where $R = 109,677\ cm^{-1}$, $n_f = 1,2,3,...$, $n_i = 2,3,4,...$, and $n_i > n_f$.

Niels Bohr, in 1913, developed a theory for atomic hydrogen that gave the energy levels in agreement with Rydberg's equation. An identical equation, based on a totally different theory for the hydrogen atom, was developed by E. Schrödinger, and independently by W. Heisenberg, in 1926.

$$E_n = -\frac{e^2}{n^2 8\pi\varepsilon_o a_H} = -\frac{13.598\ eV}{n^2} \tag{2a}$$

$$n = 1,2,3,... \tag{2b}$$

where a_H is the Bohr radius for the hydrogen atom ($52.947\ pm$), e is the magnitude of the charge of the electron, and ε_o is the vacuum permittivity.

The excited energy states of atomic hydrogen are given by Eq. (2a) for $n > 1$ in Eq. (2b). The $n = 1$ state is the "ground" state for "pure" photon transitions (the $n = 1$ state can absorb a photon and go to an excited electronic state, but it cannot release a photon and go to a lower-energy electronic state). However, an electron transition from the ground state to a lower-energy state may be possible by a nonradiative energy transfer such as multipole coupling or a resonant collision mechanism.

Processes that occur without photons and that require collisions are common. For example, the exothermic chemical reaction of $H + H$ to form H_2 does not occur with the emission of a photon. Rather, the reaction requires a collision with a third body, M, to remove the bond energy- $H + H + M \rightarrow H_2 + M^*$ [1]. The third body distributes the energy from the exothermic reaction, and the end result is the H_2 molecule and an

2

increase in the temperature of the system. Some commercial phosphors are based on nonradiative energy transfer involving multipole coupling. For example, the strong absorption strength of Sb^{3+} ions along with the efficient nonradiative transfer of excitation from Sb^{3+} to Mn^{2+}, are responsible for the strong manganese luminescence from phosphors containing these ions [2].

We propose that atomic hydrogen may undergo a catalytic reaction with certain atomized elements and ions which singly or multiply ionize at integer multiples of the potential energy of atomic hydrogen, $m \cdot 27.2\ eV$ wherein m is an integer. The theory was given previously [3-8]. The reaction involves a nonradiative energy transfer to form a hydrogen atom that is lower in energy than unreacted atomic hydrogen that corresponds to a fractional principal quantum number. That is

$$n = \frac{1}{2}, \frac{1}{3}, \frac{1}{4}, ..., \frac{1}{p}; \quad p \text{ is an integer} \tag{2c}$$

replaces the well known parameter $n = \text{integer}$ in the Rydberg equation for hydrogen excited states. The $n = 1$ state of hydrogen and the $n = \dfrac{1}{\text{integer}}$ states of hydrogen are nonradiative, but a transition between two nonradiative states is possible via a nonradiative energy transfer, say $n = 1$ to $n = 1/2$. In these cases, during the transition the electron couples to another electron transition, electron transfer reaction, or inelastic scattering reaction which can absorb the exact amount of energy that must be removed from the hydrogen atom to cause the transition. Thus, a catalyst provides a net positive enthalpy of reaction of $m \cdot 27.2\ eV$ (i.e. it absorbs $m \cdot 27.2\ eV$ where m is an integer). Certain atoms or ions serve as catalysts which resonantly accept the nonradiative energy transfer from hydrogen atoms and release the energy to the surroundings to affect electronic transitions to fractional quantum energy levels. As a consequence of the nonradiative energy transfer, the hydrogen atom becomes unstable and emits further energy until it achieves a lower-energy nonradiative state having a principal energy level given by Eqs. (2a) and (2c).

A number of independent experimental observations lead to the conclusion that atomic hydrogen can exist in fractional quantum states that are at lower energies than the traditional "ground" ($n = 1$) state. Prior

3

related studies that support the possibility of a novel reaction of atomic hydrogen which produces a chemically generated or assisted plasma and produces novel hydride compounds include extreme ultraviolet (EUV) spectroscopy [9-14, 17-21], characteristic emission from catalysis and the hydride ion products [11-12], lower-energy hydrogen emission [7, 9-10], plasma formation [11-14, 17-18, 20-21], Balmer α line broadening [15], anomalous plasma afterglow duration [20-21], power generation [13-17, 28], and analysis of chemical compounds [22-28]. We report that microwave and glow discharges of helium-hydrogen mixtures were studied by extreme ultraviolet (EUV) spectroscopy to search for line emission from transitions to fractional Rydberg states of atomic hydrogen. Since the electronic transitions are very energetic, Balmer α line broadening and an elevated electron temperature were anticipated and were measured. Since the second ionization energy of He^+ is an exact multiple of the potential energy of atomic hydrogen and microwave plasmas may have significant concentrations of He^+ as well as atomic hydrogen, fast kinetics observable as heat may be possible. Thus, power balances of microwave plasmas of helium-hydrogen mixtures were also measured.

II. EXPERIMENTAL

A. EUV Spectroscopy

EUV spectroscopy was recorded on hydrogen, helium, and helium-hydrogen (98/2%) microwave and glow discharge plasmas according to the methods given previously [9]. The glow discharge experimental set up was given previously [9]. The experimental set up comprising a microwave discharge gas cell light source and an EUV spectrometer which was differentially pumped is shown in Figure 1. Helium-hydrogen (98/2%) gas mixture was flowed through a half inch diameter quartz tube at 1 torr, 20 torr, or 760 torr. The gas pressure inside the cell was maintained by flowing the mixture while monitoring the pressure with a 10 torr and 1000 torr MKS Baratron absolute pressure gauge. By the same method, the hydrogen alone and helium alone plasmas were run at 20 torr. The tube was fitted with an Opthos coaxial microwave cavity

4

(Evenson cavity). The microwave generator was an Opthos model MPG-4M generator (Frequency: 2450 MHz). The input power to the plasma was set at 85 watts with forced air cooling of the cell.

The spectrometer was a normal incidence McPherson 0.2 meter monochromator (Model 302, Seya-Namioka type) equipped with a 1200 lines/mm holographic grating with a platinum coating. The wavelength region covered by the monochromator was $5-560\,nm$. The EUV spectrum was recorded with a channel electron multiplier (CEM) at $2500-3000\,V$. The wavelength resolution was about $0.02\,nm$ (FWHM) with an entrance and exit slit width of $50\,\mu m$. The increment was $0.2\,nm$ and the dwell time was $500\,ms$. Novel peak positions were based on a calibration against the known He I and He II lines.

To achieve higher sensitivity at the shorter EUV wavelengths, the light emission from a helium microwave plasma and a glow discharge plasma of a helium-hydrogen mixture (98/2%) maintained according to the methods given previously [9] were recorded with a McPherson 4° grazing incidence EUV spectrometer (Model 248/310G) equipped with a grating having 600 G/mm with a radius of curvature of $\approx 1\,m$. The angle of incidence was 87°. The wavelength region covered by the monochromator was $5-65\,nm$. The wavelength resolution was about $0.04\,nm$ (FWHM) with an entrance and exit slit width of $300\,\mu m$. A channel electron multiplier (CEM) at $2400\,V$ was used to detect the EUV light. The increment was $0.1\,nm$ and the dwell time was $1\,s$.

B. Line broadening and T_e measurements

The width of the 656.2 nm Balmer α line emitted from glow discharge plasmas having atomized hydrogen from pure hydrogen alone or with a mixture of 10% hydrogen and helium at 2 torr total pressure was measured according to the methods given previously [13]. The plasmas were maintained in a cylindrical stainless steel gas cell (9.21 cm in diameter and 14.5 cm in height) with an axial hollow cathode glow discharge electrode assembly comprised a stainless steel plate (4.2 cm diameter, 0.9 mm thick) anode and a circumferential stainless steel cylindrical frame (5.1 cm OD, 7.2 cm long) perforated with evenly spaced 1 cm diameter holes. The emission was viewed normal to the cell axis

5

through a 1.6 mm thick UV-grade sapphire window with a 1.5 cm view diameter. The discharge was carried out under static gas conditions with a DC voltage of about 275 V which produced about 0.2 A of current. The plasma emission from the glow discharges was fiber-optically coupled through a 220F matching fiber adapter to a high resolution visible spectrometer with a resolution of $\pm 0.025\, nm$ over the spectral range 190-860 nm. The entrance and exit slits were set to $20\,\mu m$. The spectrometer was scanned between 656-657 nm using a 0.01 nm step size. The signal was recorded by a PMT with a stand alone high voltage power supply (950 V) and an acquisition controller. The data was obtained in a single accumulation with a 1 second integration time.

T_e was measured on microwave plasmas of helium alone and helium-hydrogen mixtures (90/10%) from the ratio of the intensity of the He 501.6 nm (upper quantum level n=3) line to that of the He 492.2 nm (n=4) line as described by Griem [29]. In each case, the microwave plasma cell was run under the conditions given in section A, except that the total pressure was 0.1 torr. The visible spectrum was recorded with the normal incidence EUV spectrometer as described section A except that visible spectrum (400 − 560 nm) of the cell emission was recorded with a photomultiplier tube (PMT) and a sodium salicylate scintillator. The PMT (Model R1527P, Hamamatsu) used has a spectral response in the range of 185 − 680 nm with a peak efficiency at about 400 nm. The scan interval was 0.4 nm. The inlet and outlet slit were 300 μm with a corresponding wavelength resolution of 2 nm. The spectra were repeated five times per experiment and were found to be reproducible within less than 5%.

C. Power balance measurements

The power balances of microwave plasmas of helium, krypton, and xenon alone and each noble gas with 5% hydrogen were determined by heat loss calorimetry [30] in the cell described in section A. A K-type thermocouple ($\pm 0.1\,°C$) housed in a stainless steel tube was placed axially inside the center of the 10 cm^3 plasma volume of the quartz microwave cell. The thermocouple was read at 0.2 second intervals with a multichannel computer data acquisition system. The gas in each case was

ultrahigh purity grade or higher. Each noble gas-hydrogen mixture (95/5%) was premixed. The gas pressure inside the cell was maintained at about 300 mtorr with a gas flow rate of 9.4 sccm that was controlled by a 0-20 sccm range mass flow controller (MKS 1179A21CS1BB) with a readout (MKS type 246). The cell pressure was monitored by a 0-10 torr MKS Baratron absolute pressure gauge.

No increase in temperature was observed when the mixture containing 5% hydrogen replaced pure krypton or xenon plasmas. In contrast, with the switch from a pure helium plasma to the mixture with 5% hydrogen at 40 W input and with forced air cooling, the quartz wall was observed to begin to melt after about 90 seconds. Whereas, the helium alone plasma run under identical conditions had a maximum temperature rise to 186 °C at 90 seconds. Thus, to achieve a higher control temperature to give greater analytical accuracy, the temperature rise of the inside of the cell was measured for 90 seconds with helium at 40 W input. The input power was stopped, and a cooling curve was measured. Then the experiment was repeated with the helium-hydrogen mixture (95/5%) run at 40 W for only 60 seconds to prevent the cell from melting. In additional controls, noncatalysts krypton or xenon replaced helium.

III. RESULTS AND DISCUSSION

A. EUV Spectroscopy

The EUV emission was recorded from microwave and glow discharge plasmas of hydrogen, helium, and helium with 2% hydrogen over the wavelength range 5-125 nm. In the case of hydrogen, no peaks were observed below 78 nm, and no spurious peaks or artifacts due to the grating or the spectrometer were observed. Only known He I and He II peaks were observed in the EUV spectra of the control helium microwave or glow discharge cell emission.

The EUV spectra (15 − 50 nm) of the microwave cell emission of the helium-hydrogen mixture (98/2%) that was recorded at 1, 24, and 72 hours and the helium control (dotted curve) is shown in Figure 2. Ordinary hydrogen has no emission in these regions. Novel peaks were

observed at 45.6 nm, 37.4 nm, and 20.5 nm which do not correspond to helium and increased with time. The pressure was increased from 20 torr to 760 torr. The peaks appeared slightly more intense at the lower pressure; so, the pressure was decreased to 1 torr and spectra were recorded.

At the 1 torr condition, additional novel peaks were observed in the short wavelength region. The short wavelength EUV spectrum (5 − 50 nm) of the control hydrogen microwave cell emission (bottom curve) is shown in Figure 3. No spectrometer artifacts were observed at the short wavelengths. The short wavelength EUV spectrum (5 − 50 nm) of the helium-hydrogen mixture (98/2%) microwave cell emission with a pressure of 1 torr (top curve) is also shown in Figure 3. Novel peaks were observed at 14.15 nm, 13.03 nm, 10.13 nm, and 8.29 nm which do not correspond to helium. It is also proposed that the 30.4 nm peak shown in Figures 2 and 3 was not entirely due to the He II transition. In the case of helium-hydrogen mixture, conspicuously absent was the 25.6 nm (48.3 eV) line of He II shown in Figure 2 which implies only a minor He II transition contribution to the 30.4 nm peak.

A novel 63.3 nm peak was observed in the EUV spectrum (50 − 65 nm) of the helium-hydrogen mixture (98/2%) glow discharge cell emission shown in Figure 4. As shown in Figures 5 and 6, the ratio of the Lβ peak to the 91.2 nm peak of the helium-hydrogen microwave plasma was 2; whereas, the ratio of the Lβ peak to the 91.2 nm peak of the control hydrogen microwave plasma was 8 which indicates that the majority of the 91.2 nm peak was due to a transition other than the binding of an electron by a proton. Based on the intensity, it is proposed that the majority of the 91.2 nm peak was due to a novel peak.

The novel peaks fit two empirical relationships. In order of energy, the set comprising the peaks at 91.2 nm, 45.6 nm, 30.4 nm, 13.03 nm, 10.13 nm, and 8.29 nm correspond to energies of $q \cdot 13.6 \, eV$ where $q = 1,2,3,7,9,$ or 11. In order of energy, the set comprising the peaks at 63.3 nm, 37.4 nm, 20.5 nm, and 14.15 nm correspond to energies of $q \cdot 13.6 − 21.21 \, eV$ where $q = 3,4,6,$ or 8. These lines can be explained as electronic transitions to fractional Rydberg states of atomic hydrogen given by Eqs. (2a) and (2c) wherein the catalytic system involves helium ions because the second ionization energy of helium is 54.417 eV, which is equivalent to $2 \cdot 27.2 \, eV$. In this

case, the catalysis reaction is

$$54.417\ eV + He^+ + H[a_H] \rightarrow He^{2+} + e^- + H\left[\frac{a_H}{3}\right] + 108.8\ eV \tag{3}$$

$$He^{2+} + e^- \rightarrow He^+ + 54.417\ eV \tag{4}$$

And, the overall reaction is

$$H[a_H] \rightarrow H\left[\frac{a_H}{3}\right] + 54.4\ eV + 54.4\ eV \tag{5}$$

Since the products of the catalysis reaction have binding energies of $m \cdot 27.2\ eV$, they may further serve as catalysts. Thus, further catalytic transitions may occur: $n = \frac{1}{3} \rightarrow \frac{1}{4}, \frac{1}{4} \rightarrow \frac{1}{5}$, and so on.

Electronic transitions to Rydberg states given by Eqs. (2a) and (2c) catalyzed by the resonant nonradiative transfer of $m \cdot 27.2\ eV$ would give rise to a series of emission lines of energies $q \cdot 13.6\ eV$ where q is an integer. It is further proposed that the photons that arise from hydrogen transitions may undergo inelastic helium scattering. That is, the catalytic reaction

$$H[a_H] \xrightarrow{He^*} H\left[\frac{a_H}{3}\right] + 54.4\ eV + 54.4\ eV \tag{6}$$

yields two $54.4\ eV$ photons ($22.8\ nm$). When each of these photons strikes $He\ (1s^2)$, $21.2\ eV$ is absorbed in the excitation to $He\ (1s^1 2p^1)$. This leaves a $33.19\ eV$ ($37.4\ nm$) photon peak and a $21.2\ eV$ ($58.4\ nm$) photon from $He\ (1s^1 2p^1)$. Thus, for helium the inelastic scattered peak of $54.4\ eV$ photons from Eq. (3) is given by

$$E = 54.4\ eV - 21.21\ eV = 33.19\ eV\ (37.4\ nm) \tag{7}$$

A novel peak shown in Figures 2 and 3 was observed at $37.4\ nm$. Furthermore, the intensity of the $58.4\ nm$ shown in Figure 4 was off-scale with 56,771 photons/sec. Thus, the transition $He\ (1s^2) \rightarrow He\ (1s^1 2p^1)$ dominated the inelastic scattering of EUV peaks. The general reaction is

$$photon\ (h\nu) + He\ (1s^2) \rightarrow He\ (1s^1 2p^1) + photon\ (h\nu - 21.21\ eV) \tag{8}$$

With Eq. (8), the two empirical series may be combined. The energies for the novel lines in order of energy are $13.6\ eV$, $27.2\ eV$, $40.8\ eV$, $54.4\ eV$, $81.6\ eV$, $95.2\ eV$, $108.8\ eV$, $122.4\ eV$ and $149.6\ eV$. The corresponding peaks are $91.2\ nm$, $45.6\ nm$, $30.4\ nm$ with $63.3\ nm$, $37.4\ nm$, $20.5\ nm$, $13.03\ nm$, $14.15\ nm$, $10.13\ nm$, and $8.29\ nm$, respectively. Thus, the identified novel lines correspond to energies of $q \cdot 13.6\ eV$ where $q = 1,2,3,4,6,7,8,9,\ or\ 11$ or these lines inelastically scattered by helium atoms wherein $21.2\ eV$ was

9

absorbed in the excitation of $He(1s^2)$ to $He(1s^12p^1)$. There is remarkable agreement between the data and the proposed transitions to fractional Rydberg states and these lines inelastically scattered by helium according to Eq. (8). All other peaks could be assigned to He I, He II, second order lines, or atomic or molecular hydrogen emission. No known lines of helium or hydrogen explain the $q \cdot 13.6\,eV$ related set of peaks. Given that these spectra are readily repeatable, these peaks may have been overlooked in the past without considering the role of the helium scattering. It is also remarkable that the novel lines are moderately intense based on the low grating efficiency at these short wavelengths.

B. Line broadening and T_e measurements

The results of the 656.2 nm Balmer α line width measured with a high resolution ($\pm0.025\,nm$) visible spectrometer on glow discharge plasmas having atomized hydrogen from pure hydrogen alone and helium-hydrogen (90/10%) is given in Figure 7. Using the method of Kuraica and Konjevic [31] and Videnocic et al. [32], the energetic hydrogen atom densities and energies were calculated. It was found that helium-hydrogen showed significant broadening corresponding to an average hydrogen atom temperature of 33-$38\,eV$ and an atom density of $3 \times 10^{13}\,atoms/cm^3$; whereas, pure hydrogen showed no excessive broadening corresponding to an average hydrogen atom temperature of $\approx 3\,eV$ and an atom density of only $5 \times 10^{13}\,atoms/cm^3$ even though 10 times more hydrogen was present. Similarly, the average electron temperature for helium-hydrogen microwave plasma was 28,000 K; whereas, the corresponding temperature of helium alone was only 6800 K.

C. Power balance measurements

Since a significant increase in ion and electron temperature was observed with helium-hydrogen discharge and microwave plasmas, respectively, and energetic hydrino lines were observed at short wavelengths in the corresponding microwave plasmas that required a very significant reaction rate due to low photon detection efficiency in this region, the power balance was measured on the helium-hydrogen

1 0

microwave plasmas by heat loss calorimetry [30]. No increase in temperature with the addition of hydrogen to krypton or xenon was observed. In contrast, a remarkable temperature increase was observed when hydrogen was added to the helium microwave plasma. The temperature rise as a function of time for helium alone and the helium-hydrogen mixture (95/5%) is shown in Figure 8. The microwave input power to the helium alone and the helium-hydrogen mixture was set at 40 W. The constant microwave input was maintained for 60 seconds and 90 seconds, respectively, and then terminated. The cooling curves were then recorded.

The power balance was determined by modeling the heat flow from the quartz reactor wherein the parameters of the model were taken from the Newton cooling curves. Consider a small heat increment

$$dQ_t = P_{out}dt = dQ_m + dQ_l = CdT_h - CdT_c \tag{9}$$

where Q_t is the total heat, Q_m is the measured heat, Q_l is the lost heat, P_{out} is the power output, t is time, C is the system heat capacity, dT_h is the temperature rise due to heating, and dT_c is the temperature drop due to cooling (dT_c is negative). The system heat capacity is a function of temperature, and at a given temperature, the power output can be expressed by the following equation,

$$P_{out} = C\left(\frac{dT_h}{dt} - \frac{dT_c}{dt}\right) \tag{10}$$

The slopes dT_h/dt and dT_c/dt can be calculated from the heating and cooling curves, respectively. Assuming that, at a given temperature, the heat capacities of the two systems (system 1: helium alone; system 2: helium-hydrogen) are the same, $C_1 = C_2$, then the power ratio can be calculated by

$$R = \frac{P_{out,2}}{P_{out,1}} = \frac{\left(\dfrac{dT_{h,2}}{dt} - \dfrac{dT_{c,2}}{dt}\right)}{\left(\dfrac{dT_{h,1}}{dt} - \dfrac{dT_{c,1}}{dt}\right)} \tag{11}$$

The slopes of the heating and cooling curves were calculated using the experimental data presented in Figure 8. The power ratios were calculated by Eq. (11) in the temperature range $\Delta T = 50 - 150\,°C$, where ΔT was the difference between the plasma temperature and the room temperature, 24 °C. The following power balance existed in the

1 1

microwave plasma systems,

$$P_{out} = P_{in} + P_{ex}$$ (12)

where P_{in} was the input power and P_{ex} was the excess power. For the helium plasma, there was no excess power, $P_{ex,1} = 0$, $P_{out,1} = P_{in,1} = 40\ W$.

The calculated results are given in Table 1. The average power ratio is $R = 5.94$ with a standard deviation of 0.21. Since the temperature was recorded at 200 millisecond intervals, the data in Figure 8 shows that the temperature rise as a function of time was variable over the 60 second reaction time and significantly accelerated at temperatures above those used in the power balance determination based on Eq. (11). Thus, the analysis shown in Table 1 is conservative.

The reactor volume was $10\ cm^3$, and the hydrogen flow rate was 0.5 sccm. Therefore, with a microwave input power of $40\ W$, the thermal output power was measured to be $238 \pm 8\ W$ corresponding to a plasma gas temperature rise from room temperature to 1240 °C within 60 seconds, an unoptimized gain of about 6 times the input power, an excess power of $198 \pm 8\ W$, a power density of $24\ MW/m^3$, and an energy balance of at least $-3 \times 10^5\ kJ/mole\ H_2$ compared to the enthalpy of combustion of hydrogen of $-241.8\ kJ/mole\ H_2$.

IV. CONCLUSION

We report that extreme ultraviolet (EUV) spectroscopy was recorded on microwave and glow discharges of helium with 2% hydrogen. Novel emission lines were observed with energies of $q \cdot 13.6\ eV$ where $q = 1,2,3,4,6,7,8,9,\ or\ 11$ or these lines inelastically scattered by helium atoms wherein $21.2\ eV$ was absorbed in the excitation of $He\ (1s^2)$ to $He\ (1s^1 2p^1)$. These lines were identified as transitions to fractional Rydberg states of atomic hydrogen. In glow discharge plasmas, an average hydrogen atom temperature of $33\text{-}38\ eV$ was observed by line broadening with the presence of helium ion catalyst with hydrogen; whereas, pure hydrogen plasmas showed no excessive broadening corresponding to an average hydrogen atom temperature of $\approx 3\ eV$. Similarly, the average electron temperature for helium-hydrogen microwave plasmas was 28,000 K; whereas, the corresponding temperature of helium alone was only 6800 K.

Excess thermal power of about $240\,W$ and a gain of 6 was observed from helium-hydrogen microwave plasmas. The power from the catalytic reaction of helium ions with atomic hydrogen corresponded to a volumetric power density of over $24\,MW/m^3$ which is about 100 times that of many coal fired electric power plants, and rivals some internal combustion engines. In addition, the presently observed and previously reported energy balances [15-16] were over $100\,eV/H\,atom$ which matched the present and previously reported EUV emission that corresponded to over $100\,eV/H\,atom$ [9-11, 19]. Since the net enthalpy released is at least 100 times that of combustion, the catalysis of atomic hydrogen represents a new source of energy with H_2O as the source of hydrogen fuel. Moreover, rather that air pollutants or radioactive waste, novel hydride compounds with potential commercial applications are the products [21-28]. Since the power is in the form of a plasma that may form at room temperature, high-efficiency, low cost direct energy conversion may be possible, thus, avoiding heat engines such as turbines and the severe limitations of fuel cells [33-35]. Significantly lower capital costs and lower commercial operating costs than that of any known competing energy source are anticipated.

ACKNOWLEDGMENT

REFERENCES

1. N. V. Sidgwick, *The Chemical Elements and Their Compounds*, Volume I, Oxford, Clarendon Press, (1950), p.17.
2. M. D. Lamb, *Luminescence Spectroscopy*, Academic Press, London, (1978), p. 68.
3. R. Mills, *The Grand Unified Theory of Classical Quantum Mechanics*, September 2001 Edition, BlackLight Power, Inc., Cranbury, New Jersey, Distributed by Amazon.com; posted at www.blacklightpower.com.
4. R. Mills, "The Grand Unified Theory of Classical Quantum Mechanics", Global Foundation, Inc. Orbis Scientiae entitled *The Role of Attractive and Repulsive Gravitational Forces in Cosmic Acceleration of Particles*

The Origin of the Cosmic Gamma Ray Bursts, (29th Conference on High Energy Physics and Cosmology Since 1964) Dr. Behram N. Kursunoglu, Chairman, December 14-17, 2000, Lago Mar Resort, Fort Lauderdale, FL.

5. R. Mills, "The Grand Unified Theory of Classical Quantum Mechanics", Global Foundation, Inc. Orbis Scientiae entitled *The Role of Attractive and Repulsive Gravitational Forces in Cosmic Acceleration of Particles The Origin of the Cosmic Gamma Ray Bursts*, (29th Conference on High Energy Physics and Cosmology Since 1964) Dr. Behram N. Kursunoglu, Chairman, December 14-17, 2000, Lago Mar Resort, Fort Lauderdale, FL, Kluwer Academic/Plenum Publishers, New York, pp. 243-258.

6. R. Mills, "The Grand Unified Theory of Classical Quantum Mechanics", Int. J. of Hydrogen Energy, in press.

7. R. Mills, "The Hydrogen Atom Revisited", Int. J. of Hydrogen Energy, Vol. 25, Issue 12, December, (2000), pp. 1171-1183.

8. R. Mills, The Nature of Free Electrons in Superfluid Helium--a Test of Quantum Mechanics and a Basis to Review its Foundations and Make a Comparison to Classical Theory, Int. J. Hydrogen Energy, Vol. 26, No. 10, (2001), pp. 1059-1096.

9. R. Mills, P. Ray, "Spectral Emission of Fractional Quantum Energy Levels of Atomic Hydrogen from a Helium-Hydrogen Plasma and the Implications for Dark Matter", Int. J. Hydrogen Energy, in press.

10. R. Mills, P. Ray, "Vibrational Spectral Emission of Fractional-Principal-Quantum-Energy-Level Hydrogen Molecular Ion", Int. J. Hydrogen Energy, in press.

11. R. Mills, P. Ray, Spectroscopic Identification of a Novel Catalytic Reaction of Potassium and Atomic Hydrogen and the Hydride Ion Product, Int. J. Hydrogen Energy, Vol. 27, No. 2, December, (2001), pp. 183-192.

12. R. Mills, "Spectroscopic Identification of a Novel Catalytic Reaction of Atomic Hydrogen and the Hydride Ion Product", Int. J. Hydrogen Energy, Vol. 26, No. 10, (2001), pp. 1041-1058.

13. R. Mills and M. Nansteel, "Argon-Hydrogen-Strontium Plasma Light Source", IEEE Transactions on Plasma Science, submitted.

14. R. Mills, M. Nansteel, and Y. Lu, "Excessively Bright Hydrogen-Strontium Plasma Light Source Due to Energy Resonance of Strontium

with Hydrogen", European Journal of Physics D, submitted.

15. R. Mills, A. Voigt, P. Ray, M. Nanstell, "Measurement of Hydrogen Balmer Line Broadening and Thermal Power Balances of Noble Gas-Hydrogen Discharge Plasmas", Int. J. Hydrogen Energy, in press.

16. R. Mills, N. Greenig, S. Hicks, "Optically Measured Power Balances of Anomalous Discharges of Mixtures of Argon, Hydrogen, and Potassium, Rubidium, Cesium, or Strontium Vapor", Int. J. Hydrogen Energy, in press.

17. R. Mills, M. Nansteel, and Y. Lu, "Observation of Extreme Ultraviolet Hydrogen Emission from Incandescently Heated Hydrogen Gas with Strontium that Produced an Anomalous Optically Measured Power Balance", Int. J. Hydrogen Energy, Vol. 26, No. 4, (2001), pp. 309-326.

18. R. Mills, J. Dong, Y. Lu, "Observation of Extreme Ultraviolet Hydrogen Emission from Incandescently Heated Hydrogen Gas with Certain Catalysts", Int. J. Hydrogen Energy, Vol. 25, (2000), pp. 919-943.

19. R. Mills, "Observation of Extreme Ultraviolet Emission from Hydrogen-KI Plasmas Produced by a Hollow Cathode Discharge", Int. J. Hydrogen Energy, Vol. 26, No. 6, (2001), pp. 579-592.

20. R. Mills, "Temporal Behavior of Light-Emission in the Visible Spectral Range from a Ti-K2CO3-H-Cell", Int. J. Hydrogen Energy, Vol. 26, No. 4, (2001), pp. 327-332.

21. R. Mills, T. Onuma, and Y. Lu, "Formation of a Hydrogen Plasma from an Incandescently Heated Hydrogen-Catalyst Gas Mixture with an Anomalous Afterglow Duration", Int. J. Hydrogen Energy, Vol. 26, No. 7, July, (2001), pp. 749-762.

22. R. Mills, B. Dhandapani, M. Nansteel, J. He, A. Voigt, "Identification of Compounds Containing Novel Hydride Ions by Nuclear Magnetic Resonance Spectroscopy", Int. J. Hydrogen Energy, Vol. 26, No. 9, Sept. (2001), pp. 965-979.

23. R. Mills, B. Dhandapani, N. Greenig, J. He, "Synthesis and Characterization of Potassium Iodo Hydride", Int. J. of Hydrogen Energy, Vol. 25, Issue 12, December, (2000), pp. 1185-1203.

24. R. Mills, "Novel Inorganic Hydride", Int. J. of Hydrogen Energy, Vol. 25, (2000), pp. 669-683.

25. R. Mills, "Novel Hydrogen Compounds from a Potassium Carbonate Electrolytic Cell", Fusion Technology, Vol. 37, No. 2, March, (2000), pp.

157-182.

26. R. Mills, B. Dhandapani, M. Nansteel, J. He, T. Shannon, A. Echezuria, "Synthesis and Characterization of Novel Hydride Compounds", Int. J. of Hydrogen Energy, Vol. 26, No. 4, (2001), pp. 339-367.

27. R. Mills, "Highly Stable Novel Inorganic Hydrides", Journal of New Materials for Electrochemical Systems, in press.

28. R. Mills, W. Good, A. Voigt, Jinquan Dong, "Minimum Heat of Formation of Potassium Iodo Hydride", Int. J. Hydrogen Energy, Vol. 26, No. 11, Oct., (2001), pp. 1199-1208.

29. H. R. Griem, *Principle of Plasma Spectroscopy*, Cambridge University Press, (1987).

30. C. Chen, T. Wei, L. R. Collins, and J. Phillips, "Modeling the discharge region of a microwave generated hydrogen plasma", J. Phys. D: Appl. Phys., Vol. 32, (1999), pp. 688-698.

31. M. Kuraica, N. Konjevic, "Line shapes of atomic hydrogen in a plane-cathode abnormal glow discharge", Physical Review A, Volume 46, No. 7, October (1992), pp. 4429-4432.

32. I. R. Videnocic, N. Konjevic, M. M. Kuraica, "Spectroscopic investigations of a cathode fall region of the Grimm-type glow discharge", Spectrochimica Acta, Part B, Vol. 51, (1996), pp. 1707-1731.

33. R. Mills, "BlackLight Power Technology-A New Clean Hydrogen Energy Source with the Potential for Direct Conversion to Electricity", Proceedings of the National Hydrogen Association, 12 th Annual U.S. Hydrogen Meeting and Exposition, *Hydrogen: The Common Thread*, The Washington Hilton and Towers, Washington DC, (March 6-8, 2001), pp. 671-697.

34. R. Mills, "BlackLight Power Technology-A New Clean Energy Source with the Potential for Direct Conversion to Electricity", Global Foundation International Conference on "Global Warming and Energy Policy", Dr. Behram N. Kursunoglu, Chairman, Fort Lauderdale, FL, November 26-28, 2000, Kluwer Academic/Plenum Publishers, New York, pp. 1059-1096.

35. R. Mayo, R. Mills, M. Nansteel, "On the Potential of Direct and MHD Conversion of Power from a Novel Plasma Source to Electricity for Microdistributed Power Applications", IEEE Transactions on Plasma

Science, submitted.

17

Table 1. Calculation of Power Ratios between Helium-Hydrogen and Helium Plasmas.

ΔT (°C)	$dT_{h,1}/dt$ (°C/sec)	$dT_{c,1}/dt$ (°C/sec)	$dT_{h,2}/dt$ (°C/sec)	$dT_{c,2}/dt$ (°C/sec)	Power Ratio, R
40	4.43	-1.00	29.14	-1.16	5.59
50	3.76	-1.21	28.91	-1.35	6.10
60	3.42	-1.45	28.67	-1.57	6.21
70	3.20	-1.72	28.44	-1.81	6.14
80	3.01	-2.02	28.22	-2.07	6.03
90	2.77	-2.32	27.99	-2.34	5.95
100	2.48	-2.63	27.77	-2.60	5.94
110	2.14	-2.94	27.56	-2.84	5.99
120	1.78	-3.28	27.34	-3.06	6.00
130	1.44	-3.72	27.13	-3.25	5.88
140	1.15	-4.39	26.93	-3.41	5.47

Figure 1. The experimental set up comprising a microwave discharge gas cell light source and an EUV spectrometer which was differentially pumped.

Figure 2. The EUV spectra ($15-50\,nm$) of the microwave cell emission of the helium-hydrogen mixture (98/2%) recorded at 1, 24, and 72 hours with a normal incidence EUV spectrometer and a CEM, and control helium (dotted curve) recorded with a 4° grazing incidence EUV spectrometer and a CEM. The pressure was maintained at 20 torr. Only known He I and He II peaks were observed with the helium control. Reproducible novel emission lines that increased with time were observed at $45.6\,nm$ and $30.4\,nm$ with energies of $q \cdot 13.6\,eV$ where $q = 2\,or\,3$ and at $37.4\,nm$ and $20.5\,nm$ with energies of $q \cdot 13.6\,eV$ where $q = 4\,or\,6$ that were inelastically scattered by helium atoms wherein $21.2\,eV$ ($58.4\,nm$) was absorbed in the excitation of $He\,(1s^2)$.

Figure 3. The short wavelength EUV spectra ($5-50\,nm$) of the microwave cell emission of the helium-hydrogen mixture (98/2%) (top curve) and the control hydrogen (bottom curve) recorded with a normal incidence EUV spectrometer and a CEM. No hydrogen emission was observed in this region, and no instrument artifacts were observed. Reproducible novel emission lines were observed at $45.6\,nm$, $30.4\,nm$, $13.03\,nm$, $10.13\,nm$, and $8.29\,nm$ with energies of $q \cdot 13.6\,eV$ where $q = 2,3,7,9,\,or\,11$ and at $37.4\,nm$, $20.5\,nm$, and $14.15\,nm$ with energies of $q \cdot 13.6\,eV$ where $q = 4,6,\,or\,8$ that were inelastically scattered by helium atoms wherein $21.2\,eV$ ($58.4\,nm$) was absorbed in the excitation of $He\,(1s^2)$.

Figure 4. The EUV spectrum ($50-65\,nm$) of the helium-hydrogen mixture (98/2%) glow discharge cell emission recorded with a 4° grazing incidence EUV spectrometer and a CEM. The pressure was maintained at 400 mtorr. A novel line was observed at $63.3\,nm$ corresponding to the $30.4\,nm$ fractional Rydberg state transition shown in Figures 2 and 3 that was inelastically scattered by helium atoms wherein $21.2\,eV$ ($58.4\,nm$) was absorbed in the excitation of $He\,(1s^2)$.

Figure 5. The EUV spectrum ($88-125\,nm$) of the helium-hydrogen mixture (98/2%) microwave cell emission recorded with a normal incidence EUV spectrometer and a CEM. The pressure was maintained at
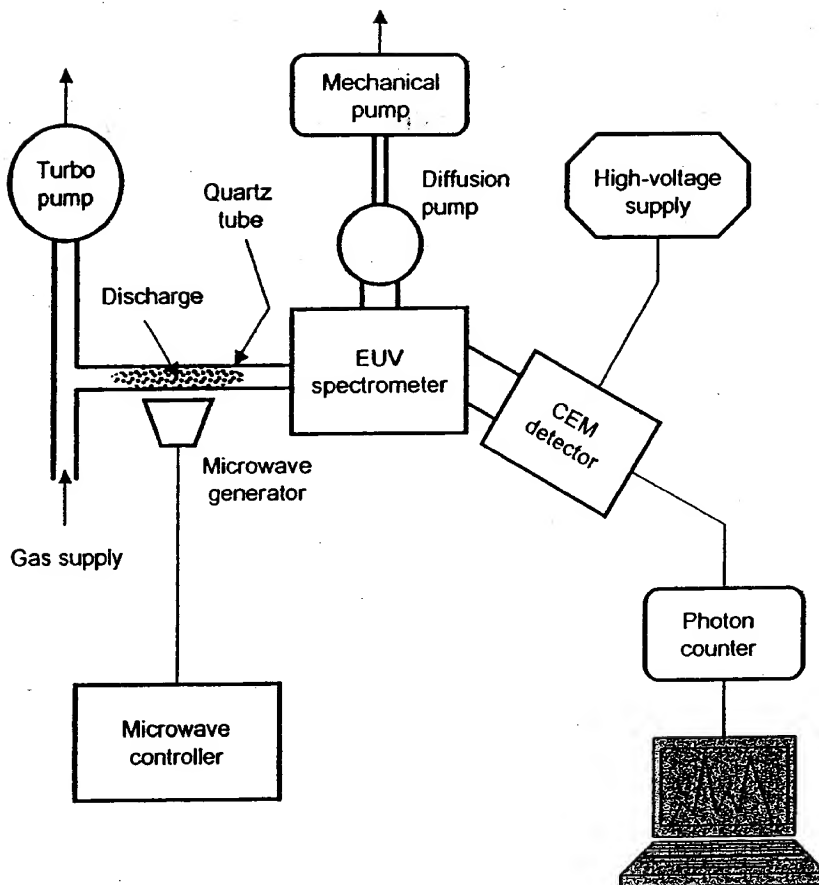
20 torr. An emission line was observed at $91.2\,nm$ with an energy of $q \cdot 13.6\,eV$ where $q = 1$ which was identified as a fractional Rydberg state transition based on the $91.2\,nm$ line intensity relative to Lβ compared to that of the control hydrogen plasma.

Figure 6. The EUV spectrum $(80 - 108\,nm)$ of the control hydrogen microwave discharge cell emission recorded with a normal incidence EUV spectrometer and a CEM.

Figure 7. The 656.2 nm Balmer α line width recorded with a high resolution ($\pm 0.025\,nm$) visible spectrometer on a helium-hydrogen mixture (90/10%) discharge plasma. Significant broadening was observed corresponding to an average hydrogen atom temperature of $33 \text{-} 38\,eV$.

Figure 8. The temperature rise as a function of time for helium alone and the helium-hydrogen mixture (95/5%) with microwave input power set at 40 W. The constant microwave input was maintained for 90 seconds and 60 seconds, respectively, and then terminated. The cooling curves were then recorded. The maximum temperature of the helium-hydrogen mixture plasma and helium alone plasma was 1240°C and 186°C, respectively. The thermal output power of the helium-hydrogen plasma was determined to be $240\,W$.

Fig. 1

Turbo pump

Quartz tube

Discharge

Mechanical pump

Diffusion pump

High-voltage supply

EUV spectrometer

CEM detector

Microwave generator

Gas supply

Microwave controller

Photon counter
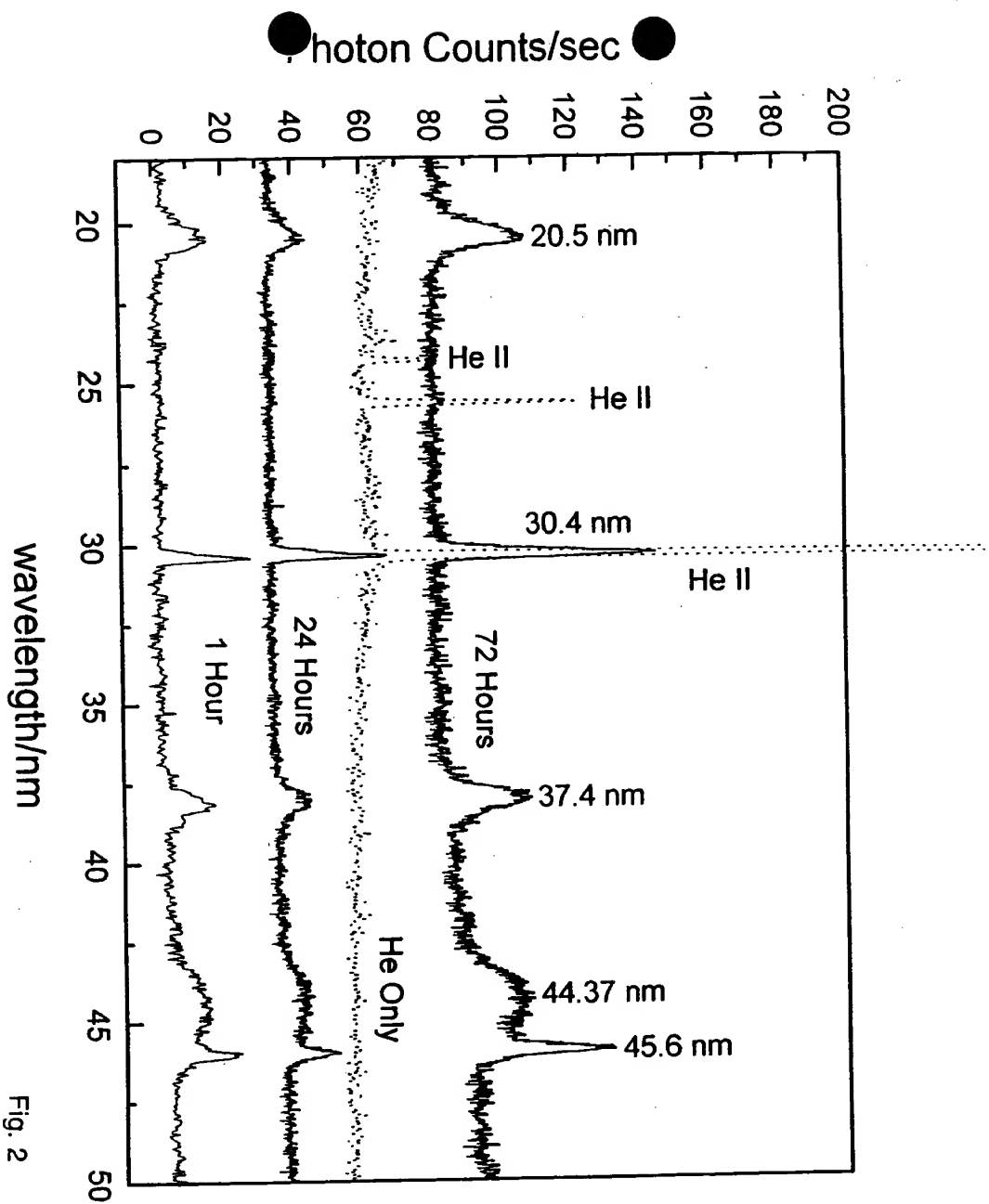
Fig. 2
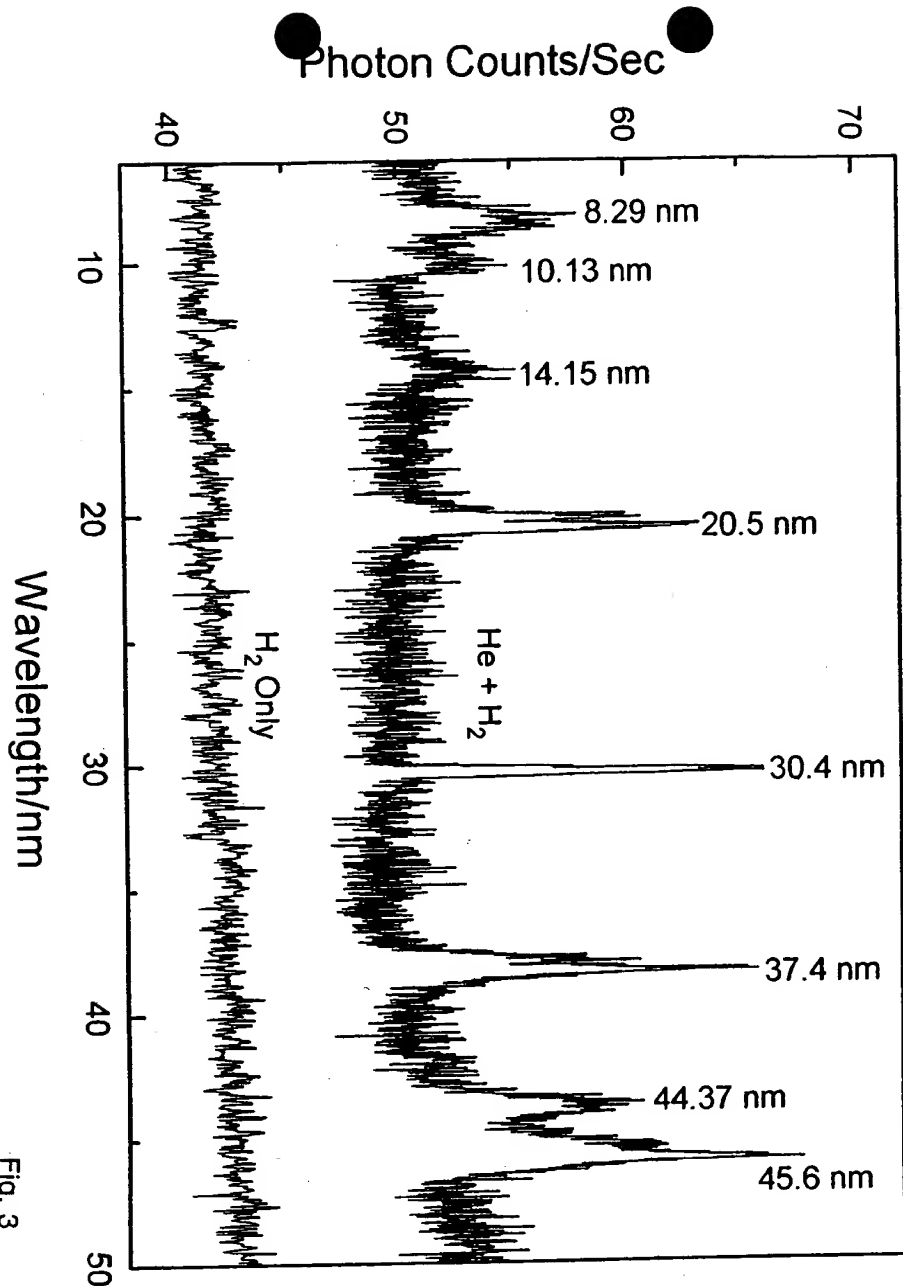
Fig. 3

Fig. 4

Photon Counts/sec

Wavelength/nm

52.4 nm

53.7 nm

58.4 nm

59.1 nm

60.2 nm

60.8 nm

61.6 nm

62.8 nm

62.5 nm

63.3 nm

63.9 nm

64.1 nm

64.5 nm

Fig. 5

Photon Counts/sec

Wavelength/nm

88.6 nm
90.7 nm
91.2 nm
91.8 nm
He I
He I
L$_\gamma$
He I
L$_\beta$
104.6 nm
106.7 nm
He I
107.36 nm
110 nm
113.5 nm
116.4 nm
He I
L$_\alpha$
124.5 nm

Fig. 6

Fig. 7

Fig. 8

New Power Source from Fractional Quantum Energy Levels of Atomic Hydrogen that Surpasses Internal Combustion

Randell L. Mills, Paresh Ray, Bala Dhandapani, Mark Nansteel, Xuemin Chen, Jiliang He

BlackLight Power, Inc.

493 Old Trenton Road

Cranbury, NJ 08512

(609) 490-1090

(609) 490-1066 FAX

ABSTRACT

Extreme ultraviolet (EUV) spectroscopy was recorded on microwave discharges of helium with 2% hydrogen. Novel emission lines were observed with energies of $q \cdot 13.6\ eV$ where $q = 1,2,3,4,6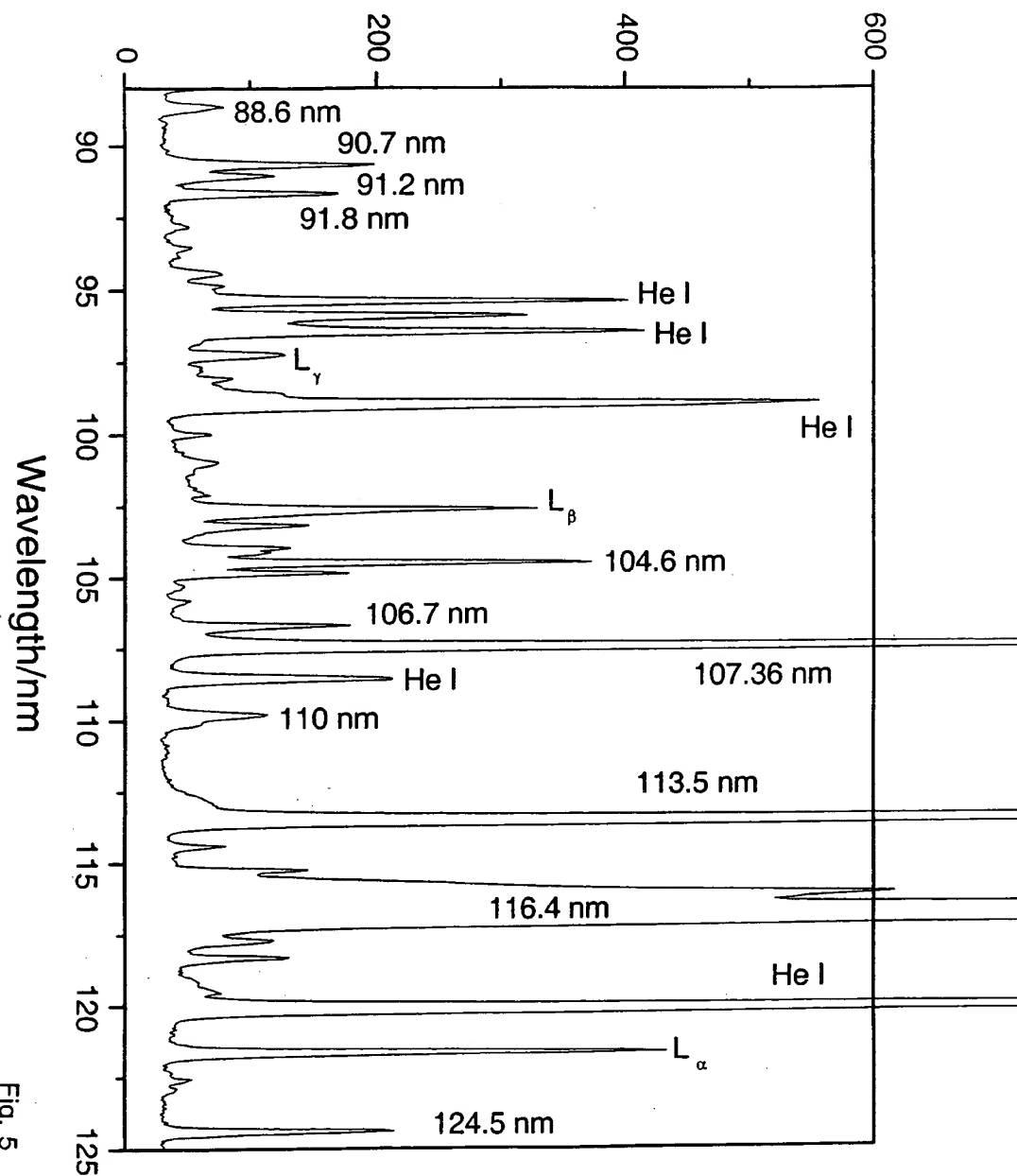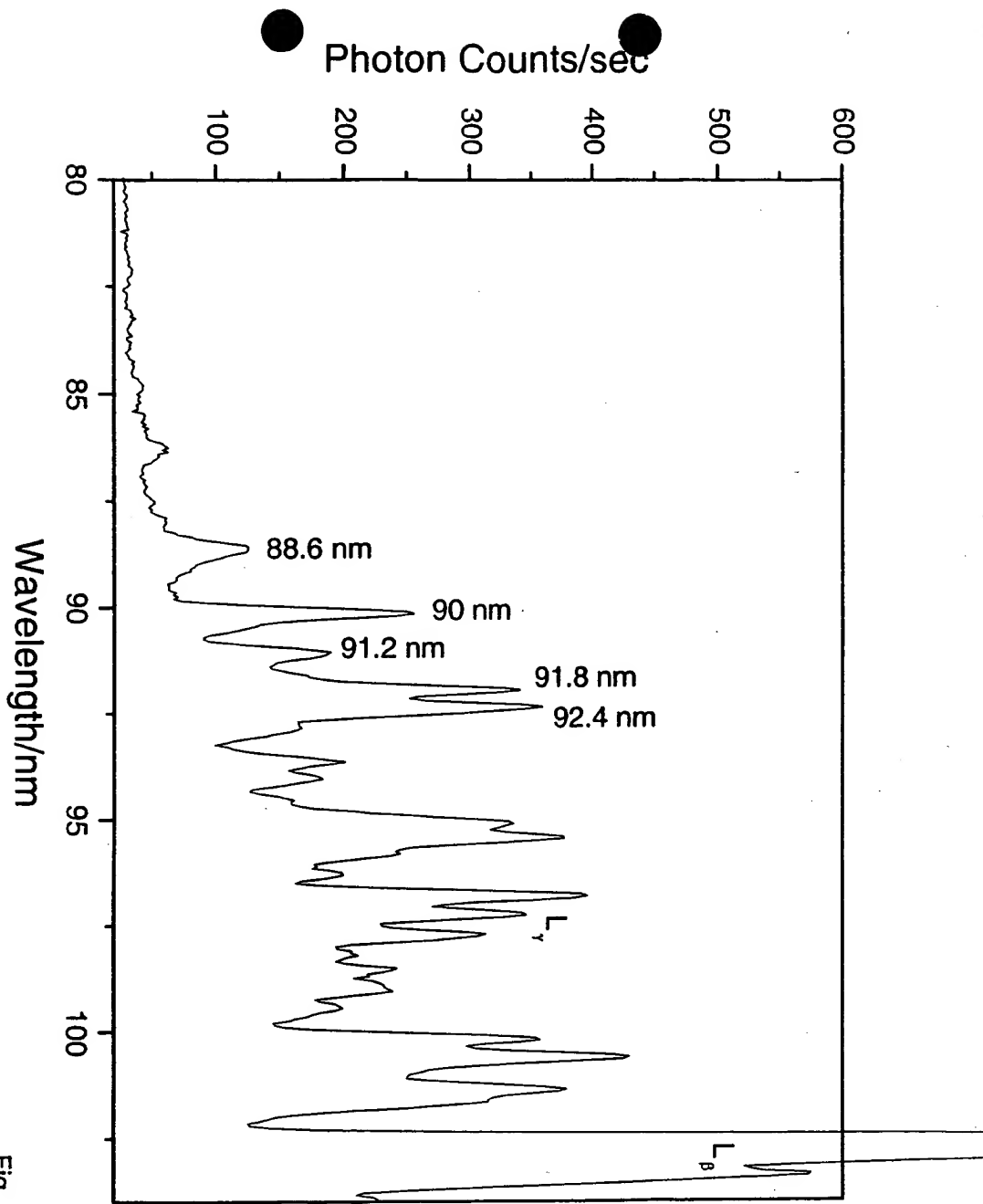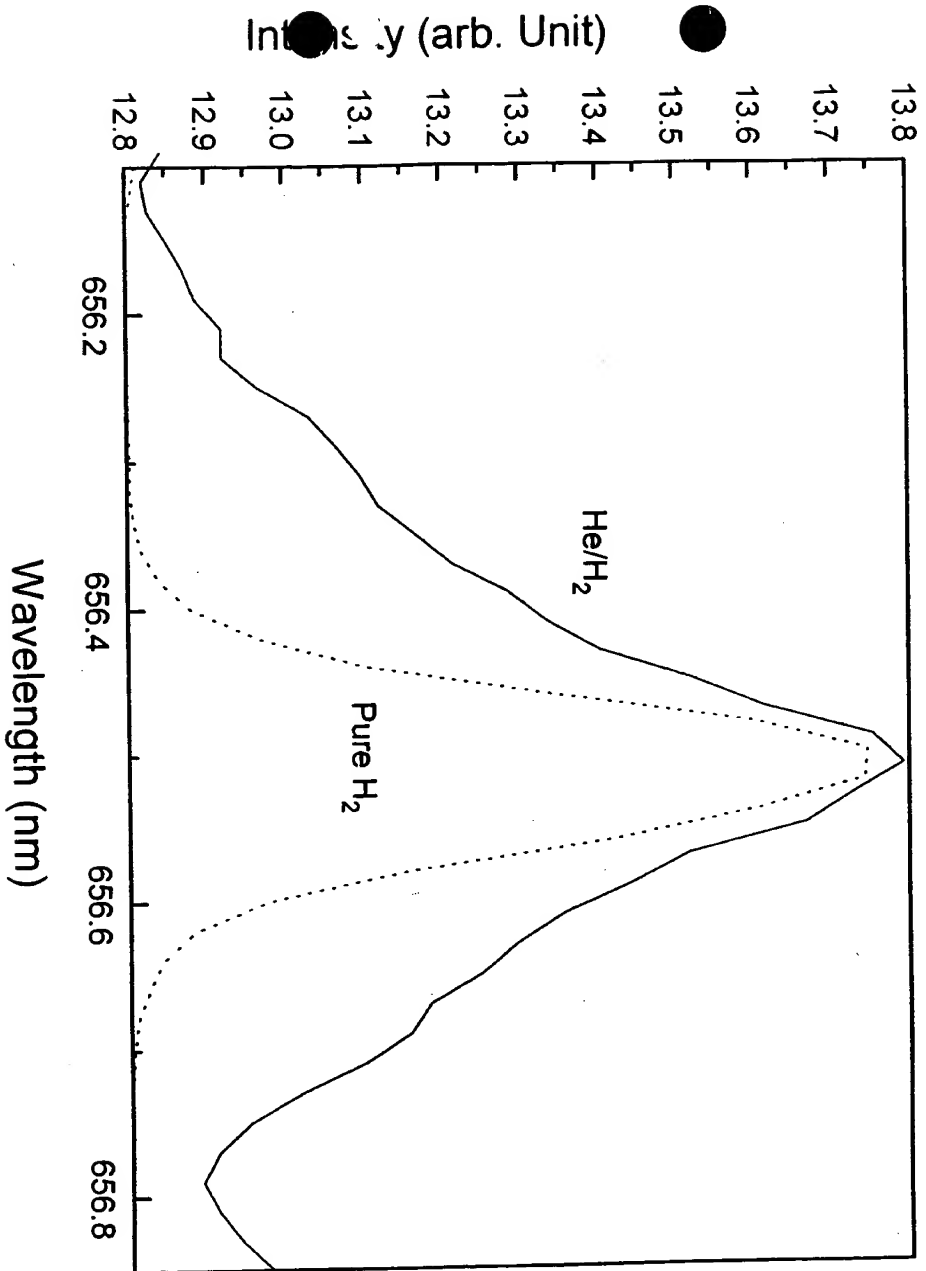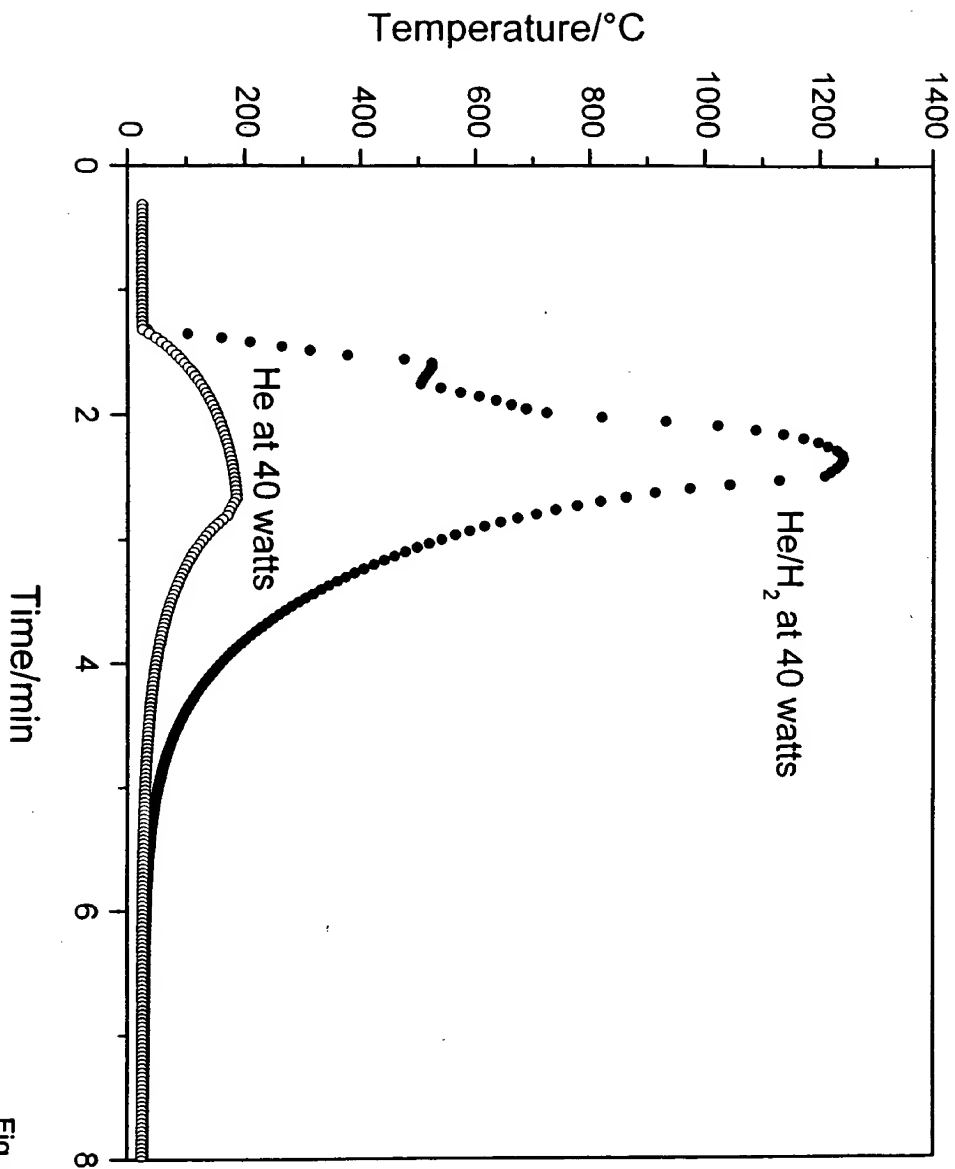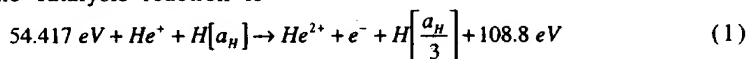,7,8,9,$ or 11 or these lines inelastically scattered by helium atoms wherein $21.2\ eV$ was absorbed in the excitation of $He\,(1s^2)$ to $He\,(1s^1 2p^1)$. These lines were identified as hydrogen transitions to electronic energy levels below the "ground" state corresponding to fractional quantum numbers. Significant line broadening corresponding to an average hydrogen atom temperature of $33 - 38\ eV$ was observed for helium-hydrogen discharge plasmas; whereas, pure hydrogen showed no excessive broadening corresponding to an average hydrogen atom temperature of $\approx 3\ eV$. Since a significant increase in ion temperature was observed with helium-hydrogen discharge plasmas, and energetic hydrino lines were observed at short wavelengths in the corresponding microwave plasmas that required a very significant reaction rate due to low photon detection efficiency in this region, the power balance was measured on the helium-hydrogen microwave plasmas. With a microwave input power of $30\ W$, the thermal output power was measured to be at least $300\ W$ corresponding to a reactor temperature rise from room temperature to $900\ °C$ within 90 seconds, a power density of $30\ MW/m^3$, and an energy balance of about $-4 \times 10^5\ kJ/mole\ H_2$ compared to the enthalpy of combustion of hydrogen of $-241.8\ kJ/mole\ H_2$.

I. INTRODUCTION

From a solution of a Schrödinger-type wave equation with a nonradiative boundary condition based on Maxwell's equations, Mills predicts that atomic hydrogen may undergo a catalytic reaction with certain atomized elements and ions which singly or multiply ionize at integer multiples of the potential energy of atomic hydrogen, $m \cdot 27.2 \, eV$ wherein m is an integer [1, 6-28]. The reaction involves a nonradiative energy transfer to form a hydrogen atom that is lower in energy than unreacted atomic hydrogen that corresponds to a fractional principal quantum number ($n = \dfrac{1}{p} = \dfrac{1}{\text{integer}}$ replaces the well known parameter $n = \text{integer}$ in the Rydberg equation for hydrogen excited states). One such atomic catalytic system involves helium ions because the second ionization energy of helium is $54.417 \, eV$, which is equivalent to $m = 2$. In this case, the catalysis reaction is

$$54.417 \, eV + He^+ + H[a_H] \rightarrow He^{2+} + e^- + H\left[\frac{a_H}{3}\right] + 108.8 \, eV \tag{1}$$

$$He^{2+} + e^- \rightarrow He^+ + 54.417 \, eV \tag{2}$$

And, the overall reaction is

$$H[a_H] \rightarrow H\left[\frac{a_H}{3}\right] + 54.4 \, eV + 54.4 \, eV \tag{3}$$

Since the products of the catalysis reaction have binding energies of $m \cdot 27.2 \, eV$, they may further serve as catalysts. Thus, further catalytic transitions may occur: $n = \dfrac{1}{3} \rightarrow \dfrac{1}{4}, \dfrac{1}{4} \rightarrow \dfrac{1}{5}$, and so on. In this process called *disproportionation*, lower-energy hydrogen atoms, *hydrinos*, can act as catalysts because each of the metastable excitation, resonance excitation, and ionization energy of a hydrino atom is $m \cdot 27.2 \, eV$. The transition reaction mechanism of a first hydrino atom affected by a second hydrino atom involves the resonant coupling between the atoms of m degenerate multipoles each having $27.21 \, eV$ of potential energy [1, 6-28]. The energy transfer of $m \cdot 27.2 \, eV$ from the first hydrino atom to the second hydrino atom causes the central field of the first atom to increase by m and its electron to drop m levels lower from a radius of $\dfrac{a_H}{p}$ to a radius of $\dfrac{a_H}{p+m}$.

The second interacting lower-energy hydrogen is either excited to a

2

metastable state, excited to a resonance state, or ionized by the resonant energy transfer.

The resonant transfer may occur in multiple stages. For example, a nonradiative transfer by multipole coupling may occur wherein the central field of the first increases by m, then the electron of the first drops m levels lower from a radius of $\dfrac{a_H}{p}$ to a radius of $\dfrac{a_H}{p+m}$ with further resonant energy transfer. The energy transferred by multipole coupling may occur by a mechanism that is analogous to photon absorption involving an excitation to a virtual level. Or, the energy transferred by multipole coupling during the electron transition of the first hydrino atom may occur by a mechanism that is analogous to two photon absorption involving a first excitation to a virtual level and a second excitation to a resonant or continuum level [29-31]. The transition energy greater than the energy transferred to the second hydrino atom may appear as a photon in a vacuum medium.

The transition of $H\left[\dfrac{a_H}{p}\right]$ to $H\left[\dfrac{a_H}{p+m}\right]$ induced by a multipole resonance transfer of $m \cdot 27.21\,eV$ and a transfer of $[(p')^2 - (p'-m')^2]\,X\,13.6\,eV - m \cdot 27.2\,eV$ with a resonance state of $H\left[\dfrac{a_H}{p'-m'}\right]$ excited in $H\left[\dfrac{a_H}{p'}\right]$ is represented by

$$H\left[\frac{a_H}{p'}\right] + H\left[\frac{a_H}{p}\right] \rightarrow H\left[\frac{a_H}{p'-m'}\right] + H\left[\frac{a_H}{p+m}\right] + [((p+m)^2 - p^2) - (p'^2 - (p'-m')^2)]\,X\,13.6\,eV$$

(4)

where p, p', m, and m' are integers.

Hydrinos may be ionized during a disproportionation reaction by the resonant energy transfer. A hydrino atom with the initial lower-energy state quantum number p and radius $\dfrac{a_H}{p}$ may undergo a transition to the state with lower-energy state quantum number $(p+m)$ and radius $\dfrac{a_H}{(p+m)}$ by reaction with a hydrino atom with the initial lower-energy state quantum number m', initial radius $\dfrac{a_H}{m'}$, and final radius a_H that provides a net enthalpy of $m \cdot 27.2\,eV$. Thus, reaction of hydrogen-type

3

atom, $H\left[\dfrac{a_H}{p}\right]$, with the hydrogen-type atom, $H\left[\dfrac{a_H}{m'}\right]$, that is ionized by the resonant energy transfer to cause a transition reaction is represented by

$$m \, X \, 27.21 \, eV + H\left[\frac{a_H}{m'}\right] + H\left[\frac{a_H}{p}\right] \rightarrow H^+ + e^- + H\left[\frac{a_H}{(p+m)}\right] + [(p+m)^2 - p^2 - (m'^2 - 2m)]X13.6 \, eV$$

$$(5)$$

$$H^+ + e^- \rightarrow H\left[\frac{a_H}{1}\right] + 13.6 \, eV \tag{6}$$

And, the overall reaction is

$$H\left[\frac{a_H}{m'}\right] + H\left[\frac{a_H}{p}\right] \rightarrow H\left[\frac{a_H}{1}\right] + H\left[\frac{a_H}{(p+m)}\right] + \left[2pm + m^2 - m'^2\right]X13.6 \, eV + 13.6 \, eV \tag{7}$$

It is further proposed that the photons that arise from hydrogen catalysis may undergo inelastic helium scattering. That is, the catalytic reaction

$$H[a_H] \xrightarrow{\;He^*\;} H\left[\frac{a_H}{3}\right] + 54.4 \, eV + 54.4 \, eV \tag{8}$$

yields two $54.4 \, eV$ photons ($22.8 \, nm$). When each of these photons strikes $He \, (1s^2)$, $21.2 \, eV$ is absorbed in the excitation to $He \, (1s^1 2p^1)$. This leaves a $33.19 \, eV$ ($37.4 \, nm$) photon peak shown in Table 1. Thus, for helium the inelastic scattered peak of $54.4 \, eV$ photons from Eq. (3) is given by

$$E = 54.4 \, eV - 21.21 \, eV = 33.19 \, eV \, (37.4 \, nm) \tag{9}$$

The general reaction is

$$photon \, (h\nu) + He \, (1s^2) \rightarrow He \, (1s^1 2p^1) + photon \, (h\nu - 21.21 \, eV) \tag{10}$$

A number of independent experimental observations lead to the conclusion that atomic hydrogen can exist in fractional quantum states that are at lower energies than the traditional "ground" ($n=1$) state. Prior related studies that support the possibility of a novel reaction of atomic hydrogen which produces a chemically generated or assisted plasma and produces novel hydride compounds include extreme ultraviolet (EUV) spectroscopy [7-12, 15-19], characteristic emission from catalysis and the hydride ion products [9-10], lower-energy hydrogen emission [5, 7-8], plasma formation [9-12, 15-16, 18-19], Balmer α line broadening [13], anomalous plasma afterglow duration [18-19], power generation [11-15, 26], and analysis of chemical compounds [20-26]. We report that microwave and glow discharges of helium-hydrogen mixtures were studied by extreme ultraviolet (EUV) spectroscopy to search for hydrino

4

lines. Since the corresponding electronic transitions are very energetic, Balmer α line broadening was anticipated and was measured. Since the second ionization energy of He^+ is an exact multiple of the potential energy of atomic hydrogen and microwave plasmas may have significant concentrations of He^+ as well as atomic hydrogen, fast kinetics observable as heat may be possible. Thus, power balances of microwave plasmas of helium-hydrogen mixtures were also measured.

II. EXPERIMENTAL

A. EUV Spectroscopy

EUV spectroscopy was recorded on hydrogen, helium, and helium-hydrogen (98/2%) microwave and glow discharge plasmas according to the methods given previously [7]. The glow discharge experimental set up was given previously [7]. The microwave experimental set up comprising a microwave discharge gas cell light source and an EUV spectrometer which was differentially pumped is shown in Figure 1. Helium-hydrogen (98/2%) gas mixture was flowed through a half inch diameter quartz tube at 1 torr, 20 torr, or 760 torr. The gas pressure inside the cell was maintained by flowing the mixture while monitoring the pressure with a 10 torr and 1000 torr MKS Baratron absolute pressure gauge. By the same method, the hydrogen alone and helium alone plasmas were run at 20 torr. The tube was fitted with an Opthos coaxial microwave cavity (Evenson cavity). The microwave generator was a Opthos model MPG-4M generator (Frequency: 2450 MHz). The input power to the plasma was set at 85 watts with air cooling of the cell.

The spectrometer was a normal incidence McPherson 0.2 meter monochromator (Model 302, Seya-Namioka type) equipped with a 1200 lines/mm holographic grating with a platinum coating. The wavelength region covered by the monochromator was $5-560\,nm$. The EUV spectrum was recorded with a channel electron multiplier (CEM) at $2500-3000\,V$. The wavelength resolution was about $0.02\,nm$ (FWHM) with an entrance and exit slit width of $50\,\mu m$. The increment was $0.2\,nm$ and the dwell time was $500\,ms$. Novel peak positions were based on a calibration against the known He I and He II lines.

To achieve higher sensitivity at the shorter EUV wavelengths, the light emission from a helium microwave plasma and a glow discharge plasma of a helium-hydrogen mixture (98/2%) maintained according to the methods given previously [7] were recorded with a McPherson 4° grazing incidence EUV spectrometer (Model 248/310G) equipped with a grating having 600 G/mm with a radius of curvature of $\approx 1\,m$. The angle of incidence was 87°. The wavelength region covered by the monochromator was $5-65\,nm$. The wavelength resolution was about $0.04\,nm$ (FWHM) with an entrance and exit slit width of $300\,\mu m$. A channel electron multiplier (CEM) at $2400\,V$ was used to detect the EUV light. The increment was $0.1\,nm$ and the dwell time was $1\,s$.

B. Line broadening measurements

The width of the 656.2 nm Balmer α line emitted from gas glow discharge plasmas having atomized hydrogen from pure hydrogen alone or with a mixture of 10% hydrogen and helium at 2 torr total pressure was measured according to the methods given previously [11]. The plasmas were maintained in a cylindrical stainless steel gas cell (9.21 cm in diameter and 14.5 cm in height) with an axial hollow cathode glow discharge electrode assembly comprised a stainless steel plate (4.2 cm diameter, 0.9 mm thick) anode and a circumferential stainless steel cylindrical frame (5.1 cm OD, 7.2 cm long) perforated with evenly spaced 1 cm diameter holes. The emission was viewed normal to the cell axis through a 1.6 mm thick UV-grade sapphire window with a 1.5 cm view diameter. The discharge was carried out under static gas conditions with a DC voltage of about 275 V which produced about 0.2 A of current. The plasma emission from the glow discharges was fiber-optically coupled through a 220F matching fiber adapter to a high resolution visible spectrometer with a resolution of $\pm 0.025\,nm$ over the spectral range $190-860\,nm$. The entrance and exit slits were set to $20\,\mu m$. The spectrometer was scanned between $656-657\,nm$ using a 0.01 nm step size. The signal was recorded by a PMT with a stand alone high voltage power supply (950 V) and an acquisition controller. The data was obtained in a single accumulation with a 1 second integration time.

C. Power balance measurements

The power balances of microwave plasmas of helium, krypton, and xenon alone and each noble gas with 10% hydrogen were determined by heat loss calorimetry [32] in the cell described in section A except that the cell was not air cooled. A K-type thermocouple ($\pm0.1\,°C$) housed in a stainless steel tube was placed axially inside the center of the 10 cm^3 plasma volume of the quartz microwave cell. The thermocouple was read with a multichannel computer data acquisition system. The gas in each case was ultrahigh purity grade or higher. The gas pressure inside the cell was maintained at about 300 mtorr with a noble gas flow rate of 9.3 sccm or an noble gas flow rate of 8.3 sccm and a hydrogen flow rate of 1 sccm. Each gas flow was controlled by a 0-20 sccm range mass flow controller (MKS 1179A21CS1BB) with a readout (MKS type 246). The cell pressure was monitored by a 0-10 torr MKS Baratron absolute pressure gauge.

No increase in temperature was observed when 10% hydrogen was added to krypton or xenon plasmas. In contrast, with the addition of 10% hydrogen to a helium plasma, the quartz wall was observed to melt in about 90 seconds unless the power was 30 W or less. Whereas, the helium alone plasma at 60 W input had a maximum temperature rise above room temperature, ΔT, of 178 °C at 90 seconds. Thus, to achieve a higher control ΔT to give greater analytical accuracy, the temperature rise of the inside of the cell was measured for 90 seconds with helium at 60 W input. The input power was stopped, and a cooling curve was measured. Then the experiment was repeated with the addition of 10% hydrogen to the helium run at only 30 W to prevent the cell from melting. In additional controls, noncatalysts krypton or xenon replaced helium.

III. RESULTS AND DISCUSSION

A. EUV Spectroscopy

The EUV emission was recorded from microwave and glow discharge plasmas of hydrogen, helium, and helium with 2% hydrogen

7

over the wavelength range $5-125\,nm$. In the case of hydrogen, no peaks were observed below $78\,nm$, and no spurious peaks or artifacts due to the grating or the spectrometer were observed. Only known He I and He II peaks were observed in the EUV spectra of the control helium microwave or glow discharge cell emission.

The EUV spectra ($15-50\,nm$) of the microwave cell emission of the helium-hydrogen mixture (98/2%) that was recorded at 1, 24, and 72 hours and the helium control (dotted curve) is shown in Figure 2. Ordinary hydrogen has no emission in these regions. Peaks observed at $45.6\,nm$, $37.4\,nm$, and $20.5\,nm$ which do not correspond to helium and increased with time were assigned to lower-energy hydrogen transitions in Table 1. The lines that corresponded to hydrogen transitions to lower electronic energy levels were not observed in the helium control. The pressure was increased from 20 torr to 760 torr. The peaks appeared slightly more intense at the lower pressure; so, the pressure was decreased to 1 torr and spectra were recorded.

At the 1 torr condition, additional novel peaks were observed in the short wavelength region. The short wavelength EUV spectrum ($5-50\,nm$) of the control hydrogen microwave cell emission (bottom curve) is shown in Figure 3. No spectrometer artifacts were observed at the short wavelengths. The short wavelength EUV spectrum ($5-50\,nm$) of the helium-hydrogen mixture (98/2%) microwave cell emission with a pressure of 1 torr (top curve) is also shown in Figure 3. Peaks observed at $14.15\,nm$, $13.03\,nm$, $10.13\,nm$, and $8.29\,nm$ which do not correspond to helium were assigned to lower-energy hydrogen transitions in Table 1. It is also proposed that the $30.4\,nm$ peak shown in Figures 2 and 3 was not entirely due to the He II transition. In the case of helium-hydrogen mixture, conspicuously absent was the $25.6\,nm$ ($48.3\,eV$) line of He II shown in Figure 2 which implies only a minor He II transition contribution to the $30.4\,nm$ peak.

A novel $63.3\,nm$ peak was observed in the EUV spectrum ($50-65\,nm$) of the helium-hydrogen mixture (98/2%) glow discharge cell emission shown in Figure 4. It is proposed that the $63.3\,nm$ peak arises from inelastic helium scattering of the $30.4\,nm$ peak. That is, the $\frac{1}{3} \to \frac{1}{4}$ transition yields a $40.8\,eV$ photon ($30.4\,nm$). When this photon strikes

$He\,(1s^2)$, $21.2\,eV$ is absorbed in the excitation to $He\,(1s^1 2p^1)$. This leaves a $19.6\,eV$ ($63.3\,nm$) photon and a $21.2\,eV$ ($58.4\,nm$) photon from $He\,(1s^1 2p^1)$. The intensity of the $58.4\,nm$ shown in Figure 4 was off-scale with 56,771 photons/sec. Thus, the transition $He\,(1s^2) \rightarrow He\,(1s^1 2p^1)$ dominated the inelastic scattering of EUV peaks. For the first nine peaks assigned as lower-energy hydrogen transitions or such transitions inelastically scattered by helium, the agreement between the predicted values and the experimental values shown in Table 1 is remarkable. It is also remarkable that the hydrino lines are moderately intense based on the low grating efficiency at these short wavelengths.

As shown in Figures 5 and 6, the ratio of the $L\beta$ peak to the $91.2\,nm$ peak of the helium-hydrogen microwave plasma was 2; whereas, the ratio of the $L\beta$ peak to the $91.2\,nm$ peak of the control hydrogen microwave plasma was 8 which indicates that the majority of the $91.2\,nm$ peak was due to a transition other than the binding of an electron by a proton. Based on the intensity, it is proposed that the majority of the $91.2\,nm$ peak was due to the $\frac{1}{2} \rightarrow \frac{1}{4}$ transition given in Table 1.

The energies for the hydrogen transitions given in Table 1 in order of energy are $13.6\,eV$, $27.2\,eV$, $40.8\,eV$, $54.4\,eV$, $81.6\,eV$, $95.2\,eV$, $108.8\,eV$, $122.4\,eV$ and $149.6\,eV$. The corresponding peaks are $91.2\,nm$, $45.6\,nm$, $30.4\,nm$ with $63.3\,nm$, $37.4\,nm$, $20.5\,nm$, $13.03\,nm$, $14.15\,nm$, $10.13\,nm$, and $8.29\,nm$, respectively. Thus, the lines identified as hydrogen transitions to electronic energy levels below the "ground" state corresponding to fractional quantum numbers correspond to energies of $q \cdot 13.6\,eV$ where $q = 1,2,3,4,6,7,8,9,$ or 11 or these lines inelastically scattered by helium atoms wherein $21.2\,eV$ was absorbed in the excitation of $He\,(1s^2)$ to $He\,(1s^1 2p^1)$. All other peaks besides those assigned to lower-energy hydrogen transitions could be assigned to He I, He II, second order lines, or atomic or molecular hydrogen emission. No known lines of helium or hydrogen explain the $q \cdot 13.6\,eV$ related set of peaks. Given that these spectra are readily repeatable, these peaks may have been overlooked in the past without considering the role of the helium scattering.

B. Line broadening measurements

9

The results of the 656.2 nm Balmer α line width measured with a high resolution ($\pm 0.025\,nm$) visible spectrometer on glow discharge plasmas having atomized hydrogen from pure hydrogen alone and helium-hydrogen (90/10%) is given in Figure 7. Using the method of Kuraica and Konjevic [33] and Videnocic et al. [34], the energetic hydrogen atom densities and energies were calculated. It was found that helium-hydrogen showed significant broadening corresponding to an average hydrogen atom temperature of 33-38 eV and an atom density of 3×10^{13} $atoms/cm^3$; whereas, pure hydrogen showed no excessive broadening corresponding to an average hydrogen atom temperature of $\approx 3\,eV$ and an atom density of only 5×10^{13} $atoms/cm^3$ ever though 10 times more hydrogen was present.

C. Power   balance   measurements

Since a significant increase in ion temperature was observed with helium-hydrogen discharge plasmas, and energetic hydrino lines were observed at short wavelengths in the corresponding microwave plasmas that required a very significant reaction rate due to low photon detection efficiency in this region, the power balance was measured on the helium-hydrogen microwave plasmas by heat loss calorimetry [32]. No increase in temperature with the addition of hydrogen to xenon was observed. In contrast, a remarkable temperature increase was observed when hydrogen was added to the helium microwave plasma. The temperature rise as a function of time for helium alone and the helium-hydrogen mixture (90/10%) is shown in Figure 8. The microwave input power to the helium alone was set at 60 W, and the input power to the helium-hydrogen mixture was 30 W. In both cases, the constant microwave input was maintained for 90 seconds and then terminated. The cooling curves were then recorded.

A conservative measure of the total output power was determined by taking the ratio of the areas of the helium-hydrogen temperature-rise-above-ambient-versus-time curve compared to that of helium only normalized by the ratio of the input powers. The ratio of the areas was determined to be about a factor of 10. The reactor volume was 10 cm^3 and the hydrogen flow rate was 1 sccm. Thus, with a microwave input power

of 30 W, the thermal output power was measured to be at least 300 W corresponding to a reactor temperature rise from room temperature to 900 °C within 90 seconds, a power density of over 30 MW/m^3, and an energy balance of over $-4 \times 10^5 \, kJ/mole \, H_2$ compared to the enthalpy of combustion of hydrogen of $-241.8 \, kJ/mole \, H_2$.

A more accurate measure was determined by modeling the heat flow from the quartz reactor wherein the parameters of the model were taken from the Newton cooling curves. Consider a small heat increment

$$dQ_t = P_{out}dt = dQ_m + dQ_l = CdT_h - CdT_c \qquad (11)$$

where Q_t is the total heat, Q_m is the measured heat, Q_l is the lost heat, P_{out} is the power output, t is time, C is the system heat capacity, dT_h is the temperature rise due to heating, and dT_c is the temperature drop due to cooling (dT_c is negative). The system heat capacity is a function of temperature, and at a given temperature, the power output can be expressed by the following equation,

$$P_{out} = C\left(\frac{dT_h}{dt} - \frac{dT_c}{dt}\right) \qquad (12)$$

The slopes dT_h/dt and dT_c/dt can be calculated from the heating and cooling curves, respectively. Assuming that, at a given temperature, the heat capacities of the two systems (system 1: helium alone; system 2: helium-hydrogen) are the same, $C_1 = C_2$, then the power ratio can be calculated by

$$R = \frac{P_{out,2}}{P_{out,1}} = \frac{\left(\dfrac{dT_{h,2}}{dt} - \dfrac{dT_{c,2}}{dt}\right)}{\left(\dfrac{dT_{h,1}}{dt} - \dfrac{dT_{c,1}}{dt}\right)} \qquad (13)$$

The slopes of the heating and cooling curves were calculated using the experimental data presented in Figure 8. The power ratios were calculated by Eq. (13) in the temperature range $\Delta T = 50 - 150 \, °C$, where ΔT was the difference between the plasma temperature and the room temperature, 24 °C. The calculated results are given in Table 2. The average power ratio is $R = 5.35$ with a standard deviation of 0.23. The following power balance existed in the microwave plasma systems,

$$P_{out} = P_{in} + P_{ex} \qquad (14)$$

where P_{in} was the input power and P_{ex} was the excess power. For the helium plasma, there was no excess power, $P_{ex,1} = 0$, $P_{out,1} = P_{in,1} = 60 \, W$.

Therefore, at microwave input power of $30\,W$, the thermal output power was measured to be $P_{out.\,2} = 321 \pm 14\,W$ corresponding to an excess power of $291 \pm 14\,W$ and an unoptimized gain of about 11 times the input power.

IV. CONCLUSION

We report that extreme ultraviolet (EUV) spectroscopy was recorded on microwave and glow discharges of helium with 2% hydrogen. Novel emission lines were observed with energies of $q \cdot 13.6\,eV$ where $q = 1,2,3,4,6,7,8,9,\,or\,11$ or these lines inelastically scattered by helium atoms wherein $21.2\,eV$ was absorbed in the excitation of $He\,(1s^2)$ to $He\,(1s^1 2p^1)$. These lines were identified as hydrogen transitions to electronic energy levels below the "ground" state corresponding to fractional quantum numbers. In glow discharge plasmas, an average hydrogen atom temperature of $33\text{-}38\,eV$ was observed by line broadening with the presence of helium ion catalyst with hydrogen; whereas, pure hydrogen plasmas showed no excessive broadening corresponding to an average hydrogen atom temperature of $\approx 3\,eV$.

Excess thermal power of about $300\,W$ and a gain of over an order of magnitude was observed from helium-hydrogen microwave plasmas. The power from the catalytic reaction of helium ions with atomic hydrogen corresponded to a volumetric power density of over $30\,MW/m^3$ which is about 100 times that of many coal fired electric power plants, and rivals some internal combustion engines. In addition, the presently observed and previously reported energy balances [13-14] were over $100\,eV/H\,atom$ which matched the present and previously reported EUV emission that corresponded to over $100\,eV/H\,atom$ [7-9, 17]. Since the net enthalpy released is at least 100 times that of combustion, the catalysis of atomic hydrogen represents a new source of energy with H_2O as the source of hydrogen fuel. Moreover, rather that air pollutants or radioactive waste, novel hydride compounds with potential commercial applications are the products [20-26]. Since the power is in the form of a plasma that may form at room temperature, high-efficiency, low cost direct energy conversion may be possible, thus, avoiding heat engines such as turbines and the severe limitations of fuel cells [27-28]. Significantly lower capital costs and lower commercial operating costs

1 2

than that of any known competing energy source are anticipated.

ACKNOWLEDGMENT

REFERENCES

1. R. Mills, *The Grand Unified Theory of Classical Quantum Mechanics*, January 2000 Edition, BlackLight Power, Inc., Cranbury, New Jersey, Distributed by Amazon.com; posted at www.blacklightpower.com.

2. R. Mills, "The Grand Unified Theory of Classical Quantum Mechanics", Global Foundation, Inc. Orbis Scientiae entitled *The Role of Attractive and Repulsive Gravitational Forces in Cosmic Acceleration of Particles The Origin of the Cosmic Gamma Ray Bursts*, (29th Conference on High Energy Physics and Cosmology Since 1964) Dr. Behram N. Kursunoglu, Chairman, December 14-17, 2000, Lago Mar Resort, Fort Lauderdale, FL.

3. R. Mills, "The Grand Unified Theory of Classical Quantum Mechanics", Global Foundation, Inc. Orbis Scientiae entitled *The Role of Attractive and Repulsive Gravitational Forces in Cosmic Acceleration of Particles The Origin of the Cosmic Gamma Ray Bursts*, (29th Conference on High Energy Physics and Cosmology Since 1964) Dr. Behram N. Kursunoglu, Chairman, December 14-17, 2000, Lago Mar Resort, Fort Lauderdale, FL, Kluwer Academic/Plenum Publishers, New York, pp. 243-258.

4. R. Mills, "The Grand Unified Theory of Classical Quantum Mechanics", Int. J. of Hydrogen Energy, in press.

5. R. Mills, "The Hydrogen Atom Revisited", Int. J. of Hydrogen Energy, Vol. 25, Issue 12, December, (2000), pp. 1171-1183.

6. R. Mills, The Nature of Free Electrons in Superfluid Helium--a Test of Quantum Mechanics and a Basis to Review its Foundations and Make a Comparison to Classical Theory, Int. J. Hydrogen Energy, Vol. 26, No. 10, (2001), pp. 1059-1096.

7. R. Mills, P. Ray, "Spectral Emission of Fractional Quantum Energy Levels of Atomic Hydrogen from a Helium-Hydrogen Plasma and the Implications for Dark Matter", Int. J. Hydrogen Energy, in press.

8. R. Mills, P. Ray, "Vibrational Spectral Emission of Fractional-Principal-Quantum-Energy-Level Hydrogen Molecular Ion", Int. J. Hydrogen Energy, in press.

9. R. Mills, P. Ray, Spectroscopic Identification of a Novel Catalytic Reaction of Potassium and Atomic Hydrogen and the Hydride Ion Product, Int. J. Hydrogen Energy, in press.

10. R. Mills, "Spectroscopic Identification of a Novel Catalytic Reaction of Atomic Hydrogen and the Hydride Ion Product", Int. J. Hydrogen Energy, Vol. 26, No. 10, (2001), pp. 1041-1058.

11. R. Mills and M. Nansteel, "Argon-Hydrogen-Strontium Plasma Light Source", IEEE Transactions on Plasma Science, submitted.

12. R. Mills, M. Nansteel, and Y. Lu, "Excessively Bright Hydrogen-Strontium Plasma Light Source Due to Energy Resonance of Strontium with Hydrogen", European Journal of Physics D, submitted.

13. R. Mills, A. Voigt, P. Ray, M. Nanstell, "Measurement of Hydrogen Balmer Line Broadening and Thermal Power Balances of Noble Gas-Hydrogen Discharge Plasmas", Int. J. Hydrogen Energy, submitted.

14. R. Mills, N. Greenig, S. Hicks, "Optically Measured Power Balances of Anomalous Discharges of Mixtures of Argon, Hydrogen, and Potassium, Rubidium, Cesium, or Strontium Vapor", Int. J. Hydrogen Energy, submitted.

15. R. Mills, M. Nansteel, and Y. Lu, "Observation of Extreme Ultraviolet Hydrogen Emission from Incandescently Heated Hydrogen Gas with Strontium that Produced an Anomalous Optically Measured Power Balance", Int. J. Hydrogen Energy, Vol. 26, No. 4, (2001), pp. 309-326.

16. R. Mills, J. Dong, Y. Lu, "Observation of Extreme Ultraviolet Hydrogen Emission from Incandescently Heated Hydrogen Gas with Certain Catalysts", Int. J. Hydrogen Energy, Vol. 25, (2000), pp. 919-943.

17. R. Mills, "Observation of Extreme Ultraviolet Emission from Hydrogen-KI Plasmas Produced by a Hollow Cathode Discharge", Int. J. Hydrogen Energy, Vol. 26, No. 6, (2001), pp. 579-592.

18. R. Mills, "Temporal Behavior of Light-Emission in the Visible Spectral Range from a Ti-K2CO3-H-Cell", Int. J. Hydrogen Energy, Vol. 26, No. 4, (2001), pp. 327-332.

19. R. Mills, T. Onuma, and Y. Lu, "Formation of a Hydrogen Plasma from an Incandescently Heated Hydrogen-Catalyst Gas Mixture with an

Anomalous Afterglow Duration", Int. J. Hydrogen Energy, Vol. 26, No. 7, July, (2001), pp. 749-762.

20. R. Mills, B. Dhandapani, M. Nansteel, J. He, A. Voigt, "Identification of Compounds Containing Novel Hydride Ions by Nuclear Magnetic Resonance Spectroscopy", Int. J. Hydrogen Energy, Vol. 26, No. 9, Sept. (2001), pp. 965-979.

21. R. Mills, B. Dhandapani, N. Greenig, J. He, "Synthesis and Characterization of Potassium Iodo Hydride", Int. J. of Hydrogen Energy, Vol. 25, Issue 12, December, (2000), pp. 1185-1203.

22. R. Mills, "Novel Inorganic Hydride", Int. J. of Hydrogen Energy, Vol. 25, (2000), pp. 669-683.

23. R. Mills, "Novel Hydrogen Compounds from a Potassium Carbonate Electrolytic Cell", Fusion Technology, Vol. 37, No. 2, March, (2000), pp. 157-182.

24. R. Mills, B. Dhandapani, M. Nansteel, J. He, T. Shannon, A. Echezuria, "Synthesis and Characterization of Novel Hydride Compounds", Int. J. of Hydrogen Energy, Vol. 26, No. 4, (2001), pp. 339-367.

25. R. Mills, "Highly Stable Novel Inorganic Hydrides", Journal of Materials Research, submitted.

26. R. Mills, W. Good, A. Voigt, Jinquan Dong, "Minimum Heat of Formation of Potassium Iodo Hydride", Int. J. Hydrogen Energy, Vol. 26, No. 11, Oct., (2001), pp. 1199-1208.

27. R. Mills, "BlackLight Power Technology-A New Clean Hydrogen Energy Source with the Potential for Direct Conversion to Electricity", Proceedings of the National Hydrogen Association, 12 th Annual U.S. Hydrogen Meeting and Exposition, *Hydrogen: The Common Thread*, The Washington Hilton and Towers, Washington DC, (March 6-8, 2001), pp. 671-697.

28. R. Mills, "BlackLight Power Technology-A New Clean Energy Source with the Potential for Direct Conversion to Electricity", Global Foundation International Conference on "Global Warming and Energy Policy", Dr. Behram N. Kursunoglu, Chairman, Fort Lauderdale, FL, November 26-28, 2000, Kluwer Academic/Plenum Publishers, New York, pp. 1059-1096.

29. B. J. Thompson, Handbook of Nonlinear Optics, Marcel Dekker, Inc., New York, (1996), pp. 497-548.

30. Y. R. Shen, The Principles of Nonlinear Optics, John Wiley & Sons, New York, (1984), pp. 203-210.

31. B. de Beauvoir, F. Nez, L. Julien, B. Cagnac, F. Biraben, D. Touahri, L. Hilico, O. Acef, A. Clairon, and J. J. Zondy, Physical Review Letters, Vol. 78, No. 3, (1997), pp. 440-443.

32. C. Chen, T. Wei, L. R. Collins, and J. Phillips, "Modeling the discharge region of a microwave generated hydrogen plasma", J. Phys. D: Appl. Phys., Vol. 32, (1999), pp. 688-698.

33. M. Kuraica, N. Konjevic, "Line shapes of atomic hydrogen in a plane-cathode abnormal glow discharge", Physical Review A, Volume 46, No. 7, October (1992), pp. 4429-4432.

34. I. R. Videnoclc, N. Konjevic, M. M. Kuraica, "Spectroscopic investigations of a cathode fall region of the Grimm-type glow discharge", Spectrochimica Acta, Part B, Vol. 51, (1996), pp. 1707-1731.

Table 1. Observed line emission from helium-hydrogen plasmas assigned to the dominant disproportionation reactions given by Eqs. (4-7) and helium inelastic scattered peaks of hydrogen transitions, wherein the photon strikes $He\,(1s^2)$ and $21.2\,eV$ is absorbed in the excitation to $He\,(1s^1 2p^1)$.

Observed Line (nm)	Predicted (Mills) (nm)	Assignment (Mills)	Figure #
8.29	8.29	$H\left[\dfrac{a_H}{3}\right] + H\left[\dfrac{a_H}{3}\right] \rightarrow H\left[\dfrac{a_H}{5}\right] + H\left[\dfrac{a_H}{2}\right] + 149.6\,eV$	3
10.13	10.13	$H\left[\dfrac{a_H}{2}\right] + H\left[\dfrac{a_H}{2}\right] \rightarrow H\left[\dfrac{a_H}{4}\right] + H\left[a_H\right] + 122.4\,eV$	3
13.03[a]	13.03	$H\left[\dfrac{a_H}{3}\right] + H\left[\dfrac{a_H}{3}\right] \rightarrow H\left[\dfrac{a_H}{5}\right] + H^+ + e^- + 95.2\,eV$	3
14.15	14.15	$H\left[\dfrac{a_H}{2}\right] + H\left[\dfrac{a_H}{2}\right] \rightarrow H\left[\dfrac{a_H}{4}\right] + H^+ + e^- + 108.8\,eV$ $108.8\,eV + He\,(1s^2) \rightarrow He\,(1s^1 2p^1) \rightarrow +87.59\,eV$	3
20.5	20.5	$H\left[\dfrac{a_H}{4}\right] + H\left[\dfrac{a_H}{2}\right] \rightarrow H\left[\dfrac{a_H}{5}\right] + H\left[a_H\right] + 81.6\,eV$ $81.6\,eV + He\,(1s^2) \rightarrow He\,(1s^1 2p^1) \rightarrow +60.39\,eV$	2, 3
30.4	30.4	$H\left[\dfrac{a_H}{3}\right] + H\left[\dfrac{a_H}{2}\right] \rightarrow H\left[\dfrac{a_H}{4}\right] + H^+ + e^- + 40.8\,eV$	2, 3
30.4	30.4	$He^+(n=2) \rightarrow He^+(n=1) + 40.8\,eV$[b]	2, 3
37.4	37.4	$H\left[a_H\right] \xrightarrow{He^*} H\left[\dfrac{a_H}{3}\right] + 54.4\,eV + 54.4\,eV$ $54.4\,eV + He\,(1s^2) \rightarrow He\,(1s^1 2p^1) \rightarrow +33.19\,eV$	2, 3
45.6	45.6	$H\left[\dfrac{a_H}{3}\right] + H\left[\dfrac{a_H}{3}\right] \rightarrow H\left[\dfrac{a_H}{4}\right] + H\left[\dfrac{a_H}{2}\right] + 27.2\,eV$	2, 3
58.4	58.4	$He\,(1s^1 2p^1) \rightarrow He\,(1s^2) + 21.2\,eV$[c]	4

63.3	63.3	$H\left[\dfrac{a_H}{3}\right] + H\left[\dfrac{a_H}{2}\right] \rightarrow H\left[\dfrac{a_H}{4}\right] + H^+ + e^- + 40.8\ eV$	4
		$40.8\ eV + He\ (1s^2) \rightarrow He\ (1s^1 2p^1) \rightarrow +19.59\ eV$	
63.3	63.3	$He^+(n=2) \rightarrow He^+(n=1) + 40.8\ eV$ [b]	4
		$40.8\ eV + He\ (1s^2) \rightarrow He\ (1s^1 2p^1) \rightarrow +19.59\ eV$	
91.2	91.2	$H\left[\dfrac{a_H}{2}\right] + H\left[\dfrac{a_H}{2}\right] \rightarrow H\left[\dfrac{a_H}{3}\right] + H^+ + e^- + 13.6\ eV$	5
91.2	91.2	$H^+ + e^- \rightarrow H[a_H] + 13.6\ eV$ [d]	6

[a] Weak shoulder on the 14.15 nm peak.

[b] In Figures 2 and 3, the peak corresponding to $He^+(n=3) \rightarrow He^+(n=1) + 48.35\ eV$ (25.6 nm)was absent which makes this assignment difficult.

[c] The intensity was 56,771 photons/sec in Figure 4; thus, the transition $He\ (1s^2) \rightarrow He\ (1s^1 2p^1)$ dominated the inelastic scattering of EUV peaks.

[d] The ratio of the Lβ peak to the 91.2 nm peak of the helium-hydrogen plasma shown in Figure 5 was 2; whereas, the ratio of the Lβ peak to the 91.2 nm peak of the control hydrogen plasma shown in Figure 6, was 8 which makes this assignment difficult.

Table 2. Calculation of Power Ratios between Helium-Hydrogen and Helium Plasmas.

ΔT (°C)	$dT_{h,1}/dt$ (°C/sec)	$dT_{c,1}/dt$ (°C/sec)	$dT_{h,2}/dt$ (°C/sec)	$dT_{c,2}/dt$ (°C/sec)	Power Ratio, R
50	10.731	-0.800	55.951	-0.989	4.938
60	9.801	-1.004	54.893	-1.118	5.183
70	9.020	-1.255	53.874	-1.266	5.367
80	8.354	-1.549	52.892	-1.433	5.486
90	7.779	-1.876	51.946	-1.619	5.548
100	7.279	-2.216	51.032	-1.819	5.566
110	6.839	-2.551	50.150	-2.025	5.557
120	6.449	-2.879	49.299	-2.222	5.523
130	6.101	-3.235	48.475	-2.390	5.448
140	5.789	-3.716	47.679	-2.507	5.280
150	5.507	-4.561	46.908	-2.555	4.913

Figure Captions

Figure 1. The experimental set up comprising a microwave discharge gas cell light source and an EUV spectrometer which was differentially pumped.

Figure 2. The EUV spectra $(15-50\ nm)$ of the microwave cell emission of the helium-hydrogen mixture (98/2%) recorded at 1, 24, and 72 hours with a normal incidence EUV spectrometer and a CEM, and control helium (dotted curve) recorded with a 4° grazing incidence EUV spectrometer and a CEM. The pressure was maintained at 20 torr. Only known He I and He II peaks were observed with the helium control. Reproducible novel emission lines that increased with time were observed at $45.6\ nm$ and $30.4\ nm$ with energies of $q \cdot 13.6\ eV$ where $q = 2\ or\ 3$ and at $37.4\ nm$ and $20.5\ nm$ with energies of $q \cdot 13.6\ eV$ where $q = 4\ or\ 6$ that were inelastically scattered by helium atoms wherein $21.2\ eV$ ($58.4\ nm$) was absorbed in the excitation of $He\,(1s^2)$. These lines were identified in Table 1 as hydrogen transitions to electronic energy levels below the "ground" state corresponding to fractional quantum numbers.

Figure 3. The short wavelength EUV spectra $(5-50\ nm)$ of the microwave cell emission of the helium-hydrogen mixture (98/2%) (top curve) and control hydrogen (bottom curve) recorded with a normal incidence EUV spectrometer and a CEM. No hydrogen emission was observed in this region, and no instrument artifacts were observed. Reproducible novel emission lines were observed at $45.6\ nm$, $30.4\ nm$, $13.03\ nm$, $10.13\ nm$, and $8.29\ nm$ with energies of $q \cdot 13.6\ eV$ where $q = 2,3,7,9,\ or\ 11$ and at $37.4\ nm$, $20.5\ nm$, and $14.15\ nm$ with energies of $q \cdot 13.6\ eV$ where $q = 4,6,\ or\ 8$ that were inelastically scattered by helium atoms wherein $21.2\ eV$ ($58.4\ nm$) was absorbed in the excitation of $He\,(1s^2)$. These lines were identified in Table 1 as hydrogen transitions to electronic energy levels below the "ground" state corresponding to fractional quantum numbers.

Figure 4. The EUV spectrum $(50-65\ nm)$ of the helium-hydrogen mixture (98/2%) glow discharge cell emission recorded with a 4° grazing incidence EUV spectrometer and a CEM. The pressure was maintained at 400 mtorr. A novel line was observed at $63.3\ nm$ corresponding to the $30.4\ nm$ lower-energy hydrogen transition line shown in Figures 2 and 3

1

and Table 1 that was inelastically scattered by helium atoms wherein 21.2 eV (58.4 nm) was absorbed in the excitation of He ($1s^2$).
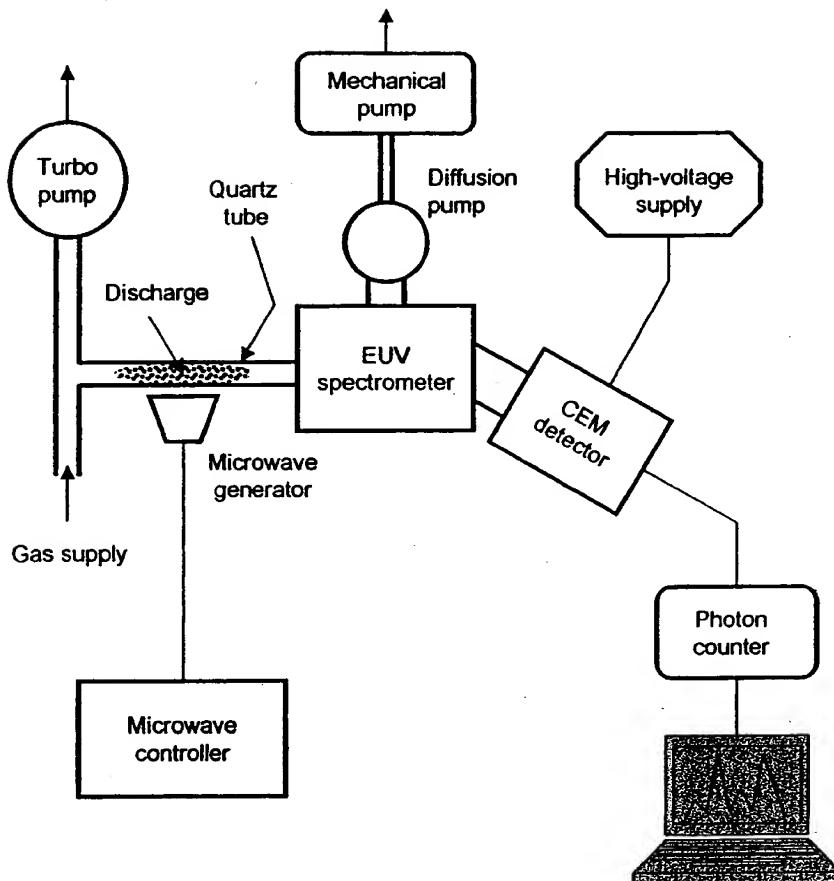
Figure 5. The EUV spectrum (88 – 125 nm) of the helium-hydrogen mixture (98/2%) microwave cell emission recorded with a normal incidence EUV spectrometer and a CEM. The pressure was maintained at 20 torr. An emission line was observed at 91.2 nm with an energy of $q \cdot 13.6\,eV$ where $q = 1$ which was identified in Table 1 as hydrogen transitions to electronic energy levels below the "ground" state corresponding to fractional quantum numbers based on the 91.2 nm line intensity relative to $L\beta$ compared to that of the control hydrogen plasma.

Figure 6. The EUV spectrum (80 – 105 nm) of the control hydrogen microwave discharge cell emission recorded with a normal incidence EUV spectrometer and a CEM.

Figure 7. The 656.2 nm Balmer α line width recorded with a high resolution (±0.025 nm) visible spectrometer on a helium-hydrogen mixture (90/10%) discharge plasma. Significant broadening was observed corresponding to an average hydrogen atom temperature of 33 - 38 eV.

Figure 8. The temperature rise as a function of time for helium alone and the helium-hydrogen mixture (90/10%) with microwave input power set at 60 W and 30 W, respectively. In both cases, the constant microwave input was maintained for 90 seconds and then terminated. The cooling curves were then recorded. The maximum ΔT for helium-hydrogen mixture and helium alone was 873 °C and 178 °C, respectively. The thermal output power of the helium-hydrogen plasma was determined to be at least 300 W.
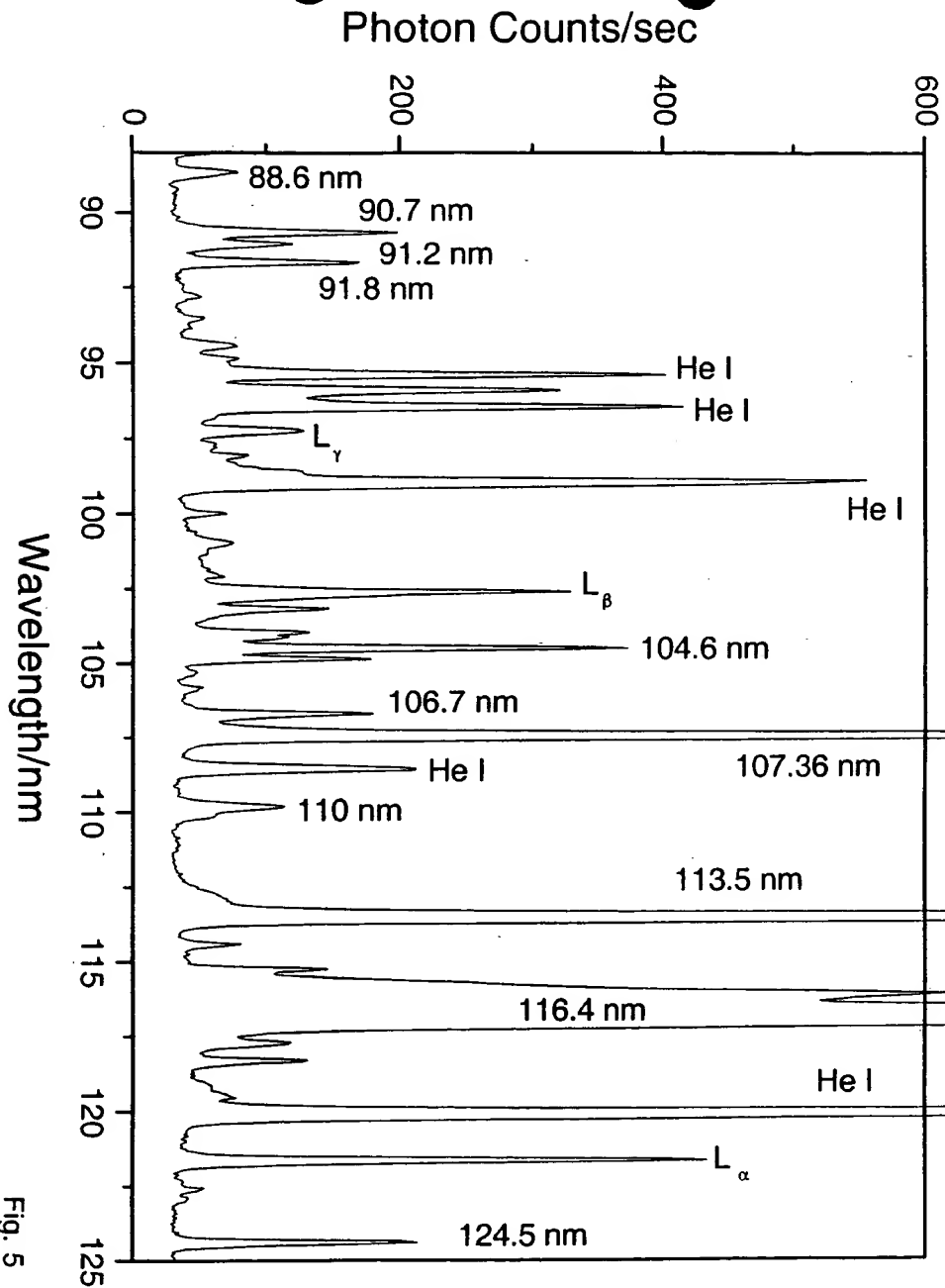
2

Fig. 1

Turbo pump

Quartz tube

Discharge

Mechanical pump

Diffusion pump

High-voltage supply

EUV spectrometer

CEM detector

Microwave generator

Gas supply

Microwave controller

Photon counter

Fig. 2

Fig. 3

Photon Counts/Sec

Wavelength/nm

H₂ Only

He + H₂

8.29 nm
10.13 nm
14.15 nm
20.5 nm
30.4 nm
37.4 nm
44.37 nm
45.6 nm

Photon Counts/sec

Wavelength/nm

52.4 nm
53.7 nm
58.4 nm
59.1 nm
60.2 nm
60.8 nm
61.6 nm
62.5 nm
62.8 nm
63.3 nm
63.9 nm
64.1 nm
64.5 nm

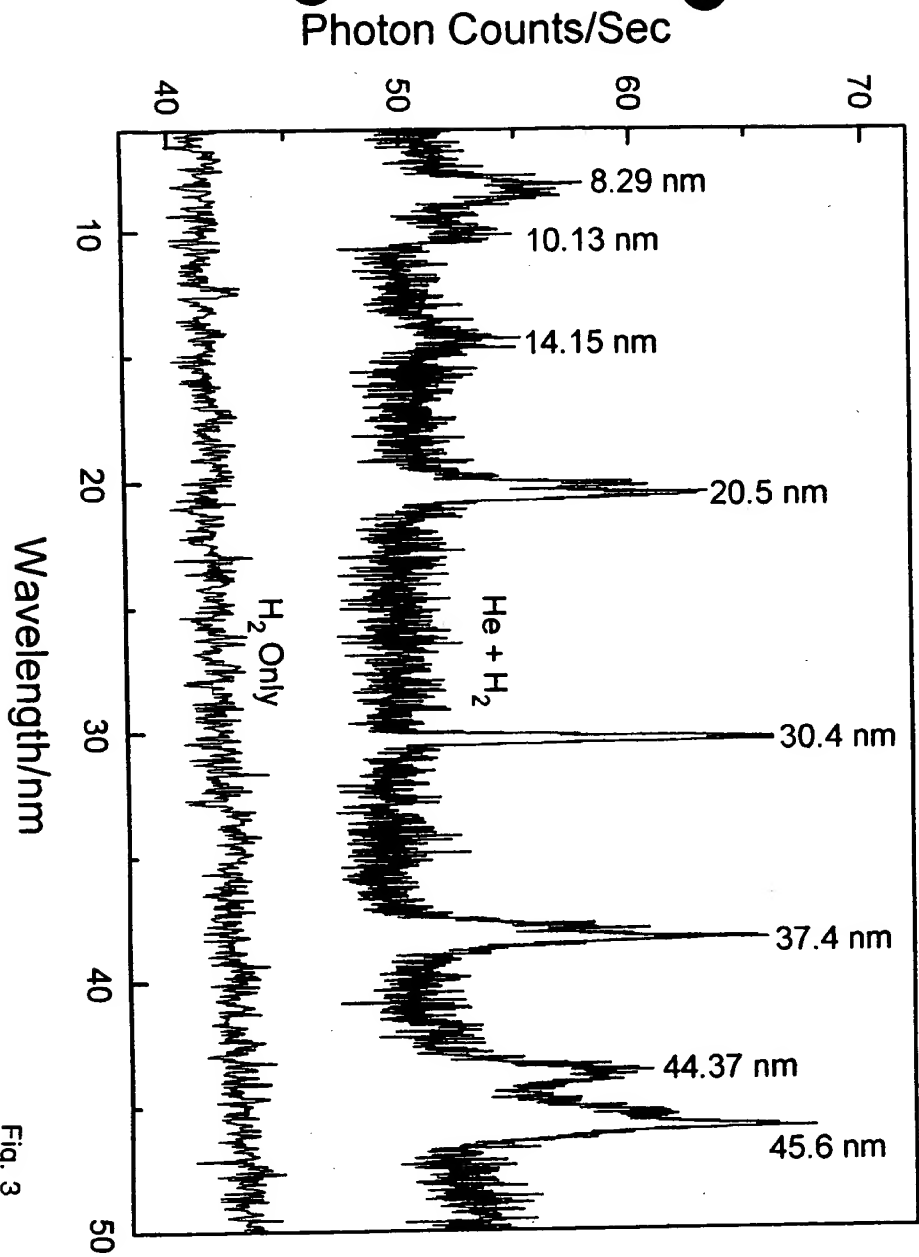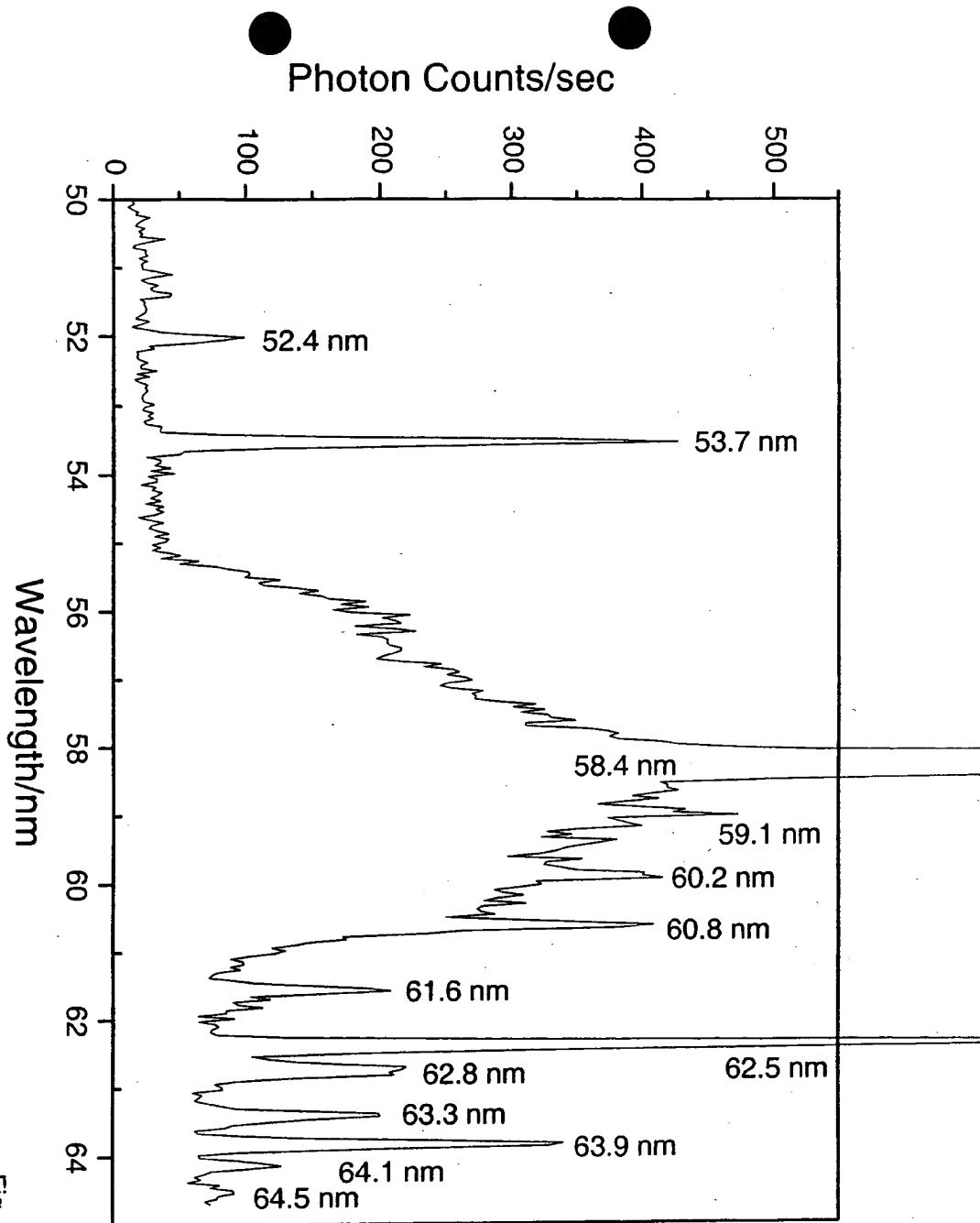Fig. 4

Fig. 5
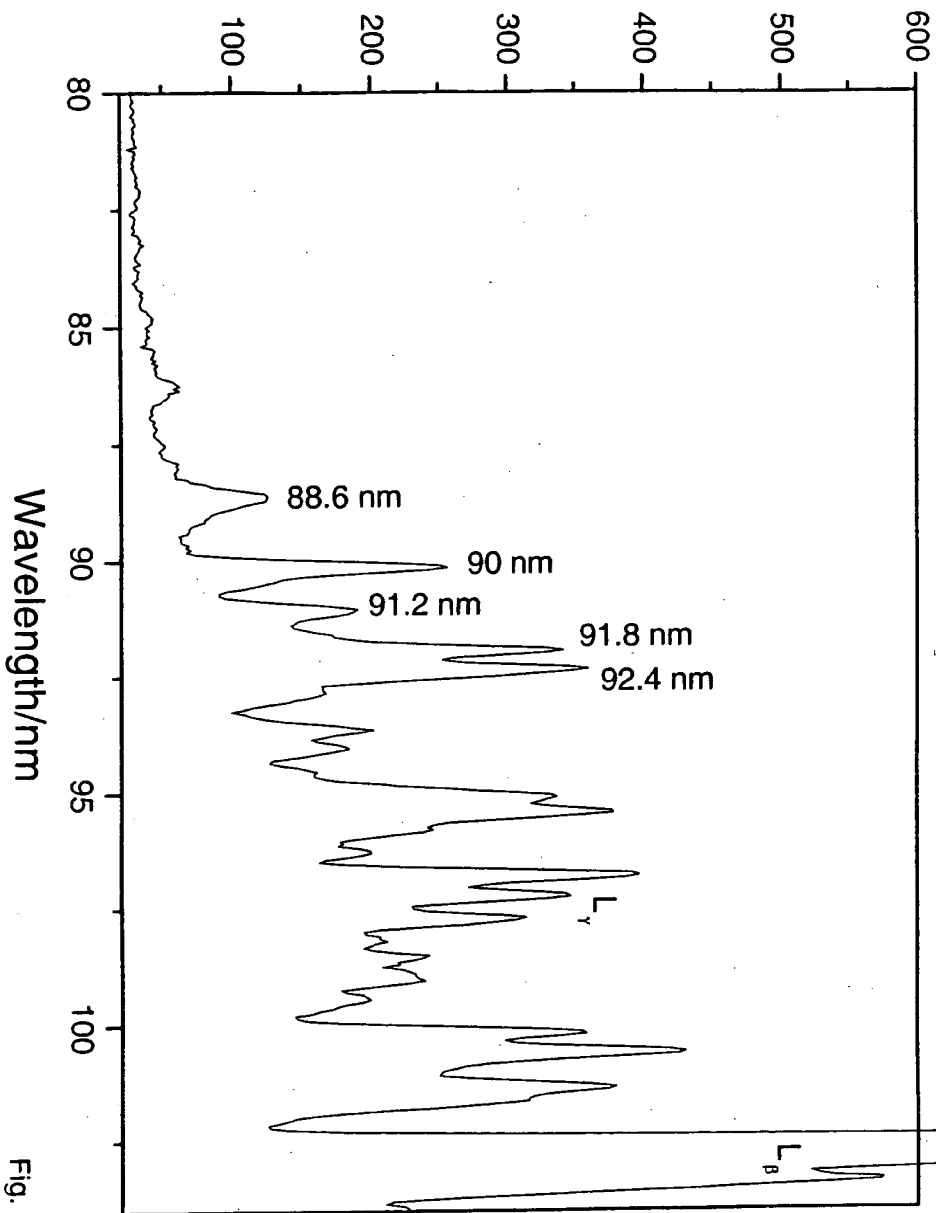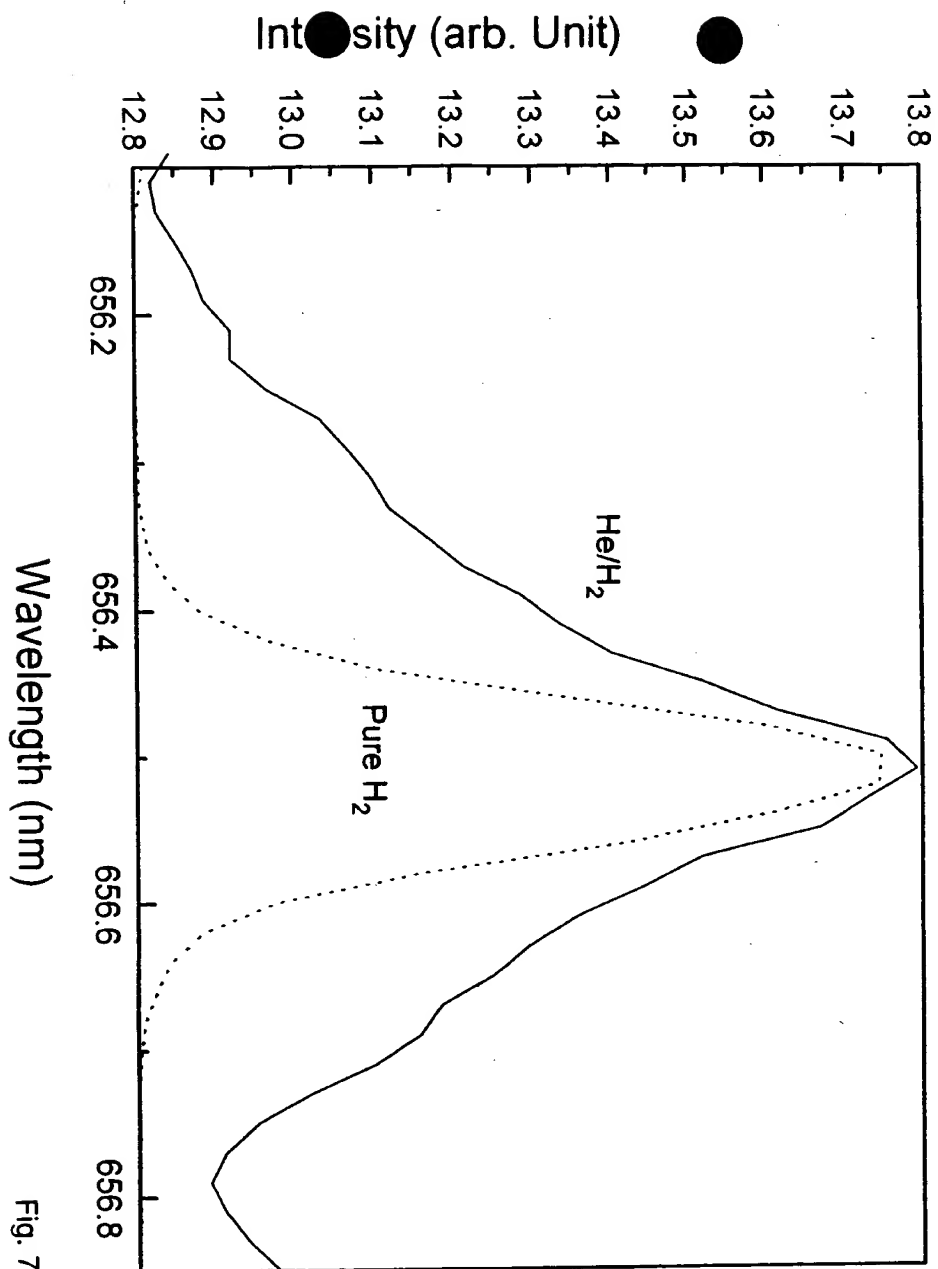
Fig. 6

Fig. 7
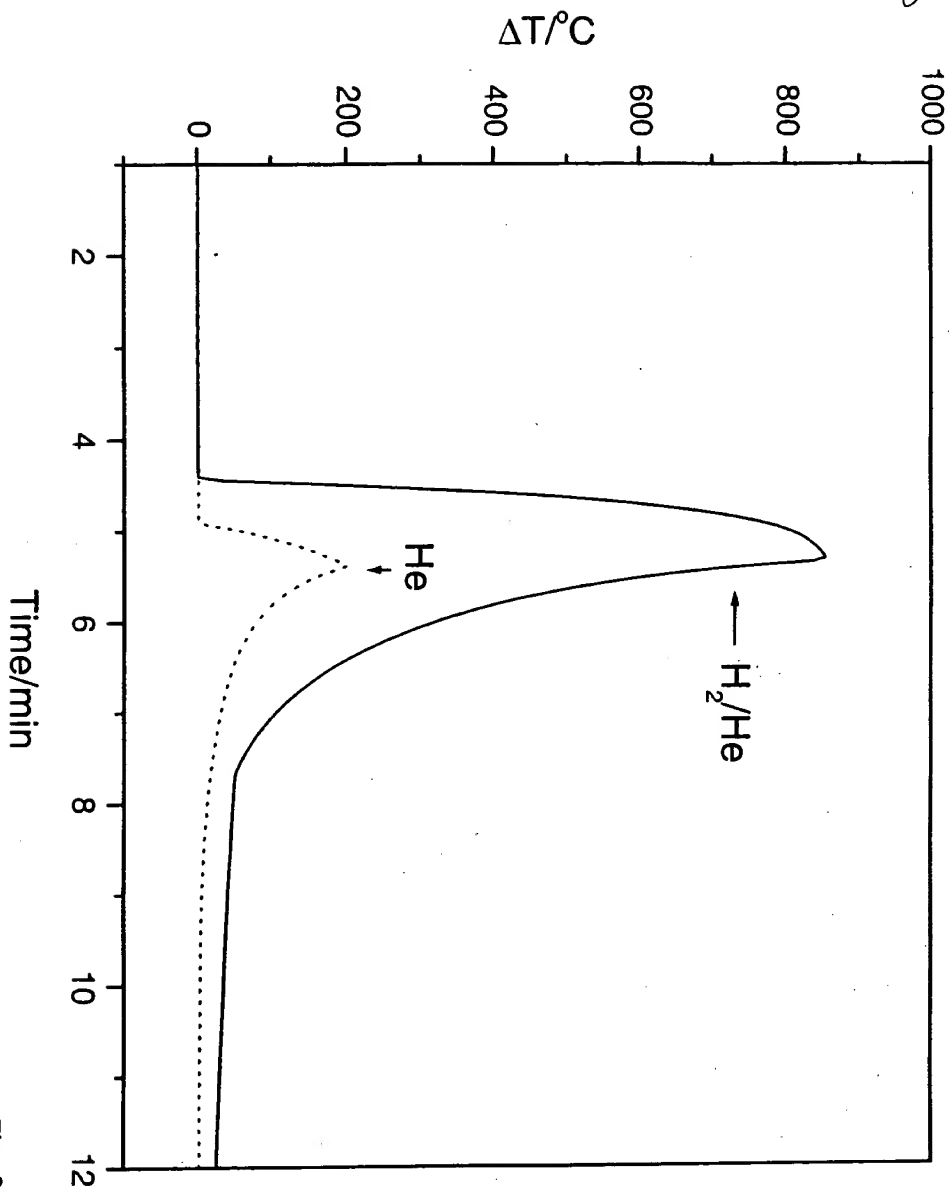
Fig. 8

Spectroscopic Identification of a Novel Catalytic Reaction of Rubidium with Atomic Hydrogen and the Hydride Ion Product

R. L. Mills

P. Ray

BlackLight Power, Inc.

493 Old Trenton Road

Cranbury, NJ 08512

ABSTRACT

From a solution of a Schrödinger-type wave equation with a nonradiative boundary condition based on Maxwell's equations, Mills predicts that atomic hydrogen may undergo a catalytic reaction with certain atomized elements and ions which singly or multiply ionize at integer multiples of the potential energy of atomic hydrogen, $27.2\,eV$. The reaction involves a nonradiative energy transfer to form a hydrogen atom that is lower in energy than unreacted atomic hydrogen with the release of energy. One such atomic catalytic system involves Rb^+ from $RbNO_3$. Since the second ionization energy of rubidium is $27.28\,eV$, the reaction Rb^+ to Rb^{2+} has a net enthalpy of reaction of $27.28\,eV$. Intense extreme ultraviolet (EUV) emission was observed from incandescently heated atomic hydrogen and the atomized Rb^+ catalyst that generated an anomalous plasma at low temperatures (e.g. $\approx 10^3\,K$) and an extraordinary low field strength of about 1-2 V/cm. No emission was observed with $RbNO_3$ or hydrogen alone or when noncatalysts, $Mg(NO_3)_2$ or $Al(NO_3)_3$, replaced $RbNO_3$ with hydrogen. Emission was observed from Rb^{2+} that confirmed the resonant nonradiative energy transfer of $27.2\,eV$ from atomic hydrogen to atomic Rb^+. The catalysis product, a lower-energy hydrogen atom, was predicted to be a highly reactive intermediate which further reacts to form a novel hydride ion. The predicted hydride ion of hydrogen catalysis by Rb^+ is the hydride ion $H^-(1/2)$. This ion was observed spectroscopically at $407\,nm$ corresponding to its predicted binding energy of $3.05\,eV$.

1

I. INTRODUCTION

Based on the solution of a Schrödinger-type wave equation with a nonradiative boundary condition based on Maxwell's equations, Mills [1-35] predicts that atomic hydrogen may undergo a catalytic reaction with certain atomized elements or certain gaseous ions which singly or multiply ionize at integer multiples of the potential energy of atomic hydrogen, $27.2\,eV$. For example, cesium atoms ionize at an integer multiple of the potential energy of atomic hydrogen, $m \cdot 27.2\,eV$. The enthalpy of ionization of Cs to Cs^{2+} has a net enthalpy of reaction of $27.05135\,eV$, which is equivalent to $m = 1$ [36]. And, the reaction Ar^+ to Ar^{2+} has a net enthalpy of reaction of $27.63\,eV$, which is equivalent to $m = 1$ [36]. In each case, the reaction involves a nonradiative energy transfer to form a hydrogen atom that is lower in energy than unreacted atomic hydrogen. The product hydrogen atom has an energy state that corresponds to a fractional principal quantum number. Recent analysis of mobility and spectroscopy data of individual electrons in liquid helium show direct experimental confirmation that electrons may have fractional principal quantum energy levels [5].

Emission was observed previously from a continuum state of Cs^{2+} and Ar^{2+} at $53.3\,nm$ and $45.6\,nm$, respectively [13]. The single emission feature with the absence of the other corresponding Rydberg series of lines from these species confirmed the resonant nonradiative energy transfer of $27.2\,eV$ from atomic hydrogen to atomic cesium or Ar^+. The catalysis product, a lower-energy hydrogen atom, was predicted to be a highly reactive intermediate which further reacts to form a novel hydride ion. The predicted hydride ion of hydrogen catalysis by either cesium atom or Ar^+ catalyst is the hydride ion $H^-(1/2)$. This ion was observed spectroscopically at $407\,nm$ corresponding to its predicted binding energy of $3.05\,eV$.

The catalyst mechanism of potassium was also confirmed spectroscopically [12]. The first, second, and third ionization energies of potassium are $4.34066\,eV$, $31.63\,eV$, and $45.806\,eV$, respectively. The triple ionization ($t = 3$) reaction of K to K^{3+}, then, has a net enthalpy of reaction of $81.7766\,eV$, which is equivalent to $3 \cdot 27.2\,eV$. Characteristic emission was observed from K^{3+} which confirmed the resonant nonradiative energy

2

transfer of $3 \cdot 27.2 \, eV$ from atomic hydrogen to atomic potassium. The predicted $H^-(1/4)$ hydride ion of hydrogen catalysis by potassium catalyst was observed at $110 \, nm$ corresponding to its predicted binding energy of $11.2 \, eV$. The catalytic reactions with the formation of the hydride ions are given in the Appendix.

Additional prior related studies that support the possibility of a novel reaction of atomic hydrogen which produces a chemically generated or assisted plasma (rt-plasma) and produces novel hydride compounds include extreme ultraviolet (EUV) spectroscopy [6-9, 11-18, 21-23], characteristic emission from catalysis and the hydride ion products [9-13], lower-energy hydrogen emission [4, 6, 7-8, 17], plasma formation [9, 11-15, 21-22, 24-25], Balmer α line broadening [7, 9, 11, 14-15, 17-19], elevated electron temperature [7, 17], anomalous plasma afterglow duration [24-25], power generation [7, 9, 14-17, 19-21, 32], and analysis of chemical compounds [26-32].

Typically the emission of vacuum ultraviolet light from hydrogen gas is achieved using discharges at high voltage, synchrotron devices, high power inductively coupled plasma generators, or a plasma is created and heated to extreme temperatures by RF coupling (e.g. $>10^6 \, K$) with confinement provided by a toroidal magnetic field. Observation of intense EUV emission at low temperatures (e.g. $\approx 10^3 \, K$) from atomic hydrogen and certain atomized elements or certain gaseous ions [9, 11-15, 21-22, 24-25] has been reported previously. The only pure elements that were observed to emit EUV were those wherein the ionization of t electrons from an atom to a continuum energy level is such that the sum of the ionization energies of the t electrons is approximately $m \cdot 27.2 \, eV$ where t and m are each an integer. K, Cs, and Sr atoms and Rb^+ ion ionize at integer multiples of the potential energy of atomic hydrogen and caused emission. Whereas, the chemically similar atoms, Na, Mg, and Ba, do not ionize at integer multiples of the potential energy of atomic hydrogen and caused no emission.

The observed EUV emission could not be explained by conventional chemistry; rather, it must have been due to a novel chemical reaction between catalyst and atomic hydrogen. The catalysis of hydrogen involves the nonradiative transfer of energy from atomic hydrogen to a catalyst which may then release the transferred energy by radiative and

3

nonradiative mechanisms. As a consequence of the nonradiative energy transfer, the hydrogen atom becomes unstable and emits further energy until it achieves a lower-energy nonradiative state having a principal energy level given by Eqs. (1-2) of the Appendix.

The energy released during catalysis may undergo internal conversion and ionize or excite molecular and atomic hydrogen resulting in hydrogen emission which includes well characterized ultraviolet lines such as the Lyman series. A search for the predicted Lyman series emission due to the catalyst mechanism comprising the nonradiative transfer of $27.2\ eV$ from atomic hydrogen to Rb^+ to form Rb^{2+}, and emission of the hydride ion product $H^-(1/2)$ was performed using EUV and visible (VIS) spectroscopy. (The catalytic reaction of Rb^+ and binding energy of the product hydride $H^-(1/2)$ are given in the Appendix.)

II. EXPERIMENTAL

A. EUV and Visible Spectroscopy

Due to the extremely short wavelength of this radiation, "transparent" optics do not exist for EUV spectroscopy. Therefore, a windowless arrangement was used wherein the source was connected to the same vacuum vessel as the grating and detectors of the EUV spectrometer. Differential pumping permitted a high pressure in the cell as compared to that in the spectrometer. This was achieved by pumping on the cell outlet and pumping on the grating side of the collimator that served as a pin-hole inlet to the optics. The spectrometer was continuously evacuated to $10^{-4}-10^{-6}$ Torr by a turbomolecular pump with the pressure read by a cold cathode pressure gauge. The EUV spectrometer was connected to the cell light source with a 1.5 mm X 5 mm collimator which provided a light path to the slits of the EUV spectrometer. The collimator also served as a flow constrictor of gas from the cell. Valves were between the cell and the mechanical pump, the cell and the monochromator, and the monochromator and its turbo pump. The cell was operated under gas flow conditions while maintaining a constant gas pressure in the cell with a mass flow controller.

EUV and VIS spectra were recorded on light emitted from plasmas of hydrogen with $RbNO_3$. The experimental set up shown in Figure 1 comprised a quartz cell which was 500 mm in length and 50 mm in diameter. The entire quartz cell was enclosed in an Alumina insulation package. Several K-type thermocouples were located in the insulation. The thermocouples were monitored with a multichannel computer data acquisition system. A Pyrex cap sealed to the quartz cell with a Viton O ring and a C-clamp incorporated ports for gas inlet, outlet, and photon detection. A tungsten filament (0.508 mm in diameter and 800 cm in length, total resistance ~2.5 Ω) heater and hydrogen dissociator were in the quartz tube as well as a cylindrical titanium screen (300 mm long and 40 mm in diameter) that served as a second hydrogen dissociator. The filament was coiled on a grooved ceramic tube support to maintain its shape when heated. The return lead passed through the inside of the ceramic tube. The filament leads were covered by a Alumina sheath.

The light emission phenomena was studied for 1.) H_2 alone, 2.) $Mg(NO_3)_2$ alone, 3.) $Al(NO_3)_3$ alone, 4.) $RbNO_3$ alone, 5.) $Mg(NO_3)_2$ with flowing hydrogen, 6.) $Al(NO_3)_3$ with flowing hydrogen, and 7.) $RbNO_3$ with flowing hydrogen. The inorganic test materials were coated on the titanium screen dissociator by the method of wet impregnation. The screen was coated by dipping it in a 0.6 M $RbNO_3/10\%$ H_2O_2, 0.6 M $Mg(NO_3)_2/10\%$ H_2O_2, or 0.6 M $Al(NO_3)_3/10\%$ H_2O_2 aqueous solution, and the crystalline material was dried on the surface by heating for 12 hours in a drying oven at 130 °C. A new dissociator was used for each experiment. The test materials were volatilized by the filament heater.

The titanium screen was electrically floated. Power was applied to the filament by a DC power supply which was controlled by a constant power controller. The cell was operated with 300 W or less input power which corresponded to a cell wall temperature of about 700 °C. The temperature of the tungsten filament was estimated to be in the range 1100 to 1500 °C.

The cell was operated under gas flow conditions while maintaining a constant gas pressure in the cell. The hydrogen was ultrahigh purity. The gas pressure inside the cell was maintained at about 300 mTorr with a hydrogen flow rate of 5.5 sccm controlled by a 0-20 sccm range mass flow controller (MKS 1179A21CS1BB) with a readout (MKS type 246).

5

The cell pressure was monitored by a 0-10 Torr MKS Baratron absolute pressure gauge.

The light emission was introduced to an EUV spectrometer for spectral measurement. The spectrometer was a McPherson 0.2 meter monochromator (Model 302, Seya-Namioka type) equipped with a 1200 lines/mm holographic grating with a platinum coating. The wavelength region covered by the monochromator was $30-560\,nm$. A channel electron multiplier (CEM) was used to detect the EUV light. The wavelength resolution was about $1\,nm$ (FWHM) with an entrance and exit slit width of $300\,\mu m$. The vacuum inside the monochromator was maintained below 5×10^{-4} Torr by a turbo pump. The Lyman α emission was recorded as a function of time after the filament was turned on. The EUV spectra ($50-90\,nm$) and ($40-160\,nm$) of the $RbNO_3/H_2$ cell emission were recorded at about the point of the maximum Lyman α emission.

The EUV/UV/VIS spectrum ($40-560\,nm$) of the cell emission with hydrogen alone was recorded with a photomultiplier tube (PMT) and a sodium salicylate scintillator. The PMT (Model R1527P, Hamamatsu) used has a spectral response in the range of $185-680\,nm$ with a peak efficiency at about $400\,nm$. The scan interval was $0.4\,nm$. The inlet and outlet slit were $500\,\mu m$ with a corresponding wavelength resolution of $1.5\,nm$.

The VIS spectrum ($380-500\,nm$) of the cell emission was according to the method of the EUV/UV/VIS spectrum ($40-560\,nm$) except that the inlet and outlet slit were $300\,\mu m$ with a corresponding wavelength resolution of $1\,nm$. The spectrum was recorded two hours after a plasma formed.

B. Standard Rubidium and Hydrogen Emission Spectra

The standard EUV emission spectrum of rubidium was obtained with a gas discharge cell comprising a five-way stainless steel cross that served as the anode with a hollow stainless steel cathode that was coated with $RbNO_3$ by the same procedure used to coat the titanium dissociator. The five-way cross was pressurized with 1 Torr of hydrogen to initiate the discharge. The hydrogen was then evacuated so that only rubidium lines were observed. The DC voltage at the time the EUV spectrum was

6

recorded was 300 V. The standard EUV emission spectrum of hydrogen was obtained in the same manner as the standard rubidium spectrum, except that the cathode was not coated.

III. RESULTS

A. EUV Spectroscopy

The intensity of the Lyman α emission as a function of time was recorded for four hours from the gas cell at a cell temperature of 700 °C comprising a tungsten filament, a titanium dissociator, and each of the controls $Mg(NO_3)_2$ alone and $Al(NO_3)_3$ alone, as well as the catalyst $RbNO_3$ alone. No Lyman α emission was observed. Similarly, a plasma did not form, and no EUV emission was observed with hydrogen alone at 300 mtorr with a flow rate of 5.5 sccm or with the control materials and the flowing hydrogen. The typical UV/VIS spectrum ($40-560\,nm$) of a control is shown in Figure 2. No emission was observed except for the blackbody filament radiation at the longer wavelengths.

The intensity of the Lyman α emission as a function of time with vaporized Rb^+ from $RbNO_3$ with flowing hydrogen was recorded. Strong EUV emission was observed from vaporized catalyst only when hydrogen was present. The EUV spectrum ($40-160\,nm$) of the cell emission recorded at about the point of the maximum Lyman α emission is shown in Figure 3.

B. EUV Emission of Rb$^+$ Catalyst

The EUV spectrum ($50-90\,nm$) of the emission of the $RbNO_3/H_2$ gas cell (top curve) and the standard rubidium discharge plasma according to Sec. IIB (bottom curve) are shown in Figure 4. Line emission corresponding to Rb^{2+} was observed at $81.59\,nm$, $59.1\,nm$, $58.1\,nm$, $55.6\,nm$, and $53.3\,nm$. Rb^+ was observed at $74.15\,nm$, $71.1\,nm$, $69.7\,nm$, and $64.38\,nm$. The assignments of the Rb^{2+} and Rb^+ lines were confirmed by the NIST tables [37].

C. 407 nm Emission with Rb⁺ Catalyst

The VIS spectra $(380-500\,nm)$ of the cell emission of the $RbNO_3/H_2$ gas cell (top curve) and of standard hydrogen (bottom curve) are shown in Figure 5. From the comparison, a novel broad peak was observed at $407\,nm$ which was not due to rubidium emission. The known Rb I peaks are indicated in Figure 5. Molecular hydrogen has emission at $407\,nm$, but the assignment to molecular hydrogen was eliminated since the other peaks of hydrogen were not observed at comparable intensity. The novel broad $407\,nm$ peak was observed only with Rb^+ and atomic hydrogen present over an extended reaction time. These results are consistent with the formation of $H^-(1/2)$ from the catalysis of atomic hydrogen by Rb^+.

IV. DISCUSSION

A plasma that emitted intense EUV formed at low temperatures (e.g. $\approx 10^3\,K$) from atomic hydrogen and Rb^+ catalyst which was vaporized by heating. No possible chemical reactions of the tungsten filament, the dissociator, the vaporized test material, and 300 mTorr hydrogen at a cell temperature of 700 °C could be found which accounted for the hydrogen Lyman α line emission. In fact, no known possible chemical reaction releases enough energy to form a hydrogen plasma and excite Lyman α emission from hydrogen. The emission was not observed with catalyst or hydrogen alone. Intense emission was observed for catalyst with hydrogen gas, but no emission was observed when magnesium or aluminum nitrate replaced rubidium nitrate catalyst with hydrogen. This result indicates that the emission was due to a reaction of the catalyst with hydrogen.

Rubidium ions ionize at an integer multiple of the potential energy of atomic hydrogen, $27.2\,eV$, $m \cdot 27.2\,eV$ wherein m is an integer. The reaction Rb^+ to Rb^{2+} has a net enthalpy of reaction of $27.28\,eV$, which is equivalent to $m=1$. Characteristic emission was observed from Rb^{2+} which confirmed the resonant nonradiative energy transfer of $27.2\,eV$ from atomic hydrogen to Rb^+ (Eq. (5)). With a highly conductive plasma, the voltage of the cell was about 20 V, and the field strength was about

8

1-2 V/cm which was too low to ionize Rb^+ to Rb^{2+}. The Rb^{2+} lines generated in the incandescently heated cell and due to the catalyst reaction of atomic hydrogen were confirmed by a high voltage discharge and NIST tables [37].

Similar low-voltage hydrogen catalysis plasmas formed with hydrogen-potassium mixtures have been reported previously [24-25] wherein the plasma decayed with a two second half-life when the electric field was actually set to zero. This was the thermal decay time of the filament which dissociated molecular hydrogen to atomic hydrogen. This experiment showed that hydrogen line emission was occurring even though the voltage between the heater wires was set to and measured to be zero and indicated that the emission was due to a reaction of potassium atoms with atomic hydrogen. Potassium atoms ionize at an integer multiple of the potential energy of atomic hydrogen, $m \cdot 27.2 \, eV$. The enthalpy of ionization of K to K^{3+} has a net enthalpy of reaction of $81.7426 \, eV$, which is equivalent to $m = 3$.

An excessive plasma afterglow duration was also previously reported for $RbNO_3$ and other catalysts [25]. A catalytic plasma of hydrogen and certain alkali ions formed at low temperatures ($< 10^3 \, K$) as recorded via EUV spectroscopy and the hydrogen Balmer and alkali line emissions in the visible range. The observed plasma formed from atomic hydrogen generated at a tungsten filament that heated a titanium dissociator and one of potassium, rubidium, cesium, and their carbonates and nitrates. These atoms and ions ionize to provide a net enthalpy of reaction of an integer multiple of the potential energy of atomic hydrogen ($m \cdot 27.2 \, eV$, $m =$ integer) to within 0.17 eV and comprise only a single ionization in the case of a potassium or rubidium ion. Whereas, the chemically similar atoms of sodium and sodium and lithium carbonates and nitrates which do not ionize with these constraints caused no emission. To test the electric dependence of the emission, the weak electric field of about 1 V/cm was set and measured to be zero in $< 0.5 \, X \, 10^{-6}$ sec. An afterglow duration of about one to two seconds was recorded in the case of potassium, rubidium, cesium, K_2CO_3, $RbNO_3$, and $CsNO_3$. Hydrogen line or alkali line emission was occurring even though the voltage between the heater wires was set to and measured to be zero. These atoms and ions ionize to provide a net enthalpy of reaction of an

integer multiple of the potential energy of atomic hydrogen to within less than the thermal energies at $\approx 10^3 \, K$ and comprise only a single ionization in the case of a potassium or rubidium ion. Since the thermal decay time of the filament for dissociation of molecular hydrogen to atomic hydrogen was similar to the plasma afterglow duration, the emission was determined to be due to a reaction of atomic hydrogen with each of the atoms or ions that did not require the presence of an electric field to be functional.

Rb^+ is predicted to catalyze hydrogen to form $H\left[\dfrac{a_H}{2}\right]$ which reacts with an electron to form $H^-(1/2)$. The predicted $H^-(1/2)$ hydride ion of hydrogen catalysis by Rb^+ was observed spectroscopically at $407 \, nm$ corresponding to its predicted binding energy of $3.05 \, eV$. The hydride reaction product formed over time.

In a recently submitted paper [11], $H^-(1/2)$, the hydride ion catalyst product of K^+/K^+ or Rb^+, was reported to have been observed by high resolution visible spectroscopy as a broad peak at $407.00 \, nm$ with a FWHM of $0.14 \, nm$ corresponding to its predicted binding energy of $3.0468 \, eV$. From the electron g factor, bound-free hyperfine structure lines of $H^-(1/2)$ were predicted with energies E_{HF} given by $E_{HF} = j^2 3.0056 \, X \, 10^{-5} + 3.0575 \, eV$ (j is an integer) as an inverse Rydberg-type series that converges at increasing wavelengths and terminates at $3.0575 \, eV$—the hydride spin-pairing energy plus the binding energy. The high resolution visible plasma emission spectra in the region of $400.0 \, nm$ to $406.0 \, nm$ matched the predicted emission lines for $j = 1$ to $j = 37$ to within a 1 part per 10^5.

The formation of compounds having novel hydride ions $H^-(1/p)$ would be substantial evidence supporting catalysis of hydrogen as the mechanism of observed rt-plasmas and further support the spectroscopic identification of $H^-(1/p)$ (p is an integer). Compounds containing novel hydride ions have been isolated as products of the reaction of atomic hydrogen with atoms and ions identified as catalysts in previously reported EUV studies [26-32]. The novel hydride compounds were identified analytically by techniques such as time of flight secondary ion mass spectroscopy, X-ray photoelectron spectroscopy, and ^1H nuclear magnetic resonance spectroscopy. For example, the time of flight

10

secondary ion mass spectroscopy showed a large hydride peak in the negative spectrum. The X-ray photoelectron spectrum showed large metal core level shifts due to binding with the hydride as well as novel hydride peaks. The ^1H nuclear magnetic resonance spectrum showed significantly upfield shifted peaks which corresponded to and identified novel hydride ions.

V. CONCLUSION

Characteristic emission was observed from Rb^{2+} which confirmed the resonant nonradiative energy transfer of $27.2\,eV$ from atomic hydrogen to Rb^+ (Eq. (5)). The predicted $H^-(1/2)$ hydride ion of hydrogen catalysis by Rb^+ catalyst given by Eqs. (5-7) and Eq. (18) was observed spectroscopically at $407\,nm$ corresponding to its predicted binding energy of $3.05\,eV$.

APPENDIX

A. Catalysts

The mechanism of EUV emission and formation of a novel hydride ion can not be explained by the conventional chemistry of hydrogen; rather, it must have been due to a novel chemical reaction between catalyst and atomic hydrogen. Mills [1-35] predicts that certain atoms or ions serve as catalysts to release energy from hydrogen to produce an increased binding energy hydrogen atom called a *hydrino atom* having a binding energy of

$$Binding\ Energy = \frac{13.6\ eV}{n^2}\tag{1}$$

where

$$n = \frac{1}{2}, \frac{1}{3}, \frac{1}{4}, ..., \frac{1}{p}\tag{2}$$

and p is an integer greater than 1, designated as $H\left[\dfrac{a_H}{p}\right]$ where a_H is the radius of the hydrogen atom. Hydrinos are predicted to form by reacting an ordinary hydrogen atom with a catalyst having a net enthalpy of reaction of about

$$m \cdot 27.2\ eV\tag{3}$$

where m is an integer. This catalysis releases energy from the hydrogen atom with a commensurate decrease in size of the hydrogen atom, $r_n = na_H$. For example, the catalysis of $H(n=1)$ to $H(n=1/2)$ releases 40.8 eV, and the hydrogen radius decreases from a_H to $\dfrac{1}{2}a_H$.

The excited energy states of atomic hydrogen are also given by Eq. (1) except that

$$n = 1,2,3,...\tag{4}$$

The $n=1$ state is the "ground" state for "pure" photon transitions (the $n=1$ state can absorb a photon and go to an excited electronic state, but it cannot release a photon and go to a lower-energy electronic state). However, an electron transition from the ground state to a lower-energy state is possible by a nonradiative energy transfer such as multipole coupling or a resonant collision mechanism. These lower-energy states

have fractional quantum numbers, $n = \dfrac{1}{\text{integer}}$. Processes that occur without photons and that require collisions are common. For example, the exothermic chemical reaction of $H + H$ to form H_2 does not occur with the emission of a photon. Rather, the reaction requires a collision with a third body, M, to remove the bond energy- $H + H + M \rightarrow H_2 + M^*$ [38]. The third body distributes the energy from the exothermic reaction, and the end result is the H_2 molecule and an increase in the temperature of the system. Some commercial phosphors are based on nonradiative energy transfer involving multipole coupling. For example, the strong absorption strength of Sb^{3+} ions along with the efficient nonradiative transfer of excitation from Sb^{3+} to Mn^{2+}, are responsible for the strong manganese luminescence from phosphors containing these ions [39].

Similarly, the $n = 1$ state of hydrogen and the $n = \dfrac{1}{\text{integer}}$ states of hydrogen are nonradiative, but a transition between two nonradiative states, say $n = 1$ to $n = 1/2$, is possible via a nonradiative energy transfer. In these cases, during the transition the electron couples to another electron transition, electron transfer reaction, or inelastic scattering reaction which can absorb the exact amount of energy that must be removed from the hydrogen atom to cause the transition. Thus, a catalyst provides a net positive enthalpy of reaction of $m \cdot 27.2\,eV$ (i.e. it absorbs $m \cdot 27.2\,eV$ where m is an integer). Certain atoms or ions serve as catalysts by accepting energy from hydrogen atoms through a nonradiative resonant transfer. The catalyst may then release the transferred energy by radiative and nonradiative mechanisms. As a consequence of the nonradiative energy transfer, the hydrogen atom becomes unstable and emits further energy until it achieves a lower-energy nonradiative state having a principal energy level given by Eqs. (1-2).

Rubidium Ion

Rubidium ions can provide a net enthalpy of a multiple of that of the potential energy of the hydrogen atom. The second ionization energy of rubidium is $27.28\,eV$. The reaction Rb^+ to Rb^{2+} has a net enthalpy of reaction of $27.28\,eV$, which is equivalent to $m = 1$ in Eq. (3).

1 3

$$27.28\ eV + Rb^+ + H\left[\frac{a_H}{p}\right] \rightarrow Rb^{2+} + e^- + H\left[\frac{a_H}{(p+1)}\right] + [(p+1)^2 - p^2]X13.6\ eV \qquad (5)$$

$$Rb^{2+} + e^- \rightarrow Rb^+ + 27.28\ eV \qquad (6)$$

The overall reaction is

$$H\left[\frac{a_H}{p}\right] \rightarrow H\left[\frac{a_H}{(p+1)}\right] + [(p+1)^2 - p^2]\ X\ 13.6\ eV \qquad (7)$$

Alkali metal nitrates are extraordinarily volatile and can be distilled at 350-500 °C [40]. $RbNO_3$ is the favored candidate for providing gaseous Rb^+ ions. Rb^+ ion emission was observed in the EUV and VIS spectrum.

Cesium

A catalytic system is provided by the ionization of two electrons from a cesium atom each to a continuum energy level such that the sum of the ionization energies of the two electrons is approximately $27.2\ eV$. The first and second ionization energies of cesium are $3.89390\ eV$ and $23.15745\ eV$, respectively [36]. The double ionization $(t=2)$ reaction of Cs to Cs^{2+}, then, has a net enthalpy of reaction of $27.05135\ eV$, which is equivalent to $m=1$ in Eq. (3).

$$27.05135\ eV + Cs(m) + H\left[\frac{a_H}{p}\right] \rightarrow Cs^{2+} + 2e^- + H\left[\frac{a_H}{(p+1)}\right] + [(p+1)^2 - p^2]X13.6\ eV$$

$$(8)$$

$$Cs^{2+} + 2e^- \rightarrow Cs(m) + 27.05135\ eV \qquad (9)$$

And, the overall reaction is

$$H\left[\frac{a_H}{p}\right] \rightarrow H\left[\frac{a_H}{(p+1)}\right] + [(p+1)^2 - p^2]X13.6\ eV \qquad (10)$$

Argon Ion

Argon ions can provide a net enthalpy of a multiple of that of the potential energy of the hydrogen atom. The second ionization energy of argon is $27.63\ eV$. The reaction Ar^+ to Ar^{2+} has a net enthalpy of reaction of $27.63\ eV$, which is equivalent to $m=1$ in Eq. (3).

$$27.63\,eV + Ar^+ + H\left[\frac{a_H}{p}\right] \rightarrow Ar^{2+} + e^- + H\left[\frac{a_H}{(p+1)}\right] + [(p+1)^2 - p^2]X13.6\,eV \tag{11}$$

$$Ar^{2+} + e^- \rightarrow Ar^+ + 27.63\,eV \tag{12}$$

And, the overall reaction is

$$H\left[\frac{a_H}{p}\right] \rightarrow H\left[\frac{a_H}{(p+1)}\right] + [(p+1)^2 - p^2]X13.6\,eV \tag{13}$$

Potassium

An additional catalytic system involves potassium atoms. The first, second, and third ionization energies of potassium are $4.34066\,eV$, $31.63\,eV$, $45.806\,eV$, respectively [36]. The triple ionization ($t=3$) reaction of K to K^{3+}, then, has a net enthalpy of reaction of $81.7766\,eV$, which is equivalent to $m=3$ in Eq. (3).

$$81.7766\,eV + K(m) + H\left[\frac{a_H}{p}\right] \rightarrow K^{3+} + 3e^- + H\left[\frac{a_H}{(p+3)}\right] + [(p+3)^2 - p^2]X13.6\,eV \tag{14}$$

$$K^{3+} + 3e^- \rightarrow K(m) + 81.7766\,eV \tag{15}$$

And, the overall reaction is

$$H\left[\frac{a_H}{p}\right] \rightarrow H\left[\frac{a_H}{(p+3)}\right] + [(p+3)^2 - p^2]X13.6\,eV \tag{16}$$

B. Hydride Ion

A novel hydride ion having extraordinary chemical properties given by Mills [1] is predicted to form by the reaction of an electron with a hydrino (Eq. (17)). The resulting hydride ion is referred to as a hydrino hydride ion, designated as $H^-(1/p)$.

$$H\left[\frac{a_H}{p}\right] + e^- \rightarrow H^-(1/p) \tag{17}$$

The hydrino hydride ion is distinguished from an ordinary hydride ion having a binding energy of 0.8 eV. The hydrino hydride ion is

15

predicted [1] to comprise a hydrogen nucleus and two indistinguishable electrons at a binding energy according to the following formula:

$$Binding\ Energy = \frac{\hbar^2\sqrt{s(s+1)}}{8\mu_e a_0^2\left[\frac{1+\sqrt{s(s+1)}}{p}\right]^2} - \frac{\pi\mu_0 e^2 \hbar^2}{m_e^2 a_0^3}\left(1 + \frac{2^2}{\left[\frac{1+\sqrt{s(s+1)}}{p}\right]^3}\right) \qquad (18)$$

where p is an integer greater than one, $s = 1/2$, $\hbar$ is Planck's constant bar, μ_o is the permeability of vacuum, m_e is the mass of the electron, μ_e is the reduced electron mass, a_o is the Bohr radius, and e is the elementary charge. The ionic radius is

$$r_1 = \frac{a_0}{p}\left(1 + \sqrt{s(s+1)}\right); \ s = \frac{1}{2} \qquad (19)$$

From Eq. (19), the radius of the hydrino hydride ion $H^-(1/p)$; $p =$ integer is $\frac{1}{p}$ that of ordinary hydride ion, $H^-(1/1)$.

ACKNOWLEDGMENT

REFERENCES

1. R. Mills, *The Grand Unified Theory of Classical Quantum Mechanics*, September 2001 Edition, BlackLight Power, Inc., Cranbury, New Jersey, Distributed by Amazon.com; posted at www.blacklightpower.com.
2. R. Mills, "The Grand Unified Theory of Classical Quantum Mechanics", Global Foundation, Inc. Orbis Scientiae entitled *The Role of Attractive and Repulsive Gravitational Forces in Cosmic Acceleration of Particles The Origin of the Cosmic Gamma Ray Bursts*, (29th Conference on High Energy Physics and Cosmology Since 1964) Dr. Behram N. Kursunoglu,

Chairman, December 14-17, 2000, Lago Mar Resort, Fort Lauderdale, FL, Kluwer Academic/Plenum Publishers, New York, pp. 243-258.

3. R. Mills, "The Grand Unified Theory of Classical Quantum Mechanics", Int. J. of Hydrogen Energy, in press.

4. R. Mills, "The Hydrogen Atom Revisited", Int. J. of Hydrogen Energy, Vol. 25, Issue 12, December, (2000), pp. 1171-1183.

5. R. Mills, The Nature of Free Electrons in Superfluid Helium—a Test of Quantum Mechanics and a Basis to Review its Foundations and Make a Comparison to Classical Theory, Int. J. Hydrogen Energy, Vol. 26, No. 10, (2001), pp. 1059-1096.

6. R. Mills, P. Ray, "Spectral Emission of Fractional Quantum Energy Levels of Atomic Hydrogen from a Helium-Hydrogen Plasma and the Implications for Dark Matter", Int. J. Hydrogen Energy, in press.

7. R. L. Mills, P. Ray, B. Dhandapani, J. He, "Spectroscopic Identification of Fractional Rydberg States of Atomic Hydrogen" J. Phys. Chem. Letts., submitted.

8. R. Mills, P. Ray, "Vibrational Spectral Emission of Fractional-Principal-Quantum-Energy-Level Hydrogen Molecular Ion", Int. J. Hydrogen Energy, in press.

9. R. Mills, P. Ray, M. Nansteel, W. Good, P. Jansson, B. Dhandapani, J. He, "Excessive Balmer α Line Broadening, Power Balance, and Novel Hydride Ion Product of Plasma Formed from Incandescently Heated Hydrogen Gas with Certain Catalysts", Int. J. Hydrogen Energy, submitted.

10. R. Mills, E. Dayalan, P. Ray, B. Dhandapani, J. He, "Highly Stable Novel Inorganic Hydrides from Aqueous Electrolysis and Plasma Electrolysis, Japanese Journal of Applied Physics, submitted.

11. R. L. Mills, P. Ray, " High Resolution Spectroscopic Observation of the Bound-Free Hyperfine Levels of a Novel Hydride Ion Corresponding to a Fractional Rydberg State of Atomic Hydrogen", Int. J. Hydrogen Energy, submitted.

12. R. Mills, P. Ray, Spectroscopic Identification of a Novel Catalytic Reaction of Potassium and Atomic Hydrogen and the Hydride Ion Product, Int. J. Hydrogen Energy, Vol. 27, No. 2, February, (2002), pp. 183-192.

13. R. Mills, "Spectroscopic Identification of a Novel Catalytic Reaction of Atomic Hydrogen and the Hydride Ion Product", Int. J. Hydrogen Energy, Vol. 26, No. 10, (2001), pp. 1041-1058.

14. R. Mills and M. Nansteel, "Argon-Hydrogen-Strontium Plasma Light Source", IEEE Transactions on Plasma Science, submitted.

15. R. Mills, M. Nansteel, and Y. Lu, "Excessively Bright Hydrogen-Strontium Plasma Light Source Due to Energy Resonance of Strontium with Hydrogen", European Journal of Physics D, submitted.

16. R. Mills, J. Dong, W. Good, P. Ray, J. He, B. Dhandapani, Measurement of Energy Balances of Noble Gas-Hydrogen Discharge Plasmas Using Calvet Calorimetry, Int. J. Hydrogen Energy, in press.

17. R. L. Mills, P. Ray, B. Dhandapani, M. Nansteel, X. Chen, J. He, "New Power Source from Fractional Quantum Energy Levels of Atomic Hydrogen that Surpasses Internal Combustion", Spectrochimica Acta, submitted.

18. R. L. Mills, P. Ray, B. Dhandapani, J. He, "Comparison of Excessive Balmer α Line Broadening of Glow Discharge and Microwave Hydrogen Plasmas with Certain Catalysts" Chem. Phys., submitted.

19. R. L. Mills, A. Voigt, P. Ray, M. Nansteel, B. Dhandapani, "Measurement of Hydrogen Balmer Line Broadening and Thermal Power Balances of Noble Gas-Hydrogen Discharge Plasmas", Int. J. Hydrogen Energy, in press.

20. R. Mills, N. Greenig, S. Hicks, "Optically Measured Power Balances of Anomalous Discharges of Mixtures of Argon, Hydrogen, and Potassium, Rubidium, Cesium, or Strontium Vapor", Int. J. Hydrogen Energy, in press.

21. R. Mills, M. Nansteel, and Y. Lu, "Observation of Extreme Ultraviolet Hydrogen Emission from Incandescently Heated Hydrogen Gas with Strontium that Produced an Anomalous Optically Measured Power Balance", Int. J. Hydrogen Energy, Vol. 26, No. 4, (2001), pp. 309-326.

22. R. Mills, J. Dong, Y. Lu, "Observation of Extreme Ultraviolet Hydrogen Emission from Incandescently Heated Hydrogen Gas with Certain Catalysts", Int. J. Hydrogen Energy, Vol. 25, (2000), pp. 919-943.

23. R. Mills, "Observation of Extreme Ultraviolet Emission from Hydrogen-KI Plasmas Produced by a Hollow Cathode Discharge", Int. J. Hydrogen Energy, Vol. 26, No. 6, (2001), pp. 579-592.

24. R. Mills, "Temporal Behavior of Light-Emission in the Visible Spectral Range from a Ti-K2CO3-H-Cell", Int. J. Hydrogen Energy, Vol. 26, No. 4, (2001), pp. 327-332.

25. R. Mills, T. Onuma, and Y. Lu, "Formation of a Hydrogen Plasma from an Incandescently Heated Hydrogen-Catalyst Gas Mixture with an Anomalous Afterglow Duration", Int. J. Hydrogen Energy, Vol. 26, No. 7, July, (2001), pp. 749-762.

26. R. Mills, B. Dhandapani, M. Nansteel, J. He, A. Voigt, "Identification of Compounds Containing Novel Hydride Ions by Nuclear Magnetic Resonance Spectroscopy", Int. J. Hydrogen Energy, Vol. 26, No. 9, Sept. (2001), pp. 965-979.

27. R. Mills, B. Dhandapani, N. Greenig, J. He, "Synthesis and Characterization of Potassium Iodo Hydride", Int. J. of Hydrogen Energy, Vol. 25, Issue 12, December, (2000), pp. 1185-1203.

28. R. Mills, "Novel Inorganic Hydride", Int. J. of Hydrogen Energy, Vol. 25, (2000), pp. 669-683.

29. R. Mills, "Novel Hydrogen Compounds from a Potassium Carbonate Electrolytic Cell", Fusion Technology, Vol. 37, No. 2, March, (2000), pp. 157-182.

30. R. Mills, B. Dhandapani, M. Nansteel, J. He, T. Shannon, A. Echezuria, "Synthesis and Characterization of Novel Hydride Compounds", Int. J. of Hydrogen Energy, Vol. 26, No. 4, (2001), pp. 339-367.

31. R. Mills, "Highly Stable Novel Inorganic Hydrides", Journal of New Materials for Electrochemical Systems, in press.

32. R. Mills, W. Good, A. Voigt, Jinquan Dong, "Minimum Heat of Formation of Potassium Iodo Hydride", Int. J. Hydrogen Energy, Vol. 26, No. 11, Oct., (2001), pp. 1199-1208.

33. R. Mills, "BlackLight Power Technology-A New Clean Hydrogen Energy Source with the Potential for Direct Conversion to Electricity", Proceedings of the National Hydrogen Association, 12 th Annual U.S. Hydrogen Meeting and Exposition, *Hydrogen: The Common Thread*, The Washington Hilton and Towers, Washington DC, (March 6-8, 2001), pp. 671-697.

34. R. Mills, "BlackLight Power Technology-A New Clean Energy Source with the Potential for Direct Conversion to Electricity", Global Foundation International Conference on "Global Warming and Energy

Policy", Dr. Behram N. Kursunoglu, Chairman, Fort Lauderdale, FL, November 26-28, 2000, Kluwer Academic/Plenum Publishers, New York, pp. 1059-1096.

35. R. Mayo, R. Mills, M. Nansteel, "On the Potential of Direct and MHD Conversion of Power from a Novel Plasma Source to Electricity for Microdistributed Power Applications", IEEE Transactions on Plasma Science, submitted.

36. David R. Linde, *CRC Handbook of Chemistry and Physics*, 79 th Edition, CRC Press, Boca Raton, Florida, (1998-9), p. 10-175 to p. 10-177.

37. NIST Atomic Spectra Database, www.physics.nist.gov/cgi-bin/AtData/display.ksh.

38. N. V. Sidgwick, *The Chemical Elements and Their Compounds*, Volume I, Oxford, Clarendon Press, (1950), p.17.

39. M. D. Lamb, *Luminescence Spectroscopy*, Academic Press, London, (1978), p. 68.

40. C. J. Hardy, B. O. Field, J. Chem. Soc., (1963), pp. 5130-5134.

Figure Captions

Figure 1. The experimental set up comprising a gas cell light source and an EUV spectrometer which was differentially pumped.

Figure 2. The EUV/UV/VIS spectrum ($40-560\,nm$) of the cell emission from the gas cell at a cell temperature of 700 °C comprising a tungsten filament, a titanium dissociator, and 300 mTorr hydrogen that was recorded with a photomultiplier tube (PMT) and a sodium salicylate scintillator with an entrance and exit slit width of $500\,\mu m$. No emission was observed except for the blackbody filament radiation at the longer wavelengths.

Figure 3. The EUV spectrum ($40-160\,nm$) of the cell emission recorded at about the point of the maximum Lyman α emission from the gas cell at a cell temperature of 700 °C comprising a tungsten filament, a titanium dissociator, 300 mTorr hydrogen, and vaporized Rb^+ from $RbNO_3$ that was recorded with a CEM. Strong Lyman series emission was observed.

Figure 4. The EUV spectrum ($50-90\,nm$) of the emission of the $RbNO_3/H_2$ gas cell (top curve) and the standard discharge rubidium plasma (bottom curve). Line emission corresponding to Rb^{2+} was observed at $81.59\,nm$, $59.1\,nm$, $58.1\,nm$, $55.6\,nm$, and $53.3\,nm$. Rb^+ was observed at $74.15\,nm$, $71.1\,nm$, $69.7\,nm$, and $64.38\,nm$.

Figure 5. The VIS spectra ($380-500\,nm$) of the cell emission of the $RbNO_3/H_2$ gas cell (top curve) and of standard hydrogen (bottom curve). A novel broad peak was observed at $407\,nm$ which was not due to rubidium or hydrogen emission. The peak was assigned to $H^-(1/2)$ emission.
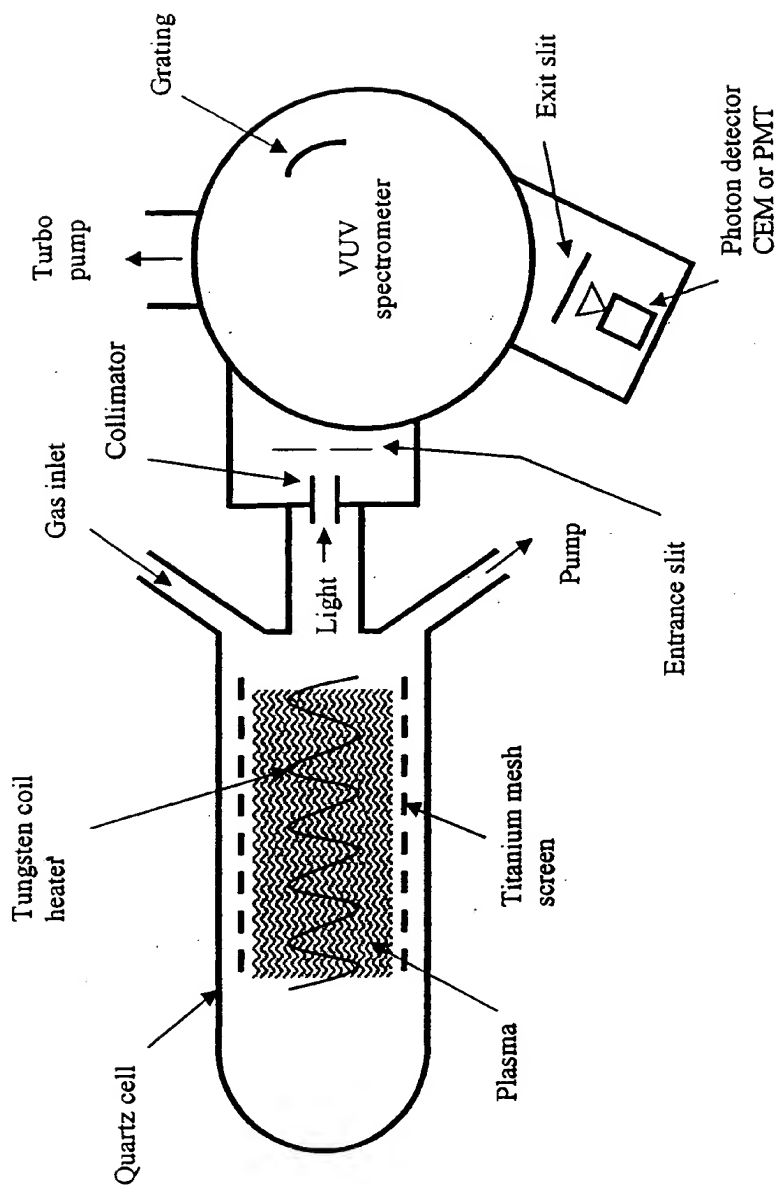
Fig. 1

Fig. 2

Hydrogen gas only

Wavelength (nm)

Photon Counts/sec

Fig. 3

Fig. 4

Graph axes: Wavelength (nm) on horizontal axis ranging from 50 to 90; Photon Counts/sec on vertical axis ranging from 0 to 500.

Plot labeled $RbNO_3/H_2$ with peaks labeled Rb^{2+}, Rb^+, Rb^+, Rb^+, Rb^+, Rb^{2+}, Rb^{2+}, Rb^+, Rb^{2+}.

Fig. 5

The figure shows a plot of Photon Counts/Sec (y-axis, ranging 0 to 4000) versus Wavelength (nm) (x-axis, ranging from below 400 to about 490). Peaks are labeled Rb$^+$, H$^-$(1/2), and B$_\beta$.

Measurement of Energy Balances of Noble Gas-Hydrogen Discharge Plasmas Using Calvet Calorimetry

R. Mills, J. Dong, W. Good, P. Ray, J. He, B. Dhandapani

BlackLight Power, Inc.
493 Old Trenton Road
Cranbury, NJ 08512

From a solution of a Schrödinger-type wave equation with a nonradiative boundary condition based on Maxwell's equations, Mills predicts that atomic hydro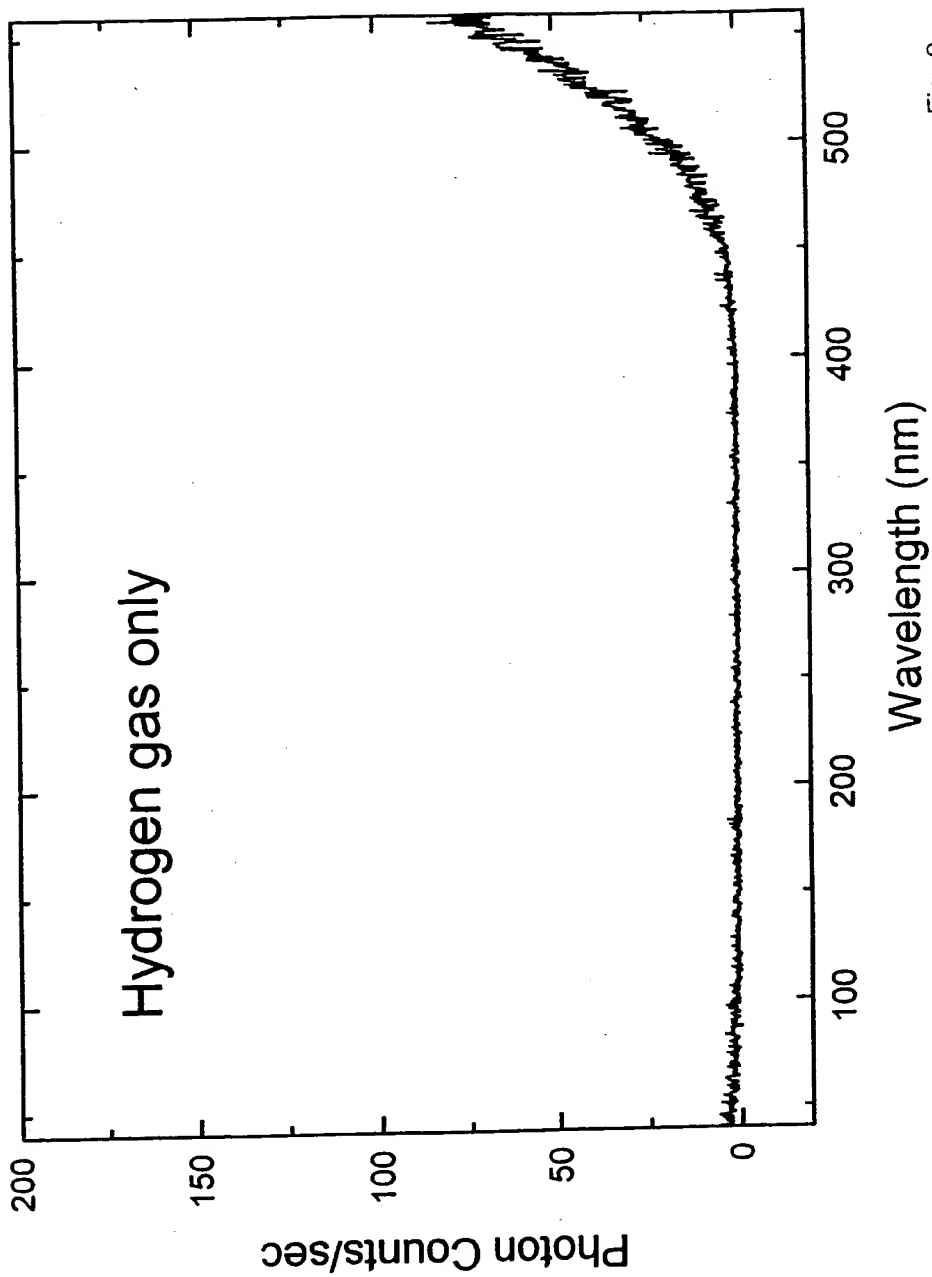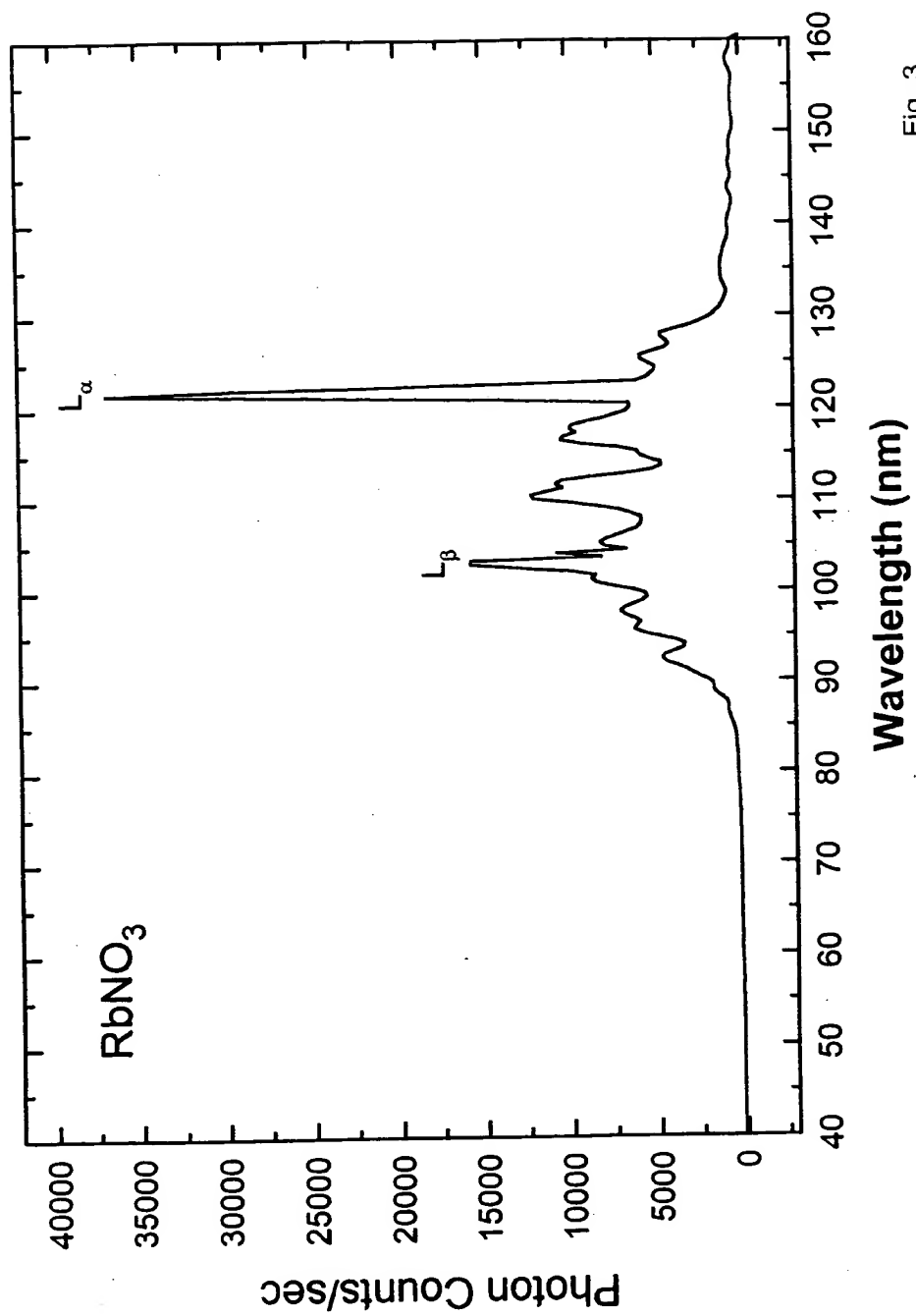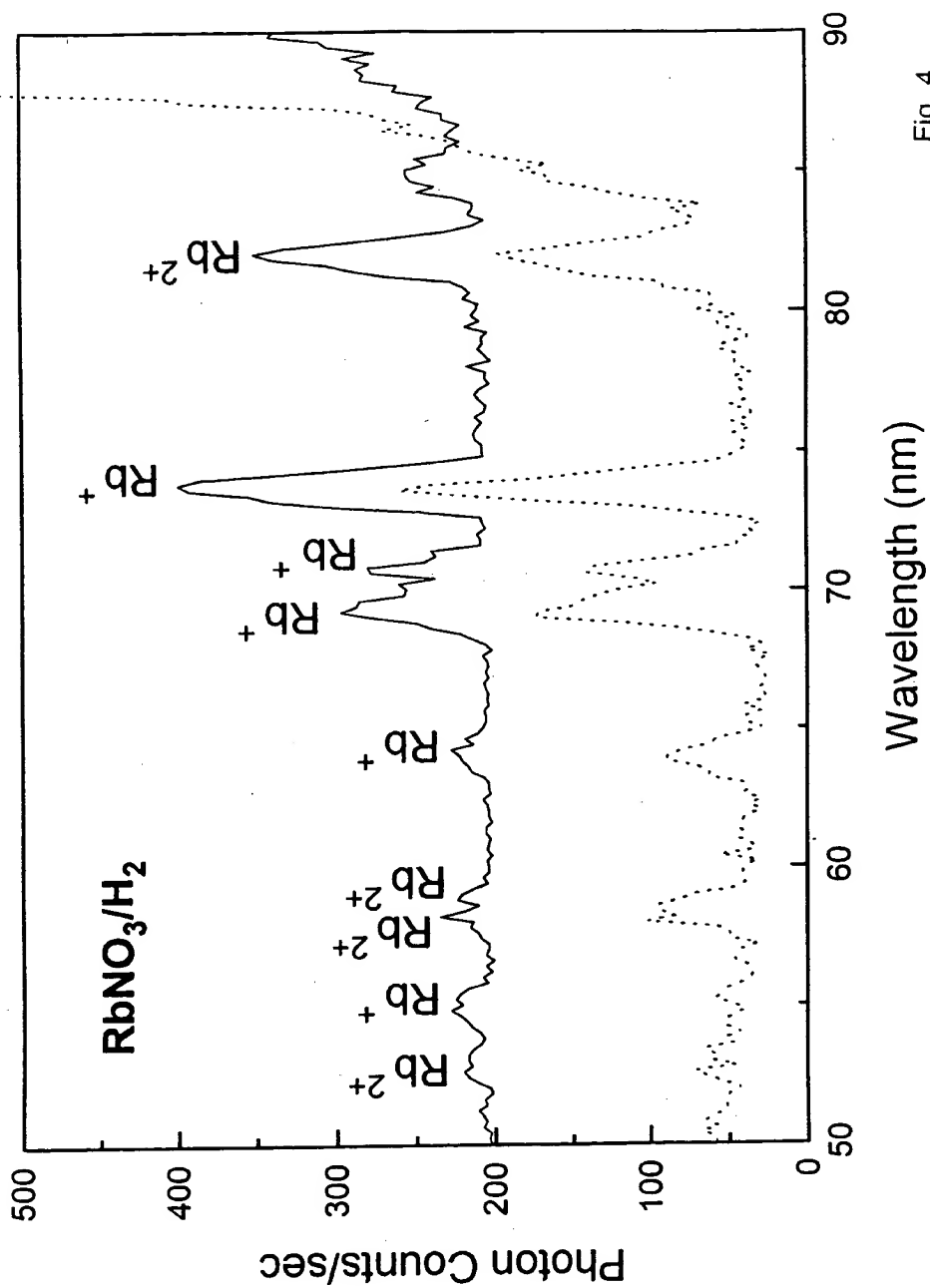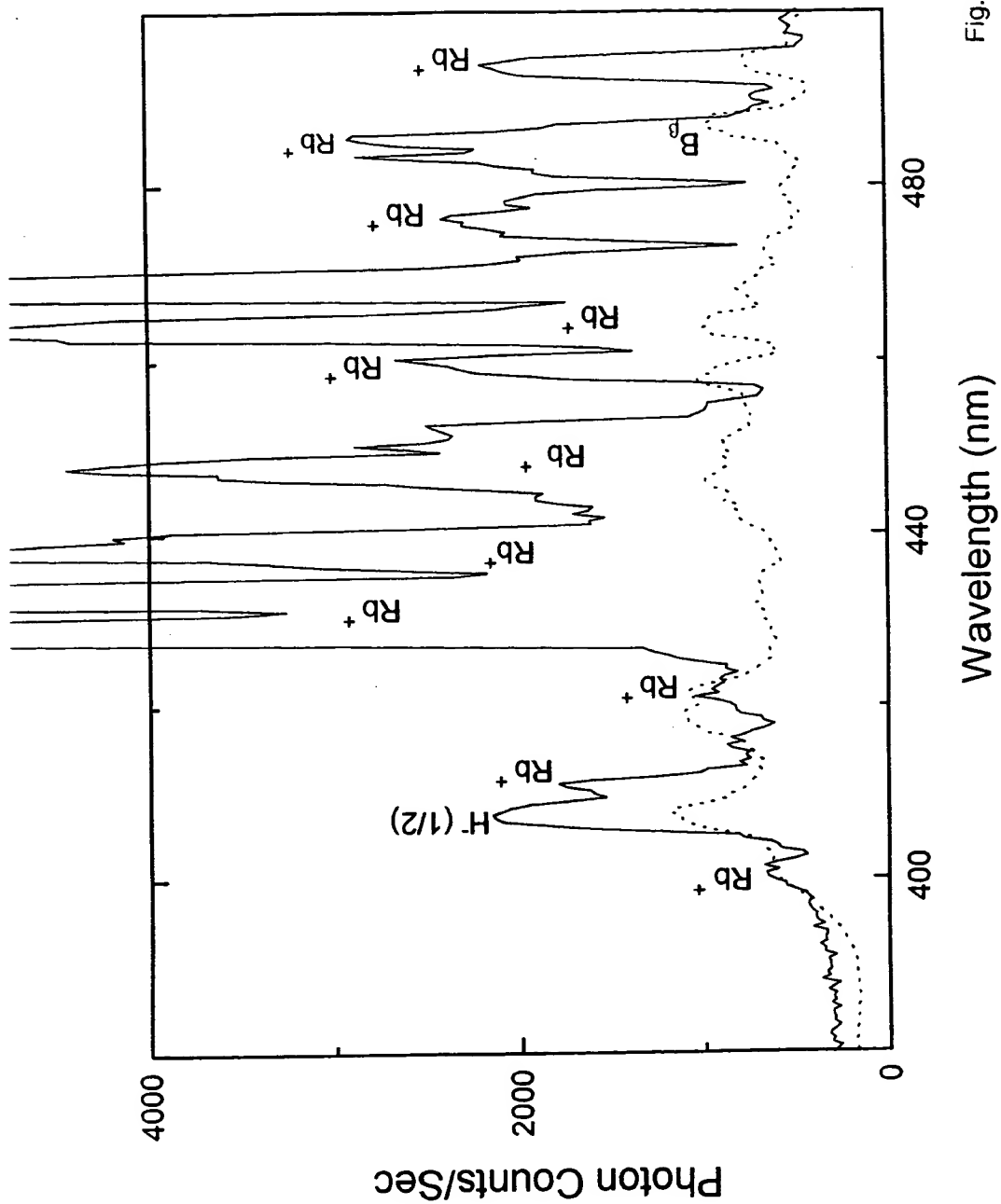gen may undergo a catalytic reaction with certain gaseous ions such as Ar^+ which ionize at integer multiples of the potential energy of atomic hydrogen, $27.2\,eV$. The reaction involves a nonradiative energy transfer to form a hydrogen atom that is lower in energy than unreacted atomic hydrogen with the release of energy. Upon the addition of 5% argon catalyst to a hydrogen plasma, the Lyman α emission was observed to increase by about an order of magnitude which indicated an increase in the plasma temperature; whereas, xenon control had no effect. Thus, the energy balances of argon-hydrogen glow discharge plasmas were measured using Calvet calorimetry. The steady state Calvet voltage significantly increased upon the addition of 3% hydrogen to an argon plasma, and the output signal was integrated until the signal returned to baseline. An energy balance of over $-151,000\,kJ\,/\,mole\,H_2$ was measured compared to the enthalpy of combustion of hydrogen of $-241.8\,kJ\,/\,mole\,H_2$. Whereas, under identical conditions no change in the Calvet voltage was observed when hydrogen was added to a plasma of xenon which does not provide a reaction with a net enthalpy of a multiple of the potential energy of atomic hydrogen under these conditions.

I. INTRODUCTION

A. Background

J. J. Balmer showed in 1885 that the frequencies for some of the lines observed in the emission spectrum of atomic hydrogen could be expressed with a completely empirical relationship. This approach was later extended by J. R. Rydberg, who showed that all of the spectral lines of atomic hydrogen were given by the equation:

$$\overline{v} = R\left(\frac{1}{n_f^2} - \frac{1}{n_i^2} \right) \tag{1}$$

where $R = 109,677\ cm^{-1}$, $n_f = 1,2,3,...$, $n_i = 2,3,4,...$, and $n_i > n_f$.

Niels Bohr, in 1913, developed a theory for atomic hydrogen that gave energy levels in agreement with Rydberg's equation. An identical equation, based on a totally different theory for the hydrogen atom, was developed by E. Schrödinger, and independently by W. Heisenberg, in 1926.

$$E_n = -\frac{e^2}{n^2 8\pi\varepsilon_o a_H} = -\frac{13.598\ eV}{n^2} \tag{2a}$$

$$n = 1,2,3,... \tag{2b}$$

where a_H is the Bohr radius for the hydrogen atom ($52.947\ pm$), e is the magnitude of the charge of the electron, and ε_o is the vacuum permittivity. Based on the solution of a Schrödinger-type wave equation with a nonradiative boundary condition based on Maxwell's equations, Mills [1-35] predicts that atomic hydrogen may undergo a catalytic reaction with certain atomized elements or certain gaseous ions which singly or multiply ionize at integer multiples of the potential energy of atomic hydrogen, 27.2 eV. The reaction involves a nonradiative energy transfer to form a hydrogen atom that is lower in energy than unreacted atomic hydrogen that corresponds to a fractional principal quantum number where Eq. (2b) should be replaced by Eq. (2c).

$$n = 1,2,3,..., \ and, \ n = \frac{1}{2},\frac{1}{3},\frac{1}{4},... \tag{2c}$$

2

A number of independent experimental observations lead to the conclusion that atomic hydrogen can exist in fractional quantum states that are at lower energies than the traditional "ground" ($n = 1$) state.

B. Lower-Energy Hydrogen Experimental Data

Prior related studies that support the possibility of a novel reaction of atomic hydrogen which produces a chemically generated or assisted plasma (rt-plasma) and produces novel hydride compounds include extreme ultraviolet (EUV) spectroscopy [6-9, 11-18, 21-23], characteristic emission from catalysis and the hydride ion products [9-14], lower-energy hydrogen emission [4, 6, 7-8, 17], plasma formation [9, 11-16, 21-22, 24-25], Balmer α line broadening [7, 9, 11, 15-19], elevated electron temperature [7, 17], anomalous plasma afterglow duration [24-25], power generation [7, 9, 15-17, 19-21, 32], and analysis of chemical compounds [26-32]. Exemplary studies include:

1.) the observation of intense extreme ultraviolet (EUV) emission at low temperatures (e.g. $\approx 10^3\,K$) from atomic hydrogen and only those atomized elements or gaseous ions which provide a net enthalpy of reaction of approximately $m \cdot 27.2\,eV$ via the ionization of t electrons to a continuum energy level where t and m are each an integer (e.g. K, Cs, and Sr atoms and Rb^+ ion ionize at integer multiples of the potential energy of atomic hydrogen and caused emission; whereas, the chemically similar atoms, Na, Mg, and Ba, do not ionize at integer multiples of the potential energy of atomic hydrogen and caused no emission) [9, 11-16, 21-22, 24-25],

2.) the observation of novel EUV emission lines from microwave and glow discharges of helium with 2% hydrogen with energies of $q \cdot 13.6\,eV$ where $q = 1,2,3,4,6,7,8,9,11,12$ or these lines inelastically scattered by helium atoms in the excitation of $He\,(1s^2)$ to $He\,(1s^1 2p^1)$ that were identified as hydrogen transitions to electronic energy levels below the "ground" state corresponding to fractional quantum numbers [6, 7, 17],

3.) the observation of novel EUV emission lines from microwave and glow discharges of helium with 2% hydrogen at $44.2\,nm$ and $40.5\,nm$ with energies of $q \cdot 13.6 + \left(\dfrac{1}{n_f^2} - \dfrac{1}{n_i^2} \right) X13.6\,eV$ where $q = 2$ and $n_f = 2,4$ $n_i = \infty$

3

that corresponded to multipole coupling to give two photon emission from a continuum excited state atom and an atom undergoing fractional Rydberg state transition [7],

4.) the identification of transitions of atomic hydrogen to lower energy levels corresponding to lower-energy hydrogen atoms in the extreme ultraviolet emission spectrum from interstellar medium and the sun [1, 4, 6, 8],

5.) the EUV spectroscopic observation of lines by the Institut für Niedertemperatur-Plasmaphysik e.V. that could be assigned to transitions of atomic hydrogen to lower energy levels corresponding to fractional principal quantum numbers and the emission from the excitation of the corresponding hydride ions [23],

6.) the recent analysis of mobility and spectroscopy data of individual electrons in liquid helium which shows direct experimental confirmation that electrons may have fractional principal quantum energy levels [5],

7.) the observation of novel EUV emission lines from microwave discharges of argon or helium with 10% hydrogen that matched those predicted for vibrational transitions of $H_2^*[n=1/4;n*=2]^+$ with energies of $v \cdot 1.185 \, eV$, $v = 17 \, to \, 38$ that terminated at the predicted dissociation limit, E_D, of $H_2[n=1/4]^+$, $E_D = 42.88 \, eV \, (28.92 \, nm)$ [8],

8.) the observation of continuum state emission of Cs^{2+} and Ar^{2+} at $53.3 \, nm$ and $45.6 \, nm$, respectively, with the absence of the other corresponding Rydberg series of lines from these species which confirmed the resonant nonradiative energy transfer of $27.2 \, eV$ from atomic hydrogen to the catalysts atomic Cs or Ar^+ [14],

9.) the spectroscopic observation of the predicted hydride ion $H^-(1/2)$ of hydrogen catalysis by either Cs atom or Ar^+ catalyst at $407 \, nm$ corresponding to its predicted binding energy of $3.05 \, eV$ [14],

10.) the observation of $H^-(1/2)$, the hydride ion catalyst product of K^+/K^+ or Rb^+, by high resolution visible spectroscopy as a broad peak at $407.00 \, nm$ with a FWHM of $0.14 \, nm$ corresponding to its predicted binding energy of $3.0468 \, eV$ [11],

11.) the observation that the high resolution visible plasma emission spectra in the region of $400.0 \, nm$ to $406.0 \, nm$ matched the predicted bound-free hyperfine structure lines E_{HF} of $H^-(1/2)$ calculated

4

from the electron g factor as $E_{HF} = j^2 3.0056 \times 10^{-5} + 3.0575\,eV$ (j is an integer) for $j = 1$ to $j = 37$ [16] to within a 1 part per 10^5 [11],

12.) the observation of characteristic emission from K^{3+} which confirmed the resonant nonradiative energy transfer of $3 \cdot 27.2\,eV$ from atomic hydrogen to atomic K [13],

13.) the spectroscopic observation of the predicted $H^-(1/4)$ ion of hydrogen catalysis by K catalyst at 110 nm corresponding to its predicted binding energy of $11.2\,eV$ [11, 13],

14.) the observation of characteristic emission from Rb^{2+} which confirmed the resonant nonradiative energy transfer of $27.2\,eV$ from atomic hydrogen to Rb^+ [12],

15.) the spectroscopic observation of the predicted $H^-(1/2)$ ion of hydrogen catalysis by Rb^+ catalyst at 407 nm corresponding to its predicted binding energy of $3.05\,eV$ [12],

16.) the observation by the Institut für Niedertemperatur-Plasmaphysik e.V. of an anomalous plasma and plasma afterglow duration formed with hydrogen-potassium mixtures [24],

17.) the observation of anomalous afterglow durations of plasmas formed by catalysts providing a net enthalpy of reaction within thermal energies of $m \cdot 27.28\,eV$ [24-25],

18.) the observation of Lyman series in the EUV that represents an energy release about 10 times that of hydrogen combustion which is greater than that of any possible known chemical reaction [9, 11-16, 21-22, 24-25],

19.) the observation of line emission by the Institut für Niedertemperatur-Plasmaphysik e.V. with a 4° grazing incidence EUV spectrometer that was 100 times more energetic than the combustion of hydrogen [23],

20.) the observation of anomalous plasmas formed with Sr and Ar^+ catalysts at 1% of the theoretical or prior known voltage requirement with a light output per unit power input up to 8600 times that of the control standard light source [15-16, 20-21],

21.) the observation that the optically measured output power of gas cells for power supplied to the glow discharge increased by over two orders of magnitude depending on the presence of less than 1% partial pressure of certain catalysts in hydrogen gas or argon-hydrogen gas

mixtures, and an excess thermal balance of 42 W was measured for the 97% argon and 3% hydrogen mixture versus argon plasma alone [20],

22.) the observation that glow discharge plasmas of the catalyst-hydrogen mixtures of strontium-hydrogen, helium-hydrogen, argon-hydrogen, strontium-helium-hydrogen, and strontium-argon-hydrogen showed significant Balmer α line broadening corresponding to an average hydrogen atom temperature of $25\text{-}45\,eV$; whereas, plasmas of the noncatalyst-hydrogen mixtures of pure hydrogen, krypton-hydrogen, xenon-hydrogen, and magnesium-hydrogen showed no excessive broadening corresponding to an average hydrogen atom temperature of $\approx 3\,eV$ [17-19],

23.) the observation that microwave helium-hydrogen and argon-hydrogen plasmas having catalyst Ar^+ or He^{2+} showed extraordinary Balmer α line broadening due to hydrogen catalysis corresponding to an average hydrogen atom temperature of $110\text{-}130\,eV$ and $180\text{-}210\,eV$, respectively; whereas, plasmas of pure hydrogen, neon-hydrogen, krypton-hydrogen, and xenon-hydrogen showed no excessive broadening corresponding to an average hydrogen atom temperature of $\approx 3\,eV$ [7, 18],

24.) the observation that microwave helium-hydrogen and argon-hydrogen plasmas showed average electron temperatures that were high, 28,000 K and 11,600 K, respectively; whereas, the corresponding temperatures of helium and argon alone were only 6800 K and 4800 K, respectively [7, 18],

25.) the observation of significant Balmer α line broadening of 17, 9, 11, 14, and 24 eV from rt-plasmas of incandescently heated hydrogen with K^+ / K^+, Rb^+, cesium, strontium, and strontium with Ar^+ catalysts, respectively, wherein the results could not be explained by Stark or thermal broadening or electric field acceleration of charged species since the measured field of the incandescent heater was extremely weak, 1 V/cm, corresponding to a broadening of much less than $1\,eV$ [9],

26.) calorimetric measurement of excess power of 20 mW/cc on rt-plasmas formed by heating hydrogen with K^+ / K^+ and Ar^+ as catalysts [9],

27.) the high resolution visible spectroscopic observation from rt-plasmas and plasma electrolysis cells of the predicted $H^-(1/2)$ ion of hydrogen catalysis by each of K^+ / K^+, Rb^+, Cs, and Ar^+ at 407 nm corresponding to its predicted binding energy of $3.05\,eV$ [9-11],

28.) the isolation of novel inorganic hydride compounds such as $KH\ KHCO_3$ and KH following each of the electrolysis and plasma electrolysis of a K_2CO_3 electrolyte which comprised high binding energy hydride ions that were stable in water with their identification by methods such as (i) ToF-SIMS on $KH\ KHCO_3$ which showed inorganic hydride clusters $K[KH\ KHCO_3]_n^+$ and a negative ToF-SIMS dominated by hydride ion, (ii) X-ray photoelectron spectroscopy which showed novel peaks corresponding to high binding energy hydride ions, and (iii) proton nuclear magnetic resonance spectroscopy which showed upfield shifted peaks corresponding to more diamagnetic, high-binding-energy hydride ions [10, 28-29, 31],

29.) the observation that the power output exceeded the power supplied to a hydrogen glow discharge plasmas by 35-184 W depending on the presence of catalysts from helium or argon and less than 1% partial pressure of strontium metal in noble gas-hydrogen mixtures; whereas, the chemically similar noncatalyst krypton had no effect on the power balance [19],

30.) the observation that upon the addition of 10% hydrogen to a helium microwave plasma maintained with a constant microwave input power of $40\ W$, the thermal output power was measured to be at least $400\ W$ corresponding to a reactor temperature rise from room temperature to 1200 °C within 150 seconds, a power density of $40\ MW/m^3$, and an energy balance of at least $-5 \times 10^5\ kJ/mole\ H_2$ compared to the enthalpy of combustion of hydrogen of $-241.8\ kJ/mole\ H_2$ [17],

31.) the differential scanning calorimetry (DSC) measurement of minimum heats of formation of KHI by the catalytic reaction of K with atomic hydrogen and KI that were over $-2000\ kJ/mole\ H_2$ compared to the enthalpy of combustion of hydrogen of $-241.8\ kJ/mole\ H_2$ [32],

32.) the isolation of novel hydrogen compounds as products of the reaction of atomic hydrogen with atoms and ions which formed an anomalous plasma as reported in the EUV studies [26-32],

33.) the identification of novel hydride compounds by a number of analytic methods as such as (i) time of flight secondary ion mass spectroscopy which showed a dominant hydride ion in the negative ion spectrum, (ii) X-ray photoelectron spectroscopy which showed novel hydride peaks and significant shifts of the core levels of the primary

elements bound to the novel hydride ions, (iii) ^1H nuclear magnetic resonance spectroscopy (NMR) which showed extraordinary upfield chemical shifts compared to the NMR of the corresponding ordinary hydrides, and iv.) thermal decomposition with analysis by gas chromatography, and mass spectroscopy which identified the compounds as hydrides [26-32],

34.) the NMR identification of novel hydride compounds $MH*X$ wherein M is the alkali or alkaline earth metal, X, is a halide, and $H*$ comprises a novel high binding energy hydride ion identified by a large distinct upfield resonance [26-31],

35.) the replication of the NMR results of the identification of novel hydride compounds by large distinct upfield resonances at Spectral Data Services, University of Massachusetts Amherst, University of Delaware, Grace Davison, and National Research Council of Canada [26],

36.) the NMR identification of novel hydride compounds $MH*$ and MH_2^* wherein M is the alkali or alkaline earth metal and $H*$ comprises a novel high binding energy hydride ion identified by a large distinct upfield resonance that proves the hydride ion is different from the hydride ion of the corresponding known compound of the same composition [26].

C. Mechanism of the Formation of Lower-Energy Atomic Hydrogen

The mechanism of the EUV emission, the formation of novel hydrides, and the observation of certain EUV lines from interstellar medium and the sun can not be explained by the conventional energy levels of hydrogen, but it is predicted by a solution of the Schrödinger equation with a nonradiative boundary constraint put forward by Mills [1]. Mills predicts that certain atoms or ions serve as catalysts to release energy from hydrogen to produce an increased binding energy hydrogen atom called a *hydrino atom* having a binding energy given by Eq. (2a) where

$$n = \frac{1}{2}, \frac{1}{3}, \frac{1}{4}, ..., \frac{1}{p} \tag{3}$$

and p is an integer greater than 1, designated as $H\left[\dfrac{a_H}{p}\right]$ where a_H is the radius of the hydrogen atom. Hydrinos are predicted to form by reacting an ordinary hydrogen atom with a catalyst having a net enthalpy of reaction of about

$$m \cdot 27.2 \; eV \tag{4}$$

where m is an integer. This catalysis releases energy from the hydrogen atom with a commensurate decrease in size of the hydrogen atom, $r_n = n a_H$. For example, the catalysis of $H(n=1)$ to $H(n=1/2)$ releases $40.8 \; eV$, and the hydrogen radius decreases from a_H to $\dfrac{1}{2} a_H$.

The excited energy states of atomic hydrogen are also given by Eq. (2a) except with Eq. (2b). The $n=1$ state is the "ground" state for "pure" photon transitions (the $n=1$ state can absorb a photon and go to an excited electronic state, but it cannot release a photon and go to a lower-energy electronic state). However, an electron transition from the ground state to a lower-energy state is possible by a nonradiative energy transfer such as multipole coupling or a resonant collision mechanism. These lower-energy states have fractional quantum numbers, $n = \dfrac{1}{\text{integer}}$.

Processes that occur without photons and that require collisions are common. For example, the exothermic chemical reaction of $H+H$ to form H_2 does not occur with the emission of a photon. Rather, the reaction requires a collision with a third body, M, to remove the bond energy- $H + H + M \rightarrow H_2 + M^*$ [36]. The third body distributes the energy from the exothermic reaction, and the end result is the H_2 molecule and an increase in the temperature of the system. Some commercial phosphors are based on nonradiative energy transfer involving multipole coupling. For example, the strong absorption strength of Sb^{3+} ions along with the efficient nonradiative transfer of excitation from Sb^{3+} to Mn^{2+} are responsible for the strong manganese luminescence from phosphors containing these ions [37].

Similarly, the $n=1$ state of hydrogen and the $n = \dfrac{1}{\text{integer}}$ states of hydrogen are nonradiative, but a transition between two nonradiative states, say $n=1$ to $n=1/2$, is possible via a nonradiative energy transfer. In these cases, during the transition the electron couples to another

9

electron transition, electron transfer reaction, or inelastic scattering reaction which can absorb the exact amount of energy that must be removed from the hydrogen atom to cause the transition. Thus, a catalyst provides a net positive enthalpy of reaction of $m \cdot 27.2\ eV$ (i.e. it absorbs $m \cdot 27.2\ eV$ where m is an integer). Certain atoms or ions serve as catalysts by accepting energy from hydrogen atoms through a nonradiative resonant transfer. The catalyst may then release the transferred energy by radiative and nonradiative mechanisms. As a consequence of the nonradiative energy transfer, the hydrogen atom becomes unstable and emits further energy until it achieves a lower-energy nonradiative state having a principal energy level given by Eqs. (2a) and (3).

D. Catalysts

Argon ions can provide a net enthalpy of a multiple of that of the potential energy of the hydrogen atom. The second ionization energy of argon is $27.63\ eV$ [38]. The reaction Ar^+ to Ar^{2+} has a net enthalpy of reaction of $27.63\ eV$, which is equivalent to $m = 1$ in Eq. (4).

$$27.63\ eV + Ar^+ + H\left[\frac{a_H}{p}\right] \rightarrow Ar^{2+} + e^- + H\left[\frac{a_H}{(p+1)}\right] + [(p+1)^2 - p^2]X13.6\ eV \tag{5}$$

$$Ar^{2+} + e^- \rightarrow Ar^+ + 27.63\ eV \tag{6}$$

And, the overall reaction is

$$H\left[\frac{a_H}{p}\right] \rightarrow H\left[\frac{a_H}{(p+1)}\right] + [(p+1)^2 - p^2]X13.6\ eV \tag{7}$$

The energy given off during catalysis is much greater than the energy lost to the catalyst. The energy released is large compared to conventional chemical reactions. For example, when hydrogen and oxygen gases undergo combustion to form water

$$H_2(g) + \frac{1}{2}O_2(g) \rightarrow H_2O(g) \tag{8}$$

the known enthalpy of formation of water is $\Delta H_f = -241.8\ kJ/mole$ or 1.25 eV per hydrogen atom. By contrast, each $(n = 1)$ ordinary hydrogen atom undergoing catalysis releases a net of $40.8\ eV$. Moreover, further catalytic transitions may occur: $n = \frac{1}{2} \rightarrow \frac{1}{3}, \frac{1}{3} \rightarrow \frac{1}{4}, \frac{1}{4} \rightarrow \frac{1}{5}$, and so on. Once catalysis

1 0

begins. hydrinos autocatalyze further in a process called *disproportionation*. This mechanism is similar to that of an inorganic ion catalysis. But, hydrino catalysis should have a higher reaction rate than that of the inorganic ion catalyst due to the better match of the enthalpy to $m \cdot 27.2 \, eV$.

II. EXPERIMENTAL

A. EUV Spectroscopy

Extreme ultraviolet (EUV) spectroscopy was recorded on a hydrogen microwave plasma alone and with 5% argon or 5% xenon. Due to the extremely short wavelength of this radiation, "transparent" optics do not exist. Therefore, a windowless arrangement was used wherein the microwave discharge cell was connected to the same vacuum vessel as the grating and detectors of the EUV spectrometer. Differential pumping permitted a high pressure in the cell as compared to that in the spectrometer. This was achieved by pumping on the cell outlet and pumping on the grating side of the collimator that served as a pin-hole inlet to the optics. The spectrometer was continuously evacuated to $10^{-4} - 10^{-6}$ Torr by a turbomolecular pump with the pressure read by a cold cathode pressure gauge. The EUV spectrometer was connected to the cell light source with a 1.5 mm X 5 mm collimator which provided a light path to the slits of the EUV spectrometer. The collimator also served as a flow constrictor of gas from the cell. The cell was operated under gas flow conditions while maintaining a constant gas pressure in the cell.

For spectral measurement, the light emission from microwave plasmas of hydrogen alone, hydrogen-argon (95/5%), and hydrogen-xenon (95/5%) were introduced to a normal incidence McPherson 0.2 meter monochromator (Model 302, Seya-Namioka type) equipped with a 1200 lines/mm holographic grating with a platinum coating. The wavelength region covered by the monochromator was $5 - 560 \, nm$. The UV spectrum $(90 - 165 \, nm)$ of the cell emission was recorded with a photomultiplier tube (PMT) and a sodium salicylate scintillator. The PMT (Model R1527P, Hamamatsu) used has a spectral response in the range of $185 - 680 \, nm$ with a peak efficiency at about $400 \, nm$. The wavelength

resolution was about 1 nm (FWHM) with an entrance and exit slit width of 300 μm. The increment was 0.1 nm and the dwell time was 500 ms.

B. Microwave Emission Spectra

The experimental set up comprising a microwave discharge gas cell light source and an EUV spectrometer which was differentially pumped is shown in Figure 1. Extreme ultraviolet emission spectra were obtained on plasmas of hydrogen alone, hydrogen-argon mixture (95/5%), and hydrogen-xenon mixture (95/5%). Hydrogen or the hydrogen-noble gas mixture was flowed through a half inch diameter quartz tube at 1 Torr that was maintained by flowing hydrogen or the gas mixture while monitoring the pressure with a 10 Torr and 1000 Torr MKS Baratron absolute pressure gauge. The tube was fitted with an Opthos coaxial microwave cavity (Evenson cavity). The microwave generator was a Opthos model MPG-4M generator (Frequency: 2450 MHz). The input power to the plasma was set at 85 watts. The EUV spectrometer was a normal incidence monochromator. (See EUV-Spectroscopy Section).

C. Calvet Calorimeter Methods

The instrument used to measure the heat of reaction was a cylindrical heat flux calorimeter (International Thermal Instrument Co., Model CA-100-1). The cylindrical calorimeter walls contained a thermopile structure composed of two sets of thermoelectric junctions. One set of junctions was in thermal contact with the internal calorimeter wall, at temperature T_i, and the second set of thermal junctions was in thermal contact with the external calorimeter wall at T_e which was held constant by a forced convection oven. When heat was generated in the calorimeter cell, the calorimeter radially transferred a constant fraction of this heat into the surrounding heat sink. As heat flowed a temperature gradient, $(T_i - T_e)$, was established between the two sets of thermopile junctions. This temperature gradient generated a voltage which was compared to the linear voltage versus power calibration curve to give the power of reaction. The calorimeter was calibrated with a precision resistor and a fixed current source at power levels

1 2

representative of the power of reaction of the catalyst runs. At constant total pressure, the calibration constant of the Calvet calorimeter was not sensitive to the flow of test gas over the range of conditions of the tests. To avoid corrosion, a cylindrical reactor, machined from 304 stainless steel to fit inside the calorimeter, was used to contain the reaction. To maintain an isothermal reaction system and improve baseline stability, the calorimeter was placed inside a commercial forced convection oven (Precision Scientific 625 S) that was operated at room temperature to $475 K$. A more complete description of a similar instrument and methods are given by Bradford, Phillips, and Klanchar [39]. The general system design of the Calvet calorimeter is shown in Figure 2.

D.   Gas Cell for Calvet Calorimeter

The cylindrical stainless steel gas discharge cell and Calvet instrument for plasma energy balance studies with argon with 3% hydrogen addition compared to xenon with 3% hydrogen addition is shown in Figure 3. The cell comprised a 800 cm^3 stainless steel vessel capable of containing a vacuum or a pressure above atmospheric. The cell was maintained at an elevated isothermal temperature by a forced convection oven. The operating temperature of the gas cell was $475 K$. The cell was used in the vertical position and was inserted into a thermopile. The flange was sealed with a silver plated copper gasket. The flange had a centered high voltage feedthrough which transmitted the power, supplied through a power connector, to a hollow cathode inside the cell. The axial hollow cathode glow discharge electrode assembly shown in Figure 3 comprised a stainless steel plate (4.2 cm diameter, 0.9 mm thick) anode and a circumferential stainless steel cylindrical frame (5.1 cm OD, 7.2 cm long) perforated with evenly spaced 1 cm diameter holes. The cathode was wound with several layers of nickel screen and was attached to the cell body by a stainless steel wire covered with ceramic beads for electrical insulation, and the cell body was grounded. The flange also had a 1/4" vacuum port through which a 1/8" inlet for argon, krypton, xenon, or hydrogen passed. The 1/8" inlet was connected to a 1/4" stainless steel tube which connected to a Tee, a needle valve, a pressure gauge, and noble gas and hydrogen supplies.

1 3

The elbow port of the Tee was attached to a vacuum gauge, a needle valve, and then a vacuum pump.

The gas in each experiment was ultrahigh pure grade or higher (Praxair). Test gases comprised hydrogen alone, krypton alone, xenon alone, xenon with the initial addition of 3% hydrogen, argon alone, and argon with the initial addition of 3% hydrogen. In the case of calibration experiments, the steady state Calvet voltage output was recorded as the power was varied over the power range of 10 W to 100 W for plasmas of pure hydrogen, krypton, or xenon at 3 Torr.

In the case of energy balance measurements, the noble gas pressure inside the cell was maintained at 3 Torr under static discharge conditions. After the calorimeter reached a steady state with 20 W of input power to the plasma, the total pressure was reduced by pumping, and hydrogen was added until the total pressure was 3 Torr for an initial noble gas-hydrogen mixture of 97/3%. Each gas flow was controlled by a 0-20 sccm range mass flow controller (MKS 1179A21CS1BB) with a readout (MKS type 246). The cell pressure was monitored by a 0-10 Torr MKS Baratron absolute pressure gauge. After achieving the desired gas mixture, the cell was run static with the input power unchanged. The Calvet output voltage was recorded as the hydrogen was consumed as indicated by a 3% drop in pressure as the elevated signal returned to baseline. No exotherm or pressure drop was observed in the case of xenon-hydrogen; so, the experiment was recorded for the same period of time as the argon-hydrogen experiment. The data was recorded with a PC based computer data acquisition system (National Instruments).

E. Energy balance measurements

Since the ambient temperature was held constant, the general form of the energy balance equation for the cell in steady state is:
$$0 = P_{in} + P_{ex} - P_{loss} \tag{9}$$
where P_{in} is the input power to the discharge, P_{ex} is the excess power generated from the hydrogen catalysis reaction, and P_{loss} is the thermal power loss from the cell. The Calvet voltage response to input power for hydrogen, krypton, or xenon alone was determined over the constant input power range of 10 W to 100 W. The data was recorded after the

14

cell had reached a thermal steady state with each increase in the input power to the glow discharge which typically occurred in 20 hours. At this point, the power lost from the cell P_{loss} was equal to the total power P_T supplied to the cell P_{in} plus any excess power P_{ex}.

$$P_T = P_{in} + P_{ex} = P_{loss} \qquad (10)$$

Since the heat transfer was dominated by conduction, the output voltage of the cell V was modeled by a linear curve

$$V = aP_T + C \qquad (11)$$

where a and C are constants for the least square curve fit of the Calvet voltage response to power input for the control experiments ($P_{ex} = 0$). V was recorded as a function of input power P_{in} for noncatalyst controls as the input power was varied. The higher voltage produced by the catalyst gas with hydrogen compared with the control gases was representative of the excess power. In the case of the catalyst run, the total output power P_T was determined by solving Eq. (11) using the measured V. The excess power P_{ex} was determined from Eq. (10). The integral of the excess power P_{ex} over time gave the excess energy E_{ex}.

III. RESULTS

A. Argon-hydrogen microwave emission spectrum

The EUV spectrum ($90-165\,nm$) of the cell emission from the hydrogen plasma (dotted line) and the hydrogen plasma to which 5% argon was added (solid line) is shown in Figure 4. Upon the addition of 5% argon, the hydrogen Lyman α emission intensity was observed to increase by about an order of magnitude which is indicative of a higher plasma temperature. Essentially no effect was observed for the addition of 5% xenon to the hydrogen plasma.

B. Power balance measurements

The Calvet voltage as a function of the power applied to each of the control gases at 3 Torr total pressure was plotted for the input power range of 10 W to 100 W as shown in Figure 5. The least squares fit of the V response to unit input power calculated from the control plasmas,

15

hydrogen, krypton, or xenon alone, (Eq. (11)) was determined to be
$$V = 7.93 + 2.25 \times P_T \tag{12}$$

An argon plasma was maintained at a constant 20 W input power until steady state. The Calvet voltage significantly increased upon the addition of 3% hydrogen, and the output signal was recorded until the signal returned to baseline as shown in Figure 6. Due to the long response time of the Calvet calorimeter (20 hours), the result shown in Figure 6 was essentially the Calvet impulse response. The excess power was determine from Eq. (12) and Eq. (10). The integral of the power over the exotherm gave an energy balance of $-151,000 \, kJ/mole \, H_2$. The experiment was repeated for xenon. The addition of hydrogen did not produce an exotherm as shown in Figure 7.

IV. DISCUSSION

Upon the addition of 5% argon to a hydrogen plasma, the Lyman alpha emission was observed to increase by about an order of magnitude which indicated an increase in the plasma temperature; whereas, no effect was observed with xenon. Thus, the energy balances of argon-hydrogen glow discharge plasmas were measured using Calvet calorimetry. The steady state Calvet voltage significantly increased upon the addition of 3% hydrogen, and the output signal was integrated until the signal returned to baseline. Energy balances of over $-151,000 \, kJ/mole \, H_2$ were measured compared to the enthalpy of combustion of hydrogen of $-241.8 \, kJ/mole \, H_2$. Whereas, under identical conditions no change in the Calvet voltage was observed when hydrogen was added to a plasma of xenon.

Argon is a source of the catalyst, Ar^+; whereas, xenon does not provide a reaction with a net enthalpy of a multiple of the potential energy of atomic hydrogen under these conditions. The presently observed energy balances were about $785 \, eV/H \, atom$. The results indicate that once a hydrino atom is formed by a catalyst (Eqs. (5-7)) further catalytic transitions: $n = \frac{1}{2} \rightarrow \frac{1}{3}, \frac{1}{3} \rightarrow \frac{1}{4}, \frac{1}{4} \rightarrow \frac{1}{5}$, and so on occur to a substantial extent. This is consistent with the previously reported series of lower-energy hydrogen lines with energies of $q \cdot 13.6 \, eV$ where

16

$q = 1,2,3,4,6,7,8,9,11,12$ [6-7, 17] and the studies given in Section B of the Introduction which show very large energy balances.

Since the net enthalpy released may be over several hundred times that of combustion, the catalysis of atomic hydrogen represents a new source of energy with H_2O as the source of hydrogen fuel. Moreover, rather than air pollutants or radioactive waste, novel hydride compounds with potential commercial applications are the products [26-32]. Since the power is in the form of a plasma, direct high-efficiency, low cost energy conversion may be possible [33-35], thus, avoiding a heat engine such as a turbine or a reformer-fuel cell system. Significantly lower capital costs and lower commercial operating costs than that of any known competing energy source are anticipated.

REFERENCES

1. R. Mills, *The Grand Unified Theory of Classical Quantum Mechanics*, September 2001 Edition, BlackLight Power, Inc., Cranbury, New Jersey, Distributed by Amazon.com; posted at www.blacklightpower.com.
2. R. Mills, "The Grand Unified Theory of Classical Quantum Mechanics", Global Foundation, Inc. Orbis Scientiae entitled *The Role of Attractive and Repulsive Gravitational Forces in Cosmic Acceleration of Particles The Origin of the Cosmic Gamma Ray Bursts*, (29th Conference on High Energy Physics and Cosmology Since 1964) Dr. Behram N. Kursunoglu, Chairman, December 14-17, 2000, Lago Mar Resort, Fort Lauderdale, FL, Kluwer Academic/Plenum Publishers, New York, pp. 243-258.
3. R. Mills, "The Grand Unified Theory of Classical Quantum Mechanics", Int. J. of Hydrogen Energy, in press.
4. R. Mills, "The Hydrogen Atom Revisited", Int. J. of Hydrogen Energy, Vol. 25, Issue 12, December, (2000), pp. 1171-1183.
5. R. Mills, The Nature of Free Electrons in Superfluid Helium—a Test of Quantum Mechanics and a Basis to Review its Foundations and Make a Comparison to Classical Theory, Int. J. Hydrogen Energy, Vol. 26, No. 10, (2001), pp. 1059-1096.
6. R. Mills, P. Ray, "Spectral Emission of Fractional Quantum Energy Levels of Atomic Hydrogen from a Helium-Hydrogen Plasma and the Implications for Dark Matter", Int. J. Hydrogen Energy, in press.

7. R. L. Mills, P. Ray, B. Dhandapani, J. He, "Spectroscopic Identification of Fractional Rydberg States of Atomic Hydrogen" J. Phys. Chem. Letts., submitted.

8. R. Mills, P. Ray, "Vibrational Spectral Emission of Fractional-Principal-Quantum-Energy-Level Hydrogen Molecular Ion", Int. J. Hydrogen Energy, in press.

9. R. Mills, P. Ray, M. Nansteel, W. Good, P. Jansson, B. Dhandapani, J. He, "Excessive Balmer α Line Broadening, Power Balance, and Novel Hydride Ion Product of Plasma Formed from Incandescently Heated Hydrogen Gas with Certain Catalysts", Int. J. Hydrogen Energy, submitted.

10. R. Mills, E. Dayalan, P. Ray, B. Dhandapani, J. He, "Highly Stable Novel Inorganic Hydrides from Aqueous Electrolysis and Plasma Electrolysis, Japanese Journal of Applied Physics, submitted.

11. R. L. Mills, P. Ray, " High Resolution Spectroscopic Observation of the Bound-Free Hyperfine Levels of a Novel Hydride Ion Corresponding to a Fractional Rydberg State of Atomic Hydrogen", Int. J. Hydrogen Energy, submitted.

12. R. L. Mills, P. Ray, "Spectroscopic Identification of a Novel Catalytic Reaction of Rubidium Ion with Atomic Hydrogen and the Hydride Ion Product", Int. J. Hydrogen Energy, in press.

13. R. Mills, P. Ray, Spectroscopic Identification of a Novel Catalytic Reaction of Potassium and Atomic Hydrogen and the Hydride Ion Product, Int. J. Hydrogen Energy, Vol. 27, No. 2, February, (2002), pp. 183-192.

14. R. Mills, "Spectroscopic Identification of a Novel Catalytic Reaction of Atomic Hydrogen and the Hydride Ion Product", Int. J. Hydrogen Energy, Vol. 26, No. 10, (2001), pp. 1041-1058.

15. R. Mills and M. Nansteel, "Argon-Hydrogen-Strontium Plasma Light Source", IEEE Transactions on Plasma Science, submitted.

16. R. Mills, M. Nansteel, and Y. Lu, "Excessively Bright Hydrogen-Strontium Plasma Light Source Due to Energy Resonance of Strontium with Hydrogen", European Journal of Physics D, submitted.

17. R. L. Mills, P. Ray, B. Dhandapani, M. Nansteel, X. Chen, J. He, "New Power Source from Fractional Quantum Energy Levels of Atomic Hydrogen that Surpasses Internal Combustion", Spectrochimica Acta,

submitted.

18. R. L. Mills, P. Ray, B. Dhandapani, J. He, "Comparison of Excessive Balmer α Line Broadening of Glow Discharge and Microwave Hydrogen Plasmas with Certain Catalysts" Chem. Phys., submitted.

19. R. L. Mills, A. Voigt, P. Ray, M. Nansteel, B. Dhandapani, "Measurement of Hydrogen Balmer Line Broadening and Thermal Power Balances of Noble Gas-Hydrogen Discharge Plasmas", Int. J. Hydrogen Energy, in press.

20. R. Mills, N. Greenig, S. Hicks, "Optically Measured Power Balances of Anomalous Discharges of Mixtures of Argon, Hydrogen, and Potassium, Rubidium, Cesium, or Strontium Vapor", Int. J. Hydrogen Energy, in press.

21. R. Mills, M. Nansteel, and Y. Lu, "Observation of Extreme Ultraviolet Hydrogen Emission from Incandescently Heated Hydrogen Gas with Strontium that Produced an Anomalous Optically Measured Power Balance", Int. J. Hydrogen Energy, Vol. 26, No. 4, (2001), pp. 309-326.

22. R. Mills, J. Dong, Y. Lu, "Observation of Extreme Ultraviolet Hydrogen Emission from Incandescently Heated Hydrogen Gas with Certain Catalysts", Int. J. Hydrogen Energy, Vol. 25, (2000), pp. 919-943.

23. R. Mills, "Observation of Extreme Ultraviolet Emission from Hydrogen-KI Plasmas Produced by a Hollow Cathode Discharge", Int. J. Hydrogen Energy, Vol. 26, No. 6, (2001), pp. 579-592.

24. R. Mills, "Temporal Behavior of Light-Emission in the Visible Spectral Range from a Ti-K2CO3-H-Cell", Int. J. Hydrogen Energy, Vol. 26, No. 4, (2001), pp. 327-332.

25. R. Mills, T. Onuma, and Y. Lu, "Formation of a Hydrogen Plasma from an Incandescently Heated Hydrogen-Catalyst Gas Mixture with an Anomalous Afterglow Duration", Int. J. Hydrogen Energy, Vol. 26, No. 7, July, (2001), pp. 749-762.

26. R. Mills, B. Dhandapani, M. Nansteel, J. He, A. Voigt, "Identification of Compounds Containing Novel Hydride Ions by Nuclear Magnetic Resonance Spectroscopy", Int. J. Hydrogen Energy, Vol. 26, No. 9, Sept. (2001), pp. 965-979.

27. R. Mills, B. Dhandapani, N. Greenig, J. He, "Synthesis and Characterization of Potassium Iodo Hydride", Int. J. of Hydrogen Energy, Vol. 25, Issue 12, December, (2000), pp. 1185-1203.

28. R. Mills, "Novel Inorganic Hydride", Int. J. of Hydrogen Energy, Vol. 25, (2000), pp. 669-683.

29. R. Mills, "Novel Hydrogen Compounds from a Potassium Carbonate Electrolytic Cell", Fusion Technology, Vol. 37, No. 2, March, (2000), pp. 157-182.

30. R. Mills, B. Dhandapani, M. Nansteel, J. He, T. Shannon, A. Echezuria, "Synthesis and Characterization of Novel Hydride Compounds", Int. J. of Hydrogen Energy, Vol. 26, No. 4, (2001), pp. 339-367.

31. R. Mills, "Highly Stable Novel Inorganic Hydrides", Journal of New Materials for Electrochemical Systems, in press.

32. R. Mills, W. Good, A. Voigt, Jinquan Dong, "Minimum Heat of Formation of Potassium Iodo Hydride", Int. J. Hydrogen Energy, Vol. 26, No. 11, Oct., (2001), pp. 1199-1208.

33. R. Mills, "BlackLight Power Technology-A New Clean Hydrogen Energy Source with the Potential for Direct Conversion to Electricity", Proceedings of the National Hydrogen Association, 12 th Annual U.S. Hydrogen Meeting and Exposition, *Hydrogen: The Common Thread*, The Washington Hilton and Towers, Washington DC, (March 6-8, 2001), pp. 671-697.

34. R. Mills, "BlackLight Power Technology-A New Clean Energy Source with the Potential for Direct Conversion to Electricity", Global Foundation International Conference on "Global Warming and Energy Policy", Dr. Behram N. Kursunoglu, Chairman, Fort Lauderdale, FL, November 26-28, 2000, Kluwer Academic/Plenum Publishers, New York, pp. 1059-1096.

35. R. Mayo, R. Mills, M. Nansteel, "On the Potential of Direct and MHD Conversion of Power from a Novel Plasma Source to Electricity for Microdistributed Power Applications", IEEE Transactions on Plasma Science, submitted.

36. N. V. Sidgwick, *The Chemical Elements and Their Compounds*, Volume I, Oxford, Clarendon Press, (1950), p.17.

37. M. D. Lamb, *Luminescence Spectroscopy*, Academic Press, London, (1978), p. 68.

38. D. R. Linde, *CRC Handbook of Chemistry and Physics*, 79 th Edition, CRC Press, Boca Raton, Florida, (1998-9), p. 10-175 to p. 10-177.

39. M. C. Bradford, J. Phillips, J., Klanchar, Rev. Sci. Instrum., 66, (1),

January, (1995), pp. 171-175.

21

Figure Captions

Figure 1.   The experimental set up comprising a microwave discharge gas cell light source and an EUV spectrometer which was differentially pumped.

Figure 2.   The general system design of the Calvet calorimeter.

Figure 3.   Cylindrical stainless steel gas discharge cell and Calvet instrument for plasma energy balance studies of argon with the addition of 3% hydrogen compared to xenon with the addition of 3% hydrogen.
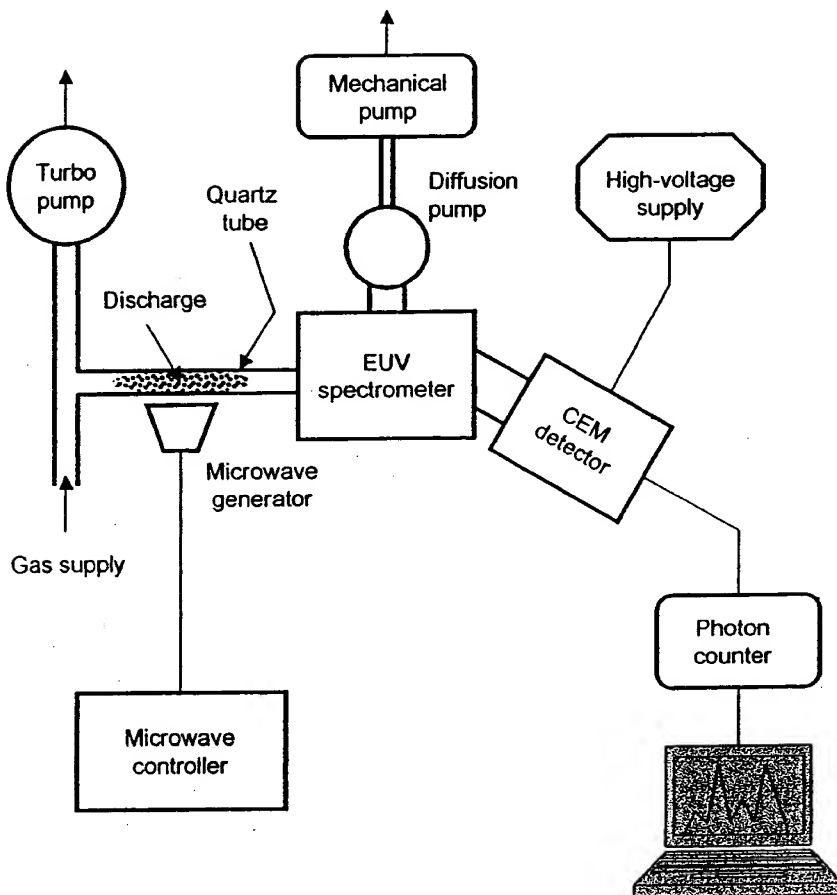
Figure 4.   The EUV spectrum ($90-165\,nm$) of the cell emission from the hydrogen plasma (dotted line) and the hydrogen plasma to which 5% argon was added (solid line).

Figure 5.   The Calvet voltage of as a function of the input power applied to each of the control gases, hydrogen, krypton, and xenon alone, at 3 Torr total pressure was plotted for the input power range of 10 W to 100 W.

Figure 6.   At constant input power, the Calvet signal response upon the switch of a 3 Torr argon plasma to plasma with 0.08 Torr of hydrogen and 2.92 Torr of argon.   The integral of the power over the exotherm gave an energy balance of $-151,000\,kJ/mole\,H_2$.

Figure 7.   At constant input power, the Calvet signal response upon the switch of a 3 Torr xenon plasma to plasma with 0.08 Torr of hydrogen and 2.92 Torr of xenon where no exotherm was observed.

1

Fig. 1

Turbo
pump

Quartz
tube

Discharge

Mechanical
pump

Diffusion
pump

High-voltage
supply

EUV
spectrometer

CEM
detector

Microwave
generator

Gas supply

Microwave
controller

Photon
counter

Fig. 2

Ni electric feedthrough

0.25" stainless steel tube (vacuum / gas port)

Cell lid

Ni screen

Stainless steel hollow cathode
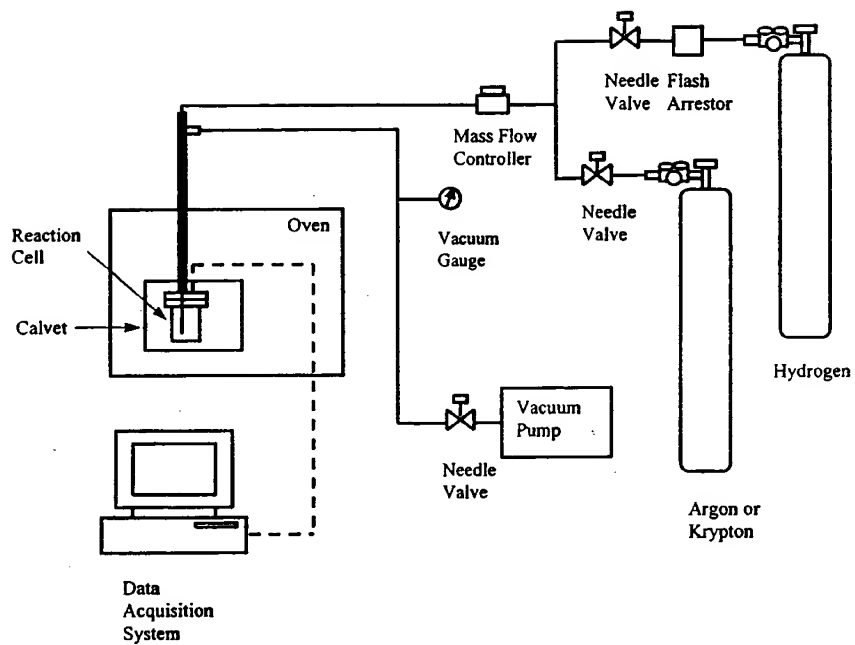
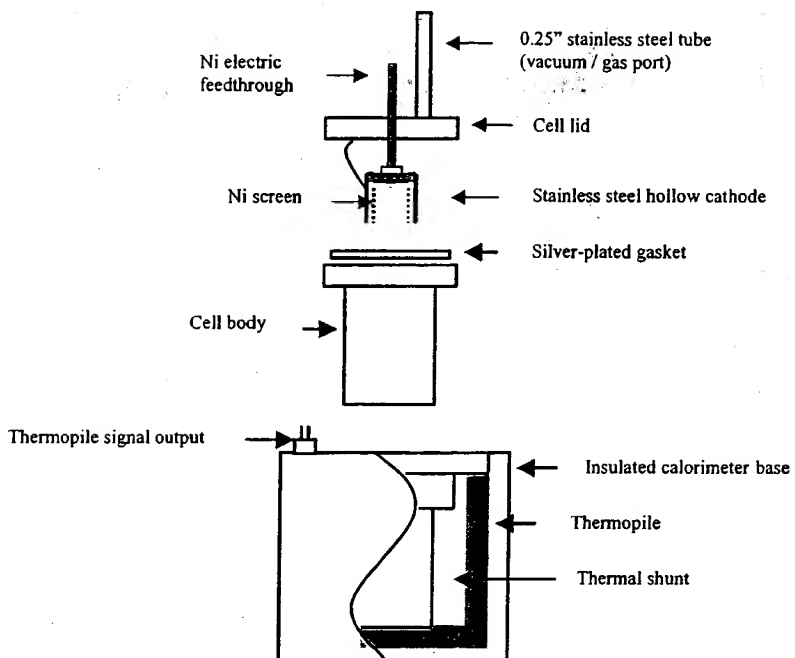Silver-plated gasket

Cell body

Thermopile signal output

Insulated calorimeter base

Thermopile

Thermal shunt

Fig. 3

Fig. 4

Fig. 5

Calvet Signal/mV (y-axis): 0, 50, 100, 150, 200, 250

Plasma Power Input/W (x-axis): 0, 20, 40, 60, 80, 100

Legend:
- ■ Kr
- ○ Xe
- △ Hydrogen
- —— Linear Fit

Fig. 6

Fig. 7

THIS PAGE BLANK (USPTO)

ARTICLE IN PRESS

Measurement of hydrogen balmer line broadening and thermal power balances of noble gas-hydrogen discharge plasmas

Randell L. Mills *, Andreas Voigt, Paresh Ray, Mark Nansteel, Bala Dhandapani

Black Light Power, Inc., 493 Old Trenton Road, Cranbury, NJ 08512, USA

Abstract

Line broadening of the hydrogen Balmer lines provides a sensitive measure of the number and energy of excited hydrogen atoms in a glow discharge plasma. The width of the 656.2 nm Balmer α line emitted from glow discharge plasmas having atomized hydrogen from pure hydrogen alone, hydrogen with magnesium or strontium, a mixture of 10% hydrogen and helium, argon, krypton, or xenon, and a mixture of 10% hydrogen and helium or argon with strontium was measured with a high resolution (± 0.025 nm) visible spectrometer. It was found that strontium–hydrogen, helium–hydrogen, argon–hydrogen, strontium–helium–hydrogen, and strontium–argon–hydrogen plasmas showed significant broadening corresponding to an average hydrogen atom temperature of 25–45 eV; whereas, pure hydrogen, krypton–hydrogen, xenon–hydrogen, and magnesium–hydrogen showed no excessive broadening corresponding to an average hydrogen atom temperature of ≈ 3 eV. Since line broadening is a measure of the plasma temperature, and a significant difference was observed between these noble gases, the power balances of glow discharge plasmas of (1) pure krypton alone, (2) a mixture of hydrogen with argon or krypton and (3) a mixture of hydrogen and helium or argon with vaporized strontium were measured. The power emitted for power supplied to the glow discharge increased by 35–83 W depending on the presence of helium or argon and less than 1% partial pressure of strontium metal in noble gas–hydrogen mixtures. Whereas, the chemically similar noble gas krypton alone or with hydrogen had no effect on the power balance. Catalyst atoms or ions which ionize at integer multiples of the potential energy of atomic hydrogen (Sr, He^+, or Ar^+) caused an increase in power; whereas, no excess power was observed in the case of krypton which does not provide a reaction with a net enthalpy of a multiple of the potential energy of atomic hydrogen under these conditions. For a power input to the glow discharge of 110 W, the excess output power of mixtures of strontium with argon–hydrogen ($\frac{95}{5}$%), strontium with hydrogen, strontium with helium–hydrogen ($\frac{95}{5}$%), and argon–hydrogen ($\frac{95}{5}$%) was 75, 58, 50, and 28 W, respectively based a comparison of the temperature rise of the cell with krypton–hydrogen mixture ($\frac{95}{5}$%) and krypton alone. The input power was varied to find conditions that resulted in the optimal output for the strontium–hydrogen plasma. At 136 W input, the excess power significantly increased to 184 W. These studies provide a useful comparison of catalysts for the optimization of a catalytic reaction of atomic hydrogen which represents an important new power source. © 2001 Published by Elsevier Science Ltd on behalf of the International Association for Hydrogen Energy.

1. Introduction

1.1. Background

Balmer showed in 1885 that the frequencies for some of the lines observed in the emission spectrum of atomic hydrogen could be expressed with a completely empirical relationship. This approach was later extended by Rydberg, who showed that all of the spectral lines of atomic hydrogen were given by the equation:

$$\bar{\nu} = R \left(\frac{1}{n_f^2} - \frac{1}{n_i^2} \right) \tag{1}$$

where $R = 109{,}677 \text{ cm}^{-1}$, $n_f = 1, 2, 3, \ldots$, $n_i = 2, 3, 4, \ldots$, and $n_i > n_f$.

Niels Bohr, in 1913, developed a theory for atomic hydrogen that gave energy levels in agreement with Rydberg's equation. An identical equation, based on a totally

* Corresponding author. Tel.: +1-609-490-1090; fax: +1-609-490-1066.

E-mail address: rmills@blacklightpower.com (R.L. Mills).

1　different theory for the hydrogen atom, was developed by Schrödinger, and independently by Heisenberg, in 1926.

$$E_n = -\frac{e^2}{n^2 8\pi\varepsilon_o a_H} = -\frac{13.598 \text{ eV}}{n^2} \qquad (2a)$$

$$n = 1, 2, 3, \ldots \qquad (2b)$$

3　where a_H is the Bohr radius for the hydrogen atom (52.947 pm), e is the magnitude of the charge of the elec-
5　tron, and ε_o is the vacuum permittivity. Based on the solution of a Schrödinger-type wave equation with a nonradiative
7　boundary condition from Maxwell's equations, Mills [1–27] predicts that atomic hydrogen may undergo a catalytic
9　reaction with certain atomized elements or certain gaseous ions which singly or multiply ionize at integer multiples
11　of the potential energy of atomic hydrogen, 27.2 eV. The reaction involves a nonradiative energy transfer to form a
13　hydrogen atom that is lower in energy than unreacted atomic hydrogen that corresponds to a fractional principal quantum
15　number where Eq. (2b) should be replaced by Eq. (2c).

$$n = 1, 2, 3, \ldots, \quad \text{and}, \quad n = \frac{1}{2}, \frac{1}{3}, \frac{1}{4}, \ldots . \qquad (2c)$$

A number of independent experimental observations lead to
17　the conclusion that atomic hydrogen can exist in fractional quantum states that are at lower energies than the traditional
19　"ground" ($n = 1$) state.

1.2. Lower-energy hydrogen experimental data

21　　Prior studies that support the possibility of a novel re-action of atomic hydrogen which produces a chemically
23　generated or assisted plasma and produces novel hydride compounds include extreme ultraviolet (EUV) spectroscopy
25　[6–11,14–18], characteristic emission from catalysis and the hydride ion products [8,9], lower-energy hydrogen
27　emission [4,6,7], plasma formation [8–11,14,15,17,18], anomalous plasma afterglow duration [17,18] power gen-
29　eration [10–14,25], and analysis of chemical compounds [19–25]. Typically the emission of vacuum ultraviolet light
31　from hydrogen gas is achieved using discharges at high voltage, synchrotron devices, high power inductively cou-
33　pled plasma generators, or a plasma is created and heated to extreme temperatures by RF coupling (e.g. $> 10^6$ K) with
35　confinement provided by a toroidal magnetic field. Obser-vation of intense extreme ultraviolet (EUV) emission at
37　low temperatures (e.g. $\leq 10^3$ K) from atomic hydrogen and certain atomized elements or certain gaseous ions [6–11,14
39　–18] has been reported previously. The only pure elements that were observed to emit EUV were those wherein the
41　ionization of t electrons from an atom to a continuum en-ergy level is such that the sum of the ionization energies of
43　the t electrons is approximately $m \cdot 27.2$ eV where t and m are each an integer. K, Cs, and Sr atoms and Rb^+ ion ionize
45　at integer multiples of the potential energy of atomic hydro-gen and caused emission. Whereas, the chemically similar
47　atoms, Na, Mg, and Ba, do not ionize at integer multiples

of the potential energy of atomic hydrogen and caused no
49　emission. Additional prior studies that support the possibil-ity of a novel reaction of atomic hydrogen which produces
51　a plasma and lower-energy-hydrogen atoms, molecules, hydride ions, and novel hydride compounds include:
53　　(1) the observation of novel EUV emission lines from mi-crowave and glow discharges of helium with 2% hydrogen
55　with energies of $q \cdot 13.6$ eV where $q = 1, 2, 3, 4, 6, 7, 8, 9,$ or 11 or these lines inelastically scattered by helium atoms
57　in the excitation of He ($1s^2$) to He ($1s^1 2p^1$) that were iden-tified as hydrogen transitions to electronic energy levels be-
59　low the "ground" state corresponding to fractional quantum numbers [6],
61　　(2) the identification of transitions of atomic hydrogen to lower energy levels corresponding to lower energy hydrogen
63　atoms in the extreme ultraviolet emission spectrum from interstellar medium and the sun [1,4,6],
65　　(3) the EUV spectroscopic observation of lines by the In-stitut für Niedertemperatur-Plasmaphysik e.V. that could be
67　assigned to transitions of atomic hydrogen to lower energy levels corresponding to fractional principal quantum num-
69　bers and the emission from the excitation of the correspond-ing hydride ions [16],
71　　(4) the recent analysis of mobility and spectroscopy data of individual electrons in liquid helium which shows direct
73　experimental confirmation that electrons may have fractional principal quantum energy levels [5],
75　　(5) the observation of novel EUV emission lines from microwave discharges of argon or helium with 10% hydro-
77　gen that matched those predicted for vibrational transitions of $H_2^*[n = \frac{1}{4}; n^* = 2]^+$ with energies of $v \cdot 1.185$ eV, $v = 17$–
79　38 that terminated at the predicted dissociation limit, E_D, of $H_2[n = \frac{1}{4}]^+$, $E_D = 42.88$ eV (28.92 nm) [7],
81　　(6) the observation of continuum state emission of Cs^{2+} and Ar^{2+} at 53.3 and 45.6 nm, respectively, with the absence
83　of the other corresponding Rydberg series of lines from these species which confirmed the resonant nonradiative energy
85　transfer of 27.2 eV from atomic hydrogen to the catalysts atomic Cs or Ar^+ [9],
87　　(7) the spectroscopic observation of the predicted hydride ion $H^-(\frac{1}{2})$ of hydrogen catalysis by either Cs atom or Ar^+
89　catalyst at 407 nm corresponding to its predicted binding energy of 3.05 eV [9],
91　　(8) which confirmed the resonant nonradiative energy transfer of $3 \cdot 27.2$ eV from atomic hydrogen to atomic K [9],
93　（observation of characteristic emission from K^{3+}
95　　(9) the spectroscopic observation of the predicted $H^-(\frac{1}{4})$ ion of hydrogen catalysis by K catalyst at 110 nm corre-
95　sponding to its predicted binding energy of 11.2 eV [9],
97　　(10) the observation by the Institut für Niedertemperatur-Plasmaphysik e.V. of an anomalous plasma and plasma af-
99　terglow duration formed with hydrogen–potassium mixtures [17],
101　　(11) the observation of anomalous afterglow durations of plasmas formed by catalysts providing a net enthalpy of
103　reaction within thermal energies of $m \cdot 27.28$ eV [17,18],

1   (12) the observation of Lyman series in the EUV that
represents an energy release about 10 times that of hydrogen
3   combustion which is greater than that of any possible known
chemical reaction [6–11,14–18],
5   (13) the observation of line emission by the Institut für
Niedertemperatur-Plasmaphysik e.V. with a 4° grazing inci-
7   dence EUV spectrometer that was 100 times more energetic
than the combustion of hydrogen [16],
9   (14) the observation of anomalous plasmas formed with
Sr and Ar^+ catalysts at 1% of the theoretical or prior known
11   voltage requirement with a light output per unit power input
up to 8600 times that of the control standard light source
13   [10,11,13,14],
(15) the observation that the optically measured output
15   power of gas cells for power supplied to the glow discharge
increased by over two orders of magnitude depending on the
17   presence of less than 1% partial pressure of certain catalysts
in hydrogen gas or argon–hydrogen gas mixtures [13],
19   (16) the differential scanning calorimetry (DSC) measure-
ment of minimum heats of formation of KHI by the catalytic
21   reaction of K with atomic hydrogen and KI that were over
-2000 kJ/mole H_2 compared to the enthalpy of combustion
23   of hydrogen of -241.8 kJ/mole H_2 [25],
(17) the isolation of novel hydrogen compounds as prod-
25   ucts of the reaction of atomic hydrogen with atoms and ions
which formed an anomalous plasma as reported in the EUV
27   studies [19–25],
(18) the identification of novel hydride compounds by
29   (i) time of flight secondary ion mass spectroscopy which
showed a dominant hydride in the negative ion spec-
31   trum, (ii) X-ray photoelectron spectroscopy which showed
novel hydride peaks and significant shifts of the core levels
33   of the primary elements bound to the novel hydride ions, (iii)
^{1}H nuclear magnetic resonance spectroscopy (NMR) which
35   showed extraordinary upfield chemical shifts compared to
the NMR of the corresponding ordinary hydrides, and (iv)
37   thermal decomposition with analysis by gas chromatogra-
phy, and mass spectroscopy which identified the compounds
39   as hydrides [19–25],
(19) the NMR identification of novel hydride compounds
41   MH^*X wherein M is the alkali or alkaline earth metal, X,
is a halide, and H^* comprises a novel high binding energy
43   hydride ion identified by a large distinct upfield resonance
[19–24],
45   (20) the replication of the NMR results of the identifica-
tion of novel hydride compounds by large distinct upfield
47   resonances at Spectral Data Services, University of Mas-
sachusetts Amherst, University of Delaware, Grace Davi-
49   son, and National Research Council of Canada [19], and
(21) the NMR identification of novel hydride compounds
51   MH^* and MH_2^* wherein M is the alkali or alkaline earth
metal and H^* comprises a novel high binding energy hy-
53   dride ion identified by a large distinct upfield resonance that
proves the hydride ion is different from the hydride ion of
55   the corresponding known compound of the same composi-
tion [19].

57   *1.3. Mechanism of the formation of lower-energy atomic
hydrogen*

59   The mechanism of the EUV emission, the formation of
novel hydrides, and the observation of certain EUV lines
61   from interstellar medium and the sun cannot be explained
by the conventional energy levels of hydrogen, but it is
63   predicted by a solution of the Schrödinger equation with a
nonradiative boundary constraint put forward by Mills [1].
65   Mills predicts that certain atoms or ions serve as catalysts
to release energy from hydrogen to produce an increased
67   binding energy hydrogen atom called a *hydrino atom* having
a binding energy given by Eq. (2a) where

$$n = \frac{1}{2}, \frac{1}{3}, \frac{1}{4}, \ldots, \frac{1}{p} \qquad (3)$$

69   and p is an integer greater than 1, designated as $H[a_H/p]$
where a_H is the radius of the hydrogen atom. Hydrinos are
71   predicted to form by reacting an ordinary hydrogen atom
with a catalyst having a net enthalpy of reaction of about

$$m \cdot 27.2 \text{ eV} \qquad (4)$$

73   where m is an integer. This catalysis releases energy from
the hydrogen atom with a commensurate decrease in size of
75   the hydrogen atom, $r_n = na_H$. For example, the catalysis of
$H(n = 1)$ to $H(n = \frac{1}{2})$ releases 40.8 eV, and the hydrogen
77   radius decreases from a_H to $\frac{1}{2}a_H$.
The excited energy states of atomic hydrogen are also
79   given by Eq. (2a) except with Eq. (2b). The $n = 1$ state is
the "ground" state for "pure" photon transitions (the $n = 1$
81   state can absorb a photon and go to an excited electronic
state, but it cannot release a photon and go to a lower-energy
83   electronic state). However, an electron transition from the
ground state to a lower-energy state is possible by a nonra-
85   diative energy transfer such as multipole coupling or a res-
onant collision mechanism. These lower-energy states have
87   fractional quantum numbers, $n = (1/\text{integer})$.
Processes that occur without photons and that require col-
89   lisions are common. For example, the exothermic chemical
reaction of $H+H$ to form H_2 does not occur with the emission
91   of a photon. Rather, the reaction requires a collision with a
third body, M, to remove the bond energy-$H + H + M \rightarrow$
93    $H_2 + H^*$ [28]. The third body distributes the energy from the
exothermic reaction, and the end result is the H_2 molecule
95   and an increase in the temperature of the system. Some com-
mercial phosphors are based on nonradiative energy trans-
97   fer involving multipole coupling. For example, the strong
absorption strength of Sb^{3+} ions along with the efficient
99   nonradiative transfer of excitation from Sb^{3+} to Mn^{2+} are
responsible for the strong manganese luminescence from
101   phosphors containing these ions [29]. Similarly, the $n = 1$
state of hydrogen and the $n = (1/\text{integer})$ states of hydro-
103   gen are nonradiative, but a transition between two nonradia-
tive states is possible via a nonradiative energy transfer, say
105    $n = 1$ to $n = \frac{1}{2}$. In these cases, during the transition the elec-
tron couples to another electron transition, electron transfer

1   reaction, or inelastic scattering reaction which can absorb
the exact amount of energy that must be removed from the
3   hydrogen atom to cause the transition. Thus, a catalyst pro-
vides a net positive enthalpy of reaction of $m \cdot 27.2$ eV (i.e. it
5   absorbs $m \cdot 27.2$ eV where m is an integer). Certain atoms or
ions serve as catalysts which resonantly accept energy from
7   hydrogen atoms and release the energy to the surroundings
to effect electronic transitions to fractional quantum energy
9   levels.

The catalysis of hydrogen involves the nonradiative trans-
11 fer of energy from atomic hydrogen to a catalyst which may
then release the transferred energy by radiative and nonra-
13 diative mechanisms. As a consequence of the nonradiative
energy transfer, the hydrogen atom becomes unstable and
15 emits further energy until it achieves a lower-energy nonra-
diative state having a principal energy level given by Eqs.
17 (2a) and (3).

1.4. Catalysts

19 *1.4.1. Argon ion*

Argon ions can provide a net enthalpy of a multiple of that
21 of the potential energy of the hydrogen atom. The second
ionization energy of argon is 27.63 eV. The reaction Ar^+ to
23 Ar^{2+} has a net enthalpy of reaction of 27.63 eV, which is
equivalent to $m = 1$ in Eq. (4).

$$27.63 \text{ eV} + Ar^+ + H\left[\frac{a_H}{p}\right] \rightarrow Ar^{2+} + e^-$$

$$+ H\left[\frac{a_H}{(p+1)}\right] + [(p+1)^2 - p^2]X13.6 \text{ eV}, \quad (5)$$

$$Ar^{2+} + e^- \rightarrow Ar^+ + 27.63 \text{ eV}, \quad (6)$$

25 and, the overall reaction is

$$H\left[\frac{a_H}{p}\right] \rightarrow H\left[\frac{a_H}{(p+1)}\right] + [(p+1)^2 - p^2]X13.6 \text{ eV}. \quad (7)$$

The energy given off during catalysis is much greater than
27 the energy lost to the catalyst. The energy released is large
compared to conventional chemical reactions. For example,
29 when hydrogen and oxygen gases undergo combustion to
form water

$$H_2(g) + \tfrac{1}{2}O_2(g) \rightarrow H_2O(l) \quad (8)$$

31 the known enthalpy of formation of water is $\Delta H_f =$
-286 kJ/mole or 1.48 eV per hydrogen atom. By contrast,
33 each ($n = 1$) ordinary hydrogen atom undergoing cataly-
sis releases a net of 40.8 eV. Moreover, further catalytic
35 transitions may occur: $n = \frac{1}{2} \rightarrow \frac{1}{3}, \frac{1}{3} \rightarrow \frac{1}{4}, \frac{1}{4} \rightarrow \frac{1}{5}$, and
so on. Once catalysis begins, hydrinos autocatalyze further
37 in a process called *disproportionation*. This mechanism is
similar to that of an inorganic ion catalysis. But, hydrino
39 catalysis should have a higher reaction rate than that of
the inorganic ion catalyst due to the better match of the
41 enthalpy to $m \cdot 27.2$ eV.

1.4.2. Helium ion

Helium ion (He^+) is also such a catalyst because the   43
second ionization energy of helium is 54.417 eV, which is
equivalent to $m = 2$ in Eq. (4). In this case, the catalysis   45
reaction is

$$54.417 \text{ eV} + He^+ + H[a_H]$$

$$\rightarrow He^{2+} + e^- + H\left[\frac{a_H}{3}\right] + 108.8 \text{ eV}, \quad (9)$$

$$He^{2+} + e^- \rightarrow He^+ + 54.417 \text{ eV}, \quad (10)$$

and, the overall reaction is   47

$$H[a_H] \rightarrow H\left[\frac{a_H}{3}\right] + 54.4 \text{ eV} + 54.4 \text{ eV}. \quad (11)$$

1.4.3. Atomic strontium

Strontium atoms can provide a net enthalpy of a multiple   49
of that of the potential energy of the hydrogen atom. The
first through the fifth ionization energies of strontium are   51
5.69484, 11.03013, 42.89, 57, and 71.6 eV, respectively
[30]. The ionization reaction of Sr to Sr^{5+}, ($t = 5$), then, has 53
a net enthalpy of reaction of 188.2 eV, which is equivalent
to $m = 7$ in Eq. (4).   55

$$188.2 \text{ eV} + Sr(m) + H\left[\frac{a_H}{p}\right]$$

$$\rightarrow Sr^{5+} + 5e^- + H\left[\frac{a_H}{(p+7)}\right]$$

$$+ [(p+7)^2 - p^2]X13.6 \text{ eV}, \quad (12)$$

$$Sr^{5+} + 5e^- \rightarrow Sr(m) + 188.2 \text{ eV}, \quad (13)$$

and, the overall reaction is

$$H\left[\frac{a_H}{p}\right] \rightarrow H\left[\frac{a_H}{(p+7)}\right] + [(p+7)^2 - p^2]X13.6 \text{ eV}. \quad (14)$$

For strontium, the ionization data is only given to two sig-   57
nificant figures [31]; whereas, at least three are needed to
calculate the enthalpy of reaction to determine whether it is   59
a catalyst. Since the available data indicates that strontium
may provide an enthalpy of reaction that is within about 1%   61
of $m \cdot 27.2$ eV, it was anticipated and confirmed to be cata-
lyst [10,11,13–15].   63

Xenon is unlikely a catalyst since the candidate reaction
involving the ionization of Xe^+ to Xe^{3+} is 53.3328 eV rather 65
than 54.4 eV. Krypton may be a catalyst, but is less likely
since the candidate reaction Kr to Kr^{6+} is 271 eV rather   67
than 272 eV; however, the available ionization data [30] is
not known to sufficient accuracy. A neon ion and a proton   69
can also provide a net enthalpy of a multiple of that of
the potential energy of the hydrogen atom; thus, neon may   71
be a catalyst in a very intense neon–hydrogen plasma. The   73

second ionization energy of neon is 40.96 eV, and H^+ releases 13.6 eV when it is reduced to H. The combination of reactions of Ne^+ to Ne^{2+} and H^+ to H, then, has a net enthalpy of reaction of 27.36 eV, which is equivalent to $m = 1$ in Eq. (4). Neon is not covered in this report, but is the subject of a report in progress.

The published ionization potentials are a good guide to predict catalysts and have been remarkably successful [8–11,14,15,17,18], but in some cases, the ionization data is incomplete [30]. Experimental condition-dependent catalytic rates are also a consideration. The absolute means to evaluate catalysts are experimental tests. Two methods are the formation of a plasma by incandescent heating the source of catalyst in the presence of atomic hydrogen [15] and line broadening which was measured in the present work.

1.5. Initial optical and thermal power balance measurements

Glow discharge devices have been developed over decades as light sources, ionization sources for mass spectroscopy, excitation sources for optical spectroscopy, and sources of ions for surface etching and chemistry [31–33]. A Grimm-type glow discharge is a well established excitation source for the analysis of conducting solid samples by optical emission spectroscopy [34–36]. Despite extensive performance characterizations, data was lacking on the plasma parameters of these devices. Kuraica and Konjevic [37] and Videnocic et al. [38] have characterized these plasmas by determining the excited hydrogen atom concentrations and energies from measurements of the line broadening of the 656.2 nm Balmer α line.

A new previously reported plasma source [8–11,14,15, 17,18] has been developed that operates by incandescently heating a hydrogen dissociator and a catalyst to provide atomic hydrogen and gaseous catalyst, respectively, such that the catalyst reacts with the atomic hydrogen to produce a plasma. It was extraordinary, that intense EUV emission was observed by Mills et al. [8–11,14,15,17,18] at low temperatures (e.g. $\approx 10^3$ K) from atomic hydrogen and certain atomized elements or certain gaseous ions which singly or multiply ionize at integer multiples of the potential energy of atomic hydrogen, 27.2 eV that comprise catalysts.

Furthermore, Mills et al. [10,11,14] have reported that strontium atoms each ionize at an integer multiple of the potential energy of atomic hydrogen and caused intense EUV emission. The enthalpy of ionization of Sr to Sr^{5+} has a net enthalpy of reaction of 188.2 eV, which is equivalent to $m = 7$. The emission intensity of the plasma generated by atomic strontium increased significantly with the introduction of argon gas only when Ar^+ emission was observed. Whereas, no emission was observed when chemically similar atoms that do not ionize at integer multiples of the potential energy of atomic hydrogen (sodium, magnesium, or barium) replaced strontium

with hydrogen, hydrogen–argon mixtures, or strontium alone.

The power balance of a gas cell having vaporized strontium and atomized hydrogen from pure hydrogen or argon–hydrogen mixture ($\frac{77}{23}$%) was measured by integrating the total light output corrected for spectrometer system response and energy over the visible range [11]. Hydrogen control cell experiments were identical except that sodium, magnesium, or barium replaced strontium. In the case of hydrogen–sodium, hydrogen–magnesium, and hydrogen–barium mixtures, 4000, 7000, and 6500 times the power of the hydrogen–strontium mixture was required, respectively, in order to achieve that same optically measured light output power. With the addition of argon to the hydrogen–strontium plasma, the power required to achieve that same optically measured light output power was reduced by a factor of about two. The power required to maintain a plasma of equivalent optical brightness with strontium atoms present was 8600 and 6300 times less than that required for argon–hydrogen and argon control, respectively. A plasma formed at a cell voltage of about 250 V for hydrogen alone and sodium–hydrogen mixtures, 140 –150 V for hydrogen–magnesium and hydrogen–barium mixtures, 224 V for an argon–hydrogen mixture, and 190 V for argon alone; whereas, a plasma formed for hydrogen–strontium mixtures and argon–hydrogen–strontium mixtures at extremely low voltages of about 2 and 6.6 V, respectively.

The power balances of gas plasmas having atomized hydrogen from pure hydrogen alone, an argon–hydrogen mixture alone, or pure hydrogen or an argon–hydrogen mixture with vaporized potassium, rubidium, cesium, strontium, sodium, or magnesium were previously reported [13]. The power was measured by integrating the total light output corrected for spectrometer system response and energy over the visible range as the input power was varied. The light emitted per unit power supplied to the glow discharge increased by over two orders of magnitude depending on the presence of less than 1% partial pressure of certain of the alkali or alkaline earth metals in hydrogen gas or argon–hydrogen gas mixtures. Whereas, other chemically similar metals had no effect on the plasma. The metal vapor enhancement of the emission was dramatically greater with an argon–hydrogen mixture versus pure hydrogen, and a 97% argon and 3% hydrogen mixture had greater emission than either gas alone. Only those atoms or ions which ionize at integer multiples of the potential energy of atomic hydrogen, K, Cs, Rb^+, Sr, and Ar^+ caused an anomalous increase in emission; whereas, no anomalous behavior was observed in the case of Mg and Na which do not provide a reaction with a net enthalpy of a multiple of the potential energy of atomic hydrogen. The light intensity versus power input of a mixture of these metals with hydrogen, argon, or argon–hydrogen gas was the same as that of the corresponding gas alone. At an input power to the glow discharge of 10 W, the optically measured light output power of a mix-

1   ture of strontium, cesium, potassium, or rubidium with 97%
    argon and 3% hydrogen was 750, 70, 16, and 13 $\mu W/cm^2$,
3   respectively [13]. Whereas, the optically measured light
    output power of the argon–hydrogen mixture ($\frac{97}{3}$%) alone
5   or with sodium or magnesium was about 11 $\mu W/cm^2$, and
    the result for hydrogen or argon alone was 1.5 $\mu W/cm^2$.
7   An excess thermal balance of 42 W was measured for
    the 97% argon and 3% hydrogen mixture versus argon
9   plasma alone.
        To further study the mechanism of the excess optical
11 power balances, the width of the 656.2 nm Balmer α line
    emitted from glow discharge plasmas having atomized
13 hydrogen from pure hydrogen alone, hydrogen with magne-
    sium or strontium, and noble gas–hydrogen mixtures alone
15 or with strontium was measured with a high resolution
    ($\pm$0.025 nm) visible spectrometer. Since line broadening
17 is a measure of the plasma temperature, and a significant
    difference was observed between these noble gases and due
19 to the presence of strontium, the power balances of glow
    discharge plasmas were measured by heat loss calorimetry
21 (determining the power balance from the temperature at
    steady state relative to that of a control power source) as
    the input power was varied.

2. Experimental

2.1. High resolution visible spectroscopy   25

    The width of the 656.2 nm Balmer α line emitted from
glow discharge plasmas having atomized hydrogen from   27
pure hydrogen alone, hydrogen with magnesium or stron-
tium, a mixture of 10% hydrogen and helium, argon, kryp-   29
ton, or xenon, and a mixture of 10% hydrogen and helium and
argon with strontium was measured with a high resolution   31
visible spectrometer at Jobin Yvon Horiba, Inc, Edison, NJ.
The plasmas were carried out in the cylindrical stainless steel 33
gas cell shown in Fig. 1 and described in Section 2.2. The
spectrometer was a TRIAX 550 Spectrometer with a stan-   35
dard PMT detector that had a resolution of $\pm$0.025 nm over
the spectral range 190–860 nm. A UV-grade sapphire win-   37
dow described in Section 2.2 provided a visible light path
from inside the cell. The plasma emission from the glow   39
discharges was fiber-optically coupled to the spectrometer
through a 220F matching fiber adapter. The entrance and   41
exit slits were set to 20 μm. The spectrometer was scanned
between 656–657 nm using a 0.01 nm step size. The signal   43
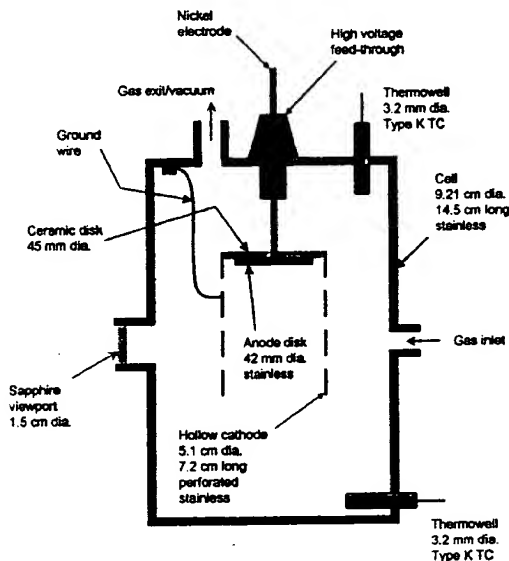was recorded by a PMT (Hamamatsu R928) with a stand

Nickel
electrode

High voltage
feed-through

Gas exit/vacuum

Thermowell
3.2 mm dia.
Type K TC

Ground
wire

Cell
9.21 cm dia.
14.5 cm long
stainless

Ceramic disk
45 mm dia.

Anode disk
42 mm dia.
stainless

Gas inlet

Sapphire
viewport
1.5 cm dia.

Hollow cathode
5.1 cm dia.
7.2 cm long
perforated
stainless

Thermowell
3.2 mm dia.
Type K TC

23   Fig. 1. Cylindrical stainless steel glow discharge cell for 656.2 nm Balmer α line width and power balance studies.
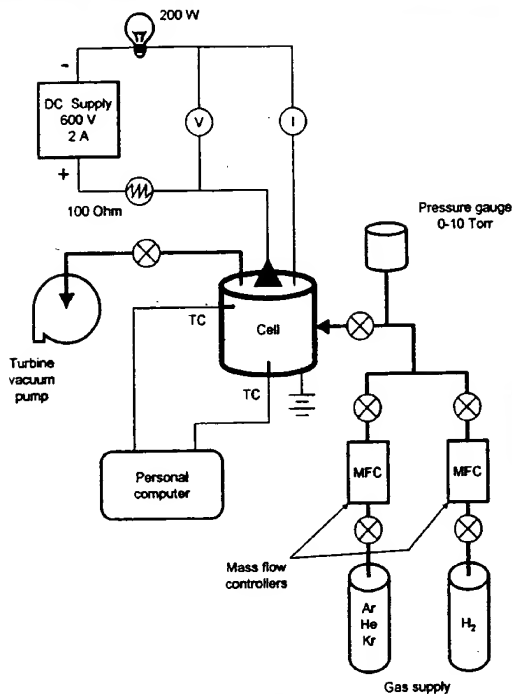
Fig. 2. The experimental setup for generating a glow discharge plasma and for measuring the power balance.

1   alone high voltage power supply (950 V) and an acquisition
controller (SpectrAcq 2). The data was obtained in a single
3   accumulation with a 1 s integration time.

2.2. Power cell apparatus and procedure

5   Power balances were measured on plasmas with (1)
krypton alone, (2) krypton–hydrogen mixture ($\frac{95}{5}$%), (3) a
7   mixture of hydrogen and vaporized strontium, (4) argon–
hydrogen mixture ($\frac{95}{5}$%), and (5) a helium–hydrogen
9   mixture ($\frac{95}{5}$%) or an argon–hydrogen mixture ($\frac{95}{5}$%) with
vaporized strontium. The plasmas were maintained in the
11 cylindrical stainless steel gas cell shown in Fig. 1, and the
power was measured by heat loss calorimetry as the input
13 power was varied. The experimental setup for generating
a glow discharge plasma and for measuring the power bal-
15 ance is shown in Fig. 2. All experiments were performed
in a clean room having a controlled ambient temperature of
17 ±0.1°C.

    The 304-stainless steel cylindrical cell was 9.21 cm in
diameter and 14.5 cm in height. The base of the cell con-   19
tained a welded-in stainless steel thermocouple well (1 cm
OD) which housed a thermocouple in the cell interior ap-   21
proximately 2 cm from the discharge and 2 cm from the cell
axis. The top end of the cell was welded to a high vacuum   23
11.75 cm diameter conflat flange. A silver plated copper gas-
ket was placed between a mating flange and the cell flange.   25
The two flanges were clamped together with 10 circumfer-
ential bolts. The mating flange contained four penetrations   27
comprising (1) a stainless steel thermocouple well (1 cm
OD) which also housed a thermocouple in the cell interior   29
approximately 2 cm from the discharge and 2 cm from the
cell axis, (2) a centered high voltage feedthrough which   31
transmitted the power, supplied through a power connector,
to a hollow cathode inside the cell, and (3) two stainless   33
steel tubes (0.95 cm diameter and 100 cm in length) with
one welded flush with the bottom surface of the top flange   35
that served as a vacuum line from the cell and the second

welded flush with the side of the cell that served as the line to supply the test gas.

The axial hollow cathode glow discharge electrode assembly shown in Fig. 1 comprised a stainless steel plate (4.2 cm diameter, 0.9 mm thick) anode and a circumferential stainless steel cylindrical frame (5.1 cm OD, 7.2 cm long) perforated with evenly spaced 1 cm diameter holes. The cathode was attached to the cell body by a stainless steel wire covered with ceramic beads for electrical insulation, and the cell body was grounded.

A 1.6 mm thick UV-grade sapphire window with 1.5 cm view diameter provided a visible light path from inside the cell. The viewing direction was normal to the cell axis.

Strontium (Alfa Aesar 99.95%) metal was loaded into the cell under a dry argon atmosphere inside a glove box. The cell was evacuated with a turbo vacuum pump to a pressure of $\leqslant 0.0001$ Torr.

The gas in each experiment was ultrahigh purity grade or higher. Test gases comprised hydrogen, or krypton alone, helium–hydrogen mixture ($\frac{95}{5}$%), argon–hydrogen mixture ($\frac{95}{5}$%), or krypton–hydrogen mixture ($\frac{95}{5}$%). The gas pressure inside the cell was maintained at 2 Torr with a hydrogen flow rate of 30 sccm, a noble gas flow rate of 30 sccm, or a noble gas flow rate of 28 sccm and a hydrogen flow rate of 2 sccm. Each gas flow was controlled by a 0–20 sccm range mass flow controller (MKS 1179A21CS1BB) with a readout (MKS type 246). The cell pressure was monitored by a 0–10 Torr MKS Baratron absolute pressure gauge. In the absence of gas flow, the gas supply tube pressure was essentially the cell pressure. The partial pressure of the strontium metal was determined by its equilibrium vapor pressure at the operating temperature of the cell as given in Table 1.

The discharge was started and maintained by a DC electric field in the hollow cathode supplied by a constant voltage DC power supply (Xantrex XRF 600-2). The input power was calculated as the product of the constant voltage times the current. The voltage between the cathode and anode was monitored by a digital multimeter (Digital Instruments 9300GB). A duplicate multimeter in series with the discharge gap was used to indicate the current. The power was increased by ramping the constant voltage.

2.3. Power balance measurements

The temperature response of the cell to input power for the test and control gases and metals was determined. The temperature at the two thermocouples was recorded and averaged about one hour after the cell had reached a thermal steady state. The time to reach a steady state temperature with each increase in the input power to the glow discharge was typically 3–4 h. At this point the power P_T lost from the cell was equal to the power supplied to the cell P_{in} plus any excess power P_{ex}.

$$P_T = P_{in} + P_{ex}. \tag{15}$$

Table 1
Vapor pressure of strontium metal versus temperature

T (°C)	Sr P_v (Torr)[a]
20	8.39E-21
70	1.27E-16
120	1.62E-13
170	4.05E-11
220	3.26E-09
270	1.16E-07
320	2.23E-06
370	2.69E-05
420	2.25E-04
470	1.41E-03
500	3.76E-03
520	6.95E-03
535	1.08E-02
540	1.24E-02
560	2.16E-02
600	6.06E-02
620	9.78E-02
650	1.93E-01

[a]Calculated [39].

Since the heat transfer was dominated by conduction from the outer cell walls, the temperature rise of the cell above ambient ΔT was modeled by a linear curve

$$\Delta T = aP_T + C \tag{16}$$

where a and C are constants for the least square curve fit of the cell temperature response to power input for the control experiments ($P_{ex} = 0$). ΔT was recorded as a function of input power P_{in} for noncatalyst krypton alone and krypton–hydrogen mixtures over the input power range of 35–165 W. The higher temperature produced by the catalyst gases compared with the control gases was representative of the excess power since the cell temperature rise was found to be insensitive to heat transfer mechanisms occurring inside of the cell — the transfer to the cell walls being very fast and heat loss from the wall to the outside ambient environment dominating the cell temperature. In the case of each catalyst run, the total output power P_T was determined by solving Eq. (16) using the measured ΔT. The excess power P_{ex} was determined from Eq. (15).

3. Results

3.1. Line broadening measurements

The results of the 656.2 nm Balmer α line width measured with a high resolution (± 0.025 nm) visible spectrometer on glow discharge plasmas of a mixture of 10% hydrogen and 90% xenon, strontium with hydrogen, a mixture of 10% hydrogen and 90% helium, or argon, 10% hydrogen with
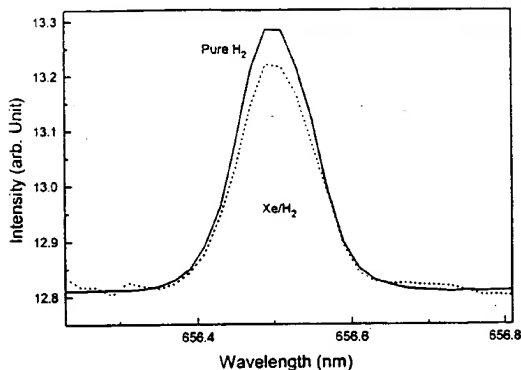
Fig. 3. The 656.2 nm Balmer α line width recorded with a high resolution (±0.025 nm) visible spectrometer on a xenon–hydrogen ($\frac{90}{10}$%) and a hydrogen glow discharge plasma. No line excessive broadening was observed corresponding to an average hydrogen atom temperature of ≈ 3 eV.

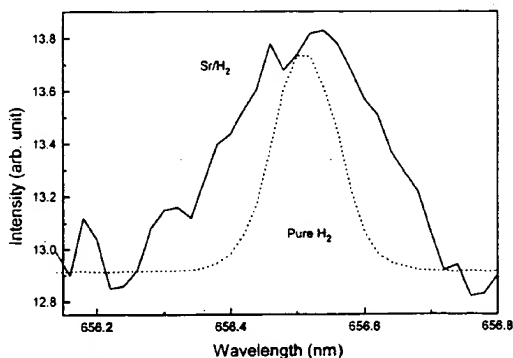

Fig. 4. The 656.2 nm Balmer α line width recorded with a high resolution (±0.025 nm) visible spectrometer on a strontium–hydrogen and a hydrogen glow discharge plasma. Significant broadening was observed corresponding to an average hydrogen atom temperature of 23–25 eV.

helium or argon and strontium each compared to control hydrogen alone are given in Figs. 3–8, respectively. To illustrate the method of displaying each line broadening result as an unsmoothed curve, the corresponding raw data points are also shown in Fig. 8 that further shows the scatter in the data. The Balmer α line width and energetic hydrogen atom densities and energies are given in Table 2. It was found that strontium–hydrogen, helium–hydrogen, argon–hydrogen, strontium–helium–hydrogen, and strontium–argon–hydrogen plasmas showed significant broadening corresponding to an average hydrogen atom temperature

of 25–45 eV; whereas, pure hydrogen, krypton–hydrogen, xenon–hydrogen, and magnesium–hydrogen showed no excessive broadening corresponding to an average hydrogen atom temperature of ≈ 3 eV.

3.2. Power balance measurements

The temperature increase above the ambient temperature of 25 ± 0.1 °C as a function of the power applied to each of the gases and metal-gas mixtures at 2 Torr total pressure was plotted for the input power range of 35–160 W as shown
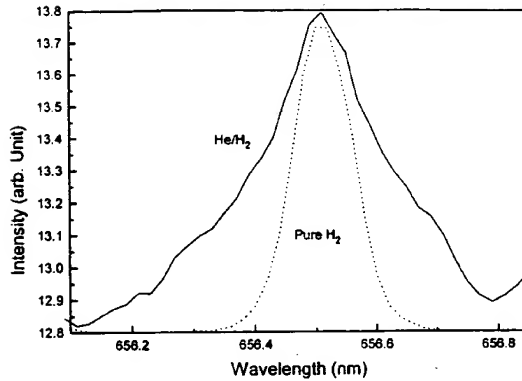
Fig. 5. The 656.2 nm Balmer α line width recorded with a high resolution (±0.025 nm) visible spectrometer on a helium–hydrogen ($\frac{90}{10}$%) and a hydrogen glow discharge plasma. Significant broadening was observed corresponding to an average hydrogen atom temperature of 30 –35 eV.

Fig. 6. The 656.2 nm Balmer α line width recorded with a high resolution (±0.025 nm) visible spectrometer on an argon–hydrogen ($\frac{90}{10}$%) and a hydrogen glow discharge plasma. Significant broadening was observed corresponding to an average hydrogen atom temperature of 30 –35 eV.
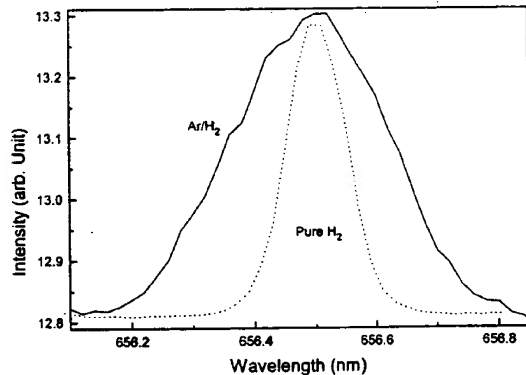
in Fig. 9. The least squares fit of the ΔT response to unit input power calculated from the control plasmas, krypton and krypton–hydrogen, (Eq. (16)) was determined to be

$$\Delta T = 7.25 + 0.687 \times P_T \qquad (17)$$

where ΔT is in $^\circ$C and P_T is in watts. At selected input powers, the total output power and excess power were determined using Eqs. (17) and (15), respectively,

for (1) a mixture of hydrogen and vaporized strontium, (2) argon–hydrogen mixture ($\frac{95}{5}$%), and (3) a helium–hydrogen mixture ($\frac{95}{5}$%) or an argon–hydrogen mixture ($\frac{95}{5}$%) with vaporized strontium as shown Tables 3–6, respectively.

For a power input to the glow discharge of 110 W, the excess output power of mixtures of strontium with argon–hydrogen ($\frac{95}{5}$%), strontium with hydrogen, strontium with helium–hydrogen ($\frac{95}{5}$%), and argon–hydrogen ($\frac{95}{5}$%) was
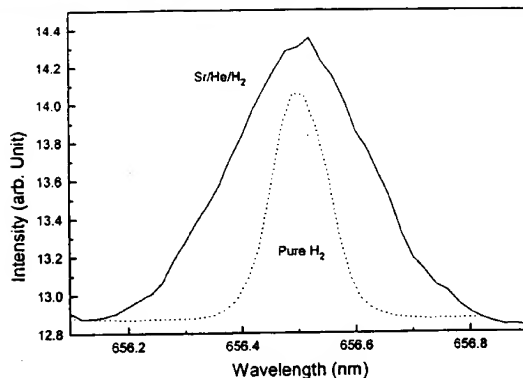
Fig. 7. The 656.2 nm Balmer α line width recorded with a high resolution (±0.025 nm) visible spectrometer on a strontium with helium–hydrogen ($\frac{90}{10}$%) and a hydrogen glow discharge plasma. Significant broadening was observed corresponding to an average hydrogen atom temperature of 40–45 eV.
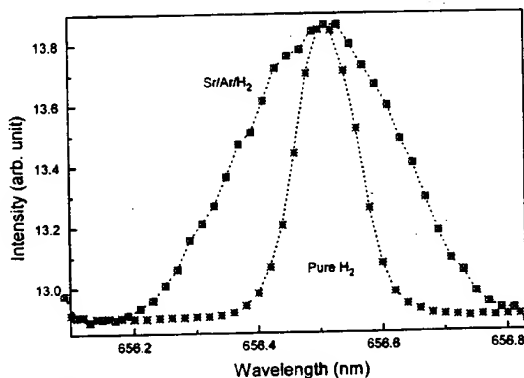

Fig. 8. The 656.2 nm Balmer α line width recorded with a high resolution (±0.025 nm) visible spectrometer on a strontium with argon–hydrogen ($\frac{90}{10}$%) and a hydrogen glow discharge plasma. Significant broadening was observed corresponding to an average hydrogen atom temperature of 35–40 eV.

1   75, 58, 50, and 28 W, respectively, based on a comparison
    of the temperature rise of the cell with krypton–hydrogen
3   mixture ($\frac{95}{5}$%) and krypton alone. The input power was
    varied to determine conditions that resulted in the optimal
5   output for the strontium–hydrogen plasma. As shown in Fig.
    9 and Table 3, at 136 W input, the excess power significantly
7   increased to 184 W. The effect was found to be repeatable
    in separate experiments.

4. Discussion

   The Balmer α line width and energetic hydrogen atom
density and energies were measured, and it was found
that plasmas of strontium–hydrogen, argon–hydrogen,
helium–hydrogen, and strontium with helium–hydrogen or
argon–hydrogen showed significant broadening. Since line
broadening is a measure of the plasma temperature, and

9

11

13

15

ARTICLE IN PRESS

Table 2

The 656.5 nm Balmer α line width (full width at half maximum) and energetic hydrogen atom densities and energies for catalyst and noncatalyst plasmas

Plasma gas	Balmer α line FWHM (nm)	Hydrogen atom density[a] (10^{12} atoms/cm^3)	Hydrogen atom energy[b] (eV)
H$_2$	0.14	50	3-4
Mg/H$_2$	0.15	60	4-5
Kr/H$_2$	0.13	10	2.5-3.5
Xe/H$_2$	0.14	10	3-4
Sr/H$_2$	0.28	100	23-25
He/H$_2$	0.31	30	33-38
Ar/H$_2$	0.30	30	30-35
Sr/He/H$_2$	0.35	40	40-45
Sr/Ar/H$_2$	0.32	40	35-40

[a]Approximate calculated [38].
[b]Calculated [38].

a significant increase was observed with the presence of a catalyst, the power balances of glow discharge plasmas were measured.

Power production was observed from discharge plasmas having a source of hydrogen and atoms or ions which ionize at integer multiples of the potential energy of atomic hydrogen (Sr, He$^+$, or Ar$^+$); whereas, no excess power was observed in the case of krypton which does not provide a reaction with a net enthalpy of a multiple of the potential energy of atomic hydrogen under these conditions. Thermal

power production was measured and observed from mixtures of strontium with argon–hydrogen ($\frac{95}{5}$%), strontium with hydrogen, strontium with helium–hydrogen ($\frac{95}{5}$%), and argon–hydrogen ($\frac{95}{5}$%). No possible chemical reactions of the 2 Torr or less hydrogen at a flow rate of 2 sccm, the electrodes, low pressure strontium, or the helium or argon gas could be found which accounted for the excess power of up to 184 W. In fact, no known chemical reaction releases enough energy (over 100 eV/H atom) to account for the power. The power was not observed when krypton or krypton–hydrogen replaced the argon–hydrogen or helium–hydrogen mixture. The power was commensurate with hydrogen fuel consumption. These results indicate that the power was due to a reaction of catalyst with hydrogen. The results of the power balance measurements are consistent with the line broadening measurements.

5. Conclusion

An average hydrogen atom temperature of 25–45 eV was observed by line broadening with the presence of strontium atoms or argon or helium ion catalysts; whereas, pure hydrogen, krypton–hydrogen, xenon–hydrogen, and magnesium–hydrogen plasmas showed no excessive broadening corresponding to an average hydrogen atom temperature of ≈ 3 eV. Excess thermal power was observed only with a catalyst present which demonstrated that line broadening was an effective method of measuring the catalysis reaction of hydrogen.
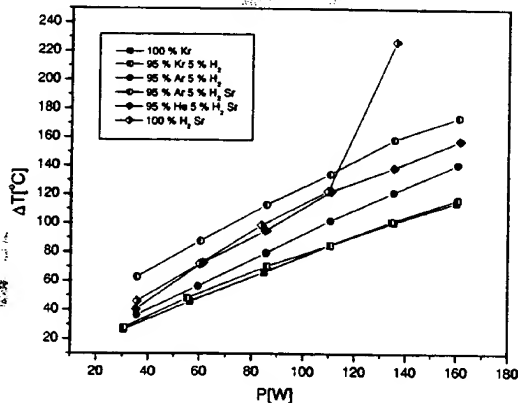

Fig. 9. The temperature increase above the ambient temperature of 25 ± 0.1°C as a function of the power applied to each of the gases and metal–gas mixtures. Significant excess power was observed in the case of catalyst–hydrogen plasmas (strontium, helium, and argon with hydrogen); whereas, no excess power was observed from noncatalyst–hydrogen plasmas.

Table 3

The total output power and excess power at selected input powers for the strontium–hydrogen plasma

Voltage (V)	Current (A)	Input power (W)	Temp. rise above ambient ΔT ($\pm 0.05^\circ$C)	Total output power P_T ($\pm 2\%$)	Excess power P_{ex} ($\pm 2\%$)
274	0.130	35.62	46.20	56.7	21.1
272	0.221	60.11	72.15	94.5	34.4
265	0.316	83.74	98.90	133.4	49.7
252	0.435	109.62	122.60	168.0	58.4
201	0.677	136.08	226.95	319.9	183.8

Table 4

The total output power and excess power at selected input powers for the argon–hydrogen plasma

Voltage (V)	Current (A)	Input power (W)	Temp. rise above ambient ΔT ($\pm 0.05^\circ$C)	Total output power P_T ($\pm 2\%$)	Excess power P_{ex} ($\pm 2\%$)
207	0.171	35.40	36.70	42.9	7.5
215	0.276	59.34	56.60	71.9	12.6
211	0.405	85.45	79.70	105.5	20.1
225	0.491	110.48	102.05	138.0	27.5
230	0.588	135.24	121.70	166.6	31.4
233	0.688	160.30	141.40	195.3	35.0

Table 5

The total output power and excess power at selected input powers for the strontium–helium–hydrogen plasma

Voltage (V)	Current (A)	Input power (W)	Temp. rise above ambient ΔT ($\pm 0.05^\circ$C)	Total output power P_T ($\pm 2\%$)	Excess power P_{ex} ($\pm 2\%$)
175	0.201	35.18	40.55	48.5	13.3
172	0.356	61.23	72.90	95.6	34.4
178	0.478	85.08	95.00	127.8	42.7
176	0.630	110.88	122.50	167.8	56.9
181	0.747	135.21	139.00	191.8	56.6
182	0.886	161.25	158.20	219.8	58.6

Table 6

The total output power and excess power at selected input powers for the strontium–argon–hydrogen plasma

Voltage (V)	Current (A)	Input powers (W)	Temp. rise above ambient ΔT ($\pm 0.05^\circ$C)	Total output power P_T ($\pm 2\%$)	Excess power P_{ex} ($\pm 2\%$)
124	0.286	35.46	62.85	81.0	45.5
151	0.399	60.25	87.85	117.4	57.1
158	0.542	85.64	113.05	154.1	68.5
163	0.677	110.35	134.50	185.3	75.0
165	0.821	135.47	158.90	220.8	85.3
167	0.962	160.65	174.35	243.3	82.7

Excess power of up to 184 W by the catalytic reaction of strontium atoms, argon ions, or helium ions with atomic hydrogen corresponded to a volumetric power density of greater than 1 W/cm^3. This is comparable to many coal fired electric power plants. The presently observed and previously reported energy balances were over 100 eV/H atom [12,13]. The results are consistent with additional previously reported studies given in Section 1.2 which show very large energy balances.

Since the net enthalpy released may be over several hundred times that of combustion, the catalysis of atomic hydrogen represents a new source of energy with H$_2$O as the source of hydrogen fuel. Moreover, rather than air pollutants or radioactive waste, novel hydride compounds with poten-

tial commercial applications are the products [19–25]. Since the power is in the form of a plasma, direct high-efficiency, low cost energy conversion may be possible, thus, avoiding a heat engine such as a turbine [26,27] or a reformer-fuel cell system. Significantly lower capital costs and lower commercial operating costs than that of any known competing energy source are anticipated.

References

[1] Mills R. The grand unified theory of classical quantum mechanics. January 2000 Edition, Cranbury, New Jersey: BlackLight Power, Inc. Distributed by Amazon.com; posted at www.blacklightpower.com.

[2] Mills R. The grand unified theory of classical quantum mechanics. Global Foundation, Inc. Orbis Scientiae entitled The Role of Attractive and Repulsive Gravitational Forces in Cosmic Acceleration of Particles. The Origin of the Cosmic Gamma Ray Bursts, (29th Conference on High Energy Physics and Cosmology Since 1964) Dr. Behram N. Kursunoglu, Chairman, December 14–17, 2000, Lago Mar Resort, Fort Lauderdale, FL, New York: Kluwer Academic/Plenum Publishers, 2000. p. 243–58.

[3] Mills R. The grand unified theory of classical quantum mechanics. Int J Hydrogen Energy, in press.

[4] Mills R. The hydrogen atom revisited. Int J Hydrogen Energy 2000;25(12):1171–83.

[5] Mills R. The nature of free electrons in superfluid helium — a test of quantum mechanics and a basis to review its foundations and make a comparison to classical theory. Int J Hydrogen Energy 2001;26(10):1059–96.

[6] Mills R, Ray P. Spectral emission of fractional quantum energy levels of atomic hydrogen from a helium-hydrogen plasma and the implications for dark matter. Int J Hydrogen Energy, in press.

[7] Mills R, Ray P. Vibrational spectral emission of fractional-principal-quantum-energy-level hydrogen molecular ion. Int J Hydrogen Energy, in press.

[8] Mills R, Ray P. Spectroscopic identification of a novel catalytic reaction of potassium and atomic hydrogen and the hydride ion product. Int J Hydrogen Energy, in press.

[9] Mills R. Spectroscopic identification of a novel catalytic reaction of atomic hydrogen and the hydride ion product. Int J Hydrogen Energy 2001;26(10):1041–58.

[10] Mills R, Nansteel M. Argon–hydrogen–strontium plasma light source. IEEE Trans Plasma Sci, submitted.

[11] Mills R, Nansteel M, Lu Y. Excessively bright hydrogen–strontium plasma light source due to energy resonance of strontium with hydrogen. Eur J Phys D, submitted.

[12] Mills RL, Ray P, Dhandapani B, Nansteel M, Chen X, He J. New power source from fractional quantum energy

levels of atomic hydrogen that surpasses internal combustion. Spectrochimica Acta, in progress.

[13] Mills R, Greenig N, Hicks S. Optically measured power balances of anomalous discharges of mixtures of argon, hydrogen, and potassium, rubidium, cesium, or strontium vapor. Int J Hydrogen Energy, submitted.

[14] Mills R, Nansteel M, Lu Y. Observation of extreme ultraviolet hydrogen emission from incandescently heated hydrogen gas with strontium that produced an anomalous optically measured power balance. Int J Hydrogen Energy 2001;26(4):309–26.

[15] Mills R, Dong J, Lu Y. Observation of extreme ultraviolet hydrogen emission from incandescently heated hydrogen gas with certain catalysts. Int J Hydrogen Energy 2000;25:919–43.

[16] Mills R. Observation of extreme ultraviolet emission from hydrogen–KI plasmas produced by a hollow cathode discharge. Int J Hydrogen Energy 2001;26(6):579–92.

[17] Mills R. Temporal behavior of light-emission in the visible spectral range from a Ti-K$_2$CO$_3$-H-Cell. Int J Hydrogen Energy 2001;26(4):327–32.

[18] Mills R, Onuma T, Lu Y. Formation of a hydrogen plasma from an incandescently heated hydrogen-catalyst gas mixture with an anomalous afterglow duration. Int J Hydrogen Energy 2001;26(7):749–62.

[19] Mills R, Dhandapani B, Nansteel M, He J, Voigt A. Identification of compounds containing novel hydride ions by nuclear magnetic resonance spectroscopy. Int J Hydrogen Energy 2001;26(9):965–79.

[20] Mills R, Dhandapani B, Greenig N, He J. Synthesis and characterization of potassium iodo hydride. Int J Hydrogen Energy 2000;25(12):1185–203.

[21] Mills R. Novel inorganic hydride. Int J Hydrogen Energy 2000;25:669–83.

[22] Mills R. Novel hydrogen compounds from a potassium carbonate electrolytic cell. Fusion Technol 2000;37(2):157–82.

[23] Mills R, Dhandapani B, Nansteel M, He J, Shannon T, Echezuria A. Synthesis and characterization of novel hydride compounds. Int J Hydrogen Energy 2001;26(4):339–67.

[24] Mills R. Highly stable novel inorganic hydrides. J Mater Res, submitted.

[25] Mills R, Good W, Voigt A, Jinquan Dong. Minimum heat of formation of potassium iodo hydride. Int J Hydrogen Energy 2001;26(11):1199–208.

[26] Mills R. Blacklight power technology — a new clean hydrogen energy source with the potential for direct conversion to electricity. Proceedings of the national hydrogen association, 12th Annual US Hydrogen Meeting and Exposition, Hydrogen: The Common Thread, The Washington Hilton and Towers, Washington DC, March 6–8, 2001. p. 671–97.

[27] Mills R. Blacklight power technology — a new clean energy source with the potential for direct conversion to electricity. Global Foundation International Conference on "Global Warming and Energy Policy", Dr. Behram N. Kursunoglu, Chairman, Fort Lauderdale, FL, New York: Kluwer Academic/Plenum Publishers, November 26–28, 2000. p. 1059–96.

[28] Sidgwick NV. The chemical elements and their compounds, vol. 1. Oxford: Clarendon Press, 1950. p. 17.

[29] Lamb MD. Luminescence spectroscopy. London: Academic Press, 1978. p. 68.

1   [30] Linde DR. CRC handbook of chemistry and physics. 79th
      Edition, Boca Raton, Florida: CRC Press, 1998–9. p. 10–175
3   to p. 10–177.

   [31] Boumans PWJM. Spectrochim. Acta B 1991;46:711.

5   [32] Broekaert JAC. Appl Spectrosc 1995;49:12A.

   [33] Boumans PWJM, Broekaert JAC, Marcus, RK, editors.
7   Spectrochim. Acta Part B, 1991;46:457.

   [34] Dogan M, Laqua K, Massmann H. Spektrochemische
9   Analysen mit einer Glimmentladungslampe als Lichtquelle —
      I. Spectrochim Acta B 1971;26:631–49.

11   [35] Dogan M, Laqua K, Massmann H. Spektrochemische
      Analysen mit einer Glimmentladungslampe als Lichtquelle —
13   II. Spectrochim Acta B 1972;27:65–88.

   [36] Broekaert JAC. J. Anal. Atmos. Spectrom. 1987;2:537.

   [37] Kuraica M, Konjevic N. Line shapes of atomic hydrogen   15
      in a plane-cathode abnormal glow discharge. Phys Rev A
      1992;46(7):4429–32.   17

   [38] Videnocic IR, Konjevic N, Kuraica MM. Spectroscopic
      investigations of a cathode fall region of the Grimm-type glow   19
      discharge. Spectrochimica Acta B 1996;51:1707–31.

   [39] Linde DR. CRC Handbook of Chemistry and Physics. 76th   21
      Edition, Boca Raton, FL: CRC Press, 1996. p. 4–121.

Vibrational spectral emission of fractional-principal-quantum-energy-level hydrogen molecular ion

Randell L. Mills *, Paresh Ray

BlackLight Power, Inc., 493 Old Trenton Road, Cranbury, NJ 08512, USA

Abstract

From a solution of a Schrödinger-type wave equation with a nonradiative boundary condition based on Maxwell's equations, Mills solves the hydrogen atom, the hydrogen molecule, the hydrogen molecular ion, the hydrogen molecular ion, and predicts corresponding species having fractional principal quantum numbers. Atomic hydrogen may undergo a catalytic reaction with certain atomized elements and ions which singly or multiply ionize at integer multiples of the potential energy of atomic hydrogen, $m27.2$ eV wherein m is an integer. The reaction involves a nonradiative energy transfer to form a hydrogen atom $H(1/p)$ that is lower in energy than unreacted atomic hydrogen that corresponds to a fractional principal quantum number ($n = 1/p = 1$/integer replaces the well known parameter n = integer in the Rydberg equation for hydrogen excited states). One such atomic catalytic system involves argon ions. The reaction Ar^+ to Ar^{2+} has a net enthalpy of reaction of 27.63 eV, which is equivalent to $m = 1$. Thus, it may serve as a catalyst to form $H(\frac{1}{2})$. Also, the second ionization energy of helium is 54.4 eV; thus, the ionization reaction of He^+ to He^{2+} has a net enthalpy of reaction of 54.4 eV which is equivalent to 2×27.2 eV. The products of the catalysis reaction $H(\frac{1}{3})$ may further serve as catalysts to form $H(\frac{1}{4})$ and $H(\frac{1}{2})$. $H(1/p)$ may react with a proton to form an excited state molecular ion $H_2^+(1/p)^+$ that has a bond energy and vibrational levels that are p^2 times those of the molecular ion comprising uncatalyzed atomic hydrogen where p is an integer. Thus, the excited state spectrum of $H_2^+[n = \frac{1}{4}; n^* = 2]^+$ was predicted to comprise rotationally broadened vibrational transitions at 1.185 eV increments to the dissociation limit of $H_2[n = \frac{1}{4}]^+$, $E_D = 42.88$ eV (28.92 nm). Extreme ultraviolet spectroscopy was recorded on microwave discharges of argon or helium with 10% hydrogen in the range 10–65 nm. Novel emission lines assigned to vibrational transitions of $H_2^+[n = \frac{1}{4}; n^* = 2]^+$ were observed in this range with energies of $v1.185$ eV, $v = 17–38$ that terminated at about 28.9 nm. In addition, fractional molecular hydrogen rotational transitions were assigned to previously unidentified lines in the Solar coronal spectrum that matched theoretical predictions to five figures. © 2001 Published by Elsevier Science Ltd on behalf of the International Association for Hydrogen Energy.

1. Introduction

1.1. Background

J.J. Balmer showed in 1885 that the frequencies for some of the lines observed in the emission spectrum of atomic hydrogen could be expressed with a completely empirical relationship. This approach was later extended by J.R. Rydberg, who showed that all of the spectral lines of atomic hydrogen were given by the equation:

$$\bar{v} = R \left(\frac{1}{n_f^2} - \frac{1}{n_i^2} \right), \qquad (1)$$

where $R = 109,677 \text{ cm}^{-1}$, $n_f = 1, 2, 3, \ldots$, $n_i = 2, 3, 4, \ldots$, and $n_i > n_f$.

Niels Bohr, in 1913, developed a theory for atomic hydrogen that gave energy levels in agreement with Rydberg's equation. An identical equation, based on a totally

* Corresponding author. Tel.: +1-609-490-1090; fax: +1-609-490-1066.

E-mail address: rmills@blacklightpower.com (R.L. Mills).

different theory for the hydrogen atom, was developed by E. Schrödinger, and independently by W. Heisenberg, in 1926

$$E_n = -\frac{e^2}{n^2 8\pi\varepsilon_0 a_H} = -\frac{13.598 \text{ eV}}{n^2}, \quad n = 1,2,3,\dots,$$

(2a,b)

where a_H is the Bohr radius for the hydrogen atom (52.947 pm), e is the magnitude of the charge of the electron, and ε_0 is the vacuum permittivity. Based on the solution of a Schrödinger-type wave equation with a nonradiative boundary condition based on Maxwell's equations, Mills [1–27] predicts that atomic hydrogen may undergo a catalytic reaction with certain atomized elements or certain gaseous ions which singly or multiply ionize at integer multiples of the potential energy of atomic hydrogen, 27.2 eV. The reaction involves a nonradiative energy transfer to form a hydrogen atom that is lower in energy than unreacted atomic hydrogen that corresponds to a fractional principal quantum number where Eq. (2b), should be replaced by

$$n = 1,2,3,\dots, \quad \text{and} \quad n = \tfrac{1}{2}, \tfrac{1}{3}, \tfrac{1}{4}, \dots . \quad (2c)$$

A number of independent experimental observations lead to the conclusion that atomic hydrogen can exist in fractional quantum states that are at lower energies than the traditional "ground" ($n = 1$) state.

1.2. Experimental data of lower-energy hydrogen

Observation of intense extreme ultraviolet (EUV) emission at low temperatures (e.g. $\approx 10^3$ K) from atomic hydrogen and certain atomized elements or certain gaseous ions [8,9,12–14,16–18] has been reported previously. The only pure elements that were observed to emit EUV were those wherein the ionization of t electrons from an atom to a continuum energy level is such that the sum of the ionization energies of the t electrons is approximately $m27.2$ eV where t and m are each an integer. Potassium, cesium, and strontium atoms and Rb^+ ion ionize at integer multiples of the potential energy of atomic hydrogen and caused emission. Whereas, the chemically similar atoms, sodium, magnesium and barium, do not ionize at integer multiples of the potential energy of atomic hydrogen and caused no emission.

Additional prior related studies that support the possibility of a novel reaction of atomic hydrogen which produces a chemically generated or assisted plasma and produces novel hydride compounds include EUV spectroscopy [7–18], characteristic emission from catalysis and the hydride ion product [8,9], lower-energy hydrogen emission [7–9], plasma formation [8,9,12–14,16–18], Balmer α line broadening [10], anomalous plasma afterglow duration [16,17], power generation [10,11,18], and analysis of chemical compounds [19–25]. Exemplary related studies include:

(1) The observation of novel EUV emission lines from microwave and glow discharges of helium with 2% hydrogen with energies of $q13.6$ eV where $q = 1,2,3,4,6,7,8,9$, or 11 or these lines inelastically scattered by helium atoms in the excitation of $He(1s^2)$ to $He(1s^12p^1)$ that were identified as hydrogen transitions to electronic energy levels below the "ground" state corresponding to fractional quantum numbers [7],

(2) the identification of transitions of atomic hydrogen to lower energy levels corresponding to lower energy hydrogen atoms in the extreme ultraviolet emission spectrum from interstellar medium and the Sun [1,5,7],

(3) the EUV spectroscopic observation of lines by the Institut für Niedertemperatur-Plasmaphysik e.V. that could be assigned to transitions of atomic hydrogen to lower energy levels corresponding to fractional principal quantum numbers and the emission from the excitation of the corresponding hydride ions [15],

(4) the recent analysis of mobility and spectroscopy data of individual electrons in liquid helium which shows direct experimental confirmation that electrons may have fractional principal quantum energy levels [6],

(5) the observation of continuum state emission of Cs^{2+} and Ar^{2+} at 53.3 and 45.6 nm, respectively, with the absence of the other corresponding Rydberg series of lines from these species which confirmed the resonant nonradiative energy transfer of 27.2 eV from atomic hydrogen to the catalysts atomic cesium or Ar^+ [9],

(6) the spectroscopic observation of the predicted hydride ion $H^-(\tfrac{1}{2})$ of hydrogen catalysis by either cesium atom or Ar^+ catalyst at 407 nm corresponding to its predicted binding energy of 3.05 eV [9],

(7) the observation of characteristic emission from K^{3+} which confirmed the resonant nonradiative energy transfer of 3.27.2 eV from atomic hydrogen to atomic potassium [8],

(8) the spectroscopic observation of the predicted $H^-(\tfrac{1}{4})$ hydride ion of hydrogen catalysis by potassium catalyst at 110 nm corresponding to its predicted binding energy of 11.2 eV [8],

(9) the observation by the Institut für Niedertemperatur-Plasmaphysik e.V. of an anomalous plasma and plasma afterglow duration formed with hydrogen–potassium mixtures [16],

(10) the observation of anomalous afterglow durations of plasmas formed by catalysts providing a net enthalpy of reaction within thermal energies of $m27.28$ eV [16,17],

(11) the observation of Lyman series in the EUV that represents an energy release 10 times hydrogen combustion which is greater than that of any possible known chemical reaction [7,18],

(12) the observation of line emission by the Institut für Niedertemperatur-Plasmaphysik e.V. with a 4° grazing incidence EUV spectrometer that was 100 times more energetic than the combustion of hydrogen [15],

(13) the observation of anomalous plasmas formed with strontium and argon catalysts at 1% of the theoretical

or prior known voltage requirement with a light output for power input up to 8600 times that of the control standard light source [12,13,18],

(14) the observation that the optically measured output power of gas cells for power supplied to the glow discharge increased by over two orders of magnitude depending on the presence of less than 1% partial pressure of certain catalysts in hydrogen gas or argon–hydrogen gas mixtures, and an excess thermal balance of 42 W was measured for the 97% argon and 3% hydrogen mixture versus argon plasma alone [11],

(15) the observation that plasmas of the catalyst–hydrogen mixtures of strontium–hydrogen, helium–hydrogen, argon–hydrogen, strontium–helium–hydrogen, and strontium–argon–hydrogen showed significant Balmer α line broadening corresponding to an average hydrogen atom temperature of 25–45 eV; whereas, plasmas of the noncatalyst–hydrogen mixtures of pure hydrogen, krypton–hydrogen, xenon–hydrogen, and magnesium–hydrogen showed no excessive broadening corresponding to an average hydrogen atom temperature of ≈ 3 eV [10],

(16) the observation that the power emitted for power supplied to a hydrogen glow discharge plasmas increased by 35–184 W depending on the presence of catalysts helium or argon and less than 1% partial pressure of strontium metal in noble gas–hydrogen mixtures; whereas, the chemically similar noncatalyst krypton had no effect on the power balance [10],

(17) the differential scanning calorimetry (DSC) measurement of minimum heats of formation of KHI by the catalytic reaction of potassium with atomic hydrogen and KI that were over −2000 kJ/mol H₂ compared to the enthalpy of combustion of hydrogen of −241.8 kJ/mol H₂ [25],

(18) the isolation of novel hydrogen compounds as products of the reaction of atomic hydrogen with atoms and ions which formed an anomalous plasma as reported in the EUV studies [19–25],

(19) the identification of novel hydride compounds by (i) time of flight secondary ion mass spectroscopy which showed a dominant hydride ion in the negative ion spectrum, (ii) X-ray photoelectron spectroscopy which showed novel hydride peaks and significant shifts of the core levels of the primary elements bound to the novel hydride ions, (iii) ¹H nuclear magnetic resonance spectroscopy (NMR) which showed extraordinary upfield chemical shifts compared to the NMR of the corresponding ordinary hydrides, and (iv) thermal decomposition with analysis by gas chromatography, and mass spectroscopy which identified the compounds as hydrides [19–25],

(20) the NMR identification of novel hydride compounds MH⁺X wherein M is the metal, X, is a halide, and H⁺ comprises a novel high binding energy hydride

ion identified by a large distinct upfield resonance [19,20,23],

(21) the replication of the NMR results of the identification of novel hydride compounds by large distinct upfield resonances at Spectral Data Services, University of Massachusetts Amherst, University of Delaware, Grace Davison, and National Research Council of Canada [19], and

(22) the NMR identification of novel hydride compounds MH⁺ and MH₂⁺ wherein M is the metal and H⁺ comprises a novel high binding energy hydride ion identified by a large distinct upfield resonance that proves the hydride ion is different from the hydride ion of the corresponding known compound of the same composition [19].

1.3. Mechanism of the formation of lower-energy atomic hydrogen

The mechanism of the EUV emission, the formation of novel hydrides, and the observation of certain EUV lines from interstellar medium and the Sun cannot be explained by the conventional energy levels of hydrogen, but it is predicted by a solution of the Schrödinger equation with a nonradiative boundary constraint put forward by Mills [1]. Mills predicts that certain atoms or ions serve as catalysts to release energy from hydrogen to produce an increased binding energy hydrogen atom called a *hydrino atom* having a binding energy given by Eq. (2a) where

$$n = \frac{1}{2}, \frac{1}{3}, \frac{1}{4}, \cdots, \frac{1}{p} \tag{3}$$

and p is an integer greater than 1, designated as $H[a_H/p]$ where a_H is the radius of the hydrogen atom. Hydrinos are predicted to form by reacting an ordinary hydrogen atom with a catalyst having a net enthalpy of reaction of about

$$m27.21 \text{ eV}, \tag{4}$$

where m is an integer. This catalysis releases energy from the hydrogen atom with a commensurate decrease in size of the hydrogen atom, $r_a = na_H$. For example, the catalysis of $H(n=1)$ to $H(n=\frac{1}{2})$ releases 40.8 eV, and the hydrogen radius decreases from a_H to $\frac{1}{2}a_H$.

The excited energy states of atomic hydrogen are also given by Eq. (2a) except with Eq. (2b). The $n=1$ state is the "ground" state for "pure" photon transitions (the $n=1$ state can absorb a photon and go to an excited electronic state, but it cannot release a photon and go to a lower-energy electronic state). However, an electron transition from the ground state to a lower-energy state is possible by a nonradiative energy transfer such as multipole coupling or a resonant collision mechanism. These lower-energy states have fractional quantum-numbers, $n = 1/\text{integer}$.

Processes that occur without photons and that require collisions are common. For example, the exothermic chemical reaction of H + H to form H₂ does not occur with the

emission of a photon. Rather, the reaction requires a collision with a third body, M, to remove the bond energy —

$$H + H + M \rightarrow H_2 + M^* \ [28].$$ The third body distributes the energy from the exothermic reaction, and the end result is the H_2 molecule and an increase in the temperature of the system. Some commercial phosphors are based on nonradiative energy transfer involving multipole coupling. For example, the strong absorption strength of Sb^{3+} ions along with the efficient nonradiative transfer of excitation from Sb^{3+} to Mn^{2+}, are responsible for the strong manganese luminescence from phosphors containing these ions [29]. Similarly, the $n = 1$ state of hydrogen and the $n = 1/$integer states of hydrogen are nonradiative, but a transition between two nonradiative states is possible via a nonradiative energy transfer, say $n = 1 - \frac{1}{2}$. In these cases, during the transition the electron couples to another electron transition, electron transfer reaction, or inelastic scattering reaction which can absorb the exact amount of energy that must be removed from the hydrogen atom to cause the transition. Thus, a catalyst provides a net positive enthalpy of reaction of $m27.21$ eV (i.e. it absorbs $m27.21$ eV where m is an integer). Certain atoms or ions serve as catalysts which resonantly accept energy from hydrogen atoms and release the energy to the surroundings to effect electronic transitions to fractional quantum energy levels. Recent analysis of mobility and spectroscopy data of individual electrons in liquid helium show direct experimental evidence that electrons may have fractional principal quantum energy levels [6].
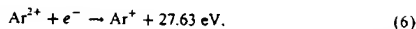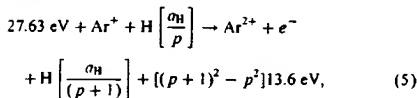
The catalysis of hydrogen involves the nonradiative transfer of energy from atomic hydrogen to a catalyst which may then release the transferred energy by radiative and nonradiative mechanisms. As a consequence of the nonradiative energy transfer, the hydrogen atom becomes unstable and emits further energy until it achieves a lower-energy nonradiative state having a principal energy level given by Eqs. (2a) and (3).
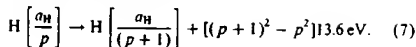
1.4. Catalysts

According to Mills [1], a catalytic system is provided by the ionization of t electrons from an atom or ion to a continuum energy level such that the sum of the ionization energies of the t electrons is approximately $m27.2$ eV where m is an integer.

1.4.1. Argon ion

Argon ions can provide a net enthalpy of a multiple of that of the potential energy of the hydrogen atom. The second ionization energy of argon is 27.63 eV. The reaction Ar^+ to Ar^{2+} has a net enthalpy of reaction of 27.63 eV, which is equivalent to $m = 1$ in Eq. (4)
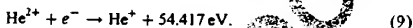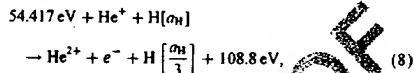
$$27.63 \text{ eV} + Ar^+ + H\left[\frac{a_H}{p}\right] \rightarrow Ar^{2+} + e^-$$
$$+ H\left[\frac{a_H}{(p+1)}\right] + [(p+1)^2 - p^2]13.6 \text{ eV}, \tag{5}$$

$$Ar^{2+} + e^- \rightarrow Ar^+ + 27.63 \text{ eV}. \tag{6}$$

And, the overall reaction is

$$H\left[\frac{a_H}{p}\right] \rightarrow H\left[\frac{a_H}{(p+1)}\right] + [(p+1)^2 - p^2]13.6 \text{ eV}. \tag{7}$$
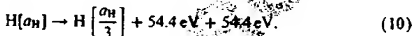
1.4.2. Helium ion

Helium ion (He^+) is also such a catalyst because the second ionization energy of helium is 54.417 eV, which is equivalent to $m = 2$ in Eq. (4). In this case, the catalysis reaction is

$$54.417 \text{ eV} + He^+ + H[a_H]$$
$$\rightarrow He^{2+} + e^- + H\left[\frac{a_H}{3}\right] + 108.8 \text{ eV}, \tag{8}$$

$$He^{2+} + e^- \rightarrow He^+ + 54.417 \text{ eV}. \tag{9}$$

And, the overall reaction is

$$H[a_H] \rightarrow H\left[\frac{a_H}{3}\right] + 54.4 \text{ eV} + 54.4 \text{ eV}. \tag{10}$$

The energy given off during catalysis is much greater than the energy lost to the catalyst. The energy released is large as compared to conventional chemical reactions. For example, when hydrogen and oxygen gases undergo combustion to form water

$$H_2(g) + \frac{1}{2}O_2(g) \rightarrow H_2O(l) \tag{11}$$

the known enthalpy of formation of water is $\Delta H_f = -286$ kJ/mol or 1.48 eV per hydrogen atom. By contrast, each ($n = 1$) ordinary hydrogen atom undergoing catalysis releases a net of 40.8 eV. Moreover, further catalytic transitions may occur: $n = \frac{1}{2} \rightarrow \frac{1}{3}, \frac{1}{3} \rightarrow \frac{1}{4}, \frac{1}{4} \rightarrow \frac{1}{5}$, and so on. Once catalysis begins, hydrinos autocatalyze further in a process called *disproportionation*. This mechanism is similar to that of an inorganic ion catalysis. But, hydrino catalysis should have a higher reaction rate than that of the inorganic ion catalyst due to the better match of the enthalpy to $m27.2$ eV.

1.4.3. Hydrino catalysis

In a process called *disproportionation*, lower-energy hydrogen atoms, *hydrinos*, can act as catalysts because each of the metastable excitation, resonance excitation, and ionization energy of a hydrino atom is $m27.2$ eV (Eq. (4)). The transition reaction mechanism of a first hydrino atom affected by a second hydrino atom involves the resonant coupling between the atoms of m degenerate multipoles each having 27.21 eV of potential energy [1]. The energy transfer of $m27.2$ eV from the first hydrino atom to the second hydrino atom causes the central field of the first atom to increase by m and its electron to drop m levels lower from a radius of a_H/p to a radius of $a_H/(p + m)$. The second interacting

lower-energy hydrogen is either excited to a metastable state, excited to a resonance state, or ionized by the resonant energy transfer. The resonant transfer may occur in multiple stages. For example, a nonradiative transfer by multipole coupling may occur wherein the central field of the first increases by m, then the electron of the first drops m levels lower from a radius of a_H/p to a radius of $a_H/(p+m)$ with further resonant energy transfer. The energy transferred by multipole coupling may occur by a mechanism that is analogous to photon absorption involving an excitation to a virtual level. Or, the energy transferred by multipole coupling during the electron transition of the first hydrino atom may occur by a mechanism that is analogous to two photon absorption involving a first excitation to a virtual level and a second excitation to a resonant or continuum level [30–32]. The transition energy greater than the energy transferred to the second hydrino atom may appear as a photon in a vacuum medium.

The transition of $H[a_H/p]$ to $H[a_H/(p+m)]$ induced by a multipole resonance transfer of $m27.21$ eV (Eq. (4)) and a transfer of $[(p')^2 - (p'-m')^2]13.6$ eV $- m27.2$ eV with a resonance state of $H[a_H/(p'-m')]$ excited in $H[a_H/p']$ is represented by

$$H\left[\frac{a_H}{p'}\right] + H\left[\frac{a_H}{p}\right] \rightarrow H\left[\frac{a_H}{p'-m'}\right] + H\left[\frac{a_H}{p+m}\right]$$

$$+[((p+m)^2 - p^2) - (p'^2 - (p'-m')^2)]13.6 \text{ eV}, \tag{12}$$

where p, p', m, and m' are integers.

Hydrinos may be ionized during a disproportionation reaction by the resonant energy transfer. A hydrino atom with the initial lower-energy state quantum number p and radius a_H/p may undergo a transition to the state with lower-energy state quantum number $(p+m)$ and radius $a_H/(p+m)$ by a reaction with a hydrino atom with the initial lower-energy state quantum number m', initial radius a_H/m' and final radius a_H that provides a net enthalpy of $m27.2$ eV (Eq. (4)). Thus, reaction of hydrogen-type atom, $H[a_H/p]$, with the hydrogen-type atom, $H[a_H/m']$, that is ionized by the resonant energy transfer to cause a transition reaction is represented by

$$m27.21 \text{ eV} + H\left[\frac{a_H}{m'}\right] + H\left[\frac{a_H}{p}\right] \rightarrow H^+$$

$$+e^- + H\left[\frac{a_H}{(p+m)}\right] + [(p+m)^2 - p^2$$

$$- (m'^2 - 2m)]13.6 \text{ eV}, \tag{13}$$

$$H^+ + e^- \rightarrow H\left[\frac{a_H}{1}\right] + 13.6 \text{ eV}. \tag{14}$$

And, the overall reaction is

$$H\left[\frac{a_H}{m'}\right] + H\left[\frac{a_H}{p}\right]$$

$$\rightarrow H\left[\frac{a_H}{1}\right] + H\left[\frac{a_H}{(p+m)}\right] + [2pm + m^2 - m'^2]$$

$$13.6 \text{ eV} + 13.6 \text{ eV}. \tag{15}$$

Helium ion catalyzes $H[a_H]$ to $H[a_H/3]$ as shown in Eqs. (8)–(10). Disproportionation reaction may then proceed to give:

$$H\left[\frac{a_H}{3}\right] + H\left[\frac{a_H}{3}\right] \rightarrow H\left[\frac{a_H}{4}\right] + H\left[\frac{a_H}{2}\right] + 27.2 \tag{16}$$

1.5. The nature of the chemical bonds of the hydrogen molecular ion, the hydrogen molecule, and hydrogen molecular ions and molecules having fractional principal quantum numbers

From the application of the nonradiative boundary condition, the instability of excited states as well as the stability of the "ground" state arise naturally in the Mills theory [1] described in Appendix B. In addition to the known states of hydrogen (Eqs. (2a) and (2b)), the theory predicts the existence of previously unknown form of matter: hydrogen atoms and molecules having electrons of lower energy than the conventional "ground" state, called *hydrinos* and *dihydrino* — the diatomic hydrino molecule, respectively, where each energy level corresponds to a fractional quantum number.

Two hydrogen atoms react to form a diatomic molecule, the hydrogen molecule

$$2H[a_H] \rightarrow H_2[2c' = \sqrt{2}a_0], \tag{17}$$

where $2c'$ is the internuclear distance. Also, two hydrino atoms react to form a diatomic molecule, a dihydrino molecule

$$2H\left[\frac{a_H}{p}\right] \rightarrow H_2\left[2c' = \frac{\sqrt{2}a_0}{p}\right], \tag{18}$$

where p is an integer. And, a hydrino atom can react with a proton to form a dihydrino molecular ion that further reacts with an electron to form a dihydrino molecule
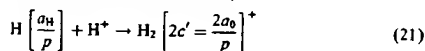
$$H\left[\frac{a_H}{p}\right] + H^+ + e^- \rightarrow H_2\left[2c' = \frac{\sqrt{2}a_0}{p}\right]. \tag{19}$$

The hydrogen-type molecular ion and molecular charge and current density functions, bond distance, and energies are solved in Appendix B from the Laplacian in ellipsoidal
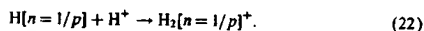
coordinates with the constraint of nonradiation

$$(\eta - \zeta)R_\xi \frac{\partial}{\partial \xi}\left(R_\xi \frac{\partial \phi}{\partial \xi}\right) + (\zeta - \xi)R_\eta \frac{\partial}{\partial \eta}\left(R_\eta \frac{\partial \phi}{\partial \eta}\right)$$

$$+ (\xi - \eta)R_\zeta \frac{\partial}{\partial \zeta}\left(R_\zeta \frac{\partial \phi}{\partial \zeta}\right) = 0. \tag{20}$$

In the case that a hydrino atom reacts with a proton to form a dihydrino molecular ion,

$$H\left[\frac{a_H}{p}\right] + H^+ \rightarrow H_2\left[2c' = \frac{2a_0}{p}\right]^+ \tag{21}$$

a designation for this reaction in terms of quantum numbers is

$$H[n = 1/p] + H^+ \rightarrow H_2[n = 1/p]^+. \tag{22}$$

The energy released is

$$E_D = E\left(H\left[\frac{a_H}{p}\right]\right) - E_T$$

$$= -p^2 13.6 + p^2 16.28\,\text{eV} = p^2 2.68\,\text{eV}, \tag{23}$$

where E_T is given by Eq. (B.77). The reaction of a hydrino atom with a proton may involve an excited electronic state and a series of corresponding vibrational and rotational states. In the reaction designated

$$H\left[\frac{a_H}{2}\right] + H^+ \rightarrow H_2^*\left[2c' = \frac{a_0}{4}; n^* = 2\right]^+ \tag{24}$$
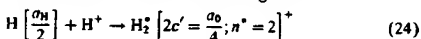
the hydrino $H[n = \frac{1}{2}]$ may react with a proton to form the first excited electronic state of the molecular ion $H_2[n = \frac{1}{4}]^+$ wherein the central field in elliptic coordinates in one half that of ground state (nonradiative state) of $H_2[n = \frac{1}{4}]^+$. This state is analogous to the $n = 2$ state of atomic hydrogen and is designated as $H_2^*[n = \frac{1}{4}; n^* = 2]^+$, except the electronic relaxation may involve a radiationless process with a radiative component involving the oscillating and rotating nuclei which undergoes transition to the state of $H_2[n = \frac{1}{4}]^+$. The nonradiative energy transfer corresponding to $H[n = \frac{1}{2}] \rightarrow H[n = \frac{1}{4}]$ may occur from the highest vibrational state (bond-continuum state) of $H_2[n = \frac{1}{4}]^+$. The bond energy of $H_2[n = 1/p]^+$ is given by Eq. (B.78). Thus, the bond energy of $H_2[n = \frac{1}{4}]^+$ is

$$E_D = p^2 2.68\,\text{eV} = 4^2 2.68\,\text{eV} = 42.88\,\text{eV}(28.92\,\text{nm}), \tag{25}$$

where $p = 4$, and the bond energy of $H_2[n = \frac{1}{2}]^+$ is

$$E_D = p^2 2.68\,\text{eV} = 2^2 2.68\,\text{eV} = 10.72\,\text{eV}(115.70\,\text{nm}), \tag{25}$$

where $p = 2$. Due to the Franck–Condon principle, the vibrational and rotational energies of $H_2^*[n = \frac{1}{4}; n^* = 2]^+$ are equivalent to those of $H_2[n = \frac{1}{2}]^+$ given by Eq. (B.122) and Eq. (B.255), respectively,

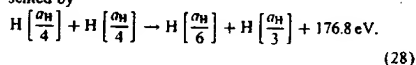$$E_{vib} = (v_f - v_i)p^2 0.2962\,\text{eV} = (v_f - v_i)1.185\,\text{eV}, \tag{26}$$

$$\lambda = \frac{169}{p^2[J + 1]}\,\mu\text{m} = \frac{42}{[J + 1]}\,\mu\text{m} \quad (J + 1 \rightarrow J), \tag{27}$$

where $p = 2$. Thus, the emission spectrum of $H_2^*[n = \frac{1}{4}; n^* = 2]^+$ is predicted to comprise vibrational peaks centered at 1.185 eV spacing slit by 42 µm spaced peaks due to rotational transitions terminating at about $E_D(H_2[n = \frac{1}{4}]^+) = 42.88\,\text{eV}(28.92\,\text{nm})$. Nonlinearity at highly excited vibrational levels with translational, vibrational, and rotational interactions are anticipated to broaden the terminal peaks.

1.6. EUV spectroscopy detects lower-energy hydrogen

It was previously reported that extreme ultraviolet spectroscopy was recorded on microwave and glow discharges of helium with 2% hydrogen wherein helium and the product hydrinos served as catalysts [7]. Novel emission lines were observed with energies of $q13.6\,\text{eV}$, where $q = 1, 2, 3, 4, 6, 7, 8, 9$, or 11 or these lines inelastically scattered by helium atoms wherein 21.2 eV was absorbed in the excitation of He(1s²) to He(1s¹2p¹). These lines were identified as hydrogen transitions to electronic energy levels below the "ground" state corresponding to fractional quantum numbers. In addition, a comparison was made between the plasma results and astrophysical data. Similar lower-energy-hydrogen transitions were found that matched the spectral lines of the extreme ultraviolet background of interstellar space and Solar lines.

Also, previously reported lines observed at the Institut für Niedertemperatur-Plasmaphysik e.V. by EUV spectroscopy could be assigned to transitions of atomic hydrogen to lower energy levels corresponding to hydrinos and the emission from the excitation of the corresponding hydride ions [15]. For example, the product of the catalysis of atomic hydrogen with potassium metal, $H[a_H/4]$ may serve as both a catalyst and a reactant to form $H[a_H/3]$ and $H[a_H/6]$. The transition of $H[a_H/4]$ to $H[a_H/6]$ induced by a multipole resonance transfer of 54.4 eV (2.27.2 eV) and a transfer of 40.8 eV with a resonance state of $H[a_H/3]$ excited in $H[a_H/4]$ is represented by

$$H\left[\frac{a_H}{4}\right] + H\left[\frac{a_H}{4}\right] \rightarrow H\left[\frac{a_H}{6}\right] + H\left[\frac{a_H}{3}\right] + 176.8\,\text{eV}. \tag{28}$$

The predicted 176.8 eV (7.02 nm) photon is a close match with the observed 7.30 nm line. The energy of this line emission corresponds to an equivalent temperature of $1,000,000\,°\text{C}$ and an energy over 100 times the energy of combustion of hydrogen.

Since the Sun and stars contain significant amounts of He⁺ and atomic hydrogen, catalysis of atomic hydrogen by He⁺ as given by Eqs. (8)–(10) may occur. Also, the simultaneous ionization of two hydrogen atoms may provide a net enthalpy given by Eq. (4) to catalyze hydrino formation. Once formed, hydrinos have binding energies given by Eqs. (2a) and (3); thus, they may serve as reactants which provide a net enthalpy of reaction given by Eq. (4). Lower-energy atomic hydrogen may react to form the corresponding dihydrino molecules. Characteristic emissions from the Sun may identify dihydrino molecules.

The detection of atomic hydrogen in fractional quantum energy levels below the traditional "ground" state — hydrinos — was previously reported [1,5,7] by the assignment of soft X-ray emissions from the interstellar medium, the Sun, and stellar flares, and by assignment of certain lines obtained by the far–infrared absolute spectrometer (FIRAS) on the Cosmic Background Explorer. The detection of a new molecular species — the diatomic hydrino molecule — was reported by the assignment of certain infrared line emissions from the Sun. The detection of a new hydride species — hydrino hydride ion — was reported by the assignment of certain soft X-ray, ultraviolet (UV), and visible emissions from the Sun. This has implications for several unresolved astrophysical problems such as the identity of dark matter and the Solar neutrino paradox [1,7].

From Eq. (26), the energy for the $v + 1 \rightarrow v$ vibrational transition is 1.185 eV. The increment of the McPherson 4° grazing incidence EUV spectrometer was 0.1 nm as described in Section 2. The corresponding energy in this spectral region is about 0.15 eV. The rotational levels given by Eq. (27) could not be resolved since the $J + 1 \rightarrow J$ corresponds to 0.03 eV. Thus, the excited state spectrum of $H_2^*[n = \frac{1}{4}; n^* = 2]^+$ was predicted to comprise rotationally broadened vibrational transitions centered on 1.185 eV increments. The series of vibrational transitions was predicted to terminate at about the dissociation limit of $H_2[n = \frac{1}{4}]^+$, $E_D = 42.88$ eV(28.92 nm) given by Eq. (25). We report that this spectrum was observed during microwave discharges of mixtures of argon or helium and 10% hydrogen. Solar astrophysical data was reviewed and emission lines from the corona were identified which matched dihydrino molecular rotational transitions to five figures.

2. Experimental

2.1. EUV spectroscopy

EUV spectroscopy was recorded on a microwave cell light source. Due to the extremely short wavelength of this radiation, "transparent" optics do not exist. Therefore, a windowless arrangement was used wherein the microwave cell was connected to the same vacuum vessel as the grating and detectors of the EUV spectrometer. Differential pumping permitted a high pressure in the cell as compared to that in the spectrometer. This was achieved by pumping on the cell outlet and pumping on the grating side of the collimator that served as a pinhole inlet to the optics. The spectrometer was continuously evacuated to 10^{-4}–10^{-6} Torr by a turbomolecular pump with the pressure read by a cold cathode pressure gauge. The EUV spectrometer was connected to the cell light source with a 1.5 mm × 5 mm collimator which provided a light path to the slits of the EUV spectrometer. The collimator also served as a flow constrictor of gas from the cell. The cell was operated under gas flow
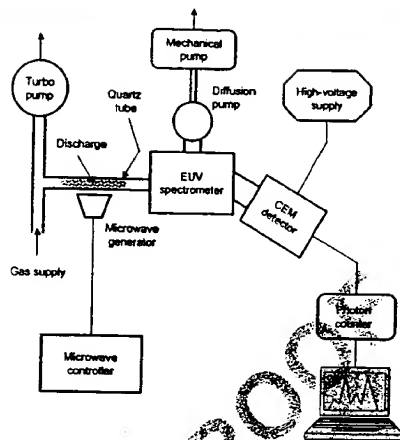

Fig. 1. The experimental setup comprising a microwave discharge gas cell light source and an EUV spectrometer which was differentially pumped.

conditions while maintaining a constant gas pressure in the cell.

EUV spectroscopy was recorded on argon–hydrogen ($\frac{90}{10}$%) and helium–hydrogen ($\frac{90}{10}$%) plasmas. The plasma source was a microwave plasma discharge cell. The microwave EUV spectra were recorded with a grazing incidence EUV spectrometer. Control plasmas of neon, krypton, xenon, hydrogen, argon, and helium alone and neon–hydrogen ($\frac{90}{10}$%), krypton–hydrogen ($\frac{90}{10}$%) and xenon–hydrogen ($\frac{90}{10}$%) were recorded.

The light emission from a microwave plasma was introduced to an EUV spectrometer for spectral measurement. The spectrometer was a McPherson 4° grazing incidence EUV spectrometer (Model 248/310G) equipped with a grating having 600 G/mm with a radius of curvature of ≈ 1 m. The angle of incidence was 87°. The wavelength region covered by the monochromator was 5–65 nm. The wavelength resolution was about 0.1 nm (FWHM) with an entrance and exit slit width of 300 µm. A channel electron multiplier (CEM) at 2400 V was used to detect the EUV light. The increment was 0.1 nm and the dwell time was 1 s.

2.2. Microwave emission spectra

The experimental setup comprising the microwave discharge gas cell light source and the EUV spectrometer which was differentially pumped is shown in Fig. 1. The extreme ultraviolet emission spectrum was obtained on plasmas of hydrogen alone, noble gases alone, or noble gas–hydrogen

ARTICLE IN PRESS

1   mixtures ($\frac{90}{10}$%) with a microwave discharge system and an
EUV spectrometer. Gas was flowed through a half-inch di-
3   ameter quartz tube. The gas pressure inside the cell was
maintained at about 300 mTorr under flow conditions where
5   the flow of each gas was controlled by 0–20 sccm range
mass flow controller (MKS 1179A21CS1BB) with a read-
7   out (MKS type 246). The flow rate for each gas tested
alone was 11 sccm, and the flow rates for the neon, kryp-
9   ton, xenon, argon, or helium 90% with 10% hydrogen was
10 and 1 sccm, respectively. The pressure was measured
11   with a 10 and 1000 Torr MKS Baratron absolute pressure
gauge. The tube was fitted with an Opthos coaxial mi-
13   crowave cavity (Evenson cavity). The microwave gener-
ator was a Opthos model MPG-4M generator (frequency:
15   2450 MHz). The output power was set at 85 W. The EUV
spectrometer was a McPherson 4° grazing incidence EUV
17   spectrometer (Model 248/310G). (See EUV-Spectroscopy
Section).

3. Results and discussion

3.1. EUV spectroscopy

21   The EUV emission spectra were recorded from micro-
wave discharge plasmas of pure neon, krypton, xenon, hy-
23   drogen, argon, and helium, as well as 10% hydrogen with
neon, krypton, xenon, argon, and helium over the wave-
25   length range 20–60 nm. The short wavelength spectra of
neon and neon–hydrogen ($\frac{90}{10}$%) were equivalent to the spec-
27   tra reported previously [7]. Only known Ne II peaks were
observed in this region. The EUV spectra of the control
29   krypton and krypton–hydrogen ($\frac{90}{10}$%), xenon and xenon–
hydrogen ($\frac{90}{10}$%), hydrogen, argon, and helium microwave
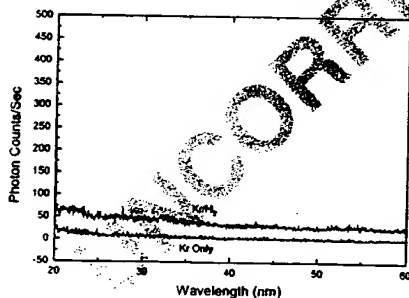31   discharge cell emission is shown in Figs. 2, 3, 4, 5, and 6,

Fig. 2. The EUV spectra (20–60 nm) of the control krypton and krypton–hydrogen microwave discharge cell emission that were recorded with a 4° grazing incidence EUV spectrometer and a CEM. No emission was observed in this region with or without hydrogen.

Fig. 3. The EUV spectra (20–60 nm) of the control xenon and xenon–hydrogen microwave discharge cell emission that were recorded with a 4° grazing incidence EUV spectrometer and a CEM. No emission was observed in this region with or without hydrogen.
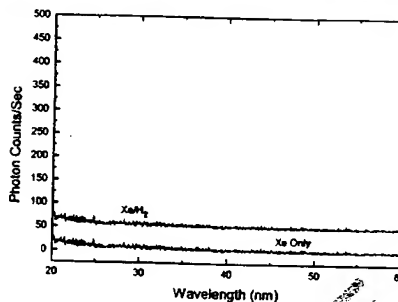

Fig. 4. The EUV spectrum (20–60 nm) of the control hydrogen microwave discharge cell emission that were recorded with a 4° grazing incidence EUV spectrometer and a CEM. No emission was observed in this region.

respectively. No spurious peaks or artifacts due to the grat-   33
ing or the spectrometer were observed. No changes in the
emission spectra were observed by the addition of hydrogen   35
to noncatalysts neon, krypton, or xenon.

The reaction Ar^+ to Ar^{2+} has a net enthalpy of reaction   37
of 27.63 eV, which is equivalent to $m = 1$. The catalysis
reaction involves a nonradiative energy transfer to form a   39
hydrogen atom that is lower in energy than unreacted atomic
hydrogen. The product hydrogen atom has an energy state   41
that corresponds to a fractional principal quantum number.
The lower-energy hydrogen atom is a highly reactive inter-   43
mediate which further reacts to form a novel hydride ion.
Emission was observed previously from a continuum state   45

Fig. 5. The EUV spectrum (27–60 nm) of the control argon microwave discharge cell emission that was recorded with a 4° grazing incidence EUV spectrometer and a CEM. No emission was observed below 45 nm.
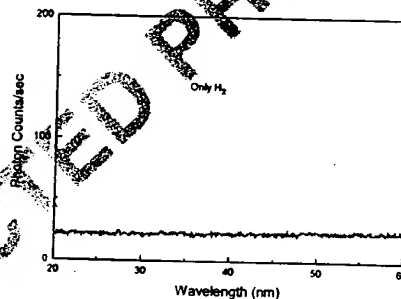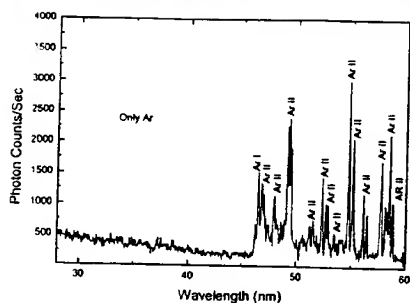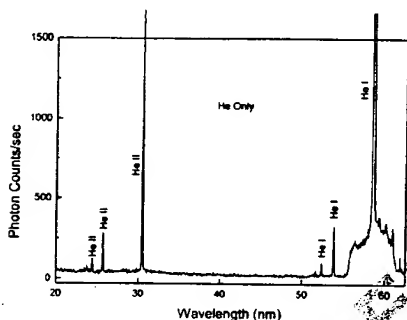

Fig. 6. The EUV spectrum (20–62 nm) of the control helium microwave discharge cell emission that was recorded with a 4° grazing incidence EUV spectrometer and a CEM. Only known line emission of He I and He II were observed.
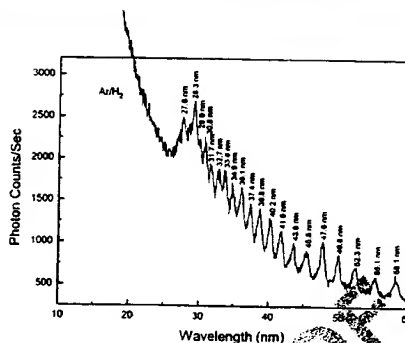

Fig. 7. The EUV spectrum (10–60 nm) of the argon–hydrogen mixture ($\frac{90}{10}$%) microwave cell emission recorded with 0.1 nm increment of the McPherson 4° grazing incidence EUV spectrometer. A series of 0.5 eV wide Gaussian-shaped peaks were observed in the spectral region 27–60 nm that were assigned to the $v = 18$–38 vibrational transitions of $H_2^*[n = \frac{1}{4}; n^* = 2]^+$ with energies $v1.185$ eV as given in Table 1. The intense continuum peak at about 28 nm that dominated the series was assigned to the dissociation energy of $H_2[\frac{1}{4}, \frac{1}{4}]^+$.
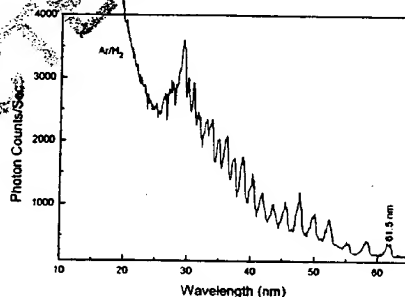
Fig. 8. The EUV spectrum (10–65 nm) of the argon–hydrogen mixture ($\frac{90}{10}$%) microwave cell emission recorded with 0.1 nm increment of the McPherson 4° grazing incidence EUV spectrometer. With an increased spectral range compared to that of Fig. 7, an addition peak was observed at 61.5 nm that was assigned to the $v = 17$ vibrational transition of $H_2^*[n = \frac{1}{4}; n^* = 2]^+$ with an energy $v1.185$ eV as given in Table 1.

1 of Ar^{2+} at 45.6 nm [9]. The single emission feature with the absence of the other corresponding Rydberg series of

3 lines from Ar^+ confirmed the resonant nonradiative energy transfer of 27.2 eV from atomic hydrogen to Ar^+. The catal-

5 ysis product, the lower-energy hydrogen atom $H(\frac{1}{2})$, was predicted to be a highly reactive intermediate which further

7 reacts to form the novel hydride ion $H^-(\frac{1}{2})$. This ion was observed spectroscopically at 407 nm corresponding to its

9 predicted binding energy of 3.05 eV. The catalytic reaction is given in Section 1.4.

11 The EUV spectra (10–60 nm) and (10–65 nm) of the argon–hydrogen mixture ($\frac{90}{10}$%) microwave cell emission

13 are shown in Figs. 7, and 8, respectively. Ordinary hydrogen has no emission in this region as shown in Fig. 4, and no

emission below 45 nm was observed with the control argon 15 microwave discharge without hydrogen as shown in Fig. 5. A series of 0.5 eV wide Gaussian-shaped peaks 17 was observed in the spectral region 27–65 nm. The

Table 1

Calculated energies of vibrational transitions of $H_2^*[n = \frac{1}{4}; n^* = 2]^+$ and the observed emission lines

Vibrational quantum number v	Calculated emission (nm) Eqs. (26) (B.80), and (B.119)	Calculated emission (eV) Eq. (26) and (B.119)	Observed lines (nm)	Observed lines (eV)	Difference between experimental and predicted (eV)
0	0	0			
1	1047	1.185			
2	523.3	2.370			
3	348.9	3.555			
4	261.7	4.740			
5	209.3	5.925			
6	174.5	7.110			
7	149.5	8.295			
8	130.8	9.480			
9	116.3	10.67			
10	104.7	11.85			
11	95.15	13.04			
12	87.22	14.22			
13	80.51	15.41			
14	74.76	16.59			
15	69.78	17.78			
16	65.42	18.96			
17	61.57	20.15			
18	58.15	21.33	61.5	20.4	0.02
19	55.09	22.52	58.1	21.3	0.02
20	52.33	23.70	55.1	22.5	0.00
21	49.84	24.89	52.3	23.7	0.02
22	47.58	26.07	49.8	24.9	0.02
23	45.51	27.26	47.0	26.1	−0.01
24	43.61	28.44	45.5	27.3	0.00
25	41.87	29.63	43.8	28.4	0.01
26	40.26	30.81	41.8	29.7	0.05
27	38.77	32.00	40.2	30.9	0.04
28	37.38	33.18	38.8	32.0	−0.03
29	36.09	34.37	37.4	33.2	−0.02
30	34.89	35.55	36.1	34.4	−0.01
31	33.76	36.74	34.9	35.5	−0.01
32	32.71	37.92	33.8	36.7	−0.04
33	31.72	39.11	32.7	37.9	0.01
34	30.78	40.29	31.7	39.1	0.02
35	29.91	41.48	30.8	40.3	−0.02
36	29.07	42.66	29.9	41.5	0.01
37	28.29	43.85	29.1	42.6	−0.04
38	27.54	45.03	28.3	43.8	−0.02
			27.6	44.9	−0.09

peaks centered on relative increments in energy of 1.185 eV terminated at about 28 nm. H(1/p) may react with a proton to form an excited state molecular ion $H_2^*(1/p)^+$ that has a bond energy and vibrational levels that are p^2 times those of the molecular ion comprising uncatalyzed atomic hydrogen where p is an integer. Ar$^+$ may serve as a catalyst to form H($\frac{1}{2}$) which may react with a proton to form $H_2^*[n = \frac{1}{4}; n^* = 2]^+$. From Eqs. (26) and (B.119), the energy for the $v + 1 \rightarrow v$ vibrational transition of $H_2^*[n = \frac{1}{4}; n^* = 2]^+$ is 1.185 eV. The increment of the McPherson 4° grazing incidence

EUV spectrometer was 0.1 nm as described in Section 2. The corresponding energy in this spectral region is about 0.15 eV. The rotational levels given by Eq. (27) could not be resolved since the $J + 1 \rightarrow J$ corresponds to 0.03 eV. Thus, the excited state spectrum of $H_2^*[n = \frac{1}{4}; n^* = 2]^+$ in this region was predicted to comprise rotationally broadened vibrational transitions at 1.185 eV increments (Eq. (26) and Eq. (B.119)) that terminated at about the dissociation limit of $H_2[n = \frac{1}{4}]^+$, $E_D = 42.88$ eV(28.92 nm) (Eq. (25)). In Table 1, the novel emission lines were assigned to the $v = 17$–38 vibrational

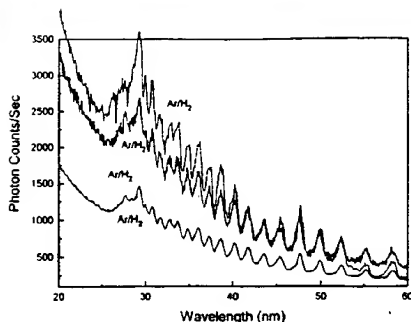Fig. 9. The three matching EUV spectra (20–60 nm) of the microwave cell emission from argon–hydrogen ($\frac{90}{10\%}$) plasmas that were equivalent to the spectrum shown in Fig. 7.

Fig. 11. The three repeatable EUV spectra (20–60 nm) of the microwave cell emission from argon–hydrogen ($\frac{90}{10\%}$) plasmas shown in Fig. 8 wherein the vibrational emission dominated the electronic emission. A fourth repeat spectrum shows other peaks that were assigned to Ar I and Ar II as shown in Fig. 5.
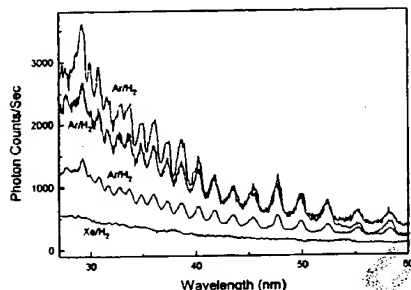

Fig. 10. The three repeatable EUV spectra (27–60 nm) of the microwave cell emission from argon–hydrogen ($\frac{90}{10\%}$) plasmas shown in Fig. 8 with an additional control xenon–hydrogen microwave discharge cell emission that was recorded with a 4° grazing incidence EUV spectrometer and a CEM. No emission was observed in this region from the control.

transitions of $H_2^*[n = \frac{1}{4}; n' = 2]^+$ with energies $v1.185$ eV that terminated at about 28.9 nm. There is remarkable agreement between the predicted vibrational energies and the observed lines. The unique continuum peak at about 28 nm was the most intense and terminated the series of peaks at the predicted dissociation energy of $H_2[n = \frac{1}{4}]^+$. Thus, this peak was assigned to the dissociation energy of $H_2[n = \frac{1}{4}]^+$. The zero order was extremely intense which corresponded to the observed high intensity of the plasma.

The spectrum of the argon–hydrogen plasma given in Figs. 7 and 8 was found to be very readily reproducible as shown in Figs. 9–11. Fig. 10 shows the region of inter-
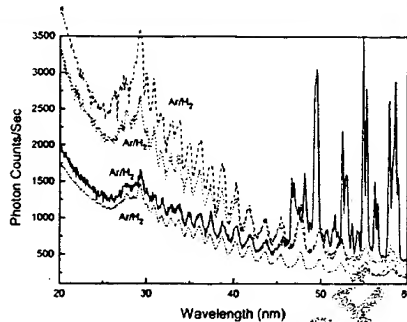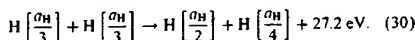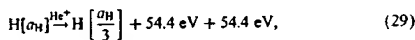
est (27–60 nm) of the EUV spectra of the argon–hydrogen plasmas compared to an additional control xenon–hydrogen microwave discharge cell emission. The series of 1.185 eV peaks were not observed from this control or the others shown in Figs. 2–9. Each argon–hydrogen plasmas experiment was performed independently on separate days, and the spectra were essentially identical. The zero order was extremely intense which corresponded to the observed high intensity of the plasma. Often the $H_2^*[n = \frac{1}{4}; n^* = 2]^+$ vibrational emission was so intense that it dominated or absorbed the electronic emission as shown in Fig. 9 compared to Fig. 11. Other peaks in the latter case were assigned to Ar I and Ar II as shown in Fig. 5.

The second ionization energy of helium is 54.4 eV; thus, the ionization reaction of He^+ to He^{2+} has a net enthalpy of reaction of 54.4 eV which is equivalent to 2.272 eV. It was previously reported that EUV spectroscopy was recorded on microwave and glow discharges of helium with 2% hydrogen at 1–760 Torr at a flow rate of 5 sccm wherein helium and the product hydrinos served as catalysts [7]. Novel emission lines were observed with energies of $q13.6$ eV where $q = 1, 2, 3, 4, 6, 7, 8, 9$, or 11 or these lines inelastically scattered by helium atoms wherein 21.2 eV was absorbed in the excitation of He ($1s^2$) to He ($1s^12p^1$). H($\frac{1}{3}$), the product with He^+ catalyst, may further serve as a catalyst to form H($\frac{1}{4}$) and H($\frac{1}{2}$). The catalysis reaction with He^+ and a favored disproportionation reaction which gives rise to H($\frac{1}{2}$) are:

$$H[a_H] \xrightarrow{He^+} H\left[\frac{a_H}{3}\right] + 54.4 \text{ eV} + 54.4 \text{ eV},\qquad(29)$$

$$H\left[\frac{a_H}{3}\right] + H\left[\frac{a_H}{3}\right] \rightarrow H\left[\frac{a_H}{2}\right] + H\left[\frac{a_H}{4}\right] + 27.2 \text{ eV}.\quad(30)$$

12   *R.L. Mills, P. Ray / International Journal of Hydrogen Energy III (IIII) III-III*

Fig. 12. The EUV spectrum (25–62 nm) of the helium–hydrogen ($\frac{90}{10}$%) microwave cell emission recorded with 0.1 nm increment of the McPherson 4° grazing incidence EUV spectrometer. A series of 0.5 eV wide Gaussian-shaped peaks were observed in the spectral region 27–55 nm that were assigned to the $v = 19, 21$–33, 35–38 vibrational transitions of $H_2^*[n = \frac{1}{4}; n^* = 2]^+$ with energies $v1.185$ eV as given in Table 1. The intense continuum peak at 28 nm that terminated the series was assigned to the dissociation energy of $H_2[n = \frac{1}{4}]^+$. Other peaks in the helium–hydrogen plasma that covered some of the vibrational peaks shown in Fig. 7 were assigned to He I and He II as shown in Fig. 6.
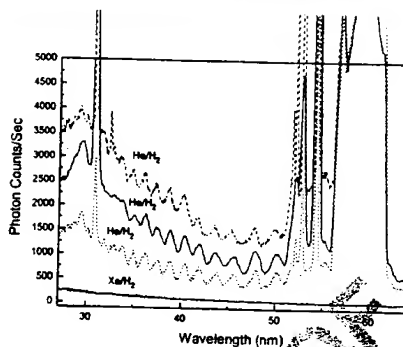

Fig. 13. Three repeatable EUV spectra (27–64 nm) of the microwave cell emission from helium–hydrogen ($\frac{90}{10}$%) plasmas that were equivalent to the spectrum shown in Fig. 12 with an additional control xenon–hydrogen microwave discharge cell emission that was recorded with a 4° grazing incidence EUV spectrometer and a CEM. No emission was observed in this region from the control.

1   The latter reaction was confirmed by the intense peak observed at 45.6 nm corresponding to $q13.6$ eV where $q = 2$.
3   As in the case of the Ar^+ catalyst, $H(\frac{1}{2})$ may react with a proton to form $H_2^*[n = \frac{1}{4}; n^* = 2]^+$.
5   The series of vibrational peaks from the argon–hydrogen plasmas shown in Figs. 7–11 were also observed with the
7   helium ion catalyst. The EUV spectrum (25–62 nm) of the helium–hydrogen ($\frac{90}{10}$%) microwave cell emission with
9   wavelengths assignments is shown in Fig. 12. The EUV spectra (27–64 nm) of the microwave cell emission from
11   three helium–hydrogen ($\frac{90}{10}$%) plasmas with an additional control xenon–hydrogen microwave discharge cell emis-
13   sion are shown in Fig. 13. Each helium–hydrogen experiment was performed independently on separate days. In
15   each case, the series of 0.5 eV wide Gaussian shaped peaks were observed in the spectral region 27–55 nm that were
17   assigned to the $v = 19, 21$–$33, 35$–38 vibrational transitions of $H_2^*[n = \frac{1}{4}; n^* = 2]^+$ with energies $v1.185$ eV as given in
19   Table 1. The intense continuum peak at about 28 nm that terminated the series was assigned to the dissociation en-
21   ergy of $H_2[n = \frac{1}{4}]^+$. The series of 1.185 eV peaks were not observed from the xenon–hydrogen control shown in Fig.
23   13 or the other controls shown in Figs. 2–4, and 6. Hydrogen has no emission in this region as shown in Fig. 4. Other
25   peaks in the helium–hydrogen plasma that covered some of the vibrational peaks shown in Fig. 7 were assigned to
27   known intense He I and He II peaks as shown in Fig. 6. In

each case, the zero order was extremely intense which corresponded to the observed high intensity of the plasma.   29

Excited state dihydrino molecular ions other than $H_2^*[n = \frac{1}{2}; n^* = 2]^+$ are predicted to emit outside the measured spectral region at shorter wavelengths, and additional vibrational transitions of $H_2^*[n = \frac{1}{4}; n^* = 2]^+$ are predicted at longer wavelengths as given in Table 1.   31   33

3.2. Identification of dihydrino molecules by the assignment of infrared line emissions from the Sun to rotational transitions   35   37

The rotational transition energies of lower-energy molecular hydrogen match closely certain spectral lines obtained by Livingston and Wallace [33] using the 1-m Fourier Transform Spectrometer at the McMath telescope on Kitt peak for which no other satisfactory assignment exists. Livingston and Wallace combined infrared solar spectra at different air masses to obtain a solar spectrum in the infrared from 1850 to 9000 cm^{-1} (1.1–5.4 µm) corrected for atmospheric absorption by a point-by-point extrapolation to zero air mass. The spectra were obtained at disk center. The observed region was free of sunspots, and a 1-m out-of-focus image (∼ 40 arc-sec diameter area) assured that any surface velocity and brightness structure was averaged over. The spectra band width was set at long wavelengths (∼ 5.4 µm) by the response of the InSb detectors and at the short wavelength end (∼ 1.1 µm) by a silicon filter. The infrared lines corrected for atmospheric absorption that match the rotational transitions of lower-energy molecular hydrogen are given in Table 2. Similar observations of spectral lines obtained   39   41   43   45   47   49   51   53   55

Table 2
The $J + 1$ to J rotational energy of Solar dihydrino molecules

Observed line wave number (cm^{-1})	Predicted Mills (cm^{-1}) Eq. (27)	p Eq. (B.2)	Assignment Mills Transition $J + 1$ to J Eq. (27)	Ref.	Assignment (other)
1898.2	1898.1	2	4–3	[33]	CO, $\Delta v = 1$ peak
1897.9	1898.1	2	4–3	[34]	None
1894.4					
1898.1	1898.1	2	4–3	[35]	Solar in origin CO
2846.8	2847.1	2	6–5	[33]	None
2847.7	2847.1	2	6–5	[34]	None
2847.1	2847.1	2	6–5	[35]	CH_4 (telluric)
3322	3321.6	2	7–6	[33]	None
3320.4	3321.6	2	7–6	[34]	None
3322					
3321.6	3321.6	2	7–6	[35]	Solar in origin Not identified
4270.8	4270.7	2	9–8	[33]	CO, $\Delta v = 2$ peak
4270.7	4270.7	2	9–8	[34]	None
4745.3	4745.2	2	10–9	[34]	None
1067.7	1067.7	3	1–0	[35]	O_3 (telluric)
2135.3	2135.3	3	2–1	[33]	CO, $\Delta v = 1$ peak
2135.5	2135.3	3	2–1	[34]	None
2135.3	2135.3	3	2–1	[35]	CO (telluric)
3203.1	3203.0	3	3–2	[34]	None
3203.0	3203.0	3	3–2	[35]	Not identified
4270.8	4270.7	3	4–3	[33]	CO, $\Delta v = 2$ peak
4270.7	4270.7	3	4–3	[34]	None
6406.18	6406.0	3	6–5	[33]	Ni, 6406.18
6406.2	6406.0	3	6–5	[34]	None
7473.7	7473.7	3	7–6	[34]	None
8540.9	8541.4	3	8–7	[34]	None
8542.3					
1898.2	1898.1	4	1–0	[33]	CO, $\Delta v = 1$ peak
1897.8	1898.1	4	1–0	[34]	None
1898.4					
5693.8	5694.2	4	3–2	[33]	None
5693.7	5694.2	4	3–2	[34]	None
5694.4					
7592.2	7592.3	4	4–3	[33]	None
7592.6	7592.3	4	4–3	[34]	None
9490.5	9490.4	4	5–4	[34]	None
2967.12	2965.8	5	1–0	[33]	None
2965.7	2965.8	5	1–0	[34]	None
2966					
2965.8	2965.8	5	1–0	[35]	$H_2O, 2v_2$ (telluric)
5931.3	5931.5	5	2–1	[33]	None
5931.5	5931.5	5	2–1	[34]	None
8896.7	8897.3	5	3–2	[33]	None
8897.3	8897.3	5	3–2	[34]	None
4270.8	4270.7	6	1–0	[33]	CO, $\Delta v = 2$ peak
4270.7	4270.7	6	1–0	[34]	None
8540.9	8541.4	6	2–1	[34]	None
8542.3					
5812.26	5812.9	7	1–0	[33]	Fe at 5812.26
5814.2					None

Table 2
Continued

Observed line wave number (cm^{-1})	Predicted Mills (cm^{-1}) Eq. (27)	p Eq. (B.2)	Assignment Mills Transition $J + 1$ to J Eq. (27)	Ref.	Assignment (other)
5812.7	5812.9	7	1–0	[34]	None
7592.2	7592.3	8	1–0	[33]	None
7592.6	7592.3	8	1–0	[34]	None
60,124	60,142	13	3–2	[36]	Fe(II)
69,783	69,750	14	3–2	[36]	None
53,362	53,381	15	2–1	[36]	Active region unidentified
80,038	80,071	15	3–2	[36]	None
60,710	60,735	16	2–1	[36]	Active region unidentified
68,582	68,564	17	2–1	[36]	S(I)
76,869	76,868	18	2–1	[36]	None

by Brault et al. at Kitt Peak National Observatory [34], M. Migeotte made at Jungfraujoch International Scientific Station of Switzerland [35], and Cohen [36] recorded on Skylab with the NRL's Apollo Telescope also appear in Table 2. The frequency corresponding to the $J + 1$ to J rotational transition of the dihydrino molecule (Eq. (B.251) where p is an integer which corresponds to $n = 1/p$, the fractional quantum number of the hydrogen-type molecule) are given in Table 2. The assignment of additional lines to rotational transitions of lower-energy hydrogen molecules was limited by the range of the spectrum, the weakness of the spectrum in certain regions, and strong atmospheric components in some regions. The intensity of these forbidden lines supports the possibility of a substantial abundance of dihydrino molecules in the Sun.

4. Conclusion

Transitions to fractional quantum energy levels were previously recorded on microwave and glow discharges of helium with 2% hydrogen. Novel emission lines were observed with energies of $q13.6$ eV where $q = 1, 2, 3, 4, 6, 7, 8, 9,$ or 11 or these lines inelastically scattered by helium atoms wherein 21.2 eV was absorbed in the excitation of He ($1s^2$) to He ($1s^1 2p^1$) [7]. EUV lines that could be assigned to transitions of atomic hydrogen to lower energy levels corresponding to fractional principal quantum numbers were also previously recorded at the Institut für Niedertemperatur Plasmaphysik e.V. [15]. Novel hydride compounds were previously reported as final stable products of the catalysis reaction with alkaline or alkaline earth metals or halides as reactants [19–25]. We report that a novel molecular ion corresponding to the diatomic hydrino, dihydrino molecular ion, was observed when noble gas ions Ar^+ or He^+ served as catalysts. Ar^+ may serve as a catalyst to form $H(\frac{1}{2})$. The products of the He^+ catalysis reaction $H(\frac{1}{3})$ may further serve as catalysts to form

$H(\frac{1}{4})$ and $H(\frac{1}{2})$. $H(1/p)$ may react with a proton to form an excited state molecular ion $H_2^+(1/p)$ that has a bond energy and vibrational levels that are p^2 times those of the molecular ion comprising uncatalyzed atomic hydrogen where p is an integer. Thus, the excited state spectrum of $H_2^+[n = \frac{1}{4}; n^* = 2]^+$ was predicted to comprise rotationally broadened vibrational transitions at 1.185 eV increments that terminated at about the dissociation limit of $H_2[n = \frac{1}{4}]^+$, $E_D = 42.88$ eV(28.92 nm). EUV spectroscopy was recorded on microwave discharges of argon or helium with 10% hydrogen in the region 10–65 nm. Novel emission lines in this region were assigned to the $v = 17$–38 vibrational transitions of $H_2^+[n = \frac{1}{4}; n^* = 2]^+$ with energies $v1.185$ eV that terminated at about 28.9 nm. Furthermore, astrophysical data was reviewed, and fractional molecular hydrogen rotational transitions were assigned to previously unidentified lines in the Solar coronal spectrum that matched theoretical predictions to five figures. Fractional hydrogen transitions were previously assigned to lines in the Solar EUV spectrum which may resolve the solar neutrino problem, the mystery of the cause of sunspots and other solar activity, and why the Sun emits X-rays [7]. In addition to producing power on the Sun, the catalysis of hydrogen represents a new powerful energy source with the potential for direct conversion of plasma to electricity with the production of novel compounds [26,27]. Helium or argon as the source of catalyst with the formation of stable hydrogen-type molecules offers the possibility of room temperature operation with a gaseous product which may be ventable.

Appendix A. Introduction[1]

A theory of classical quantum mechanics (CQM), derived from first principles, successfully applies physical laws on all scales [1]. The classical wave equation is solved with the constraint that a bound electron cannot radiate energy. The mathematical formulation for zero radiation based on Maxwell's equations follows from a derivation by Haus [37]. The function that describes the motion of the electron must not possess spacetime Fourier components that are synchronous with waves traveling at the speed of light. CQM gives closed form solutions for the atom including the stability of the $n = 1$ state and the instability of the excited states, the equation of the photon and electron in excited states, the equation of the free electron, and photon which predict the wave particle duality behavior of particles and light. The current and charge density functions of the electron may be directly physically interpreted. For example, spin angular momentum results from the motion of negatively charged mass moving systematically, and the equation for angular momentum, $\mathbf{r} \times \mathbf{p}$, can be applied directly to the wave function (a current density function) that describes the electron. The magnetic moment of a Bohr magneton, Stern Gerlach experiment, g factor, Lamb shift, resonant line width and shape, selection rules, correspondence principle, excited states, reduced mass, rotational energies, and momenta, orbital and spin splitting, spin–orbital coupling, Knight shift, and spin–nuclear coupling, ionization of two electron atoms, inelastic electron scattering from helium atoms, and the nature of the chemical bond are derived in closed form equations based on Maxwell's equations. The calculations agree with experimental observations.

A.1. Classical quantum theory

One-electron atoms include the hydrogen atom, He$^+$, Li^{2+}, Be^{3+}, and so on. The mass-energy and angular momentum of the electron are constant; this requires that the equation of motion of the electron be temporally and spatially harmonic. Thus, the classical wave equation applies and

$$\left[\nabla^2 - \frac{1}{v^2}\frac{\delta^2}{\delta t^2}\right]\rho(r,\theta,\phi,t) = 0, \qquad \text{(A.i)}$$

where $\rho(r,\theta,\phi,t)$ is the charge density function of the electron in time and space. In general, the wave equation has an infinite number of solutions. To arrive at the solution which represents the electron, a suitable boundary condition must be imposed. It is well known from experiments that each single atomic electron of a given isotope radiates to the same stable state. Thus, Mills chose the physical boundary condition of nonradiation of the bound electron to be

imposed on the solution of the wave equation for the charge density function of the electron. The condition for radiation by a moving point charge given by Haus [37] is that its spacetime Fourier transform does possess components that are synchronous with waves traveling at the speed of light. Conversely, it is proposed that the condition for nonradiation by an ensemble of moving point charges that comprises a charge density function is

> *For non-radiative states, the current-density function*
> *must NOT possess spacetime Fourier components that*
> *are synchronous with waves traveling at the speed of*
> *light.*

The Haus derivation applies to a moving charge-density function as well because charge obeys superposition.

From the application of the nonradiative boundary condition, the instability of excited states as well as the stability of the "ground" state arise naturally in the Mills theory as derived in Stability of Atoms and Hydrinos Section [1]. In addition to the above known states of hydrogen (Eq. (1)), the theory predicts the existence of a previously unknown form of matter: hydrogen atoms and molecules having electrons of lower energy than the conventional "ground" state, called *hydrinos* and *dihydrinos*, respectively, where each energy level corresponds to a fractional quantum number.

The central field of the proton corresponds to integer one charge. Excited states comprise an electron with a trapped photon. In all energy states of hydrogen, the photon has an electric field which superposes with the field of the proton. In the $n = 1$ state, the sum is one, and the sum is zero in the ionized state. In an excited state, the sum is a fraction of one (i.e. between zero and one). Derivations from first principles given by Mills demonstrate that each "allowed" fraction corresponding to an excited state is 1/integer. The relationship between the electric field equation and the "trapped photon" source charge-density function is given by Maxwell's equation in two dimensions

$$\mathbf{n} \bullet (\mathbf{E}_1 - \mathbf{E}_2) = \frac{\sigma}{\epsilon_0}, \qquad \text{(A.ii)}$$

where $\mathbf{n}$ is the radial normal unit vector, $\mathbf{E}_1 = 0$ ($\mathbf{E}_1$ is the electric field outside of the electron), $\mathbf{E}_2$ is given by the total electric field at $r_n = na_H$, and σ is the surface charge-density. The electric field of an excited state is fractional; therefore, the source charge function is fractional. It is well known that fractional charge is not "allowed". The reason is that fractional charge typically corresponds to a radiative current density function. The excited states of the hydrogen atom are examples. They are radiative; consequently, they are not stable. Thus, an excited electron decays to the first nonradiative state corresponding to an integer field, $n = 1$ (i.e. a field of integer one times the central field of the proton).

Equally valid from first principles are electronic states where the magnitude of the sum of the electric field of the photon and the proton central field are an integer greater than one times the central field of the proton. These states are nonradiative. A catalyst can effect a transition between

these states via a nonradiative energy transfer. Substantial experimental evidence exists that supports the existence of this novel hydrogen chemistry and its applications [7–27]. Laboratory experiments that confirm the novel hydrogen chemistry include EUV spectroscopy [7–18], characteristic emission from catalysis and the hydride ion products [8,9], lower-energy hydrogen emission [7–9], plasma formation [8,9,12–14,16–18], Balmer α line broadening [10], anomalous plasma afterglow duration [16,17], power generation [10,11,18], and analysis of chemical compounds [19–25].

Appendix B The nature of the chemical bond of hydrogen-type molecules and molecular ions

Two hydrogen atoms react to form a diatomic molecule, the hydrogen molecule

$$2H[a_H] \rightarrow H_2[2c' = \sqrt{2}a_0],\tag{B.1}$$

where $2c'$ is the internuclear distance. Also, two hydrino atoms react to form a diatomic molecule, a dihydrino molecule

$$2H\left[\frac{a_H}{p}\right] \rightarrow H_2\left[2c' = \frac{\sqrt{2}a_0}{p}\right],\tag{B.2}$$
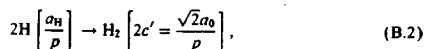
where p is an integer.

Hydrogen molecules form hydrogen molecular ions when they are singly ionized

$$H_2[2c' = \sqrt{2}a_0] \rightarrow H_2[2c' = 2a_0]^+ + e^-.\tag{B.3}$$

Also, dihydrino molecules form dihydrino molecular ions when they are singly ionized

$$H_2\left[2c' = \frac{\sqrt{2}a_0}{p}\right] \rightarrow H_2\left[2c' = \frac{2a_0}{p}\right]^+ + e^-.\tag{B.4}$$
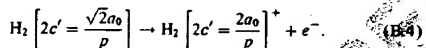
B.1. Hydrogen-type molecular ions

Each hydrogen-type molecular ion comprises two protons and an electron where the equation of motion of the electron is determined by the central field which is p times that of a proton at each focus (p is one for the hydrogen molecular ion, and p is an integer greater than one for each dihydrino molecular ion). The differential equations of motion in the case of a central field are

$$m(\ddot{r} - r\dot{\theta}^2) = f(r),\tag{B.5}$$

$$m(2\dot{r}\dot{\theta} + r\ddot{\theta}) = 0.\tag{B.6}$$

The second or transverse equation, Eq. (A.6), gives the result that the angular momentum is constant

$$r^2\dot{\theta} = \text{constant} = L/m.\tag{B.7}$$

where L is the angular momentum ($\hbar$ in the case of the electron). The central force equations can be transformed into an orbital equation by the substitution, $u = 1/r$. The differential equation of the orbit of a particle moving under a central force is

$$\frac{\delta^2 u}{\delta\theta^2} + u = \frac{-1}{mL^2u^2/m^2}f(u^{-1}).\tag{B.8}$$

Because the angular momentum is constant, motion in only one plane need be considered; thus, the orbital equation is given in polar coordinates. The solution of Eq. (B.8) for an inverse-squared force

$$f(r) = -\frac{k}{r^2}\tag{B.9}$$

is

$$r = r_0\frac{1+e}{1+e\cos\theta},\tag{B.10}$$

$$e = A\frac{mL^2/m^2}{k},\tag{B.11}$$

$$r_0 = \frac{mL^2/m^2}{k(1+e)},\tag{B.12}$$

where e is the eccentricity of the ellipse and A is a constant. The equation of motion due to a central force can also be expressed in terms of the energies of the orbit. The square of the speed in polar coordinates is

$$v^2 = (\dot{r}^2 + r^2\dot{\theta}^2).\tag{B.13}$$

Since a central force is conservative, the total energy, E, is equal to the sum of the kinetic, T, and the potential, V, and is constant. The total energy is

$$\frac{1}{2}m(\dot{r}^2 + r^2\dot{\theta}^2) + V(r) = E = \text{constant}.\tag{B.14}$$

Substitution of the variable $u = 1/r$ and Eq. (B.7) into Eq. (B.14) gives the orbital energy equation

$$\frac{1}{2}mL^2/m^2\left[\left(\frac{\delta^2 u}{\delta\theta^2}\right) + u^2\right] + V(u^{-1}) = E.\tag{B.15}$$

Because the potential energy function $V(r)$ for an inverse-squared force field is

$$V(r) = -\frac{k}{r} = -ku\tag{B.16}$$

the energy equation of the orbit, Eq. (B.15),

$$\frac{1}{2}mL^2/m^2\left[\left(\frac{\delta^2 u}{\delta\theta^2}\right) + u^2\right] - ku = E,\tag{B.17}$$

which has the solution

$$r = \frac{m(L^2/m^2)k^{-1}}{1 + [1 + 2Em(L^2/m^2)k^{-2}]^{1/2}\cos\theta}.\tag{B.18}$$

where the eccentricity, e, is

$$e = \left[1 + 2Em\frac{L^2}{m^2}k^{-2}\right]^{1/2}. \qquad (B.19)$$

Eq. (B.19) permits the classification of the orbits according to the total energy, E, as follows:

$E < 0$, $\quad e < 1$ $\quad$ closed orbits (ellipse or circle),

$E = 0$, $\quad e = 1$ $\quad$ parabolic orbit,

$E > 0$, $\quad e > 1$ $\quad$ hyperbolic orbit.

Since $E = T + V$ and is constant, the closed orbits are those for which $T < |V|$, and the open orbits are those for which $T \geqslant |V|$. It can be shown that the time average of the kinetic energy, $\langle T \rangle$, for elliptic motion in an inverse-squared field is $\frac{1}{2}$ that of the time average of the potential energy, $\langle V \rangle$.
$\langle T \rangle = \frac{1}{2}\langle V \rangle$.

As demonstrated in the One Electron Atom section of Mills [1], the electric inverse-squared force is conservative; thus, the angular momentum of the electron, $\hbar$, and the energy of atomic orbitspheres (orbitsphere refers to the function which represents the bound electron) is constant. In addition, the orbitspheres are nonradiative when the boundary condition is met.

The central force equation, Eq. (B.14), has orbital solutions which are circular, elliptic, parabolic, or hyperbolic. The former two types of solutions are associated with atomic and molecular orbitals. These solutions are nonradiative. The boundary condition for nonradiation given in the One Electron Atom section, is the absence of components of the space-time Fourier transform of the charge-density function synchronous with waves traveling at the speed of light. The boundary condition is met when the velocity for every point on the orbitsphere is

$$v_n = \frac{\hbar}{m_e r_n}. \qquad (B.20)$$

The allowed velocities and angular frequencies are related to r_n by

$$v_n = r_n \omega_n, \qquad (B.21)$$

$$\omega_n = \frac{\hbar}{m_e r_n^2}. \qquad (B.22)$$

As demonstrated in the One Electron Atom section and by Eq. (B.22), this condition is met for the product function of a radial Dirac delta function and a time harmonic function where the angular frequency, ω, is constant and given by Eq. (B.22).

$$\omega_n = \frac{\hbar}{m_e r_n^2} = \frac{\pi L/m_e}{A}, \qquad (B.23)$$

where L is the angular momentum and A is the area of the closed geodesic orbit. Consider the solution of the central force equation comprising the product of a two-dimensional ellipsoid and a time harmonic function. The spatial part of the product function is the convolution of a radial Dirac delta function with the equation of an ellipsoid. The Fourier transform of the convolution of two functions is the product of the individual Fourier transforms of the functions; thus, the boundary condition is met for an ellipsoidal-time harmonic function when

$$\omega_n = \frac{\pi\hbar}{m_e A} \simeq \frac{\hbar}{m_e ab}, \qquad (B.24)$$

where the area of an ellipse is

$$A = \pi ab, \qquad (B.25)$$

where $2b$ is the length of the semiminor axis and $2a$ is the length of the semimajor axis. The geometry of molecular hydrogen is elliptic with the internuclear axis as the principal axis; thus, the electron orbital is a two-dimensional ellipsoidal-time harmonic function. The mass follows geodesics time harmonically as determined by the central field of the protons at the foci. Rotational symmetry about the internuclear axis further determines that the orbital is a prolate spheroid. In general, ellipsoidal orbits of molecular bonding, hereafter referred to as ellipsoidal molecular orbitals (MOs), have the general equation

$$\frac{x^2}{a^2} + \frac{y^2}{b^2} + \frac{z^2}{c^2} = 1. \qquad (B.26)$$

The semiprincipal axes of the ellipsoid are a, b, c.

In ellipsoidal coordinates the Laplacian is

$$(\eta - \xi)R_\zeta\frac{\partial}{\partial\xi}\left(R_\xi\frac{\partial\phi}{\partial\xi}\right) + (\zeta - \xi)R_\eta\frac{\partial}{\partial\eta}\left(R_\eta\frac{\partial\phi}{\partial\eta}\right)$$

$$+ (\xi - \eta)R_\zeta\frac{\partial}{\partial\zeta}\left(R_\zeta\frac{\partial\phi}{\partial\zeta}\right) = 0. \qquad (B.27)$$

An ellipsoidal MO is equivalent to a charged conductor whose surface is given by Eq. (B.26). It carries a total charge q, and its potential is a solution of the Laplacian in ellipsoidal coordinates, Eq. (B.27).

Excited states of orbitspheres are discussed in the Excited States of the One Electron Atom (Quantization) section. In the case of ellipsoidal MOs, excited electronic states are created when photons of discrete frequencies are trapped in the ellipsoidal resonator cavity of the MO. The photon changes the effective charge at the MO surface where the central field is ellipsoidal and arises from the protons and the effective charge of the "trapped photon" at the foci of the MO. Force balance is achieved at a series of ellipsoidal equipotential two-dimensional surfaces confocal with the ground state ellipsoid. The "trapped photons" are solutions of the Laplacian in ellipsoidal coordinates, Eq. (B.27).

As is the case with the orbitsphere, higher and lower energy states are equally valid. The photon standing wave in both cases is a solution of the Laplacian in ellipsoidal coordinates. For an ellipsoidal resonator cavity, the relationship between an allowed circumference, $4aE$, and the photon standing wavelength, λ, is

$$4aE = n\lambda, \qquad (B.28)$$

where n is an integer and where

$$k = \frac{\sqrt{a^2 - b^2}}{a} \qquad \text{(B.29)}$$

is used in the elliptic integral E of Eq. (B.28). Applying Eqs. (B.28) and (B.29), the relationship between an allowed angular frequency given by Eq. (B.24) and the photon standing wave angular frequency, ω, is

$$\frac{\pi\hbar}{m_e A} = \frac{\hbar}{m_e n a_1 n b_1} = \frac{\hbar}{m_e a_n b_n} = \frac{1}{n^2}\omega_1 = \omega_n, \qquad \text{(B.30)}$$

where $n = 1, 2, 3, 4, \ldots$

$$n = \tfrac{1}{2}, \tfrac{1}{3}, \tfrac{1}{4}, \ldots,$$

ω_1 is the allowed angular frequency for $n = 1$, a_1 and b_1 are the allowed semimajor and semiminor axes for $n = 1$.

Let us compute the potential of an ellipsoidal MO which is equivalent to a charged conductor whose surface is given by Eq. (B.26). It carries a total charge q, and we assume initially that there is no external field. We wish to know the potential, ϕ, and the distribution of charge, σ, over the conducting surface. To solve this problem a potential function must be found which satisfies Eq. (B.27), which is regular at infinity, and which is constant over the given ellipsoid. Now ξ is the parameter of a family of ellipsoids all confocal with the standard surface $\xi = 0$ whose axes have the specified values a, b, c. The variables ζ and η are the parameters of confocal hyperboloids and as such serve to measure position on any ellipsoid $\xi = \text{constant}$. On the surface $\xi = 0$; therefore, ϕ must be independent of ζ and η. If we can find a function depending only on ξ which satisfies Eq. (B.27) and behaves properly at infinity, it can be adjusted to represent the potential correctly at any point outside the ellipsoid $\xi = 0$.

Let us assume, then, that $\phi = \phi(\xi)$. The Laplacian reduces to

$$\frac{\delta}{\delta\xi}\left(R_\xi \frac{\partial\phi}{\partial\xi}\right) = 0, \quad R_\xi = \sqrt{(\xi + a^2)(\xi + b^2)(\xi + c^2)} \qquad \text{(B.31)}$$

which on integration leads to

$$\phi(\xi) = C_1 \int_\xi^\infty \frac{\delta\xi}{R_\xi}, \qquad \text{(B.32)}$$

where C_1 is an arbitrary constant. The choice of the upper limit is such as to ensure the proper behavior at infinity. When ξ becomes very large, R_ξ approaches $\xi^{3/2}$ and

$$\phi \sim \frac{2C_1}{\sqrt{\xi}} \quad (\xi \to \infty). \qquad \text{(B.33)}$$

On the other hand, the equation of an ellipsoid can be written in the form

$$\frac{x^2}{1 + a^2/\xi} + \frac{y^2}{1 + b^2/\xi} + \frac{z^2}{1 + c^2/\xi} = \xi. \qquad \text{(B.34)}$$

If $r^2 = x^2 + y^2 + z^2$ is the distance from the origin to any point on the ellipsoid ξ, it is apparent that as ξ becomes very

large $\xi \to r^2$ and hence at great distances from the origin

$$\phi \sim \frac{2C_1}{r}. \qquad \text{(B.35)}$$

The solution Eq. (B.32) is, therefore, regular at infinity. Moreover, Eq. (B.35) enables us to determine at once the value of C_1; for it has been shown that whatever the distribution, the dominant term of the expansion at remote points is the potential of a point charge at the origin equal to the total charge of the distribution — in this case q. Hence $C_1 = q/8\pi\varepsilon_0$, and the potential at any point is

$$\phi(\xi) = \frac{q}{8\pi\varepsilon_0}\int_\xi^\infty \frac{\partial\xi}{R_\xi}. \qquad \text{(B.36)}$$

The equipotential surfaces are the ellipsoids $\xi = \text{constant}$. Eq. (B.36) is a elliptic integral and its values have been tabulated [38].

To obtain the normal derivative we must remember that distance along a curvilinear coordinate u^1 is measured not by du^1 but by $h_1 du^1$. In ellipsoidal coordinates

$$h_1 = \frac{1}{2}\frac{\sqrt{(\xi - \eta)(\xi - \zeta)}}{R_\xi}, \qquad \text{(B.37)}$$

$$\frac{\delta\phi}{\delta n} = \frac{1}{h_1}\frac{\delta\phi}{\delta\xi} = \frac{-q}{4\pi\varepsilon_0}\frac{1}{\sqrt{(\xi - \eta)(\xi - \zeta)}}. \qquad \text{(B.38)}$$

The density of charge, σ, over the surface $\xi = 0$ is

$$\sigma = \varepsilon_0 \left(\frac{\delta\phi}{\delta n}\right)_{\xi=0} = \frac{q}{4\pi\sqrt{\eta\zeta}}. \qquad \text{(B.39)}$$

Defining x, y, z in terms of ξ, η, ζ we put $\xi = 0$, it may be easily verified that

$$\frac{x^2}{a^4} + \frac{y^2}{b^4} + \frac{z^2}{c^4} = \frac{\zeta\eta}{a^2 b^2 c^2} \quad (\xi = 0). \qquad \text{(B.40)}$$

Consequently, the charge-density in rectangular coordinates is

$$\sigma = \frac{q}{4\pi abc}\frac{1}{\sqrt{(x^2/a^4 + y^2/b^4 + z^2/c^4)}}. \qquad \text{(B.41)}$$

(The mass density function of an MO is equivalent to its charge-density function where m replaces q of Eq. (B.41)). The equation of the plane tangent to the ellipsoid at the point x_0, y_0, z_0 is

$$X\frac{x_0}{a^2} + Y\frac{y_0}{b^2} + Z\frac{z_0}{c^2} = 1, \qquad \text{(B.42)}$$

where X, Y, Z are running coordinates in the plane. After dividing through by the square root of the sum of the squares of the coefficients of X, Y, and Z, the right member is the distance D from the origin to the tangent plane. That is

$$D = \frac{1}{\sqrt{(x^2/a^4 + y^2/b^4 + z^2/c^4)}} \qquad \text{(B.43)}$$

so that

$$\sigma = \frac{q}{4\pi abc}D. \qquad \text{(B.44)}$$

In other words, the surface density at any point on a charged ellipsoidal conductor is proportional to the perpendicular distance from the center of the ellipsoid to the plane tangent to the ellipsoid at the point. The charge is thus greater on the more sharply rounded ends farther away from the origin.

In the case of hydrogen-type molecules and molecular ions, rotational symmetry about the internuclear axis requires that two of the axes be equal. Thus, the MO is a spheroid, and Eq. (B.36) can be integrated in terms of elementary functions. If $a > b = c$, the spheroid is prolate, and the potential is given by

$$\phi = \frac{1}{8\pi\varepsilon_0} \frac{q}{\sqrt{a^2 - b^2}} \ln \frac{\sqrt{\xi + a^2} + \sqrt{a^2 - b^2}}{\sqrt{\xi + a^2} - \sqrt{a^2 - b^2}}. \tag{B.45}$$

Spheroidal force equations electric force. The spheroidal MO is a two-dimensional surface of constant potential given by Eq. (B.45) for $\xi = 0$. For an isolated electron MO the electric field inside is zero as given by Gauss' Law

$$\int_S \mathbf{E} \, dA = \int_V \frac{\rho}{\varepsilon_0} \, dV, \tag{B.46}$$

where the charge-density, ρ, inside the MO is zero. Gauss' Law at a two-dimensional surface is

$$\mathbf{n} \cdot (\mathbf{E}_1 - \mathbf{E}_2) = \frac{\sigma}{\varepsilon_0} \tag{B.47}$$

$\mathbf{E}_2$ is the electric field inside which is zero. The electric field of an ellipsoidal MO is given by substituting σ given by Eq. (B.38) and Eq. (B.39) into Eq. (B.47)

$$\mathbf{E} = \frac{\sigma}{\varepsilon_0} = \frac{q}{4\pi\varepsilon_0} \frac{1}{\sqrt{(\xi - \eta)(\xi - \zeta)}}. \tag{B.48}$$

The electric field in spheroid coordinates is

$$\mathbf{E} = \frac{q}{8\pi\varepsilon_0} \frac{1}{\sqrt{\xi + a^2}} \frac{1}{\sqrt{\xi + b^2}} \frac{1}{c} \sqrt{\frac{\xi^2 - 1}{\xi^2 - \eta^2}}. \tag{B.49}$$

From Eq. (B.30), the magnitude of the elliptic field corresponding to a below "ground state" hydrogen-type molecular ion is an integer. The integer is one in the case of hydrogen molecular ion and an integer greater than one in the case of each dihydrino molecular ion. The central electric force from the two protons, $\mathbf{F}_e$, is

$$\mathbf{F}_e = Ze\mathbf{E} = \frac{p2e^2}{8\pi\varepsilon_0} \frac{1}{\sqrt{\xi + a^2}} \frac{1}{\sqrt{\xi + b^2}} \frac{1}{c} \sqrt{\frac{\xi^2 - 1}{\xi^2 - \eta^2}}, \tag{B.50}$$

where p is one for the hydrogen molecular ion, and p is an integer greater than one for each dihydrino molecule and molecular ion.

Centripetal force. Each infinitesimal point mass of the electron MO moves along a geodesic orbit of a spheroidal MO in such a way that its eccentric angle, θ, changes at a constant rate. That is $\theta = \omega t$ at time t where ω is a constant, and

$$r(t) = \mathbf{i}a \cos \omega t + \mathbf{j}b \sin \omega t \tag{B.51}$$

is the parametric equation of the ellipse of the geodesic. If $a(t)$ denotes the acceleration vector, then

$$a(t) = -\omega^2 r(t). \tag{B.52}$$

In other words, the acceleration is centripetal as in the case of circular motion with constant angular speed ω. The centripetal force, $\mathbf{F}_c$, is

$$\mathbf{F}_c = ma = -m\omega^2 r(t). \tag{B.53}$$

Recall that nonradiation results when $\omega = $ constant given by Eq. (B.30). Substitution of ω given by Eq. (B.30) into Eq. (B.53) gives

$$\mathbf{F}_c = \frac{-\hbar^2}{m_e a^2 b^2} r(t) = \frac{-\hbar^2}{m_e a^2 b^2} D, \tag{B.54}$$

where D is the distance from the origin to the tangent plane as given by Eq. (B.43). If X is defined as follows:

$$X = \frac{1}{\sqrt{\xi + a^2}} \frac{1}{\sqrt{\xi + b^2}} \frac{1}{c} \sqrt{\frac{\xi^2 - 1}{\xi^2 - \eta^2}} \tag{B.55}$$

Then, it follows from Eqs. (B.38), (B.44), (B.48), and (B.50) that

$$D = 2ab^2 X. \tag{B.56}$$

B.1. Force balance of hydrogen-type molecular ions Force balance between the electric and centripetal forces is

$$\frac{\hbar^2}{m_e a^2 b^2} 2ab^2 X = \frac{pe^2}{4\pi\varepsilon_0} X, \tag{B.57}$$

which has the parametric solution given by Eq. (B.51) when

$$a = \frac{2a_0}{p}. \tag{B.58}$$

B.1.2. Energies of hydrogen-type molecular ions From Eq. (B.30), the magnitude of the elliptic field corresponding to a below "ground state" hydrogen-type molecule is an integer, p. The potential energy, V_e, of the electron MO in the field of magnitude p times that of the protons at the foci ($\xi = 0$) is

$$V_e = \frac{-4pe^2}{8\pi\varepsilon_0 \sqrt{a^2 - b^2}} \ln \frac{a + \sqrt{a^2 - b^2}}{a - \sqrt{a^2 - b^2}}, \tag{B.59}$$

where

$$\sqrt{a^2 - b^2} = c' \tag{B.60}$$

$2c'$ is the distance between the foci which is the internuclear distance. The kinetic energy, T, of the electron MO is given

by the integral of the left-hand side of Eq. (B.57)

$$T = \frac{2\hbar^2}{m_e a\sqrt{a^2 - b^2}} \ln \frac{a + \sqrt{a^2 - b^2}}{a - \sqrt{a^2 - b^2}}. \tag{B.61}$$

From the orbital equations in polar coordinates, Eqs. (B.10)–(12), the following relationship can be derived:

$$a = \frac{mL^2/m^2}{k(1 - e^2)}. \tag{B.62}$$

For any ellipse,

$$b = a\sqrt{1 - e^2}. \tag{B.63}$$

Thus,

$$b = a\sqrt{\frac{(L^2/m^2)m}{ka}} \quad \text{(polar coordinates)}. \tag{B.64}$$

Using Eqs. (B.54) and (B.61), and (B.16) and (B.61), respectively, it can be appreciated that b of polar coordinates corresponds to $c' = \sqrt{a^2 - b^2}$ of elliptic coordinates, and k of polar coordinates with one attracting focus is replaced by $2k$ of elliptic coordinates with two attracting foci. In elliptic coordinates, k is given by Eq. (B.48) and (B.50)

$$k = \frac{2pe^2}{4\pi\varepsilon_0} \tag{B.65}$$

and L for the electron equals $\hbar$; thus, in elliptic coordinates

$$c' = a\sqrt{\frac{\hbar^2 4\pi\varepsilon_0}{me^2 2pa}} = \sqrt{\frac{aa_0}{2p}}. \tag{B.66}$$

Substitution of a given by Eq. (B.58) into Eq. (B.66) is

$$c' = \frac{a_0}{p}. \tag{B.67}$$

The internuclear distance from Eq. (B.67) is $2c' = 2a_0/p$. One-half the length of the semiminor axis of the prolate spheroidal MO, $b = c$, is

$$b = \sqrt{a^2 - c'^2}. \tag{B.68}$$

Substitution of $a = 2a_0/p$ and $c' = a_0/p$ into Eq. (B.68) is

$$b = \frac{\sqrt{3}}{p} a_0. \tag{B.69}$$

The eccentricity, e, is

$$e = \frac{c'}{a}. \tag{B.70}$$

Substitution of $a = 2a_0/p$ and $c' = a_0/p$ into Eq. (B.70) is

$$e = \frac{1}{2}. \tag{B.71}$$

The potential energy, V_p, due to proton–proton repulsion in the field of magnitude p times that of the protons at the foci ($\xi = 0$) is

$$V_p = \frac{pe^2}{8\pi\varepsilon_0\sqrt{a^2 - b^2}}. \tag{B.72}$$

Substitution of a and b given by Eqs. (B.58) and (B.69), respectively, into Eqs. (B.59), (B.61), and (B.72) is

$$V_e = \frac{-4 p^2 e^2}{8\pi\varepsilon_0 a_0} \ln 3, \tag{B.73}$$

$$V_p = \frac{p^2 e^2}{8\pi\varepsilon_0 a_0}, \tag{B.74}$$

$$T = \frac{2 p^2 e^2}{8\pi\varepsilon_0 a_0} \ln 3, \tag{B.75}$$

$$E_T = V_e + V_p + T, \tag{B.76}$$

$$E_T = 13.6 \text{ eV}(-4 p^2 \ln 3 + p^2 + 2 p^2 \ln 3)$$

$$= - p^2 16.28 \text{ eV}. \tag{B.77}$$

The bond dissociation energy, E_D, is the difference between the total energy of the corresponding hydrogen atom or hydrino atom and E_T

$$E_D = E\left(H\left[\frac{a_H}{p}\right]\right) - E_T$$

$$= - p^2 13.6 + p^2 16.28 \text{ eV} = p^2 2.68 \text{ eV}. \tag{B.78}$$

B.1.3. Vibration of hydrogen-type molecular ions

An oscillating charge $r_0(t) = d \sin \omega_0 t$ has a Fourier spectrum

$$J(k, \omega) = \frac{q\omega_0 d}{2} J_m(k \cos\theta d)\{\delta[\omega - (m + 1)\omega_0]$$

$$+ \delta[\omega - (m - 1)\omega_0]\}, \tag{B.79}$$

where $J'_m s$ are Bessel functions of order m. These Fourier components can, and do, acquire phase velocities that are equal to the velocity of light [37]. The protons of hydrogen-type molecular ions and molecules oscillate as simple harmonic oscillators; thus, vibrating protons will radiate. Moreover, nonoscillating protons may be excited by one or more photons that are resonant with the oscillatory resonance frequency of the molecule or molecular ion, and oscillating protons may be further excited to higher energy vibrational states by resonant photons. The energy of a photon is quantized according to Planck's equation

$$E = \hbar\omega = h\frac{c}{\lambda}. \tag{B.80}$$

The energy of a vibrational transition corresponds to the energy difference between the initial and final vibrational states. Each state has an electromechanical resonance frequency, and the emitted or absorbed photon is resonant with the difference in frequencies. Thus, as a general principle, quantization of the vibrational spectrum is due to the quantized energies of photons and the electromechanical resonance of the vibrationally excited ion or molecule.

It can be shown that a perturbation of the orbit determined by an inverse-squared force results in simple harmonic

1 oscillatory motion of the orbit [39]. In a circular orbit in spherical coordinates, the transverse equation of motion
3 gives

$$\dot{\theta} = \frac{L/m}{r^2}, \quad (B.81)$$

where L is the angular momentum. The radial equation of
5 motion is

$$m(\ddot{r} - r\dot{\theta}^2) = f(r). \quad (B.82)$$

Substitution of Eq. (B.81) into Eq. (B.82) gives

$$m\ddot{r} - \frac{m(L/m)^2}{r^3} = f(r). \quad (B.83)$$

7 For a circular orbit, r is a constant and $\ddot{r} = 0$. Thus, the radial equation of motion is given by

$$-\frac{m(L/m)^2}{a^3} = f(a), \quad (B.84)$$

9 where a is the radius of the circular orbit for central force $f(a)$ at $r = a$. A perturbation of the radial motion may be
11 expressed in terms of a variable x defined by

$$x = r - a. \quad (B.85)$$

The differential equation can then be written as

$$m\ddot{x} - m(L/m)^2 (x + a)^{-3} = f(x + a). \quad (B.86)$$

13 Expanding the two terms involving $x + a$ as a power series in x, gives

$$m\ddot{x} - m(L/m)^2 a^{-3} \left(1 - 3\frac{x}{a} + \cdots\right)$$
$$= f(a) + f'(a)x + \cdots. \quad (B.87)$$

15 Substitution of Eq. (B.84) into Eq. (B.87) and neglecting terms involving x^2 and higher powers of x gives

$$m\ddot{x} + \left[\frac{-3}{a}f(a) - f'(a)\right]x = 0. \quad (B.88)$$

17 For an inverse-squared central field, the coefficient of x in Eq. (B.88) is positive, and the equation is the same as that
19 of the simple harmonic oscillator. In this case the particle, if perturbed, oscillates harmonically about the circle $r = a$, and
21 an approximation of the angular frequency of this oscillation is

$$\omega = \sqrt{\frac{[(-3/a)f(a) - f'(a)]}{m}} = \sqrt{\frac{k}{m}}. \quad (B.89)$$

23 An apsis is a point in an orbit at which the radius vector assumes an extreme value (maximum or minimum). The
25 angle swept out by the radius vector between two consecutive apsides is called the apsidal angle. Thus, the apsidal
27 angle is π for elliptic orbits under the inverse-squared law of force. In the case of a nearly circular orbit, Eq. (B.88)
29 shows that r oscillates about the circle $r = a$, and the period of oscillation is given by

$$\tau_r = 2\pi \sqrt{\frac{m}{-[(3/a)f(a) + f'(a)]}}. \quad (B.90)$$

The apsidal angle in this case is just the amount by which the polar angle θ increases during the time that r oscillates from
33 a minimum value to the succeeding maximum value which is τ_r. From Eq. (B.81), $\dot{\theta} = L/m/r^2$, therefore, θ remains
35 constant, and Eq. (B.84) gives

$$\dot{\theta} \approx \frac{L/m}{a^2} = \left[-\frac{f(a)}{ma}\right]^{1/2}. \quad (B.91)$$

37 Thus, the apsidal angle is given by

$$\psi = \frac{1}{2}\tau_r\dot{\theta} = \pi\left[3 + a\frac{f'(a)}{f(a)}\right]^{-1/2}. \quad (B.92)$$

Thus, the power force of $f(r) = -cr^n$ gives

$$\psi = \pi(3 + n)^{-1/2}. \quad (B.93)$$

39 The apsidal angle is independent of the size of the orbit in this case. The orbit is re-entrant, or repetitive, in the case of
41 the inverse-squared law ($n = -2$) for which $\psi = \pi$.

In the case of a hydrogen molecule or molecular ion, the
43 electrons which have a mass of $1/1836$ that of the protons move essentially instantaneously. Thus, a stable electron
45 orbit is maintained with oscillatory motion of the protons. Hydrogen molecules and molecular ions are symmetrical
47 along the semimajor axis; thus, the oscillatory motion of protons is along this axis. Let x be the displacement of the
49 protons along the semimajor axis from the position of the initial foci of the stationary state. The equation of proton
51 motion due to the perturbation of an orbit having a central inverse-squared central force [39] and neglecting terms in-
53 volving x^2 and higher is given by

$$\mu\ddot{x} + kx = 0 \quad (B.94)$$

which has the solution in terms of the maximum amplitude
55 of oscillation of the protons from the initial foci A, the reduced mass μ, the restoring constant or spring constant k,
57 the resonance frequency ω_0, and the vibrational energy E_{vib} [40]

$$A\cos\omega_0 t, \quad (B.95)$$

59 where

$$\omega_0 = \sqrt{\frac{k}{\mu}}. \quad (B.96)$$

For the two protons which undergo a symmetrical displace-
61 ment x from the foci, the potential energy corresponding to the oscillation E_{Pvib} is given by

$$E_{Pvib} = 2(\tfrac{1}{2}kx^2) = kx^2. \quad (B.97)$$

63 The total energy of the oscillating protons $E_{Totalvib}$ is given as the sum of the kinetic and potential energies

$$E_{Totalvib} = \tfrac{1}{2}\mu\dot{x}^2 + kx^2. \quad (B.98)$$

65 The velocity is zero when x is the maximum amplitude A. The total energy of the oscillating protons $E_{Totalvib}$ is then

given as the potential energy with $x = A$

$$E_{Totalvib} = kA^2. \tag{B.99}$$

Thus,

$$A = \sqrt{\frac{E_{Totalvib}}{k}}. \tag{B.100}$$

It is shown in the Excite States of the One Electron Atom (Quantization) section that the change in angular velocity of the electron orbitsphere, Eq. (2.21), is identical to the angular velocity of the photon necessary for the excitation, ω_{photon} (Eq. (2.19)). The energy of the photon necessary to excite the equivalent transition in an electron orbitsphere is one-half of the excitation energy of the stationary cavity because the change in kinetic energy of the electron orbitsphere supplies one-half of the necessary energy. The change in the angular frequency of the orbitsphere during a transition and the angular frequency of the photon corresponding to the superposition of the free space photon and the photon corresponding to the kinetic energy change of the orbitsphere during a transition are equivalent. The correspondence principle holds. It can be demonstrated that the resonance condition between these frequencies is to be satisfied in order to have a net change of the energy field [41]. The bound electrons are excited with the oscillating protons. Thus, the mechanical resonance frequency ω_0 is only one that of the electromechanical frequency which is equal to the frequency of the free space photon ω which excites the vibrational mode of the hydrogen molecular ion. The vibrational energy E_{vib} corresponding to the photon is given by

$$E_{vib} = \hbar\omega = \hbar\omega_0 = \hbar\sqrt{\frac{k}{\mu}} = 2kA^2, \tag{B.101}$$

where Planck's equation (Eq. (B.80)) was used. The reduced mass is given by

$$\mu = \frac{m_1 m_2}{m_1 + m_2}. \tag{B.102}$$

Thus,

$$A = \sqrt{\frac{\hbar\omega_0}{2k}} \tag{B.103}$$

Since the protons are not fixed and vibrate about the center of mass, the maximum amplitude is given by the reduced amplitude $A_{reduced}$ given by

$$A_{reduced} = \frac{A_1 A_2}{A_1 + A_2} \tag{B.104}$$

where A_n is the amplitude of proton n if the origin is fixed. Thus, Eq. (B.103) becomes

$$A_{reduced} = \frac{1}{2}\sqrt{\frac{\hbar\omega_0}{2k}} \tag{B.105}$$

and from Eq. (B.96), $A_{reduced}$ is

$$A_{reduced} \frac{1}{2}\sqrt{\frac{\hbar\omega_0}{2k}} = \frac{1}{2}\sqrt{\frac{\hbar}{2k}}\left(\frac{k}{\mu}\right)^{1/4} = \frac{\sqrt{\hbar}}{2^{3/2}(k\mu)^{1/4}}. \tag{B.106}$$

The total energy of a hydrogen-type molecular ion is given by substituting Eqs. (B.59), (B.61), and (B.72) into Eq. (B.76)

$$\begin{aligned}
E_T &= V_e + V_p + T \\
&= \frac{-4pe^2}{8\pi\varepsilon_0\sqrt{a^2 - b^2}}\ln\frac{a + \sqrt{a^2 - b^2}}{a - \sqrt{a^2 - b^2}} + \frac{pe^2}{8\pi\varepsilon_0\sqrt{a^2 - b^2}} \\
&\quad + \frac{2\hbar^2}{m_e a\sqrt{a^2 - b^2}}\ln\frac{a + \sqrt{a^2 - b^2}}{a - \sqrt{a^2 - b^2}} \\
&= \left[\frac{2\hbar^2}{m_e a} - \frac{4pe^2}{8\pi\varepsilon_0}\right]\frac{1}{\sqrt{a^2 - b^2}}\ln\frac{a + \sqrt{a^2 - b^2}}{a - \sqrt{a^2 - b^2}} \\
&\quad + \frac{pe^2}{8\pi\varepsilon_0\sqrt{a^2 - b^2}}.
\end{aligned} \tag{B.107}$$

From Eq. (B.68), the internuclear distance $2c'$ is given by

$$2c' = 2\sqrt{a^2 - b^2} \tag{B.108}$$

A hydrogen-type molecular ion comprises two nuclei at the foci and an electron at a prolate spheroid MO. To conserve momentum, the oscillation of the molecular ion comprises a time averaged increase in the internuclear distance with a time averaged increase in the semiminor axis. This corresponds to motion of the nuclei in phase with the electron. The total energy is a function of the semimajor axis a and c'. The displacement x corresponds to the amplitude of the time averaged increase in the distance from the origin to each focus c' with a time averaged semimajor axis a. Thus, the perturbated internuclear distance $2c''$ is given by

$$2c'' = 2(c' + x) = 2(\sqrt{a^2 - b^2} + x). \tag{B.109}$$

The relationship between $2c''$ and the perturbated semimajor axis a' follows from Eq. (B.66)

$$c'' = c' + x = a'\sqrt{\frac{\hbar^2 4\pi\varepsilon_0}{me^2 2pa'}} = \sqrt{\frac{a'a_0}{2p}}. \tag{B.110}$$

Thus,

$$a' = \frac{2p}{a_0}(c' + x)^2. \tag{B.111}$$

The solution to the force balance equation (Eq. (B.57)) for a is $2a_0/p$, and the solution for c' given by Eq. (B.67) is

$$c' = \frac{a_0}{p}. \tag{B.112}$$

From Eq. (B.107), E_{Tvib}, the total energy including vibration with the perturbated origin-to-nucleus distance c'' and the perturbated semimajor axis a' is given by

$$E_{Tvib} = \left[\frac{2\hbar^2}{m_e a'} - \frac{4pe^2}{8\pi\varepsilon_0} \right] \frac{1}{c''} \ln \frac{a' + c''}{a' - c''} + \frac{pe^2}{8\pi\varepsilon_0 c''}. \tag{B.113}$$

Substitution of Eqs. (A.12.110), (A.111) and (B.111) into Eq. (B.113) gives

$$E_{Tvib} = \left[\frac{2\hbar^2}{m_e \frac{2p}{a_0}\left(\frac{a_0}{p} + x\right)^2} - \frac{4pe^2}{8\pi\varepsilon_0} \right] \frac{1}{\left(\frac{a_0}{p} + x\right)}$$

$$\ln \frac{\frac{2p}{a_0}\left(\frac{a_0}{p} + x\right)^2 + \left(\frac{a_0}{p} + x\right)}{\frac{2p}{a_0}\left(\frac{a_0}{p} + x\right)^2 - \left(\frac{a_0}{p} + x\right)} + \frac{pe^2}{8\pi\varepsilon_0 \left(\frac{a_0}{p} + x\right)}, \tag{B.114}$$

$$E_{Tvib} = \left[\frac{p^2\hbar^2}{m_e a_0^2 \left(1 + \frac{p}{a_0}x\right)^2} - \frac{4p^2 e^2}{8\pi\varepsilon_0 a_0} \right] \frac{1}{\left(1 + \frac{p}{a_0}x\right)}$$

$$\ln \frac{\left(3 + \frac{2p}{a_0}x\right)}{\left(1 + \frac{2p}{a_0}x\right)} + \frac{p^2 e^2}{8\pi\varepsilon_0 a_0 \left(1 + \frac{p}{a_0}x\right)}, \tag{B.115}$$

$$E_{Tvib} = \frac{p^2 13.6 \text{ eV}}{\left(1 + \frac{p}{a_0}x\right)} \left\{ \left[\frac{2}{\left(1 + \frac{p}{a_0}x\right)^2} - 4 \right] \right.$$

$$\left. \ln \frac{\left(3 + \frac{2p}{a_0}x\right)}{\left(1 + \frac{2p}{a_0}x\right)} + 1 \right\}. \tag{B.116}$$

The vibrational energy E_{vib} is given by the difference in the total energy of the nonoscillating molecular ion E_T (Eq. (B.77)) and that of the oscillating molecular ion E_{Tvib} (Eq. (B.116))

$$E_{vib} = E_{Tvib} - E_T = p^2 13.6 \text{ eV} \frac{1}{\left(1 + \frac{p}{a_0}x\right)}$$

$$\times \left[\left[\frac{2}{\left(1 + \frac{p}{a_0}x\right)^2} - 4 \right] \ln \frac{\left(3 + \frac{2p}{a_0}x\right)}{\left(1 + \frac{2p}{a_0}x\right)} + 1 \right] + 2\ln 3 - 1 \right]. \tag{B.117}$$

The maximum displacement x is the reduced amplitude $A_{reduced}$ given by Eq. (B.106). Substitution of $A_{reduced}$ into

Eq. (B.117) gives

$$E_{vib} = \hbar\omega_0 = \hbar\sqrt{k/\mu}$$

$$= p^2 13.6 \text{ eV} \left[\frac{1}{\left(1 + \frac{p}{a_0}\frac{\sqrt{\hbar}}{2^{3/2}(k\mu)^{1/4}}\right)} \right.$$

$$\left[\left[\frac{2}{\left(1 + \frac{p}{a_0}\frac{\sqrt{\hbar}}{2^{3/2}(k\mu)^{1/4}}\right)^2} - 4 \right] \right.$$

$$\left. \ln \frac{\left(3 + \frac{2p}{a_0}\frac{\sqrt{\hbar}}{2^{3/2}(k\mu)^{1/4}}\right)}{\left(1 + \frac{2p}{a_0}\frac{\sqrt{\hbar}}{2^{3/2}(k\mu)^{1/4}}\right)} + 1 \right] + 2\ln 3 - 1 \right]. \tag{B.118}$$

A solution to

$$p^2 13.6 \text{ eV} \left[\frac{1}{\left(1 + \frac{p}{a_0}\frac{\sqrt{\hbar}}{2^{3/2}(k\mu)^{1/4}}\right)} \right.$$

$$\left[\left[\frac{2}{\left(1 + \frac{p}{a_0}\frac{\sqrt{\hbar}}{2^{3/2}(k\mu)^{1/4}}\right)^2} - 4 \right] \right.$$

$$\left. \ln \frac{\left(3 + \frac{2p}{a_0}\frac{\sqrt{\hbar}}{2^{3/2}(k\mu)^{1/4}}\right)}{\left(1 + \frac{2p}{a_0}\frac{\sqrt{\hbar}}{2^{3/2}(k\mu)^{1/4}}\right)} + 1 \right] + 2\ln 3 - 1 \right]$$

$$- \hbar\sqrt{\frac{k}{\mu}} = 0 \tag{B.119}$$

found by reiteration is

$$k = p^4 168 \text{ Nm}^{-1}. \tag{B.120}$$

A harmonic oscillator is a linear system as given by Eq. (B.94); thus, the resonant vibrational frequencies for hydrogen-type molecular ions with protons given by Eq. (B.96) and Eq. (B.120) for the vibrational transition $v_i \rightarrow v_f$ are

$$\omega_{0f} - \omega_{0i} = \Delta\omega = p^2 \sqrt{\frac{v_f^2 k}{\mu}} - p^2 \sqrt{\frac{v_i^2 k}{\mu}}$$

$$= (v_f - v_i)p^2 \sqrt{\frac{k}{\mu}}$$

$$= p^2 \sqrt{\frac{168 \text{ Nm}^{-1}}{\mu}} = p^2 4.48 \times 10^{14} \text{ radians/s}, \tag{B.121}$$

where v is an integer. From Planck's equation (Eq. (B.80)) and the vibrational frequencies (Eq. (B.121)), the vibrational energies E_{vib} of hydrogen-type molecular ions are

$$E_{vib} = (v_f - v_i)p^2 0.2962 \text{ eV}. \tag{B.122}$$

1 The experimental vibrational energy of the hydrogen molec-
ular ion [43] is

$$E_{vib} = 0.288 \text{ eV}. \tag{B.123}$$

3 The amplitude of oscillation given by Eqs. (B.106) and
(B.120) is

$$A = (v_f - v_i) \frac{\sqrt{\hbar}}{2^{3/2} (p^4 168 \text{ Nm}^{-1} \mu)^{1/4}}$$

$$= (v_f - v_i) \frac{5.93 \times 10^{-12} \text{ m}}{p}. \tag{B.124}$$

5 The energy spacing of each of the transitions of the
vibrational spectrum is approximately given by Eq. (B.122).
7 However, slight departure is anticipated as higher states are
excited due to the distortion of the molecular ion in these
9 states. The actual transition energy may be calculated from
Eq. (B.117) wherein the energy difference corresponds to
11 the initial and final states as opposed to the ground vibra-
tional state and the first vibrational state, and higher order
13 terms in the perturbation series are included.

B.2. Hydrogen-type molecules

15 B.2.1. Force balance of hydrogen-type molecules
Hydrogen-type molecules comprise two indistinguishable
17 electrons bound by an elliptic field. Each electron experi-
ences a centrifugal force, and the balancing centripetal force
19 (on each electron) is produced by the electric force between
the electron and the elliptic electric field and the magnetic
21 force between the two electrons causing the electrons to
pair. In the present case of hydrogen-type molecules, if the
23 eccentricity equals $1/\sqrt{2}$, then the vectorial projection of the
magnetic force between the electrons, $\sqrt{3/4}$ of Eq. (7.15)
25 of the Two Electron Atom section, is one. The molecules
will be solved by self-consistency. Assume $e = 1/\sqrt{2}$, then
27 the force balance equation given by Eq. (7.18) of the Two
Electron Atom section and Eq. (B.57) is

$$\frac{\hbar^2}{m_e a^2 b^2} 2ab^2 X = \frac{pe^2}{4\pi\varepsilon_0} X + \frac{\hbar^2}{2m_e b^2} \tag{B.125}$$

$$\frac{2a_0}{pa} - \frac{a_0}{pa} = 1, \tag{B.126}$$

$$a = \frac{a_0}{p}. \tag{B.127}$$

29 Substitution of Eq. (B.127) into (B.66) is

$$c' = \frac{1}{p\sqrt{2}} a_0. \tag{B.128}$$

Substitution of Eqs. (B.127) and (B.128) into Eq. (B.68) is

$$b = c' = \frac{1}{p\sqrt{2}} a_0. \tag{B.129}$$

31

Substitution of Eqs. (B.127) and (B.128) into Eq. (B.70) is

$$e = \frac{1}{\sqrt{2}}. \tag{B.130}$$

The eccentricity is $1/\sqrt{2}$; thus, the present self-consistent   33
solution which was obtained as a boundary value problem
is correct. The internuclear distance given by multiplying   35
Eq. (B.128) by two is $a_0\sqrt{2}/p$.

B.2.2. Energies of hydrogen-type molecules   37
The energy components defined previously for the mole-
cular ion, Eqs. (B.73)–(12.77), apply in the case of the   39
corresponding molecule. And, each molecular energy com-
ponent is given by the integral of corresponding force in   41
Eq. (B.125) where each energy component is the total for
the two equivalent electrons. The parameters a and b are   43
given by Eqs. (B.127) and (B.129), respectively.

$$V_e = \frac{-2pe^2}{8\pi\varepsilon_0\sqrt{a^2 - b^2}} \ln \frac{a + \sqrt{a^2 - b^2}}{a - \sqrt{a^2 - b^2}}, \tag{B.131}$$

$$V_p = \frac{p}{8\pi\varepsilon_0} \frac{e^2}{\sqrt{a^2 - b^2}}, \tag{B.132}$$

$$T = \frac{\hbar^2}{2m_e a\sqrt{a^2 - b^2}} \ln \frac{a + \sqrt{a^2 - b^2}}{a - \sqrt{a^2 - b^2}}. \tag{B.133}$$

The energy, V_m, corresponding to the magnetic force of Eq.   45
(B.125) is

$$V_m = \frac{-\hbar^2}{4m_e a\sqrt{a^2 - b^2}} \ln \frac{a + \sqrt{a^2 - b^2}}{a - \sqrt{a^2 - b^2}}, \tag{B.134}$$

$$E_T = V_e + T + V_m + V_p, \tag{B.135}$$

$$E_T = -13.6 \text{ eV} \left[\left(2p^2\sqrt{2} - p^2\sqrt{2} + \frac{p^2\sqrt{2}}{2} \right) \right.$$

$$\left. \ln \frac{\sqrt{2} + 1}{\sqrt{2} - 1} - p^2\sqrt{2} \right] = -p^2 31.63, \tag{B.136}$$

$$E \left(2H \left[\frac{a_H}{p} \right] \right) = -2p^2 13.6 \text{ eV}. \tag{B.137}$$

The bond dissociation energy, E_D, is the difference between   47
the total energy of the corresponding hydrogen atoms or
hydrino atoms and E_T 49

$$E_D = E \left(2H \left[\frac{a_H}{p} \right] \right) - E_T = -2p^2 13.6 + p^2 31.63 \text{ eV}$$

$$= p^2 4.43 \text{ eV}. \tag{B.138}$$

B.2.3. Vibration of hydrogen-type molecules
The vibrational energy levels of hydrogen-type molecules   51
may be solved in the same manner as hydrogen-type

molecular ions given in Section B.1.3. The total energy of a hydrogen-type molecule is given by substituting Eqs. (B.59), (B.61) and (B.72) into Eq. (B.76)

$$E_T = V_e + T + V_m + V_p$$

$$= \frac{-2pe^2}{8\pi\varepsilon_0\sqrt{a^2-b^2}}\ln\frac{a+\sqrt{a^2-b^2}}{a-\sqrt{a^2-b^2}} + \frac{\hbar^2}{2m_e a\sqrt{a^2-b^2}}$$

$$\ln\frac{a+\sqrt{a^2-b^2}}{a-\sqrt{a^2-b^2}} + \frac{-\hbar^2}{4m_e a\sqrt{a^2-b^2}}$$

$$\ln\frac{a+\sqrt{a^2-b^2}}{a-\sqrt{a^2-b^2}} + \frac{pe^2}{8\pi\varepsilon_0\sqrt{a^2-b^2}}, \qquad (B.139)$$

$$E_T = \left[\frac{\hbar^2}{2m_e a} - \frac{2pe^2}{8\pi\varepsilon_0} - \frac{\hbar^2}{4m_e a}\right]\frac{1}{\sqrt{a^2-b^2}}$$

$$\ln\frac{a+\sqrt{a^2-b^2}}{a-\sqrt{a^2-b^2}} + \frac{pe^2}{8\pi\varepsilon_0\sqrt{a^2-b^2}}, \qquad (B.140)$$

$$E_T = \left[\frac{\hbar^2}{4m_e a} - \frac{2pe^2}{8\pi\varepsilon_0}\right]\frac{1}{\sqrt{a^2-b^2}}\ln\frac{a+\sqrt{a^2-b^2}}{a-\sqrt{a^2-b^2}}$$

$$+ \frac{pe^2}{8\pi\varepsilon_0\sqrt{a^2-b^2}}. \qquad (B.141)$$

From Eq. (B.68), the internuclear distance $2c'$ is given by

$$2c' = 2\sqrt{a^2-b^2}. \qquad (B.142)$$

Thus, the total energy of the nonoscillating molecule is

$$E_T = \left[\frac{\hbar^2}{4m_e a} - \frac{2pe^2}{8\pi\varepsilon_0}\right]\frac{1}{c'}\ln\frac{a+c'}{a-c'} + \frac{pe^2}{8\pi\varepsilon_0 c'}. \qquad (B.143)$$

The relationship between $2c'$ and the semimajor axis a follows from Eq. (B.66)

$$2c' = 2a\sqrt{\frac{\hbar^2 4\pi\varepsilon_0}{me^2 2 pa'}} = 2\sqrt{\frac{aa_0}{2p}}. \qquad (B.144)$$

Substitution of Eq. (B.144) into Eq. (B.143) gives

$$E_T = \left[\frac{\hbar^2}{4m_e a} - \frac{2pe^2}{8\pi\varepsilon_0}\right]\frac{1}{c'}\frac{\sqrt{\frac{2p}{a_0}} + 1}{\sqrt{\frac{2p}{a_0}} - 1} \frac{pe^2}{8\pi\varepsilon_0 c'}. \qquad (B.145)$$

A hydrogen-type molecule comprises two nuclei at the foci and two indistinguishable electrons at the same prolate spheroid MO. The two electrons are spin-paired with the motion of one electron being the mirror image of that of the other. To conserve momentum, the oscillation of the molecule comprises a time averaged decrease in the internuclear distance and a time averaged increase in the semiminor axis relative to the stationary molecule. This corresponds to in-phase motion of the electrons that is opposite to that of the protons. The total energy is a function of the semimajor axis a and the distance from the origin to each focus c'.

The energy terms which are a function of the internuclear distance increase in magnitude and those that depend on the semiminor axis decrease in magnitude. The displacement x corresponds to the amplitude of the time averaged decrease in the distance from the origin to each focus c' and increase the time averaged semimajor axis a. Thus, the perturbated semimajor axis a' is given by

$$a' = a + x. \qquad (B.146)$$

From Eq. (B.144), the perturbated origin-to-nucleus distance c'' is given by

$$c'' = \sqrt{\frac{(a-x)a_0}{2p}}. \qquad (B.147)$$

From Eqs. (B.145), (B.146), and (B.147), then, the total energy including vibration with the perturbated origin-to-nucleus distance c'' and the perturbated semimajor axis a' is given by

$$E_{Tvib} = \left[\frac{\hbar^2}{4m_e a'} - \frac{2pe^2}{8\pi\varepsilon_0}\right]\frac{1}{c''}\ln\frac{\sqrt{2pa'/a_0} + 1}{\sqrt{2pa'/a_0} - 1} + \frac{pe^2}{8\pi\varepsilon_0 c''}. \qquad (B.148)$$

The solution to the force balance equation (Eq. (B.125)) for a given by Eq. (B.127) is

$$a = \frac{a_0}{p}. \qquad (B.149)$$

From Eq. (B.146),

$$a' = \frac{a_0}{p} + x, \qquad (B.150)$$

and from Eq. (B.147) and Eq. (B.150)

$$c'' = \sqrt{\frac{(a_0/p - x)a_0}{2p}}. \qquad (B.151)$$

Substitution of Eqs. (B.150), and (B.151) into Eq. (B.148) gives

$$E_{Tvib} = \left[\frac{\hbar^2}{4m_e\left(\frac{a_0}{p}+x\right)} - \frac{2pe^2}{8\pi\varepsilon_0}\right]\frac{1}{\sqrt{\frac{\left(\frac{a_0}{p}-x\right)a_0}{2p}}}$$

$$\ln\frac{\sqrt{\frac{2p}{a_0}\left(\frac{a_0}{p}+x\right)} + 1}{\sqrt{\frac{2p}{a_0}\left(\frac{a_0}{p}+x\right)} - 1} + \frac{pe^2}{8\pi\varepsilon_0\sqrt{\frac{\left(\frac{a_0}{p}-x\right)a_0}{2p}}}, \qquad (B.152)$$

$$E_{Tvib} = \left[\frac{p^2\hbar^2}{4m_e a_0^2\left(1+\frac{p}{a_0}x\right)} - \frac{2p^2e^2}{8\pi\varepsilon_0 a_0}\right]\frac{\sqrt{2}}{\sqrt{\left(1-\frac{p}{a_0}x\right)}}$$

$$\ln\frac{\sqrt{\frac{2p}{a_0}\left(\frac{a_0}{p}+x\right)} + 1}{\sqrt{\frac{2p}{a_0}\left(\frac{a_0}{p}+x\right)} - 1} + \frac{\sqrt{2}p^2e^2}{8\pi\varepsilon_0 a_0\sqrt{\left(1-\frac{p}{a_0}x\right)}}. \qquad (B.153)$$

$$E_{\text{Tvib}} = \frac{\sqrt{2}\,p^2\,13.6\,\text{eV}}{\sqrt{\left(1 - \frac{p}{a_0}x\right)}}$$

$$\left[\left[\frac{1/2}{\left(1 + \frac{p}{a_0}x\right)} - 2\right] \ln\frac{\sqrt{\frac{2p}{a_0}\left(\frac{a_0}{p} + x\right)} + 1}{\sqrt{\frac{2p}{a_0}\left(\frac{a_0}{p} + x\right)} - 1} + 1\right],$$

(B.154)

$$E_{\text{Tvib}} = \frac{\sqrt{2}\,p^2\,13.6\,\text{eV}}{\sqrt{\left(1 - \frac{p}{a_0}x\right)}}$$

$$\left[\left[\frac{1/2}{\left(1 + \frac{p}{a_0}x\right)} - 2\right] \ln\frac{\sqrt{2 + \frac{2p}{a_0}x} + 1}{\sqrt{2 + \frac{2p}{a_0}x} - 1} + 1\right].$$

(B.155)

1   The vibrational energy E_{vib} is given by the difference in the total energy of the nonoscillating molecule E_T (Eq. (B.136))
3   and that of the oscillating molecule E_{Tvib} (Eq. (B.155))

$$E_{\text{vib}} = E_{\text{Tvib}} - E_T = p^2\,13.6\,\text{eV}$$

$$\left[\frac{\sqrt{2}}{\sqrt{\left(1 - \frac{p}{a_0}x\right)}}\left[\left[\frac{1/2}{\left(1 + \frac{p}{a_0}x\right)} - 2\right]\right.\right.$$

$$\left.\ln\frac{\sqrt{2 + \frac{2p}{a_0}x} + 1}{\sqrt{2 + \frac{2p}{a_0}x} - 1} + 1\right]$$

$$\left.+ \left[\left(\sqrt{2} + \frac{\sqrt{2}}{2}\right)\ln\frac{\sqrt{2} + 1}{\sqrt{2} - 1} - \sqrt{2}\right]\right]$$

(B.156)

The maximum displacement x is the reduced amplitude
5   A_{reduced} given by Eq. (B.106). Substitution of A_{reduced} into Eq. (B.156) gives

$$E_{\text{vib}} = \hbar\omega_0 = \hbar\sqrt{\frac{k}{\mu}}$$

$$= p^2\,13.6\,\text{eV}\left[\frac{\sqrt{2}}{\sqrt{\left(1 - \frac{p}{a_0}\frac{\sqrt{\hbar}}{2^{3/2}(k\mu)^{1/4}}\right)}}\right.$$

$$\left[\left[\frac{1/2}{\left(1 + \frac{p}{a_0}\frac{\sqrt{\hbar}}{2^{3/2}(k\mu)^{1/4}}\right)} - 2\right]\right.$$

$$\left.\ln\frac{\sqrt{2 + \frac{2p}{a_0}\frac{\sqrt{\hbar}}{2^{3/2}(k\mu)^{1/4}}} + 1}{\sqrt{2 + \frac{2p}{a_0}\frac{\sqrt{\hbar}}{2^{3/2}(k\mu)^{1/4}}} - 1} + 1\right]$$

$$\left.+ \left[\left(\sqrt{2} + \frac{\sqrt{2}}{2}\right)\ln\frac{\sqrt{2} + 1}{\sqrt{2} - 1} - \sqrt{2}\right]\right]$$

7   (B.157)

A solution to

$$p^2\,13.6\,\text{eV}\left[\frac{\sqrt{2}}{\sqrt{\left(1 - \frac{p}{a_0}\frac{\sqrt{\hbar}}{2^{3/2}(k\mu)^{1/4}}\right)}}\right.$$

$$\left[\left[\frac{1/2}{\left(1 + \frac{p}{a_0}\frac{\sqrt{\hbar}}{2^{3/2}(k\mu)^{1/4}}\right)} - 2\right]\right.$$

$$\left.\ln\frac{\sqrt{2 + \frac{2p}{a_0}\frac{\sqrt{\hbar}}{2^{3/2}(k\mu)^{1/4}}} + 1}{\sqrt{2 + \frac{2p}{a_0}\frac{\sqrt{\hbar}}{2^{3/2}(k\mu)^{1/4}}} - 1}\right]$$

$$\left.+ \left[\left(\sqrt{2} + \frac{\sqrt{2}}{2}\right)\ln\frac{\sqrt{2} + 1}{\sqrt{2} - 1} - \sqrt{2}\right]\right]$$

$$-\hbar\sqrt{\frac{k}{\mu}} = 0$$

(B.158)

found by reiteration is   9

$$k = p^4\,570\,\text{Nm}^{-1}.$$

(B.159)

The resonant vibrational frequencies for hydrogen-type   11
molecules with proton nuclei given by Eq. (B.96) and Eq.
(B.159) are

$$\omega_0 = p^2\sqrt{\frac{k}{\mu}}$$

$$= \sqrt{\frac{570\,\text{Nm}^{-1}}{\mu}} = p^2\,8.2 \times 10^{14}\,\text{radians/s}.$$ (B.160)

From Planck's equation (Eq. (B.80)) and the vibrational   13
frequencies (Eq. (B.160)), the vibrational energies E_{vib} of
hydrogen-type molecules are   15

$$E_{\text{vib}} = p^2\,0.543\,\text{eV}.$$

(B.161)

The experimental vibrational energy of the hydrogen   17
molecule [43] is

$$E_{\text{vib}} = 0.545\,\text{eV}.$$

(B.162)

The amplitude of oscillation given by Eqs. (B.106) and   19
(B.159) is

$$A = \frac{\sqrt{\hbar}}{2^{3/2}(p^4\,570\,\text{Nm}^{-1}\,\mu)^{1/4}} = \frac{4.37 \times 10^{-12}\,\text{m}}{p}.$$ (B.163)

Due to the pairing of the two electrons, the vibrational   21
energies of hydrogen-type molecules are nonlinear as a
function of the vibrational quantum number v. The energy   23
spacing of each of the transitions of the vibrational spec-
trum is approximately given by Eq. (B.158) wherein the   25
corresponding amplitude of the proton displacement of each
state is approximately vA_{reduced}. The lines do become more   27
closely spaced as higher states are excited due to the distor-
tion of the molecule in these states. The actual transition en-   29
ergy may be better calculated from Eq. (B.156) wherein the
energy difference corresponds to the initial and final states

as opposed to the ground vibrational state and the first vibrational state, and higher order terms in the perturbation series are included.

B.3. The hydrogen molecular ion $H_2[2c' = 2a_0]^+$

B.3.1. Force balance of the hydrogen molecular ion

Force balance between the electric and centripetal forces is given by Eq. (B.57) where $p = 1$

$$\frac{\hbar^2}{m_e a^2 b^2} 2ab^2 X = \frac{e^2}{4\pi\varepsilon_0} X, \tag{B.164}$$

which has the parametric solution given by Eq. (B.51) when

$$a = 2a_0. \tag{B.165}$$

The semimajor axis, a, is also given by Eq. (B.58) where $p = 1$. The internuclear distance, $2c'$, which is the distance between the foci is given by Eq. (B.67) where $p = 1$

$$2c' = 2a_0. \tag{B.166}$$

The experimental internuclear distance is $2a_0$. The semiminor axis is given by Eq. (B.69) where $p = 1$

$$b = \sqrt{3}a_0. \tag{B.167}$$

The eccentricity, e, is given by Eq. (B.71)

$$e = \tfrac{1}{2}. \tag{B.168}$$

B.3.2. Energies of the hydrogen molecular ion

The potential energy, V_e, of the electron MO in the field of the protons at the foci ($\xi = 0$) is given by Eq. (B.69) where $p = 1$

$$V_e = \frac{-4e^2}{8\pi\varepsilon_0\sqrt{a^2 - b^2}} \ln\frac{a + \sqrt{a^2 - b^2}}{a - \sqrt{a^2 - b^2}}. \tag{B.169}$$

The potential energy, V_p, due to proton–proton repulsion is given by Eq. (B.72) where $p = 1$

$$V_p = \frac{e^2}{8\pi\varepsilon_0\sqrt{a^2 - b^2}}. \tag{B.170}$$

The kinetic energy, T, of the electron MO is given by Eq. (B.61) where $p = 1$

$$T = \frac{2\hbar^2}{m_e a\sqrt{a^2 - b^2}} \ln\frac{a + \sqrt{a^2 - b^2}}{a - \sqrt{a^2 - b^2}}. \tag{B.171}$$

Substitution of a and b given by Eqs. (B.165) and (B.167), respectively, into Eqs. (B.169), (B.170), and (B.171) is

$$V_e = \frac{-4e^2}{8\pi\varepsilon_0 a_0} \ln 3 = -59.763 \text{ eV}, \tag{B.172}$$

$$V_p = \frac{e^2}{8\pi\varepsilon_0 a_0} = 13.6 \text{ eV}, \tag{B.173}$$

$$T = \frac{2e^2}{8\pi\varepsilon_0 a_0} \ln 3 = 29.88 \text{ eV}, \tag{B.174}$$

$$E_T = V_e + V_p + T, \tag{B.175}$$

$$E_T = -16.282 \text{ eV}, \tag{B.176}$$

$$E(H[a_H]) = -13.6 \text{ eV},$$

$$E_T = V_e + V_p + T, \tag{B.177}$$

$$E_T = 13.6 \text{ eV}(-4\ln 3 + 1 + 2\ln 3) = -16.28 \text{ eV}. \tag{B.178}$$

The bond dissociation energy, E_D, is the difference between the total energy of the corresponding hydrogen atom and E_T

$$E_D = E\left(H\left[\frac{a_H}{p}\right]\right) - E_T = -13.6 + 16.28 \text{ eV} = 2.68 \text{ eV}. \tag{B.179}$$

Eqs. (B.172)–(12.179) are equivalent to Eqs. (B.73)–(12.78) where $p = 1$. The experimental bond energy of the hydrogen molecular ion [42] is

$$E_D = 2.651 \text{ eV}. \tag{B.180}$$

B.3.3. Vibration of the hydrogen molecular ion

It can be shown that a perturbation of the orbit determined by an inverse-squared force results in simple harmonic oscillatory motion of the orbit [39]. The spring constant k for the hydrogen molecular ion with protons given by Eq. (B.120)

$$k = 168 \text{ Nm}^{-1}, \tag{B.181}$$

wherein $p = 1$. The resonant vibrational frequency for the hydrogen molecular ion with protons given by Eq. (B.121) is

$$\omega_0 = \sqrt{\frac{k}{\mu}} = \sqrt{\frac{168 \text{ Nm}^{-1}}{\mu}} = 4.48 \times 10^{14} \text{ radians/s}. \tag{B.182}$$

The vibrational energy E_{vib} of the hydrogen molecular ion given by Eq. (B.122) is

$$E_{vib} = 0.2962 \text{ eV}. \tag{B.183}$$

The experimental vibrational energy of the hydrogen molecular ion [42] is

$$E_{vib} = 0.288 \text{ eV}. \tag{B.184}$$

The amplitude of oscillation given by Eq. (B.124) is

$$A = \frac{\sqrt{\hbar}}{2^{3/2}(168 \text{ Nm}^{-1}\mu)^{1/4}} = 5.93 \times 10^{-12} \text{ m}. \tag{B.185}$$

B.4. The hydrogen molecule $H_2[2c' = \sqrt{2}a_0]$

B.4.1. Force balance of the hydrogen molecule

The force balance equation for the hydrogen molecule is given by Eq. (B.125) where $p = 1$

$$\frac{\hbar^2}{m_e a^2 b^2} 2ab^2 X = \frac{e^2}{4\pi\varepsilon_0} X + \frac{\hbar^2}{2m_e a^2 b^2} 2ab^2 X, \quad (B.186)$$

which has the parametric solution given by Eq. (B.51) when

$$a = a_0. \quad (B.187)$$

The semimajor axis, a, is also given by Eq. (B.127) where $p = 1$. The internuclear distance, $2c'$, which is the distance between the foci is given by Eq. (B.128) where $p = 1$

$$2c' = \sqrt{2}a_0. \quad (B.188)$$

The experimental internuclear distance is $\sqrt{2}a_0$. The semiminor axis is given by Eq. (B.129) where $p = 1$

$$b = \frac{1}{\sqrt{2}}a_0. \quad (B.189)$$

The eccentricity, e, is given by Eq. (B.130)

$$e = \frac{1}{\sqrt{2}}. \quad (B.190)$$

The finite dimensions of the hydrogen molecule are evident in the plateau of the resistivity versus pressure curve of metallic hydrogen [43].

B.4.2. Energies of the hydrogen molecule

The energies of the hydrogen molecule are given by Eqs. (B.131)–(12.137) where $p = 1$

$$V_e = \frac{-2e^2}{8\pi\varepsilon_0\sqrt{a^2 - b^2}} \ln\frac{a + \sqrt{a^2 - b^2}}{a - \sqrt{a^2 - b^2}} = -67.813 \text{ eV}. \quad (B.191)$$

$$V_p = \frac{e^2}{8\pi\varepsilon_0\sqrt{a^2 - b^2}} = 19.23 \text{ eV}, \quad (B.192)$$

$$T = \frac{\hbar^2}{2m_e a\sqrt{a^2 - b^2}} \ln\frac{a + \sqrt{a^2 - b^2}}{a - \sqrt{a^2 - b^2}} = 33.906 \text{ eV}. \quad (B.193)$$

The energy, V_m, of the magnetic force is

$$V_m = \frac{-\hbar^2}{4m_e a\sqrt{a^2 - b^2}} \ln\frac{a + \sqrt{a^2 - b^2}}{a - \sqrt{a^2 - b^2}} = -16.9533 \text{ eV}, \quad (B.194)$$

$$E_T = V_e + T + V_m + V_p, \quad (B.195)$$

$$E_T = -13.6 \text{ eV} \left[\left(2\sqrt{2} - \sqrt{2} + \frac{\sqrt{2}}{2} \right) \ln\frac{\sqrt{2}+1}{\sqrt{2}-1} - \sqrt{2} \right] = -31.63 \text{ eV}, \quad (B.196)$$

$$E(2H[a_H]) = -27.21 \text{ eV}. \quad (B.197)$$

The bond dissociation energy, E_D, is the difference between the total energy of the corresponding hydrogen atoms and E_T

$$E_D = E(2H[a_H]) - E_T = -27.2 + 31.63 \text{ eV} = 4.43 \text{ eV}. \quad (B.198)$$

The experimental bond energy of the hydrogen molecule [42] is

$$E_D = 4.478 \text{ eV}. \quad (B.199)$$

B.4.3. Vibration of the hydrogen molecule

It can be shown that a perturbation of the orbit determined by an inverse-squared force results in simple harmonic oscillatory motion of the orbit [39]. The spring constant k for the hydrogen molecule with protons given by Eq. (B.159) is

$$k = 570 \text{ Nm}^{-1}, \quad (B.200)$$

wherein $p = 1$. The resonant vibrational frequency for the hydrogen molecule with protons given by Eq. (B.160) is

$$\omega_0 = \sqrt{\frac{k}{\mu}} = \sqrt{\frac{570 \text{ Nm}^{-1}}{\mu}} = 8.2 \times 10^{14} \text{ radians/s}. \quad (B.201)$$

The vibrational energy E_{vib} of the hydrogen molecule given by Eq. (B.161) is

$$E_{vib} = 0.543 \text{ eV}. \quad (B.202)$$

The experimental vibrational energy of the hydrogen molecule [43] is

$$E_{vib} = 0.545 \text{ eV}. \quad (B.203)$$

The amplitude of oscillation given by Eq. (B.163) is

$$A = \frac{\sqrt{\hbar}}{2^{3/2}(570 \text{ Nm}^{-1} \mu)^{1/4}} = 4.37 \times 10^{-12} \text{ m}. \quad (B.204)$$

B.5. The dihydrino molecular ion $H_2[2c' = a_0]^+$

B.5.1. Force balance of the dihydrino molecular ion

Force balance between the electric and centripetal forces is given by Eq. (B.57) where $p = 2$

$$\frac{\hbar^2}{m_e a^2 b^2} 2ab^2 X = \frac{2e^2}{4\pi\varepsilon_0} X, \quad (B.205)$$

which has the parametric solution given by Eq. (B.51) when

$$a = a_0. \quad (B.206)$$

The semimajor axis, a, is also given by Eq. (B.58) where $p = 2$. The internuclear distance, $2c'$, which is the distance

between the foci is given by Eq. (B.67) where $p = 2$

$$2c' = a_0. \tag{B.207}$$

The semiminor axis is given by Eq. (B.69) where $p = 2$

$$b = \frac{\sqrt{3}}{2} a_0. \tag{B.208}$$

The eccentricity, e, is given by Eq. (B.71).

$$e = \frac{1}{2}. \tag{B.209}$$

B.5.2. Energies of the dihydrino molecular ion

The potential energy, V_e, of the electron MO in the field of magnitude twice that of the protons at the foci ($\xi = 0$) is given by Eq. (B.59) where $p = 2$

$$V_e = \frac{-8e^2}{8\pi\varepsilon_0\sqrt{a^2 - b^2}} \ln\frac{a + \sqrt{a^2 - b^2}}{a - \sqrt{a^2 - b^2}}. \tag{B.210}$$

The potential energy, V_p, due to proton–proton repulsion in the field of magnitude twice that of the protons at the foci ($\xi = 0$) is given by Eq. (B.72) where $p = 2$

$$V_p = \frac{2e^2}{8\pi\varepsilon_0\sqrt{a^2 - b^2}}. \tag{B.211}$$

The kinetic energy, T, of the electron MO is given by Eq. (B.61) where $p = 2$

$$T = \frac{2\hbar^2}{m_e a\sqrt{a^2 - b^2}} \ln\frac{a + \sqrt{a^2 - b^2}}{a - \sqrt{a^2 - b^2}}. \tag{B.212}$$

Substitution of a and b given by Eqs. (B.206) and (B.208), respectively, into Eqs. (B.210), (B.211), and (B.212) is

$$V_e = \frac{-16e^2}{8\pi\varepsilon_0 a_0} \ln 3 = -239.058 \text{ eV}, \tag{B.213}$$

$$V_p = \frac{4e^2}{8\pi\varepsilon_0 a_0} = 54.42 \text{ eV}, \tag{B.214}$$

$$T = \frac{8e^2}{8\pi\varepsilon_0 a_0} \ln 3 = 119.53 \text{ eV}, \tag{B.215}$$

$$E\left(H\left[\frac{a_H}{2}\right]\right) = -54.4 \text{ eV}, \tag{B.216}$$

$$E_T = V_e + V_p + T, \tag{B.217}$$

$$E_T = 13.6 \text{ eV}(-16\ln 3 + 4 + 8\ln 3) = -65.09 \text{ eV}. \tag{B.218}$$

The bond dissociation energy, E_D, is the difference between the total energy of the corresponding hydrino atom and E_T

$$E_D = E\left(H\left[\frac{a_H}{2}\right]\right) - E_T = -54.4 + 65.09 \text{ eV} = 10.69 \text{ eV}. \tag{B.219}$$

Eqs. (B.213)–(12.219) are equivalent to Eqs. (B.73)–(12.78) where $p = 2$.

B.5.3. Vibration of the dihydrino molecular ion

It can be shown that a perturbation of the orbit determined by an inverse-squared force results in simple harmonic oscillatory motion of the orbit [39]. The spring constant k for the dihydrino molecular ion with protons given by Eq. (B.120) is

$$k = 2^4 168 \text{ Nm}^{-1} = 2688 \text{ Nm}^{-1}, \tag{B.220}$$

wherein $p = 2$. The resonant vibrational frequency for the dihydrino molecular ion with protons given by Eq. (B.121) is

$$\omega_0 = 2^2 \sqrt{\frac{k}{\mu}} = 2^2 \sqrt{\frac{168 \text{ Nm}^{-1}}{\mu}} = 1.79 \times 10^{15} \text{ radians/s}. \tag{B.221}$$

The vibrational energy E_{vib} of the dihydrino molecular ion given by Eq. (B.122) is

$$E_{vib} = 2^2(0.2962) \text{ eV} = 1.185 \text{ eV}. \tag{B.222}$$

The amplitude of oscillation given by Eq. (B.124) is

$$A = \frac{\sqrt{\hbar^2}}{2^{3/2}(2^4(168) \text{ Nm}^{-1}\mu)^{1/4}}$$
$$= \frac{5.93 \times 10^{-12} \text{ m}}{2} = 2.97 \times 10^{-12} \text{ m}. \tag{B.223}$$

B.6. The dihydrino molecule $H_2[2c' = a_0/\sqrt{2}]$

B.6.1. Force balance of the dihydrino molecule

The force balance equation for the dihydrino molecule $H_2[2c' = a_0/\sqrt{2}]$ is given by Eq. (B.125) where $p = 2$

$$\frac{\hbar^2}{m_e a^2 b^2} 2ab^2 X = \frac{2e^2}{4\pi\varepsilon_0} X + \frac{\hbar^2}{2m_e a^2 b^2} 2ab^2 X, \tag{B.224}$$

which has the parametric solution given by Eq. (B.51) when

$$a = \frac{a_0}{2}. \tag{B.225}$$

The semimajor axis, a, is also given by Eq. (B.127) where $p = 2$. The internuclear distance, $2c'$, which is the distance between the foci is given by Eq. (B.128) where $p = 2$

$$2c' = \frac{1}{\sqrt{2}} a_0. \tag{B.226}$$

The semiminor axis is given by Eq. (B.129) where $p = 2$

$$b = c = \frac{1}{2\sqrt{2}} a_0. \tag{B.227}$$

1   The eccentricity, e, is given by Eq. (B.130)

$$e = \frac{1}{\sqrt{2}}. \tag{B.228}$$

B.6.2. Energies of the dihydrino molecule

3   The energies of the dihydrino molecule $H_2[2c' = a_0/\sqrt{2}]$ are given by Eqs. (B.131)–(12.137) where $p = 2$

$$V_e = \frac{-4e^2}{8\pi\varepsilon_0\sqrt{a^2 - b^2}} \ln\frac{a + \sqrt{a^2 - b^2}}{a - \sqrt{a^2 - b^2}} = -271.23 \text{ eV}, \tag{B.229}$$

$$V_p = \frac{2}{8\pi\varepsilon_0}\frac{e^2}{\sqrt{a^2 - b^2}} = 76.93 \text{ eV}, \tag{B.230}$$

$$T = \frac{\hbar^2}{2m_e a\sqrt{a^2 - b^2}} \ln\frac{a + \sqrt{a^2 - b^2}}{a - \sqrt{a^2 - b^2}} = 135.614 \text{ eV}. \tag{B.231}$$

5   The energy, V_m, of the magnetic force is

$$V_m = \frac{-\hbar^2}{4m_e a\sqrt{a^2 - b^2}} \ln\frac{a + \sqrt{a^2 - b^2}}{a - \sqrt{a^2 - b^2}} = -67.8069 \text{ eV}, \tag{B.232}$$

$$E_T = V_e + T + V_m + V_p, \tag{B.233}$$

$$E_T = -13.6 \text{ eV}\left[\left(8\sqrt{2} - 4\sqrt{2} + \frac{4\sqrt{2}}{2}\right)\right.$$
$$\left.\ln\frac{\sqrt{2} + 1}{\sqrt{2} - 1} - 4\sqrt{2}\right] = -126.5 \text{ eV}, \tag{B.234}$$

$$E\left(2H\left[\frac{a_H}{2}\right]\right) = -2(54.4) \text{ eV}. \tag{B.235}$$

The bond dissociation energy, E_D, is the difference between

7   the total energy of the corresponding hydrino atoms and E_T

$$E_D = E\left(2H\left[\frac{a_H}{2}\right]\right) - E_T$$
$$= -108.8 + 126.5 \text{ eV} = 17.7 \text{ eV}. \tag{B.236}$$

B.6.3. Vibration of the dihydrino molecule

9   It can be shown that a perturbation of the orbit determined by an inverse-squared force results in simple harmonic

11   oscillatory motion of the orbit [39]. The spring constant k for the dihydrino molecule with protons given by Eq.

13   (B.159) is

$$k = 2^4 570 \text{ Nm}^{-1} = 9120 \text{ Nm}^{-1}, \tag{B.237}$$

wherein $p = 2$. The resonant vibrational frequency for the

15   dihydrino molecule with protons given by Eq. (B.160) is

$$\omega_0 = 2^2\sqrt{\frac{k}{\mu}} = 2^2\sqrt{\frac{570 \text{ Nm}^{-1}}{\mu}} = 3.28 \times 10^{15} \text{ radians/s}. \tag{B.238}$$

The vibrational energy E_{vib} of the dihydrino molecule given   17
by Eq. (B.161) is

$$E_{vib} = 2^2(0.543) \text{ eV} = 2.17 \text{ eV}. \tag{B.239}$$

The amplitude of oscillation given by Eq. (B.163) is   19

$$A = \frac{\sqrt{\hbar}}{2^{3/2}(2^4(570) \text{ Nm}^{-1}\mu)^{1/4}}$$
$$= \frac{4.37 \times 10^{-12} \text{ m}}{2} = 2.19 \times 10^{-12} \text{ m}. \tag{B.240}$$

B.7. Diatomic molecular rotation

A molecule with a permanent dipole moment can res-   21
onantly absorb a photon which excites a rotational mode
about the center of mass of the molecule. Momentum must   23
be conserved with excitation of a rotational mode. The
photon carries $\hbar$ of angular momentum, thus the rotational   25
angular momentum of the molecule changes by $\hbar$. And,
the rotational charge-density function is equivalent to the   27
rigid rotor problem considered in the Rotational Parameters
of the Electron (Angular Momentum, Rotational Energy,   29
Moment of Inertia) section with the exception that for a
diatomic molecule having atoms of masses m_1 and m_2, the   31
moment of inertia is

$$I = \mu r^2, \tag{B.241}$$

where μ is the reduced mass   33

$$\mu = \frac{m_1 m_2}{m_1 + m_2} \tag{B.242}$$

and where r is the distance between the centers of the atoms,
the internuclear distance. The rotational energy levels follow   35
from Eq. (1.95)

$$E_{\text{rotational orbital}} = \frac{\hbar^2}{2I}J(J + 1), \tag{B.243}$$

where J is an integer. For Eq. (B.243), $J = 0$ corresponds to   37
rotation about the z-axis where the internuclear axis is along
the y-axis, and $J \neq 0$ corresponds to a linear combination   39
of rotations about the z- and x-axis.

As given in the Selection Rules section, the radiation of a   41
multipole of order (l, m) carries $m\hbar$ units of the z component
of angular momentum per photon of energy $\hbar\omega$. Thus, the z   43
component of the angular momentum of the corresponding
excited rotational state is   45

$$L_z = m\hbar. \tag{B.244}$$

Thus, the selection rule for rotational transitions is

$$\Delta J = \pm 1. \tag{B.245}$$

In addition, the molecule must posses a permanent dipole   47
moment. In the case of absorption of electromagnetic radi-
ation, the molecule goes from a state with a quantum num-   49
ber J to one with a quantum number of $J + 1$. Using Eq.
(B.243), the energy difference is   51

$$\Delta E = E_{J+1} - E_J = \frac{\hbar^2}{I}[J + 1]. \tag{B.246}$$

B.7.1. Diatomic molecular rotation of hydrogen-type molecules

The reduced mass of hydrogen-type molecules, μ_{H_2}, having two protons is given by Eq. (B.242) where $m_1 = m_2 = m_p$, and m_p is the mass of the proton

$$\mu_{H_2} = \frac{m_p m_p}{m_p + m_p} = \frac{1}{2} m_p. \tag{B.247}$$

The moment of inertia of hydrogen-type molecules is given by substitution of the reduced mass, Eq. (B.247), for μ of Eq. (B.241) and substitution of the internuclear distance, two times Eq. (B.128), for r of Eq. (B.241)

$$I = m_p \frac{a_0^2}{p^2}, \tag{B.248}$$

where p is an integer which corresponds to, $n = 1/p$, the fractional quantum number of the hydrogen-type molecule. Using Eqs. (B.246) and (B.248), the rotational energy absorbed by a hydrogen-type molecule with the transition from the state with the rotational quantum number J to one with the rotational quantum number $J + 1$ is

$$\Delta E = E_{J+1} - E_J = \frac{p^2 \hbar^2}{m_p a_0^2} [J + 1]$$

$$= p^2 [J + 1] 2.37 \times 10^{-21} J. \tag{B.249}$$

The energy can be expressed in terms of wavelength in angstroms (Å) using the Planck relationship, Eq. (2.65)

$$\lambda = 10^{10} \frac{hc}{\Delta E} = \frac{8.38 \times 10^5}{p^2 [J + 1]}. \tag{B.250}$$

Vibration increases the internuclear distance, r of Eq. (B.241), which decreases the rotational energy. The rotational wavelength including vibration given in Section B.2.3 (Eq. (B.163)) is

$$\lambda = \frac{8.43 \times 10^5}{p^2 [J + 1]}. \tag{B.251}$$

The calculated wavelength for the $J = 0 \to 1$ transition of the hydrogen molecule $H_2(n = 1)$ including vibration is 8.43×10^5 Å. The experimental value is 8.43×10^5 Å [44].

B.7.2. Diatomic molecular rotation of hydrogen-type molecular ions

The moment of inertia of hydrogen-type molecular ions is given by substitution of the reduced mass, Eq. (B.247), for μ of Eq. (B.241) and substitution of the internuclear distance, two times Eq. (B.67), for r of Eq. (B.241)

$$I = m_p \frac{2a_0^2}{p^2}, \tag{B.252}$$

where p is an integer which corresponds to, $n = 1/p$, the fractional quantum number of the hydrogen-type molecular

ion. Using Eqs. (B.246) and (B.242), the rotational energy absorbed by a hydrogen-type molecular ion with the transition from the state with the rotational quantum number J to one with the rotational quantum number $J + 1$ is

$$\Delta E = E_{J+1} - E_J = \frac{p^2 \hbar^2}{m_p 2a_0^2} [J + 1]$$

$$= p^2 [J + 1] 1.89 \times 10^{-21} J. \tag{B.253}$$

The energy can be expressed in terms of wavelength in microns (μm) using the Planck relationship, Eq. (2.65).

$$\lambda = 10^6 \frac{hc}{\Delta E} \ \mu m = \frac{168}{p^2 [J + 1]} \ \mu m. \tag{B.254}$$

Vibration increases the internuclear distance, r of Eq. (B.241), which decreases the rotational energy. The rotational wavelength including vibration given in Section B.1.3 (Eq. (B.124)) is

$$\lambda = \frac{169}{p^2 [J + 1]} \ \mu m. \tag{B.255}$$

The calculated wavelength for the $J = 0 \to 1$ transition of the hydrogen molecular ion $H_2[2c' = 2a_0]^+$ including vibration is 169 μm. The experimental value is 169 μm [43].

References

[1] Mills R. The grand unified theory of classical quantum mechanics. January 2000 ed. Cranbury, New Jersey: BlackLight Power, Inc. Distributed by Amazon.com; posted at www.blacklightpower.com.

[2] Mills R. The grand unified theory of classical quantum mechanics, Global Foundation, Inc. Orbis Scientiae entitled The role of attractive and repulsive gravitational forces in cosmic acceleration of particles the origin of the cosmic gamma ray bursts. 29th Conference on High Energy Physics and Cosmology Since 1964. Dr. Behram N. Kursunoglu, Chairman, December 14–17, 2000, Lago Mar Resort, Fort Lauderdale, FL.

[3] Mills R. The grand unified theory of classical quantum mechanics, Global Foundation, Inc. Orbis Scientiae entitled The role of attractive and repulsive gravitational forces in cosmic acceleration of particles the origin of the cosmic gamma ray bursts. 29th Conference on High Energy Physics and Cosmology Since 1964. Dr. Behram N. Kursunoglu, Chairman, December 14–17, 2000, Lago Mar Resort, Fort Lauderdale, FL, New York: Kluwer Academic/Plenum Publishers, p. 243–258.

[4] Mills R. The grand unified theory of classical quantum mechanics. Int J Hydrogen Energy, in press.

[5] Mills R. The hydrogen atom revisited. Int J Hydrogen Energy 2000;25(12):1171–83.

[6] Mills R. The nature of free electrons in superfluid helium — a test of quantum mechanics and a basis to review its foundations and make a comparison to classical theory. Int J Hydrogen Energy 2001;26(10):1059–96.

[7] Mills R, Ray P. Spectral emission of fractional quantum energy levels of atomic hydrogen from a helium–hydrogen plasma and the implications for dark matter. Int J Hydrogen Energy, in press.

ARTICLE IN PRESS

[8] Mills R, Ray P. Spectroscopic identification of a novel catalytic reaction of potassium and atomic hydrogen and the hydride ion product. Int J Hydrogen Energy, in press.

[9] Mills R. Spectroscopic identification of a novel catalytic reaction of atomic hydrogen and the hydride ion product. Int J Hydrogen Energy 2001;26(10):1041–58.

[10] Mills RL, Voigt A, Ray P, Nansteel M, Dhandapani B. Measurement of hydrogen balmer line broadening and thermal power balances of noble gas-hydrogen discharge plasmas. Int J Hydrogen Energy, submitted.

[11] Mills R, Greenig N, Hicks S. Optically measured power balances of anomalous discharges of mixtures of argon, hydrogen, and potassium, rubidium, cesium, or strontium vapor. Int J Hydrogen Energy, submitted.

[12] Mills R, Nansteel M. Argon–hydrogen–strontium plasma light source. IEEE Trans Plasma Sci., submitted.

[13] Mills R, Nansteel M, Lu Y. Excessively bright hydrogen-strontium plasma light source due to energy resonance of strontium with hydrogen. Europ J Phys D, submitted.

[14] Mills R, Dong J, Lu Y. Observation of extreme ultraviolet hydrogen emission from incandescently heated hydrogen gas with certain catalysts. Int J Hydrogen Energy 2000; 25:919–43.

[15] Mills R. Observation of extreme ultraviolet emission from hydrogen–KI plasmas produced by a hollow cathode discharge. Int J Hydrogen Energy 2001;26(6):579–92.

[16] Mills R. Temporal behavior of light-emission in the visible spectral range from a Ti–K₂CO₃-H-Cell. Int J Hydrogen Energy 2001;26(4):327–32.

[17] Mills R, Onuma T, Lu Y. Formation of a hydrogen plasma from an incandescently heated hydrogen-catalyst gas mixture with an anomalous afterglow duration. Int J Hydrogen Energy 2001;26(7):749–62.

[18] Mills R, Nansteel M, Lu Y. Observation of extreme ultraviolet hydrogen emission from incandescently heated hydrogen gas with strontium that produced an anomalous optically measured power balance. Int J Hydrogen Energy 2001;26(4):309–26.

[19] Mills R, Dhandapani B, Nansteel M, He J, Voigt A. Identification of compounds containing novel hydride ions by nuclear magnetic resonance spectroscopy. Int J Hydrogen Energy 2001;26(9):965–79.

[20] Mills R, Dhandapani B, Greenig N, He J. Synthesis and characterization of potassium iodo hydride. Int J Hydrogen Energy 2000;25(12):1185–203.

[21] Mills R. Novel inorganic hydride. Int J Hydrogen Energy 2000;25:669–83.

[22] Mills R. Novel hydrogen compounds from a potassium carbonate electrolytic cell. Fusion Technol 2000;37(2): 157–82.

[23] Mills R, Dhandapani B, Nansteel M, He J, Shannon T, Echezuria A. Synthesis and characterization of novel hydride compounds. Int J Hydrogen Energy 2001;26(4):pp. 339–67.

[24] Mills R. Highly stable novel inorganic hydrides. J Mater Res, submitted.

[25] Mills R, Good W, Voigt A. Jinquan Dong, Minimum heat of formation of potassium iodo hydride. Int J Hydrogen Energy, in press.

[26] Mills R. BlackLight power technology — a new clean hydrogen energy source with the potential for direct conversion to electricity. Proceedings of the National

Hydrogen Association, 12th Annual US Hydrogen Meeting and Exposition. Hydrogen: The Common Thread, The Washington Hilton and Towers, Washington DC, March 6–8, 2001, p. 671–97.

[27] Mills R. BlackLight power technology — a new clean energy source with the potential for direct conversion to electricity. Global Foundation International Conference on Global Warming and Energy Policy, Dr. Behram N. Kursunoglu, Chairman, Fort Lauderdale, FL, November 26–28, 2000, New York: Kluwer Academic/Plenum Publishers, p. 1059–96.

[28] Sidgwick NV. The chemical elements and their compounds, Vol. I. Oxford: Clarendon Press, 1950. p. 17.

[29] Lamb MD. Luminescence spectroscopy. London: Academic Press, 1978. p. 68.

[30] Thompson BJ. Handbook of nonlinear optics. New York: Marcel Dekker, Inc., 1996. p. 497–548.

[31] Shen YR. The principles of nonlinear optics. New York: Wiley, 1984. p. 203–10.

[32] de Beauvoir B, Nez F, Julien L, Cagnac B, Biraben F, Touahri D, Hilico L, Acef O, Clairon A, Zondy JJ. Phys Rev Lett 1997;78(3):440–3.

[33] Livingston W, Wallace L. An atlas of the solar spectrum in the infrared from 1850 to 9000 cm⁻¹ (1.1–5.4 µm) with identifications of the main solar features. Published by the National Optical Astronomy Observatories, December 18, 1990.

[34] Delbouille L, Roland G, Brault J, Testerman L. Photometric atlas of the solar spectrum from 1850 to 10,000 cm⁻¹, Kitt Peak National Observatory, Tucson, AZ.

[35] Migeotte M, Neven L, Swensson J. The solar spectrum from 2.8 to 23.7 microns, Part II. Measurements and identifications with WS. Benedict, Comments on the spectra of telluric H₂O and CO₂ as observed in the solar spectrum. 2.8–23.7 microns, Institut D'Astrophysique De L'Universite' De Liege Observatoire Royal De Belgique, Technical Final Report-Phase A (Part II) Under Contract AF 61 (514)–432.

[36] Cohen L. An atlas of solar spectra between 1175 and 1950 Angstroms recorded on skylab with the NRL's Apollo telescope mount experiment, Laboratory for Astronomy and Solar Physics, Goddard Space Flight Center, NASA Reference Publication 1069, March, 1981.

[37] Haus HA. On the radiation from point charges. Amer J Phys 1986;54:1126–9.

[38] Jahnke-Emde, Tables of functions. 2nd ed. Stuttgart: Teubner, 1933.

[39] Fowles GR. Analytical mechanics. 3rd ed. New York: Holt, Rinehart, and Winston, 1977. p. 154–5.

[40] Fowles GR. Analytical Mechanics. 3rd ed. New York: Holt, Rinehart, and Winston, 1977. p. 57–66.

[41] Mizushima M. Quantum mechanics of atomic spectra and atomic structure. New York: W.A. Benjamin, Inc., 1970. p. 17.

[42] Atkins PW. Physical chemistry. 2nd ed. San Francisco: W.H. Freeman, 1982. p. 589.

[43] Nellis WJ. Making metallic hydrogen. Sci Amer 2000; p. 84–90.

[44] Roncin JY, Launay F, Larzilliere M. High resolution emission spectrum of H₂ between 78 and 118 nm. Can J Phys 1984;62:1686–705.

Spectral emission of fractional quantum energy levels of atomic hydrogen from a helium–hydrogen plasma and the implications for dark matter

Randell L. Mills *, Paresh Ray

BlackLight Power, Inc., 493 Old Trenton Road, Cranbury, NJ 08512, USA

Abstract

From a solution of a Schrödinger-type wave equation with a nonradiative boundary condition based on Maxwell's equations, Mills predicts that atomic hydrogen may undergo a catalytic reaction with certain atomized elements and ions which singly or multiply ionize at integer multiples of the potential energy of atomic hydrogen, $m27.2$ eV wherein m is an integer. The reaction involves a nonradiative energy transfer to form a hydrogen atom that is lower in energy than unreacted atomic hydrogen that corresponds to a fractional principal quantum number ($n = 1/p = 1/$integer replaces the well-known parameter $n =$ integer in the Rydberg equation for hydrogen excited states). One such atomic catalytic system involves helium ions. The second ionization energy of helium is 54.4 eV; thus, the ionization reaction of He^+ to He^{2+} has a net enthalpy of reaction of 54.4 eV which is equivalent to 2×27.2 eV. Since the products of the catalysis reaction have binding energies of $m27.2$ eV, they may further serve as catalysts. Extreme ultraviolet (EUV) spectroscopy was recorded on microwave and glow discharges of helium with 2% hydrogen. Novel emission lines were observed with energies of $q13.6$ eV where $q = 1, 2, 3, 4, 6, 7, 8, 9,$ or 11 or these lines inelastically scattered by helium atoms wherein 21.2 eV was absorbed in the excitation of He ($1s^2$) to He ($1s^1 2p^1$). These lines were identified as hydrogen transitions to electronic energy levels below the "ground" state corresponding to fractional quantum numbers. Furthermore, astrophysical data was reviewed and such transitions were found to match the spectral lines of the extreme ultraviolet background of interstellar space. They may resolve the paradox of the identity of dark matter and account for many celestial observations such as diffuse $H\alpha$ emission is ubiquitous throughout the Galaxy and widespread sources of flux shortward of 912 Å are required. Additional hydrogen transitions were also assigned to unidentified lines in the solar EUV spectrum which may resolve the solar neutrino problem, the mystery of the cause of sunspots and other solar activity, and why the Sun emits X-rays. © 2001 Published by Elsevier Science Ltd. on behalf of the International Association for Hydrogen Energy.

1. Introduction

1.1. Background

J. J. Balmer showed in 1885 that the frequencies for some of the lines observed in the emission spectrum of atomic hydrogen could be expressed with a completely empirical relationship. This approach was later extended by J. R. Rydberg, who showed that all of the spectral lines of atomic hydrogen were given by the equation

$$\bar{v} = R \left(\frac{1}{n_f^2} - \frac{1}{n_i^2} \right), \tag{1}$$

where $R = 109{,}677\ \mathrm{cm}^{-1}$, $n_f = 1, 2, 3, \ldots$, $n_i = 2, 3, 4, \ldots$, and $n_i > n_f$.

Niels Bohr, in 1913, developed a theory for atomic hydrogen that gave energy levels in agreement with Rydberg's equation. An identical equation, based on a totally differ-

* Corresponding author. Tel.: +1-609-490-1090; fax: +1-609-490-1066.

E-mail address: rmills@blacklightpower.com (R.L. Mills).

ent theory for the hydrogen atom, was developed by E. Schrödinger, and independently by W. Heisenberg, in 1926.

$$E_n = -\frac{e^2}{n^2 8\pi\varepsilon_0 a_H} = -\frac{13.598 \text{ eV}}{n^2}, \qquad (2a)$$

$$n = 1, 2, 3, \dots, \qquad (2b)$$

where a_H is the Bohr radius for the hydrogen atom (52.947 pm), e is the magnitude of the charge of the electron, and ε_0 is the vacuum permittivity. Based on the solution of a Schrödinger-type wave equation with a nonradiative boundary condition based on Maxwell's equations, Mills [1–41] predicts that atomic hydrogen may undergo a catalytic reaction with certain atomized elements or certain gaseous ions which singly or multiply ionize at integer multiples of the potential energy of atomic hydrogen, 27.2 eV. The reaction involves a nonradiative energy transfer to form a hydrogen atom that is lower in energy than unreacted atomic hydrogen that corresponds to a fraction principal quantum number where Eq. (2b), should be replaced by Eq. (2c).

$$n = 1, 2, 3, \dots \quad \text{and} \quad n = \frac{1}{2}, \frac{1}{3}, \frac{1}{4}, \dots . \qquad (2c)$$

A number of independent experimental observations lead to the conclusion that atomic hydrogen can exist in fractional quantum states that are at lower energies than the traditional "ground" ($n = 1$) state.

1.2. Experimental data of lower-energy hydrogen

Observation of intense extreme ultraviolet (EUV) emission at low temperatures (e.g. $\approx 10^3$ K) from atomic hydrogen and certain atomized elements or certain gaseous ions [7–24] has been reported previously. The only pure elements that were observed to emit EUV were those wherein the ionization of t electrons from an atom to a continuum energy level is such that the sum of the ionization energies of the t electrons is approximately $m27.2$ eV where t and m are each an integer. Potassium, cesium, and strontium atoms and Rb^+ ion ionize at integer multiples of the potential energy of atomic hydrogen and caused emission. Whereas, the chemically similar atoms, sodium, magnesium and barium, do not ionize at integer multiples of the potential energy of atomic hydrogen and caused no emission.

Prior studies that support the possibility of a novel reaction of atomic hydrogen which produces a chemically generated or assisted plasma, fractional-principal-quantum-energy-level hydrogen atoms, molecules, and hydride ions, and novel hydride compounds include extreme ultraviolet (EUV) spectroscopy [7–9,11–24], plasma formation [7–24], power generation [10–12,17,25], and analysis of chemical compounds [8,9,20,22–39]. Exemplary studies include:

(1) The recent analysis of mobility and spectroscopy data of individual electrons in liquid helium which shows direct experimental confirmation that electrons may have fractional principal quantum energy levels [6].

(2) The observation of continuum state emission of Cs^{2+} and Ar^{2+} at 533 and 456 Å, respectively, with the absence of the other corresponding Rydberg series of lines from these species which confirmed the resonant nonradiative energy transfer of 27.2 eV from atomic hydrogen to the catalysts atomic Cs or Ar^+ [9].

(3) The spectroscopic observation of the predicted hydride ion $H^-(1/2)$ of hydrogen catalysis by either Cs or Ar^+ catalyst at 4070 Å corresponding to its predicted binding energy of 3.05 eV [9].

(4) The observation of characteristic emission from K^{3+} which confirmed the resonant nonradiative energy transfer of 3×27.2 eV from atomic hydrogen to atomic potassium [8].

(5) The spectroscopic observation of the predicted $H^-(1/4)$ hydride ion of hydrogen catalysis by potassium catalyst at 1100 Å corresponding to its predicted binding energy of 11.2 eV [8].

(6) The identification of transitions of atomic hydrogen to lower-energy levels corresponding to fractional principal quantum numbers in the extreme ultraviolet emission spectrum from interstellar medium [1,5].

(7) The EUV spectroscopic observation of lines by the Institut für Niedertemperatur-Plasmaphysik e.V. that could be assigned to transitions of atomic hydrogen to lower-energy levels corresponding to fractional principal quantum numbers and the emission from the excitation of the corresponding hydride ions [14].

(8) The observation of novel EUV emission lines from microwave discharges of argon or helium with 10% hydrogen that matched those predicted for vibrational transitions of H_2^* $[n = 1/4; n^* = 2]^+$ with energies of $v1.185$ eV, $v = 17$–38 that terminated at the predicted dissociation limit, E_D, of H_2 $[n = 1/4]^+$, $E_D = 42.88$ eV (28.92 nm) [7].

(9) The observation by the Institut für Niedertemperatur-Plasmaphysik e.V. of an anomalous plasma and plasma afterglow duration formed with hydrogen–potassium mixtures [15].

(10) The observation of anomalous afterglow durations of plasmas formed by catalysts providing a net enthalpy of reaction within thermal energies of $m27.28$ eV [15,16].

(11) The observation of Lyman series in the EUV that represents an energy release 10 times hydrogen combustion which is greater than that of any possible known chemical reaction [8–24].

(12) The observation of line emission by the Institut für Niedertemperatur-Plasmaphysik e.V. with a 4° grazing incidence EUV spectrometer that was 100 times more energetic than the combustion of hydrogen [14].

(13) The observation of anomalous plasmas formed with strontium and argon catalysts at 1% of the theoretical or prior known voltage requirement with a light output for power input up to 8600 times that of the control standard light source [11,12,17].

(14) The observation that the optically measured output power of gas cells for power supplied to the glow discharge increased by over two orders of magnitude depending on the presence of less than 1% partial pressure of certain catalysts in hydrogen gas or argon–hydrogen gas mixtures [10].

(15) The isolation of novel hydrogen compounds as products of the reaction of atomic hydrogen with atoms and ions which formed an anomalous plasma as reported in the EUV studies [20,22–39].

(16) The identification of novel hydride compounds by (i) time of flight secondary ion mass spectroscopy which showed a dominant hydride ion in the negative ion spectrum, (ii) X-ray photoelectron spectroscopy which showed novel hydride peaks and significant shifts of the core levels of the primary elements bound to the novel hydride ions, (iii) ^{1}H nuclear magnetic resonance spectroscopy (NMR) which showed extraordinary upfield chemical shifts compared to the NMR of the corresponding ordinary hydrides, and (iv) thermal decomposition with analysis by gas chromatography, and mass spectroscopy which identified the compounds as hydrides [20,22–39].

(17) The NMR identification of novel hydride compounds MH^-X wherein M is the metal, X, is a halide, and H^- comprises a novel high binding energy hydride ion identified by a large distinct upfield resonance [25,26,29].

(18) The replication of the NMR results of the identification of novel hydride compounds by large distinct upfield resonances at Spectral Data Services, University of Massachusetts Amherst, University of Delaware, Grace Davison, and National Research Council of Canada [25].

(19) The NMR identification of novel hydride compounds MH^+ and MH_2^+ wherein M is the metal and H^- comprises a novel high binding energy hydride ion, identified by a large distinct upfield resonance that proves the hydride ion is different from the hydride ion of the corresponding known compound of the same composition [25].

(20) The differential scanning calorimetry (DSC) measurement of minimum heat of formation of KHI by the catalytic reaction of potassium with atomic hydrogen and KI that were over -2000 kJ mol^{-1} H$_2$ compared to the enthalpy of combustion of hydrogen of -241.8 kJ mol^{-1} H$_2$ [39].

1.3. Mechanism of the formation of lower-energy hydrogen

The mechanism of EUV emission, formation of novel hydrides, and certain EUV lines from interstellar medium cannot be explained by the conventional energy levels of hydrogen, but it is predicted by a solution of the Schrödinger equation with a nonradiative boundary constraint put forward by Mills [1]. Mills predicts that certain atoms or ions serve as catalysts to release energy from hydrogen to produce an increased binding energy hydrogen atom called a *hydrino atom* having a binding energy given by Eq. (2a) where

$$n = \frac{1}{2}, \frac{1}{3}, \frac{1}{4}, \ldots, \frac{1}{p} \tag{3}$$

and p is an integer greater than 1, designated as $H[a_H/p]$ where a_H is the radius of the hydrogen atom. Hydrinos are predicted to form by reacting an ordinary hydrogen atom with a catalyst having a net enthalpy of reaction of about

$$m27.2 \text{ eV}, \tag{4}$$

where m is an integer. This catalysis releases energy from the hydrogen atom with a commensurate decrease in size of the hydrogen atom, $r_n = na_H$. For example, the catalysis of $H(n=1)$ to $H(n=1/2)$ releases 40.8 eV, and the hydrogen radius decreases from a_H to $1/2a_H$.

The excited energy states of atomic hydrogen are also given by Eq. (2a) except with Eq. (2b). The $n=1$ state is the "ground" state for "pure" photon transitions (the $n=1$ state can absorb a photon and go to an excited electronic state, but it cannot release a photon and go to a lower-energy electronic state). However, an electron transition from the ground state to a lower-energy state is possible by a nonradiative energy transfer such as multipole coupling or a resonant collision mechanism. These lower-energy states have fractional quantum numbers $n=1/\text{integer}$. Processes that occur without photons and that require collisions are common. For example, the exothermic chemical reaction of $H + H$ to form H_2 does not occur with the emission of a photon. Rather, the reaction requires a collision with a third body, M, to remove the bond energy — $H + H + M \rightarrow H_2 + M^*$ [42]. The third body distributes the energy from the exothermic reaction, and the end result is the H_2 molecule and an increase in the temperature of the system.

Some commercial phosphors are based on nonradiative energy transfer involving multipole coupling. For example, the strong absorption strength of Sb^{3+} ions along with the efficient nonradiative transfer of excitation from Sb^{3+} to Mn^{2+}, are responsible for the strong manganese luminescence from phosphors containing these ions [43].
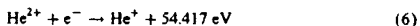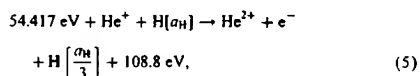
Similarly, the $n=1$ state of hydrogen and the $n=1/\text{integer}$ states of hydrogen are nonradiative, but a transition between two nonradiative states is possible via a nonradiative energy transfer, say $n=1$ to $1/2$. In these cases, during the transition the electron couples to another electron transition, electron transfer reaction, or inelastic scattering reaction which can absorb the exact amount of energy that must be removed from the hydrogen atom. Thus, a catalyst provides a net positive enthalpy of reaction of $m27.2$ eV (i.e. it absorbs $m27.2$ eV where m is an integer). Certain atoms or ions serve as catalysts which resonantly accept energy from hydrogen atoms and release the energy to the surroundings to effect electronic transitions to fractional quantum energy levels.

1   The catalysis of hydrogen involves the nonradiative trans-
fer of energy from atomic hydrogen to a catalyst which may
3   then release the transferred energy by radiative and nonra-
diative mechanisms. As a consequence of the nonradiative
5   energy transfer, the hydrogen atom becomes unstable and
emits further energy until it achieves a lower-energy nonra-
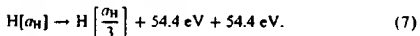7   diative state having a principal energy level given by Eqs.
(2a) and (3).

9   *1.4. Catalysts*

1.4.1. Helium ion
11   Helium ion (He$^+$) is such a catalyst because the second
ionization energy of helium is 54.417 eV, which is equiva-
13   lent to $m = 2$ in Eq. (4). In this case, the catalysis reaction is

$$54.417 \text{ eV} + \text{He}^+ + \text{H}[a_H] \rightarrow \text{He}^{2+} + e^-$$

$$+ \text{H}\left[\frac{a_H}{3}\right] + 108.8 \text{ eV}, \tag{5}$$

$$\text{He}^{2+} + e^- \rightarrow \text{He}^+ + 54.417 \text{ eV} \tag{6}$$

and, the overall reaction is

$$\text{H}[a_H] \rightarrow \text{H}\left[\frac{a_H}{3}\right] + 54.4 \text{ eV} + 54.4 \text{ eV}. \tag{7}$$

15   The energy given off during catalysis is much greater than
the energy lost to the catalyst. The energy released is large as
17   compared to conventional chemical reactions. For example,
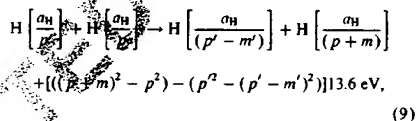when hydrogen and oxygen gases undergo combustion to
19   form water

$$\text{H}_2(g) + \frac{1}{2}\text{O}_2(g) \rightarrow \text{H}_2\text{O}(l) \tag{8}$$
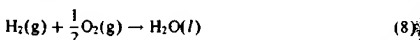
the known enthalpy of formation of water is $\Delta H_f = -$
21   286 kJ mol^{-1} or 1.48 eV per hydrogen atom. By contrast,
each ($n = 1$) ordinary hydrogen atom undergoing cataly-
23   sis releases a net of 40.8 eV. Moreover, further catalytic
transitions may occur: $n = \frac{1}{2} \rightarrow \frac{1}{3}, \frac{1}{3} \rightarrow \frac{1}{4}, \frac{1}{4} \rightarrow \frac{1}{5}$, and
25   so on. Once catalysis begins, hydrinos autocatalyze further
in a process called *disproportionation*. This mechanism is
27   similar to that of an inorganic ion catalyst. But, hydrino
catalysis should have a higher reaction rate than that of
29   the inorganic ion catalyst due to the better match of the
enthalpy to $m27.2$ eV.

31   *1.4.2. Hydrino catalysis*
In a process called *disproportionation*, lower-energy hy-
33   drogen atoms, *hydrinos*, can act as catalysts because each of
the metastable excitation, resonance excitation, and ioniza-
35   tion energy of a hydrino atom is $m27.2$ eV (Eq. (4)). The
transition reaction mechanism of a first hydrino atom af-
37   fected by a second hydrino atom involves the resonant cou-
pling between the atoms of m degenerate multipoles each
39   having 27.21 eV of potential energy [1]. The energy trans-
41   fer of $m27.2$ eV from the first hydrino atom to the second
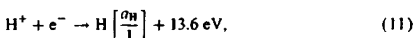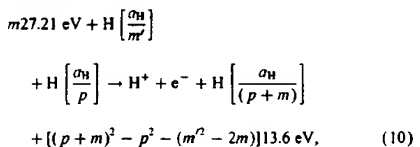
hydrino atom causes the central field of the first atom to
increase by m and its electron to drop m levels lower from   43
a radius of a_H/p to a radius of $a_H/(p + m)$. The second
interacting lower-energy hydrogen is either excited to a   45
metastable state, excited to a resonance state, or ionized by
the resonant energy transfer. The resonant transfer may oc-   47
cur in multiple stages. For example, a nonradiative transfer
by multipole coupling may occur wherein the central field of   49
the first increases by m, then the electron of the first drops m
levels lower from a radius of a_H/p to a radius of $a_H/(p + m)$ 51
with further resonant energy transfer. The energy transferred
by multipole coupling may occur by a mechanism that is   53
analogous to photon absorption involving an excitation to a
virtual level. Or, the energy transferred by multipole cou-   55
pling during the electron transition of the first hydrino atom
may occur by a mechanism that is analogous to two-photon   57
absorption involving a first excitation to a virtual level and a
second excitation to a resonant or continuum level [44–46].   59
The transition energy greater than the energy transferred
to the second hydrino atom may appear as a photon in a   61
vacuum medium.

The transition of $\text{H}[a_H/p]$ to $\text{H}[a_H/(p + m)]$ induced by   63
a multipole resonance transfer of $m27.21$ eV (Eq. (4)) and
a transfer of $[(p')^2 - (p' - m')^2]13.6$ eV $- m27.2$ eV with   65
a resonance state of $\text{H}[a_H/(p' - m')]$ excited in $\text{H}[a_H/p']$ is
represented by   67

$$\text{H}\left[\frac{a_H}{p}\right] + \text{H}\left[\frac{a_H}{p'}\right] \rightarrow \text{H}\left[\frac{a_H}{(p' - m')}\right] + \text{H}\left[\frac{a_H}{(p + m)}\right]$$

$$+[((p + m)^2 - p^2) - (p'^2 - (p' - m')^2)]13.6 \text{ eV}, \tag{9}$$

where p, p', m, and m' are integers.
Hydrinos may be ionized during a disproportionation re-   69
action by the resonant energy transfer. A hydrino atom with
the initial lower-energy state quantum number p and radius   71
a_H/p may undergo a transition to the state with lower-energy
state quantum number $(p + m)$ and radius $a_H/(p + m)$ by   73
reaction with a hydrino atom with the initial lower-energy
state quantum number m', initial radius a_H/m', and final ra-   75
dius a_H that provides a net enthalpy of $m27.2$ eV (Eq. (4)).
Thus, reaction of hydrogen-type atom, $\text{H}[a_H/p]$, with the   77
hydrogen-type atom, $\text{H}[a_H/m']$, that is ionized by the reso-
nant energy transfer to cause a transition reaction is repre-   79
sented by

$$m27.21 \text{ eV} + \text{H}\left[\frac{a_H}{m'}\right]$$

$$+ \text{H}\left[\frac{a_H}{p}\right] \rightarrow \text{H}^+ + e^- + \text{H}\left[\frac{a_H}{(p + m)}\right]$$

$$+ [(p + m)^2 - p^2 - (m'^2 - 2m)]13.6 \text{ eV}, \tag{10}$$

$$\text{H}^+ + e^- \rightarrow \text{H}\left[\frac{a_H}{1}\right] + 13.6 \text{ eV}, \tag{11}$$

81

and, the overall reaction is

$$H\left[\frac{a_H}{m'}\right] + H\left[\frac{a_H}{p}\right] \rightarrow H\left[\frac{a_H}{1}\right] + H\left[\frac{a_H}{(p+m)}\right]$$
$$+ [2pm + m^2 - m'^2]13.6 + 13.6 \text{ eV}. \quad (12)$$

Helium ion catalyzes $H[a_H]$ to $H[a_H/3]$ as shown in Eqs. (5)–(7). Further disproportionation reactions may then proceed

$$H\left[\frac{a_H}{3}\right] + H\left[\frac{a_H}{3}\right] \rightarrow H\left[\frac{a_H}{4}\right] + H\left[\frac{a_H}{2}\right] + 27.2 \text{ eV}, \quad (13)$$

$$H[a_H] + H\left[\frac{a_H}{2}\right] \rightarrow H\left[\frac{a_H}{3}\right] + H^+ + e^- + 54.4 \text{ eV}, \quad (14)$$

$$H\left[\frac{a_H}{2}\right] + H\left[\frac{a_H}{2}\right] \rightarrow H\left[\frac{a_H}{3}\right] + H^+ + e^- + 13.6 \text{ eV}, \quad (15)$$

$$H\left[\frac{a_H}{2}\right] + H\left[\frac{a_H}{2}\right] \rightarrow H\left[\frac{a_H}{3}\right] + H[a_H] + 27.2 \text{ eV}, \quad (16)$$

$$H\left[\frac{a_H}{2}\right] + H\left[\frac{a_H}{2}\right] \rightarrow H\left[\frac{a_H}{4}\right] + H^+ + e^- + 108.8 \text{ eV}, \quad (17)$$

$$H\left[\frac{a_H}{2}\right] + H\left[\frac{a_H}{2}\right] \rightarrow H\left[\frac{a_H}{4}\right] + H[a_H] + 122.4 \text{ eV}, \quad (18)$$

$$H\left[\frac{a_H}{3}\right] + H\left[\frac{a_H}{2}\right] \rightarrow H\left[\frac{a_H}{4}\right] + H^+ + e^- + 40.8 \text{ eV}, \quad (19)$$

$$H\left[\frac{a_H}{3}\right] + H\left[\frac{a_H}{2}\right] \rightarrow H\left[\frac{a_H}{4}\right] + H[a_H] + 54.4 \text{ eV}, \quad (20)$$

$$H\left[\frac{a_H}{4}\right] + H\left[\frac{a_H}{2}\right] \rightarrow H\left[\frac{a_H}{5}\right] + H^+ + e^- + 68 \text{ eV}, \quad (21)$$

$$H\left[\frac{a_H}{4}\right] + H\left[\frac{a_H}{2}\right] \rightarrow H\left[\frac{a_H}{5}\right] + H[a_H] + 81.6 \text{ eV}, \quad (22)$$

$$H\left[\frac{a_H}{2}\right] + He^+ \rightarrow H[a_H] + He^{2+} + e^- + 108.8 \text{ eV}, \quad (23)$$

$$H[a_H] + H\left[\frac{a_H}{3}\right] \rightarrow H\left[\frac{a_H}{4}\right] + H^+ + e^- + 81.6 \text{ eV}, \quad (24)$$

$$H\left[\frac{a_H}{3}\right] + H\left[\frac{a_H}{3}\right] \rightarrow H\left[\frac{a_H}{5}\right] + H\left[\frac{a_H}{2}\right] + 149.6 \text{ eV}, \quad (25)$$

$$H\left[\frac{a_H}{3}\right] + H\left[\frac{a_H}{3}\right] \rightarrow H\left[\frac{a_H}{5}\right] + H[a_H] + 108.8 \text{ eV}, \quad (26)$$

$$H\left[\frac{a_H}{3}\right] + H\left[\frac{a_H}{3}\right] \rightarrow H\left[\frac{a_H}{5}\right] + H^+ + e^- + 95.2 \text{ eV}, \quad (27)$$

$$H\left[\frac{a_H}{4}\right] + H\left[\frac{a_H}{3}\right] \rightarrow H\left[\frac{a_H}{5}\right] + H\left[\frac{a_H}{2}\right] + 54.4 \text{ eV}, \quad (28)$$

$$H\left[\frac{a_H}{4}\right] + H\left[\frac{a_H}{3}\right] \rightarrow H\left[\frac{a_H}{5}\right] + H[a_H] + 13.6 \text{ eV}, \quad (29)$$

$$H\left[\frac{a_H}{5}\right] + H\left[\frac{a_H}{2}\right] \rightarrow H\left[\frac{a_H}{6}\right] + H^+ + e^- + 95.2 \text{ eV}, \quad (30)$$

$$H\left[\frac{a_H}{5}\right] + H\left[\frac{a_H}{2}\right] \rightarrow H\left[\frac{a_H}{6}\right] + H[a_H] + 108.8 \text{ eV}, \quad (31)$$

$$H\left[\frac{a_H}{6}\right] + H\left[\frac{a_H}{2}\right] \rightarrow H\left[\frac{a_H}{7}\right] + H^+ + e^- + 122.4 \text{ eV}, \quad (32)$$

$$H\left[\frac{a_H}{6}\right] + H\left[\frac{a_H}{2}\right] \rightarrow H\left[\frac{a_H}{7}\right] + H[a_H] + 136 \text{ eV}, \quad (33)$$

$$H\left[\frac{a_H}{7}\right] + H\left[\frac{a_H}{2}\right] \rightarrow H\left[\frac{a_H}{8}\right] + H^+ + e^- + 149.6 \text{ eV}, \quad (34)$$

$$H\left[\frac{a_H}{7}\right] + H\left[\frac{a_H}{2}\right] \rightarrow H\left[\frac{a_H}{8}\right] + H[a_H] + 163.2 \text{ eV}. \quad (35)$$

1.4.3. Inelastic scattering by atomic helium

It is proposed that the photons that arise from hydrogen catalysis may undergo inelastic helium scattering. That is, the catalytic reaction

$$H[a_H] \xrightarrow{He^*} H\left[\frac{a_H}{3}\right] + 54.4 + 54.4 \text{ eV} \quad (36)$$

yields two 54.4 eV photons (228 Å). When each of these photons strikes He $(1s^2)$, 21.2 eV is absorbed in the excitation to He $(1s^1 2p^1)$. This leaves a 33.19 eV (374 Å) photon peak shown in Table 1. Thus, for helium the inelastic scattered peak of 54.4 eV photons from Eqs. (7), (14), (20), and (28) is given by

$$E = 54.4 - 21.21 \text{ eV} = 33.19 \text{ eV} \ (374 \text{ Å}). \quad (37)$$

For helium, the inelastic scattered peak of 27.2 eV photons from Eqs. (13) and (16) is given by

$$E = 27.2 - 21.21 \text{ eV} = 5.99 \text{ eV} \ (2071 \text{ Å}). \quad (38)$$

Table 1

Observed line emission from helium–hydrogen plasmas assigned to the disproportionation reactions given by Eqs. (9)–(12) and helium inelastic scattered peaks of hydrogen transitions, wherein the photon strikes He ($1s^2$) and 21.2 eV is absorbed in the excitation to He ($1s^1 2p^1$)

Observed line (Å)	Predicted (Mills) (Å)	Assignment (Mills)	Equation no.	Figures
82.9	82.9	$H\left[\frac{a_H}{3}\right] + H\left[\frac{a_H}{4}\right] \rightarrow H\left[\frac{a_H}{3}\right] + H\left[\frac{a_H}{2}\right] + 149.6\,\text{eV},$	(25)	12
		$H\left[\frac{a_H}{4}\right] + H\left[\frac{a_H}{4}\right] \rightarrow H\left[\frac{a_H}{8}\right] + H^+ + e^- + 149.6\,\text{eV},$	(34)	
101.3	101.3	$H\left[\frac{a_H}{2}\right] + H\left[\frac{a_H}{2}\right] \rightarrow H\left[\frac{a_H}{4}\right] + H[a_H] + 122.4\,\text{eV},$	(18)	12
		$H\left[\frac{a_H}{6}\right] + H\left[\frac{a_H}{2}\right] \rightarrow H\left[\frac{a_H}{7}\right] + H^+ + e^- + 122.4\,\text{eV},$	(32)	
130.3[a]	130.3	$H\left[\frac{a_H}{3}\right] + H\left[\frac{a_H}{4}\right] \rightarrow H\left[\frac{a_H}{5}\right] + H^+ + e^- + 95.2\,\text{eV},$	(27)	12
		$H\left[\frac{a_H}{5}\right] + H\left[\frac{a_H}{2}\right] \rightarrow H\left[\frac{a_H}{6}\right] + H^+ + e^- + 95.2\,\text{eV},$	(30)	
141.5	141.5	$H\left[\frac{a_H}{2}\right] + H\left[\frac{a_H}{2}\right] \rightarrow H\left[\frac{a_H}{4}\right] + H^+ + e^- + 108.8\,\text{eV},$	(17)	
		$H\left[\frac{a_H}{2}\right] + He^+ \rightarrow H\left[\frac{a_H}{4}\right] + He^{2+} + e^- + 108.8\,\text{eV},$	(23)	
		$H\left[\frac{a_H}{4}\right] + H\left[\frac{a_H}{3}\right] \rightarrow H\left[\frac{a_H}{5}\right] + H[a_H] + 108.8\,\text{eV},$	(26)	
		$H\left[\frac{a_H}{5}\right] + H\left[\frac{a_H}{2}\right] \rightarrow H\left[\frac{a_H}{6}\right] + H[a_H] + 108.8\,\text{eV},$	(31)	
		$108.8\,\text{eV} + He\,(1s^2) \rightarrow He\,(1s^1 2p^1) \rightarrow +87.59\,\text{eV},$	(43)	
205	205	$H\left[\frac{a_H}{4}\right] + H\left[\frac{a_H}{4}\right] \rightarrow H\left[\frac{a_H}{5}\right] + H[a_H] + 81.6\,\text{eV},$	(22)	7, 8, 9, 10, 12
		$H[a_H] + H\left[\frac{a_H}{3}\right] \rightarrow H\left[\frac{a_H}{4}\right] + H^+ + e^- + 81.6\,\text{eV},$	(24)	
		$81.6\,\text{eV} + He\,(1s^2) \rightarrow He\,(1s^1 2p^1) \rightarrow +60.39\,\text{eV},$	(41)	
304	304	$H\left[\frac{a_H}{3}\right] + H\left[\frac{a_H}{2}\right] \rightarrow H\left[\frac{a_H}{4}\right] + H^+ + e^- + 40.8\,\text{eV},$	(19)	7, 8, 9, 10, 12
304	304	$He^+ \,(n=2) \rightarrow He^+ \,(n=1) + 40.8\,\text{eV}^b,$		7, 8, 9, 10, 12
374	374	$H[a_H] \xrightarrow{He^+} H\left[\frac{a_H}{3}\right] + 54.4 + 54.4\,\text{eV},$	(5)–(7)	7, 8, 9, 10, 12
		$H[a_H] + H\left[\frac{a_H}{2}\right] \rightarrow H\left[\frac{a_H}{3}\right] + H^+ + e^- + 54.4\,\text{eV},$	(14)	
		$H\left[\frac{a_H}{3}\right] + H\left[\frac{a_H}{2}\right] \rightarrow H\left[\frac{a_H}{4}\right] + H[a_H] + 54.4\,\text{eV},$	(20)	
		$H\left[\frac{a_H}{4}\right] + H\left[\frac{a_H}{2}\right] \rightarrow H\left[\frac{a_H}{3}\right] + H\left[\frac{a_H}{2}\right] + 54.4\,\text{eV},$	(28)	
		$54.4\,\text{eV} + He\,(1s^2) \rightarrow He\,(1s^1 2p^1) \rightarrow +33.19\,\text{eV},$	(37)	
456	456	$H\left[\frac{a_H}{3}\right] + H\left[\frac{a_H}{3}\right] \rightarrow H\left[\frac{a_H}{4}\right] + H\left[\frac{a_H}{2}\right] + 27.2\,\text{eV},$	(13)	7, 8, 9, 10, 12
		$H\left[\frac{a_H}{2}\right] + H\left[\frac{a_H}{4}\right] \rightarrow H\left[\frac{a_H}{3}\right] + H[a_H] + 27.2\,\text{eV},$	(16)	
584	584	$He\,(1s^1 2p^1) \rightarrow He\,(1s^2) + 21.2\,\text{eV}^c,$		6, 7, 10, 13
633	633	$H\left[\frac{a_H}{3}\right] + H\left[\frac{a_H}{2}\right] \rightarrow H\left[\frac{a_H}{4}\right] + H^+ + e^- + 40.8\,\text{eV},$	(19)	13
		$40.8\,\text{eV} + He\,(1s^2) \rightarrow He\,(1s^1 2p^1) \rightarrow +19.59\,\text{eV},$	(39)	
633	633	$He^+ \,(n=2) \rightarrow He^+ \,(n=1) + 40.8\,\text{eV}^b,$		13
		$40.8\,\text{eV} + He\,(1s^2) \rightarrow He\,(1s^1 2p^1) \rightarrow +19.59\,\text{eV},$	(39)	

Table. 1 (*continued*).

Observed line (Å)	Predicted (Mills) (Å)	Assignment (Mills)	Equation no.	Figures
912	912	$H\left[\frac{a_H}{2}\right] + H\left[\frac{a_H}{2}\right] \longrightarrow H\left[\frac{a_H}{3}\right] + H^+ + e^- + 13.6 \text{ eV},$	(15)	14
		$H\left[\frac{a_H}{4}\right] + H\left[\frac{a_H}{3}\right] \longrightarrow H\left[\frac{a_H}{3}\right] + H[a_H] + 13.6 \text{ eV}.$	(29)	
912	912	$H^+ + e^- \longrightarrow H[a_H] + 13.6 \text{ eV}^d.$		15

ᵃ Weak shoulder on the 141.5 Å peak.

ᵇ In Figs. 7–10, and 12, the peak corresponding to He⁺ (n = 3) → He⁺ (n = 1) + 48.35 eV (256 Å) was absent which makes this assignment difficult.

ᶜ The intensity which is off-scale in Fig. 13 as 56,771 photons/s; thus, the transition He (1s²) → He (1s¹2p¹) dominated the inelastic scattering of EUV peaks.

ᵈ The ratio of the Lβ peak to the 912 Å peak of the helium–hydrogen plasma shown in Fig. 14 was 2; whereas, the ratio of the Lβ peak to the 912 Å peak of the control hydrogen plasma shown in Fig. 15, was 8 which makes this assignment difficult.

1 For helium, the inelastic scattered peak of 40.8 eV photons from Eq. (19) is given by

$$E = 40.8 - 21.21 \text{ eV} = 19.59 \text{ eV} \ (633 \text{ Å}). \tag{39}$$

3 For helium, the inelastic scattered peak of 68 eV photons from Eq. (21) is given by

$$E = 68 - 21.21 \text{ eV} = 46.79 \text{ eV} \ (265 \text{ Å}). \tag{40}$$

5 For helium, the inelastic scattered peak of 81.6 eV photons from Eqs. (22) and (24) is given by

$$E = 81.6 - 21.21 \text{ eV} = 60.39 \text{ eV} \ (205 \text{ Å}). \tag{41}$$

7 For helium, the inelastic scattered peak of 95.2 eV photons from Eqs. (27) and (30) is given by

$$E = 95.2 - 21.21 \text{ eV} = 73.99 \text{ eV} \ (167.6 \text{ Å}). \tag{42}$$

9 For helium, the inelastic scattered peak of 108.8 eV photons from Eqs. (17), (23), (26), and (31) is given by

$$E = 108.8 - 21.21 \text{ eV} = 87.59 \text{ eV} \ (141.6 \text{ Å}). \tag{43}$$

11 *1.5. EUV spectroscopy detects lower-energy hydrogen*

13 Previously reported lines observed at the Institut für Niedertemperatur-Plasmaphysik e.V. by EUV spectroscopy 15 could be assigned to transitions of atomic hydrogen to lower-energy levels corresponding to hydrinos and the emission from the excitation of the corresponding hy- 17 dride ions [14]. For example, the product of the catalysis of atomic hydrogen with potassium metal, H[a_H/4], may 19 serve as both a catalyst and a reactant to form H[a_H/3] and H[a_H/6]. The transition of H[a_H/4] to H[a_H/6] induced by 21 a multipole resonance transfer of (54.4 eV) (2 × 27.2 eV) and a transfer of 40.8 eV with a resonance state of H[a_H/3] 23

excited in H[a_H/4] is represented by

$$H\left[\frac{a_H}{4}\right] + H\left[\frac{a_H}{4}\right] \longrightarrow H\left[\frac{a_H}{6}\right] + H\left[\frac{a_H}{3}\right] + 176.8 \text{ eV}.$$

$$\tag{44}$$

The predicted 176.8 eV (70.2 Å) photon is a close match 25 with the observed 73.0 Å line. The energy of this line emission corresponds to an equivalent temperature of 27 1,000,000 °C and an energy over 100 times the energy of combustion of hydrogen. 29

Since the sun and stars contain significant amounts of He⁺ and atomic hydrogen, catalysis of atomic hydrogen by He⁺ 31 as given by Eqs. (5)–(7) may occur. Also, the simultaneous ionization of two hydrogen atoms may provide a net en- 33 thalpy given by Eq. (4) to catalyze hydrino formation. Once formed, hydrinos have binding energies given by Eqs. (2a) 35 and (3); thus, they may serve as reactants which provide a net enthalpy of reaction given by Eq. (4). Characteris- 37 tic emissions from the Sun corresponding to these reactions may be observed, and stellar production may be a source of 39 hydrinos in interstellar space where further transitions may occur with corresponding emission of characteristic EUV 41 lines.

The detection of atomic hydrogen in fractional quantum 43 energy levels below the traditional "ground" state — hydrinos — was previously reported [1,5] by the assignment 45 of soft X-ray emissions from the interstellar medium, the Sun, and stellar flares, and by assignment of certain lines 47 obtained by the far-infrared absolute spectrometer (FIRAS) on the cosmic background explorer (COBE) on the new 49 molecular species — the diatomic hydrino molecule — was reported by the assignment of certain infrared line emissions 51 from the Sun. The detection of a new hydride species — hydrino hydride ion — was reported by the assignment of 53 certain soft X-ray, ultraviolet (UV), and visible emissions from the Sun. This has implications for several unresolved 55 astrophysical problems such as the identity of dark matter and the solar neutrino paradox. 57

1   We report that extreme ultraviolet (EUV) spectroscopy
was recorded on microwave and glow discharges of he-
3   lium with 2% hydrogen. Novel emission lines were observed
with energies of $q13.6$ eV where $q = 1, 2, 3, 4, 6, 7, 8, 9,$ *or*
5   11 or these lines inelastically scattered by helium atoms
wherein 21.2 eV was absorbed in the excitation of He($1s^2$)
7   to He ($1s^1 2p^1$). These lines were identified as hydrogen tran-
sitions to electronic energy levels below the "ground" state
9   corresponding to fractional quantum numbers. A compari-
son was made between the plasma results and astrophysical
11 data. Similar lower-energy-hydrogen transitions were found
that matched the spectral lines of the extreme ultraviolet
13 background of interstellar space and solar lines.

2. Experimental

15 *2.1. EUV spectroscopy*

Extreme ultraviolet (EUV) spectroscopy was recorded on
17 microwave and discharge cell light sources. Due to the ex-
tremely short wavelength of this radiation, "transparent" op-
19 tics do not exist. Therefore, a windowless arrangement was
used wherein the microwave or discharge cell was connected
21 to the same vacuum vessel as the grating and detectors of the
extreme ultraviolet (EUV) spectrometer. Differential pump-
23 ing permitted a high pressure in the cell as compared to that
in the spectrometer. This was achieved by pumping on the
25 cell outlet and pumping on the grating side of the collimator
that served as a pin-hole inlet to the optics. The spectrome-
27 ter was continuously evacuated to 10^{-4}–10^{-6} Torr by a tur-
bomolecular pump with the pressure read by a cold cathode
29 pressure gauge. The EUV spectrometer was connected to
the cell light source with a 1.5 mm × 5 mm collimator which
31 provided a light path to the slits of the EUV spectrometer.
The collimator also served as a flow constrictor of gas from
33 the cell. The cell was operated under gas flow conditions
while maintaining a constant gas pressure in the cell.
35 Spectra were obtained on hydrogen, helium and xenon
(not a catalyst in this system) and mixtures of 2% hydro-
37 gen with helium, neon, or xenon. The noble gas-hydrogen
mixtures (98/2%) were made from ultrahigh purity gases by
39 addition of hydrogen to the noble gas to achieve a 98/2%
mixture based on the individual gas partial pressures.
41 For spectral measurement, the light emission from mi-
crowave plasmas of hydrogen alone, helium–hydrogen
43 (98/2%), and neon–hydrogen (98/2%), and light emission
from a discharge plasma of hydrogen alone were introduced
45 to a normal incidence McPherson 0.2 meter monochro-
mator (Model 302, Seya-Namioka type) equipped with a
47 1200 lines/mm holographic grating with a platinum coat-
ing. The wavelength region covered by the monochromator
49 was 50–5600 Å. The EUV spectrum was recorded with a
channel electron multiplier (CEM) at 2500–3000 V. The
51 wavelength resolution was about 0.2 Å (FWHM) with an
entrance and exit slit width of 50 μm. The increment was
53 2 Å and the dwell time was 500 ms.

To achieve higher sensitivity at the shorter EUV wave-
55 lengths, the light emission of control microwave plasmas of
hydrogen alone, helium alone, and glow discharge plasmas
57 of hydrogen, xenon, helium–hydrogen mixture (98/2%),
and xenon–hydrogen mixture (98/2%) were recorded with a
59 McPherson 4° grazing incidence EUV spectrometer (Model
248/310G) equipped with a grating having 600 G/mm with
61 a radius of curvature of ≈ 1 m. The angle of incidence was
87°. The wavelength region covered by the monochromator
63 was 50–650 Å. The wavelength resolution was about 0.4 Å
(FWHM) with an entrance and exit slit width of 300 μm.
65 A CEM at 2400 V was used to detect the EUV light. The
increment was 1 Å and the dwell time was 1 s.

67 *2.2. Microwave emission spectra*

The experimental set up comprising a microwave dis-
69 charge gas cell light source and an EUV spectrometer
which was differentially pumped is shown in Fig. 1. Ex-
71 treme ultraviolet emission spectra were obtained on plasmas
of hydrogen alone, helium alone, helium–hydrogen mix-
73 ture (98/2%), and neon–hydrogen mixture (98/2%) with
a microwave discharge system and an EUV spectrometer.
75 The microwave generator was a Opthos model MPG-4M
generator (Frequency: 2450 MHz). The output power was
77 set at 85 W. Helium–hydrogen (98/2%) gas mixture was
flowed through a half-inch diameter quartz tube at 1, 20, or
79 760 Torr. The gas pressure inside the cell was maintained
by flowing the mixture while monitoring the pressure with
81 a 10 and 1000 Torr MKS Baratron absolute pressure gauge.
By the same method, hydrogen alone plasmas were run
83 at 1 and 20 Torr, and plasmas of helium alone and neon–
hydrogen mixture (98/2%) were run at 20 Torr. The tube
85 was fitted with an Opthos coaxial microwave cavity (Even-
son cavity). The EUV spectrometer was a normal incidence
87 monochromator except for the helium alone plasma and an
additional hydrogen alone plasma which were recorded with
89 a 4° grazing incidence EUV spectrometer (see Section 2.1).

2.3. Glow discharge emission spectra

91 A diagram of the discharge plasma source is given in
Fig. 2. The hollow cathode and EUV spectrograph were
93 aligned on a common optical axis using a laser. The experi-
mental setup for the discharge measurements is illustrated in
95 Fig. 3. Extreme ultraviolet emission spectra were obtained
on plasmas of hydrogen, xenon, helium–hydrogen mixture
97 (98/2%), and xenon–hydrogen mixture (98/2%) with a gas
discharge cell that comprised a five-way stainless-steel cross
99 that served as the anode with a hollow stainless-steel cath-
ode. The plasma was generated at the hollow cathode inside
101 the discharge cell. The hollow cathode was constructed of
a stainless-steel rod inserted into a steel tube, and this as-
103 sembly was inserted into an alumina tube. A flange opposite
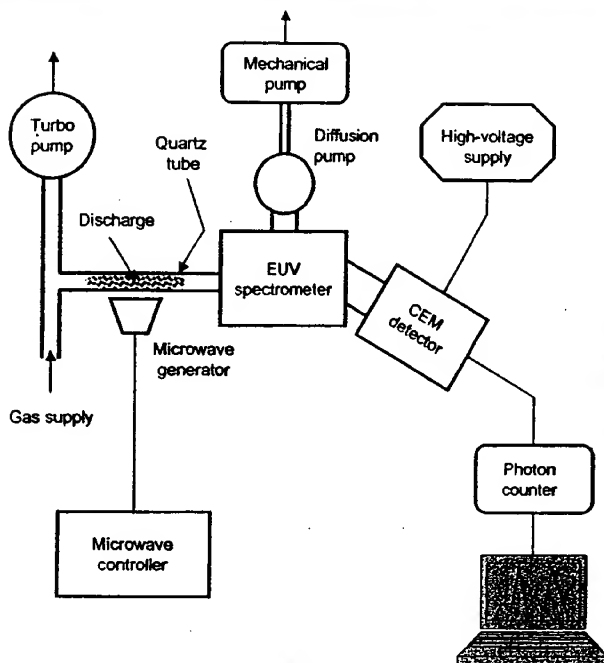the end of the hollow cathode connected the spectrometer

Fig. 1. The experimental set up comprising a microwave discharge gas cell light source and an EUV spectrometer which was differentially pumped.
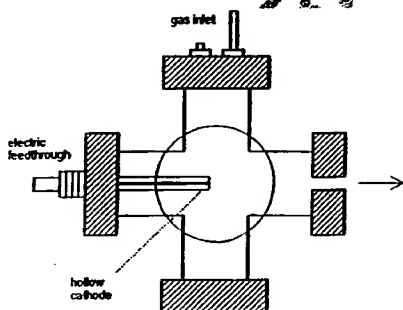

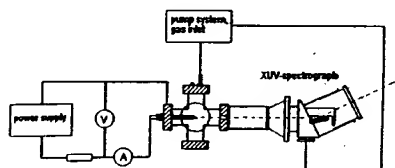Fig. 2. Cross-sectional view of the discharge cell.

Fig. 3. The experimental set up comprising a discharge gas cell light source and an EUV spectrometer which was differentially pumped.

with the cell. It had a small hole that permitted radiation to pass to the spectrometer. An AC power supply ($U = 0$–1 kV, $I = 0$–100 mA) was connected to the hollow cathode to generate a discharge. The AC voltage and current at the time the EUV spectrum was recorded were 200 V and 40 mA, respectively. A Swagelok adapter at the very end of
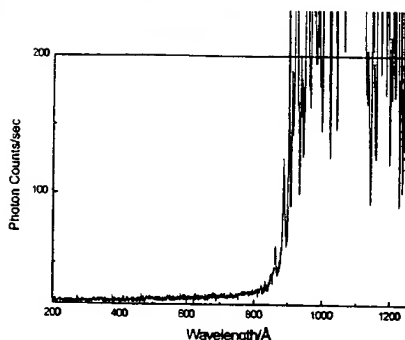
Fig. 4. The EUV spectrum (200–1250 Å) of the control hydrogen discharge cell emission that was recorded with a normal incidence EUV spectrometer and a CEM. No emission was observed below 800 Å.
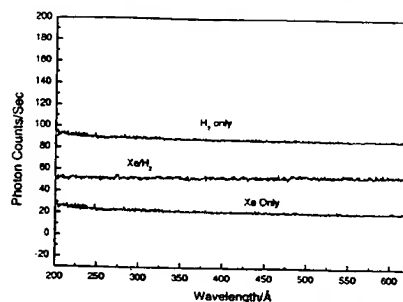

Fig. 5. The EUV spectra (200–645 Å) of the control hydrogen (top curve), control xenon–hydrogen mixture (98/2%) (middle curve), and control xenon (bottom curve) discharge cell emission that were recorded with a 4° grazing incidence EUV spectrometer and a CEM. No peaks were observed in this region from xenon alone or with the addition of hydrogen. No instrument artifacts were observed.

1   the steel cross provided a gas inlet and a connection with the
    pumping system, and the cell was pumped with a mechani-
3   cal pump. Valves were between the cell and the mechanical
    pump, the cell and the monochromator, and the monochro-
5   mator and its turbo pump. The five-way cross was pressur-
    ized with 400 mTorr of gas which was maintained by flow-
7   ing the gas while monitoring the pressure with a 1 Torr MKS
    Baratron absolute pressure gauge. The EUV spectrometer
9   was a 4° grazing incidence EUV spectrometer except for an
    additional hydrogen alone plasma which was recorded with
11   a normal incidence monochromator (see Section 2.1).

3. Results and discussion

13   *3.1. EUV spectroscopy*

     The EUV emission was recorded from microwave and
15   glow discharge plasmas of hydrogen, helium, and xenon,
    and helium, neon, and xenon with 2% hydrogen over the
17   wavelength range 50–1250 Å. The EUV spectrum (200–
    1250 Å) of the control hydrogen discharge cell emission
19   is shown in Fig. 4. The hydrogen glow discharge and mi-
    crowave discharge emission recorded with the normal inci-
21   dence monochromator and the 4° grazing EUV spectrometer
    were the same. The EUV spectra (200–645 Å) of the con-
23   trol hydrogen (top curve), control xenon–hydrogen mixture
    (98/2%) (middle curve), and control xenon (bottom curve)
25   discharge cell emission are shown in Fig. 5. No peaks were
    observed in this region from xenon alone or with the ad-
27   dition of hydrogen. Thus, xenon did not catalyze hydrogen
    to give novel peaks, and no spurious peaks or artifacts due
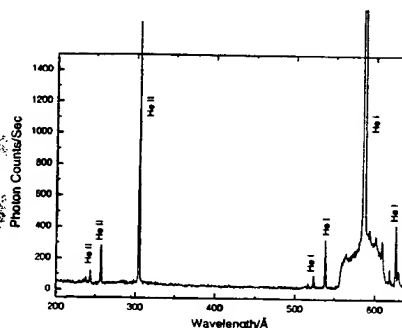29   to the grating or the spectrometer were observed. The EUV

Fig. 6. The EUV spectrum (200–650 Å) of the control helium microwave discharge cell emission that was recorded with a 4° grazing incidence EUV spectrometer and a CEM. Only known He I and He II peaks were observed.

spectrum (200–650 Å) of the control helium microwave cell
emission is shown in Fig. 6. Only known He I and He II   31
peaks were observed.

     The EUV spectrum (150–650 Å) of the helium–hydrogen   33
mixture (98/2%) microwave cell emission that was recorded
at 1, 24, and 72 h is shown in Fig. 7. Ordinary hydrogen has   35
no emission in these regions as shown in Fig. 4. Peaks ob-
served at 205, 374 and 456 Å which do not correspond to he-   37
lium and increase with time were assigned to lower-energy
hydrogen transitions in Table 1. A control helium was ob-   39
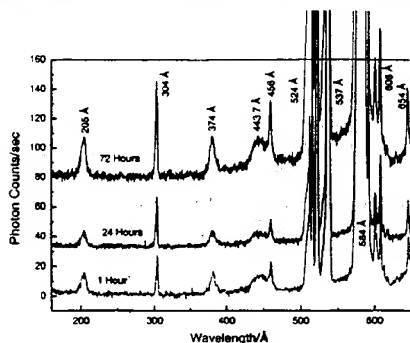tained with the 4° grazing incidence EUV spectrometer since

Fig. 7. The EUV spectra (150–650 Å) of the helium–hydrogen mixture (98/2%) microwave cell emission that was recorded at 1, 24, and 72 h with a normal incidence EUV spectrometer and a CEM. The pressure was maintained at 20 Torr. Reproducible novel emission lines that increased with time were observed at 456 and 304 Å with energies of $q13.6$ eV where $q = 2$ *or* 3 and at 374 and 205 Å with energies of $q13.6$ eV where $q = 4$ or 6 that were inelastically scattered by helium atoms wherein 21.2 eV (584 Å) was absorbed in the excitation of He ($1s^2$). These lines were identified in Table 1 as hydrogen transitions to electronic energy levels below the "ground" state corresponding to fractional quantum numbers.
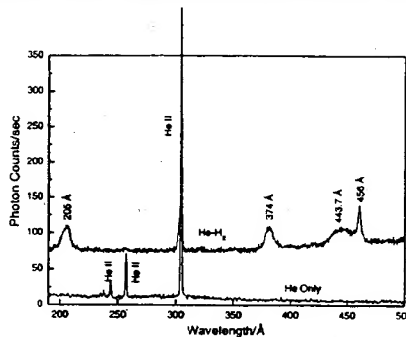

Fig. 8. The EUV spectra (190–500 Å) of the helium–hydrogen mixture (98/2%) (top curve) and control helium (bottom curve) microwave discharge cell emission that were recorded with a normal incidence and a 4° grazing incidence EUV spectrometer, respectively, and a CEM. The lines that corresponded to hydrogen transitions to lower electronic energy levels were not observed in the helium control.
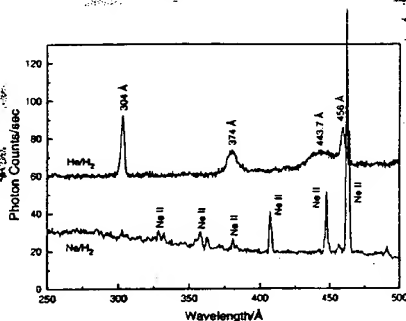

Fig. 9. The EUV spectra (250–500 Å) of the helium–hydrogen mixture (98/2%) (top curve) and control neon–hydrogen mixture (98/2%) (bottom curve) microwave discharge cell emission that were recorded with a normal incidence EUV spectrometer and a CEM. The lines that corresponded to hydrogen transitions to lower electronic energy levels were not observed in the neon–hydrogen control, and a series of Ne II lines were observed only in the control.

1   the spectrum with helium alone had very low intensity at the short wavelengths below 584 Å; whereas, the plasma of the
3   helium–hydrogen mixture (98/2%) was much more intense and was obtained on the normal incidence monochromator.
5   The EUV spectra (190–500 Å) of the helium–hydrogen mixture (98/2%) (top curve) and control helium (bottom
7   curve) microwave discharge cell emission is shown in Fig. 8. The lines that corresponded to hydrogen transitions
9   to lower electronic energy levels were not observed in the helium control.
11   Neon has peaks at 456.35 and 455.27 Å. To eliminate the possibility that the 456 Å peak shown in Fig. 8 was
13   due to the presence of neon as an impurity, the EUV spectra (250–500 Å) of the helium-by-hydrogen mixture (98/2%)
15   (top curve) and control neon–hydrogen mixture (98/2%) (bottom curve) microwave discharge cell emission were
17   recorded with a normal incidence EUV spectrometer and a CEM as shown in Fig. 9. The lines that corresponded to hy-
19   drogen transitions to lower electronic energy levels were not observed in the neon–hydrogen control, and a series of Ne
21   II lines were observed only in the control. The neon peaks at 456.35 and 455.27 Å were resolved in Fig. 9; whereas,
23   the 456 Å peak in the helium–hydrogen plasma was about 30 Å broad. Thus, it was not due to neon impurity.
25   The pressure was increased from 20 to 760 Torr, and the corresponding spectra were compared in Fig. 10. The

peaks appeared slightly more intense at the lower pressure; 27
so, the pressure was decreased to 1 Torr and spectra were
recorded. The short-wavelength EUV spectrum (50–600 Å) 29
of the control hydrogen microwave discharge cell emission
is shown in Fig. 11. No spectrometer artifacts were observed 31
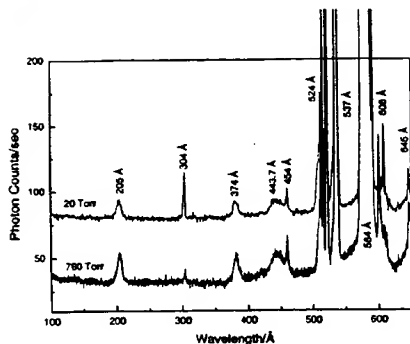at the short wavelengths. The short-wavelength EUV spec-

Fig. 10. The EUV spectrum (100–650 Å) of the helium–hydrogen mixture (98/2%) microwave cell emission that was recorded with a normal incidence EUV spectrometer and a CEM. The pressure was maintained at 20 and 760 Torr for the top and bottom curves, respectively. The lines that corresponded to hydrogen transitions to lower electronic energy levels appeared more intense at the lower pressure.
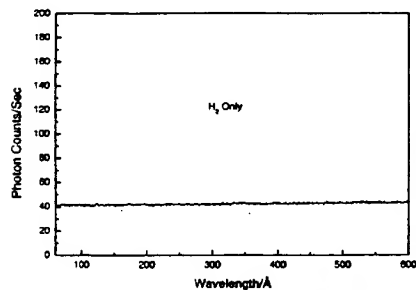

Fig. 11. The short-wavelength EUV spectrum (50–600 Å) of the control hydrogen microwave cell emission that was recorded with a normal incidence EUV spectrometer and a CEM. The pressure was maintained at 1 Torr. No hydrogen emission was observed in this region, and no instrument artifacts were observed.

1   trum (50–460 Å) of the helium–hydrogen mixture (98/2%)
    microwave cell emission with a pressure of 1 Torr is shown
3   in Fig. 12. The plasma was the brightest and had an increased
    background at this condition which is demonstrated by com-
5   parison with the control plasma recorded at the same detector
    sensitivity. At the 1 Torr condition, additional novel peaks
7   were observed in the short-wavelength region. Peaks ob-
    served at 82.9, 101.3, 130.3, and 141.5 Å which do not cor-
9   respond to helium were assigned to lower-energy hydrogen
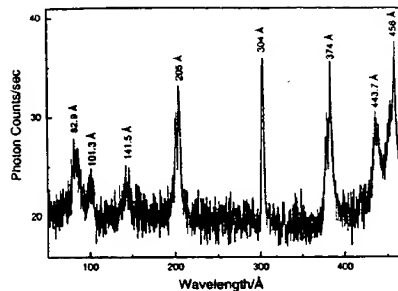   transitions in Table 1. It is also proposed that the 304 Å peak

Fig. 12. The short-wavelength EUV spectrum (50–460 Å) of the helium–hydrogen mixture (98/2%) microwave cell emission that was recorded with a normal incidence EUV spectrometer and a CEM. The pressure was maintained at 1 Torr. Reproducible novel emission lines were recorded at 456, 304, 130.3, 101.3, and 82.9 Å with energies of q13.6 eV where $q = 2, 3, 7, 9,$ or 11 and at 374, 205, and 141.5 Å with energies of q13.6 eV where $q = 4, 6,$ or 8 that were inelastically scattered by helium atoms wherein 21.2 eV (584 Å) was absorbed in the excitation of He ($1s^2$). These lines were identified in Table 1 as hydrogen transitions to electronic energy levels below the "ground" state corresponding to fractional quantum numbers.

shown in Figs. 7–10 and 12 was not entirely due to the He II   11
transition. Conspicuously absent was the 256 Å (48.3 eV)
line of He II shown in Figs. 6 and 8 which implies only a   13
minor He II transition contribution to the 304 Å peak.
    The EUV spectrum (500–650 Å) of the helium–hydrogen   15
mixture (98/2%) discharge cell emission is shown in
Fig. 13. It is proposed that the 633 Å peak shown in Fig.   17
13 arises from inelastic helium scattering of the 304 Å
peak. That is, the $\frac{1}{3} \rightarrow \frac{1}{4}$ transition yields a 40.8 eV pho-   19
ton (304 Å). When this photon strikes He ($1s^2$), 21.2 eV
is absorbed in the excitation to He ($1s^1 2p^1$). This leaves   21
a 19.6 eV (633 Å) photon and a 21.2 eV (584 Å) photon
from He ($1s^1 2p^1$). The intensity of the 584 Å line in   23
Fig. 13 is off-scale with 56.771 photons s^{-1}. Thus, the
transition He ($1s^2$) $\rightarrow$ He ($1s^1 2p^1$) dominated the inelastic   25
scattering of EUV peaks. For the first nine peaks assigned
as lower-energy hydrogen transitions or such transitions   27
inelastically scattered by helium, the agreement between
the predicted values and the experimental values shown in   29
Table 1 is remarkable. It is also remarkable that the hy-
drino lines are moderately intense based on the low grating   31
efficiency at these short wavelengths.
    The EUV spectrum (880–1250 Å) of the helium–   33
hydrogen mixture (98/2%) microwave cell emission is
shown in Fig. 14. The EUV spectrum (800–1050 Å) of   35
the control hydrogen microwave cell emission is shown in
Fig. 15. The ratio of the Lβ peak to the 912 Å peak of the   37
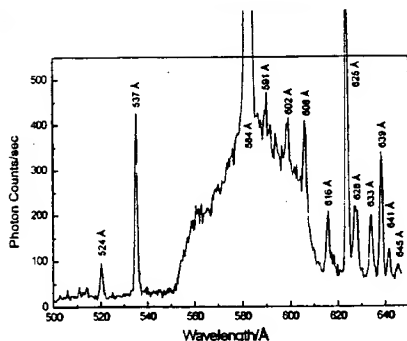helium–hydrogen plasma shown in Fig. 14 was 2; whereas,

13

Fig. 13. The EUV spectrum (500–650 Å) of the helium–hydrogen mixture (98/2%) discharge cell emission that was recorded with a 4° grazing incidence EUV spectrometer and a CEM. The pressure was maintained at 400 mTorr. An important astrophysical line was observed at 633 Å corresponding to the 304 Å lower-energy hydrogen transition line shown in Figs. 5, 6 and 8 and Table 1 that was inelastically scattered by helium atoms wherein 21.2 eV (584 Å) was absorbed in the excitation of He ($1s^2$).
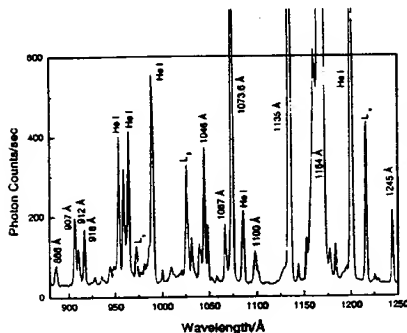

Fig. 14. The EUV spectrum (880–1250 Å) of the helium–hydrogen mixture (98/2%) microwave cell emission that was recorded with a normal incidence EUV spectrometer and a CEM. The pressure was maintained at 20 Torr. An emission line was observed at 912 Å with an energy of $q13.6$ eV where $q=1$ which was identified in Table 1 as hydrogen transitions to electronic energy levels below the "ground" state corresponding to fractional quantum numbers based on the 912 Å line intensity relative to Lß compared to that of the control hydrogen plasma.

1 the ratio of the Lβ peak to the 912 Å peak of the control hydrogen plasma shown in Fig. 15, was 8 which indicates
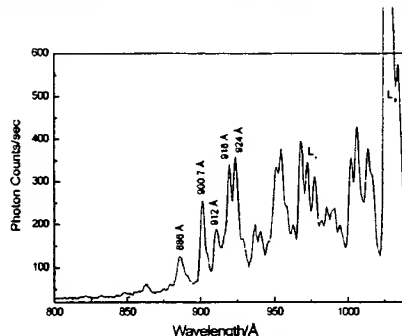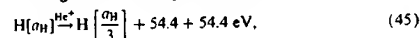3 that the majority of the 912 Å peak was due to a transition

Fig. 15. The EUV spectrum (800–1050 Å) of the control hydrogen microwave discharge cell emission that was recorded with a normal incidence EUV spectrometer and a CEM.

other than the binding of an electron by a proton. Based on
the intensity, it is proposed that the majority of the 912 Å   5
peak shown in Fig. 14 was due to the $\frac{1}{2} \rightarrow \frac{1}{4}$ and $\frac{1}{4} \rightarrow \frac{1}{5}$
transitions given in Table 1.   7

The energies for the hydrogen transitions given in
Table 1 in order of energy are 13.6, 27.2, 40.8, 54.4,   9
81.6, 95.2, 108.8, 122.4 and 149.6 eV. The correspond-
ing peaks are 912, 456, 304 Å with 633, 374, 205, 130.3,   11
141.5, 103.3, and 82.9 Å, respectively. Thus, the lines
identified in Figs. 7–10 and 12–14 as hydrogen tran-   13
sitions to electronic energy levels below the "ground"
state corresponding to fractional quantum numbers corre-   15
spond to energies of $q13.6$ eV where $q=1,2,3,4,6,7,8,9$,
or 11 or these lines inelastically scattered by helium   17
atoms wherein 21.2 eV was absorbed in the excitation
of He ($1s^2$) to He ($1s^12p^1$). The absence of the se-   19
ries members corresponding to $q=5$ and 10 may be
due to a slow reaction rate due to selection rules, low   21
cross-section, or low relative reactant concentrations
with only one dominant reaction pathway given by Eqs.   23
(21) and (33), respectively. For example, the data is
consistent with the reaction given by Eq. (22) which   25
gives rise to the helium-scattered peak at 205 Å being
favored over that given by Eq. (21) corresponding to   27
$q=5$. And, the reaction cross-section and concentration
of $H[a_H/6]$ required in the case of the reaction given by   29
Eq. (33) corresponding to $q=10$ may have been relatively
lower.   31

The disproportionation reaction assignments given in Ta-
ble 1 start with the product of the catalysis of atomic hydro- 33
gen by He$^+$ given by Eqs. (5)–(7). One cascade of reactions
which gives rise to the peaks assigned in Table 1 is   35

$$H[a_H]\overset{He^+}{\longrightarrow} H\left[\frac{a_H}{3}\right] + 54.4 + 54.4 \text{ eV}, \qquad (45)$$

$$H\left[\frac{a_H}{3}\right] + H\left[\frac{a_H}{3}\right] \rightarrow H\left[\frac{a_H}{2}\right] + H\left[\frac{a_H}{4}\right] + 27.2 \text{ eV}, \quad (46)$$

$$H\left[\frac{a_H}{2}\right] + H\left[\frac{a_H}{2}\right] \rightarrow H^+ + e^- + H\left[\frac{a_H}{3}\right] + 13.6 \text{ eV}, \quad (47)$$

$$H\left[\frac{a_H}{3}\right] + H\left[\frac{a_H}{2}\right] \rightarrow H^+ + e^- + H\left[\frac{a_H}{4}\right] + 40.8 \text{ eV}, \quad (48)$$

$$H\left[\frac{a_H}{4}\right] + H\left[\frac{a_H}{2}\right] \rightarrow H[a_H] + H\left[\frac{a_H}{5}\right] + 81.6 \text{ eV}, \quad (49)$$

$$H\left[\frac{a_H}{3}\right] + H\left[\frac{a_H}{3}\right] \rightarrow H\left[\frac{a_H}{5}\right] + H^+ + e^- + 95.2 \text{ eV}, \quad (50)$$

$$H\left[\frac{a_H}{3}\right] + H\left[\frac{a_H}{3}\right] \rightarrow H\left[\frac{a_H}{5}\right] + H[a_H] + 108.8 \text{ eV}, \quad (51)$$

$$H\left[\frac{a_H}{2}\right] + H\left[\frac{a_H}{2}\right] \rightarrow H\left[\frac{a_H}{4}\right] + H[a_H] + 122.4 \text{ eV}, \quad (52)$$

$$H\left[\frac{a_H}{3}\right] + H\left[\frac{a_H}{3}\right] \rightarrow H\left[\frac{a_H}{5}\right] + H\left[\frac{a_H}{2}\right] + 149.6 \text{ eV}, \quad (53)$$

wherein peaks inelastically scattered by helium are given by

photon (hv) + He $(1s^2)$ $\rightarrow$ He $(1s^1 2p^1)$

+ photon $(hv - 21.21 \text{ eV})$. $\qquad (54)$

All other peaks besides those assigned to lower-energy hydrogen transitions could be assigned to He I (e.g. 524, 537, 591, 602, 625, 628, 639, 641, 645 Å), He II (assigned in figures), second-order lines (608, 615, 886, 1046, 1079, 6, 1135, 1164, 1245 Å), or atomic (e.g. 1216, 1026, 973 Å) or molecular hydrogen (e.g. 907, 918, 1067, 1190 Å) emission [47,48]. No known lines of helium or hydrogen explain the q13.6 eV related set of peaks. Given that these spectra are readily repeatable, these peaks may have been overlooked in the past without considering the role of the helium scattering. The 633 Å peak which arises from the helium scattered 304 Å peak has significant astrophysical importance as discussed in the identification of lower-energy hydrogen by soft X-rays from dark interstellar medium section.

3.2. Identification of lower-energy hydrogen by soft X-rays from dark interstellar medium

3.2.1. Dark matter

The universe is predominantly comprised of hydrogen and a small amount of helium. These elements exist in interstellar regions of space, and they are expected to comprise the majority of interstellar matter. However, the observed constant angular velocity of many galaxies as the distance from the luminous galactic center increases can only be accounted for by the existence of nonluminous weakly interacting matter, dark matter. Dark matter exists at the cold fringes of galaxies and in cold interstellar space. It may account for the majority of the universal mass.

The identity of dark matter has been a cosmological mystery. Postulated assignments include τ neutrinos, but a detailed search for signature emissions has yielded nil [49]. The search for signatures by the cryogenic dark matter search (CDMS) developed to detect theorized weakly interacting massive particles (WIMPs) has similarly yielded nil [50,51]. WIMP theory's main competitor known as MACHO theory which assigns the dark matter to massive compact halo objects (MACHOs) which rather than elusive subatomic particles comprises ordinary baryonic matter in the form of burned-out dark stars, stray planets, and other large, heavy, but dark objects that must be ubiquitous throughout the universe. However, MACHO theory has also recently been ruled out based on lack of evidence of these dark objects observable by the brief ellipses caused by them moving in front of distant stars. Only a few such objects have been observed after exhaustively searching for over five years [50,52].

It is anticipated that the emission spectrum of the extreme ultraviolet background of interstellar matter possesses the spectral signature of dark matter. Labov and Bowyer designed a grazing incidence spectrometer to measure and record the diffuse extreme ultraviolet background [53]. The instrument was carried aboard a sounding rocket, and data were obtained between 80 and 650 Å (data points approximately every 1.5 Å). Several lines including an intense 635 Å emission associated with dark matter were observed [53] which has considerable astrophysical importance as indicated by the authors:

Regardless of the origin, the 635 Å emission observed could be a major source of ionization. Reynolds (1983–1985) has shown that diffuse Hα emission is ubiquitous throughout the Galaxy, and widespread sources of flux shortward of 912 Å are required. Pulsar dispersion measures (Reynolds, 1989) indicate a high scale height for the associated ionized material. Since the path length for radiation shortward of 912 Å is low, this implies that the ionizing source must also have a large scale height and be widespread. Transient heating appears unlikely, and the steady-state ionization rate is more than can be provided by cosmic rays, the soft X-ray background, B stars, or hot white dwarfs (Reynolds, 1986; Brushweiler and Cheng, 1988). Sciama (1990) and Salucci and Sciama (1990) have argued that a variety of observations can be explained by the presence of dark matter in the galaxy which decays with the emission of radiation below 912 Å.

The flux of 635 Å radiation required to produce hydrogen ionization is given by $F = \zeta_H/\sigma_i = 4.3 \times 10^4 \zeta_{-13}$ photons cm^{-2}s^{-1}, where ζ_{-13} is the ionizing rate in units of 10^{-13} s^{-1} per H atom. Reynolds (1986) estimates that in the immediate vicinity of the Sun, a steady-state ionizing rate of ζ_{-13} between 0.4 and 3.0 is required. To produce this range of ionization, the 635 Å intensity we observe would have to be distributed over 7–54% of the sky.

The first soft X-ray background was detected and reported [54] about 25 years ago. Quite naturally, it was assumed that these soft X-ray emissions were from ionized atoms within hot gases. Labov and Bowyer also interpreted the data as emissions from hot gases. However, the authors left the door open for some other interpretation with the following statement from their introduction:

It is now generally believed that this diffuse soft X-ray background is produced by a high-temperature component of the interstellar medium. However, evidence of the thermal nature of this emission is indirect in that it is based not on observations of line emission, but on indirect evidence that no plausible non-thermal mechanism has been suggested which does not conflict with some component of the observational evidence.

The authors also state that "if this interpretation is correct, gas at several temperatures is present". Specifically, emissions were attributed to gases in three ranges: $5.5 < \log T < 5.7$; $\log T = 6$; $6.6 < \log T < 6.8$.

The explanation proposed herein about the observed dark interstellar medium spectrum hinges on the possibility of energy states below the $n = 1$ state, as given by Eqs. (2a) and (3). A number of experimental observations discussed in Section 1 lead to the conclusion that atomic hydrogen can exist in fractional quantum states that are at lower energies than the traditional "ground" ($n = 1$) state. The existence of fractional quantum states of hydrogen atoms explains the spectral observations of the extreme ultraviolet background emission from interstellar space [53], which may characterize dark matter as demonstrated in Table 3. In these cases, a hydrogen atom in a fractional quantum state, H(n_i), collides, for example, with a $n = \frac{1}{2}$ hydrogen atom, H($\frac{1}{2}$), and the result is an even lower-energy hydrogen atom, H(n_f), and H($\frac{1}{2}$) is ionized.

$$H(n_i) + H(\tfrac{1}{2}) \rightarrow H(n_f) + H^+ + e^- + \text{photon.} \quad (55)$$
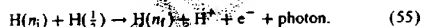
The energy released, as a photon, is the difference between the energies of the initial and final states given by Eqs. (2a) and (3) minus the ionization energy of H($\frac{1}{2}$), 54.4 eV.

Thus, lower-energy transitions of the type

$$\Delta E = \left(\frac{1}{n_f^2} - \frac{1}{n_i^2}\right) 13.6 - 54.4 \text{ eV} \quad n = 1, \tfrac{1}{2}, \tfrac{1}{3}, \tfrac{1}{4}, \ldots$$

$$\text{and} \quad n_i > n_f \quad (56)$$

Table 2
Energies (Eq. (56)) of several fractional-state transitions catalyzed by H[$a_H/2$]

n_i	n_f	ΔE (eV)	λ (Å)
$\frac{1}{2}$	$\frac{1}{3}$	13.6	912
$\frac{1}{3}$	$\frac{1}{4}$	40.80	303.9
$\frac{1}{4}$	$\frac{1}{5}$	68.00	182.4
$\frac{1}{5}$	$\frac{1}{6}$	95.20	130.2
$\frac{1}{6}$	$\frac{1}{7}$	122.4	101.3
$\frac{1}{7}$	$\frac{1}{8}$	149.6	82.9

induced by a disproportionation reaction with H[$\frac{a_H}{2}$] ought to occur. The wavelength is related to ΔE by

$$\lambda \text{ (in Å)} = \frac{1.240 \times 10^4}{\Delta E \text{ (in eV)}} \quad (57)$$

The energies and wavelengths of several of these proposed transitions are shown in Table 2. Note that the lower-energy transitions are in the soft X-ray region.

3.2. The data and its interpretation

In their analysis of the data, Labov and Bowyer [53] established several tests to separate emission features from the background. There were seven features (peaks) that passed their criteria. The wavelengths and other aspects of these peaks are shown in Table 3. Peaks 2 and 5 were interpreted by Labov and Bowyer as instrumental second-order images of peaks 4 and 7, respectively. Peak 3, the strongest feature, is clearly a helium resonance line: He ($1s^12p^1 \rightarrow 1s^2$). At issue here, is the interpretation of peaks 1, 4, 6, and 7. It is proposed that peaks 4, 6, and 7 arise from the $\frac{1}{3} \rightarrow \frac{1}{4}$, $\frac{1}{4} \rightarrow \frac{1}{5}$, and $\frac{1}{6} \rightarrow \frac{1}{7}$ hydrogen atoms transitions given by Eq. (55). It is also proposed that peak 1 arises from inelastic helium scattering of peak 4. That is, the $\frac{1}{3} \rightarrow \frac{1}{4}$ transition yields a 40.8 eV photon (303.9 Å). Conspicuously absent is the 256 Å (48.3 eV) line of He II which eliminates the assignment of the majority of the 303 Å line to the He II transition. When this photon strikes He ($1s^2$), 21.2 eV is absorbed in the excitation to He ($1s^12p^1$). This leaves a 19.6 eV photon (632.6 Å), peak 1. For these four peaks, the agreement between the predicted (Table 2) and the experimental values (Table 3) is remarkable.

One argument against this new interpretation of the data is that the transition $\frac{1}{5} \rightarrow \frac{1}{6}$ is missing — predicted at 130.2 Å by Eqs. (56)–(57). This missing peak cannot be explained into existence, but a reasonable rationale can be provided as to why it might be missing from these data. The data obtained by Labov and Bowyer are outstanding

Table 3
Emission features of the Labov and Bowyer spectrum and their interpretation

Peak	λ (Å)	Confidence limit (Å)	Intensity photons $cm^{-2} s^{-1} sr^{-1}$	Assignment (Labov and Bowyer)	Assignment (Mills)	Predicted λ (Eq. (56), (57)) (Å)
1	633.0	-4.7 to $+4.7$	19,000	O^{4+}; Log $T = 5.5$	He scattering of 303.9 line (peak 4)	633.0
2	607.5	-4.9 to $+4.9$	Second order	Second order of 302.5 line	Second order of 303.9 line	607.8
3	584	-4.5 to $+4.5$	70,400	He resonance $(1s^1 2p^1 \rightarrow 1s^2)$	He resonance $(1s^1 2p^1 \rightarrow 1s^2)$	584
4	302.5	-6.0 to $+5.9$	2080	He^+; $(2p^1$ to $1s^1)$	$n = 1/3 - 1/4$	303.9
5	200.6	-4.4 to $+5.3$	Second order	Second order of 101.5 line	Second order of 101.3 line	202.6
6	181.7	-4.6 to $+5.1$	1030	Fe^{9+} and Fe^{10+}; Log $T = 6$	$n = 1/4 - 1/5$	182.3
7	101.5	-5.3 to $+4.2$	790	Fe^{17+} and Fe^{18+}; Log $T = 6.6 - 6.8$	$n = 1/6 - 1/7$	101.3

Table 4
Data (Labov and Bowyer) near the predicted $\frac{1}{5} \rightarrow \frac{1}{6}$ transition (130.2 Å)

λ (Å)	Counts	Background	Counts-background
125.82	26	21.58	4.42
127.10	22	21.32	0.68
128.37	18	19.50	-1.50
129.64	29	20.28	8.72
130.90	18	19.76	-1.76
132.15	20	19.50	0.50
133.41	19	19.50	-0.50
134.65	19	20.80	-1.80

1   when the region of the spectrum, the time allotted for data collection, and the logistics are considered. Nonetheless, it
3   is clear that the signal-to-noise ratio is low and that considerable effort had to be expended to differentiate emis-
5   sion features from the background. This particular peak, $\frac{1}{5} \rightarrow \frac{1}{6}$, is likely to be only slightly stronger than the $\frac{1}{6} \rightarrow$
7    $\frac{1}{7}$ peak (the intensities, Table 3, appear to decrease as n decreases), which has low intensity. Labov and Bowyer
9   provided their data (wavelength, count, count error, background, and background error). The counts minus back-
11   ground values for the region of interest, 130.2 ± 5 Å, are shown in Table 4 (the confidence limits for the wavelength
13   of about ±5 Å are the single-side 1 confidence levels and include both the uncertainties in the fitting procedure and

uncertainties in the wavelength calibration). Note that the   15
largest peak (count-background) is at 129.64 Å and has a
counts-background = 8.72. The counts-background for the   17
strongest signal of the other hydrino transitions are: $n = 1/3–$
$1/4$, 20.05; $n = 1/4–1/5$, 11.36; $n = 1/6–1/7$, 10.40. Thus,   19
there is fair agreement with the wavelength and the strength
of the signal. This, of course, does not mean that there is a   21
peak at 130.2 Å. However, it is not unreasonable to conclude
that a spectrum with a better signal-to-noise ratio might un-   23
cover the missing peak. With the assignment of the $\frac{1}{5} \rightarrow \frac{1}{6}$
transition, all of the hydrogen transitions $\frac{1}{3} \rightarrow \frac{1}{4}$, $\frac{1}{4} \rightarrow \frac{1}{5}$,   25
$\frac{1}{5} \rightarrow \frac{1}{6}$, and $\frac{1}{6} \rightarrow \frac{1}{7}$ are observed over the recorded spectral
range, and the 632.6 Å peak is identified.   27

3.3. Identification of lower-energy hydrogen by soft X-rays from the sun   29

3.3.1. Solar neutrino problem

   Another cosmological mystery unresolved for three   31
decades is the discrepancy between solar neutrino flux ob-
served with the Homestake detector, 2.1±0.03SNU, and that   33
predicted based on conservative predictions of the standard
solar model (SSM), 7.9 ± 2.6SNU [55–57]. According to   35
the SSM, the pp chain is the predominant energy source of
main-sequence stars which commences with proton–proton   37
fusion according to the following reaction [55];

$$^1H + {}^1H \rightarrow {}^2H + e^+ + v_e \qquad (58)$$

and, according to this model, strong coupling exists between   39
luminosity and neutrino flux because they are both based

on nuclear reactions. An experiment with a radioactive so- 1
lar surrogate at the Gallex solar neutrino detector in Italy
performed over 15 years ago supports the results that over 3
the preceding several years the Gallex and Russia's SAGE,
the other large gallium detector, saw only about 60% of 5
the solar neutrino signal predicted to within 1–2% by astro-
physical models [58]. The Homestake experiment detects 7
the neutrinos from the pp chain indirectly by detecting ^{8}B
neutrinos. A direct measure of neutrinos from the pp chain 9
provides a more definitive test of the SSM. Historically,
GALLEX and SAGE were the only two experiments which 11
directly detected electron neutrinos from the pp chain. Re-
cently, GALLEX was upgraded and recommissioned as the 13
Gallium Neutrino Observatory (GNO) which also directly
detects pp chain neutrinos to test the deficit observed by 15
GALLEX and SAGE [59–66]. The most recent results from
all three experiments show a 50% discrepancy [59–66] 17
which confirms the paradox observed by the Homestake ex-
periment (GNO 65.8$^{+10.7}_{-10.2}$SNU [65], GALLEX 74.1$^{+6.7}_{-6.8}$SNU 19
[65], SAGE 75.4$^{+7.0}_{-6.8}$SNU [61], SSM theoretical 129$^{+8}_{-6}$SNU
[61,66]). Furthermore, Super-Kamiokande operated since 21
1996 which detects ^{8}B neutrinos by electron scattering (ES)
on ordinary water and the recently commissioned Sudbury 23
Neutrino Observatory [67,68] which detects ^{8}B neutrinos
by charge current (CC) reaction on deuterium and elec- 25
tron scattering (ES) also reproduced the deficit observed
by Homestake (Sudbury 1.75 ± 0.07 (stat.)$^{+0.12}_{0.11}$ (sys.) ± 27
0.05 (theor.) × 10^6 cm^{-2} s^{-1} (CC) where the theoreti-
cal uncertainty is the CC cross-section uncertainty and 29
2.39 ± 0.34 (stat.)$^{+0.16}_{-0.14}$ (sys.) × 10^6 cm^{-2} s^{-1} (ES) [67],
Super-Kamiokande 2.32 ± 0.03 (stat.)$^{+0.08}_{-0.07}$(sys.)SNU (ES) 31
[67], SSM theoretical 5.05 × 10^6 cm^{-2} s^{-1} [67]).

The recent results from different neutrino detectors around 33
the world all show that the observed solar neutrino flux is
only about 34–50% of that predicted. *There is unequivo-* 35
cally a solar neutrino paradox that is directly observable.
Assuming the experiments are accurate with large mar- 37
gins for error (50% or greater), the explanations are: (1) a
problem with the standard solar model and (2) neutrino os- 39
cillation. However, oscillation violates the standard model
— it does not conserve family Lepton number and requires 41
mass different from zero [64]. Furthermore, if neutrinos os-
cillate, then the universe should be full of tau neutrinos 43
which were once proposed as the identity of dark matter.
But, a detailed search for signature emissions has yielded nil 45
[49]. Neutrino oscillation has never been directly observed.
The Sudbury [67] results showed no evidence for a devia- 47
tion of the spectral shape from the predicted shape under the
non-oscillation hypothesis. In addition, the precise measure- 49
ment of the spectrum shape and day/night fluxes measured
by Super-Kamiokande does not show evidence of neutrino 51
oscillation [69,70].

The paradox of the paucity of solar neutrinos to account 53
for the solar energy output by the pp chain is resolved by
assigning a major portion of the solar output to hydrogen 55
transitions. Hydrogen transitions to electronic energy levels

below the "ground" state corresponding to fractional quan- 57
tum numbers can yield energies comparable to nuclear en-
ergies. For example, all transitions to the $n = \frac{1}{100}$ state of 59
hydrogen taken together release 136 keV. Data strongly sup-
porting this tenant is the observation by Labov and Bowyer 61
of an intense 304 Å (40.8 eV) solar emission line corre-
sponding to the transition given by Eq. (55) 63

$$H\left[\frac{a_H}{3}\right] \xrightarrow{H[a_H/3]} H\left[\frac{a_H}{4}\right] \qquad (59)$$

in the absence of the 256 Å (48.3 eV) line of He II which
challenges the assignment of the 304 Å line to the He II 65
transition. Solar lines which match lower-energy hydrogen
transitions shown in Table 5 are also observed on the Sun 67
which is consistent with a stellar origin of lower-energy
hydrogen in interstellar space. 69

3.3.2. Temperature of the solar corona problem

In addition to the questions of what powers the Sun 71
and why the solar neutrino flux is significantly deficient,
there exists no satisfactory answer to two additional solar 73
questions: The cause of sunspots and other solar activ-
ity and why the Sun emits X-rays is unknown [75]. In 75
fact, a possible anticorrelation exists between the abun-
dance of sunspots and the solar neutrino flux observed 77
with the Homestake detector [76]. The photosphere of the
Sun is 6000 K, whereas, the temperature of the corona 79
based on the assignment of the emitted X-rays to highly
ionized heavy elements is in excess of 10^6 K. No satis- 81
factory power transfer mechanism is known which ex-
plains the excessive temperature of the corona relative 83
to that of the photosphere. The mechanism must explain
the constant transfer over time of energy from the pho- 85
tosphere at 6000 K to the corona at 10^6 K which radiates
energy into cold space. Further compounding the tem- 87
perature mystery is the observation of a strong coronal
hydrogen Lyman series, beginning with Lα at 1216 Å 89
and ending at 912 Å, corresponding to unionized hy-
drogen atoms. The hydrogen lines would indicate that 91
the corona is less than 10^4 K. The paradox is resolved
by the existence of a power source associated with the 93
corona.

The cause of sunspots and other solar activity, and why 95
the Sun emits X-rays can be explained by energy releas-
ing transitions of hydrogen to lower-energy levels. The 97
energy which maintains the corona at a temperature that
appears in excess of 10^6 K may be that released by 99
disproportionation reactions of lower-energy hydrogen as
given by Eqs. (10)–(12). Hydrogen transitions to electronic 101
energy levels below the "ground" state corresponding to
fractional quantum numbers match lines of the solar emis- 103
sion spectrum in the extreme ultraviolet and X-ray regions.
The solar lines that match the energy of disproportionation 105
reactions of lower-energy hydrogen given by Eqs. (10)–
(12) are given in Table 5. 107

Table 5

Observed solar line emission assigned to the disproportionation reactions given by Eqs. (10)–(12). (Raw extreme ultraviolet solar spectral data taken from Figs. 3a–k of [71], Figs. 1a–d (observed lines from Table 1) of [72]; Fig. 7.5 of [73], and Fig. 4.10 of Phillips [74].)

Observed line (Å)	Predicted (Mills)[b] (Å)	m, m'	Assignment (Mills)	Ref	Assignment (Other)
		f			
1215.7	1215.67	d	$H(2p^1) \rightarrow H(1s^1) + 10.2$ eV	[73,74]	Collisional excitation, $L\alpha$ scattering
911.8	911.78	1, 1;1[c]	$1 \rightarrow 1/2$ H transition	[73,74]	$H^+ + e^- \rightarrow H + 13.6$ eV at $T > 20,000$ K
		1, 2	$1/2 \rightarrow 1/3$ H transition		
584.5	584.5	e	He $(1s^12p^1) \rightarrow$ He $(1s^2) + 21.2$ eV	[73,74]	Collisional excitation
373.7	373.73	2, 2	Inelastic scattering (He) of $1 \rightarrow 1/3$ H transition	[71]	None
303.784	303.92	1, 2	$1/3 \rightarrow 1/4$ transition	[71]	He II
280.2[a] 280.8[a]	280.54	2, 2	Inelastic scattering (H) of $1 \rightarrow 1/3$ H transition	[72]	None
264.80	265.08	1, 2	Inelastic scattering (He) of $1/4 \rightarrow 1/5$ H transition	[72]	Fe XIV
228[a]	227.95	2, 2	$1 \rightarrow 1/3$ H transition	[72]	None
215.16	214.54	1, 2	Inelastic scattering (H) of $1/4 \rightarrow 1/5$ H transition	[72]	S XII
182.16	182.36	1, 2	$1/4 \rightarrow 1/5$ H transition	[72]	Fe XI
167.50	167.62	1, 2	Inelastic scattering (He) of $1/5 \rightarrow 1/6$ H transition	[72]	Fe VIII
152.15	151.97	3, 3	$1 \rightarrow 1/4$ transition	[72]	Ni XII
145.9[a]	145.88	1, 2	Inelastic scattering (H) of $1/5 \rightarrow 1/6$ H transition	[72]	None
141[a]	141.59	2, 2	Inelastic scattering (He) of $1/2 \rightarrow 1/4$ H transition	[72]	None
129.87	130.26	1, 2	$1/5 \rightarrow 1/6$ H transition	[72]	O VI
125.5a	125.76	2, 2	Inelastic scattering (H) of $1/2 \rightarrow 1/4$ H transition	[72]	None
122.2[a]	122.56	1, 2	Inelastic scattering (He) of $1/6 \rightarrow 1/7$ H transition	[72]	None
114[a]	113.97	2, 2	$1/2 \rightarrow 1/4$ transition	[72]	None
110.5[a]	110.52	1, 2	Inelastic scattering (H) of $1/6 \rightarrow 1/7$ H transition	[72]	None
101.3[a]	101.31	1, 2	$1/6 \rightarrow 1/7$ transition	[72]	None
96.7[a]	96.59	1, 2	Inelastic scattering (He) of $1/7 \rightarrow 1/8$ H transition	[72]	None
88.8	88.95	1, 2	Inelastic scattering (H) of $1/7 \rightarrow 1/8$ H transition	[72]	None
87.0[a]	87.34	2, 2	Inelastic scattering (He) of $1/3 \rightarrow 1/5$ H transition	[72]	None
82.9[a]	82.89	1, 2	$1/7 \rightarrow 1/8$ H transition	[72]	None
81.1[a]	81.05	2, 2	Inelastic scattering (H) of $1/3 \rightarrow 1/5$ H transition	[72]	None
79.58	79.76	1, 2	Inelastic scattering (He) of $1/8 \rightarrow 1/9$ H transition	[72]	Fe XII
76.0[a]	75.98	2, 2	$1/3 \rightarrow 1/5$ H transition	[72]	None
70.1[a]	70.14	1, 2	$1/8 \rightarrow 1/9$ H transition	[72]	None
67.5[a]	67.84	1, 2	Inelastic scattering (He) of $1/9 \rightarrow 1/10$ H transition	[72]	None
63.12	63.14	2, 2	Inelastic scattering (He) of $1/4 \rightarrow 1/6$ H transition	[72]	Mg X

Table 5. (*Continued*).

Observed line (Å)	Predicted (Mills)[b] (Å)	m, m'	Assignment (Mills)	Ref	Assignment (Other)
61.0[a]	60.78	1, 2	1/9 → 1/10 H transition	[72]	None
59.7[a]	59.79	2, 2	Inelastic scattering (H) of 1/4 → 1/6 H transition	[72]	None

[a]Wavelength read from Fig. 1 of [72]; wavelength not given in Table of [72].

[b]For lower-energy transitions, $n = 1, \frac{1}{2}, \frac{1}{3}, \frac{1}{4}, \ldots$, and $n_i > n_f$ induced by a disproportionation reaction with $H[a_H/2]$, $E = (1/n_f^2 - 1/n_i^2)13.6 \text{ eV} - m'^2 13.6 \text{ eV}$. [b] For helium inelastic scattered peaks of hydrogen transitions, $n_i \rightarrow n_f$, $E = (1/n_f^2 - 1/n_i^2)13.6 \text{ eV} - m'^2 13.6 - 21.21 \text{ eV}$ (when this photon strikes He ($1s^2$), 21.2 eV is absorbed in the excitation to He ($1s^1 2p^1$)). [b] For hydrogen inelastic scattered peaks of hydrogen transitions, $n_i \rightarrow n_f$, $E = (1/n_f^2 - 1/n_i^2)13.6 \text{ eV} - m'^2 13.6 - 10.2 \text{ eV}$ (when this photon strikes H ($1s^1$), 10.2 eV is absorbed in the excitation to H($2p^1$)).

[c]H $[n = 1] \xrightarrow{2H} $ H $[n = \frac{1}{2}] + h\nu$ (911.8 Å).

[d]H ($2p^1$) → H ($1s^1$) + 10.2 eV (excitation by emission of lower-energy hydrogen transitions).

[e]He ($1s^1 2p^1$) → He ($1s^2$) + 21.2 eV (excitation by emission of lower-energy hydrogen transitions).

[f]Eqs. (10)–(12).

The agreement between the calculated and the experimental values is remarkable, and several match those identified by EUV spectroscopy of the helium–hydrogen plasma as shown in Table 1. Furthermore, many of the lines of Table 5 had no previous assignment, or the assignment was unsatisfactory. Some lines assigned in the literature may have been assigned incorrectly by trying to fit the spectrum to known lines. But, inconsistencies arise. For example, the intensity of the peak assigned to He II by Thomas [71] is extremely strong ($I = 62,200$). The laboratory He II transition intensities are: $I(303.780) = 1000$; $I(303.786) = 500$; $I(256) = 300$. Therefore, the predicted peak intensity of the 256 Å (48.3 eV) line of He II is $I = 12,440$; whereas the observed intensity is too weak ($I = 1580$) which challenges the assignment of the 304 Å line solely to the He II transition.

Temporal variation in the disproportionation line intensities may reflect solar activity. For example, the coronal power is ≅ 0.01% of the solar power in the case of a quite Sun and as high as 100% of the solar power in the case of an active Sun [77]. Emission lines corresponding to lower-energy hydrogen transitions and assigned as such in Table 5 greatly increase in intensity during flare events [1,78–80] which is evidence that lower-energy hydrogen transitions may be a factor in the cause of solar flares.

4. Conclusion

Transitions to fractional quantum energy levels were previously recorded at the Institut für Niedertemperatur-Plasmaphysik e.V. We report that extreme ultraviolet (EUV) spectroscopy was recorded on microwave and glow discharges of helium with 2% hydrogen. Novel emission lines were observed with energies of $q13.6$ eV where $q = 1, 2, 3, 4, 6, 7, 8, 9,$ or 11 or these lines inelastically

scattered by helium atoms wherein 21.2 eV was absorbed in the excitation of He ($1s^2$) to He ($1s^1 2p^1$). These lines were identified as hydrogen transitions to electronic energy levels below the "ground" state corresponding to fractional quantum numbers. Furthermore, astrophysical data was reviewed, and such transitions were found to match the spectral lines of the extreme ultraviolet background of interstellar space. These transitions may resolve the paradox of the identity of dark matter and account for many celestial observations such as: diffuse Hα emission is ubiquitous throughout the Galaxy and widespread sources of flux shortward of 912 Å are required. The origin of the 633 Å emission observed by Labov and others [53] that could be a major source of ionization of interstellar hydrogen was also observed in our helium–hydrogen plasma. We assigned the 633 Å emission to atomic helium scattered 304 Å emission from the H$[a_H/3] \xrightarrow{H[a_H/2]} [a_H/4]$ hydrogen transition.

Furthermore, fractional hydrogen transitions were also assigned to lines in the solar EUV spectrum which may resolve the solar neutrino problem, the mystery of the cause of sunspots and other solar activity, and why the Sun emits X-rays. In addition to producing power on the Sun, the catalysis of hydrogen represents a new powerful energy source with the potential for direct conversion of plasma to electricity with the production of novel compounds [40,41].

References

[1] Mills R. The grand unified theory of classical quantum mechanics, January 2000 edn. Cranbury, NJ: BlackLight Power, Inc. Distributed by Amazon.com.

[2] Mills R. The grand unified theory of classical quantum mechanics. Global foundation, Inc. Orbis Scientiae entitled The Role of Attractive and Repulsive Gravitational Forces in Cosmic Acceleration of Particles The Origin of the Cosmic Gamma Ray Bursts, 29th Conference on High Energy Physics and Cosmology Since 1964, Dr. Behram N. Kursunoglu, Chairman, December 14–17, 2000, Lago Mar Resort, Fort Lauderdale, FL.

[3] Mills R. The grand unified theory of classical quantum mechanics. Global Foundation, Inc. Orbis Scientiae entitled The Role of Attractive and Repulsive Gravitational Forces in Cosmic Acceleration of Particles The Origin of the Cosmic Gamma Ray Bursts, 29th Conference on High Energy Physics and Cosmology Since 1964, Dr. Behram N. Kursunoglu, Chairman, Lago Mar Resort, Fort Lauderdale, FL, New York: Kluwer Academic/Plenum Publishers, December 14–17, 2000. p. 243–58.

[4] Mills R. The grand unified theory of classical quantum mechanics. Int J Hydrogen Energy, submitted for publication.

[5] Mills R. The hydrogen atom revisited. Int J Hydrogen Energy 2000;25(12):1171–83.

[6] Mills R. The nature of free electrons in superfluid helium — a test of quantum mechanics and a basis to review its foundations and make a comparison to classical theory. Int J Hydrogen Energy 2001;26(10):1059–96.

[7] Mills R, Ray P. Vibrational spectral emission of fractional-principal-quantum-energy-level hydrogen molecular ion. Int J Hydrogen Energy, submitted for publication.

[8] Mills R, Ray P. Spectroscopic identification of a novel catalytic reaction of potassium and atomic hydrogen and the hydride ion product. Int J Hydrogen Energy, in press.

[9] Mills R. Spectroscopic identification of a novel catalytic reaction of atomic hydrogen and the hydride ion product. Int J Hydrogen Energy 2001;26(10):1041–58.

[10] Mills R, Greenig N, Hicks S. Optically measured power balances of anomalous discharges of mixtures of argon, hydrogen, and potassium, rubidium, cesium, or strontium vapor. Int J Hydrogen Energy, submitted for publication.

[11] Mills R, Nansteel M. Argon–hydrogen–strontium plasma light source. IEEE Trans Plasma Sci, submitted for publication.

[12] Mills R, Nansteel M, Lu Y. Excessively bright hydrogen–strontium plasma light source due to an energy resonance of strontium with hydrogen. European J Phys D, submitted for publication.

[13] Mills R, Dong J, Lu Y. Observation of extreme ultraviolet hydrogen emission from incandescently heated hydrogen gas with certain catalysts. Int J Hydrogen Energy 2000;25:919–43.

[14] Mills R. Observation of extreme ultraviolet emission from hydrogen-KI plasmas produced by a hollow cathode discharge. Int J Hydrogen Energy 2001;26(6):579–92.

[15] Mills R. Temporal behavior of light-emission in the visible spectral range from a Ti-K2CO3-H-Cell. Int J Hydrogen Energy 2001;26(4):327–32.

[16] Mills R, Onuma T, Lu Y. Formation of a hydrogen plasma from an incandescently heated hydrogen-catalyst gas mixture with an anomalous afterglow duration. Int J Hydrogen Energy 2001;26(7):749–62.

[17] Mills R, Nansteel M, Lu Y. Observation of extreme ultraviolet hydrogen emission from incandescently heated hydrogen gas with strontium that produced an anomalous optically measured power balance. Int J Hydrogen Energy 2001;26(4):309–26.

[18] Mills R, Dong J, Lu Y, Conrads J. Observation of extreme ultraviolet hydrogen emission from incandescently heated hydrogen gas with certain catalysts. 1999 Pacific Conference on Chemistry and Spectroscopy and the 35th ACS Western Regional Meeting, Ontario Convention Center, California, October 6–8, 1999.

[19] Mills R, Dong J, Greenig N, Lu Y. Observation of extreme ultraviolet hydrogen emission from incandescently heated hydrogen gas with certain catalysts. 11th Annual US Hydrogen Meeting, Vienna, VA, National Hydrogen Association, February 29–March 2, 2000.

[20] Mills R, Dhandapani B, Greenig N, He J, Dong J, Lu Y, Conrads H. Formation of an energetic plasma and novel hydrides from incandescently heated hydrogen gas with certain catalysts. 11th Annual US Hydrogen Meeting, Vienna, VA, National Hydrogen Association, February 29–March 2, 2000.

[21] Mills R, Dong J, Greenig N, Lu Y. Observation of extreme ultraviolet hydrogen emission from incandescently heated hydrogen gas with certain catalysts. 219th National ACS Meeting, San Francisco, CA, March 26–30, 2000.

[22] Mills R, Dhandapani B, Greenig N, He J, Dong J, Lu Y, Conrads H. Formation of an energetic plasma and novel hydrides from incandescently heated hydrogen gas with certain catalysts. 219th National ACS Meeting, San Francisco, CA, March 26–30, 2000.

[23] Mills R, Dhandapani B, Greenig N, He J, Dong J, Lu Y, Conrads H. Formation of an energetic plasma and novel hydrides from incandescently heated hydrogen gas with certain catalysts. 29th Northeast Regional Meeting, University of Connecticut, Storrs, CT, June 18–21, 2000.

[24] Mills R, Dhandapani B, Greenig N, He J, Dong J, Lu Y, Conrads H. Formation of an energetic plasma and novel hydrides from incandescently heated hydrogen gas with certain catalysts. 220th ACS National Meeting, Washington, DC, August 20–24, 2000.

[25] Mills R, Dhandapani B, Nansteel M, He J, Voigt A. Identification of compounds containing novel hydride ions by nuclear magnetic resonance spectroscopy. Int J Hydrogen Energy 2001;26(9):965–79.

[26] Mills R, Dhandapani B, Greenig N, He J. Synthesis and characterization of potassium iodo hydride. Int J Hydrogen Energy 2000;25(12):1185–203.

[27] Mills R. Novel inorganic hydride. Int J Hydrogen Energy 2000;25:669–83.

[28] Mills R. Novel hydrogen compounds from a potassium carbonate electrolytic cell. Fusion Technol 2000;37(2):157–82.

[29] Mills R, Dhandapani B, Nansteel M, He J, Shannon T, Echezuria A. Synthesis and characterization of novel hydride compounds. Int J Hydrogen Energy 2001;26(4):339–67.

[30] Mills R. Highly stable novel inorganic hydrides. J Mater Res, submitted for publication.

[31] Mills R. Novel hydride compound. 1999 Pacific Conference on Chemistry and Spectroscopy and the 35th ACS Western

Regional Meeting, Ontario Convention Center, California, October 6–8, 1999.

[32] Mills R, Dhandapani B, Greenig N, He J. Synthesis and characterization of potassium iodo hydride. 1999 Pacific Conference on Chemistry and Spectroscopy and the 35th ACS Western Regional Meeting, Ontario Convention Center, California, October 6–8, 1999.

[33] Mills R, He J, Dhandapani B. Novel hydrogen compounds. 1999 Pacific Conference on Chemistry and Spectroscopy and the 35th ACS Western Regional Meeting, Ontario Convention Center, California, October 6–8, 1999.

[34] Mills R. Novel hydride compound. 11th Annual US Hydrogen Meeting, Vienna, VA, National Hydrogen Association, February 29–March 2, 2000.

[35] Mills R, He J, Dhandapani B. Novel alkali and alkaline earth hydrides. 11th Annual US Hydrogen Meeting, Vienna, VA, National Hydrogen Association, February 29–March 2, 2000.

[36] Mills R. Novel hydride compound. 219th National ACS Meeting, San Francisco, CA, March 26–30, 2000.

[37] Mills R, He J, Dhandapani B. Novel alkali and alkaline earth hydrides. 219th National ACS Meeting, San Francisco, CA, March 26–30, 2000.

[38] Mills R, He J, Dhandapani B. Novel alkali and alkaline earth hydrides. 220th ACS National Meeting, Washington, DC, August 20–24, 2000.

[39] Mills R, Good W, Voigt A, Jinquan Dong, Minimum heat of formation of potassium iodo hydride. Int J Hydrogen Energy, in press.

[40] Mills R. BlackLight power technology — a new clean hydrogen energy source with the potential for direct conversion to electricity. Proceedings of the National Hydrogen Association, 12th Annual US Hydrogen Meeting and Exposition, Hydrogen: The Common Thread, The Washington Hilton and Towers, Washington DC, March 6–8, 2001. p. 671–97.

[41] Mills R. BlackLight power technology — a new clean energy source with the potential for direct conversion to electricity. Global Foundation International Conference on Global Warming and Energy Policy, Dr. Behram N. Kursunoghu, Chairman, Fort. Lauderdale, FL, Kluwer Academic/Plenum Publishers, New York: November 26–28, 2000. p. 1059–96.

[42] Sidgwick NV, The chemical elements and their compounds, vol. 1. Oxford: Clarendon Press, 1950. p. 171.

[43] Lamb MD. Luminescence spectroscopy. London: Academic Press, 1978. p. 68.

[44] Thompson BJ. Handbook of nonlinear optics. New York: Marcel Dekker, Inc., 1996. p. 427–548.

[45] Shen YR, The principles of nonlinear optics. New York: Wiley, 1984. p. 203–10.

[46] de Beauvoir B, Nez F, Julien L, Cagnac B, Biraben F, Touahri D, Hilico L, Acef O, Clairon A, Zondy JJ. Phys Rev Lett 1977;78(3):440–3.

[47] Kelly R. Atomic and ionic spectrum lines below 2000 angstroms: hydrogen through krypton, Part 1 (H-Cr), J Phys Chem Ref. Data. 1987;16 (Supp(1)):20–1. American Chemical Society and the American Institute of Physics for the National Bureau of Standards.

[48] NIST Atomic Spectra Database, www.physics.nist.gov/cgi-bin/AtData/display.ksh.

[49] Davidsen A, et al. Test of the decaying dark matter hypothesis using the Hopkins ultraviolet telescope. Nature 1991;351:128–30.

[50] Milan W. Shall the WIMPs inherit the universe. SPACE.com, 28 February, 2000. http://space.com/scienceastronomy/generalscience/dark_matter_000228.html.

[51] Abusaidi R. Exclusion limits on the WIMP-nucleon cross section from the cryogenic dark matter search. Phys Rev Lett 2000;84(25):5699–703.

[52] Oppenheimer BR, Hambly NC, Digby AP, Hodgkin ST, Saumon D. Direct detection of galactic halo dark matter. Science 2000;292:698–702.

[53] Labov S, Bowyer S. Spectral observations of the extreme ultraviolet background. Astrophys J 1991;371:810–9.

[54] Bower S, Field G, Mack J. Detection of an anisotrophic soft X-ray background flux. Nature 1968;217:32.

[55] Bahcall J et al. Solar neutrinos: a field in transition. Nature 1988;334 (11):487–93.

[56] Taubes G. Science 1992;256:1512–3.

[57] Taubes G. Science 1992;256:731–3.

[58] Schwarzschild B. Phys Today 1995;19–21.

[59] Kirsten TA. GALLEX solar neutrino results and status of GNO. Nucl Phys B (Proc Suppl) 1999;77:26–34.

[60] Anselmann P, Fockenbrock R, Hampel W, Heusser G, Kiko J, Kirsten T, Laubenstein M, Pernicka E, Pezzoni S, Rönn U, Sann M, Spielker F, Wink R, Wójcik M, Ammon Rv, Ebert KH, Fritsch T, Heidt D, Henrich E, Schlosser C, Stieglitz L, Weirich F, Balata M, Lalla H, Bellotti E, Cattadori X, Cremonesi O, Ferrari N, Fiorini E, Zanotti L, Altmann M, Feilitzsch Fv, Mössbauer R, Schandra U, Berthomieu G, Schatzman E, Carmi I, Dostrovsky I, Bacci C, Belli P, Bernabei R, d'Angelo S, Paoluzi L, Bevilacqua A, Charbit S, Cribier M, Dupont G, Gosset L, Rich J, Spiro M, Stolarczyk T, Tao C, Vignaud D, Boger J, Hahn RL, Hartmann FX, Rowley JK, Stoerner RW, Weneser J. First results from the Cr neutrino source experiment with the GALLEX detector. Nucl Phys B 1995;342:440–50.

[61] Gavrin VN. Solar neutrino results from SAGE. Nucl Phys B (Proc Suppl) 2001;91:36–43.

[62] Hampel W et al. GALLEX coll. Phys Lett B 1999;477:127.

[63] Abdyrashitov JN et al. SAGE coll. Phys Rev Lett 1999;83:4686.

[64] Bellotti E. First results from GNO. Nucl Phys B (Proc Suppl) 2001;91:44–9.

[65] Alltmann M, Balata M, Belli P, Bellotti E, Bernabei R, Burkert E, Cattadori C, Cerichelli G, Cribier M, d'Angelo S, Del Re G, Ebert KH, Feilitzsch FV, Ferrari N, Hampel W, Handt J, Henrich E, Heusser G, Kiko J, Kirsten T, Lachenmaier T, Lanfranchi J, Laubenstein M, Motta D, Rau W, Richter H, Wänninger H, Wójcik M, Zanotti L. GNO solar neutrino observations: results for GNO I. Nucl Phys B 2000;490:16–26.

[66] Belotti E. Measurement of low energy solar neutrino interaction rate. Excerpts from the presentation the XIX International Conference on Neutrino Physics and Astrophysics, September 16–21, 2000, Sudbury, ON, Canada, http://www.mpi-hd.mpg.de/kirsten/papers.html.

[67] Ahmad QR, et al. Measurement of charged current interactions produced by ^8B solar neutrinos at the Sudbury Neutrino Observatory. Phys Rev Lett 2001, submitted for publication.

[68] McDonald AB. First neutrino observations from the Sudbury neutrino observatory. Nucl Phys B (Proc Suppl) 2001;91:21–8.

[69] Suzuki Y. Solar neutrino results from Super-Kamiokande. Nucl Phys B (Proc Suppl) 2001;91:29–35.

BEST AVAILABLE COPY

1

[70] Svoboda R. Neutrino mass mixing measurements at Super-Kamiokande. Nucl Phys B (Proc Suppl) 2001;98:165–74.

3

[71] Thomas RJ, Neupert WM. Astrophys J Suppl Ser 1994;91:461–82.

5

[72] Malinovsky M, Heroux L. Astrophys J 1973;181:1009–30.

[73] Noyes R. The Sun, our star. Cambridge, MA: Harvard

7

University Press, 1982, p. 172.

[74] Phillips JH, Guide to the Sun. Cambridge, Great Britain:

9

Cambridge University Press, 1992. p 118–119; 120, 121; 144, 145.

[75] Harvey J. Phys Today 1995;32–8.

11

[76] Schwarzschild B. Phys Today 1990;17–20.

[77] Stix M. The Sun. Berlin: Springer, 1991, p. 351–6.

13

[78] Cowen R. Sci News 1992;141:344–6.

[79] Bowyer S. Science 1994;263:55–9.

15

[80] Fossi BCM et al. Astrophys J 1995;449:376–85.

Spectroscopic identification of a novel catalytic reaction of potassium and atomic hydrogen and the hydride ion product

Randell L. Mills *, Paresh Ray

BlackLight Power, Inc., 493 Old Trenton Road, Cranbury, NJ 08512, USA

Abstract

From a solution of a Schrödinger-type wave equation with a nonradiative boundary condition based on Maxwell's equations, Mills predicts that atomic hydrogen may undergo a catalytic reaction with certain atomized elements and ions which singly or multiply ionize at integer multiples of the potential energy of atomic hydrogen, 2.72 eV, i.e. $m \times 27.2$ eV, wherein m is an integer. The reaction involves a nonradiative energy transfer to form a hydrogen atom that is lower in energy than unreacted atomic hydrogen with the release of energy. One such atomic catalytic system involves potassium atoms. The first, second, and third ionization energies of potassium are 4.34066, 31.63, and 45.806 eV, respectively. The triple ionization ($t = 3$) reaction of to K–K^{3+}, then, has a net enthalpy of reaction of 81.7766 eV, which is equivalent to 3×27.2 eV. Intense extreme ultraviolet (EUV) emission was observed from incandescently heated atomic hydrogen and the atomized potassium catalyst that generated an anomalous plasma at low temperatures (e.g. $\approx 10^3$ K) and an extraordinary low field strength of about 1–2 V/cm. No emission was observed with potassium or hydrogen alone or when sodium replaced potassium with hydrogen. Emission was observed from K^{3+} confirmed the resonant nonradiative energy transfer of 3×27.2 eV from atomic hydrogen to atomic potassium. The catalysis product, a lower-energy hydrogen atom, was predicted to be a highly reactive intermediate which further reacts to form a novel hydride ion. The predicted hydride ion of hydrogen catalysis by atomic potassium is the hydride ion H$^-$(1/4). This ion was observed spectroscopically at 110 nm corresponding to its predicted binding energy of 11.2 eV. © 2001 Published by Elsevier Science Ltd. on behalf of the International Association for Hydrogen Energy.

Keywords: ■; ■; ■

1. Introduction

Based on the solution of a Schrödinger-type wave equation with a nonradiative boundary condition based on Maxwell's equations, Mills [1–38] predicts that atomic hydrogen may undergo a catalytic reaction with certain atomized elements or certain gaseous ions which singly or multiply ionize at integer multiples of the potential energy of atomic hydrogen, 27.2 eV. For example, cesium atoms ionize at an integer multiple of the potential energy of atomic hydrogen, $m \times 27.2$ eV. The enthalpy of ionization of Cs–Cs^{2+} has a net enthalpy of reaction of 27.05135 eV,

which is equivalent to $m = 1$ [39]. The reaction Ar$^+$–Ar^{2+} has a net enthalpy of reaction of 27.63 eV, which is equivalent to $m = 1$ [39]. In each case, the reaction involves a nonradiative energy transfer to form a hydrogen atom that is lower in energy than unreacted atomic hydrogen. The product hydrogen atom has an energy state that corresponds to a fractional principal quantum number. Recent analysis of mobility and spectroscopy data of individual electrons in liquid helium show direct experimental confirmation that electrons may have fractional principal quantum energy levels [35]. The lower-energy hydrogen atom is a highly reactive intermediate which further reacts to form a novel hydride ion. Emission was observed previously from a continuum state of Cs^{2+} and Ar^{2+} at 53.3 and 45.6 nm, respectively [5]. The single emission feature with the absence of the other corresponding Rydberg series of lines from these species

* Corresponding author. Tel.: +1-609-490-1090; fax: +1-609-490-1066.

E-mail address: rmills@blacklightpower.com (R.L. Mills).

1   confirmed the resonant nonradiative energy transfer of
     27.2 eV from atomic hydrogen to atomic cesium or Ar⁺.
3   The catalysis product, a lower-energy hydrogen atom, was
     predicted to be a highly reactive intermediate which further
5   reacts to form a novel hydride ion. The predicted hydride
     ion of hydrogen catalysis by either cesium atom or Ar⁺
7   catalyst is the hydride ion H⁻(1/2). This ion was observed
     spectroscopically at 407 nm corresponding to its predicted
9   binding energy of 3.05 eV. The catalytic reactions and
     formation of the hydride ions are given in Appendix A.

11   Additional prior studies that support the possibility of
     a novel reaction of atomic hydrogen which produces an
13   anomalous discharge and produces novel hydride com-
     pounds include extreme ultraviolet (EUV) spectroscopy
15   [5,7–20], plasma formation [5–20], power generation
     [6–8,13,36], and analysis of chemical compounds [16,18–34].
17   Typically, the emission of extreme ultraviolet light from
     hydrogen gas is achieved via a discharge at high voltage,
19   a high power inductively coupled plasma, or a plasma cre-
     ated and heated to extreme temperatures by RF coupling
21   (e.g. > 10⁶ K) with confinement provided by a toroidal
     magnetic field. Observation of intense extreme ultraviolet
23   (EUV) emission at low temperatures (e.g. ≈ 10³ K) from
     atomic hydrogen and certain atomized elements or certain
25   gaseous ions has been reported previously [5,7–20]. The
     only pure elements that were observed to emit EUV were
27   those predicted [1–38] wherein the ionization of t electrons
     from an atom or ion to a continuum energy level is such
29   that the sum of the ionization energies of the t electrons
     is approximately $m \times 27.2$ eV where t and m are each an
31   integer.
         The observed EUV emission could not be explained by
33   conventional chemistry; rather it must have been due to a
     novel chemical reaction between catalyst and atomic hy-
35   drogen. The catalysis of hydrogen involves the nonradiative
     transfer of energy from atomic hydrogen to a catalyst which
37   may then release the transferred energy by radiative and
     nonradiative mechanisms. As a consequence of the nonra-
39   diative energy transfer, the hydrogen atom becomes unsta-
     ble and emits further energy until it achieves a lower-energy
41   nonradiative state having a principal energy level given by
     Eqs. (A.1) and (A.2) of Appendix A.
43   The energy released during catalysis may undergo inter-
     nal conversion and ionize or excite molecular and atomic
45   hydrogen resulting in hydrogen emission which includes
     well characterized ultraviolet lines such as the Lyman se-
47   ries. Lyman series emission, emission due to the catalyst
     mechanism, and emission of the hydride ion product were
49   measured by EUV spectroscopy. The catalytic reactions and
     binding energies of the product hydride ions are given in
51   Appendix A.
         Potassium, cesium, and strontium atoms and Rb⁺ ion
53   ionize at integer multiples of the potential energy of atomic
     hydrogen. In prior studies [5,7–20] and in the current
55   experiments, these catalysts caused intense extreme ultra-
     violet (EUV) emission from incandescently heated atomic

57   hydrogen and the atomized catalyst that generated a plasma
     at low temperatures (e.g. ≈ 10³ K). Whereas, the chemi-
59   cally similar noncatalyst atoms, sodium, magnesium and
     barium, do not ionize at integer multiples of the potential
61   energy of atomic hydrogen, did not generate a plasma,
     and caused no emission. In the case of atomic potassium
63   catalyst, the first, second, and third ionization energies are
     4.34066, 31.63, 45.806 eV, respectively. The triple ioniza-
65   tion ($t = 3$) reaction of K–K³⁺, then, has a net enthalpy of
     reaction of 81.7766 eV, which is equivalent to 3×27.2 eV.
67   Emission was observed from K³⁺ that confirmed the res-
     onant nonradiative energy transfer of 3×27.2 eV from
69   atomic hydrogen to atomic potassium. The predicted hy-
     dride ion of hydrogen catalysis by atomic potassium is the
71   hydride ion H⁻(1/4). This ion was observed spectroscop-
     ically at 110 nm corresponding to its predicted binding
73   energy of 11.2 eV.

2. Experimental

2.1. EUV spectroscopy   75

         Due to the extremely short wavelength of this radiation,
77   "transparent" optics do not exist. Therefore, a windowless
     arrangement was used wherein the source was connected
79   to the same vacuum vessel as the grating and detectors of
     the EUV spectrometer. Windowless EUV spectroscopy was
81   performed with an extreme ultraviolet spectrometer that was
     mated with the cell. Differential pumping permitted a high
83   pressure in the cell as compared to that in the spectrome-
     ter. This was achieved by pumping on the cell outlet and
85   pumping on the grating side of the collimator that served
     as a pin-hole inlet to the optics. The cell was operated un-
87   der hydrogen flow conditions while maintaining a constant
     hydrogen pressure in the cell with a mass flow controller.

89   The experimental set up shown in Fig. 1 comprised a
     quartz cell which was 500 mm in length and 50 mm in
91   diameter. Three ports for gas inlet, outlet, and photon
     detection were on the cap of the cell. The cell pump was a
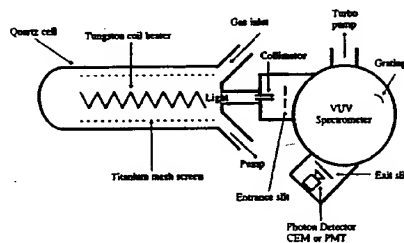

Fig. 1. The experimental set up comprising a gas cell light source
and an EUV spectrometer which was differentially pumped.

mechanical pump. The spectrometer was continuously evac-
uated to 10^{-4}–10^{-6} Torr by a turbomolecular pump with the
pressure read by a cold cathode pressure gauge. The EUV
spectrometer was connected to the cell light source with a
1.5 mm × 5 mm collimator which provided a light path to the
slits of the EUV spectrometer. The collimator also served
as a flow constrictor of gas from the cell. Valves were be-
tween the cell and the mechanical pump, the cell and the
monochromator, and the monochromator and its turbo pump.

A tungsten filament (0.508 mm in diameter and 800 cm
in length, total resistance $\sim 2.5\ \Omega$) and a titanium cylin-
drical screen (300 mm long and 40 mm in diameter) that
performed as a hydrogen dissociator were inside the quartz
cell. A new dissociator was used for each experiment. A
filament was coiled on a grooved ceramic support to main-
tain its shape when heated. The return lead ran through the
middle of the ceramic support. The filament leads were cov-
ered by an alumina sheath. The titanium screen was elec-
trically floated. The power was applied to the filament by
a power supply (Sorensen 80-13) which was controlled by
a constant power controller. For the catalysts, the cell was
operated with a maximum of 300 W of input power which
corresponded to a cell wall temperature of about 700°C. The
temperature of the tungsten filament was estimated to be
about 1500°C. In the case of the noncatalysts, the cell power
was increased to the maximum of 500 W. The gas was ultra-
high purity hydrogen. The gas pressure inside the cell was
maintained at about 300 mTorr with a hydrogen flow rate of
5.5 sccm controlled by a 0–20 sccm range mass flow con-
troller (MKS 1179A21CS1BB) with a readout (MKS type
246). The entire quartz cell was enclosed inside an insula-
tion package (Zircar AL-30). Several K-type thermocouples
were placed in the insulation to measure key temperatures
of the cell and insulation. The thermocouples were read with
a multichannel computer data acquisition system.

In the present study, the light emission phenom-
ena was studied for (1) hydrogen, argon, neon, and
helium alone, (2) sodium, rubidium, magnesium,
strontium, and barium metals, and (3) Na$_2$CO$_3$, K$_2$CO$_3$,
and Cs$_2$CO$_3$. The inorganic test materials were coated
on a titanium screen dissociator by the method of wet
impregnation. The screen was coated by dipping it in a
0.6 M Na$_2$CO$_3$/10% H$_2$O$_2$, 0.6 M K$_2$CO$_3$/10% H$_2$O$_2$, or
0.6 M Cs$_2$CO$_3$/10% H$_2$O$_2$ solution, and the crystalline ma-
terial was dried on the surface by heating for 12 h in a
drying oven at 130°C. A new dissociator was used for each
experiment. The metals were placed in the bottom of the
cell and volatilized by the filament heater.

The light emission was introduced to an EUV spec-
trometer for spectral measurement. The spectrometer
was a McPherson 0.2 m monochromator (Model 302,
Seya-Namioka type) equipped with a 1200 lines/mm holo-
graphic grating with a platinum coating. The wavelength
region covered by the monochromator was 30–560 nm. The
vacuum inside the monochromator was maintained below
5×10^{-4} Torr by a turbo pump.

The EUV spectrum (40–160 nm) of the cell emission
was recorded with a channel electron multiplier (CEM). The
wavelength resolution was about 1 nm (FWHM) with an
entrance and exit slit width of 300 µm.

The EUV/UV/VIS spectrum (40–560 nm) of the cell
emission with hydrogen alone was recorded with a photo-
multiplier tube (PMT) and a sodium salicylate scintillator.
The PMT (Model R1527P, Hamamatsu) used has a spectral
response in the range of 185–680 nm with a peak efficiency
at about 400 nm. The scan interval was 0.4 nm. The inlet and
outlet slit were 500 µm with a corresponding wavelength
resolution of 2 nm.

2.2. Standard potassium emission spectrum

The standard extreme ultraviolet emission spectrum of
potassium was obtained with a gas discharge cell comprised
a five-way stainless steel cross that served as the anode
with a hollow stainless steel cathode that was coated with
K$_2$CO$_3$ by the same procedure used to coat the titanium
dissociator. The five-way cross was pressurized with 1 Torr
of hydrogen to initiate the discharge. The hydrogen was then
evacuated so that only potassium lines were observed. The
DC voltage at the time the EUV spectrum was recorded was
300 V.

3. Results

3.1. EUV spectroscopy

The intensity of the Lyman α emission as a function
of time from the gas cell at a cell temperature of 700°C
comprising a tungsten filament, a titanium dissociator, and
300 mTorr hydrogen with a flow rate of 5.5 sccm was tested
for several controls and catalysts. The cell was run with hy-
drogen but without any test material present to establish the
baseline of the spectrometer. The intensity of the Lyman α
emission as a function of time was measured for 3 h, and no
emission was observed. The corresponding UV/VIS spec-
trum (40–560 nm) is shown in Fig. 2. The spectrum was
recorded with a photomultiplier tube (PMT) and a sodium
salicylate scintillator. No emission was observed except for
the blackbody filament radiation at the longer wavelengths.
No emission was also observed for the pure elements alone
or when argon, neon, or helium replaced hydrogen. Sodium,
magnesium, or barium metal was vaporized by filament
heating. Sodium metal was also vaporized from Na$_2$CO$_3$
as the source. No emission was observed in any case. The
maximum filament power was greater than 500 W. A metal
coating formed in the cap of the cell over the course of the
experiment in all cases.

The intensity of the Lyman α emission as a function of
time with each of vaporized cesium from Cs$_2$CO$_3$, potas-
sium from K$_2$CO$_3$, Rb$^+$ from rubidium metal, and stron-
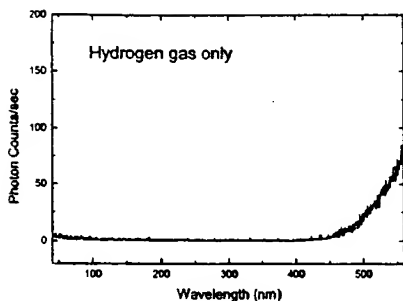tium from strontium metal was recorded. In all cases, strong

Fig. 2. The UV/VIS spectrum (40–560 nm) of the cell emission from the gas cell at a cell temperature of 700°C comprising a tungsten filament, a titanium dissociator, and 300 mTorr hydrogen that was recorded with a photomultiplier tube (PMT) and a sodium salicylate scintillator with an entrance and exit slit width of 500 μm. No emission was observed except for the blackbody filament radiation at the longer wavelengths.

Fig. 4. The EUV spectrum (45–80 nm) of the cell emission recorded at about the point of the maximum Lyman α emission from the gas cell at a cell temperature of 700°C comprising a tungsten filament, a titanium dissociator, 300 mTorr hydrogen, and vaporized potassium from K_2CO_3 that was recorded with a CEM. Line emission corresponding to K^{3+} was observed at 65–67 and 74–76 nm.
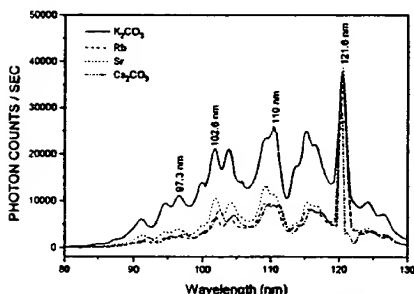

Fig. 3. The EUV spectrum (80–130 nm) of the cell emission recorded at about the point of the maximum Lyman α emission from the gas cell at a cell temperature of 700°C comprising a tungsten filament, a titanium dissociator, 300 mTorr hydrogen, and each of vaporized cesium from Cs_2CO_3, potassium from K_2CO_3, Rb^+ from rubidium metal, and strontium from strontium metal that was recorded with a CEM. The ratio of the intensities of the hydrogen peaks $B^{1}{}^{1}\Sigma_u^+ \rightarrow X^{1}\Sigma_g^+$ for $J = 1\text{–}6$ and $1\text{–}5$ at 109.989 and 108.946 nm, respectively is 0.88.

Fig. 5. The EUV spectrum (45–80 nm) of the cell emission recorded at about the point of the maximum Lyman α emission from a repeat gas cell at a cell temperature of 700°C comprising a tungsten filament, a titanium dissociator, 300 mTorr hydrogen, and vaporized potassium from K_2CO_3 that was recorded with a CEM. Line emission corresponding to K^{3+} was observed at 65–67 and 74–76 nm.

1   EUV emission was observed from vaporized catalyst with
     hydrogen. The superposition of the EUV spectra (80–
3   130 nm) of the cell emission recorded at about the point of
     the maximum Lyman α emission for each of the catalysts
5   is shown in Fig. 3. In each case, no emission was observed
     in the absence of hydrogen, and no emission occurred until
7   the catalyst was vaporized as indicated by the appearance
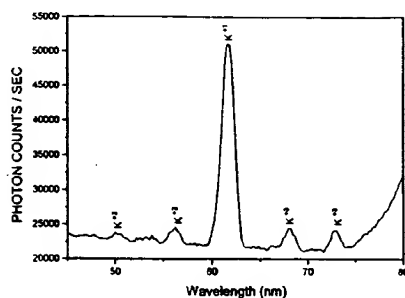
of a metal coating in the cap of the cell over the course of
the experiment.   9

3.2. EUV emission of potassium catalyst

   The EUV spectrum (45–80 nm) of the emission of the   11
potassium–hydrogen gas cell and a replication experiment
are shown in Figs. 4 and 5. Line emission corresponding   13
to K^{3+} was observed at 65–67 and 74–76 nm. K^{2+} was
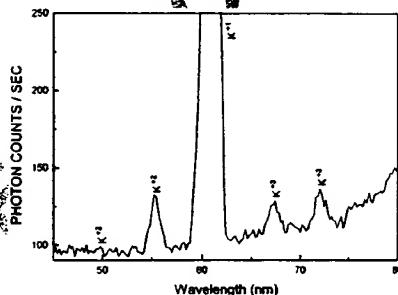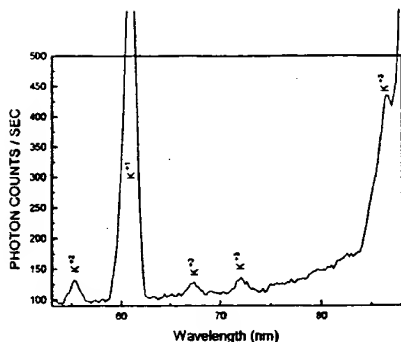observed at 51 and 55 nm, and K^+ was observed at 62 nm. 15

Fig. 6. The EUV spectrum (53–89 nm) of the cell emission recorded at about the point of the maximum Lyman α emission from a repeat gas cell at a cell temperature of 700°C comprising a tungsten filament, a titanium dissociator, 300 mTorr hydrogen, and vaporized potassium from K_2CO_3 that was recorded with a CEM. A large K^{3+} peak was observed at 89.2 nm.
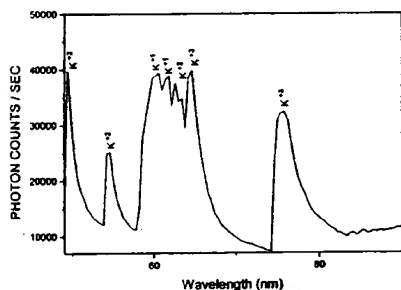

Fig. 7. The EUV spectrum (50–90 nm) recorded of a standard potassium plasma excited by a discharge that comprised a five-way stainless steel cross that serves the anode with a hollow stainless steel cathode. The assignment of the K^{3+}, K^{2+}, and K^+ lines were confirmed by the standard potassium plasma spectrum.

1 A large K^{3+} peak shown in Fig. 6 was also observed at 89.2 nm. The assignments of the K^{3+}, K^{2+}, and K^+ lines
3 were confirmed by the standard potassium plasma spectrum shown in Fig. 7 and NIST tables [40,41].

5 3.3. 110 nm emission with potassium catalyst

7 The EUV spectrum (80–130 nm) of the cell emission from the potassium gas cell and a replication experiment are shown in Figs. 8 and 9. The EUV spectrum (80–130 nm)
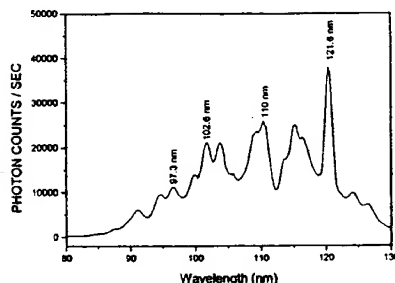

Fig. 8. The EUV spectrum (80–130 nm) of the cell emission recorded at about the point of the maximum Lyman α emission from the gas cell at a cell temperature of 700°C comprising a tungsten filament, a titanium dissociator, 300 mTorr hydrogen, and vaporized potassium from K_2CO_3 that was recorded with a CEM. The ratio of the peak at 110 nm versus the hydrogen peak at 108.946 nm is 1.19. Whereas, the peaks at these wavelengths in the controls shown in Fig. 3 is 0.883. The increase in intensity at 110 nm compared to hydrogen emission alone was assigned to a contribution from $H^-(1/4)$.
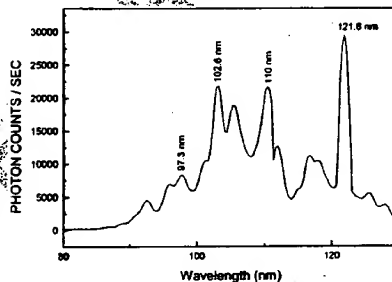
Fig. 9. The EUV spectrum (80–130 nm) of the cell emission recorded at about the point of the maximum Lyman α emission from a repeat gas cell at a cell temperature of 700°C comprising a tungsten filament, a titanium dissociator, 300 mTorr hydrogen, and vaporized potassium from K_2CO_3 that was recorded with a CEM. The ratio of the peak at 110 nm versus the hydrogen peak at 108.946 nm is 1.61. Whereas, the peaks at these wavelengths in the controls shown in Fig. 3 is 0.883. The increase in intensity at 110 nm compared to hydrogen emission alone was assigned to a contribution from $H^-(1/4)$.

9 of the cell emission from the cesium, potassium, rubidium, and strontium gas cells are superimposed in Fig. 3. Only
11 potassium is predicted to form the hydride $H^-(1/4)$ with emission at 110 nm as shown in Appendix A and Table 1.
13 Molecular hydrogen has peaks in this region as shown in Fig. 3 for catalysts which form a plasma in hydrogen but

Table 1
The ionization energy of the hydrino hydride ion $H^-(n = 1/p)$ as a function of p

Hydride ion	Catalyst	r_1 $(a_0)^a$	Calculated ionization energy[b] (eV)	Calculated wavelength (nm)
$H^-(n = 1)$		1.8660	0.754	1645
$H^-(n = 1/2)$	Rb$^+$,Cs	0.9330	3.047	407
$H^-(n = 1/3)$		0.6220	6.610	188
$H^-(n = 1/4)$	K	0.4665	11.23	110
$H^-(n = 1/5)$		0.3732	16.70	74.2
$H^-(n = 1/6)$		0.3110	22.81	54.4
$H^-(n = 1/7)$		0.2666	29.34	42.3
$H^-(n = 1/8)$	Sr	0.2333	36.08	34.4
$H^-(n = 1/9)$		0.2073	42.83	28.9
$H^-(n = 1/10)$		0.1866	49.37	25.1
$H^-(n = 1/11)$		0.1696	55.49	22.34
$H^-(n = 1/12)$		0.1555	60.98	20.33
$H^-(n = 1/13)$		0.1435	65.62	18.89
$H^-(n = 1/14)$		0.1333	69.21	17.91
$H^-(n = 1/15)$		0.1244	71.53	17.33
$H^-(n = 1/16)$		0.1166	72.38	17.13
$H^-(n = 1/17)$		0.1098	71.54	17.33
$H^-(n = 1/18)$		0.1037	68.80	18.02
$H^-(n = 1/19)$		0.0982	63.95	19.39
$H^-(n = 1/20)$		0.0933	56.78	21.83
$H^-(n = 1/21)$		0.0889	47.08	26.33
$H^-(n = 1/22)$		0.0848	34.63	35.80
$H^-(n = 1/23)$		0.0811	19.22	64.49
$H^-(n = 1/24)$		0.0778	0.6535	1897
$H^-(n = 1/25)$			Not stable	

[a] From Eq. (A.15).
[b] From Eq. (A.16).

are predicted to form a hydride different from $H^-(1/4)$. The hydrogen peaks in the region of 110 nm are due to the transition $B^1\Sigma_u^+ \rightarrow X^1\Sigma_g^+$. A peak at 109.989 nm is due to $v = 1-6$, and a peak at 108.946 nm is due to $v = 1-5$. The experimental emission intensity ratio from Fig. 3 is

$$\frac{\text{Intensity}(109.989)}{\text{Intensity}(108.946)} = \frac{13,701 \text{ photon counts/s}}{15,506 \text{ photon counts/s}} = 0.883, \quad (1)$$

whereas the ratio of the peak at 110 nm versus the peak at 108.946 nm with potassium catalyst and hydrogen shown in Fig. 8 is

$$\frac{\text{Intensity}(110)}{\text{Intensity}(108.946)} = \frac{27,897 \text{ photon counts/s}}{23,280 \text{ photon counts/s}} = 1.19. \quad (2)$$

The ratio of the peak at 110 nm versus the peak at 108.946 nm with potassium catalyst and hydrogen shown in Fig. 9 is

$$\frac{\text{Intensity}(110)}{\text{Intensity}(108.946)} = \frac{21,723 \text{ photon counts/s}}{13,462 \text{ photon counts/s}} = 1.61. \quad (3)$$

The 110 nm peak is twice that of the control molecular hydrogen peak. This peak dominated the molecular hydrogen

peak at 108.946 nm such that the counts due to each peak were determined by expanding the scale and deconvolving the superimposed peaks. Potassium does not have emission lines in the region of 110 nm. Thus, from the comparison, a novel continuum feature is observed at 110 nm which was not due to hydrogen or potassium emission. The novel 110 nm continuum peak was observed only with potassium and atomic hydrogen present over an extended reaction time. As shown in Figs. 8 and 3, the Lyman β and Lyman δ lines of the potassium gas cell at 102.6 and 97.3 nm, respectively, have a greater intensity relative to Lyman α line at 121.6 nm than the other catalysts which indicates a high plasma temperature. These results are consistent with the formation of $H^-(1/4)$ from the catalysis of atomic hydrogen by $K(m)$.

4. Discussion

A plasma that emitted intense EUV formed at low temperatures (e.g. $\approx 10^3$ K) from atomic hydrogen and each of Rb$^+$, cesium, potassium, and strontium catalyst which was vaporized by heating. No possible chemical reactions of the tungsten filament, the dissociator, the vaporized test material, and 300 mTorr hydrogen at a cell temperature of 700°C could be found which accounted for the hydrogen Lyman α line emission. In fact, no known chemical reaction releases enough energy to excite Lyman α emission from hydrogen. The emission was not observed with catalyst or hydrogen alone. Intense emission was observed for catalyst with hydrogen gas, but no emission was observed when sodium, magnesium, or barium replaced a catalyst with hydrogen. This result indicates that the emission was due to a reaction of the catalyst with hydrogen.

The only pure elements that were observed to emit EUV were those wherein the ionization of t electrons from an atom or ion to a continuum energy level is such that the sum of the ionization energies of the t electrons is approximately $m \times 27.2$ eV where t and m are each an integer. Rubidium ions and potassium, cesium, and strontium atoms ionize at an integer multiple of the potential energy of atomic hydrogen, $m \times 27.2$ eV. The triple ionization ($t = 3$) reaction of $K-K^{3+}$ has a net enthalpy of reaction of 81.7766 eV, which is equivalent to $m = 3$. The reaction Rb$^+$ to Rb^{2+} has a net enthalpy of reaction of 27.28 eV, which is equivalent to $m = 1$. The double ionization ($t = 2$) of Cs–Cs^{2+} has a net enthalpy of reaction of 27.05135 eV, which is equivalent to $m = 1$ [39]. The ionization reaction of Sr–Sr^{5+}, ($t = 5$) has a net enthalpy of reaction of 188.2 eV, which is equivalent to $m = 7$. In each case, the reaction involves a nonradiative energy transfer to form a hydrogen atom that is lower in energy than unreacted atomic hydrogen.

Characteristic emission was observed from K^{3+} which confirmed the resonant nonradiative energy transfer of 3×27.2 eV from atomic hydrogen to atomic potassium (Eq. (A.5)). With a highly conductive plasma, the voltage of the cell was about 20 V, and the field strength was about

1–2 V/cm which was too low to ionize potassium to K^{3+} which requires at least 81.7766 eV. The K^{3+} lines generated in the incandescently heated cell and due to the catalyst reaction of atomic hydrogen were confirmed by a high voltage discharge and NIST tables [40,41].

$K(m)$ is predicted to catalyze hydrogen to form $H[a_H/4]$ which reacts with an electron to form $H^-(1/4)$. The predicted $H^-(1/4)$ hydride ion of hydrogen catalysis by potassium was observed spectroscopically at 110 nm corresponding to its predicted binding energy of 11.2 eV. The hydride reaction product formed over time.

The release of energy from hydrogen as evidenced by the EUV emission must result in a lower-energy state of hydrogen. The present study identified the formation of a novel hydride ion. The formation of novel compounds based on novel hydride ions would be a substantial evidence supporting catalysis of hydrogen as the mechanism of the observed EUV emission and further support the present spectroscopic identification of $H^-(1/4)$. Compounds containing novel hydride ions have been isolated as products of the reaction of atomic hydrogen with atoms and ions identified as catalysts in the present study and previously reported EUV studies [5,7–34,36]. The novel hydride compounds were identified analytically by techniques such as time of flight secondary ion mass spectroscopy, X-ray photoelectron spectroscopy, and ^{1}H nuclear magnetic resonance spectroscopy. For example, the time of flight secondary ion mass spectroscopy showed a large hydride peak in the negative spectrum. The X-ray photoelectron spectrum showed large metal core level shifts due to binding with the hydride as well as novel hydride peaks. The ^{1}H nuclear magnetic resonance spectrum showed significantly upfield shifted peaks which corresponded to and identified novel hydride ions.

The hydride ion $H^-(1/4)$ has been reported previously [22]. KHI containing $H^-(1/4)$ was synthesized by reaction of potassium metal, atomic hydrogen, and KI. The XPS spectrum of the product blue crystals differed from that of KI by having additional features at 9.1 and 11.1 eV. The XPS peaks centered at 9.0 and 11.1 eV that did not correspond to any other primary element peaks were assigned to $H^-(n=1/4)E_b = 11.2$ eV hydride ion (Eq. (A.18)) in two different chemical environments, where E_b is the predicted vacuum binding energy. Furthermore, the reported minimum heats of formation of KHI by the catalytic reaction of potassium with atomic hydrogen and KI were over -2000 kJ/mol H_2 compared to the enthalpy of combustion of hydrogen of -241.8 kJ/mol H_2 [36]. The implications are that a new field of novel hydrogen chemistry has been discovered that represents a new source of energy with the potential for direct conversion of plasma to electricity [37,38].

5. Conclusion

Characteristic emission was observed from K^{3+} which confirmed the resonant nonradiative energy transfer of 3 · 27.2 eV from atomic hydrogen to atomic potassium (Eq. (A.5)). The predicted $H^-(1/4)$ hydride ion of hydrogen catalysis by potassium catalyst given by Eqs. (A.5)–(A.7) and Eq. (A.18) was observed spectroscopically at 110 nm corresponding to its predicted binding energy of 11.2 eV.

Appendix A.

A.1. Catalysts

The mechanism of EUV emission and formation of novel hydrides cannot be explained by the conventional chemistry of hydrogen; rather it must have been due to a novel chemical reaction between catalyst and atomic hydrogen. Mills [1–38] predicts that certain atoms or ions serve as catalysts to release energy from hydrogen to produce an increased binding energy hydrogen atom called a *hydrino atom* having a binding energy of

$$\text{Binding energy} = \frac{13.6 \text{ eV}}{n^2}, \quad (A.1)$$

where

$$n = 1, \frac{1}{2}, \frac{1}{3}, \frac{1}{4}, \ldots, \frac{1}{p}   \quad (A.2)$$

and p is an integer greater than 1, designated as $H[a_H/p]$ where a_H is the radius of the hydrogen atom. Hydrinos are predicted to form by reacting an ordinary hydrogen atom with a catalyst having a net enthalpy of reaction of about

$$m \times 27.2 \text{ eV},   \quad (A.3)$$

where m is an integer. This catalysis releases energy from the hydrogen atom with a commensurate decrease in size of the hydrogen atom, $r_n = na_H$. For example, the catalysis of $H(n=1)$–$H(n=1/2)$ releases 40.8 eV, and the hydrogen radius decreases from a_H to $\frac{1}{2}a_H$.

The excited energy states of atomic hydrogen are also given by Eq. (A.1) except that

$$n = 1, 2, 3, \ldots .   \quad (A.4)$$

The $n=1$ state is the "ground" state for "pure" photon transitions (the $n=1$ state can absorb a photon and go to an excited electronic state, but it cannot release a photon and go to a lower-energy electronic state). However, an electron transition from the ground state to a lower-energy state is possible by a nonradiative energy transfer such as multipole coupling or a resonant collision mechanism. These lower-energy states have fractional quantum numbers, $n = 1/$integer. Processes that occur without photons and that

8

require collisions are common. For example, the exothermic chemical reaction of $H + H$ to form H_2 does not occur with the emission of a photon. Rather, the reaction requires a collision with a third body, M, to remove the bond energy— $H + H + M \rightarrow H_2 + M^*$ [43]. The third body distributes the energy from the exothermic reaction, and the end result is the H_2 molecule and an increase in the temperature of the system. Some commercial phosphors are based on nonradiative energy transfer involving multipole coupling. For example, the strong absorption strength of Sb^{3+} ions along with the efficient nonradiative transfer of excitation from Sb^{3+} to Mn^{2+}, are responsible for the strong manganese luminescence from phosphors containing these ions [44]. Similarly, the $n = 1$ state of hydrogen and the $n = 1/integer$ states of hydrogen are nonradiative, but a transition between two nonradiative states is possible via a nonradiative energy transfer, say $n = 1–1/2$. In these cases, during the transition the electron couples to another electron transition, electron transfer reaction, or inelastic scattering reaction which can absorb the exact amount of energy that must be removed from the hydrogen atom. Thus, a catalyst provides a net positive enthalpy of reaction of $m \times 27.2$ eV (i.e. it absorbs $m \times 27.2$ eV where m is an integer). Certain atoms or ions serve as catalysts which resonantly accept energy from hydrogen atoms and release the energy to the surroundings to effect electronic transitions to fractional quantum energy levels. Recent analysis of mobility and spectroscopy data of individual electrons in liquid helium show direct experimental evidence that electrons may have fractional principal quantum energy levels [35].
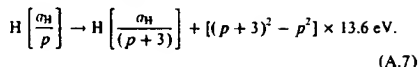
According to Mills [1–38], a catalytic system is provided by the ionization of t electrons from an atom or ion to a continuum energy level such that the sum of the ionization energies of the t electrons is approximately $m \times 27.2$ eV where m is an integer.

A.2. Potassium

One such atomic catalytic system involves potassium atoms. The first, second, and third ionization energies of potassium are 4.34066, 31.63, 45.806 eV respectively [39]. The triple ionization ($t = 3$) reaction of $K–K^{3+}$, then, has a net enthalpy of reaction of 81.7766 eV, which is equivalent to $m = 3$ in Eq. (A.3).
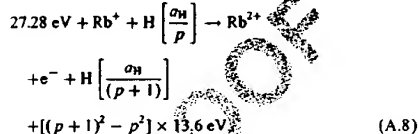
$$81.7766 \text{ eV} + K(m) + H\left[\frac{a_H}{p}\right] \rightarrow K^{3+}$$

$$+3e^- + H\left[\frac{a_H}{(p+3)}\right]$$

$$+[(p+3)^2 - p^2] \times 13.6 \text{ eV}, \tag{A.5}$$

$$K^{3+} + 3e^- \rightarrow K(m) + 81.7766 \text{ eV}. \tag{A.6}$$

The overall reaction is

$$H\left[\frac{a_H}{p}\right] \rightarrow H\left[\frac{a_H}{(p+3)}\right] + [(p+3)^2 - p^2] \times 13.6 \text{ eV}. \tag{A.7}$$
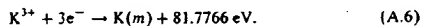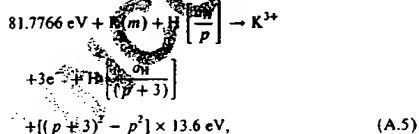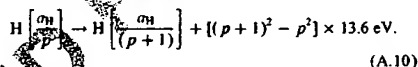
Vaporized atomic potassium was formed by hydrogen reduction and thermal decomposition of potassium carbonate.

A.3. Rubidium ion

Rubidium ions can also provide a net enthalpy of a multiple of that of the potential energy of the hydrogen atom. The second ionization energy of rubidium is 27.28 eV. The reaction $Rb^+–Rb^{2+}$ has a net enthalpy of reaction of 27.28 eV, which is equivalent to $m = 1$ in Eq. (A.3).

$$27.28 \text{ eV} + Rb^+ + H\left[\frac{a_H}{p}\right] \rightarrow Rb^{2+}$$

$$+e^- + H\left[\frac{a_H}{(p+1)}\right]$$

$$+[(p+1)^2 - p^2] \times 13.6 \text{ eV} \tag{A.8}$$

$$Rb^{2+} + e^- \rightarrow Rb^+ + 27.28 \text{ eV}. \tag{A.9}$$

The overall reaction is

$$H\left[\frac{a_H}{p}\right] \rightarrow H\left[\frac{a_H}{(p+1)}\right] + [(p+1)^2 - p^2] \times 13.6 \text{ eV}. \tag{A.10}$$

Rubidium metal may form RbH which may provide gas phase Rb^+ ions, or rubidium metal may be ionized to provide gas phase Rb^+ ions. Rb^+ ion emission was observed in the EUV spectrum of rubidium metal.

A.4. Cesium

A catalytic system is provided by the ionization of two electrons from a cesium atom each to a continuum energy level such that the sum of the ionization energies of the two electrons is approximately 27.2 eV. The first and second ionization energies of cesium are 3.89390 and 23.15745 eV, respectively [39]. The double ionization ($t = 2$) reaction of $Cs–Cs^{2+}$, then, has a net enthalpy of reaction of 27.05135 eV, which is equivalent to $m = 1$ in Eq. (A.3).

$$27.05135 \text{ eV} + Cs(m) + H\left[\frac{a_H}{p}\right] \rightarrow Cs^{2+}$$

$$+2e^- + H\left[\frac{a_H}{(p+1)}\right]$$

$$+[(p+1)^2 - p^2] \times 13.6 \text{ eV}, \tag{A.11}$$

$$Cs^{2+} + 2e^- \rightarrow Cs(m) + 27.05135 \text{ eV}. \tag{A.12}$$

9
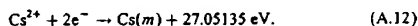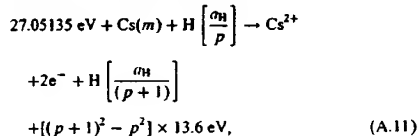
The overall reaction is

$$H\left[\frac{a_H}{p}\right] \rightarrow H\left[\frac{a_H}{(p+1)}\right] + [(p+1)^2 - p^2] \times 13.6 \text{ eV}. \tag{A.13}$$

Vaporized atomic cesium was formed by hydrogen reduction and thermal decomposition of the carbonate.

A.5. Strontium

One such catalytic system involves strontium. The first through the fifth ionization energies of strontium are 5.69484, 11.03013, 42.89, 57, and 71.6 eV, respectively [39]. The ionization reaction of Sr–Sr^{5+}, $(t = 5)$, then, has a net enthalpy of reaction of 188.2 eV, which is equivalent to $m = 7$ in Eq. (A.3).

$$188.2 \text{ eV} + Sr(m) + H\left[\frac{a_H}{p}\right] \rightarrow Sr^{5+}$$

$$+ 5e^- + H\left[\frac{a_H}{(p+7)}\right]$$

$$+ [(p+7)^2 - p^2] \times 13.6 \text{ eV}, \tag{A.14}$$

$$Sr^{5+} + 5e^- \rightarrow Sr(m) + 188.2 \text{ eV}. \tag{A.15}$$

The overall reaction is

$$H\left[\frac{a_H}{p}\right] \rightarrow H\left[\frac{a_H}{(p+7)}\right] + [(p+7)^2 - p^2] \times 13.6 \text{ eV}. \tag{A.16}$$

Vaporized atomic strontium was formed by heating the metal to 700°C.

A.6. Hydride ion

A novel hydride ion having extraordinary chemical properties given by Mills [1] is predicted to form by the reaction of an electron with a hydrino (Eq. (A.17)). The resulting hydride ion is referred to as a hydrino hydride ion designated as H$^-(1/p)$.

$$H\left[\frac{a_H}{p}\right] + e^- \rightarrow H^-(1/p). \tag{A.17}$$

The hydrino hydride ion is distinguished from an ordinary hydride ion having a binding energy of 0.8 eV. The hydrino hydride ion is predicted to comprise a hydrogen nucleus and two indistinguishable electrons at a binding energy according to the following formula:

Binding energy

$$= \frac{\hbar^2 \sqrt{s(s+1)}}{8\mu_e a_0^2[(1+\sqrt{s(s+1)})/p]^2} - \frac{\pi\mu_0 e^2 \hbar^2}{m_e^2 a_0^3}$$

$$\left(1 + \frac{2^2}{[(1+\sqrt{s(s+1)})/p]^3}\right), \tag{A.18}$$

where p is an integer greater than one, $s = 1/2$, $\hbar$ is Planck's constant bar, μ_0 is the permeability of vacuum, m_e is the mass of the electron, μ_e is the reduced electron mass, a_0 is the Bohr radius, and e is the elementary charge. The ionic radius is

$$r_1 = \frac{a_0}{p}(1 + \sqrt{s(s+1)}), \qquad s = \frac{1}{2} \tag{A.19}$$

From Eq. (A.19), the radius of the hydrino hydride ion H$^-(1/p)$; $p =$ integer is $1/p$ that of ordinary hydride ion, H$^-(1/1)$. Compounds containing hydrino hydride ions have been isolated as products of the reaction of atomic hydrogen with atoms and ions identified as catalysts by EUV emission [5,7–34,36].

6. Uncited Reference

[42]

References

[1] Mills R. The grand unified theory of classical quantum mechanics, January 2000 Ed. Cranbury, NJ: BlackLight Power, Inc. Distributed by Amazon.com.

[2] Mills R. The grand unified theory of classical quantum mechanics. Global Foundation, Inc. Orbis Scientiae entitled. The role of attractive and repulsive gravitational forces in cosmic acceleration of particles. The origin of the cosmic gamma ray bursts. 29th Conference on High Energy Physics and Cosmology Since 1964, Dr. Behram N. Kursunoglu, Chairman, December 14–17, 2000, Lago Mar Resort, Fort Lauderdale, FL, in press.

[3] Mills R. The grand unified theory of classical quantum mechanics, Il Nuovo Cimento, submitted for publication.

[4] Mills R. The hydrogen atom revisited. Int J Hydrogen Energy 2000;25(12):1171–83.

[5] Mills R. Spectroscopic identification of a novel catalytic reaction of atomic hydrogen and the hydride ion product. Int J Hydrogen Energy, in press.

[6] Mills R, Greenig N, Hicks S. Optically measured power balances of anomalous discharges of mixtures of argon, hydrogen, and potassium, rubidium, cesium, or strontium vapor. Int J Hydrogen Energy, submitted for publication.

[7] Mills R, Nansteel M. Anomalous argon–hydrogen–strontium discharge. IEEE Trans. Plasma Science, submitted for publication.

[8] Mills R, Nansteel M, Lu Y. Anomalous hydrogen/strontium discharge. Eur J Phys D, submitted for publication.

[9] Mills R, Dong J, Lu Y. Observation of extreme ultraviolet hydrogen emission from incandescently heated hydrogen gas with certain catalysts. Int J Hydrogen Energy 2000;25: 919–43.

[10] Mills R. Observation of extreme ultraviolet emission from hydrogen–KI plasmas produced by a hollow cathode discharge. Int J Hydrogen Energy 2001;26(6):579–92.

[11] Mills R. Temporal behavior of light-emission in the visible spectral range from a Ti–K$_2$CO$_3$–H-cell. Int J Hydrogen Energy 2001;26(4):327–32.

[12] Mills R, Onuma T, Lu Y. Formation of a hydrogen plasma from an incandescently heated hydrogen–catalyst gas mixture with an anomalous afterglow duration. Int J Hydrogen Energy, in press.

HE 1265

[13] Mills R, Nansteel M, Lu Y. Observation of extreme ultraviolet hydrogen emission from incandescently heated hydrogen gas with strontium that produced an anomalous optically measured power balance. Int J Hydrogen Energy 2001;26(4):309–26.

[14] Mills R, Dong J, Lu Y, Conrads J. Observation of extreme ultraviolet hydrogen emission from incandescently heated hydrogen gas with certain catalysts. 1999 Pacific Conference on Chemistry and Spectroscopy and the 35th ACS Western Regional Meeting, Ontario Convention Center, California, October 6–8, 1999.

[15] Mills R, Dong J, Greenig N, Lu Y. Observation of extreme ultraviolet hydrogen emission from incandescently heated hydrogen gas with certain catalysts. National Hydrogen Association. 11th Annual US Hydrogen Meeting, Vienna, VA, February 29–March 2, 2000.

[16] Mills R, Dhandapani B, Greenig N, He J, Dong J, Lu Y, Conrads H. Formation of an energetic plasma and novel hydrides from incandescently heated hydrogen gas with certain catalysts. National Hydrogen Association, 11th Annual US Hydrogen Meeting, Vienna, VA, February 29–March 2, 2000.

[17] Mills R, Dong J, Greenig N, Lu Y. Observation of extreme ultraviolet hydrogen emission from incandescently heated hydrogen gas with certain catalysts. 219th National ACS Meeting, San Francisco, California, March 26–30, 2000.

[18] Mills R, Dhandapani B, Greenig N, He J, Dong J, Lu Y, Conrads H. Formation of an energetic plasma and novel hydrides from incandescently heated hydrogen gas with certain catalysts. 219th National ACS Meeting, San Francisco, California, March 26–30, 2000.

[19] Mills R, Dhandapani B, Greenig N, He J, Dong J, Lu Y, Conrads H. Formation of an energetic plasma and novel hydrides from incandescently heated hydrogen gas with certain catalysts. June ACS Meeting, 29th Northeast Regional Meeting, University of Connecticut, Storrs, CT, June 18–21, 2000.

[20] Mills R, Dhandapani B, Greenig N, He J, Dong J, Lu Y, Conrads H. Formation of an energetic plasma and novel hydrides from incandescently heated hydrogen gas with certain catalysts. August National ACS Meeting, 220th ACS National Meeting, Washington, DC, August 20–24, 2000.

[21] Mills R, Dhandapani B, He J, Voigt A. Identification of compounds containing novel hydride ions by nuclear magnetic resonance spectroscopy. Int J Hydrogen Energy, in press.

[22] Mills R, Dhandapani B, Greenig N, He J. Synthesis and characterization of potassium iodo hydride. Int J Hydrogen Energy 2000;25(12):1185–203.

[23] Mills R. Novel inorganic hydride. Int J Hydrogen Energy 2000;25:669–83.

[24] Mills R. Novel hydrogen compounds from a potassium carbonate electrolytic cell. Fusion Technology 2000; 37(2):157–82.

[25] Mills R, Dhandapani B, Nansteel M, He J, Shannon T, Echezuria A. Synthesis and characterization of novel hydride compounds. Int J Hydrogen Energy 2001;26(4):339–67.

[26] Mills R. Highly stable novel inorganic hydrides. J Mater Res, submitted.

[27] Mills R. Novel hydride compound. 1999 Pacific Conference on Chemistry and Spectroscopy and the 35th ACS Western Regional Meeting, Ontario Convention Center, California, October 6–8, 1999.

[28] Mills R, Dhandapani B, Greenig N, He J. Synthesis and characterization of potassium iodo hydride. 1999 Pacific Conference on Chemistry and Spectroscopy and the 35th ACS Western Regional Meeting, Ontario Convention Center, California, October 6–8, 1999.

[29] Mills R, He J, Dhandapani B. Novel hydrogen compounds. 1999 Pacific Conference on Chemistry and Spectroscopy and the 35th ACS Western Regional Meeting, Ontario Convention Center, California, October 6–8, 1999.

[30] Mills R. Novel hydride compound. National Hydrogen Association, 11th Annual US Hydrogen Meeting, Vienna, VA, February 29–March 2, 2000.

[31] Mills R, He J, Dhandapani B. Novel alkali and alkaline earth hydrides. National Hydrogen Association, 11th Annual US Hydrogen Meeting, Vienna, VA, February 29–March 2, 2000.

[32] Mills R. Novel hydride compound, 219th National ACS Meeting, San Francisco, California, March 26–30, 2000.

[33] Mills R, He J, Dhandapani B. Novel alkali and alkaline earth hydrides. 219th National ACS Meeting, San Francisco, California, March 26–30, 2000.

[34] Mills R, He J, Dhandapani B. Novel alkali and alkaline earth hydrides. August National ACS Meeting, 220th ACS National Meeting, Washington, DC, August 20–24, 2000.

[35] Mills R. The nature of free electrons in superfluid helium—a test of quantum mechanics and a basis to review its foundations and make a comparison to classical theory. Int J Hydrogen Energy, in press.

[36] Mills R, Good W, Voigt A, Jinquan Dong. Minimum heat of formation of potassium iodo hydride. Int J Hydrogen Energy, in press.

[37] Mills R. BlackLight power technology—a new clean hydrogen energy source with the potential for direct conversion to electricity. Proceedings of the National Hydrogen Association, 12th Annual US Hydrogen Meeting and Exposition. Hydrogen: the common thread, The Washington Hilton and Towers, Washington, DC, March 6–8, 2001, in press.

[38] Mills R. BlackLight power technology—a new clean energy source with the potential for direct conversion to electricity, Global Foundation International Conference on Global Warming and Energy Policy, Dr. Behram N. Kursunoglu, Chairman, Fort Lauderdale, FL, November 26–28, 2000, in press.

[39] Linde DR. CRC handbook of chemistry and physics, 79th Ed. Boca Raton, FL: CRC Press, 1998–1999. p. 10-175 to 10–177.

[40] Kelly R, Atomic and ionic spectrum lines below 2000 Angstroms: hydrogen through Krypton. Part 1 (H–Cr). J Phys Chem Ref Data, 1987; 16 (Suppl. No. 1): 418–22. Washington, DC: American Chemical Society and the American Institute of Physics for the National Bureau of Standards.

[41] NIST Atomic Spectra Database, www.physics.nist.gov/cgi-bin/AtData/display.ksh.

[42] Linde DR. CRC Handbook of Chemistry and Physics, 79th Ed. Boca Raton, FL: CRC Press, 1999. p. 9–51 to 9–69.

[43] Sidgwick NV. The chemical elements and their compounds vol. I, Oxford: Clarendon Press, 1950. p. 17.

[44] Lamb MD. Luminescence spectroscopy. London: Academic Press, 1978. p. 68.

BlackLight Power Technology
A New Hydrogen Energy Source with the Potential for Direct Conversion to Electricity

Randell L. Mills
BlackLight Power, Inc.

1. Introduction

BlackLight Power, Inc. (the Company), a Delaware corporation based in its 53,000 sq. ft. headquarters in Cranbury, New Jersey, believes it has developed a new hydrogen chemical process that generates power, plasma (a hot ionized glowing gas), and a vast class of new compositions of matter. Specifically, the Company has designed and tested a new proprietary energy-producing chemical process. The Company has developed high-power density, high-temperature, hydrogen gas cells that produce intense light, power orders of magnitude greater than that of the combustion of hydrogen at high temperatures, and power densities equal to those of many electric power plants. The Company is focusing on cells for generating light and plasma for lighting applications and direct conversion to electricity, respectively.

The cells generate energy through a chemical process (BlackLight Process) which the Company believes causes the electrons of hydrogen atoms to drop to lower orbits thus releasing energy in excess of the energy required to start the process. The lower-energy atomic hydrogen product of the BlackLight Process reacts with an electron to form a hydride ion which further reacts with elements other than hydrogen to form novel compounds called hydrino hydride compounds (HHCs) which are proprietary to the Company. The Company is developing the vast class of proprietary chemical compounds formed via the BlackLight Process. Its technology has far-reaching applications in many industries.

The power may be in the form of a plasma, a hot ionized glowing gas. The plasma may be converted directly to electricity with high efficiency, thus, avoiding a heat engine such as a turbine. The Company is working on direct plasma to electricity conversion. The device may be linearly scaleable from the size of hand held units to large units which could replace large turbines.

1

There are many advantages of the technology. The energy balance permits the use of electrolysis of water to split water into its elemental constituents of hydrogen and oxygen as the source of hydrogen fuel using a small fraction of the output electricity. Additionally, pollution produced by fossil and nuclear fuels should be eliminated since no green house gases, air pollutants, or hazardous wastes are produced. As no fossil fuels are required, the projected commercial operating costs are much less than that of any known competing energy source.

The Company's process may start with water as the hydrogen source and convert it to HHCs; whereas, fuel cells typically require a hydrocarbon fuel and an expensive reformer to convert hydrocarbons to hydrogen and carbon dioxide. The Company's plasma to electric conversion technology with no reformer, no fuel cost, creation of a valuable chemical by-product rather than pollutants or green house gases such as carbon dioxide, and significantly lower capital costs and operating and maintenance (O&M) costs are anticipated to result in household units that are competitive with central power and significantly superior to competing microdistributed power technologies such as fuel cells.

2. The BlackLight Process

Based on physical laws of nature, Dr. Mills theory predicts that additional lower energy states are possible for the hydrogen atom, but are not normally achieved because transitions to these states are not directly associated with the emission of radiation. Thus, the ordinary hydrogen atom as well as lower-energy hydrogen atoms (termed hydrinos by Dr. Mills) are stable in isolation. Mills theory further predicts that hydrogen atoms can achieve these states by a radiationless energy transfer with a nearby atom, ion, or combination of ions (a catalyst) having the capability to absorb the energy required to effect the transition. Radiationless energy transfer is common. For example, it is the basis of the performance of the most common phosphor used in fluorescent lighting. Thus, the Company believes hydrogen atoms can be induced to collapse to a lower-energy state, with release of the net energy difference between states. Successive stages of collapse of the hydrogen atom are predicted, resulting in the release of energy in amounts many times greater than the energy released by the combustion of hydrogen. Since the combustion energy is equivalent to the energy required to liberate hydrogen from water, a process which takes water as a feed material and produces net energy is possible. The equivalent energy content of water would thus be several hundred to several thousand times that of crude oil, depending on the average number of stages of collapse.

The Company is the pioneer of technology based on the chemical process of releasing chemical energy from hydrogen called the "BlackLight Process". More specifically, energy is released as the electrons of hydrogen atoms are induced by a catalyst to transition to lower-

2

energy levels (i.e. drop to lower base orbits around each atom's nucleus) corresponding to fractional quantum numbers. The lower energy atomic hydrogen product is called "hydrino", and the hydrogen catalyst to form hydrino is called a "transition catalyst". As hydrogen atoms are normally found bound together as molecules, a hot dissociator is used to break hydrogen molecules into individual hydrogen atoms. A vaporized catalyst then causes the normal hydrogen atoms to transition to lower-energy states by allowing their electrons to fall to smaller radii around the nucleus with a release of energy that is intermediate between chemical and nuclear energies. The products are power, plasma, light, and novel HHCs.

The catalysts used and the BlackLight Process are the proprietary intellectual property of the Company. The theory, data, and analysis supporting the existence of this new form of energy have been made publicly available [1-22]. Also see the BlackLight Power web page: www.blacklightpower.com. Laboratory scale devices demonstrating means of extracting the energy have been operated at the Company and at independent laboratories. Results to date indicate that the process can eventually provide economically competitive products in a wide range of applications including lighting, thermal, and electric power generation. The Company's gas energy cells, even in prototype stage, are frequently operating at power densities and temperatures equivalent to those of many coal fired electric power plants and produce about 100 times the energy of the combustion of the hydrogen fuel. The plasma is permissive of a direct plasma to electricity conversion technology as well as the production of electricity by conventional heat engines. The Company currently believes that the scale-up of energy cells to commercial power generation level will require mainly the application of existing industry knowledge in catalysis and power engineering.

The lower-energy atomic hydrogen product of the BlackLight Process reacts with an electron to form a hydride ion which further reacts with elements other than hydrogen to form novel compounds which are proprietary to the Company. The Company is developing the vast class of proprietary chemical compounds formed via the BlackLight Process. Test results indicate that the properties of HHCs are rich in diversity due to their extraordinary binding energy (i.e. the energy required to remove an electron which determines the chemical reactivity and properties). This new class of matter may be comparable to carbon in terms of the possibilities of new compositions of matter. Carbon is a base element for many useful compounds ranging from diamonds, to synthetic fibers, to liquid gasoline, to pharmaceuticals. The Company believes hydrino hydride ions have the potential to be as useful as carbon as a base "element". The novel compositions of matter and associated technologies have far-reaching applications in many industries including the chemical, lighting, computer, defense, energy, battery, propellant, munitions, surface coatings, electronics, telecommunications, aerospace, and automotive industries. The Company is focusing on developing a high voltage

3

battery and silane materials based on the novel hydride chemical products. Many additional applications of the chemical compounds are possible.

2.1 Confirmation of the BlackLight Process

Based on the solution of a Schrödinger-type wave equation with a nonradiative boundary condition based on Maxwell's equations, Mills [1-22] predicts that atomic hydrogen may undergo a catalytic reaction with certain atomized elements or certain gaseous ions which singly or multiply ionize at integer multiples of the potential energy of atomic hydrogen, $27.2 \ eV$. For example, cesium atoms ionize at an integer multiple of the potential energy of atomic hydrogen, $m \cdot 27.2 \ eV$. The enthalpy of ionization of Cs to Cs^{2+} has a net enthalpy of reaction of $27.05135 \ eV$, which is equivalent to $m = 1$ [23]. And, the reaction Ar^{+} to Ar^{2+} has a net enthalpy of reaction of $27.63 \ eV$, which is equivalent to $m = 1$ [23]. In each case, the reaction involves a nonradiative energy transfer to form a hydrogen atom that is lower in energy than unreacted atomic hydrogen. The product hydrogen atom has an energy state that corresponds to a fractional principal quantum number. Recent analysis of mobility and spectroscopy data of individual electrons in liquid helium show direct experimental confirmation that electrons may have fractional principal quantum energy levels [5]. The lower-energy hydrogen atom is a highly reactive intermediate which further reacts to form a novel hydride ion. Emission was observed from a continuum state of Cs^{2+} and Ar^{2+} at $53.3 \ nm$ and $45.6 \ nm$, respectively [7]. The single emission feature with the absence of the other corresponding Rydberg series of lines from these species confirmed the resonant nonradiative energy transfer of $27.2 \ eV$ from atomic hydrogen to atomic cesium or Ar^{+}. The catalysis product, a lower-energy hydrogen atom, was predicted to be a highly reactive intermediate which further reacts to form a novel hydride ion. The predicted hydride ion of hydrogen catalysis by either cesium atom or Ar^{+} catalyst is the hydride ion $H^{-}(1/2)$. This ion was observed spectroscopically at $407 \ nm$ corresponding to its predicted binding energy of $3.05 \ eV$ [7].

Typically, the emission of extreme ultraviolet (EUV) light from hydrogen gas is achieved by a discharge at high voltage, a high power inductively coupled plasma, or in hot fusion research, a plasma is created and heated by radio waves to 10s of millions of degrees with confinement of the hot plasma by a toroidal (donut shaped) magnetic field. The Company has observed intense EUV emission at low temperatures (e.g. $\approx 10^{3} \ K$) from atomic hydrogen and certain atomized elements or certain gaseous ions [7, 9-15] that served as catalysts. The Company has tested over 130 elements and compounds which covers essentially all of the elements of the periodic chart. The chemical interaction of catalysts with atomic hydrogen at

temperatures below 1000 K has shown surprising results in terms of the emission of the Lyman and Balmer lines [7, 9-15] (atomic hydrogen emission ten times more energetic than the combustion of hydrogen), emission of lines corresponding to lower-energy hydrogen states and the corresponding hydride ions, and the formation of novel chemical compounds [16-22].

Over 20 independent labs have performed 25 types of analytical experiments that confirm the Company's novel catalytic reaction of atomic hydrogen which produces an anomalous discharge or plasma and produces novel hydride compounds [7-22]. Experiments that confirm the novel hydrogen chemistry include extreme ultraviolet (EUV) spectroscopy [7, 9-12, 15], plasma formation [7-15], power generation [8-10, 15, 22], and analysis of chemical compounds [16-22]. For example:

1.) Pennsylvania State University, Chemical Engineering Department has determined heat production associated with hydrino formation with a Calvet calorimeter that showed the generation of $10^7 \, J/mole$ of hydrogen, as compared to $2.5 \times 10^5 \, J/mole$ of hydrogen anticipated for standard hydrogen combustion [24]. Thus, the total heats generated appear to be 100 times too large to be explained by conventional chemistry, but the results are completely consistent with Mills model.

2.) Lines observed at the Institut Fur Niedertemperatur-Plasmaphysik e.V. by EUV spectroscopy could be assigned to transitions of atomic hydrogen to lower energy levels corresponding to lower energy hydrogen atoms and the emission from the excitation of the corresponding hydride ions [12]. For example, the product of the catalysis of atomic hydrogen with potassium metal, $H\left[\dfrac{a_H}{4}\right]$ may serve as both a catalyst and a reactant to form $H\left[\dfrac{a_H}{3}\right]$ and $H\left[\dfrac{a_H}{6}\right]$. The transition of $H\left[\dfrac{a_H}{4}\right]$ to $H\left[\dfrac{a_H}{6}\right]$ induced by a multipole resonance transfer of $54.4 \, eV$ ($2 \cdot 27.2 \, eV$) and a transfer of $40.8 \, eV$ with a resonance state of $H\left[\dfrac{a_H}{3}\right]$ excited in $H\left[\dfrac{a_H}{4}\right]$ is represented by $H\left[\dfrac{a_H}{4}\right] + H\left[\dfrac{a_H}{4}\right] \to H\left[\dfrac{a_H}{6}\right] + H\left[\dfrac{a_H}{3}\right] + 176.8 \, eV$. The predicted $176.8 \, eV$ (70.2 Å) photon is a close match with the observed 73.0 Å line. The energy of this line emission corresponds to an equivalent temperature of 1,000,000 °C and an energy over 100 times the energy of combustion of hydrogen.

3.) Transitions of atomic hydrogen to lower energy levels corresponding to lower energy hydrogen atoms has been identified in the extreme ultraviolet emission spectrum from interstellar medium [4].

4.) Observation of intense extreme ultraviolet (EUV) emission has been reported at low temperatures (e.g. $\approx 10^3 \, K$) from atomic hydrogen and certain atomized elements or certain

5

gaseous ions [7, 9-15]. The only pure elements that were observed to emit EUV were those wherein the ionization of t electrons from an atom to a continuum energy level is such that the sum of the ionization energies of the t electrons is approximately $m \cdot 27.2\, eV$ where t and m are each an integer. Potassium, cesium, and strontium atoms and Rb^+ ion ionize at integer multiples of the potential energy of atomic hydrogen and caused emission. Whereas, the chemically similar atoms, sodium, magnesium and barium, do not ionize at integer multiples of the potential energy of atomic hydrogen and caused no emission. A catalyst may also be provided by the transfer of t electrons between participating ions. The transfer of t electrons from one ion to another ion provides a net enthalpy of reaction whereby the sum of the ionization energy of the electron donating ion minus the ionization energy of the electron accepting ion equals approximately $m \cdot 27.2\, eV$ where t and m are each an integer. Potassium ions can also provide a net enthalpy of a multiple of that of the potential energy of the hydrogen atom. The second ionization energy of potassium is $31.63\, eV$; and K^+ releases $4.34\, eV$ when it is reduced to K [23]. The combination of reactions K^+ to K^{2+} and K^+ to K, then, has a net enthalpy of reaction of $27.28\, eV$, which is equivalent to $1 \cdot 27.2\, eV$. Observation of intense extreme ultraviolet (EUV) emission has been reported at low temperatures (e.g. $\approx 10^3\, K$) from K_2CO_3; whereas, chemically similar Na_2CO_3 caused no emission [11].

5.) An energetic plasma in hydrogen was generated using strontium atoms as the catalyst. The plasma formed at 1% of the theoretical or prior known voltage requirement with 4,000-7,000 times less power input power compared to noncatalyst controls, sodium, magnesium, or barium atoms, wherein the plasma reaction was controlled with a weak electric field [10, 15]. The light output for power input increased to 8600 times that of the control when argon was added to the hydrogen strontium plasma to form Ar^+ catalyst [9].

6.) The optically measured output power of gas cells for power supplied to the glow discharge increased by over two orders of magnitude depending on the presence of less than 1% partial pressure of certain catalysts in hydrogen gas or argon-hydrogen gas mixtures [8].

7.) In experiments performed at the Institut Fur Niedertemperatur-Plasmaphysik e.V., an anomalous plasma formed with hydrogen-potassium mixtures wherein the plasma decayed with a two second half-life which was the thermal decay time of the filament which dissociated molecular hydrogen to atomic hydrogen when the electric field was set to zero [13]. This experiment showed that hydrogen line emission was occurring even though the voltage between the heater wires was set to and measured to be zero and indicated that the emission was due to a reaction of potassium catalyst with atomic hydrogen which confirms a new chemical source of power.

8.) A plasma of hydrogen and certain alkali ions formed at low temperatures (e.g. $\approx 10^3\, K$) as recorded via EUV spectroscopy and the hydrogen Balmer and alkali line emissions

in the visible range. The observed plasma formed at low temperatures (e.g. $\approx 10^3 K$) from atomic hydrogen generated at a tungsten filament that heated a titanium dissociator and a catalyst comprising one of potassium, rubidium, cesium, and their carbonates and nitrates. These atoms and ions ionize to provide a catalyst with a net enthalpy of reaction of an integer multiple of the potential energy of atomic hydrogen ($m \cdot 27.2\ eV$, $m = $ integer) to within 0.17 eV and comprise only a single ionization in the case of a potassium or rubidium ion. Whereas, the chemically similar atoms of sodium and sodium and lithium carbonates and nitrates which do not ionize with these constraints caused no emission. To test the electric dependence of the emission, a weak electric field of about 1 V/cm was set and measured to be zero in $< 0.5\ X\ 10^{-6}$ sec. An anomalous afterglow duration of about one to two seconds was recorded in the case of potassium, rubidium, cesium, K_2CO_3, $RbNO_3$, and $CsNO_3$. Hydrogen line or alkali line emission was occurring even though the voltage between the heater wires was set to and measured to be zero. These atoms and ions ionize to provide a catalyst with a net enthalpy of reaction of an integer multiple of the potential energy of atomic hydrogen to within less than the thermal energies at $\approx 10^3 K$ and comprise only a single ionization in the case of a potassium or rubidium ion. Since the thermal decay time of the filament for dissociation of molecular hydrogen to atomic hydrogen was similar to the anomalous plasma afterglow duration, the emission was determined to be due to a reaction of atomic hydrogen with a catalyst that did not require the presence of an electric field to be functional.

9.) The formation of novel compounds provide substantial evidence supporting a novel reaction of hydrogen as the mechanism of the observed EUV emission and anomalous discharge. Novel hydrogen compounds have been isolated as products of the reaction of atomic hydrogen with atoms and ions identified as catalysts in the reported EUV studies [7-22]. Novel inorganic alkali and alkaline earth hydrides of the formula MH^* and MH^*X wherein M is the metal, X, is a singly negatively charged anion, and H^* comprises a novel high binding energy hydride ion were synthesized in a high temperature gas cell by reaction of atomic hydrogen with a catalyst such as potassium metal and MH, MX or MX_2 corresponding to an alkali metal or alkaline earth metal compound, respectively [16-17, 19]. Novel hydride compounds were identified by 1.) time of flight secondary ion mass spectroscopy which showed a dominant hydride ion in the negative ion spectrum, 2.) X-ray photoelectron spectroscopy which showed novel hydride peaks and significant shifts of the core levels of the primary elements bound to the novel hydride ions, 3.) ^1H nuclear magnetic resonance spectroscopy (NMR) which showed extraordinary upfield chemical shifts compared to the NMR of the corresponding ordinary hydrides, and 4.) thermal decomposition with analysis by gas chromatography, and mass spectroscopy which identified the compounds as hydrides [17, 19].

7

An upfield shifted ^1H NMR peak is consistent with a hydride ion with a smaller radius as compared with ordinary hydride since a smaller radius increases the shielding or diamagnetism. Thus, the NMR shows that the hydride formed in the catalytic reaction has been reduced in distance to the nucleus indicating that the electrons are in a lower-energy state. Compared to the shift of known corresponding hydrides the NMR provides direct evidence of reduced energy state hydride ions.

The NMR results confirm the identification of novel hydride compounds MH^*X, MH^*, and MH_2^* wherein M is the metal, X, is a halide, and H^* comprises a novel high binding energy hydride ion. For example, large distinct upfield resonances were observed at -4.6 ppm and -2.8 ppm in the case of KH^*Cl and KH^*, respectively. Whereas, the resonances for the ordinary hydride ion of KH were observed at 0.8 and 1.1 ppm. The presence of a halide in each compound MH^*X does not explain the upfield shifted NMR peak since the same NMR spectrum was observed for an equimolar mixture of the pure hydride and the corresponding alkali halide (MH/MX) as was observed for the pure hydride, MH. The synthesis of novel hydrides such as KH^* with upfield shifted peaks prove that the hydride ion is different from the hydride ion of the corresponding known compound of the same composition. The reproducibility of the syntheses and the results from five independent laboratories confirm the formation of novel hydride ions [16].

3. Business Units

The Company believes that it has created a commercially competitive new source of energy, a new source of plasma which releases rather than consumes energy, a new source of light, and a revolutionary new field of hydrogen chemistry. With its achievements of a sustained 100,000+ °C plasma of hydrogen with essentially no power input to its power cell and synthesis of over 40 novel compounds in bulk with extraordinary properties the Company is focusing on product development. Initial target products are a direct plasma to electric power cell targeted at the residential and commercial microdistributed markets and the premium power market. Additional market objectives for the plasma and chemistry technologies are lighting sources, a high voltage battery to power portable electronics and electric vehicles, and chemical products and processes based on silicon and hydrino chemistry.

The Company has two basic business units—power and chemical. The plasma-electric technology may represent a near-term huge energy market. But, in the case of a large central power plant, the Company estimates that the potential revenues from the chemicals produced with power generation may eclipse the electricity sales. However, both offer extraordinary

potential revenue and profit. Since enormous power (easily convertible to electricity) is a product of the BlackLight Process, the two units can operate in tandem seamlessly.

The priorities of the Company's power business is the residential and commercial microdistributed markets and the premium power market based on its plasma-electric power cell technology. The time to market should be near term for these relatively small-scale, simple devices that are projected to be inexpensive to manufacture, service, and use, and vastly superior to competing technologies such as internal combustion engine gensets, fuel cells, and microturbines. Selected statistics on electric generation are given in Table 1.

Table 1. Statistics on electric generation.

US Electric Market
- $217 billion in annual US sales (1998).
- 43% Residential
- 32% Commercial
- 22% Industrial
- 5% Other

Capital Expenditures Required to Meet New Generation Demand
- Estimated at $90 Billion Globally with 10% in US in 1999
- $21 Billion will be spent on Premium Power in 2000
- $30 Billion in 2002
- $50 Billion in 2005

Premium Power Consumption/Demand
- Estimated to be 30,000 MW in 1999
- Estimated to be 500,000 MW in 2000
- Double digit growth expected over next five years

Early adopters of BlackLight power systems are expected to be those that require premium power generated on-site. The premium power market* includes businesses where brief electrical outages can cause severe monetary loss: telecommunication sites, computer centers, server hotels, e-commerce centers, semiconductor fabrication facilities, and others. The market size was estimated to be 30,000 MW in 1999 and growth to be multiples of the

---

* The premium power market is also known as the 9's market and the powercosm market. Utility grids provide 99.9% reliability, or 8 hours of disruption per year. For the Internet economy, even small fractions of a second can cost millions of dollars. In high technology manufacturing industries, even hours of disruption can shut down operations for days, again costing millions. More reliability is measured in %, the more 9's required (99.999...%), the smaller the fractions of a second power is disrupted and the more valuable the power.

entire energy market rate [25-26]. The Glider Group and Stephens Inc. estimates [27-28] that this market is 15% of the current US energy market, and it will be 30—50% within 3—5 years as the internet economy build-out continues. This market is characterized by early adoption of emerging technologies and an insensitivity to cost. For example, a typical rate is over $1,000 per kWh, and the rate for the upper-end of the reliability scale, six 9's reliable power, is about $1 million per kWh compared to 5 ¢ per kWh for three 9's power supplied by the grid. The premium power market is a multi-billion dollar market. The current equipment market is $21 billion in hardware alone and is projected to eclipse the profitability of the entire utility market in the near term [29].

Table 2. Competitive Advantages of The BlackLight Power Process.

Cost Per KWH of Alternative Energy Sources

Coal	4-5 ¢
Natural Gas	4-5 ¢
Oil	4-5 ¢
Nuclear Power	5-6 ¢
Hydroelectric	4-7 ¢
Geothermal	5-8 ¢
Wind	5-9 ¢
Solar	10-12 ¢
Photovoltaic	30-40 ¢
BlackLight *	<1 ¢

*Cost figures include operating, maintenance, capital generating expense of plasma-electric system (Source: EPRI, BlackLight Power, Inc.)

BlackLight's Energy Systems design advantages are: virtually instantaneous turn on/off, simplicity, easy logistics, low capital cost, low operational and maintenance cost, easy redundancy (for reliability), and no pollution. With our current design, BlackLight projects capital costs around $25—100 per kW, and very low generation cost (<$0.01 per kWh). This is lower than competitive solutions, but in this market segment cost is not a driver. Our chief competitors are reciprocating engine-based gensets built by Catapillar, Cummins, and others. Additional competition might be from newer entrants: microturbines and fuel cells. The former competitors, fossil-fueled engines, have an advantage because they are an incumbent technology, but 1.) they will not be able to significantly improve their reliability, 2.) they have a short lifetime, 3.) they do not meet pollution requirements, and 4.) they can not reduce their O&M costs to be competitive with our solution. The latter competitors have a slight advantage

in name recognition relative to BlackLight, but microturbines and fuel cells are not suited for the premium power market. Fuel cells and turbine systems take too long to start up, and are difficult to harmonize with grid-supplied power. Thus, they are ineffective at improving power reliability.

Due to superior performance of its technology, the Company expects early adoption by the premium power market with expansion into the broader microdistributed market. The broader market which includes hundreds of millions of homes and businesses in the US and Europe will be drawn by significant cost savings and increasing unreliability of the grid with a lack of viable microdistributed alternatives. The populace of the third world, particularly Asia, represents a further enormous market opportunity for which BlackLight technology is particularly suited, since in addition to very low capital and O&M costs, no fuel or electrical grid infrastructure is required.

In terms of its development strategy for large scale systems, the Company has decided to focus on developing the chemical business unit as a first priority over large power plants. In addition to the possibility of larger revenue, the chemical business offers several other initial advantages. A power generation plant based on thermal energy would have to be scaled-up while maintaining current or higher levels of power density before it could be commercialized. Scaling up to a power plant of very large proportions has engineering risks. While there are engineering risks associated with the scale-up for chemical production, they are not as daunting. Some potential product areas such as electronics are projected to have very high value in small quantity. Moreover, in terms of gaining widespread scientific and commercial acceptance for the BlackLight Process, it is relatively easy to validate the properties of a chemical compound. A solid chemical compound is a product that can be examined directly and its existence proven unequivocally—it either exists or it doesn't. This also means that its patents are well defined and easy to defend. The products are much more diverse, so broad industry adoption is anticipated.

In addition to direct cell power to electric power conversion, thermal power from the plasma produced by the BlackLight Process may be converted to electricity by powering a turbine. Contemporary central station thermal generation systems have been optimized to match their respective thermal sources. Since BlackLight-technology is not combustion or nuclear, an opportunity exists to dramatically reduce the complexity of the generation station. The BlackLight Process may be used as a thermal source for central or distributed power through use of a modified steam or gas turbine. The BlackLight adaptation of the steam-based system replaces the heat source of the boiler with a BlackLight gas cell. The BlackLight adaptation of the gas turbine replaces the combustor of a conventional machine with a gas cell and a heat exchanger incorporating the BlackLight Process. High pressure air from the

11

compressor is heated by the BlackLight energy cell heat exchanger before expanding through the power turbine. The exhaust would contain no combustion products. With energy production from hydrogen at a hundred times combustion energy, fuel cost would become an inconsequential consideration, and refueling intervals would be consistent with other maintenance. Alternatively, an on-site electrolysis system producing hydrogen from water could provide unlimited fuel with periodic additions of small quantities of water.

A typical chemical plant is projected to produce 100 MW electric power as a side product. Power and chemical cells may be fabricated using readily available materials, and systems such as steam or gas turbine systems are scalable over a large range [e.g. distributed units (1 MW) to central power plants (1 GW)]. The projected cost for a combined chemical and energy plant is about $250/kW. The two functions could work seamlessly together and generate a dual income stream with a reduction of business risk. Rather than producing nuclear or fossil fuel waste which requires disposal, the BlackLight chemical plant will produce HHCs which have potential for far-reaching applications in many industries such as batteries for electric vehicles at significant earnings. For example, a 100 MW chemical plant is projected to produce $300 M in electric vehicle battery revenue from 200,000 batteries with $23 M from electricity sales at 3 ¢ kWh.

4. Solution to the Energy Problem?

The world's current energy system is unsustainable. Furthermore, the world's current energy system is not sufficiently reliable or affordable to support widespread economic growth. The productivity of one-third of the world's people is compromised by lack of access to commercial energy, and perhaps another third suffer economic hardships and insecurity due to unreliable energy supplies [30]. Solar and wind power are prohibitively expensive. Billions of dollars have been spent to harness the energy of hydrogen through hot fusion using extremely hot plasmas created with enormous energy input using complex, expensive systems. By contrast, the Company's reactions indicate that over 100 times the energy of its combustion is released from hydrogen with the formation of a plasma as a by-product at relatively low temperatures with simple, inexpensive systems. And, in the Company's power cells, the plasma may be converted directly to electricity with high efficiency avoiding a heat engine such as a turbine. In addition, rather than producing radioactive waste, the BlackLight Process produces compounds having extraordinary properties. The implications are that a vast new energy source and a new field of hydrogen chemistry have been discovered.

The advantages of the BlackLight process over existing energy forms, such as fossil fuels and nuclear power, include: (1) the water, which is the fuel for the process, is safe and

inexpensive to contain; (2) the reaction is prospectively easily controlled; and (3) the byproduct, HHCs, have great potential commercial value. The projection of the capital cost per kilowatt capacity of BlackLight's system may be an order of magnitude less than that of the typical capital cost for a fossil fuel system and two orders of magnitude less than that of the typical capital cost for a nuclear system. The power cell may also be interfaced with conventional steam-cycle or gas turbine equipment used in fossil fuel power plants. In either case, fuel costs are eliminated since the fuel, hydrogen, can be generated by a fraction of the electrical output power. The cost factors per kilowatt/hour are the capital, maintenance and operation costs of the gas cell and plant. These costs are further reduced by elimination of the costs of handling fossil fuels and managing the pollution of air, water, and ground caused by the ash generated by fossil fuels.

4.1. BlackLight Distributed Generation

Central station generation and distribution, the mainstay of electrical power production for the last 100 years worldwide, is now being supplemented in an increasing number of areas by smaller power units closer to the end-user group. Most distributed-generation units are in the capacity range of 100 kW—3 MW (electric), but some could be as large as 250 MW (electric). Distributed generation solves some of centralized power's inherent problems of transmission and distribution line losses, electromagnetic pollution fears from high-tension lines, cost and difficulty of transmission-line maintenance, and inefficiencies in load factor design of power plants (wherein the use of a 20% capacity safety factor is still a common industry practice when estimating peak loading). The Company's technology may be ideal for distributed generation with significant reductions in grid complexity and generation capital equipment requirements.

The Company projects that the residential market may be broadly served by a 25 kW unit, and the commercial market may be broadly served by modular 1 MW units. This approach may replace the grid since in addition to avoidance of line losses, a major economic advantage of distributed power is the avoidance of transmission tariffs which could amount to 50% of the cost of electricity to a customer. Using BlackLight's distributed power generation technology, considerable savings can be realized by eliminating the transmission and distribution capital equipment, operations, and maintenance costs. Also, energy can be saved, given that electricity "demand" also includes substantial transmission and distribution losses from the traditional central-station type power generation systems. These considerations are important considerations for developing nations.

As the world's population grows from about 6 billion (in 1999) to an estimated 7 billion by 2010, most of the new energy demand will come from less-developed countries (LDCs), as these countries' living standards increase. LDC energy demand has long been answered by economic development programs generally aimed at the development of large, central-station power plants. These do not adequately address the thermal and lighting needs of half the world's population which is poor, many of whom still use carbon fuels for these purposes. The solution for LDC's may be distributed power facilitated by BlackLight Power technology since no fuel, power plant, or transmission grid infrastructure is required.

5. BlackLight Power Technology—A New Paradigm in Energy and Electricity Generation

The products of the BlackLight Process are power, plasma, light, and novel HHCs. Using advanced catalysts in its gas power cell, the Company has sustained an energetic plasma in hydrogen at 1% of the theoretical or prior-known voltage requirement and with 1000's of times less power input in a system wherein the plasma reaction is controlled with a weak electric field. A plasma is a very hot, glowing, ionized gas. The plasma is produced from reactions which release energies over 100 times the energy of the combustion of hydrogen and correspond to an equivalent electron temperature of over 1,000,000 °C. The plasma produced in the Company's cells cannot be produced by any chemical reaction other than the Company's process.

5.1. Plasma-Electric Power Converter

Typically, a heat engine such as a turbine is used for converting heat into electricity. However, plasma power may be directly converted into electrical power. The technology is not based on heat. Thus, heat sinks such as a river or cooling towers as well as thermal pollution are largely eliminated. Based on research and development in this area of converters, the Company expects that routine engineering will result in devices that have higher conversion efficiencies than turbines. The device may be linearly scaleable from the size of hand held units to large units which could replace large turbines. And, unlike turbine technology wherein the cost per unit capacity soars with miniaturization, the Company anticipates that the unit cost per capacity will be insensitive to scale. The Company anticipates applications for its technology in broad markets such as premium power, microdistributed power, motive power, consumer electronics, portable electronics, telecommunications, aerospace, and uninterruptable, remote, and satellite power supplies.

14

Plasma may be directly converted into electricity using a direct converter. Several examples being studied and tested by BlackLight are microwave devices such as a gyrotron, a magnetic mirror magnetohydrodynamic power converter, a charge drift direct power converter, and a Post or Venetian blind direct power converter.

5.1.1. Gyrotron Converter

A gyrotron is an established technology for converting energetic electrons into microwaves. Conventionally the source of energetic electrons comprises an electron beam or a plasma formed by electrical input such as a high voltage discharge. Prior to the development of the Company's technology, it was not possible to generate a plasma in hydrogen chemically. The BlackLight Process generates an energetic plasma in hydrogen which is *a new source of energy*.

The energy released by the catalysis of hydrogen to form HHCs produces a plasma in the cell. The energetic electrons of the plasma produced by the BlackLight Process are introduced into an axial magnetic field where they undergo cyclotron motion. The force on a charged ion in a magnetic field is perpendicular to both its velocity and the direction of the applied magnetic field. The electrons of the plasma orbit in a circular path in a plane transverse to the applied magnetic field for sufficient field strength at an ion cyclotron frequency ω_c that is independent of the electron velocity. Thus, a typical case which involves a large number of electrons with a distribution of velocities will be characterized by a unique cyclotron frequency that is only dependent on the electron charge to mass ratio and the strength of the applied magnetic field. There is no dependence on their velocities. The velocity distribution will, however, be reflected by a distribution of orbital radii. The electrons emit electromagnetic radiation with a maximum intensity at the cyclotron frequency. The velocity and radius of each electron may decrease due to loss of energy and a decrease of the temperature.

The gyrotron comprises a resonator cavity which has a dominant resonator mode at the cyclotron frequency. The plasma contains electrons with a range of energies and trajectories (momenta) and randomly distributed phases initially. Electromagnetic oscillations are generated from the electrons to produce induced radiation due to the grouping of electrons under the action of the self-consistent field produced by the electrons themselves with coherent radiation of the resulting packets. In this case, the device is a feedback oscillator. The theory of induced radiation of excited classical oscillators such as electrons under the action of an external field and its use in high-frequency electronics is described by A. Gaponov et al. [31]. The electromagnetic radiation emitted from the electrons excites the mode of the cavity and is received by a resonant receiving antenna.

The engineering of the BlackLight gyrotron converter is based on established microwave technology which may achieve very high conversion efficiencies (e.g. 80%) of energetic electrons into microwaves [32]. A 0.1 Tesla magnetic field will produce about 2.5 GHz microwaves. The microwaves are then rectified into DC electricity. Rectification efficiency at 2.5 GHz is about 95% [33-36]. The DC electricity may be inverted and transformed into any desired voltage and frequency with conventional power conditioning equipment.

5.1.2. Magnetic Mirror Magnetohydrodynamic (Mirror-MHD) Power Converter

The BlackLight plasma comprises energetic electrons and ions which may be converted into a directional flow using a magnetic mirror described by Jackson [37] and directly converted into electricity. A magnetic mirror has a magnetic field gradient in a desired direction of ion flow (e.g. z-axis) where the initial parallel velocity of plasma electrons $v_{\|0}$ increases as the orbital velocity $v_\perp$ decreases with conservation of energy according to the adiabatic invariant $\dfrac{v_\perp^2}{B} = \text{constant}$, the linear energy being drawn from that of orbital motion. As the magnetic flux **B** decreases the radius a will increase such that the flux $\pi a^2 B$ remains constant. The adiabatic invariance of flux through the orbit of an ion is a means to form a flow of ions along the z-axis with the conversion of $v_\perp$ to $v_\|$ such that $v_\| > v_\perp$.

The plasma is generated selectively in a desired region of the BlackLight power cell. A magnetic mirror of a magnetic mirror magnetohydrodynamic power converter is located in the desired region such that electrons and ions are forced from a homogeneous distribution of velocities in x, y, and z to a preferential velocity along the axis of magnetic field gradient of the magnetic mirror, the z-axis. The mirror-MHD power converter further comprises a magnetohydrodynamic power converter comprising a source of magnetic flux transverse to the z-axis. Thus, the ions have a preferential velocity along the z-axis and propagate into the region of the transverse magnetic flux from the source of transverse flux. The Lorentzian force on the propagating electrons and ions with charge e is given by $F = e\mathbf{v} \times \mathbf{B}$. The force is transverse to the ion velocity and the magnetic field and in opposite directions for positive and negative ions. Thus, charge separation occurs for electrons and positive ions. The magnetohydrodynamic power converter further comprises at least two electrodes which may be transverse to the magnetic field to receive the transversely Lorentzian deflected ions which creates a voltage across the electrodes. The Lorentzian deflector or magnetohydrodymanic generator may be a segmented Faraday generator as described by Petrick [38]. The voltage may drive a current through an electrical load.

16

According to the adiabatic invariant $\dfrac{v_\perp^2}{B} = \text{constant}$, the parallel velocity at any position along the z-axis is given by $v_{\parallel 0}^2 = v_0^2 - v_{\perp 0}^2 \dfrac{B(z)}{B_0}$ where the zero subscript represents the original condition. In the case that $v_{\parallel 0}^2 = v_{\perp 0}^2 = 0.5 v_0^2$ and $\dfrac{B(z)}{B_0} = 0.1$ at the magnetohydrodymanic power converter, the velocity is 95% parallel to the z-axis. The deflection of the ions may be essentially 100%. Thus, very high efficiency may be achieved. Furthermore, very high power may be achieved since very large currents are possible for a given ion energy corresponding to a maximum electrode voltage, and series magnetohydrodymanic power converters may achieve high voltages.

5.1.3. Charge Drift Direct Power Converter

The charge drift direct power converter described by Timofeev and Glagolev [39-40] comprises a magnetic field gradient in a direction transverse to the direction of a source of a magnetic flux **B** and a source of magnetic flux **B** having a curvature of the field lines. Jackson [41] shows that if charged particles move through regions where a magnetic field gradient exists in a direction transverse to the direction of a magnetic flux **B** or the magnetic field has curvature in a plane, drifting negatively and positively charged ions move in opposite directions perpendicular to the plane formed by **B** and the direction of the magnetic field gradient or the plane in which **B** has curvature. Jackson [42] also shows that the motion of a charged particle in crossed electric and magnetic fields with the electric field **E** less that the magnetic field **B** is gyration around the magnetic field with a uniform drift at velocity **u** in the direction perpendicular to both the perpendicular electric and magnetic fields.

A flow of ions from a BlackLight cell may be received at a plasma injection port of the charge drift power converter, or the plasma generating reaction may be within the converter. In both the case of the gradient field and the curved field, the thermal energy of the plasma is converted into electrical energy as the charged particles drift in crossed fields: an inhomogeneous magnetic field and an electric field perpendicular to the magnetic field. The ions move across the gradient or curved field due to the $\mathbf{E} \times \mathbf{B}$ drift velocity affected by the crossed fields [42]. The drifting negatively and positively charged ions move in opposite directions perpendicular to plane formed by **B** and the direction of the magnetic field gradient or the plane in which **B** has curvature. In each case, the separated ions generate a voltage at opposing capacitors that are parallel to the plane with a concomitant decrease of the thermal energy of the ions. The generated voltage has a corresponding electric field which is

perpendicular to the magnetic flux **B** having a perpendicular gradient or curvature. Thus, the energy is converted in crossed imposed magnetic and resultant electric fields. The magnetic flux **B** perpendicular to the electric field prevents the charges from flowing along the electric field and canceling it.

High conversion efficiencies are possible. In the case that the magnetic field decreases by a factor of three across the transverse gradient, and the initial kinetic energy is primarily in the parallel direction, the efficiency may be 90% [39-40].

5.1.4. Post or Venetian Blind Direct Power Converter

A Post or Venetian blind direct power converter described by Moir and Freis [43-44] comprises a magnetic mirror which is a source of a directional flow of ions from the BlackLight power cell as described for the mirror-MHD case. The Post converter further comprises an electrostatic collector which deflects electrons at a first set of negatively biased electrodes, then stops the positive ions at a series of positively biased electrodes to convert the axial kinetic energy into electrical energy. High efficiencies (e.g. 86 %) have been achieved [43].

In the plasma formed by the BlackLight Process, the electrons have greater energy than the positive ions. Thus, in the application of a Post direct converter to the BlackLight plasma, the positive ions are separated from the electrons at a first set of electrodes, and the energetic electrons are stopped at a second set of electrodes as the primary source of power conversion.

The power produced by the BlackLight Process and the converted power may be matched such that a steady state of power production and power flow from the cell may be achieved. The rate of the hydrogen catalysis reaction may be controlled by controlling the total pressure, the atomic hydrogen pressure, the catalyst pressure, the particular catalyst, and the cell temperature. Very fast response times may be achieved by controlling the rate of reaction and plasma formation with an applied electric or magnetic field which influences the catalysis rate. Plasma and a direct converter can respond essentially instantaneously. Thus, unprecedented load following capability is possible.

The plasma formed by the BlackLight Process shown in Figure 1 and a direct energy converter test-bed shown in Figure 2 have been tested independently. Current work is in progress on selecting the most commercially competitive option for converting the BlackLight Process generated plasma into electricity.

18

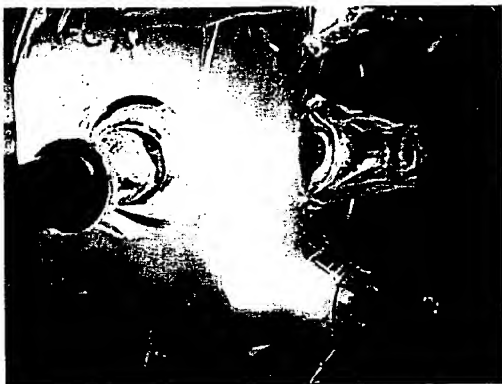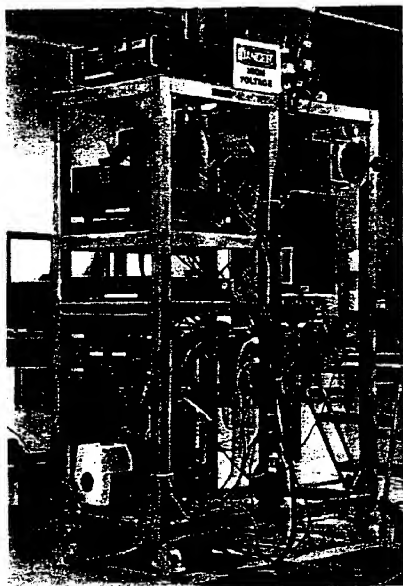**Figure 1. Plasma Generated by the BlackLight Process.**

Figure 2. Direct Plasma-Electric Converter Test-bed.

5.2. Power Balance Analysis

The commercial unit would comprise a 3-stage power generator. Stage 1 would be electrolysis to provide hydrogen fuel; stage 2—production of plasma in a gas cell; and stage 3—conversion of plasma to electricity.

Using even relatively conservative assumptions for reaction yield and power density, a competitive power generation unit appears easily possible: (1) Production of about 100 times electrical power as electrolysis power; (2) Production of green emission (oxygen only) zero CO_2 emission; (3) No fossil-fuel combustion by-products; (4) Essentially no waste heat since the direct converter is not a heat engine; (5) Tremendously more efficient at energy conversion to electricity; and (5) Projected to dominate the home and microdistributed markets.

5.3. Comparison with Competing Microdistributed Technologies

The Company's process may start with water as the hydrogen source and convert it to HHCs; whereas, fuel cells typically require a hydrocarbon fuel and an expensive reformer to convert hydrocarbons to hydrogen and carbon dioxide. The Company's plasma to electric conversion technology with no reformer, no fuel cost, creation of a valuable chemical by-product, and significantly lower capital costs and O&M costs are anticipated to result in household units that are competitive with central power and significantly superior to competing microdistributed power technology such as fuel cells and micro combustion turbines. With a focus on large scale production of microdistributed devices, the Company anticipates rapid penetration of the electricity energy market. In this case, the Company plans to form strategic alliances with component manufacturers, systems assemblers, and service companies to provide power for consumers with units under lease or by sale. The service companies may be utilities. Other services or utility companies such as water, gas, telephone, cable, plumbing, and HVAC companies are also potential partners. The Company may have its plasma-electric power cell manufactured under contract or license. Alternatively, the Company may manufacture the units itself.

Table 3. Economics of International Fuel Cells Corp.

Basis: Installed Cost < $1,000/kW DOE Credit—$3,000 kW
Capital Recovery Factor—12%
Annual Load Factor—95% (8,322 hrs of operation)
Electric Efficiency (higher heating value)—36%
Heat Rate—9,480 Btu / kWh
Waste Heat Recovery as Hot Water
(Equivalent to 875,000 Btu/hr of fuel input at 80% efficiency)
Implicit Overall Thermal Efficiency—82%
Natural Gas Cost—$3.50 / million Btu

Cents/kWh	
Capital Charges	4.3
Fuel	3.3
O&M	2.0*
Subtotal	9.6
Hot Water Credit	-1.5
Net Power Cost	8.1

* Includes $600/kW overhaul costs every six years

Some of the competitive advantages of BlackLight Power generation over the competing microdistributed technologies fuel cells and micro combustion turbines are no fuel costs, no fuel handling issues nor pollution, not a heat engine and not electrochemical, no reformer, solid state device, chemically-generated plasma with proven microwave technology, linearly scalable, cost competitive (lower capital and O&M costs), long product lifetime, appliance-like, load following, no grid connection (gas or electric for fuel or load leveling), high 9's power capability, closed system, and valuable solid chemical by-product.

With strategic alliances, the Company plans to develop, manufacture, and market a unit of approximately twenty five kilowatt electric (25 kWe) which is a desirable size for a modular uninterruptable power supply for the premium power market. 25 kWe is also capable of providing for the total power requirements of a single family residence or a light commercial load. The potential advantages of the Company's power system compared to fuel cells are (1) zero fuel costs, (2) capital and O&M costs that are 10% that of fuel cells, and (3) valuable chemicals are produced rather than pollutants such as carbon dioxide. Thereby, the cost per kilowatt of electric generated by the Company's plasma-electric power cell is projected to be about 10% of that of a fuel cell. In addition, an energy consumer may also derive revenue by

selling power back onto the distribution system when the full capacity of the system is not required by such consumer.

The components required to produce a BlackLight power system such as a vacuum vessel and magnets are mass manufacturable. For implementation in the third world and acquisition of market share in the first world, the plasma-electric cell requires essentially no fuel and fuel distribution infrastructure, no regional or on-site pipelines, no utility connection (gas or electrical), no electric lines, and no specialized or centralized manufacturing expertise. In each category, competing technologies are at a competitive disadvantage which could prevent broad adoption even if they were viable based on logistics and costs.

Fuel cells are not cost competitive with BlackLight technology. The cost of electricity with a molten carbonate fuel cell which has a much lower capital cost compared to a proton exchange membrane fuel (PEM) is given in Table 3. The projected capital cost for a BlackLight 5—25 kW plasma-electric system is about $25/kW based on Freis' projections for a Post converter [43] which is comparable to projections for a gyrotron system [6]. A mirror MHD system is projected to be less than that of a Post converter.

Also with strategic alliances, the Company further plans to develop, manufacture, and market a unit of approximately 1 MWe. One to ten of these units should provide the total power load requirements of a central power grid substation. The potential advantages of the Company's power system compared to central power are the same as with plasma-electric power cell. The cost per kilowatt of electric generated by the Company's plasma-electric power cell is projected to be about 20% of that of central power (see Table 2). With the installation of substation units, light commercial, and residential units, all components of the present central power generation infrastructure upstream from the substation may be eliminated. Some infrastructure components that may be eliminated by the Company's technology with associated cost savings are: (1) high voltage transformers, (2) high voltage transmission lines, and (3) central power plants, including their associated turbines, fuel and pollution handling systems, ash, pollution, coal trains, coal mines, gas pipelines, gas fields, super tankers, oil fields, nuclear power plants, uranium processing plants, and uranium mines.

5.4. Motive Power—Plasma-Electric and Battery

The capital cost for BlackLight power for motive power are comparable to the cost of an automotive internal combustion engine. Whereas, fuel cells are two orders of magnitude too expensive and require trillions of dollars to be invested in a hydrocarbon to hydrogen refueling system. In contrast, a motive power plant based on BlackLight technology uses water as the fuel and requires no infrastructure. The Company is considering several promising options to

commercialize its process in the motive power market. In addition to stationary power, the plasma-electric system may be used for motive power. The Company is also developing a high voltage battery which may power an electric vehicle.

5.6. Conclusion

The BlackLight Process has potentially very broad applications including: electrical power generation, space and process heating, motive power, and production of HHCs.

The technology generates plasma and heat from hydrogen, which may be obtained from ordinary water. The implications of this development could be significant. If the technology becomes proven, then the energy from this process could possibly be used to cleanly and cheaply meet the world's demand for thermal, chemical, and mechanical energy as well as electricity. Over time, it may be possible to replace or retrofit coal-fired, gas-fired, and oil-fired electric power plants. This would help to abate global warming and air and water pollution. Moreover, it may be possible to replace or retrofit some of the world's nuclear power plants. With BlackLight technology, an opportunity exists to dramatically reduce the complexity and the cost of the generation station, which includes fuel handling, thermal generation, thermal to electrical conversion, pollution abatement and spent fuel disposal or storage systems.

The Company is focusing on possible electrical and heating applications for its technology including a fit with a converter to make electricity. Electrical power generation with the Company's plasma-electric power technology may represent a major opportunity to use a microdistributed system to replace existing infrastructure at considerable savings in capital and generation costs. Residential/light commercial units, substation units, and a low voltage local distribution system could replace the central power based current system. Adaptation of the Company's technology is facilitated by the deregulation of the utility industry and the demand for autonomous microdistributed power in developing countries.

6. REFERENCES

1. R. Mills, *The Grand Unified Theory of Classical Quantum Mechanics*, January 2000 Edition, BlackLight Power, Inc., Cranbury, New Jersey, Distributed by Amazon.com.
2. R. Mills, "The Grand Unified Theory of Classical Quantum Mechanics", Global Foundation, Inc. Orbis Scientiae entitled *The Role of Attractive and Repulsive Gravitational Forces in Cosmic Acceleration of Particles The Origin of the Cosmic Gamma Ray Bursts*, (29th Conference on High Energy Physics and Cosmology Since 1964) Dr. Behram N.

Kursunoglu, Chairman, December 14-17, 2000, Lago Mar Resort, Fort Lauderdale, FL, in press.

3. R. Mills, "The Grand Unified Theory of Classical Quantum Mechanics", Il Nuovo Cimento, submitted.

4. R. Mills, "The Hydrogen Atom Revisited", Int. J. of Hydrogen Energy, Vol. 25, Issue 12, December, (2000), pp. 1171-1183.

5. R. Mills, The Nature of Free Electrons in Superfluid Helium--a Test of Quantum Mechanics and a Basis to Review its Foundations and Make a Comparison to Classical Theory, Int. J. Hydrogen Energy, in press.

6. R. Mills, "BlackLight Power Technology-A New Clean Energy Source with the Potential for Direct Conversion to Electricity", Global Foundation International Conference on "Global Warming and Energy Policy", Dr. Behram N. Kursunoglu, Chairman, Fort Lauderdale, FL, November 26-28, 2000, in press.

7. R. Mills, "Spectroscopic Identification of a Novel Catalytic Reaction of Atomic Hydrogen and the Hydride Ion Product", Int. J. Hydrogen Energy, submitted.

8. R. Mills, N. Greenig, S. Hicks, "Optically Measured Power Balances of Anomalous Discharges of Mixtures of Argon, Hydrogen, and Potassium, Rubidium, Cesium, or Strontium Vapor", Int. J. Hydrogen Energy, submitted.

9. R. Mills and M. Nansteel, "Anomalous Argon-Hydrogen-Strontium Discharge", IEEE Transactions on Plasma Science, submitted.

10. R. Mills, M. Nansteel, and Y. Lu, "Anomalous Hydrogen-Strontium Discharge", European Journal of Physics D, submitted.

11. R. Mills, J. Dong, Y. Lu, "Observation of Extreme Ultraviolet Hydrogen Emission from Incandescently Heated Hydrogen Gas with Certain Catalysts", Int. J. Hydrogen Energy, Vol. 25, (2000), pp. 919-943.

12. R. Mills, "Observation of Extreme Ultraviolet Emission from Hydrogen-KI Plasmas Produced by a Hollow Cathode Discharge", Int. J. Hydrogen Energy, in press.

13. R. Mills, "Temporal Behavior of Light-Emission in the Visible Spectral Range from a Ti-K2CO3-H-Cell", Int. J. Hydrogen Energy, Vol. 26, No. 4, (2001), pp. 327-332.

14. R. Mills, T. Onuma, and Y. Lu, "Formation of a Hydrogen Plasma from an Incandescently Heated Hydrogen-Catalyst Gas Mixture with an Anomalous Afterglow Duration", Int. J. Hydrogen Energy, in press.

15. R. Mills, M. Nansteel, and Y. Lu, "Observation of Extreme Ultraviolet Hydrogen Emission from Incandescently Heated Hydrogen Gas with Strontium that Produced an Anomalous Optically Measured Power Balance", Int. J. Hydrogen Energy, Vol. 26, No. 4, (2001), pp. 309-326.

24

16. R. Mills, B. Dhandapani, M. Nansteel, J. He, A. "Voigt, Identification of Compounds Containing Novel Hydride Ions by Nuclear Magnetic Resonance Spectroscopy", Int. J. Hydrogen Energy, in press.

17. R. Mills, B. Dhandapani, N. Greenig, J. He, "Synthesis and Characterization of Potassium Iodo Hydride", Int. J. of Hydrogen Energy, Vol. 25, Issue 12, December, (2000), pp. 1185-1203.

18. R. Mills, "Novel Inorganic Hydride", Int. J. of Hydrogen Energy, Vol. 25, (2000), pp. 669-683.

19. R. Mills, B. Dhandapani, M. Nansteel, J. He, T. Shannon, A. Echezuria, "Synthesis and Characterization of Novel Hydride Compounds", Int. J. of Hydrogen Energy, Vol. 26, No. 4, (2001), pp. 339-367.

20. R. Mills, "Highly Stable Novel Inorganic Hydrides", Journal of Materials Research, submitted.

21. R. Mills, "Novel Hydrogen Compounds from a Potassium Carbonate Electrolytic Cell", Fusion Technology, Vol. 37, No. 2, March, (2000), pp. 157-182.

22. R. Mills, W. Good, A. Voigt, Jinquan Dong, "Minimum Heat of Formation of Potassium Iodo Hydride", Int. J. Hydrogen Energy, submitted.

23. David R. Linde, CRC Handbook of Chemistry and Physics, 79 th Edition, CRC Press, Boca Raton, Florida, (1998-9), p. 10-175 to p. 10-177.

24. J. Phillips, J. Smith, S. Kurtz, Report On Calorimetric Investigations Of Gas-Phase Catalyzed Hydrino Formation, Final Report for Period October-December 1996, January 1, 1997, A Confidential Report submitted to BlackLight Power, Inc. provided by BlackLight Power, Inc., 493 Old Trenton Road, Cranbury, NJ, 08512.

25. USDOE 1999 Report

26. Merrill Lynch Report on Plug Power and Fuel Cell Market Size. December 6, 1999

27. S. Sanders, J. Chumbler, M. P. Zhang, Powering the Digital Economy/Digital Power Demand Meets Industrial Power Supply/Emerging Power Technologies for the Next 100 Years, Published by Stephens Inc. Investment Bankers, 111 Center Street, Little Rock, Arkansas, 72201, August, (2000).

28. T. Cooper, H. Harvey, Power Electronics, "Power Semiconductors and Power Supplies-The Building Blocks of the Digital Power Revolution", Published by Stephens Inc. Investment Bankers, 111 Center Street, Little Rock, Arkansas, 72201, (2000).

29. P. Huber, M. Mills, The Huber Mills Digital Power Report, Powering the Telecosm, Gilder Publishing, June 2000, Issue 3.

30. World Energy Assessment, http://services.sciencewise.com/content/index.cfm?objectid=309.

31. A. Gaponov, M. I. Petelin, V. K. Yulpatov, Izvestiya VUZ. Radiofizika, 10(9-10) 1414-1453 (1965).

32. V. A. Flyagin, A. V. Gaponov, M. I. Petelin, and V. K. Yulpatov, IEEE Transactions on Microwave Theory and Techniques, Vol. MTT-25, No. 6, June (1977), pp. 514-521.

33. R. M. Dickinson, Performance of a high-power, 2.388 GHz receiving array in wireless power transmission over 1.5 km, in 1976 IEEE MTT-S International Microwave Symposium, (1976), pp. 139-141.

34. R. M. Dickinson, Bill Brown's Distinguished Career, http://www.mtt.org/awards/WCB's%20distinquished %20career.htm.

35. J. O. McSpadden, Wireless power transmission demonstration, Texas A&M University, http://www.tsgc.utexas.edu/power/general/wpt.html; History of microwave power transmission before 1980, http://rasc5.kurasc.kyoto-u.ac.jp/docs/plasma-group/sps/history2-e.html.

36. J. O. McSpadden, R. M. Dickson, L. Fan, K. Chang, A novel oscillating rectenna for wireless microwave power transmission, Texas A&M University, Jet Propulsion Laboratory, Pasadena, CA, http://www.tamu.edu, Microwave Engineering Department.

37. J. D. Jackson, *Classical Electrodynamics*, Second Edition, John Wiley & Sons, New York, (1962), pp. 588-593.

38. J. F. Louis, V. I. Kovbasyuk, Open-cycle Magnetohydrodynamic Electrical Power Generation, M Petrick, and B. Ya Shumyatsky, Editors, Argonne National Laboratory, Argonne, Illinois, (1978), pp. 157-163.

39. A. V. Timofeev, "A scheme for direct conversion of plasma thermal energy into electrical energy," Sov. J. Plasma Phys., Vol. 4, No. 4, July-August, (1978), pp. 464-468.

40. V. M. Glagolev, and A. V. Timofeev, "Direct Conversion of thermonuclear into electrical energy a drakon system," Plasma Phys. Rep., Vol. 19, No. 12, December (1993), pp. 745-749.

41. J. D. Jackson, *Classical Electrodynamics*, Second Edition, John Wiley & Sons, New York, (1962), pp. 584-588.

42. J. D. Jackson, *Classical Electrodynamics*, Second Edition, John Wiley & Sons, New York, (1962), pp. 582-584.

43. R. W. Moir, W. L. Barr, and G. A. Carlson, "Direct conversion of plasma energy to electricity for mirror fusion reactors, Lawrence Livermore Laboratory, IAEA-CN-33/G3-1, pp. 583-592.

44. R. P. Freis, Computed efficiencies of a direct-conversion collector for a fusion reactor", Nuclear Fusion, Vol. 13, (1973), pp. 247-257.

Contact information: Randell L Mills, President, BlackLight Power, Inc., 493 Old Trenton Road, Cranbury, NJ 08512, Phone: 609-490-1090, e-mail: rmills@blacklightpower.com; www.blacklightpower.com

THIS PAGE BLANK (USPTO)

THE GRAND UNIFIED THEORY OF CLASSICAL QUANTUM MECHANICS

Randell L. Mills[*]

1. INTRODUCTION

A theory of classical quantum mechanics (CQM), derived from first principles,[1] successfully applies physical laws on all scales. The classical wave equation is solved with the constraint that a bound electron cannot radiate energy. The mathematical formulation for zero radiation based on Maxwell's equations follows from a derivation by Haus.[2] The function that describes the motion of the electron must not possess spacetime Fourier components that are synchronous with waves traveling at the speed of light. CQM gives closed form solutions for the atom, including the stability of the $n=1$ state and the instability of the excited states, the equation of the photon and electron in excited states, the equation of the free electron, and photon which predict the wave particle duality behavior of particles and light. The current and charge density functions of the electron may be directly physically interpreted. For example, spin angular momentum results from the motion of negatively charged mass moving systematically, and the equation for angular momentum, r x p, can be applied directly to the wave function, called an orbitsphere (a current density function), that describes the electron. The magnetic moment of a Bohr magneton, Stern Gerlach experiment, g factor, Lamb shift, resonant line width and shape, selection rules, correspondence principle, wave particle duality, excited states, reduced mass, rotational energies, and momenta, orbital and spin splitting, spin-orbital coupling, Knight shift, and spin-nuclear coupling are derived in closed form equations based on Maxwell's equations. The calculations agree with experimental observations.

For or any kind of wave advancing with limiting velocity and capable of transmitting signals, the equation of front propagation is the same as the equation for the front of a light wave. By applying this condition to electromagnetic and gravitational fields at

[*] Randell L Mills, President, BlackLight Power, Inc., 493 Old Trenton Road, Cranbury, NJ 08512, Phone: 609-490-1090, e-mail: rmills@blacklightpower.com; www.blacklightpower.com

particle production, the Schwarzschild metric (SM) is derived from the classical wave equation which modifies general relativity to include conservation of spacetime in addition to momentum and matter/energy. The result gives a natural relationship between Maxwell's equations, special relativity, and general relativity. It gives gravitation from the atom to the cosmos. The Universe is time harmonically oscillatory in matter energy and spacetime expansion and contraction with a minimum radius that is the gravitational radius. In closed form equations with fundamental constants only, CQM gives the deflection of light by stars, the precession of the perihelion of Mercury, the particle masses, the Hubble constant, the age of the Universe, the observed acceleration of the expansion, the power of the Universe, the power spectrum of the Universe, the microwave background temperature, the uniformity of the microwave background radiation, the microkelvin spatial variation of the microwave background radiation, the observed violation of the GZK cutoff, the mass density, the large scale structure of the Universe, and the identity of dark matter which matches the criteria for the structure of galaxies. In a special case wherein the gravitational potential energy density of a blackhole equals that of the Plank mass, matter converts to energy and spacetime expands with the release of a gamma-ray burst. The singularity in the SM is eliminated.

2. COSMOLOGICAL THEORY BASED ON MAXWELL'S EQUATIONS

Maxwell's equations and special relativity are based on the law of propagation of a electromagnetic wave front in the form

$$1/c^2 (\delta\omega/\delta t)^2 - \left[(\delta\omega/\delta x)^2 + (\delta\omega/\delta y)^2 + (\delta\omega/\delta\omega)^2\right] = 0 \qquad (1)$$

For any kind of wave advancing with limiting velocity and capable of transmitting signals, the equation of front propagation is the same as the equation for the front of a light wave. Thus, the equation $1/c^2 (\delta\omega/\delta t)^2 - (grad\omega)^2 = 0$ acquires a general character; it is more general than Maxwell's equations from which Maxwell originally derived it.

A discovery of the present work is that the classical wave equation governs: (1) the motion of bound electrons, (2) the propagation of any form of energy, (3) measurements between inertial frames of reference such as time, mass, momentum, and length (Minkowski tensor), (4) fundamental particle production and the conversion of matter to energy, (5) a relativistic correction of spacetime due to particle production or annihilation (Schwarzschild metric), (6) the expansion and contraction of the Universe, (7) the basis of the relationship between Maxwell's equations, Planck's equation, the de Broglie equation, Newton's laws, and special, and general relativity.

The relationship between the time interval between ticks t of a clock in motion with velocity v relative to an observer and the time interval t_0 between ticks on a clock at rest relative to an observer [3] is

$$(ct)^2 = (ct_0)^2 + (vt)^2. \qquad (2)$$

Thus, the time dilation relationship based on the constant maximum speed of light c in any inertial frame is $t = t_0 / \sqrt{1 - (v^2/c^2)}$. The metric $g_{\mu\nu}$ for Euclidean space is the

Minkowski tensor $\eta_{\mu\nu}$. In this case, the separation of proper time between two events x^μ and $x^\mu + dx^\mu$ is $d\tau^2 = -\eta_{\mu\nu} dx^\mu dx^\nu$.

3. THE EQUIVALENCE OF THE GRAVITATIONAL MASS AND THE INERTIAL MASS

The equivalence of the gravitational mass and the inertial mass m_g/m_i = universal constant which is predicted by Newton's law of mechanics and gravitation is experimentally confirmed to less $1 \; X \; 10^{-11}$.[4] In physics, the discovery of a universal constant often leads to the development of an entirely new theory. From the universal constancy of the velocity of light c, the special theory of relativity was derived; and from Planck's constant h, the quantum theory was deduced. Therefore, the universal constant m_g/m_i should be the key to the gravitational problem. The energy equation of Newtonian gravitation is

$$E = \frac{1}{2}mv^2 - \frac{GMm}{r} = \frac{1}{2}mv_0^2 - \frac{GMm}{r_0} = \text{constant} \tag{3}$$

Since h, the angular momentum per unit mass, is $h = L/m = |\mathbf{r} \times \mathbf{v}| = r_0 v_0 \sin\phi$, the eccentricity e may be written as

$$e = [1 + \left(v_0^2 - \frac{2GM}{r_0} \right) \frac{r_0^2 v_0^2 \sin^2\phi}{G^2 M^2}]^{1/2}, \tag{4}$$

where m is the inertial mass of a particle, v_0 is the speed of the particle, r_0 is the distance of the particle from a massive object, ϕ is the angle between the direction of motion of the particle and the radius vector from the object, and M is the total mass of the object (including a particle). The eccentricity e given by Newton's differential equations of motion in the case of the central field permits the classification of the orbits according to the total energy E [5] (column 1) and the orbital velocity squared, v_0^2, relative to the gravitational velocity squared, $2GM/r_0$ [5] (column 2):

$E < 0$	$v_0^2 < 2GM/r_0$	$e < 1$	ellipse
$E < 0$	$v_0^2 < 2GM/r_0$	$e = 0$	circle (special case of ellipse)
$E = 0$	$v_0^2 = 2GM/r_0$	$e = 1$	parabolic orbit
$E > 0$	$v_0^2 > 2GM/r_0$	$e > 1$	hyperbolic orbit

4. CONTINUITY CONDITIONS FOR THE PRODUCTION OF A PARTICLE FROM A PHOTON TRAVELING AT LIGHT SPEED

A photon traveling at the speed of light gives rise to a particle with an initial radius equal to its Compton wavelength bar.

$$r = \lambda_C = \frac{\hbar}{m_0 c} = r_\alpha^* , \tag{5}$$

The particle must have an orbital velocity equal to Newtonian gravitational escape velocity v_g of the antiparticle.

$$v_g = \sqrt{\frac{2Gm}{r}} = \sqrt{\frac{2Gm_0}{\lambda_C}} . \tag{6}$$

The eccentricity is one. The orbital energy is zero. The particle production trajectory is a parabola relative to the center of mass of the antiparticle.

4.1 A Gravitational Field as a Front Equivalent to Light Wave Front

The particle with a finite gravitational mass gives rise to a gravitational field that travels out as a front equivalent to a light wave front. The form of the outgoing gravitational field front traveling at the speed of light is $f(t - r/c)$ and $d\tau^2$ is given by

$$d\tau^2 = f(r)dt^2 - \frac{1}{c^2}\left[f(r)^{-1} dr^2 + r^2 d\theta^2 + r^2 \sin^2 \theta d\phi^2 \right] \tag{7}$$

The speed of light as a constant maximum as well as phase matching and continuity conditions of the electromagnetic and gravitational waves require the following form of the squared displacements:

$$(c\tau)^2 + (v_g t)^2 = (ct)^2 , \tag{8}$$

$$f(r) = \left(1 - \left(\frac{v_g}{c} \right)^2 \right). \tag{9}$$

In order that the wave front velocity does not exceed c in any frame, spacetime must undergo time dilation and length contraction due to the particle production event. *The derivation and result of spacetime time dilation is analogous to the derivation and result of special relativistic time dilation* wherein the relative velocity of two inertial frames replaces the gravitational velocity.

The general form of the metric due to the relativistic effect on spacetime due to mass m_0 with v_g given by Eq. (6) is

$$d\tau^2 = \left(1 - \left(\frac{v_g}{c} \right)^2 \right)dt^2 - \frac{1}{c^2}\left[\left(1 - \left(\frac{v_g}{c} \right)^2 \right)^{-1} dr^2 + r^2 d\theta^2 + r^2 \sin^2 \theta d\phi^2 \right]. \tag{10}$$

The gravitational radius, r_g, of each orbitsphere of the particle production event, each of

mass m_0 and the corresponding general form of the metric are respectively

$$r_g = \frac{2Gm_0}{c^2},$$ (11)

$$d\tau^2 = \left(1 - \frac{r_g}{r}\right)dt^2 - \frac{1}{c^2}\left[\left(1 - \frac{r_g}{r}\right)^{-1}dr^2 + r^2d\theta^2 + r^2\sin^2\theta d\phi^2\right].$$ (12)

The metric $g_{\mu\nu}$ for non-euclidean space due to the relativistic effect on spacetime due to mass m_0 is

$$g_{\mu\nu} = \begin{pmatrix} -\left(1 - \frac{2Gm_0}{c^2r}\right) & 0 & 0 & 0 \\ 0 & \frac{1}{c^2}\left(1 - \frac{2Gm_0}{c^2r}\right)^{-1} & 0 & 0 \\ 0 & 0 & \frac{1}{c^2}r^2 & 0 \\ 0 & 0 & 0 & \frac{1}{c^2}r^2\sin^2\theta \end{pmatrix}$$ (12a)

Masses and their effects on spacetime *superimpose*. The separation of proper time between two events x^μ and $x^\mu + dx^\mu$ is

$$d\tau^2 = \left(1 - \frac{2GM}{c^2r}\right)dt^2 - \frac{1}{c^2}\left[\left(1 - \frac{2GM}{c^2r}\right)^{-1}dr^2 + r^2d\theta^2 + r^2\sin^2\theta d\phi^2\right].$$ (13)

The *Schwarzschild metric[Eq. (12a)] gives the relationship whereby matter causes relativistic corrections to spacetime that determines the curvature of spacetime and is the origin of gravity.*

4.2. Particle Production Continuity Conditions from Maxwell's Equations, and the Schwarzchild Metric

The photon to particle event requires a transition state that is continuous wherein the velocity of a transition state orbitsphere is the speed of light. The radius, r, is the Compton wavelength bar, λ_c, given by Eq. (5). At production, the Planck equation energy, the electric potential energy, and the magnetic energy are equal to m_0c^2.

The Schwarzschild metric gives the relationship whereby matter causes relativistic corrections to spacetime that determines the masses of fundamental particles. Substitution of $r = \lambda_c$; $dr = 0$; $d\theta = 0$; $\sin^2\theta = 1$ into the Schwarzschild metric gives

$$d\tau = dt\left(1 - \frac{2Gm_0}{c^2r_\alpha^*} - \frac{v^2}{c^2}\right)^{\frac{1}{2}},$$ (14)

with $v^2 = c^2$, the relationship between the proper time and the coordinate time is

$$\tau = ti\sqrt{\frac{2GM}{c^2 r_a^*}} = ti\sqrt{\frac{2GM}{c^2 \lambda_c}} = ti\frac{v_g}{c} . \tag{15}$$

When the orbitsphere velocity is the speed of light, continuity conditions based on the constant maximum speed of light given by Maxwell's equations are mass energy = Planck equation energy = electric potential energy = magnetic energy = mass/spacetime metric energy. Therefore, $m_o c^2 = \hbar\omega^* = V = E_{mag} = E_{spacetime}$

$$m_0 c^2 = \hbar\omega^* = \frac{\hbar^2}{m_0 \lambda_c^2} = \alpha^{-1}\frac{e^2}{4\pi\varepsilon_0 \lambda_c} = \alpha^{-1}\frac{\pi\mu_o e^2 \hbar^2}{(2\pi m_0)^2 \lambda_c^3} = \frac{\alpha h}{1\sec}\sqrt{\frac{\lambda_c c^2}{2Gm}} . \tag{16}$$

The continuity conditions based on the constant maximum speed of light given by the Schwarzschild metric are:

$$\frac{\text{proper time}}{\text{coordinate time}} = \frac{\text{gravitational wave condition}}{\text{electromagnetic wave condition}} = \frac{\text{gravitational mass phase matching}}{\text{charge/inertial mass phase matching}} \tag{17}$$

$$\frac{\text{proper time}}{\text{coordinate time}} = i\frac{\sqrt{\frac{2Gm}{c^2 \lambda_c}}}{\alpha} = i\frac{v_g}{\alpha c} . \tag{18}$$

5. MASSES OF FUNDAMENTAL PARTICLES

Each of the Planck equation energy, electric energy, and magnetic energy corresponds to a particle given by the relationship between the proper time and the coordinate time. The electron and down-down-up neutron correspond to the Planck equation energy. The muon and strange-strange-charmed neutron correspond to the electric energy. The tau and bottom-bottom-top neutron correspond to the magnetic energy. The particle must possess the escape velocity v_g relative to the antiparticle where $v_g < c$. According to Newton's law of gravitation, the eccentricity is one and the particle production trajectory is a parabola relative to the center of mass of the antiparticle.

5.1. The Electron-Antielectron Lepton Pair

A clock is defined in terms of a self consistent system of units used to measure the particle mass. The proper time of the particle is equated with the coordinate time according to the Schwarzschild metric corresponding to light speed. The special relativistic condition corresponding to the Planck energy gives the mass of the electron.

$$2\pi\frac{\hbar}{mc^2} = sec\sqrt{\frac{2Gm^2}{c\alpha^2\hbar}} , \tag{19}$$

$$m_e = \left(\frac{h\alpha}{sec\,c^2}\right)^{\frac{1}{2}}\left(\frac{c\hbar}{2G}\right)^{\frac{1}{4}} = 9.1097\,X\,10^{-31}\,kg \;, \tag{20}$$

$$m_e = 9.1097\,X\,10^{-31}\,kg - 18\,eV/c^2\,(v_e) = 9.1094\,X\,10^{-31}\,kg \;, \tag{21}$$

$$m_{e\,experimental} = 9.1095\,X\,10^{-31}\,kg \;. \tag{22}$$

5.2. Down-Down-Up Neutron (DDU)

The corresponding equation for production of the neutron is

$$2\pi\frac{2\pi\hbar}{\dfrac{m_N}{3}\left[\dfrac{1}{2\pi}-\dfrac{\alpha}{2\pi}\right]c^2} = sec\sqrt{\frac{2G\left[\dfrac{m_N}{3}\left[\dfrac{1}{2\pi}-\dfrac{\alpha}{2\pi}\right]\right]^2}{3c(2\pi)^2\hbar}} \;, \tag{23}$$

$$m_{N\,calculated} = (3)(2\pi)\left(\frac{1}{1-\alpha}\right)\left(\frac{2\pi h}{sec\,c^2}\right)^{\frac{1}{2}}\left(\frac{2\pi(3)ch}{2G}\right)^{\frac{1}{4}} = 1.6744 X 10^{-27}\,kg \tag{24}$$

$$m_{N\,experimental} = 1.6749 X 10^{-27}\,kg \;. \tag{25}$$

6. GRAVITATIONAL POTENTIAL ENERGY

The gravitational radius, α_G or r_G, of an orbitsphere of mass m_0 is defined as

$$\alpha_G = r_G = \frac{Gm_0}{c^2} \;, \tag{26}$$

when the $r_G = r_a^* = \lambda_C$, the gravitational potential energy equals $m_0 c^2$

$$r_G = \frac{Gm_0}{c^2} = \lambda_c = \frac{\hbar}{m_0 c} \;, \tag{27}$$

$$E_{grav} = \frac{Gm_0^2}{r} = \frac{Gm_0^2}{\lambda_C} = \frac{Gm_0^2}{r_a^*} = \hbar\omega^* = m_0 c^2 \;. \tag{28}$$

The mass m_0 is the Planck mass, m_u,

$$m_u = m_0 = \sqrt{\frac{\hbar c}{G}} \tag{29}$$

the corresponding gravitational velocity, v_G, is defined as

$$v_G = \sqrt{\frac{Gm_0}{r}} = \sqrt{\frac{Gm_0}{\lambda_C}} = \sqrt{\frac{Gm_u}{\lambda_C}} \ . \tag{30}$$

6.1. Relationship of the Equivalent Planck Mass Particle Production Energies

For the Plank mass particle, the relationships corresponding to Eq. (16) are: (mass energy = Planck equation energy = electric potential energy = magnetic energy = gravitational potential energy = mass/spacetime metric energy)

$$m_0 c^2 = \hbar \omega^* = V = E_{mag} = E_{grav} = E_{spacetime} , \tag{31}$$

$$m_0 c^2 = \hbar \omega^* = \frac{\hbar^2}{m_0 \lambda_C^2} = \alpha^{-1} \frac{e^2}{4\pi\varepsilon_0 \lambda_C} = \alpha^{-1} \frac{\pi\mu_0 e^2 \hbar^2}{(2\pi m_0)^2 \lambda_C^3} = \alpha^{-1} \frac{\mu_0 e^2 c^2}{2h} \sqrt{\frac{Gm_0}{\lambda_C}} \sqrt{\frac{\hbar c}{G}} = \frac{\alpha h}{1 \sec} \sqrt{\frac{\lambda_C c^2}{2Gm}} \tag{32}$$

These equivalent energies give the particle masses in terms of the gravitational velocity, v_G, and the Planck mass, m_u

$$m_0 = \alpha^{-1} \frac{\mu_0 e^2 c}{2h} \frac{\sqrt{\frac{Gm_0}{\lambda_C}}}{c} m_u = \alpha^{-1} \frac{\mu_0 e^2 c}{2h} \sqrt{\frac{Gm_0}{c^2 \lambda_C}} m_u = \alpha^{-1} \frac{\mu_0 e^2 c}{2h} \frac{v_G}{c} m_u = \frac{v_G}{c} m_u \ . \tag{33}$$

6.2. Planck Mass Particles

A pair of particles each of the Planck mass corresponding to the gravitational potential energy is not observed since the velocity of each transition state orbitsphere is the gravitational velocity, v_G that in this case is the speed of light; whereas, the Newtonian gravitational escape velocity v_g is $\sqrt{2}$ the speed of light. In this case, an electromagnetic wave of mass energy equivalent to the Planck mass travels in a circular orbit about the center of mass of another electromagnetic wave of mass energy equivalent to the Planck mass wherein the eccentricity is equal to zero and the escape velocity can never be reached. The Planck mass is a "measuring stick." The extraordinarily high Planck mass ($\sqrt{\hbar c/G} = 2.18 \times 10^{-8} \ kg$) is the unobtainable mass bound imposed by the angular momentum and speed of the photon relative to the gravitational constant. It is analogous to the unattainable bound of the speed of light for a particle possessing finite rest mass imposed by the Minkowski tensor.

6.3. Astrophysical Implications of Planck Mass Particles

The limiting speed of light eliminates the singularity problem of Einstein's equation that arises as the radius of a blackhole equals the Schwarzschild radius. General relativity with the singularity eliminated resolves the paradox of the infinite propagation velocity required for the gravitational force in order to explain why the angular momentum of objects orbiting a gravitating body does not increase due to the finite propagation delay of the gravitational force according to special relativity.[6] When the gravitational potential energy density of a massive body such as a blackhole equals that of a particle having the Planck mass, the matter may transition to photons of the Planck mass. Even light from a

blackhole will escape when the decay rate of the trapped matter with the concomitant spacetime expansion is greater than the effects of gravity which oppose this expansion. Gamma-ray bursts are the most energetic phenomenon known that can release an explosion of gamma rays packing 100 times more energy than a supernova explosion.[7] The annihilation of a blackhole may be the source of γ-*ray bursts*. The source may be due to conversion of matter to photons of the Planck mass/energy which may also give rise to cosmic rays which are the most energetic particles known, and their origin is also a mystery.[8] According to the GZK cutoff, the cosmic spectrum cannot extend beyond 5 X $10^{19}eV$, but AGASA, the world's largest air shower array, has shown that the spectrum is extending beyond $10^{20}eV$ without any clear sign of cutoff.[9] Photons each of the Planck mass may be the source of these inexplicably energetic cosmic rays.

7. RELATIONSHIP OF MATTER TO ENERGY AND SPACETIME EXPANSION

The Schwarzschild metric gives the relationship whereby matter causes relativistic corrections to spacetime. The limiting velocity c results in the contraction of spacetime due to particle production, which is given by $2\pi r_g$ where r_g is the gravitational radius of the particle. This has implications for the expansion of spacetime when matter converts to energy. Q the mass/energy to expansion/contraction quotient of spacetime is given by the ratio of the mass of a particle at production divided by T the period of production.

$$Q = \frac{m_0}{T} = \frac{m_0}{\frac{2\pi r_g}{c}} = \frac{m_0}{\frac{2\pi \frac{2Gm_0}{c^2}}{c}} = \frac{c^3}{4\pi G} = 3.22 \times 10^{34} \frac{kg}{sec} .$$ (34)

The gravitational equations with the equivalence of the particle production energies [Eq. (16)] permit the conservation of mass/energy ($E=mc^2$) and spacetime ($c^3/4\pi G$=3.22 X 10^{34} *kg/sec*). With the conversion of 3.22 X 10^{34} *kg* of matter to energy, spacetime expands by 1 sec. The photon has inertial mass and angular momentum, but due to Maxwell's equations and the implicit special relativity it does not have a gravitational mass.

7.1. Cosmological Consequences

The Universe is closed (it is *finite but with no boundary*). It is a 3-sphere Universe-Riemannian three dimensional hyperspace plus time of constant positive curvature at each r-sphere. The *Universe is oscillatory in matter/energy and spacetime* with a finite minimum radius, the gravitational radius. Spacetime expands as mass is released as energy which provides the basis of the atomic, thermodynamic, and cosmological arrows of time. Different regions of space are isothermal even though they are separated by greater distances than that over which light could travel during the time of the expansion of the Universe.[10] Presently, stars and large scale structures exist which are older than the elapsed time of the present expansion as stellar, galaxy, and supercluster evolution occurred during the contraction phase.[11–17] The maximum power radiated by the Universe which occurs at the beginning of the expansion phase is $P_U=c^5/4\pi G = 2.89 \times 10^{51} W$.

Observations beyond the beginning of the expansion phase are not possible since the Universe is entirely matter filled.

7.2. The Period of Oscillation of the Universe Based on Closed Propagation of Light

Mass/energy is conserved during harmonic expansion and contraction. The gravitational potential energy E_{grav} given by Eq. (28) with $m_0 = m_U$ is equal to $m_U c^2$ when the radius of the Universe r is the gravitational radius r_G. The gravitational velocity v_G [Eq. (30) with $r=r_G$ and $m_0 = m_U$] is the speed of light in a circular orbit wherein the eccentricity is equal to zero and the escape velocity from the Universe can never be reached. The period of the oscillation of the Universe and the period for light to transverse the Universe corresponding to the gravitational radius r_G must be equal. The harmonic oscillation period, T, is

$$T = \frac{2\pi r_G}{c} = \frac{2\pi G m_U}{c^3} = \frac{2\pi G \left(2 \times 10^{54} \ kg\right)}{c^3} = 3.10 \times 10^{19} \ sec = 9.83 \times 10^{11} \ years , \tag{35}$$

where the mass of the Universe, m_U, is approximately $2 \times 10^{54} kg$. (The initial mass of the Universe of $2 \times 10^{54} kg$ is based on internal consistency with the size, age, Hubble constant, temperature, density of matter, and power spectrum.) Thus, the observed Universe will expand as mass is released as photons for $4.92 \times 10^{11} years$. At this point in its world line, the Universe will obtain its maximum size and begin to contract.

8. THE DIFFERENTIAL EQUATION OF THE RADIUS OF THE UNIVERSE

Based on conservation of mass/energy ($E=mc^2$) and spacetime ($c^3/4\pi G=3.22 \times 10^{34}$ kg/sec). The Universe behaves as a simple harmonic oscillator having a restoring force, F, which is proportional to the radius. The proportionality constant, k, is given in terms of the potential energy, E, gained as the radius decreases from the maximum expansion to the minimum contraction.

$$\frac{E}{\aleph^2} = k . \tag{36}$$

Since the gravitational potential energy E_{grav} is equal to $m_U c^2$ when the radius of the Universe r is the gravitational radius r_G

$$F = -k\aleph = -\frac{m_U c^2}{r_G^2}\aleph = -\frac{m_U c^2}{\left(\frac{G m_U}{c^2}\right)^2}\aleph . \tag{37}$$

And, the differential equation of the radius of the Universe, $\aleph$ is

$$m_U \ddot{\aleph} + \frac{m_U c^2}{r_G^2}\aleph = m_U \ddot{\aleph} + \frac{m_U c^2}{\left(\frac{G m_U}{c^2}\right)^2}\aleph = 0 . \tag{38}$$

The *maximum radius of the Universe*, the amplitude, r_0, of the time harmonic variation in the radius of the Universe, is given by the quotient of the total mass of the Universe and Q, the mass/energy to expansion/contraction quotient.

$$r_0 = \frac{m_U}{Q} = \frac{m_U}{\dfrac{c^3}{4\pi G}} = \frac{2\,X\,10^{54}\,kg}{\dfrac{c^3}{4\pi G}} = 1.97\,X\,10^{12}\;light\;years\,. \tag{39}$$

The *minimum radius* which corresponds to the gravitational radius r_g, given by Eq. (11) with $m_0 = m_U$ is $3.12\,X\,10^{11}$ *light years*. When the radius of the Universe is the gravitational radius, r_g, the proper time is equal to the coordinate time by Eq. (15) and the gravitational escape velocity v_g of the Universe is the speed of light. The radius of the Universe as a function of time is

$$\aleph = \left(r_g + \frac{cm_U}{Q}\right) - \frac{cm_U}{Q}\cos\left(\frac{2\pi t}{\dfrac{2\pi r_G}{c}}\right) = \left(\frac{2Gm_U}{c^2} + \frac{cm_U}{\dfrac{c^3}{4\pi G}}\right) - \frac{cm_U}{\dfrac{c^3}{4\pi G}}\cos\left(\frac{2\pi t}{\dfrac{2\pi Gm_U}{c^3}}\right). \tag{40}$$

The expansion/contraction rate, $\dot{\aleph}$, is given by time derivative of Eq. (40)

$$\dot{\aleph} = 4\pi c\,X\,10^{-3}\sin\left(\frac{2\pi t}{\dfrac{2\pi Gm_U}{c^3}}\right)\frac{km}{sec}\,. \tag{41}$$

9. THE HUBBLE CONSTANT

The *Hubble constant* is given by the ratio of the expansion rate given in units of *km/sec* divided by the radius of the expansion in *Mpc*. The radius of expansion is equivalent to the radius of the light sphere with an origin at the time point when the Universe stopped contracting and started to expand.

$$H = \frac{\dot{\aleph}}{t\,Mpc} = \frac{4\pi c\,X\,10^{-3}\sin\left(\dfrac{2\pi t}{\dfrac{2\pi Gm_U}{c^3}}\right)\dfrac{km}{sec}}{t\,Mpc}\,, \tag{42}$$

for $t = 10^{10}$ *light years* $= 3.069\,X\,10^3\,Mpc$, the Hubble constant, H_0, is 78.6 *km/sec·Mpc*. The experimental value is[18] $H_0 = 80 \pm 17$ *km/sec·Mpc*.

10. THE DENSITY OF THE UNIVERSE AS A FUNCTION OF TIME

The density of the Universe as a function of time $\rho_U(t)$ is given by the ratio of the

mass as a function of time and the volume as a function of time.

$$\rho_U(t) = \frac{m_U(t)}{V(t)} = \frac{m_U(t)}{\frac{4}{3}\pi\aleph(t)} = \frac{\frac{m_U}{2}\left(1 + cos\left(\frac{2\pi t}{\frac{2\pi G m_U}{c^3}}\right)\right)}{\frac{4}{3}\pi\left(\left(\frac{2G m_U}{c^2} + \frac{c m_U}{\frac{c^3}{4\pi G}}\right) - \frac{c m_U}{\frac{c^3}{4\pi G}} cos\left(\frac{2\pi t}{\frac{2\pi G m_U}{c^3}}\right)\right)^3}, \tag{43}$$

for $t = 10^{10}$ *light years*, $\rho_U = 1.7 \times 10^{-32}$ *g / cm³* The density of luminous matter of stars and gas of galaxies is about $\rho_U = 2 \times 10^{-31}$ *g / cm³*.[19–20]

11. THE POWER OF THE UNIVERSE AS A FUNCTION OF TIME, $P_U(t)$

From $E = mc^2$ and Eq. (34),

$$P_U(t) = \frac{c^5}{8\pi G}\left(1 + cos\left(\frac{2\pi t}{\frac{2\pi r_G}{c}}\right)\right) \tag{44}$$

For $t = 10^{10}$ *light years*, $P_U(t) = 2.88 \times 10^{51} W$. The observed power is consistent with that predicted.

12. THE TEMPERATURE OF THE UNIVERSE AS A FUNCTION OF TIME

The temperature of the Universe as a function of time, $T_U(t)$, follows from the Stefan-Boltzmann law.

$$T_U(t) = \left(\frac{1}{1 + \frac{G m_U(t)}{c^2 \aleph(t)}}\right)\left[\frac{R_U(t)}{e\sigma}\right]^{\frac{1}{4}} = \left(\frac{1}{1 + \frac{G m_U(t)}{c^2 \aleph(t)}}\right)\left[\frac{\frac{P_U(t)}{4\pi\aleph(t)^2}}{e\sigma}\right]^{\frac{1}{4}}. \tag{45}$$

The calculated uniform temperature is about 2.7 K which is in agreement with the observed microwave background temperature.[10]

13. POWER SPECTRUM OF THE COSMOS

The power spectrum of the cosmos, as measured by the Las Campanas Survey,

generally follows the prediction of cold dark matter on the scales of 200 million to 600 million light-years. However, the power increases dramatically on scales of 600 million to 900 million light-years. The infinitesimal temporal displacement, $d\tau^2$, is given by Eq. (13).

The relationship between the proper time and the coordinate time is

$$\tau = t\sqrt{1 - \frac{2Gm_U}{c^2 r}} = t\sqrt{1 - \frac{r_s}{r}} . \tag{46}$$

The power maximum in the proper frame occurs at

$$\tau = 5 \times 10^9 \; light \; years \sqrt{1 - \frac{3.12 \times 10^{11} \; light \; years}{3.22 \times 10^{11} \; light \; years}} = 880 \times 10^6 \; light \; years . \tag{47}$$

The power maximum of the current observable Universe is predicted to occur on the scale of 880×10^6 *light years*. There is excellent agreement between the predicted value and the experimental value of 600–900 $\times 10^6$ *light years.*[17]

14. THE EXPANSION/CONTRACTION ACCELERATION, $\ddot{\aleph}$

The expansion/contraction acceleration rate, $\ddot{\aleph}$, is given by the time derivative of Eq. (41).

$$\ddot{\aleph} = 2\pi \frac{c^4}{Gm_U} cos\left(\frac{2\pi t}{\frac{2\pi Gm_U}{c^3} \; sec} \right) = \ddot{\aleph} = H_o = 78.7 cos\left(\frac{2\pi t}{3.01 \times 10^5 \; Mpc} \right) \frac{km}{sec \cdot Mpc} \tag{48}$$

The differential in the radius of the Universe, $\Delta\aleph$, due to its acceleration is given by $\Delta\aleph = 1/2 \ddot{\aleph} t^2$. The differential in expanded radius for the elapsed time of expansion, $t = 10^{10}$ *light years* corresponds to a decease in brightness of a supernovae standard candle of about an order of magnitude of that expected where the distance is taken as $\Delta\aleph$. This result based on the predicted rate of acceleration of the expansion is consistent with the experimental observation.[21-23]

Furthermore, the microwave background radiation image obtained by the Boomerang telescope[24] is consistent with a Universe of nearly flat geometry since the commencement of its expansion. The data is consistent with a large offset radius of the Universe with a fractional increase in size since the commencement of expansion about 10 billion years ago.

15. THE PERIODS OF SPACETIME EXPANSION/CONTRACTION AND PARTICLE DECAY/PRODUCTION FOR THE UNIVERSE ARE EQUAL

The period of the expansion/contraction cycle of the radius of the Universe, T, is given by Eq. (35). It follows from the Poynting power theorem with spherical radiation that the transition lifetimes are given by the ratio of energy and the power of the transition.

$$\tau = \frac{energy}{power} = \frac{[\hbar\omega]}{\left[\dfrac{2\pi c}{[(2l+1)!!]^2}\left(\dfrac{l+1}{l}\right)k^{2l+1}|Q_{lm}+Q'_{lm}|^2\right]}$$

$$= \frac{1}{2\pi}\left(\frac{h}{e^2}\right)\sqrt{\frac{\varepsilon_0}{\mu_0}}\frac{[(2l+1)!!]^2}{2\pi}\left(\frac{l}{l+1}\right)\left(\frac{l+3}{3}\right)^2\frac{1}{(k r_n)^{2l}\omega}. \tag{49}$$

Exponential decay applies to electromagnetic energy decay $h(t)=e^{-\frac{1}{T}t}u(t)$. The coordinate time is imaginary because energy transitions are spacelike due spacetime expansion from matter to energy conversion. For example, the mass of the electron (a fundamental particle) is given by

$$\frac{2\pi\lambda_C}{\sqrt{\dfrac{2Gm_e}{\lambda_C}}} = \frac{2\pi\lambda_C}{v_g} = i\alpha^{-1}\,sec, \tag{50}$$

where v_g is Newtonian gravitational velocity [Eq. (6)]. When the gravitational radius r_g is the radius of the Universe, the proper time is equal to the coordinate time by Eq. (15), and the gravitational escape velocity v_g of the Universe is the speed of light. Replacement of the coordinate time, t, by the spacelike time, it, gives

$$h(t) = Re\left[e^{-i\frac{1}{T}t}\right] = cos\frac{2\pi}{T}t, \tag{51}$$

where the period is T [Eq. (35)]. The continuity conditions based on the constant maximum speed of light (Maxwell's equations) are given by Eqs. (16). The continuity conditions based on the constant maximum speed of light (Schwarzschild metric) are given by Eqs. (17-18). The periods of spacetime expansion/contraction and particle decay/production for the Universe are equal because only the particles which satisfy Maxwell's equations and the relationship between proper time and coordinate time imposed by the Schwarzschild metric may exist.

16. WAVE EQUATION

The general form of the light front wave equations is given by Eq. (1). The equation

of the radius of the Universe, $\aleph$, may be written as

$$\aleph = \left(\frac{2Gm_U}{c^2} + \frac{cm_U}{\frac{c^3}{4\pi G}} \right) - \frac{cm_U}{\frac{c^3}{4\pi G}} \cos \left(\frac{2\pi}{\frac{2\pi Gm_U}{c^3} \, sec} \left(t - \frac{\aleph}{c} \right) \right) m \; , \tag{52}$$

which is a solution of the wave equation for a light wave front.

17. CONCLUSION

Maxwell's equations, Planck's equation, the de Broglie equation, Newton's laws, and special, and general relativity are unified.

REFERENCES

1. R. Mills, *The Grand Unified Theory of Classical Quantum Mechanics*, January 2000 Edition, BlackLight Power, Inc., Cranbury, New Jersey, Distributed by Amazon.com.
2. H. A. Haus, On the radiation from point charges, *American Journal of Physics*, **54**, 1126–1129 (1986).
3. A. Beiser., *Concepts of Modern Physics*, 4th Edition, McGraw-Hill Book Company, New York, (1978), 2–10.
4. E. G. Adelberger, C. W. Stubbs, B. R. Heckel, Y. Su, H. E.Swanson, G. Smith, J. H. Gundlach, *Phys. Rev. D*, **42**(10), 3267-3292 (1990).
5. G. R. Fowles, *Analytical Mechanics*, Third Edition, Holt, Rinehart, and Winston, New York, (1977), pp. 154–155.
6. T. Van Flandern, The Speed of Gravity—What the Experiments Say, *Physics Letters A*, **250**, 1–11 (1998).
7. R Cowen, Gamma-ray burst makes quite a bang, *Science News*,**153**(19), 292(1998).
8. M. Chown, The ultimate free lunch, *New Scientist*, **154**(2081), 50–51 (1997)ʾ
9. B. Schwarzschild, Giant air shower array shows cosmic-ray spectrum violating greisen cutoff, *Physics Today*, **51**(10), 19–21 (1998).
10. J. C. Mather, E. S. Cheng, A preliminary measurement of the cosmic microwave background spectrum by the Cosmic Background Explorer (COBE) satellite, *Astrophysical Journal Letters*, **354**, L37–L40 (May 10, 1990).
11. W. Saunders, C. Frenk; et al; The density field of the local universe; *Nature*, **349**(6304), 32–38 (1991).
12. R. P. Kirshner, A. Oemler, Jr., P.L. Schechter, S. A. Shectman, A deep survey of galaxies, *Astronomical Journal*, **88**, 1285–1300 (September 1983).
13. V. de Lapparent, M.J. Geller, J.P. Huchra, The mean density and two-point correlation function for the CfA redshift survey slices, *Astrophysical Journal*, **332**(9) 44–56 (September 1, 1988).
14. A. Dressler, D. Lynden-Bell, D. Burstein, et. al., Spectroscopy and photometry of elliptical galaxies. I–A new distance estimator, *Astrophysical Journal*, **313**(2), 42–58 (1987).
15. S. Flamsteed, Crisis in the Cosmos, *Discover*, **16**(3), 66(1995).
16. J. Glanz, CO in the early universe clouds cosmologists' views, *Science*, **273**(5275), 581 (1996)
17. S. D. Landy, Mapping the Universe, *Scientific American*, **280**(6), 38–45 (1999).
18. W.L. Freeman, et al., Distance to the Virgo cluster galaxy M100 from Hubble Space, *Nature*, **371**(6500), 757–762 (1994).
19. R. M. Wald, *General Relativity*, University of Chicago Press, Chicago, (1984), pp. 114–116.
20. P. J. E. Peebles, J. Silk, Joseph, A cosmic book of phenomena, *Nature*, **346**(6281), 233 (1990)
21. J. Glanz; Astronomers see a cosmic antigravity force at work, *Science*, **279**(5355), 1298–1299 (1998).

22. R. Cowen, Living with lambda, *Science News*, 153(22), 344 (1998).
23. R. Cowen, Studies support an accelerating Universe, *Science News*, 154(18), 277 (1998).
24. P. de Bernardis et al., A flat Universe from high-resolution maps of the cosmic microwave
     background radiation, *Nature*, 404, (2000), p. 955; http://www.physics.ucsb.edu/~boomerang.

The grand unified theory of classical quantum mechanics

Randell L. Mills [*,1]

Black Light Power, Inc., 493 Old Trenton Road, Cranbury, NJ 08512, USA

Abstract

A theory of classical quantum mechanics (CQM) is derived from first principles that successfully applies physical laws on all scales. Using Maxwell's equations, the classical wave equation is solved with the constraint that a bound electron cannot radiate energy. By further application of Maxwell's equations to electromagnetic and gravitational fields at particle production, the Schwarzschild metric (SM) is derived from the classical wave equation which modifies general relativity to include conservation of spacetime in addition to momentum and matter/energy. The result gives a natural relationship between Maxwell's equations, special relativity, and general relativity. It gives gravitation from the atom to the cosmos. © 2001 Published by Elsevier Science Ltd on behalf of the International Association for Hydrogen Energy.

1. Introduction

A theory of classical quantum mechanics (CQM), derived from first principles, successfully applies physical laws on all scales [1]. The classical wave equation is solved with the constraint that a bound electron cannot radiate energy. The mathematical formulation for zero radiation based on Maxwell's equations follows from a derivation by Haus [2]. The function that describes the motion of the electron must not possess spacetime Fourier components that are synchronous with waves traveling at the speed of light. CQM gives closed form solutions for the atom including the stability of the $n = 1$ state and the instability of the excited states, the equation of the photon and electron in excited states, the equation of the free electron and photon which predict the wave particle duality behavior of particles and light. The current and charge-density functions of the electron may be directly physically interpreted. For example, spin angular momentum results from the motion of negatively charged mass moving systematically, and the equation for angular momentum, $r \times p$, can be applied directly to the wave function (a current density function) that describes the electron. The magnetic moment of a Bohr magneton, Stern

Gerlach experiment, g factor, Lamb shift, resonant line width and shape, selection rules, correspondence principle, wave particle duality, excited states, reduced mass, rotational energies, and momenta, orbital and spin splitting, spin-orbital coupling, Knight shift, and spin-nuclear coupling, ionization energies of two electron atoms, elastic electron scattering from helium atoms, and the nature of the chemical bond are derived in closed form equations based on Maxwell's equations. The calculations agree with experimental observations.

For any kind of wave advancing with limiting velocity and capable of transmitting signals, the equation of front propagation is the same as the equation for the front of a light wave. By applying this condition to electromagnetic and gravitational fields at particle production, the Schwarzschild metric (SM) is derived from the classical wave equation which modifies general relativity to include conservation of spacetime in addition to momentum and matter/energy. The result gives a natural relationship between Maxwell's equations, special relativity, and general relativity. It gives gravitation from the atom to the cosmos. The universe is time harmonically oscillatory in matter energy and spacetime expansion and contraction with a minimum radius that is the gravitational radius. In closed form equations with fundamental constants only, CQM gives the deflection of light by stars, the precession of the perihelion of Mercury, the particle masses, the Hubble constant, the age of the universe, the observed acceleration of the expansion, the power of the

* Corresponding author. Tel.: +1-609-490-1090; fax: +1-609-490-1066.

E-mail address: rmills@blacklightpower.com (R.L. Mills).

[1] URL: www.blacklightpower.com

1   universe, the power spectrum of the universe, the microwave
    background temperature, the uniformity of the microwave
3   background radiation at 2.7 K with the microkelvin spa-
    tial variation observed by the DASI, the observed violation
5   of the GZK cutoff, the mass density, the large-scale struc-
    ture of the universe, and the identity of dark matter which
7   matches the criteria for the structure of galaxies. In a special
    case wherein the gravitational potential energy density of a
9   blackhole equals that of the Plank mass, matter converts to
    energy and spacetime expands with the release of a gamma
11 ray burst. The singularity in the SM is eliminated.

2. Classical quantum theory of the atom based on Maxwell's equations

One-electron atoms include the hydrogen atom, He$^+$,
15 Li^{2+}, Be^{3+}, and so on. The mass–energy and angular
    momentum of the electron are constant; this requires that
17 the equation of motion of the electron be temporally and
    spatially harmonic. Thus, the classical wave equation
19 applies and

$$\left[\nabla^2 - \frac{1}{v^2}\frac{\partial^2}{\partial t^2}\right]\rho(r,\theta,\phi,t) = 0, \qquad (1)$$

where $\rho(r,\theta,\phi,t)$ is the time-dependent charge-density
21 function of the electron in time and space. In general, the
    wave equation has an infinite number of solutions. To ar-
23 rive at the solution which represents the electron, a suitable
    boundary condition must be imposed. It is well known from
25 experiments that each single atomic electron of a given
    isotope radiates to the same stable state. Thus, the physical
27 boundary condition of nonradiation of the bound electron
    was imposed on the solution of the wave equation for the
29 time-dependent charge-density function of the electron.
    The condition for radiation by a moving point charge is given
31 by Haus [2] is that its spacetime Fourier transform does
    possess components that are synchronous with waves trav-
33 eling at the speed of light. Conversely, it is proposed that
    the condition for nonradiation of an ensemble of moving
35 point charges that comprises a current-density function is

For nonradiative states, the current-density function
37 *must NOT possess spacetime Fourier components that*
    are synchronous with waves traveling at the speed of
39 *light.*

The time, radial, and angular solutions of the wave equa-
41 tion are separable. The motion is time harmonic with fre-
    quency ω_n. A constant angular function is a solution to the
43 wave equation. The solution for the radial function which
    satisfies the boundary condition is a radial delta function

$$f(r) = \frac{1}{r^2}\delta(r - r_n) \qquad (2)$$

The orbitsphere has zero thickness.
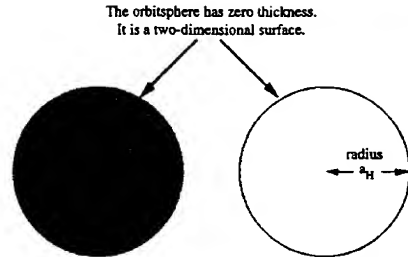It is a two-dimensional surface.

Fig. 1. The orbitsphere is a two-dimensional spherical shell with the Bohr radius of the hydrogen atom.

which defines a constant charge function of a spherical shell
where $r_n = nr_1$. Given time harmonic motion and a radial
47 delta function, the relationship between an allowed radius
    and the electron wavelength is given by
49

$$2\pi r_n = \lambda_n. \qquad (3)$$

Using the de Broglie relationship for the electron mass where
the coordinates are spherical,
51

$$\lambda_n = \frac{h}{p_n} = \frac{\hbar}{m_e v_n} \qquad (4)$$

and the magnitude of the velocity for *every* point on the
orbitsphere is
53

$$v_n = \frac{\hbar}{m_e r_n}. \qquad (5)$$

The sum of the L_i, the magnitude of the angular momentum
of each infinitesimal point of the orbitsphere of mass m_i,
55 must be constant. The constant is $\hbar$.

$$\sum |L_i| = \sum |r \times m_i v| = m_e r_n \frac{\hbar}{m_e r_n} = \hbar. \qquad (6)$$

Thus, an electron is a spinning, two-dimensional spherical
57 surface, called an *electron orbitsphere*, that can exist in a
    bound state at only specified distances from the nucleus as
59 shown in Fig. 1. The corresponding current function shown
    in Fig. 2 which gives rise to the phenomenon of *spin* is
61 derived in the "Spin Function" section.
    Nonconstant functions are also solutions for the angu-
63 lar functions. To be a harmonic solution of the wave equa-
    tion in spherical coordinates, these angular functions must
65 be spherical harmonic functions. A zero of the spacetime
    Fourier transform of the product function of two spherical
67 harmonic angular functions, a time harmonic function, and
    an unknown radial function is sought. The solution for the
69 radial function which satisfies the boundary condition is also
    a delta function given by Eq. (2). Thus, bound electrons
71 are described by a charge-density (mass-density) function
    which is the product of a radial delta function, two angular
73
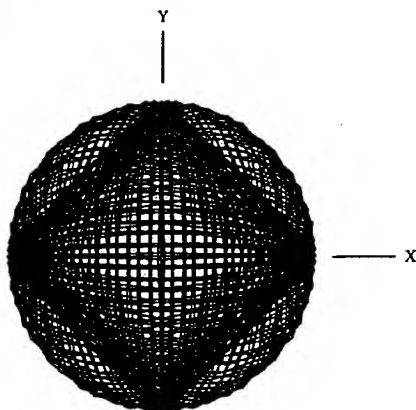
VIEW ALONG THE Z AXIS

Fig. 2. The current pattern of the orbitsphere from the perspective of looking along the z-axis. The current and charge density are confined to two dimensions at $r_n = nr_1$. The corresponding charge density function is uniform.

Fig. 3. The orbital function modulates the constant (spin) function shown for $\ell = 0$; cross-sectional view).

1 functions (spherical harmonic functions), and a time harmonic function.

$$\rho(r, \theta, \phi, t) = f(r)A(\theta, \phi, t) = \frac{1}{r^2}\delta(r - r_n)A(\theta, \phi, t),$$

$$A(\theta, \phi, t) = Y(\theta, \phi)k(t).$$

3 In these cases, the spherical harmonic function corresponds to a traveling charge-density wave confined to the spherical
5 shell which gives rise to the phenomenon of orbital angular momentum. The orbital functions which modulate the constant "spin" function shown graphically in Fig. 3 are given
7 in the "Angular Functions" section.

3. Spin function

The orbitsphere spin function comprises a constant
11 charge-density function with moving charge confined to a two-dimensional spherical shell. The current pattern of
13 the orbitsphere spin function comprises an infinite series of correlated orthogonal great circle current loops
15 wherein each point moves time harmonically with angular velocity
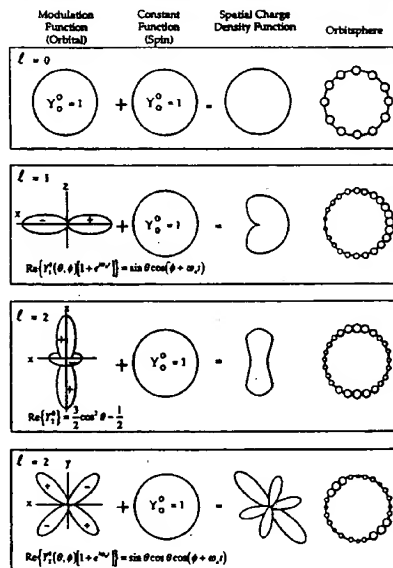
17 $$\omega_n = \frac{\hbar}{m_e r_n^2}.$$ (8)

The current pattern is generated over the surface by a 19
series of nested rotations of two orthogonal great circle
current loops where the coordinate axes rotate with the 21
two orthogonal great circles. Half of the pattern is generated as the z-axis rotates to the negative z-axis during 23
a 1st set of nested rotations. The mirror image, second half of the pattern is generated as the z-axis rotates 25
back to its original direction during a 2nd set of nested rotations.

3.1. Points on great circle current loop one 27

$$\begin{bmatrix} x_1 \\ y_1 \\ z_1 \end{bmatrix} =$$

$$\begin{bmatrix} \cos(\Delta\alpha) & -\sin^2(\Delta\alpha) & -\sin(\Delta\alpha)\cos(\Delta\alpha) \\ 0 & \cos(\Delta\alpha) & -\sin(\Delta\alpha) \\ \sin(\Delta\alpha) & \cos(\Delta\alpha)\sin(\Delta\alpha) & \cos^2(\Delta\alpha) \end{bmatrix} \begin{bmatrix} x_1' \\ y_1' \\ z_1' \end{bmatrix}$$ (9)

and $\Delta\alpha' = -\Delta\alpha$ replaces $\Delta\alpha$ for $\sum_{n=1}^{\sqrt{2}\pi/\Delta\alpha} \Delta\alpha = \sqrt{2}\pi$;
$\sum_{n=1}^{\sqrt{2}\pi/|\Delta\alpha'|} |\Delta\alpha'| = \sqrt{2}\pi.$ 29

3.2. Points on great circle current loop two

$$
\begin{bmatrix} x_2 \\ y_2 \\ z_2 \end{bmatrix} =
$$

$$
\begin{bmatrix} \cos(\Delta\alpha) & -\sin^2(\Delta\alpha) & -\sin(\Delta\alpha)\cos(\Delta\alpha) \\ 0 & \cos(\Delta\alpha) & -\sin(\Delta\alpha) \\ \sin(\Delta\alpha)\cos(\Delta\alpha)\sin(\Delta\alpha) & \cos^2(\Delta\alpha) \end{bmatrix} \begin{bmatrix} x_2' \\ y_2' \\ z_2' \end{bmatrix}
\tag{10}
$$

and $\Delta\alpha' = -\Delta\alpha$ replaces $\Delta\alpha$ for $\sum_{m=1}^{\sqrt{2}\pi/\Delta\alpha} \Delta\alpha = \sqrt{2}\pi$; $\sum_{m=1}^{\sqrt{2}\pi/|\Delta\alpha'|} |\Delta\alpha'| = \sqrt{2}\pi$.

The orbitsphere is given by reiterations of Eqs. (9) and (10). The output given by the nonprimed coordinates is the input of the next iteration corresponding to each successive nested rotation by the infinitesimal angle where the summation of the rotation about each of the x-axis and the y-axis is $\sum_{m=1}^{\sqrt{2}\pi/\Delta\alpha} \Delta\alpha = \sqrt{2}\pi$ (1st set) and $\sum_{m=1}^{\sqrt{2}\pi/|\Delta\alpha'|} |\Delta\alpha'| = \sqrt{2}\pi$ (2nd set). The current pattern corresponding to great circle current loop one and two shown with 8.49° increments of the infinitesimal angular variable $\Delta\alpha(\Delta\alpha')$ of Eqs. (9) and (10) is shown from the perspective of looking along the z-axis in Fig. 2. The true orbitsphere current pattern is given as $\Delta\alpha(\Delta\alpha')$ approaches zero. This current pattern gives rise to the phenomenon corresponding to the spin quantum number of the electron.

4. Magnetic field equations of the electron

The orbitsphere is a shell of negative charge current comprising correlated charge motion along great circles. For $\ell = 0$, the orbitsphere gives rise to a magnetic moment of 1 Bohr magneton [3].

$$
\mu_B = \frac{e\hbar}{2m_e} = 9.274 \times 10^{-24} \ JT^{-1}.
$$

The magnetic field of the electron shown in Fig. 4 is given by

$$
H = \frac{e\hbar}{m_e r_n^3}(i_r \cos\theta - i_\theta \sin\theta) \quad \text{for } r < r_n
\tag{12}
$$

$$
H = \frac{e\hbar}{2m_e r^3}(i_r 2\cos\theta - i_\theta \sin\theta) \quad \text{for } r > r_n.
\tag{13}
$$

The energy stored in the magnetic field of the electron is

$$
E_{mag} = \frac{1}{2}\mu_0 \int_0^{2\pi} \cdots r^2 \sin\theta \, dr \, d\theta \, d\Phi,
\tag{14}
$$

$$
E_{mag\ total} = \frac{\pi\mu_0 e^2\hbar^2}{m_e^2 r^3}
\tag{15}
$$

5. Stern–Gerlach experiment

The Stern–Gerlach experiment implies a magnetic moment of one Bohr magneton and an associated angular

The magnetic field is constant inside of the orbitsphere.
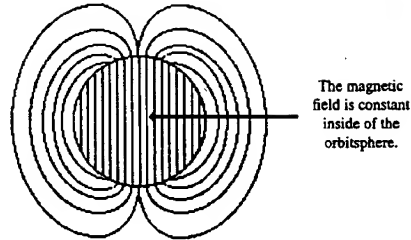
Fig. 4. The magnetic field of an electron orbitsphere.

momentum quantum number of $1/2$. Historically, this quantum number is called the spin quantum number, s $(s = \frac{1}{2}; m_s = \pm\frac{1}{2})$. The superposition of the vector projection of the orbitsphere angular momentum on to an axis S that precesses about the z-axis called the spin axis at an angle of $\theta = \pi/3$ and an angle of $\frac{2}{3}\pi$ with respect to $\langle L_{xy}\rangle_{\sum\Delta\alpha}$ is

$$
S = \pm\sqrt{\frac{3}{4}}\hbar.
\tag{16}
$$

S rotates about the z-axis at the Larmor frequency. $\langle S_z\rangle$, the time averaged projection of the orbitsphere angular momentum onto the axis of the applied magnetic field is

$$
\langle L_z\rangle = \pm\frac{\hbar}{2}
\tag{17}
$$

Electron g factor

Conservation of angular momentum of the orbitsphere permits a discrete change of its kinetic angular momentum $(r \times mv)$ by the applied magnetic field of $\hbar/2$, and concomitantly the potential angular momentum $(r \times eA)$ must change by $-\hbar/2$.

$$
\Delta L = \frac{\hbar}{2} - r \times eA
\tag{18}
$$

$$
= \left[\frac{\hbar}{2} - \frac{e\phi}{2\pi}\right]\hat{z}.
\tag{19}
$$

In order that the change of angular momentum, ΔL, equals zero, ϕ must be $\Phi_0 = h/2e$, the magnetic flux quantum. The magnetic moment of the electron is parallel or antiparallel to the applied field only. During the spin-flip transition, power must be conserved. Power flow is governed by the Poynting power theorem,

$$
\nabla \cdot (E \times H) = -\frac{\partial}{\partial t}\left[\frac{1}{2}\mu_0 H \cdot H\right]
$$

$$
-\frac{\partial}{\partial t}\left[\frac{1}{2}\varepsilon_0 E \cdot E\right] - J \cdot E
\tag{20}
$$

Eq. (21) gives the total energy of the flip transition which is the sum of the energy of reorientation of the magnetic moment (1st term), the magnetic energy (2nd term), the electric energy (3rd term), and the dissipated energy of a fluxon treading the orbitsphere (4th term), respectively,

$$\Delta E_{mag}^{spin} = 2\left(1 + \frac{\alpha}{2\pi} + \frac{2}{3}\alpha^2\left(\frac{\alpha}{2\pi}\right) - \frac{4}{3}\left(\frac{\alpha}{2\pi}\right)^2\right)\mu_B B, \quad (21)$$

$$\Delta E_{mag}^{spin} = g\mu_B B, \quad (22)$$

where the stored magnetic energy corresponding to the $\partial/\partial t[\frac{1}{2}\mu_0 H \bullet H]$ term increases, the stored electric energy corresponding to the $\partial/\partial t[\frac{1}{2}\varepsilon_0 E \bullet E]$ term increases, and the $J \bullet E$ term is dissipative. The spin-flip transition can be considered as involving a magnetic moment of g times that of a Bohr magneton. The g factor is redesignated the fluxon g factor as opposed to the anomalous g factor. The calculated value of $g/2$ is 1.001159652137. The experimental value [4] of $g/2$ is 1.001159652188(4).

7. Angular functions

The time, radial, and angular solutions of the wave equation are separable. Also based on the radial solution, the angular charge and current-density functions of the electron, $A(\theta, \phi, t)$, must be a solution of the wave equation in two dimensions (plus time),

$$\left[\nabla^2 - \frac{1}{v^2}\frac{\partial^2}{\partial t^2}\right]A(\theta, \phi, t) = 0, \quad (23)$$

where $\rho(r, \theta, \phi, t) = f(r)A(\theta, \phi, t) = (1/r^2)\delta(r - r_n)A(\theta, \phi, t)$ and $A(\theta, \phi, t) = Y(\theta, \phi)k(t)$

$$\left[\frac{1}{r^2\sin\theta}\frac{\partial}{\partial\theta}\left(\sin\theta\frac{\partial}{\partial\theta}\right)_{r,\phi} + \frac{1}{r^2\sin^2\theta}\left(\frac{\partial^2}{\partial\phi^2}\right)_{r,\theta}\right.$$

$$\left. - \frac{1}{v^2}\frac{\partial^2}{\partial t^2}\right]A(\theta, \phi, t) = 0, \quad (24)$$

where v is the linear velocity of the electron. The charge-density functions including the time function factor are

$\ell = 0,$

$$\rho(r, \theta, \phi, t) = \frac{e}{8\pi r_n^2}[\delta(r - r_n)][Y_0^0(\theta, \phi) + Y_0^0(\theta, \phi)]. \quad (25)$$

$\ell > 0,$

$$\rho(r, \theta, \phi, t) = \frac{e}{4\pi r_n^2}[\delta(r - r_n)][Y_0^0(\theta, \phi)$$

$$+ Re\{Y_\ell^m(\theta, \phi)[1 + e^{i\omega_n t}]\}], \quad (26)$$

$$Re\{Y_\ell^m(\theta, \phi)[1 + e^{i\omega_n t}]\} = Re\{Y_\ell^m(\theta, \phi) + Y_\ell^m(\theta, \phi)e^{i\omega_n t}\}$$
$$= P_\ell^m(\cos\theta)\cos m\phi + P_\ell^m(\cos\theta)\cos(m\phi + \omega_n t) \text{ and } \omega_n = 0$$
for $m = 0.$

8. Spin and orbital parameters

The total function that describes the spinning motion of each electron orbitsphere is composed of two functions. One function, the spin function, is spatially uniform over the orbitsphere, spins with a quantized angular velocity, and gives rise to spin angular momentum. The other function, the modulation function, can be spatially uniform in which case there is no orbital angular momentum and the magnetic moment of the electron orbitsphere is one Bohr magneton or not spatially uniform in which case there is orbital angular momentum. The modulation function also rotates with a quantized angular velocity.

The spin function of the electron corresponds to the nonradiative $n = 1$, $\ell = 0$ state of atomic hydrogen which is well known as an *s* state or orbital. (See Fig. 1 for the charge function and Fig. 2 for the current function.) For orbitals with the ℓ quantum number not equal to zero, the constant spin function is modulated by a time and spherical harmonic function as given by Eq. (26) and shown in Fig. 3. The modulation or traveling charge-density wave corresponds to an orbital angular momentum in addition to a spin angular momentum. These states are typically referred to as p, d, f, etc. orbitals. Application of Haus's [2] condition also predicts nonradiation for a constant spin function modulated by a time and spherically harmonic orbital function. There is acceleration without radiation. (Also see Abbott and Griffiths and Goedecke [5, 6].) However, in the case that such a state arises as an excited state by photon absorption, it is radiative due to a radial dipole term in its current-density function since it possesses spacetime Fourier Transform components synchronous with waves traveling at the speed of light [2]. (See Instability of Excited States" section.)

8.1. Moment of inertia and spin and rotational energies

$\ell = 0,$

$$I_z = I_{spin} = \frac{m_e r_n^2}{2}, \quad (27)$$

$$L_z = I\omega I_z = \pm\frac{\hbar}{2}, \quad (28)$$

$$E_{rotational} = E_{rotational, spin} = \frac{1}{2}\left[I_{spin}\left(\frac{\hbar}{m_e r_n^2}\right)^2\right]$$

$$= \frac{1}{2}\left[\frac{m_e r_n^2}{2}\left(\frac{\hbar}{m_e r_n^2}\right)^2\right] = \frac{1}{4}\left[\frac{\hbar^2}{2I_{spin}}\right]. \quad (29)$$

$\ell > 0,$

$$I_{orbital} = m_e r_n^2\left[\frac{\ell(\ell + 1)}{\ell^2 + \ell + 1}\right]^{1/2}, \quad (30)$$

$$L_z = m\hbar, \quad (31)$$

$$L_{z\,total} = L_{z\,spin} + L_{z\,orbital}, \quad (32)$$

$$E_{\text{rotational, orbital}} = \frac{\hbar^2}{2I}\left[\frac{\ell(\ell+1)}{\ell^2+2\ell+1}\right], \tag{33}$$

$$T = \frac{\hbar^2}{2m_e r_n^2}, \tag{34}$$

$$\langle E_{\text{rotational, orbital}} \rangle = 0. \tag{35}$$

From Eq. (35), the time average rotational energy is zero; thus, the principal levels are degenerate except when a magnetic field is applied.

9. Nonradiation condition (acceleration without radiation)

The Fourier transform of the electron charge-density function is a solution of the four-dimensional wave equation in frequency space (k, ω space). Then the corresponding Fourier transform of the current-density function $K(s, \Theta, \Phi, \omega)$ is given by multiplying by the constant angular frequency.

$$K(s, \Theta, \Phi, \omega) = 4\pi\omega_n \frac{\sin(2s_n r_n)}{2s_n r_n} \otimes 2\pi\sum_{v=1}^{\infty}$$

$$\times \frac{(-1)^{v-1}(\pi\sin\Theta)^{2(v-1)}}{(v-1)!(v-1)!}\frac{\Gamma(\frac{1}{2})\Gamma(v+\frac{1}{2})}{(\pi\cos\Theta)^{2v+1}2^{v+1}}\frac{2v!}{(v-1)!}s^{-2v}, \tag{36}$$

$$\otimes 2\pi\sum_{v=1}^{\infty}\frac{(-1)^{v-1}(\pi\sin\Phi)^{2(v-1)}}{(v-1)!(v-1)!}\frac{\Gamma(\frac{1}{2})\Gamma(v+\frac{1}{2})}{(\pi\cos\Phi)^{2v+1}2^{v+1}}$$

$$\times \frac{2v!}{(v-1)!}s^{-2v}\frac{1}{4\pi}[\delta(\omega-\omega_n)+\delta(\omega+\omega_n)],$$

$s_n \bullet v_n = s_n \bullet c = \omega_n$ implies $r_n = \lambda_n$. Spacetime harmonics of $\omega_n/c = k$ or $\omega_n/c\sqrt{\varepsilon/\varepsilon_0} = k$ for which the Fourier transform of the current-density function is nonzero do exist. Radiation due to charge motion does not occur in any medium when this boundary condition is met. The nonradiation is also determined from the fields based on Maxwell's equations [1].)

10. Force balance equation

The radius of the nonradiative ($n=1$) state is solved using the electromagnetic force equations of Maxwell relating the charge and mass-density functions wherein the angular momentum of the electron is given by Planck's constant bar. The reduced mass arises naturally from an electrodynamic interaction between the electron and the proton.

$$\frac{m_e}{4\pi r_1^2}\frac{v_1^2}{r_1} = \frac{e}{4\pi r_1^2}\frac{Ze}{4\pi\varepsilon_0 r_1^2} - \frac{1}{4\pi r_1^2}\frac{\hbar^2}{mr_n^2}, \tag{37}$$

$$r_1 = \frac{a_H}{Z}. \tag{38}$$

11. Energy calculations

From Maxwell's equations, the potential energy V, kinetic energy T, electric energy or binding energy E_{ele} are

$$V = \frac{-Ze^2}{4\pi\varepsilon_0 r_1} = \frac{-Z^2 e^2}{4\pi\varepsilon_0 a_H} = -Z^2 \times 4.3675 \times 10^{-18}\,\text{J}$$

$$= -Z^2 \times 27.2\,\text{eV}, \tag{39}$$

$$T = \frac{Z^2 e^2}{8\pi\varepsilon_0 a_H} = Z^2 \times 13.59\,\text{eV}, \tag{40}$$

$$T = E_{\text{ele}} = -\frac{1}{2}\varepsilon_0 \int_{\infty}^{r_1}\mathbf{E}^2\,dv \quad\text{where}\quad \mathbf{E} = -\frac{Ze}{4\pi\varepsilon_0 r^2}, \tag{41}$$

$$E_{\text{ele}} = -\frac{Z^2 e^2}{8\pi\varepsilon_0 a_H} = -Z^2 \times 2.1786 \times 10^{-18}\,\text{J}$$

$$= -Z^2 \times 13.598\,\text{eV}. \tag{42}$$

The calculated Rydberg constant is 109,677.58 cm^{-1}; the experimental Rydberg constant is 109,677.58 cm^{-1}.

12. Excited states

CQM gives closed form solutions for the resonant photons and excited state electron functions. The angular momentum of the photon given by

$$m = \frac{1}{\mu_0 c^2}Re[r \times (E \times B^*)] = \hbar \tag{43}$$

is constant [7, pp. 739–779]. The change in angular velocity of the electron is equal to the angular frequency of the resonant photon. The energy is given by Planck's equation. The predicted energies, Lamb shift, hyperfine structure, resonant line shape, line width, selection rules, etc. are in agreement with observation.

The orbitsphere is a dynamic spherical resonator cavity which traps photons of discrete frequencies. The relationship between an allowed radius and the photon standing wave wavelength is

$$2\pi r = n\lambda, \tag{44}$$

where n is an integer. The relationship between an allowed radius and the electron wavelength is

$$2\pi(nr_1) = 2\pi r_n = n\lambda_1 = \lambda_n, \tag{45}$$

where $n = 1, 2, 3, 4, \ldots$. The radius of an orbitsphere increases with the absorption of electromagnetic energy. The radii of excited states are solved using the electromagnetic force equations of Maxwell relating the field from the charge of the proton, the electric field of the photon, and charge- and mass-density functions of the electron wherein the angular momentum of the electron is given by Planck's constant bar (Eq. (37)). The solutions to Maxwell's equations for modes that can be excited in the orbitsphere resonator cavity give rise to four quantum numbers, and the energies of the modes are the experimentally known

7

hydrogen spectrum. The relationship between the electric field equation and the trapped photon source charge-density function is given by Maxwell's equation in two dimensions.

$$\mathbf{n} \bullet (\mathbf{E}_1 - \mathbf{E}_2) = \frac{\sigma}{\varepsilon_0}. \qquad (46)$$

The photon standing electromagnetic wave is phase matched with the electron

$$\mathbf{E}_{r\,\text{photon}\,n,\ell,m} = \frac{e(na_H)^\ell}{4\pi\varepsilon_0}\frac{1}{r^{(\ell+2)}}\left[-Y_0^0(\theta,\phi)+\frac{1}{n}[Y_0^0(\theta,\phi)\right.$$
$$\left. +Re\{Y_\ell^m(\theta,\phi)[1+e^{i\omega_n t}]\}\right]\delta(r-r_n), \quad (47)$$

$$\omega_n = 0 \quad for \ m=0,$$

$$\ell = 1, 2, \ldots, n-1,$$

$$m = -\ell, -\ell+1, \ldots, 0, \ldots, +\ell,$$

$$\mathbf{E}_{r\,\text{total}} = \frac{e}{4\pi\varepsilon_0 r^2}+\frac{e(na_H)^\ell}{4\pi\varepsilon_0}\frac{1}{r^{(\ell+2)}}\left[-Y_0^0(\theta,\phi)+\frac{1}{n}[Y_0^0(\theta,\phi)\right.$$
$$\left. +Re\{Y_\ell^m(\theta,\phi)[1+e^{i\omega_n t}]\}\right]\delta(r-r_n), \quad (48)$$

$$\omega_n = 0 \quad \text{for } m=0.$$

For $r = na_H$ and $m = 0$, the total radial electric field is

$$\mathbf{E}_{r\,\text{total}} = \frac{1}{n}\frac{e}{4\pi\varepsilon_0(na_H)^2}. \qquad (49)$$

The energy of the photon which excites a mode in the electron spherical resonator cavity from radius a_H to radius na_H is

$$E_{\text{photon}} = \frac{e^2}{8\pi\varepsilon_0 a_H}\left[1-\frac{1}{n^2}\right] = h\nu = \hbar\omega. \qquad (50)$$

The change in angular velocity of the orbitsphere for excitation from $n=1$ to n is

$$\Delta\omega = \frac{\hbar}{m_e(a_H)^2}-\frac{\hbar}{m_e(na_H)^2} = \frac{\hbar}{m_e(a_H)^2} \qquad (51)$$

The kinetic energy change of the transition is

$$\frac{1}{2}m_e(\Delta v)^2 = \frac{e^2}{8\pi\varepsilon_0 a_H}\left[1-\frac{1}{n^2}\right] \qquad (52)$$

The change in angular velocity of the electron orbitsphere is identical to the angular velocity of the photon necessary for the excitation. Thus the correspondence principle holds. It can be demonstrated that the resonance condition between these frequencies is to be satisfied in order to have a net change of the energy field [8].

13. Orbital and spin splitting

The ratio of the square of the angular momentum, M^2, to the square of the energy, U^2, for a pure (ℓ, m) multipole is

[7, pp. 739–752]

$$\frac{M^2}{U^2} = \frac{m^2}{\omega^2}. \qquad (53)$$

The magnetic moment is defined as

$$\mu = \frac{\text{charge} \times \text{angular momentum}}{2 \times \text{mass}}. \qquad (54)$$

The radiation of a multipole of order (ℓ, m) carries $m\hbar$ units of the z component of angular momentum per photon of energy $\hbar\omega$. Thus, the z component of the angular momentum of the corresponding excited state electron orbitsphere is

$$L_z = m\hbar. \qquad (55)$$

Therefore,

$$\mu_z = \frac{em\hbar}{2m_e} = m\mu_B, \qquad (56)$$

where μ_B is the Bohr magneton. The orbital splitting energy is

$$E_{\text{mag}}^{\text{orb}} = m\mu_B B. \qquad (57)$$

The spin and orbital splitting energies superimpose; thus, the principal excited state energy levels of the hydrogen atom are split by the energy $E_{\text{mag}}^{\text{spin/orb}}$.

$$E_{\text{mag}}^{\text{spin/orb}} = m\frac{e\hbar}{2m_e}B + m_s g\frac{e\hbar}{m_e}B \quad \text{where} \qquad (58)$$

$$n = 2, 3, 4,$$

$$\ell = 1, 2, \ldots, n-1,$$

$$m = -\ell, -\ell+1, \ldots, 0, \ldots, +\ell,$$

$$m_s = \pm\frac{1}{2}.$$

For the electric dipole transition, the selection rules are

$$\Delta m = 0, \pm 1, \qquad (59)$$

$$\Delta m_s = 0.$$

14. Resonant line shape and lamb shift

The spectroscopic linewidth shown in Fig. 5 arises from the classical rise-time band-width relationship, and the Lamb shift is due to conservation of energy and linear momentum and arises from the radiation reaction force between the electron and the photon. It follows from the Poynting power theorem with spherical radiation that the transition probabilities are given by the ratio of power and the energy of the transition [7, pp. 758–763]. The transition probability in the
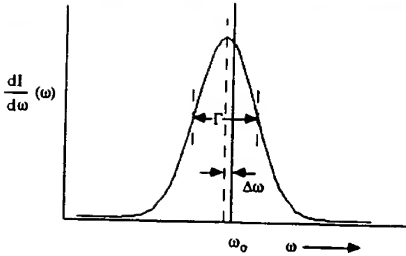
Fig. 5. Broadening of the spectral line due to the rise-time and shifting of the spectral line due to the radiative reaction. The resonant line shape has width Γ. The level shift is $\Delta\omega$.

case of the electric multipole moment is

$$\frac{1}{\tau} = \frac{power}{energy},\tag{60}$$

$$\frac{1}{\tau} = \frac{\left[\frac{2\pi c}{[(2l+1)!!]^2}\left(\frac{l+1}{l}\right)k^{2l+1}|Q_{lm}+Q'_{lm}|^2\right]}{[\hbar\omega]}$$

$$= 2\pi\left(\frac{e^2}{h}\right)\sqrt{\frac{\mu_0}{\varepsilon_0}}\frac{2\pi}{[(2l+1)!!]^2}\left(\frac{l+1}{l}\right)$$

$$\times\left(\frac{3}{l+3}\right)^2(kr_n)^{2l}\omega,\tag{61}$$

$$E(\omega)\propto\int_0^\infty e^{-\alpha t}e^{-i\omega t}\,dt = \frac{1}{\alpha-i\omega}.\tag{62}$$

The relationship between the rise-time and the band width for exponential decay is

$$\tau\Gamma = \frac{1}{\pi}.\tag{63}$$

The energy radiated per unit frequency interval is

$$\frac{dI(\omega)}{d\omega} = I_0\frac{\Gamma}{2\pi}\frac{1}{(\omega-\omega_0-\Delta\omega)^2+(\Gamma/2)^2}.\tag{64}$$

15. Lamb shift

The Lamb shift of the $^2P_{1/2}$ state of the hydrogen atom is due to conservation of linear momentum of the electron, atom, and photon. The electron component is

$$\Delta f = \frac{\Delta\omega}{2\pi} = \frac{E_{h\nu}}{h} = 3\frac{(E_{h\nu})^2}{h2m_ec^2} = 1052\ MHz,\tag{65}$$

where $E_{h\nu}$ is

$$E_{h\nu} = 13.6\left(1-\frac{1}{n^2}\right)\frac{1}{|X_{lm}|^2_{\ell=1}} - h\Delta f,\tag{66}$$

$$E_{h\nu} = 13.6\left(1-\frac{1}{n^2}\right)\frac{3}{8\pi} - h\Delta f,\tag{67}$$

$$h\Delta f <<<1.\tag{68}$$

Therefore,

$$E_{h\nu} = 13.6\left(1-\frac{1}{n^2}\right)\frac{3}{8\pi}.\tag{69}$$

The atom component is

$$\Delta f = \frac{\Delta\omega}{2\pi} = \frac{E_{h\nu}}{h} = \frac{1}{2}\frac{(E_{h\nu})^2}{2m_Hc^2} = 6.5\ MHz,\tag{70}$$

The sum of the components is

$$\Delta f = 1052\ MHz + 6.5\ MHz = 1058.5\ MHz.\tag{71}$$

The experimental Lamb shift is 1058 MHz.

16. Instability of excited states

For the excited energy states of the hydrogen atom, σ_{photon}, the two-dimensional surface charge due to the trapped photons and the electron orbitsphere, given by Eqs. (46) and (47) is

$$\sigma_{photon} = \frac{e}{4\pi(r_n)^2}\left[Y_0^0(\theta,\phi) - \frac{1}{n}[Y_0^0(\theta,\phi)\right.$$
$$\left. + Re\{Y_\ell^m(\theta,\phi)[1+e^{i\omega_nt}]\}]\right]\delta(r-r_n),\tag{72}$$

where $n = 2,3,4,\ldots,$. Whereas, $\sigma_{electron}$, the two-dimensional surface charge of the electron orbitsphere given by Eq. (26) is

$$\sigma_{electron} = \frac{-e}{4\pi(r_n)^2}[Y_0^0(\theta,\phi)$$
$$+ Re\{Y_\ell^m(\theta,\phi)[1+e^{i\omega_nt}]\}]\delta(r-r_n).\tag{73}$$

The superposition of σ_{photon} (Eq. (72)) and $\sigma_{electron}$ is equivalent to the sum of a radial electric dipole represented by a doublet function and a radial electric monopole represented by a delta function.

$$\sigma_{photon} + \sigma_{electron}$$

$$= \frac{e}{4\pi(r_n)^2}\left[Y_0^0(\theta,\phi)\overset{\bullet}{\delta}(r-r_n) - \frac{1}{n}Y_0^0(\theta,\phi)\delta(r-r_n)\right.$$

$$\left. - \left(1+\frac{1}{n}\right)[Re\{Y_\ell^m(\theta,\phi)[1+e^{i\omega_nt}]\}]\delta(r-r_n)\right],\tag{74}$$

where $n = 2, 3, 4, \ldots,$. Due to the radial doublet, excited states are radiative since spacetime harmonics of $\omega_n/c = k$ or $(\omega_n/c)\sqrt{\varepsilon/\varepsilon_0} = k$ do exist for which the spacetime Fourier transform of the current-density function is nonzero.

17. Photon equations

The time-averaged angular-momentum density, $\mathbf{m}$, of an emitted photon is

$$\mathbf{m} = \frac{1}{8\pi} Re[\mathbf{r} \times (\mathbf{E} \times \mathbf{B}^*)] = \hbar. \tag{75}$$

A linearly polarized photon orbitsphere is generated from two orthogonal great circle field lines shown in Fig. 6 rather than two great circle current loops as in the case of the electron spin function. The right-handed circularly polarized photon orbitsphere shown in Fig. 7 corresponds to the case wherein the summation of the rotation about each of the x-axis and the y-axis is $\sum_{m=1}^{\sqrt{2}\pi/\Delta\alpha} \Delta\alpha = \sqrt{2}\pi$, and the mirror image left-handed circularly polarized photon orbitsphere corresponds to the case wherein the summation of the rotation about each of the x-axis and the y-axis is $\sum_{m=1}^{\sqrt{2}\pi/|\Delta\alpha'|} |\Delta\alpha'| = \sqrt{2}\pi$.

17.1. Nested set of great circle field lines generates the photon function

H Field

$$\begin{bmatrix} x_1 \\ y_1 \\ z_1 \end{bmatrix} =$$

$$\begin{bmatrix} \cos(\Delta\alpha) & -\sin^2(\Delta\alpha) & -\sin(\Delta\alpha)\cos(\Delta\alpha) \\ 0 & \cos(\Delta\alpha) & -\sin(\Delta\alpha) \\ \sin(\Delta\alpha) & \cos(\Delta\alpha)\sin(\Delta\alpha) & \cos^2(\Delta\alpha) \end{bmatrix} \begin{bmatrix} x_1' \\ y_1' \\ z_1' \end{bmatrix} \tag{76}$$

and $\Delta\alpha' = -\Delta\alpha$ replaces $\Delta\alpha$ for $\sum_{m=1}^{\sqrt{2}\pi/\Delta\alpha} \Delta\alpha = \sqrt{2}\pi$; $\sum_{m=1}^{\sqrt{2}\pi/|\Delta\alpha'|} |\Delta\alpha'| = \sqrt{2}\pi$.

E Field

$$\begin{bmatrix} x_2 \\ y_2 \\ z_2 \end{bmatrix} =$$

$$\begin{bmatrix} \cos(\Delta\alpha) & -\sin^2(\Delta\alpha) & -\sin(\Delta\alpha)\cos(\Delta\alpha) \\ 0 & \cos(\Delta\alpha) & -\sin(\Delta\alpha) \\ \sin(\Delta\alpha) & \cos(\Delta\alpha)\sin(\Delta\alpha) & \cos^2(\Delta\alpha) \end{bmatrix} \begin{bmatrix} x_2' \\ y_2' \\ z_2' \end{bmatrix} \tag{77}$$

and $\Delta\alpha' = -\Delta\alpha$ replaces $\Delta\alpha$ for $\sum_{m=1}^{\sqrt{2}\pi/\Delta\alpha} \Delta\alpha = \sqrt{2}\pi$; $\sum_{m=1}^{\sqrt{2}\pi/|\Delta\alpha'|} |\Delta\alpha'| = \sqrt{2}\pi$.

The field lines in the lab frame follow from the relativistic invariance of charge as given by Purcell [9]. The relationship
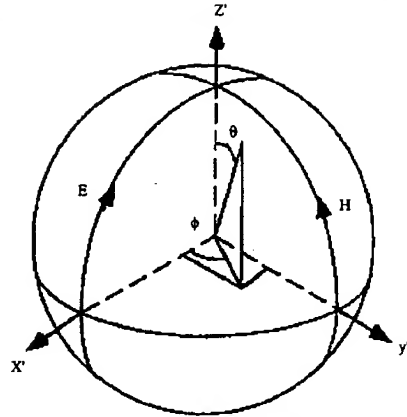
Fig. 6. The Cartesian coordinate system wherein the first great circle magnetic field line lies in the yz-plane, and the second great circle electric field lines lies in the xy-plane is designated the photon orbitsphere reference frame of a photon orbitsphere.
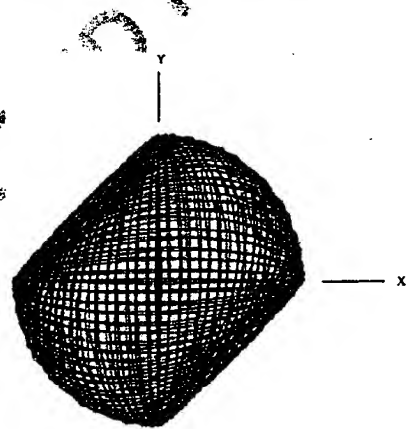
VIEW ALONG THE Z AXIS

Fig. 7. The field line pattern from the perspective of looking along the z-axis of a right-handed circularly polarized photon.

between the relativistic velocity and the electric field of a moving charge shown schematically in Fig. 8. From Eqs. (76)–(77) with $\sum_{m=1}^{\sqrt{2}\pi/\Delta\alpha} \Delta\alpha = \sqrt{2}\pi$, the photon equation in the lab frame of a right-handed circularly polarized
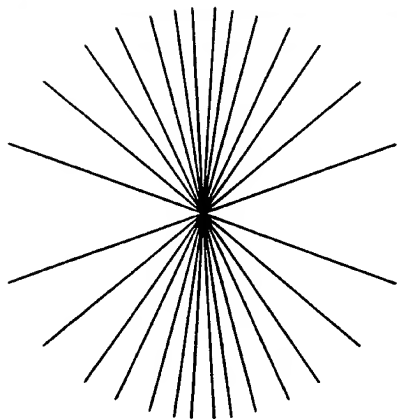
Fig. 8. The electric field of a moving point charge ($v = \frac{1}{3}c$).

$$2\pi r_n = \lambda_n$$
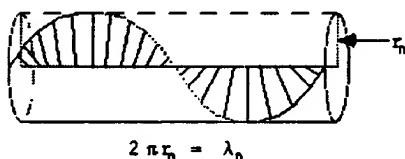
Fig. 9. The electric field lines of a right-handed circularly polarized photon orbitsphere as seen along the axis of propagation in the lab inertial reference frame as it passes a fixed point.

photon orbitsphere is

$$E = E_0[x + iy]e^{-jk_z z}e^{-j\omega t}, \tag{78}$$

$$H = \left(\frac{E_0}{\eta}\right)[y - ix]e^{-jk_z z}e^{-j\omega t} = E_0\sqrt{}[y - ix]e^{-jk_z z}e^{-j\omega t} \tag{79}$$

with a wavelength of

$$\lambda = 2\pi\frac{c}{\omega}. \tag{80}$$

The relationship between the photon orbitsphere radius and wavelength is

$$2\pi r_0 = \lambda_0. \tag{81}$$

The electric field lines of a right-handed circularly polarized photon orbitsphere as seen along the axis of propagation in the lab inertial reference frame as it passes a fixed point is shown in Fig. 9.

9   *17.2. Spherical wave*

Photons superimpose, and the amplitude due to N photons is

$$E_{total} = \sum_{n=1}^{N}\frac{e^{-ik_r|r-r'|}}{4\pi|r - r'|}f(\theta, \phi). \tag{82}$$

In the far field, the emitted wave is a spherical wave

$$E_{total} = E_0\frac{e^{-ikr}}{r}. \tag{83}$$

The Green Function is given as the solution of the wave equation. Thus, the superposition of photons gives the classical result. As r goes to infinity, the spherical wave becomes a plane wave. The double slit interference pattern is predicted. From the equation of a photon, the wave–particle duality arises naturally. The energy is always given by Planck's equation; yet, an interference pattern is observed when photons add over time or space.

18. Equations of the free electron

18.1. Charge-density function

The radius of the electron orbitsphere increases with the absorption of electromagnetic energy [10]. With the absorption of a photon of energy exactly equal to the ionization energy, the electron becomes ionized and is a plane wave (spherical wave in the limit) with the de Broglie wavelength. The ionized electron traveling at constant velocity is nonradiative and is a two-dimensional surface having a total charge of e and a total mass of m_e. The solution of the boundary value problem of the free electron is given by the projection of the orbitsphere into a plane that linearly propagates along an axis perpendicular to the plane where the velocity of the plane and the orbitsphere is given by

$$v = \frac{\hbar}{m_e\rho_0} \tag{84}$$

and the radius of the orbitsphere in spherical coordinates is equal to the radius of the free electron in cylindrical coordinates ($\rho_0 = r_0$). The mass-density function of a free electron shown in Fig. 10 is a two-dimensional disk having the mass-density distribution in the $xy(\rho)$-plane

$$\rho_m(\rho, \phi, z) = \frac{m_e}{\frac{2}{3}\pi\rho_0^2}\pi\left(\frac{\rho}{2\rho_0}\right)\sqrt{\rho_0^2 - \rho^2}\delta(z) \tag{85}$$

and charge-density distribution, $\rho_e(\rho, \phi, z)$, in the xy-plane given by replacing m_e with e. The charge-density distribution of the free electron has recently been confirmed experimentally [11,12]. Researchers working at the Japanese National Laboratory for High Energy Physics (KEK) demonstrated that the charge of the free electron increases toward the particle's core and is symmetrical as a function of ϕ. In addition, the wave–particle duality arises naturally,

Front View of Electron

$$\rho_0 = \frac{\hbar}{m v_z}$$

electron moving in this direction

Side View of Electron
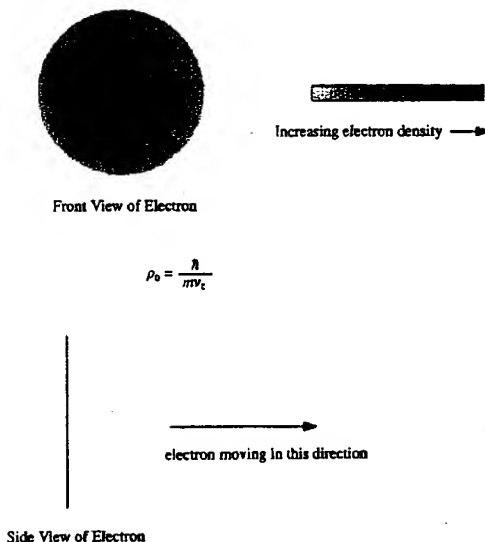
Fig. 10. The front view of the magnitude of the mass (charge) density function in the xy-plane of a free electron; side view of a free electron along the axis of propagation — z-axis.

and the result is consistent with scattering experiments from helium and the double split experiment [1].

18.2. Current-density function

Consider an electron initially bound as an orbitsphere of radius $r = r_n = r_0$ ionized from a hydrogen atom with the magnitude of the angular velocity of the orbitsphere is given by

$$\omega = \frac{\hbar}{m_e r^2}. \tag{86}$$

The current-density function of the free electron propagating with velocity v_z along the z-axis in the inertial frame of the proton is given by the vector projection of the current into xy-plane as the radius increases from $r = r_0$ to $r = \infty$. The current-density function of the free electron, is

$$J(\rho, \phi, z, t) = \left[\pi \left(\frac{\rho}{2\rho_0} \right) \frac{e}{\frac{4}{3}\pi\rho_0^3} \frac{\hbar}{m_e \sqrt{\rho_0^2 - \rho^2}} \mathbf{i}_\phi \right], \tag{87}$$

where $\rho_0 = r_0$. The angular momentum, L, is given by

$$\mathbf{L}\mathbf{i}_z = m_e r^2 \omega. \tag{88}$$

Substitution of m_e for e in Eq. (87) followed by substitution into Eq. (88) gives the angular momentum density function, L

$$\mathbf{L}\mathbf{i}_z = \pi \left(\frac{\rho}{2\rho_0} \right) \frac{m_e}{\frac{4}{3}\pi\rho_0^3} \frac{\hbar}{m_e \sqrt{\rho_0^2 - \rho^2}} \rho^2. \tag{89}$$

The total angular momentum of the free electron is given by integration over the two-dimensional disk having the angular momentum density given by Eq. (89).

$$\mathbf{L}\mathbf{i}_z = \int_0^{2\pi} \int_0^{\rho_0} \pi \left(\frac{\rho}{2\rho_0} \right) \frac{m_e}{\frac{4}{3}\pi\rho_0^3} \frac{\hbar}{m_e \sqrt{\rho_0^2 - \rho^2}} \rho^2 \, d\rho \, d\phi = \hbar. \tag{90}$$

The four-dimensional spacetime current-density function of the free electron that propagates along the z-axis with velocity given by Eq. (84) corresponding to $r = r_0 = \rho_0$ is given by substitution of Eq. (84) into Eq. (88).

$$J(\rho, \phi, z, t) = \left[\pi \left(\frac{\rho}{2\rho_0} \right) \frac{e}{\frac{4}{3}\pi\rho_0^3} \frac{\hbar}{m_e \sqrt{\rho_0^2 - \rho^2}} \mathbf{i}_\phi \right]$$
$$+ \frac{e\hbar}{m_e \rho_0} \delta \left(z - \frac{\hbar}{m_e \rho_0} t \right) \mathbf{i}_z. \tag{91}$$

Table 1
The calculated electric (per electron), magnetic (per electron), and ionization energies for some two-electron atoms

Atom	r_1 $(a_0)^a$	Electric energy[b] (eV)	Magnetic energy[c] (eV)	Calculated ionization energy[d] (eV)	Experimental ionization [12,13] energy (eV)
He	0.567	−23.96	0.63	24.59	24.59
Li$^+$	0.356	−76.41	2.54	75.56	75.64
Be^{2+}	0.261	−156.08	6.42	154.48	153.89
B^{3+}	0.207	−262.94	12.96	260.35	259.37
C^{++}	0.171	−396.98	22.83	393.18	392.08
N^{5+}	0.146	−558.20	36.74	552.95	552.06
O^{6+}	0.127	−746.59	55.35	739.67	739.32
F^{7+}	0.113	−962.17	79.37	953.35	953.89

[a]From Eq. (96).
[b]From Eq. (98).
[c]From Eq. (99).
[d]From Eqs. (97) and (100).

1   The spacetime Fourier Transform is

$$\frac{e}{\frac{4}{3}\pi\rho_0^3}\frac{\hbar}{m_e}\operatorname{sinc}(2\pi s\rho_0) + 2\pi e\frac{\hbar}{m_e\rho_0}\delta(\omega - \mathbf{k}_e \bullet \mathbf{v}_z). \quad (92)$$

Spacetime harmonics of $\omega_n/c = k$ or $(\omega_n/c)\sqrt{\varepsilon/\varepsilon_0} = k$ do
3   not exist. Radiation due to charge motion does not occur in
any medium when this boundary condition is met. Thus, no
5   Fourier components that are synchronous with light veloc-
ity with the propagation constant $|\mathbf{k}_e| = \omega/c$ exist. Radiation
7   due to charge motion does not occur when this boundary
condition is met. It follows from Eq. (84) and the relation-
9   ship $2\pi\rho_0 = \lambda_0$ that the wavelength of the free electron is
the de Broglie wavelength.

$$\lambda_0 = \frac{h}{m_e v_z} = 2\pi\rho_0. \quad (93)$$

11   In the presence of a z-axis applied magnetic field, the
free electron precesses. The time average vector projection
13   of the total angular momentum of the free electron onto
an axis S that rotates about the z-axis is $\frac{\sqrt{3}}{4}\hbar$, and the
15   time averaged projection of the angular momentum onto the
axis of the applied magnetic field is $\pm\hbar/2$. Magnetic flux is
17   linked by the electron in units of the magnetic flux quantum
with conservation of angular momentum as in the case of
19   the orbitsphere as the projection of the angular momentum
along the magnetic field axis of $\hbar/2$ reverses direction. The
21   energy, ΔE_{mag}^{spin} of the spin flip transition corresponding to
the $m_s = \frac{1}{2}$ quantum number is given by Eq. (22).

$$\Delta E_{mag}^{spin} = g\mu_B B. \quad (94)$$

23   The Stern–Gerlach experiment implies a magnetic moment
of one Bohr magneton and an associated angular momentum
25   quantum number of 1/2. Historically, this quantum number
is called the spin quantum number, m_s, and that designation
27   is maintained.

19. Two electron atoms

29   Two electron atoms may be solved from a central force
balance equation with the nonradiation condition. The force
31   balance equation is

$$\frac{m_e}{4\pi r_2^2}\frac{v_2^2}{r_2} = \frac{e_{sc}(Z-1)e}{4\pi r_2^2}\frac{e}{4\pi\varepsilon_0 r_2^2} + \frac{1}{4\pi r_2^2}\frac{\hbar^2}{Zm_e r_2^3}\sqrt{s(s+1)} \quad (95)$$

which gives the radius of both electrons as

$$r_1 = \left(\frac{1}{Z-1} - \frac{\sqrt{s(s+1)}}{Z(Z-1)}\right), \quad s = \frac{1}{2}. \quad (96)$$

19.1. Ionization energies calculated using the Poynting
33   power theorem

35   For helium, which has no electric field beyond r_1

ionization energy(He) $= -E(\text{electric}) + E(\text{magnetic})$.
$$\quad (97)$$

where,

$$E(\text{electric}) = -\frac{(Z-1)e^2}{8\pi\varepsilon_0 r_1}, \quad (98)$$

$$E(\text{magnetic}) = \frac{2\pi\mu_0 e^2\hbar^2}{m_e^2 r_1^3}. \quad (99)$$

For $3 \leqslant Z$ 37

ionization energy $= -$electric energy

$$-\frac{1}{Z}\text{magnetic energy.} \quad (100)$$

The energies of several two-electron atoms are given in
Table 1.   39

20. Elastic electron scattering from helium atoms

The aperture distribution function, $a(\rho, \phi, z)$, for the elastic scattering of an incident electron plane wave represented by $\pi(z)$ by a helium atom represented by

$$\frac{2}{4\pi(0.567a_0)^2}[\delta(r - 0.567a_0)] \tag{101}$$

is given by the convolution of the plane wave with the helium atom function:

$$a(\rho, \phi, z) = \pi(z) \otimes \frac{2}{4\pi(0.567a_0)^2}[\delta(r - 0.567a_0)]. \tag{102}$$

The aperture function is

$$a(\rho, \phi, z) = \frac{2}{4\pi(0.567a_0)^2}$$
$$\sqrt{(0.567a_0)^2 - z^2}\delta(r - \sqrt{(0.567a_0)^2 - z^2}). \tag{103}$$

20.1. Far field scattering (circular symmetry)

Applying Huygens' principle to a disturbance caused by the plane wave electron over the helium atom as an aperture gives the amplitude of the far field or Fraunhofer diffraction pattern $F(s)$ as the Fourier Transform of the aperture distribution. The intensity $I_1^{\rm ed}$ is the square of the amplitude.

$$F(s) = \frac{2}{4\pi(0.567a_0)^2} 2\pi \int_0^\infty \int_{-\infty}^\infty$$
$$\sqrt{(0.567a_0)^2 - z^2}\delta(\rho - \sqrt{(0.567a_0)^2 - z^2})$$
$$\times J_0(s\rho)e^{-i w \tau}\rho\, d\rho\, dz, \tag{104}$$

$$I_1^{\rm ed} = F(s)^2 =$$

$$I_e \left\{ \begin{array}{c} \left[\frac{2\pi}{(z_0 w)^2 + (z_0 s)^2}\right]^{1/2} \\ \left\{2\left[\frac{z_0 s}{(z_0 w)^2 + (z_0 s)^2}\right]J_{3/2}[((z_0 w)^2 \\ - \left[\frac{z_0 s}{(z_0 w)^2 + (z_0 s)^2}\right]^2 J_{5/2}((z_0 w)^2 + (z_0 s)^2)^{1/2}]\right\} \end{array} \right\}, \tag{105}$$

$$s = \frac{4\pi}{\lambda}\sin\frac{\theta}{2}, \quad w = 0 \text{ (units of Å}^{-1}\text{)}. \tag{106}$$

The experimental results of Bromberg [15], the extrapolated experimental data of Hughes [15], the small angle data of Geiger [16] and the semiexperimental results of Lassettre [15] for the elastic differential cross-section for the elastic scattering of electrons by helium atoms is shown graphically in Fig. 11. The elastic differential cross-section as a function of angle numerically calculated by Khare [15] using the first Born approximation and first-order exchange approximation also appear in Fig. 11. These results which are based on a
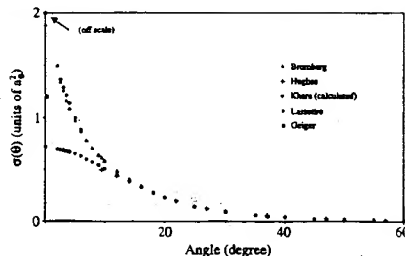
Fig. 11. The experimental results for the elastic differential cross-section for the elastic scattering of electrons by helium atoms and a Born approximation prediction.

quantum mechanical model are compared with experimentation [15,16]. The closed form functions (Eqs. (105) and (106)) for the elastic differential cross-section for the elastic scattering of electrons by helium atoms is shown graphically in Fig. 12. The scattering amplitude function, $F(s)$ (Eq. (104), is shown as an insert. It is apparent from Fig. 11 that the quantum mechanical calculations fail completely at predicting the experimental results at small scattering angles; whereas, there is good agreement between Eq. (105) and the experimental results.

21. The nature of the chemical bond of hydrogen

The hydrogen molecule charge and current-density functions, bond distance and energies are solved from the Laplacian in ellipsoidal coordinates with the constraint of nonradiation.

$$(\eta - \zeta)R_\zeta \frac{\partial}{\partial \xi}\left(R_\zeta \frac{\partial\phi}{\partial\xi}\right) + (\zeta - \xi)R_\eta \frac{\partial}{\partial\eta}\left(R_\eta \frac{\partial\phi}{\partial\eta}\right)$$
$$+ (\xi - \eta)R_\zeta \frac{\partial}{\partial\zeta}\left(R_\zeta \frac{\partial\phi}{\partial\zeta}\right) = 0. \tag{107}$$

The force balance equation for the hydrogen molecule is

$$\frac{\hbar^2}{m_e a^2 b^2}2ab^2X = \frac{e^2}{4\pi\varepsilon_0}X + \frac{\hbar^2}{2m_e a^2 b^2}2ab^2X, \tag{108}$$

where

$$X = \frac{1}{\sqrt{\xi + a^2}}\frac{1}{\sqrt{\xi + b^2}}\frac{1}{c}\sqrt{\frac{\xi^2 - 1}{\xi^2 - \eta^2}}. \tag{109}$$

Eq. (108) has the parametric solution

$$r(t) = ia\cos\omega t + jb\sin\omega t \tag{110}$$

when the semimajor axis, a, is
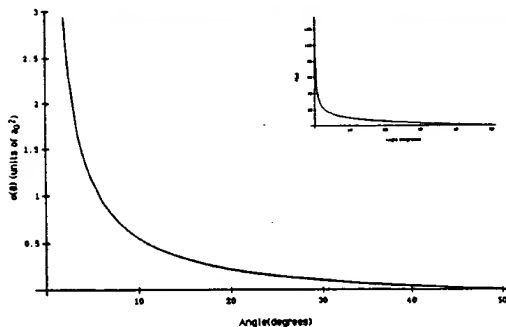
$$a = a_0. \tag{111}$$

Fig. 12. The closed form function (Eqs. (105) and (106)) for the elastic differential cross section for the elastic scattering of electrons by helium atoms. The scattering amplitude function, $F(s)$ (Eq. (104)), is shown as an insert.

1   The internuclear distance, $2c'$, which is the distance between the foci is

$$2c' = \sqrt{2}a_0. \tag{112}$$

3   The experimental internuclear distance is $\sqrt{2}a_0$. The semiminor axis is

$$b = \frac{1}{\sqrt{2}}a_0. \tag{113}$$

5   The eccentricity, e, is

$$e = \frac{1}{\sqrt{2}}. \tag{114}$$

21.1. The energies of the hydrogen molecule

7   The potential energy of the two electrons in the central field of the protons at the foci is

$$V_e = \frac{-2e^2}{8\pi\varepsilon_0\sqrt{a^2-b^2}} \ln\frac{a+\sqrt{a^2-b^2}}{a-\sqrt{a^2-b^2}} \qquad \text{eV}. \tag{115}$$

9   The potential energy of the two protons is

$$V_p = \frac{e^2}{8\pi\varepsilon_0\sqrt{a^2-b^2}} \qquad \qquad \tag{116}$$

The kinetic energy of the electrons is

$$T = \frac{\hbar^2}{2m_e a\sqrt{a^2-b^2}} \ln\frac{a+\sqrt{a^2-b^2}}{a-\sqrt{a^2-b^2}} = 33.906 \text{ eV}. \tag{117}$$

11   The energy, V_m, of the magnetic force between the electrons is

$$V_m = \frac{-\hbar^2}{4m_e a\sqrt{a^2-b^2}} \ln\frac{a+\sqrt{a^2-b^2}}{a-\sqrt{a^2-b^2}} = -16.9533 \text{ eV}. \tag{118}$$

13

The total energy is

$$E_T = V_e + T + V_m + V_p \tag{119}$$

$$E_T = -13.6 \text{ eV}\left[\left(2\sqrt{2}-\sqrt{2}+\frac{\sqrt{2}}{2}\right)\ln\frac{\sqrt{2}+1}{\sqrt{2}-1} - \sqrt{2}\right]$$

$$= -31.6\ \text{eV}. \tag{120}$$

The energy of two hydrogen atoms is   15

$$E2H[a_H] = -27.21 \text{ eV}. \tag{121}$$

The bond dissociation energy, E_D, is the difference between   17
the total energy of the corresponding hydrogen atoms
(Eq. (121)) and E_T (Eq. (120)).

$$E_D = E(2H[a_H]) - E_T = 4.43 \text{ eV}. \tag{122}$$

The experimental energy determined by calorimetry is   19

$$E_D = 4.45 \text{ eV}. \tag{123}$$

22. Cosmological theory based on Maxwell's equations

Maxwell's equations and special relativity are based on   21
the law of propagation of a electromagnetic wave front in
the form   23

$$\frac{1}{c^2}\left(\frac{\partial\omega}{\partial t}\right)^2 - \left[\left(\frac{\partial\omega}{\partial x}\right)^2 + \left(\frac{\partial\omega}{\partial y}\right)^2 + \left(\frac{\partial\omega}{\partial z}\right)^2\right] = 0. \tag{124}$$

For any kind of wave advancing with limiting velocity and   25
capable of transmitting signals, the equation of front prop-
agation is the same as the equation for the front of a light
wave. Thus, the equation   27

$$\frac{1}{c^2}\left(\frac{\partial\omega}{\partial t}\right)^2 - (\text{grad }\omega)^2 = 0 \tag{125}$$

acquires a general character; it is more general than Maxwell's equations from which Maxwell originally derived it.

A discovery of the present work is that the classical wave equation governs: (1) the motion of bound electrons, (2) the propagation of any form of energy, (3) measurements between inertial frames of reference such as time, mass, momentum, and length (Minkowski tensor), (4) fundamental particle production and the conversion of matter to energy, (5) a relativistic correction of spacetime due to particle production or annihilation (Schwarzschild metric), (6) the expansion and contraction of the universe, (7) the basis of the relationship between Maxwell's equations, Planck's equation, the de Broglie equation, Newton's laws, and special, and general relativity.

The relationship between the time interval between ticks t of a clock in motion with velocity v relative to an observer and the time interval t_0 between ticks on a clock at rest relative to an observer is [17]

$$(ct)^2 = (ct_0)^2 + (vt)^2. \tag{126}$$

Thus, the time dilation relationship based on the constant maximum speed of light c in any inertial frame is

$$t = \frac{t_0}{\sqrt{1 - v^2/c^2}}. \tag{127}$$

The metric $g_{\mu\nu}$ for Euclidean space is the Minkowski tensor $\eta_{\mu\nu}$. In this case, the separation of proper time between two events x^μ and $x^\mu + dx^\mu$ is $d\tau^2 = -\eta_{\mu\nu} dx^\mu dx^\nu$.

23. The equivalence of the gravitational mass and the inertial mass

The equivalence of the gravitational mass and the inertial mass, $m_g/m_i =$ universal constant, which is predicted by Newton's law of mechanics and gravitation is experimentally confirmed to less 1×10^{-11} [18]. In physics, the discovery of a universal constant often leads to the development of an entirely new theory. From the universal constancy of the velocity of light, c the special theory of relativity was derived; and from Planck's constant, the quantum theory was deduced. Therefore, the universal constant m_g/m_i should be the key to the gravitational problem. The energy equation of Newtonian gravitation is

$$E = \frac{1}{2}mv^2 - \frac{GMm}{r} = constant. \tag{128}$$

Since h, the angular momentum per unit mass, is

$$h = L/m = |\mathbf{r} \times \mathbf{v}| = r_0 v_0 \sin\phi$$

the eccentricity e may be written as

$$e = \left[1 + \left(v_0^2 - \frac{2GM}{r_0} \right) \frac{r_0^2 v_0^2 \sin^2\phi}{G^2 M^2} \right]^{1/2}, \tag{129}$$

where m is the inertial mass of a particle, v_0 is the speed of the particle, r_0 is the distance of the particle from a massive object, ϕ is the angle between the direction of motion of the particle and the radius vector from the object, and M is the total mass of the object (including a particle). The eccentricity e given by Newton's differential equations of motion in the case of the central field permits the classification of the orbits according to the total energy E [19] (column 1) and the orbital velocity squared, v_0^2, relative to the gravitational velocity squared, $2GM/r_0$ [19] (column 2):

$$E < 0 \quad v_0^2 < \frac{2GM}{r_0} \quad e < 1 \quad \text{ellipse},$$

$$E < 0 \quad v_0^2 < \frac{2GM}{r_0} \quad e = 0 \quad \text{circle (special case of ellipse)},$$

$$E = 0 \quad v_0^2 = \frac{2GM}{r_0} \quad e = 1 \quad \text{parabolic orbit},$$

$$E > 0 \quad v_0^2 > \frac{2GM}{r_0} \quad e > 1 \quad \text{hyperbolic orbit}. \tag{130}$$

24. Continuity conditions for the production of a particle from a photon travelling at light speed

A photon traveling at the speed of light gives rise to a particle with an initial radius equal to its Compton wavelength bar.

$$r = -\lambda_C = \frac{\hbar}{mc} r_e. \tag{131}$$

The particle must have an orbital velocity equal to Newtonian gravitational escape velocity v_g of the antiparticle.

$$v_g = \sqrt{\frac{2Gm}{r}} = \sqrt{\frac{2Gm_0}{-\lambda_C}}. \tag{132}$$

The eccentricity is one. The orbital energy is zero. The particle production trajectory is a parabola relative to the center of mass of the antiparticle.

24.1. A gravitational field as a front equivalent to light wave front

The particle with a finite gravitational mass gives rise to a gravitational field that travels out as a front equivalent to a light wave front. The form of the outgoing gravitational field front traveling at the speed of light is $f(t - r/c)$, and $d\tau^2$ is given by

$$d\tau^2 = f(r) dt^2 - \frac{1}{c^2}[f(r)^{-1} dr^2 + r^2 d\theta^2 + r^2 \sin^2\theta d\phi^2]. \tag{133}$$

The speed of light as a constant maximum as well as phase matching and continuity conditions of the electromagnetic and gravitational waves require the following form of the squared displacements:

$$(c\tau)^2 + (v_g t)^2 = (ct)^2, \tag{134}$$

$$f(r) = \left(1 - \left(\frac{v_g}{c} \right)^2 \right). \tag{135}$$

In order that the wave front velocity does not exceed c in any frame, spacetime must undergo time dilation and length contraction due to the particle production event. *The derivation and result of spacetime time dilation is analogous to the derivation and result of special relativistic time dilation* wherein the relative velocity of two inertial frames replaces the gravitational velocity.

The general form of the metric due to the relativistic effect on spacetime due to mass m_0 with v_g given by Eq. (132) is

$$d\tau^2 = \left(1 - \left(\frac{v_g}{c}\right)^2\right)dt^2 - \frac{1}{c^2}\left[\left(1 - \left(\frac{v_g}{c}\right)^2\right)^{-1}dr^2 + r^2\,d\theta^2 + r^2\sin^2\theta\,d\phi^2\right]. \tag{136}$$

The gravitational radius, r_g, of each orbitsphere of the particle production event, each of mass m_0, and the corresponding general form of the metric are respectively

$$r_g = \frac{2Gm}{c^2}, \tag{137}$$

$$d\tau^2 = \left(1 - \frac{r_g}{r}\right)dt^2 - \frac{1}{c^2}\left[\left(1 - \frac{r_g}{r}\right)^{-1}dr^2 + r^2\,d\theta^2 + r^2\sin^2\theta\,d\phi^2\right]. \tag{138}$$

The metric $g_{\mu\nu}$ for non-Euclidean space due to the relativistic effect on spacetime due to mass m_0 is

$$g_{\mu\nu} = \begin{pmatrix} -(1 - \frac{2Gm}{c^2 r}) & 0 & 0 & 0 \\ 0 & \frac{1}{c^2}(1 - \frac{2Gm}{c^2 r})^{-1} & 0 & 0 \\ 0 & 0 & \frac{1}{c^2}r^2 & 0 \\ 0 & 0 & 0 & \frac{1}{c^2}r^2\sin^2\theta \end{pmatrix}. \tag{139}$$

Masses and their effects on spacetime *superimpose*. The separation of proper time between two events x^μ and x^ν is

$$d\tau^2 = \left(1 - \frac{2GM}{c^2 r}\right)dt^2 - \frac{1}{c^2}\left[\left(1 - \frac{2GM}{c^2 r}\right)^{-1}dr^2 + r^2\,d\theta^2 + r^2\sin^2\theta\,d\phi^2\right]. \tag{140}$$

The *Schwarzschild metric* (Eq. (140)) *gives the relationship whereby matter causes relativistic corrections to spacetime that determine the curvature of spacetime and is the origin of gravity.*

24.2. Particle production continuity conditions from Maxwell's equations, and the Schwarzschild metric

The photon to particle event requires a transition state that is continuous wherein the velocity of a transition state orbitsphere is the speed of light. The radius, r, is the Compton wavelength bar, $-\lambda_C$, given by Eq. (131). At production, the Planck equation energy, the electric potential energy, and the magnetic energy are equal to m_0c^2.

The Schwarzschild metric gives the relationship whereby matter causes relativistic corrections to spacetime that determines the masses of fundamental particles. Substitution of $r = -\lambda_C$; $dr = 0$; $d\theta = 0$; $\sin^2\theta = 1$ into the Schwarzschild metric gives

$$d\tau = dt\left(1 - \frac{2Gm_0}{c^2 r_e^2} - \frac{v^2}{c^2}\right)^{1/2} \tag{141}$$

with $v^2 = c^2$, the relationship between the proper time and the coordinate time is

$$\tau = ti\sqrt{\frac{2GM}{c^2 r_e^2}} = ti\sqrt{\frac{2GM}{c^2 - \lambda_C}} = ti\frac{v_g}{c}. \tag{142}$$

When the orbitsphere velocity is the speed of light, continuity conditions based on the constant maximum speed of light given by Maxwell's equations are mass energy = Planck equation energy = electric potential energy = magnetic energy = mass/spacetime metric energy. Therefore,

$$m_0c^2 = \hbar\omega^* = V = E_{mag} = \dots \tag{143}$$

$$m_0c^2 = \hbar\omega^* = \frac{\hbar^2}{m_0 - \lambda_C^2} = \alpha^{-1}\frac{e^2}{4\pi\varepsilon_0 - \lambda_C} = \alpha^{-1}\frac{\pi\mu_0 e^2\hbar^2}{(2\pi m_0)^2 - \lambda_C^3}$$

$$= \frac{\alpha^{-1}}{i\frac{1}{sec}}\sqrt{\frac{-c^2}{Gm}} \tag{144}$$

The continuity conditions based on the constant maximum speed of light given by the Schwarzschild metric are:

$$\frac{\text{proper time}}{\text{coordinate time}} = \frac{\text{gravitational wave condition}}{\text{electromagnetic wave condition}}$$

$$= \frac{\text{gravitational mass phase matching}}{\text{charge/inertial mass phase matching}},$$

$$\frac{\text{proper time}}{\text{coordinate time}} = i\frac{\sqrt{2Gm/c^2 - \lambda_C}}{\alpha} = i\frac{v_g}{\alpha c}. \tag{145}$$

25. Masses of fundamental particles

Each of the Planck equation energy, electric energy, and magnetic energy corresponds to a particle given by the relationship between the proper time and the coordinate time. The electron and down-down-up neutron correspond to the Planck equation energy. The muon and strange-strange-charmed neutron correspond to the electric energy. The tau and bottom-bottom-top neutron correspond to the magnetic energy. The particle must possess the escape velocity v_g relative to the antiparticle where $v_g < c$. According to Newton's law of gravitation, the eccentricity is one and the particle production trajectory is a parabola relative to the center of mass of the antiparticle.

17

25.1. The electron–antielectron lepton pair

A clock is defined in terms of a self-consistent system of units used to measure the particle mass.[2] The proper time of the particle is equated with the coordinate time according to the Schwarzschild metric corresponding to light speed. The special relativistic condition corresponding to the Planck energy gives the mass of the electron.

$$2\pi \frac{\hbar}{mc^2} = \sec\sqrt{\frac{2Gm^2}{c\alpha^2\hbar}}, \tag{146}$$

$$m_e = \left(\frac{\hbar\alpha}{\sec c^2}\right)^{1/2}\left(\frac{c\hbar}{2g}\right)^{1/4} = 9.1097\times10^{-31}\ \text{kg}, \tag{147}$$

$$m_e = 9.1097\times10^{-31}\ \text{kg} - 18\ \text{eV}(v_e) = 9.1094\times10^{-31}\ \text{kg}, \tag{148}$$

$$m_{e\ \text{experimental}} = 9.1095\times10^{-31}\ \text{kg}. \tag{149}$$

25.2. Down-down-up neutron (DDU)

The corresponding equation for production of the neutron is

$$2\pi\frac{2\pi\hbar}{(m_N/3)[1/2\pi - \alpha/2\pi]c^2}$$

$$= \sec\sqrt{\frac{2G[(m_N/3)[1/2\pi - \alpha/2\pi]]^2}{3c(2\pi)^2\hbar}}, \tag{150}$$

$$m_{N\text{calculated}} = (3)(2\pi)\left(\frac{1}{1-\alpha}\right)\left(\frac{2\pi h}{\sec c^2}\right)^{1/2}\left(\frac{2\pi(3)ch}{2G}\right)^{1/4}$$

$$= 1.6744\times10^{-27}\ \text{kg}, \tag{151}$$

$$m_{N\text{experimental}} = 1.6749\times10^{-27}\ \text{kg}. \tag{152}$$

26. Gravitational potential energy

The gravitational radius, α_G or r_G, of the orbitsphere of mass m_0 is defined as

$$\alpha_G = r_G = \frac{Gm_0}{c^2}. \tag{153}$$

[2] Presently the second is defined as the time required for 9,192,631,770 vibrations within the cesium-133 atom. The "sec" as defined in Eq. (146) is a fundamental constant, namely, the metric of spacetime that is almost identically equal to the present value for reasons explained in Ref. [1]). A unified theory can only provide the relationships between all measurable observables in terms of a clock defined in terms of fundamental constants according to those observables and used to measure them. The so *defined "clock"* *measures "clicks" on an observable in one aspect, and in another,* *it is the ruler of spacetime of the universe with the implicit depen-* *dence of spacetime on matter–energy conversion* as shown in the Relationship of Matter to Energy and Spacetime Expansion section.

When $r_G = r_a^* = -\lambda_C$, the gravitational potential energy equals m_0c^2

$$r_G = \frac{Gm_0}{c^2} = -\lambda_C = \frac{\hbar}{m_0c}, \tag{154}$$

$$E_{\text{grav}} = \frac{Gm_0^2}{r} = \frac{Gm_0^2}{-\lambda_C} = \frac{Gm_0^2}{r_a^*} = \hbar\omega^* = m_0c^2. \tag{155}$$

The mass m_0 is the Planck mass, m_u,

$$m_u = m_0 = \sqrt{\frac{\hbar c}{G}}. \tag{156}$$

The corresponding gravitational velocity, v_G, is defined as

$$v_G = \sqrt{\frac{Gm_0}{r}} = \sqrt{\frac{Gm_0}{-\lambda_C}} = \sqrt{\frac{Gm_u}{-\lambda_C}}. \tag{157}$$

26.1. Relationship of the equivalent Planck mass particle production energies

For the Planck mass particle, the relationships corresponding to Eq. (144) are: (mass energy = Planck equation energy = electric potential energy = magnetic energy = gravitational potential energy = mass/spacetime metric energy)

$$m_0c^2 = \hbar\omega^* = E_{\text{ele}} = E_{\text{mag}} = E_{\text{grav}} = E_{\text{spacetime}} \tag{158}$$

$$m_0c^2 = \hbar\omega^* = \frac{2\hbar c}{m_0 - \lambda_C^2} = \alpha^{-1}\frac{e^2}{4\pi\varepsilon_0 - \lambda_C} = \alpha^{-1}\frac{\pi\mu_0e^2\hbar^2}{(2\pi m_0)^2 - \lambda_C^3}$$

$$= \alpha^{-1}\frac{\mu_0e^2c^2}{2h}\sqrt{\frac{Gm_0}{-\lambda_C}}\sqrt{\frac{\hbar c}{G}} = \frac{\alpha h}{1\ \sec}\sqrt{\frac{-\lambda_C c^2}{2Gm}}. \tag{159}$$

These equivalent energies give the particle masses in terms of the gravitational velocity, v_G and the Planck mass, m_u

$$m_0 = \alpha^{-1}\frac{\mu_0e^2c}{2h}\frac{\sqrt{Gm_0/-\lambda_C}}{c}m_u = \alpha^{-1}\frac{\mu_0e^2c}{2h}\sqrt{\frac{Gm_0}{c^2 - \lambda_C}}m_u$$

$$= \alpha^{-1}\frac{\mu_0e^2c}{2h}\frac{v_G}{c}m_u = \frac{v_G}{c}m_u. \tag{160}$$

26.2. Planck mass particles

A pair of particles each of the Planck mass corresponding to the gravitational potential energy is not observed since the velocity of each transition state orbitsphere is the gravitational velocity v_G that in this case is the speed of light; whereas, the Newtonian gravitational escape velocity v_g is $\sqrt{2}$ the speed of light. In this case, an electromagnetic wave of mass energy equivalent to the Planck mass travels in a circular orbit about the center of mass of another electromagnetic wave of mass energy equivalent to the Planck mass wherein the eccentricity is equal to zero and the escape velocity can never be reached. The Planck mass is a measuring stick. The extraordinarily high Planck mass

($\sqrt{\hbar c/G} = 2.18 \times 10^{-8}$ kg) is the unobtainable mass bound imposed by the angular momentum and speed of the photon relative to the gravitational constant. It is analogous to the unattainable bound of the speed of light for a particle possessing finite rest mass imposed by the Minkowski tensor.

26.3. Astrophysical implications of Planck mass particles

The limiting speed of light eliminates the singularity problem of Einstein's equation that arises as the radius of a blackhole equals the Schwarzschild radius. General relativity with the singularity eliminated resolves the paradox of the infinite propagation velocity required for the gravitational force in order to explain why the angular momentum of objects orbiting a gravitating body does not increase due to the finite propagation delay of the gravitational force according to special relativity [20]. When the gravitational potential energy density of a massive body such as a blackhole equals that of a particle having the Planck mass, the matter may transition to photons of the Planck mass. Even light from a blackhole will escape when the decay rate of the trapped matter with the concomitant spacetime expansion is greater than the effects of gravity which oppose this expansion. Gamma-ray bursts are the most energetic phenomenon known that can release an explosion of gamma rays packing 100 times more energy than a supernova explosion [21]. The annihilation of a blackhole may be the source of *gamma-ray bursts*. The source may be due to conversion of matter to photons of the Planck mass/energy which may also give rise to cosmic rays which are the most energetic particles known, and their origin is also a mystery [22]. According to the GZK cutoff, the cosmic spectrum cannot extend beyond 5×10^{19} eV, but AGASA, the world's largest air shower array, has shown that the spectrum is extending beyond 10^{20} eV without any clear sign of cutoff [23]. Photons each of the Planck mass may be the source of these inexplicably energetic cosmic rays.

27. Relationship of matter to energy and spacetime expansion

The Schwarzschild metric gives the relationship whereby matter causes relativistic corrections to spacetime. The limiting velocity c results in the contraction of spacetime due to particle production, which is given by $2\pi r_g$ where r_g is the gravitational radius of the particle. This has implications for the expansion of spacetime when matter converts to energy. Q the mass/energy to expansion/contraction quotient of spacetime is given by the ratio of the mass of a particle at production divided by T, the period of production.

$$Q = \frac{m_0}{T} = \frac{m_0}{\frac{2\pi r_g}{c}} = \frac{m_0}{\frac{2\pi \frac{2Gm_0}{c^2}}{c}} = \frac{c^3}{4\pi G} = 3.22 \times 10^{34} \text{ kg/sec.}$$
(161)

The gravitational equations with the equivalence of the particle production energies (Eq. (144)) permit the conservation of mass/energy ($E = mc^2$) and spacetime ($c^3/4\pi G = 3.22 \times 10^{34}$ kg/sec). With the conversion of 3.22×10^{34} kg of matter to energy, spacetime expands by 1 sec. The photon has inertial mass and angular momentum, but due to Maxwell's equations and the implicit special relativity it does not have a gravitational mass.

27.1. Cosmological consequences

The universe is closed (it *is finite but with no boundary*). It is a 3-sphere universe–Riemannian three-dimensional hyperspace plus time of constant positive curvature at each r-sphere. The *universe is oscillatory in matter/energy and spacetime* with a finite minimum radius, the gravitational radius. Spacetime expands as mass is released as energy which provides the basis of the atomic, thermodynamic, and cosmological arrows of time. Different regions of space are isothermal even though they are separated by greater distances than that over which light could travel during the time of the expansion of the universe [24]. Presently, stars and large-scale structures exist which are older than the elapsed time of the present expansion as stellar, galaxy, and supercluster evolution occurred during the contraction phase [25–31]. The maximum power radiated by the universe which occurs at the beginning of the expansion phase is $P_U = c^5/4\pi G = 2.89 \times 10^{51}$ W. Observations beyond the beginning of the expansion phase are not possible since the universe was entirely matter filled.

27.2. The period of oscillation of the universe based on closed propagation of light

Mass/energy is conserved during harmonic expansion and contraction. The gravitational potential energy E_{grav} given by Eq. (155) with $m_0 = m_U$ is equal to when the radius of the universe r is the gravitational radius r_G. The gravitational velocity v_G (Eq. (157) with $r = r_G$ and $m_0 = m_U$) is the speed of light in a circular orbit wherein the eccentricity is equal to zero and the escape velocity from the universe can never be reached. The period of the oscillation of the universe and the period for light to transverse the universe corresponding to the gravitational radius r_G must be equal. The harmonic oscillation period, T, is

$$T = \frac{2\pi r_G}{c} = \frac{2\pi G m_U}{c^3} = \frac{2\pi G (2 \times 10^{54} \text{ kg})}{c^3}$$
$$= 3.10 \times 10^{19} \text{ sec} = 9.83 \times 10^{11} \text{ years,} \quad (162)$$

where the mass of the universe, m_U, is approximately 2×10^{54} kg. (The initial mass of the universe of 2×10^{54} kg is based on internal consistency with the size, age, Hubble constant, temperature, density of matter, and power spectrum.) Thus, the observed universe will expand as mass is released as photons for 4.92×10^{11} years. At this point in its world line, the universe will obtain its maximum size and begin to contract.
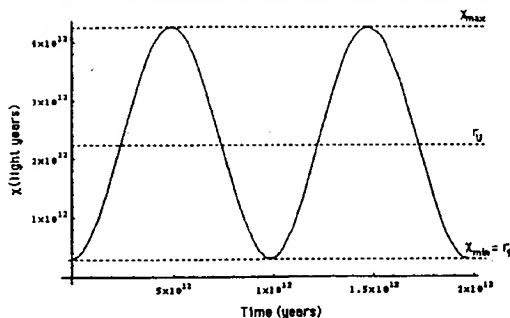
Fig. 13. The radius of the universe as a function of time.

28. The differential equation of the radius of the universe

Based on conservation of mass/energy ($E = mc^2$) and spacetime ($c^3/4\pi G = 3.22 \times 10^{34}$ kg/sec). The universe behaves as a simple harmonic oscillator having a restoring force, F, which is proportional to the radius. The proportionality constant, k, is given in terms of the potential energy, E, gained as the radius decreases from the maximum expansion to the minimum contraction.

$$\frac{E}{\aleph^2} = k. \tag{163}$$

Since the gravitational potential energy E_{grav} is equal to $m_U c^2$ when the radius of the universe r is the gravitational radius, r_G

$$F = -k\aleph = -\frac{m_U c^2}{r_G^2}\aleph = -\frac{m_U c^2}{(Gm_U/c^2)^2}\aleph. \tag{164}$$

And, the differential equation of the radius of the universe, $\aleph$ is

$$m_U \overset{\cdot\cdot}{\aleph} + \frac{m_U c^2}{r_G^2}\aleph = m_U \overset{\cdot\cdot}{\aleph} + \frac{m_U c^2}{(Gm_U/c^2)^2}. \tag{165}$$

The *maximum radius of the universe*, the amplitude, r_0, of the time harmonic variation in the radius of the universe, is given by the quotient of the total mass of the universe and Q (Eq. (161)), the mass energy to expansion/contraction quotient.

$$r_0 = \frac{m_U}{Q} = \frac{2 \times 10^{54} \text{ kg}}{c^3/4\pi G} = \frac{c^3/4\pi G}{}$$

$$= 1.97 \times 10^{12} \text{ light years.} \tag{166}$$

The *minimum radius* which corresponds to the gravitational radius, r_g, given by Eq. (137) with $m_0 = m_U$ is

$$r_g = \frac{2Gm_U}{c^2} = 2.96 \times 10^{27} \text{ m} = 3.12 \times 10^{11} \text{ light years.} \tag{167}$$

When the radius of the universe is the gravitational radius, r_g, the proper time is equal to the coordinate time by Eq. (142), and the gravitational escape velocity v_g of the universe is the speed of light. The radius of the universe as a function of time as shown in Fig. 13 is

$$\aleph = \left(r_g + \frac{cm_U}{Q}\right) - \frac{cm_U}{Q}\cos\left(\frac{2\pi t}{(2\pi r_0/c)}\right)$$

$$= \left(\frac{2Gm_U}{c^2} + \frac{cm_U}{(c^3/4\pi G)}\right) - \frac{cm_U}{(c^3/4\pi G)}\cos\left(\frac{2\pi t}{(2\pi Gm_U/c^3)}\right). \tag{168}$$

The expansion/contraction rate, $\overset{\cdot}{\aleph}$, as shown in Fig. 14 is given by time derivative of Eq. (168)

$$\overset{\cdot}{\aleph} = 4\pi c \times 10^{-3}\sin\left(\frac{2\pi t}{(2\pi Gm_U/c^3)}\right) \text{ km/sec.} \tag{169}$$

29. The Hubble constant

The *Hubble constant* is given by the ratio of the expansion rate given in units of km/sec divided by the radius of the expansion in Mpc. The radius of expansion is equivalent to the radius of the light sphere with an origin at the time point when the universe stopped contracting and started to expand.

$$H = \frac{\overset{\cdot}{\aleph}}{t\text{Mpc}} = \frac{4\pi c \times 10^{-3}\sin\left(\frac{2\pi t}{(2\pi Gm_U/c^3)}\right) \text{ km/sec}}{t\text{Mpc}}. \tag{170}$$

For $t = 10^{10}$ light years $= 3.069 \times 10^3$ Mpc, the Hubble constant, H_0, is

$$H_0 = 78.6 \text{ km/sec Mpc.} \tag{171}$$
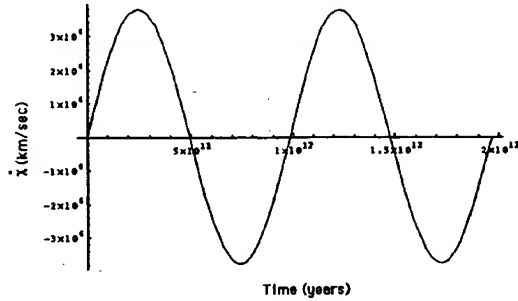
Fig. 14. The expansion/contraction rate of the universe as a function of time.
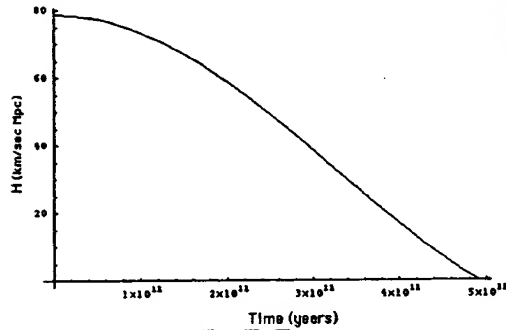
Fig. 15. The Hubble constant of the universe as a function of time.

1   The experimental value [34] as shown in Fig. 15 is

$$H_0 = 80 \pm 17 \text{ km/sec Mpc.} \tag{172}$$

30. The density of the universe as a function of time

3   The density of the universe as a function of time $\rho_U(t)$ given by the ratio of the mass as a function of time and the

5   volume as a function of time as shown in Fig. 16 is

$$\rho_U(t) = \frac{m_U(t)}{V(t)} = \frac{m_U(t)}{\frac{4}{3}\pi \aleph(t)^3} =$$

$$\frac{\frac{m_U}{2}\left(1 + \cos\left(\frac{2\pi t}{\frac{2\pi G m_U}{c^3}}\right)\right)}{\frac{4}{3}\pi\left(\left(\frac{2Gm_U}{c^2} + \frac{cm_U}{4\pi G}\right) - \frac{cm_U}{4\pi G}\cos\left(\frac{2\pi t}{\frac{2\pi G m_U}{c^3}}\right)\right)^3}.$$

$$\tag{173}$$

For $t = 10^{10}$ light years, $\rho_U = 1.7 \times 10^{-32}$ g/cm^3. The density of luminous matter of stars and gas of galaxies is about   7
$\rho_U = 2 \times 10^{-31}$ g/cm^3 [33,34].

31. The power of the universe as a function of time $P_U(t)$ 9

From $E = mc^2$ and Eq. (161),

$$P_U(t) = \frac{c^5}{8\pi G}\left(1 + \cos\left(\frac{2\pi t}{2\pi r_0/c}\right)\right). \tag{174}$$

For $t = 10^{10}$ light years, $P_U(t) = 2.88 \times 10^{51}$ W. The   11
observed power is consistent with that predicted. The power of the universe as a function of time is shown   13
in Fig. 17.
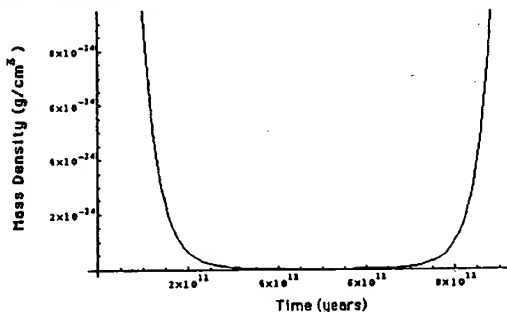
Fig. 16. The density of the universe as a function of time.
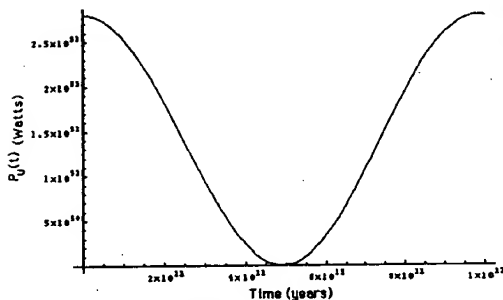
Fig. 17. The power of the universe as a function of time.

32. The temperature of the universe as a function of time

3 The temperature of the universe as a function of time, $T_U(t)$, as shown in Fig. 18, follows from the Stefan–Boltzmann law.

$$T_U(t) = \left(\frac{1}{1 + \frac{Gm_U(t)}{c^2 \aleph(t)}} \left[\frac{P_U(t)}{e\sigma} \right] \right)^{1/4}$$

$$= \left(\frac{1}{1 + \frac{Gm_U(t)}{c^2 \aleph(t)}} \right) \left[\frac{P_U(t)}{4\pi\aleph(t)^2}}{e\sigma} \right]^{1/4} . \qquad (175)$$

5 The calculated uniform temperature is about 2.7 K which is in agreement with the observed microwave background
7 temperature [32].

33. Power spectrum of the cosmos

The power spectrum of the cosmos, as measured by   9
the Las Campanas survey, generally follows the predic-
tion of cold dark matter on the scales of 200–600 million   11
light-years. However, the power increases dramatically on
scales of 600–900 million light-years [31]. This discrep-   13
ancy means that the universe is much more structured on
those scales than current theories can explain.   15

The universe is oscillatory in matter/energy and space-
time with a finite minimum radius. The *minimum radius*   17
which corresponds to the gravitational radius, r_g, given
by Eq. (167) is 3.12×10^{11} light years. The minimum ra-   19
dius is larger than that provided by the current expansion,
approximately 10 billion light years [32]. The universe is   21
a four-dimensional hyperspace of constant positive curva-
ture at each r-sphere. The coordinates are spherical, and   23
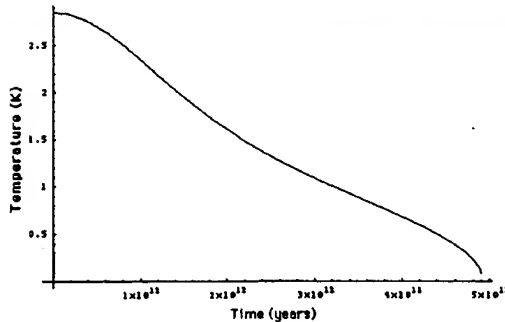
Fig. 18. The temperature of the universe as a function of time during the expansion phase.

1   the space can be described as a series of spheres each of
     constant radius r whose centers coincide at the origin. The
3   existence of the mass m_U causes the area of the spheres to
     be less than $4\pi r^2$ and causes the clock of each r-sphere to
5   run so that it is no longer observed from other r-spheres to
     be at the same rate. The Schwarzschild metric given by Eq.
7   (140) is the general form of the metric which allows for
     these effects. Consider the present observable universe that
9   has undergone expansion for 10 billion years. The radius
     of the universe as a function of time from the coordinate
11   r-sphere is of the same form as Eq. (168). The average size
     of the universe, r_U, is given as the sum of the gravitational
13   radius, r_g, and the observed radius, 10 billion light years.

$$r_U = r_g + 10^{10} \text{ light years} = 3.12 \times 10^{11} \text{ light years}$$

$$+10^{10} \text{ light years} = 3.22 \times 10^{11} \text{ light years} \qquad (176)$$

     The frequency of Eq. (168) is one-half the amplitude of
15   spacetime expansion from the conversion of the mass of uni-
     verse into energy according to Eq. (169). Thus, keeping the
17   same relationships, the frequency of the current expansion
     function is the reciprocal of one-half the current age. Substi-
19   tution of the average size of the universe, the frequency of
     expansion, and the amplitude of expansion, 10 billion light
21   years, into Eq. (168) gives the radius of the universe as a
     function of time for the coordinate r-sphere.

$$\aleph = 3.22 \times 10^{11} - 1 \times 10^{10}$$

$$\cos\left(\frac{2\pi t}{5 \times 10^9 \text{ light years}}\right) \text{ light years.} \qquad (177)$$

23   The Schwarzschild metric gives the relationship between
     the proper time and the coordinate time. The infinitesimal

temporal displacement, $d\tau$ is given by Eq. (140). In the   25
case that $dr^2 = d\theta^2 = d\phi^2 = 0$, the relationship between the
proper time and the coordinate time is   27

$$d\tau^2 = \left(1 - \frac{2Gm_U}{c^2 r}\right) dt^2 \qquad (178)$$

$$\tau = \sqrt{1 - \frac{r_g}{r}} \qquad (179)$$

The maximum power radiated by the universe is given by
Eqs. (174) which occurs when the proper radius, the co-   29
ordinate radius, and the gravitational radius r_g are equal.
For the present universe, the coordinate radius is given by   31
Eq. (176). The gravitational radius is given by Eq. (167).
The maximum of the power spectrum of a trigonometric   33
function occurs at its frequency [35]. Thus, the coordi-
nate maximum power according to Eq. (177) occurs at   35
5×10^9 light years. The maximum power corresponding to
the proper time is given by the substitution of the coordi-   37
nate radius, the gravitational radius r_g, and the coordinate
power maximum into Eq. (179). The power maximum in   39
the proper frame occurs at

$$\tau = 5 \times 10^9 \text{ light years}\sqrt{1 - \frac{3.12 \times 10^{11} \text{ light years}}{3.22 \times 10^{11} \text{ light years}}},$$

$$\tau = 880 \times 10^6 \text{ light years.} \qquad (180)$$

The power maximum of the current observable universe is   41
predicted to occur on the scale of 880×10^6 light years.
There is excellent agreement between the predicted value   43
and the experimental value of $600–900 \times 10^6$ light years
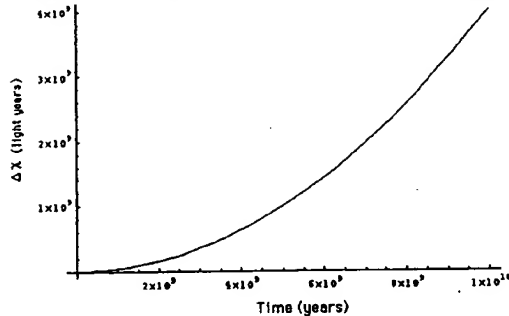[31].   45

Fig. 19. The differential expansion of the light sphere due to the acceleration of the expansion of the cosmos as a function of time.

34. The expansion/contraction acceleration, $\overset{\cdot\cdot}{\aleph}$

The expansion/contraction acceleration rate, $\overset{\cdot\cdot}{\aleph}$, as shown in Fig. 19, is given by the time derivative of Eq. (169).

$$\overset{\cdot\cdot}{\aleph} = 2\pi \frac{c^4}{Gm_U} \cos\left(\frac{2\pi t}{2\pi Gm_U/c^3} \sec\right) \overset{\cdot\cdot}{\aleph} = H_o$$

$$= 78.7 \cos\left(\frac{2\pi t}{3.01 \times 10^5 \text{ Mpc}}\right) \text{ km/sec Mpc.} \quad (181)$$

The differential in the radius of the universe, $\Delta\aleph$, due to its acceleration is given by $\Delta\aleph = 1/2\overset{\cdot\cdot}{\aleph} t^2$. The differential in expanded radius for the elapsed time of expansion, $t = 10^{10}$ light years corresponds to a decease in brightness of a supernovae standard candle of about an order of magnitude of that expected where the distance is taken as $\Delta\aleph$. This result based on the predicted rate of acceleration of the expansion is consistent with the experimental observation [36–38].

Furthermore, the microwave background radiation image obtained by the Boomerang telescope [39] consistent with a universe of nearly flat geometry since the commencement of its expansion. The data is consistent with a large offset radius of the universe with a fractional increase in size since the commencement of expansion about 10 billion years ago.

35. Power spectrum of the cosmic microwave background

When the universe reaches the maximum radius corresponding to the maximum contribution of the amplitude, r_0, of the time harmonic variation in the radius of the universe, (Eq. (166)), it is entirely radiation filled. Since the photon has no gravitational mass, the radiation is uniform. As energy converts into matter the power of the universe may be considered negative for the first quarter cycle starting from the point of maximum expansion as given by Eq. (187), and spacetime contracts according to Eq. (161). The gravitational field from particle production travels as a light wave front. As the universe contracts to a minimum radius, the gravitational radius given by Eq. (167), constructive interference of the gravitational fields occurs for distances which are integer of the amplitude, r_0, of the time harmonic variation in the radius of the universe for the times when the power is negative according to Eq. (187). The resulting slight variations in the density of matter are observed from our present sphere. The observed radius of expansion is equivalent to the radius of the light sphere with an origin at the time point when the universe stopped contracting and started to expand. The spherical harmonic parameter ℓ is given by the ratio of the amplitude, r_0, of the time harmonic variation in the radius of the universe, (Eq. (166)) divided by the present radius of the light sphere where the universe is a 3-sphere universe–Riemannian three-dimensional hyperspace plus time of constant positive curvature at each r-sphere. For $t = 10^{10}$ light years $= 3.069 \times 10^3$ Mpc, the fundamental ℓ is given by

$$\ell = \frac{r_0}{t} = \frac{2 \times 10^{54} \text{ kg}c^3/4\pi G}{t}$$

$$= \frac{1.97 \times 10^{12} \text{ light years}}{10^{10} \text{ light years}} = 197. \quad (182)$$

The number of constructive interferences is given by the maximum integer of the ratio of the amplitude, r_0, of the time harmonic variation in the radius of the universe, (Eq. (166)) divided by the minimum radius, the gravitational radius (Eq. (167)). The number of peaks are

$$\frac{r_0}{r_g} = \frac{\frac{2 \times 10^{54} \text{ kg}}{c^3/4\pi G}}{2Gm_U/c^2} = \frac{1.97 \times 10^{12} \text{ light years}}{3.12 \times 10^{11} \text{ light years}} = 6.3 \rightarrow 6. \quad (183)$$

Table 2
Predicted harmonic parameters ℓ and relative intensities $I(n)$ as a function of peak n

n	ℓ^a	$I(n)^b$
1	197	1
2	591	0.50
3	788	0.33
4	985	0.25
5	1182	0.20
6	1379	0.17

^{a}Eq. (184).
^{b}Eq. (188).

The peaks are predicted to occur at the fundamental plus harmonics of the fundamental-integer multiples, $n = 2, 3, 4, 5,$ and 6, of the fundamental $\ell = 197$.

$$\ell = 197 \text{ (fundamental)},$$
$$\ell = 197 + n197 \quad n = 2, 3, 4, 5, \text{ and } 6 \text{ (harmonics)}. \tag{184}$$

From Eq. (184), the predicted harmonic parameters ℓ are given in Table 2.

The harmonic peaks correspond to the condition that the amplitude of the harmonic term of the radius of the universe $r_0(n)$ is a reciprocal integer that of the maximum amplitude r_0. Thus, $r_0(n)$ is given by

$$r_0(n) = \frac{r_0}{n} = \frac{\frac{2 \times 10^{54} \text{ kg}}{c^2/4\pi G}}{n} = \frac{1.97 \times 10^{12} \text{ light years}}{n}. \tag{185}$$

The power flow of radiant energy into mass decreases as the radius contracts, and the relative intensities of the peaks follow from the power flow. The relative intensities are given by the normalized power as a function of time, the time at which the magnitude of the amplitude of the harmonic term of the radius of the universe $r_0(n)$ given by Eq. (185) corresponding to each contraction radius at which constructive interference occurs. Starting the clock at the point of the maximum expansion where the universe is entirely radiation filled and the CMB is uniform, the time at which the magnitude of the amplitude of the harmonic term of the radius of the universe $r_0(n)$ is given by Eq. (185) follows from Eq. (166).

$$r_0(n) = \frac{r_0}{n} = \frac{1.97 \times 10^{12}}{n}$$

$$= 1.97 \times 10^{12} \cos\left(\frac{2\pi t(n)}{9.83 \times 10^{11} \text{ years}}\right) \text{ light years},$$

$$t(n) = \frac{9.83 \times 10^{11}}{2\pi} \cos^{-1}\left(\frac{1}{n}\right) \text{ years}$$

$$= 1.564 \times 10^{11} \cos^{-1}\left(\frac{1}{n}\right) \text{ years}. \tag{186}$$

The power of the universe as a function of time is given by Eq. (174) and is shown in Fig. 17. To express the negative power flow relative to the radiant energy of the universe corresponding to the conversion of energy into matter, the power of the universe as a function of time may be expressed as

$$P_U(t) = -\frac{c^5}{4\pi G} \cos\left(\frac{2\pi t}{9.83 \times 10^{11} \text{ years}}\right) W,$$

$$P_U(t) = -2.9 \times 10^{51} \cos\left(\frac{2\pi t}{9.83 \times 10^{11} \text{ years}}\right) W, \quad (187)$$

where $t = 0$ corresponds to the time when the universe reaches the maximum radius corresponding to the maximum contribution of the amplitude, r_0, of the time harmonic variation in the radius of the universe (Eq. (166)). At $t = 0$ as defined, the universe is entirely radiation filled, and the power into particle production is a maximum. At $t = (\pi/2)/(2\pi/9.83 \times 10^{11} \text{ years})$ according to Eq. (187), particle production is in balance with matter to energy conversion, and the latter dominates for the following half cycle.

The relative intensities are given by substitution of Eq. (186) into Eq. (187) that is normalized by the magnitude of the maximum power which occurs at the maximum radius. Thus, the relative intensities are given by

$$I(n) = \cos\left(\frac{2\pi(1.564 \times 10^{11} \cos^{-1}(\frac{1}{n})\text{years})}{9.83 \times 10^{11} \text{ years}}\right) = \frac{1}{n}. \quad (188)$$

The relative intensities $I(n)$ as a function of peak n are given in Table 2.

The cosmic microwave background radiation is an average temperature of 2.7 K, with deviations of 30 or so μK in different parts of the sky representing slight variations in the density of matter. The measurements of the anisotropy in the Cosmic Microwave Background (CMB) have been measured with the Degree Angular Scale Interferometer (DASI) [40]. The angular power spectrum was measured in the range $100 < \ell < 900$, and peaks in the power spectrum from the temperature fluctuations of the cosmic microwave background radiation appear at certain values of ℓ of spherical harmonics. Peaks were observed at $\ell \approx 200$, $\ell \approx 550$, and $\ell \approx 800$ with relative intensities of 1, 0.5, and 0.3, respectively (Fig. 1 of Ref. [40]). There is excellent agreement between the predicted parameters given in Table 2 and the observed peaks.

36. The periods of spacetime expansion/contraction and particle decay/production for the universe are equal

The period of the expansion/contraction cycle of the radius of the universe, T, is given by Eq. (162). It follows from the Poynting power theorem with spherical radiation that the transition lifetimes are given by the ratio of energy

and the power of the transition (Eqs. (60)–(61)). Exponential decay applies to electromagnetic energy decay

$$h(t) = e^{-(1/T)t} u(t). \tag{189}$$

The coordinate time is imaginary because energy transitions are spacelike due spacetime expansion from matter to energy conversion. For example, the mass of the electron (a fundamental particle) is given by

$$\frac{2\pi - \lambda_C}{\sqrt{2Gm_e/-\lambda_C}} = \frac{2\pi - \lambda_C}{v_g} = i\alpha^{-1} \text{ sec}, \tag{190}$$

where v_g is Newtonian gravitational velocity (Eq. (132)). When the gravitational radius r_g is the radius of the universe, the proper time is equal to the coordinate time by Eq. (142), and the gravitational escape velocity v_g of the universe is the speed of light. Replacement of the coordinate time, t, by the spacelike time, it, gives

$$h(t) = Re[e^{-i(1/T)t}] = \cos\frac{2\pi}{T}t, \tag{191}$$

where the period is T (Eq. (162)). The continuity conditions based on the constant maximum speed of light (Maxwell's equations) are given by Eqs. (143)–(144). The continuity conditions based on the constant maximum speed of light (Schwarzschild metric) are given by Eq. (145). The periods of spacetime expansion/contraction and particle decay/production for the universe are equal because only the particles which satisfy Maxwell's equations and the relationship between proper time and coordinate time imposed by the Schwarzschild metric may exist.

37. Wave equation

The general form of the light front wave equation is given by Eq. (124). The equation of the radius of the universe, $\aleph$, may be written as

$$\aleph = \left(\frac{2Gm_U}{c^2} + \frac{cm_U}{(c^3/4\pi G)} \right)$$
$$- \frac{cm_U}{c^3/4\pi G} \cos\left(\frac{2\pi}{(2\pi Gm_U/c^3)\sec} \left(t \right) \right) m, \tag{192}$$

which is a solution of the wave equation for a light wave front.

38. Conclusion

Maxwell's equations, Planck's equation, the de Broglie equation, Newton's laws, and special, and general relativity are unified.

39. Uncited References

[14]

References

[1] Mills R. The grand unified theory of classical quantum mechanics, January 2000 ed. Cranbury, NJ: BlackLight Power, Inc., Distributed by Amazon.com; April 2001 Edition posted at www.blacklightpower.com.

[2] Haus HA. On the radiation from point charges. American Journal of Physics 1986;54:1126–9.

[3] McQuarrie DA. Quantum chemistry. Mill Valley, CA: University Science Books, 1983. p. 238–41.

[4] Van Dyck Jr RS, Schwinberg P, Dehmelt H. New high precision comparison of electron and positron g factors. Phys Rev Lett 1987;21:26–9.

[5] Abbott TA, Griffiths DJ. Am J Phys 1985;153(12):1203–11.

[6] Goedecke G. Phys Rev 1964;135B:281.

[7] Jackson JD. Classical electrodynamics. 2nd ed. New York: Wiley, 1962. p. 739–79.

[8] Mizushima M. Quantum mechanics of atomic spectra and atomic structure. New York: W.A. Benjamin, Inc., 1970. p. 17.

[9] Purcell E. Electricity and magnetism, New York: McGraw-Hill, 1965. p. 156–67.

[10] Clark D. Very large hydrogen atoms in interstellar space. J Chem Education 1991;68(6):454.

[11] Gribbin J. New Scientist 1994;25:15.

[12] Levine I. Phys Rev Lett 1997;78(3):424–7.

[13] Moore CE. Ionization potentials and ionization limits derived from the analyses of optical spectra. Nat Stand Ref Data Ser-Nat Bur Stand (US), No. 34, 1970.

[14] Weast RC. CRC handbook of chemistry and physics, 58 ed. West Palm Beach, FL: CRC Press, 1977, p. E-68.

[15] Bromberg PJ. Absolute differential cross sections of elastically scattered electrons. I. He, N_2, and CO at 500 eV. J Chem Phys 1969;50(9):3906–21.

[16] Geiger J. Elastische und unelastische streuung von elektronen an gasen. Z Phys 1963;175:530–42.

[17] Beiser A. Concepts of modern physics, 4th ed. New York: McGraw-Hill, 1978. p. 2–10.

[18] Adelberger EG, Stubbs CW, Heckel BR, Su Y, Swanson HE, Smith G, Gundlach JH. Phys Rev D 1990;42(10):3267–92.

[19] Fowles GR. Analytical mechanics, 3rd ed. New York: Holt, Rinehart, and Winston, 1977. p. 154–5.

[20] Van Flandern T. The speed of gravity what the experiments say. Phys Lett A 1998;250:1–11.

[21] Cowen R. Gamma-ray burst makes quite a bang. Sci News 1998;153(19):292.

[22] Chown M. The ultimate free lunch. New Scientist 1997;154(2081):50–1.

[23] Schwarzschild B. Giant air shower array shows cosmic-ray spectrum violating greisen cutoff. Phys Today 1998;51(10):19–21.

[24] Mather JC, Cheng ES. A preliminary measurement of the cosmic microwave background spectrum by the cosmic background explorer (COBE) satellite. Astrophys J Lett 1990;354:L37–40.

[25] Saunders W, Frenk C. The density field of the local universe. Nature 1991;349(6304):32–8.

[26] Kirshner RP, Oemler Jr A, Schechter PL, Shectman SA. A deep survey of galaxies. Astron J 1983;88:1285–300.

[27] de Lapparent V, Geller MJ, Huchra JP. The mean density and two-point correlation function for the CfA redshift survey slices. Astrophys J 1988;332(9):44–56.

[28] Dressler A, Lynden-Bell D, Burstein D. Spectroscopy and photometry of elliptical galaxies. I — A new distance estimator. Astrophys J 1987;313(2):42–58.

[29] Flamsteed S. Crisis in the cosmos. Discover 1995;16(3):66.

[30] Glanz J. CO in the early universe clouds cosmologists' views. Science 1996;273(5275):581.

[31] Landy SD. Mapping the universe. Sci Am 1999;280(6):38–45.

[32] Freeman WL. Distance to the Virgo cluster galaxy M100 from Hubble Space. Nature 1994;371(6500):757–62.

[33] Wald RM, General relativity. Chicago: University of Chicago Press, 1984. p. 114–6.

[34] Peebles PJE, Silk J. Joseph, A cosmic book of phenomena. Nature 1990;346(6281):233.

[35] Siebert WMcC. Circuits, signals, and systems, Cambridge, MA: The MIT Press, 1986, p. 597–603.

[36] Glanz J. Astronomers see a cosmic antigravity force at work. Science 1998;279(5355):1298–9.

[37] Cowen R. Living with lambda. Sci News 1998;153(22):344.

[38] Cowen R. Studies support an accelerating universe. Sci News 1998;154(18):277.

[39] de Bernardis et al., P. A flat Universe from high-resolution maps of the cosmic microwave background radiation. Nature 2000;404:955; http://www.physics.ucsb.edu/ ~ boomerang.

[40] Halverson NW, Leitch EM, Pryke C, Kovac J, Carlstrom JE, Holzapfel WL, Dragovan M, Cartwright JK, Mason BS, Padin S, Pearson TJ, Shepard MC, Readhead ACS. DASI first results: a measurement of the cosmic microwave background angular power spectrum, arXiv:astro-ph/0104489, 30 April 2001.

BLACKLIGHT POWER TECHNOLOGY

A New Clean Energy Source with the Potential for Direct Conversion to Electricity

Randell L. Mills[*]

1. INTRODUCTION

BlackLight Power, Inc. (the Company), a Delaware corporation based in its 53,000 sq. ft. headquarters in Cranbury, New Jersey, believes it has developed a new hydrogen chemical process that generates power, plasma (a hot ionized glowing gas), and a vast class of new compositions of matter. Specifically, the Company has designed and tested a new proprietary energy-producing chemical process. The Company has developed high-power density, high-temperature, hydrogen gas cells that produce intense light, power of orders of magnitude greater than that of the combustion of hydrogen at high temperatures, and power densities equal to those of many electric power plants. The Company is focusing on cells for generating light and plasma for lighting applications and direct conversion to electricity, respectively.

The cells generate energy through a chemical process (BlackLight Process) which the Company believes causes the electrons of hydrogen atoms to drop to lower orbits thus releasing energy in excess of the energy required to start the process. The lower-energy atomic hydrogen product of the BlackLight Process reacts with an electron to form a hydride ion which further reacts with elements other than hydrogen to form novel compounds called hydrino hydride compounds (HHCs) which are proprietary to the Company. The Company is developing the vast class of proprietary chemical compounds formed via the BlackLight Process. Its technology has far-reaching applications in many industries.

The power may be in the form of a plasma, a hot ionized glowing gas. The plasma may be converted directly to electricity with high efficiency using a known microwave device called a gyrotron, thus, avoiding a heat engine such as a turbine. The Company is

[*] Randell L Mills, President, BlackLight Power, Inc., 493 Old Trenton Road, Cranbury, NJ 08512, Phone: 609-490-1090, e-mail: rmills@blacklightpower.com; www.blacklightpower.com

working on direct plasma to electricity conversion. The device is linearly scaleable from the size of hand held units to large units which could replace large turbines.

There are many advantages of the technology. The energy balance permits the use of electrolysis of water to split water into its elemental constituents of hydrogen and oxygen as the source of hydrogen fuel using a small fraction of the output electricity. Additionally, pollution produced by fossil and nuclear fuels should be eliminated since no green house gases, air pollutants, or hazardous wastes are produced. As no fossil fuels are required, the projected commercial operating costs are much less than that of any known competing energy source.

The Company's process may start with water as the hydrogen source and convert it to HHCs; whereas, fuel cells typically require a hydrocarbon fuel and an expensive reformer to convert hydrocarbons to hydrogen and carbon dioxide. The Company's plasma to electric conversion technology with no reformer, no fuel cost, creation of a valuable chemical by-product rather than pollutants such as carbon dioxide, and significantly lower capital costs and operating and maintenance (O&M) costs are anticipated to result in household units that are competitive with central power and significantly superior to competing microdistributed power technologies such as fuel cells.

2. THE BLACKLIGHT PROCESS

Based on physical laws of nature, Dr. Mills theory predicts that additional lower energy states are possible for the hydrogen atom, but are not normally achieved because transitions to these states are not directly associated with the emission of radiation. Thus, the ordinary hydrogen atom as well as lower-energy hydrogen atoms (termed hydrinos by Dr. Mills) are stable in isolation. Mills theory further predicts that hydrogen atoms can achieve these states by a radiationless energy transfer with a nearby atom, ion, or combination of ions (a catalyst) having the capability to absorb the energy required to effect the transition. Radiationless energy transfer is common. For example, it is the basis of the performance of the most common phosphor used in fluorescent lighting. Thus, the Company believes hydrogen atoms can be induced to collapse to a lower-energy state, with release of the net energy difference between states. Successive stages of collapse of the hydrogen atom are predicted, resulting in the release of energy in amounts many times greater than the energy released by the combustion of hydrogen. Since the combustion energy is equivalent to the energy required to liberate hydrogen from water, a process which takes water as a feed material and produces net energy is possible. The equivalent energy content of water would thus be several hundred to several thousand times that of crude oil, depending on the average number of stages of collapse.

The Company is the pioneer of technology based on the chemical process of releasing further chemical energy from hydrogen called the "BlackLight Process." More specifically, energy is released as the electrons of hydrogen atoms are induced by a catalyst to transition to lower-energy levels (i.e. drop to lower base orbits around each atom's nucleus) corresponding to fractional quantum numbers. The lower energy atomic hydrogen product is called "hydrino," and the hydrogen catalyst to form hydrino is called a "transition catalyst." As hydrogen atoms are normally found bound together as molecules, a hot dissociator is used to break hydrogen molecules into individual hydrogen atoms. A vaporized catalyst then causes the normal hydrogen atoms to transition to lower-energy states by allowing their electrons to fall to smaller radii around the nucleus with a

release of energy that is intermediate between chemical and nuclear energies. The products are power, plasma, light, and novel HHCs.

The catalysts used and the BlackLight Process are the proprietary intellectual property of the Company. The theory, data, and analysis supporting the existence of this new form of energy have been made publicly available.[1-15] Also see the BlackLight Power web page: www.blacklightpower.com. Laboratory scale devices demonstrating means of extracting the energy have been operated at the Company and at independent laboratories. Results to date indicate that the process can eventually provide economically competitive products in a wide range of applications including lighting, thermal, and electric power generation. The Company's gas energy cells, even in prototype stage, are frequently operating at power densities and temperatures equivalent to those of many coal fired electric power plants and produce about 100 times the energy of the combustion of the hydrogen fuel. The plasma is permissive of a direct plasma to electricity conversion technology as well as the production of electricity by conventional heat engines. The Company currently believes that the scale-up of energy cells to commercial power generation level will require mainly the application of existing industry knowledge in catalysis and power engineering.

The lower-energy atomic hydrogen product of the BlackLight Process reacts with an electron to form a hydride ion which further reacts with elements other than hydrogen to form novel compounds which are proprietary to the Company. The Company is developing the vast class of proprietary chemical compounds formed via the BlackLight Process. Test results indicate that the properties of HHCs are rich in diversity due to their extraordinary binding energy (i.e. the energy required to remove an electron which determines the chemical reactivity and properties). This new class of matter may be comparable to carbon in terms of the possibilities of new compositions of matter. Carbon is a base element for many useful compounds ranging from diamonds, to synthetic fibers, to liquid gasoline, to pharmaceuticals. The Company believes hydrino hydride ions have the potential to be as useful as carbon as a base "element." The novel compositions of matter and associated technologies have far-reaching applications in many industries including the chemical, lighting, computer, defense, energy, battery, propellant, munitions, surface coatings, electronics, telecommunications, aerospace, and automotive industries. The Company is focusing on developing a high voltage battery and silane materials based on the novel hydride chemical products. Many additional applications of the chemical compounds are possible.

2.1 Validation

Based on the solution of a Schrödinger-type wave equation with a nonradiative boundary condition based on Maxwell's equations, Mills[1-15] predicts that atomic hydrogen may undergo a catalytic reaction with certain atomized elements or certain gaseous ions which singly or multiply ionize at integer multiples of the potential energy of atomic hydrogen, 27.2 eV.

For example, potassium ions can provide a net enthalpy of a multiple of that of the potential energy of the hydrogen atom. The second ionization energy of potassium is 31.63 eV, and K^+ releases 4.34 eV when it is reduced to K.[16] The combination of reactions K^+ to K^{2+} and K^+ to K, then, has a net enthalpy of reaction of 27.28 eV.

The reaction involves a nonradiative energy transfer to form a hydrogen atom that is lower in energy than unreacted atomic hydrogen. The product hydrogen atom has an

energy state that corresponds to a fractional principal quantum number. Recent analysis of mobility and spectroscopy data of individual electrons in liquid helium show direct experimental confirmation that electrons may have fractional principal quantum levels.[14] The lower-energy hydrogen atom is a highly reactive intermediate which further reacts to form a novel hydride ion. Single line emission from the excited catalyst ion having accepted the energy from atomic hydrogen has been observed with the emission from the predicted hydride ion product.[15] Thus, the catalytic reaction with the formation the novel hydride ions is confirmed spectroscopically.

Typically, the emission of extreme ultraviolet (EUV) light from hydrogen gas is achieved by a discharge at high voltage, a high power inductively coupled plasma, or in hot fusion research, a plasma is created and heated by radio waves to 10s of millions of degrees with confinement of the hot plasma by a toroidal (donut shaped) magnetic field. The Company has observed intense EUV emission at low temperatures from atomic hydrogen and certain atomized pure elements or certain gaseous ions which ionize at integer multiples of the potential energy of atomic hydrogen. The Company has tested over 130 elements and compounds which covers essentially all of the elements of the periodic chart. The chemical interaction of catalysts with atomic hydrogen at temperatures below 1000 K has shown surprising results in terms of the emission of the Lyman and Balmer lines[2-7] (atomic hydrogen emission ten times more energetic than the combustion of hydrogen), emission of lines corresponding to lower-energy hydrogen states and the corresponding hydride ions, and the formation of novel chemical compounds.[8-13]

Over 20 independent labs have performed 25 types of analytical experiments that confirm the Company's novel catalytic reaction of atomic hydrogen which produces an anomalous discharge or plasma and produces novel hydride compounds.[2-13]

Experiments that confirm the novel hydrogen chemistry include extreme ultraviolet (EUV) spectroscopy, plasma formation, power generation, and analysis of chemical compounds. For example:

1. Pennsylvania State University Chemical Engineering Department has determined heat production associated with hydrino formation with a Calvet calorimeter that showed the generation of 10^7 *J/mole* of hydrogen, as compared to 2.5×10^5 *J/mole* of hydrogen anticipated for standard hydrogen combustion.[17] Thus, the total heats generated appear to be 100 times too large to be explained by conventional chemistry, but the results are completely consistent with Mills model.

2. Lines observed by EUV spectroscopy could be assigned to transitions of atomic hydrogen to lower-energy levels corresponding to lower-energy hydrogen atoms and to the emission from the excitation of the corresponding hydride ions.[4]

For example, the product of the catalysis of atomic hydrogen with potassium metal, $H[a_H/4]$ may serve as both a catalyst and a reactant to form $H[a_H/3]$ and $H[a_H/6]$. The transition of $H[a_H/4]$ to $H[a_H/6]$ induced by a multipole resonance transfer of 54.4 *eV* ($2 \cdot 27.2 \ eV$) and a transfer of 40.8 *eV* with a resonance state of $H[a_H/3]$ excited in $H[a_H/4]$ is represented by $H[a_H/4] + H[a_H/4] \rightarrow H[a_H/6] + H[a_H/3] + 176.8 \ eV$.

The predicted 176.8 *eV* (70.2 Å) photon is a close match with the 73.0 Å line observed by a team headed by Dr. Johannes P. F. Conrads, then Director and Chairman of the Board, of Institut Fur Niedertemperatur–Plasmaphysik e.V. and the Ernst–Moritz Arndt–Univeristat Greifswald ("INP"), a top plasma physics laboratory in Greifswald, Germany. The energy of this line emission corresponds to an equivalent temperature of 1,000,000 °C and an energy over 100 times the energy of combustion of hydrogen.

3. Observation of intense extreme ultraviolet (EUV) emission has been reported at low temperatures (e.g $\approx 10^3$ K) from atomic hydrogen and certain atomized elements or certain gaseous ions.[2-7] The only pure elements that were observed to emit EUV were those wherein the ionization of t electrons from an atom to a continuum energy level is such that the sum of the ionization energies of the t electrons is approximately $m \cdot 27.2$ eV where t and m are each an integer. Potassium, cesium, and strontium atoms and Rb^+ ion ionize at integer multiples of the potential energy of atomic hydrogen and caused emission. Whereas, the chemically similar atoms, sodium, magnesium, and barium do not ionize at integer multiples of the potential energy of atomic hydrogen and caused no emission.

4. An energetic plasma in hydrogen was generated using strontium atoms as the catalyst. The plasma formed at 1% of the theoretical or prior known voltage requirement with 4,000–7,000 times less power input power compared to noncatalyst controls, sodium, magnesium, or barium atoms, wherein the plasma reaction was controlled with a weak electric field.[2, 7]

5. An anomalous plasma with hydrogen/potassium mixtures has been reported wherein the plasma decayed with a two second half-life which was the thermal decay time of the filament which dissociated molecular hydrogen to atomic hydrogen when the electric field was set to zero.[5-6] This experiment showed that hydrogen line emission was occurring even though the voltage between the heater wires was set to and measured to be zero and indicated that the emission was due to a reaction of potassium atoms with atomic hydrogen which confirms a new chemical source of power.

Reports of the formation of novel compounds provide substantial evidence supporting a novel reaction of hydrogen as the mechanism of the observed EUV emission and anomalous discharge. Novel hydrogen compounds have been isolated as products of the reaction of atomic hydrogen with atoms and ions identified as catalysts in the reported EUV studies.[2-13] Novel inorganic alkali and alkaline earth hydrides of the formula MH^* and MH^* X wherein M is the metal, X, is a singly negatively charged anion, and H^* comprises a novel high binding energy hydride ion were synthesized in a high temperature gas cell by reaction of atomic hydrogen with a catalyst such as potassium metal and MH, MX or MX_2, corresponding to an alkali metal or alkaline earth metal compound, respectively.[8, 11] Novel hydride compounds were identified by (1) time of flight secondary ion mass spectroscopy which showed a dominate hydride ion in the negative ion spectrum, (2) X-ray photoelectron spectroscopy which showed novel hydride peaks and significant shifts of the core levels of the primary elements bound to the novel hydride ions, (3) proton nuclear magnetic resonance spectroscopy (NMR) which showed extraordinary upfield chemical shifts compared to the NMR of the corresponding ordinary hydrides, and (4) thermal decomposition with analysis by gas chromatography, and mass spectroscopy which identified the compounds as hydrides.[8, 11]

An upfield shifted NMR peak is consistent with a hydride ion with a smaller radius as compared with ordinary hydride since a smaller radius increases the shielding or diamagnetism. Thus, the NMR shows that the hydride formed in the catalytic reaction has been reduced in distance to the nucleus indicating that the electrons are in a lower-energy state. Compared to the shift of known corresponding hydrides the NMR provides direct evidence of reduced energy state hydride ions.

The NMR results confirm the identification of novel hydride compounds MH^*X, MH^* , and MH_2^* wherein M is the metal, H, is a halide, and H^* comprises a novel high binding energy hydride ion. For example, large distinct upfield resonances were observed at –4.6 ppm and –2.8 ppm in the case of KH^*Cl and KH^*, respectively. Whereas, the

resonances for the ordinary hydride ion of *KH* were observed at 0.8 and 1.1 ppm. The presence of a halide in each compound *MH*X* does not explain the upfield shifted NMR peak since the same NMR spectrum was observed for an equimolar mixture of the pure hydride and the corresponding alkali halide (*MH/MX*) as was observed for the pure hydride, *MH*. The synthesis of novel hydrides such as *KH** with upfield shifted peaks prove that the hydride ion is different from the hydride ion of the corresponding known compound of the same composition. The reproducibility of the syntheses and the results from independent laboratories confirm the formation of novel hydride ions.

3. BUSINESS UNITS

The Company believes that it has created a commercially competitive new source of energy, a new source of plasma which releases rather than consumes energy, a new source of light, and a revolutionary new field of hydrogen chemistry. With its achievements of a sustained 100,000+ °C plasma of hydrogen with essentially no power input to its power cell and synthesis of over 40 novel compounds in bulk with extraordinary properties the Company is focusing on product development. Initial target products are a direct plasma to electric power cell targeted at the residential and commercial microdistributed markets and the premium power market. Additional market objectives for the plasma and chemistry technologies are lighting sources, a high voltage battery to power portable electronics and electric vehicles, and chemical products and processes based on silicon and hydrino chemistry.

The Company has two basic business units—power and chemical. The plasma-electric technology may represent a near-term huge energy market. But, in the case of a large central power plant, the Company estimates that the potential revenues from the chemicals produced with power generation may eclipse the electricity sales. However, both offer extraordinary potential revenue and profit. Since enormous power (easily convertible to electricity) is a product of the BlackLight Process, the two units can operate in tandem seamlessly.

The priorities of the Company's power business is the residential and commercial microdistributed markets and the premium power market based on its plasma-electric power cell technology. The time to market should be near term for these relatively small-scale, simple devices that are projected to be inexpensive to manufacture, service, and use, and vastly superior to competing technologies such as internal combustion engine gensets, fuel cells, and microturbines. Selected statistics on electric generation are given in Table 1.

Early adopters of BlackLight power systems are expected to be those that require premium power generated on-site. The premium power market* includes businesses where brief electrical outages can cause severe monetary loss: telecommunications sites, computer centers, server hotels, e-commerce centers, semiconductor fabrication facilities, and others. The market size was estimated to be 30,000 MW in 1999 and growth to be multiples of the entire energy market rate.[18-19] The Glider Group and Stephens Inc.

---

*The premium power market is also known as the 9's market and the powercosm market. Utility grids provide 99.9% reliability, or 8 hours of disruption per year. For the Internet economy even small fractions of a second can cost millions of dollars. In high technology manufacturing industries even hours of disruption can shut down operations for days, again costing millions. More reliability is measured in %, the more 9's required (99.999…%), the smaller the fractions of a second power is disrupted, and the more valuable the power.

Table 1. Statistics on electric generation.

US Electric Market
• $217 billion in annual US sales (1998).
• 43% Residential
• 32% Commercial
• 22% Industrial
• 5% Other
Capital Expenditures Required to Meet New Generation Demand
• Estimated at $90 Billion Globally with 10% in US in 1999
• $21 Billion will be spent on Premium Power in 2000 .
• $30 Billion in 2002
• $50 Billion in 2005
Premium Power Consumption/Demand
• Estimated to be 30,000 MW in 1999
• Estimated to be 500,000 MW in 2000
• Double digit growth expected over next five years

Table 2. Competitive Advantages of The BlackLight Power Process.

Cost Per KWH of Alternative Energy Sources	
Coal	4-5 ¢
Natural Gas	4-5 ¢
Oil	4-5 ¢
Nuclear Power	5-6 ¢
Hydroelectric	4-7 ¢
Geothermal	5-8 ¢
Wind	5-9 ¢
Solar	10-12 ¢
Photovoltaic	30-40 ¢
BlackLight *	<1 ¢

*Cost figures include operating, maintenance, capital generating expense of plasma-electric system (Source: EPRI, BLP)

estimates[20-21] that this market is 15% of the current US energy market; and will be 30–50% within 3–5 years as the internet economy build-out continues. This market is characterized by early adoption of emerging technologies and an insensitivity to cost. For example, a typical rate is over $1,000 per kWh rate and the rate for the upper-end of the reliability scale, six 9's reliable power, is about $1 million per kWh compared to 5 ¢ per kWh for three 9's power supplied by the grid. The premium power market is a multi-billion dollar market. The current equipment market is $21 billion in hardware alone and is projected to ellipse the profitability of the entire utility market in the near term.[22]

BlackLight's Energy Systems design advantages are: virtually instantaneous turn on/off, simplicity, easy logistics, low capital cost, low operational and maintenance cost, easy redundancy (for reliability), and no pollution. With our current design, BlackLight projects capital costs around $25–100 per kW, and very low generation cost (<$0.01 per kWh). This is lower than competitive solutions, but in this market segment cost is not a driver. Our chief competitors are reciprocating engine-based gensets built by Catapillar, Cummins, and others. Additional competition might be from newer entrants: microturbines and fuel cells. The former competitors, fossil-fueled engines, have an advantage because they are an incumbent technology, but they will not be able to significantly improve their reliability, have a short lifetime, do not meet pollution requirements, and can not reduce their O&M costs to be competitive with our solution. The latter competitors have a slight advantage in name recognition relative to BlackLight, but microturbines and fuel cells are not suited for the premium power market. Fuel cells and turbine systems take too long to start up, and are difficult to harmonize with grid-supplied power. Thus they are ineffective at improving power reliability.

Due to superior performance of its technology, the Company expects early adoption by the premium power market with expansion into the broader microdistributed market. The broader market which includes hundreds of millions of homes and businesses in the US and Europe will be drawn by significant cost savings and increasing unreliability of the grid with a lack of viable microdistributed alternatives. The populace of the third world, particularly Asia, represents a further enormous market opportunity for which

BlackLight technology is particularly suited, since in addition to very low capital and O&M costs, no fuel or electrical grid infrastructure is required.

In terms of its development strategy for large scale systems, the Company has decided to focus on developing the chemical business unit as a first priority over large power plants. In addition to the possibility of larger revenue, the chemical business offers several other initial advantages. A power generation plant based on thermal energy would have to be scaled-up while maintaining current or higher levels of power density before it could be commercialized. Scaling up to a power plant of very large proportions has engineering risks. While there are engineering risks associated with the scale-up for chemical production, they are not as daunting. Some potential product areas such as electronics are projected to have very high value in small quantity. Moreover, in terms of gaining widespread scientific and commercial acceptance for the BlackLight Process, it is relatively easy to validate the properties of a chemical compound. A solid chemical compound is a product that can be examined directly and its existence proven unequivocally—it either exists or it doesn't. This also means that its patents are well defined and easy to defend. The products are much more diverse, so broad industry adoption is anticipated.

In addition to direct cell power to electric power conversion, thermal power from the plasma produced by the BlackLight Process may be converted to electricity by powering a turbine. Contemporary central station thermal generation systems have been optimized to match their respective thermal sources. Since BlackLight-technology is not combustion or nuclear, an opportunity exists to dramatically reduce the complexity of the generation station. The BlackLight Process may be used as a thermal source for central or distributed power through use of a modified steam or gas turbine. The BlackLight adaptation of the steam-based system replaces the heat source of the boiler with the gas cell. The BlackLight adaptation of the gas turbine replaces the combustor of a conventional machine with a gas cell and a heat exchanger incorporating the BlackLight Process. High pressure air from the compressor is heated by the BlackLight energy cell heat exchanger before expanding through the power turbine. The exhaust would contain no combustion products. With energy production from hydrogen at a hundred times combustion energy, fuel cost would become an inconsequential consideration, and refueling intervals would be consistent with other maintenance. Alternatively, an on-site electrolysis system producing hydrogen from water could provide unlimited fuel with periodic additions of small quantities of water.

A typical chemical plant is projected to produce 100 MW electric power as a side product. Power and chemical cells may be fabricated using readily available materials, and systems such as steam or gas turbine systems are scalable over a large range [e.g. distributed units (1 MW) to central power plants (1 GW)]. The projected cost for a combined chemical and energy plant is about $250/kW. The two functions could work seamlessly together and generate a dual income stream with a reduction of business risk. Rather than producing nuclear or fossil fuel waste which requires disposal, the BlackLight chemical plant will produce HHCs which have potential for far-reaching applications in many industries such as batteries for electric vehicles at significant earnings. For example, a 100 MW chemical plant is projected to produce $300 M in electric vehicle battery revenue from 200,000 batteries with $23 M from electricity sales at 3 ¢ kWh.

4. SOLUTION TO THE ENERGY PROBLEM?

The world's current energy system is unsustainable. Furthermore, the world's current energy system is not sufficiently reliable or affordable to support widespread economic growth. The productivity of one-third of the world's peoples is compromised by lack of access to commercial energy, and perhaps another third suffer economic hardships and insecurity due to unreliable energy supplies.[23]

Solar and wind power are prohibitively expensive. Billions of dollars have been spent to harness the energy of hydrogen through hot fusion using extremely hot plasmas created with enormous energy input using complex, expensive systems. By contrast, the Company's reactions indicate that over 100 times the energy of its combustion is released from hydrogen with the formation of a plasma as a by-product at relatively low temperatures with simple, inexpensive systems. And, in the Company's reactors, the plasma may be converted directly to electricity with high efficiency avoiding a heat engine such as a turbine. In addition, rather than producing radioactive waste, the BlackLight Process produces compounds having extraordinary properties. The implications are that a vast new energy source and a new field of hydrogen chemistry have been discovered.

The advantages of the BlackLight process over existing energy forms, such as fossil fuels and nuclear power, include: (1) the water, which is the fuel for the process, is safe and inexpensive to contain; (2) the reaction is prospectively easily controlled; and (3) the byproduct, HHCs, have great potential commercial value. The projection of the capital cost per kilowatt capacity of a gyrotron system may be an order of magnitude less than that of the typical capital cost for a fossil fuel system and two orders of magnitude less than that of the typical capital cost for a nuclear system. The power cell may also be interfaced with conventional steam-cycle or gas turbine equipment used in fossil fuel power plants. In either case, fuel costs are eliminated since the fuel, hydrogen, can be generated by a fraction of the electrical output power. The cost factors per kilowatt/hour are the capital, maintenance and operation costs of the gas cell and plant. These costs are further reduced by elimination of the costs of handling fossil fuels and managing the pollution of the air, water, and ground caused by the ash generated by fossil fuels.

4.1. BlackLight Distributed Generation

Central station generation and distribution, the mainstay of electrical power production for the last 100 years worldwide, is now being supplemented in an increasing number of areas by smaller power units closer to the end-user group. Most distributed-generation units are in the capacity range of 100 kW–3 MW (electric), but some could be as large as 250 MW (electric). Distributed generation solves some of centralized power's inherent problems of transmission and distribution line losses, electromagnetic pollution fears from high-tension lines, cost and difficulty of transmission-line maintenance, and inefficiencies in load factor design of power plants (wherein the use of a 20% capacity safety factor is still a common industry practice when estimating peak loading). The Company's technology may be ideal for distributed generation with significant reductions in grid complexity and generation capital equipment requirements.

The Company projects that the residential market may be broadly served by a 25 kW unit, and the commercial market may be broadly served by modular 1 MW units. This approach may replace the grid since in addition to avoidance of line losses, a major economic advantage of distributed power is the avoidance of transmission tariffs which

could amount to 50% of the cost of electricity to a customer. Using BlackLight's distributed power generation technology, considerable savings can be realized by eliminating the transmission and distribution capital equipment, operations, and maintenance costs. Also, energy can be saved, given that electricity "demand" also includes substantial transmission and distribution losses from the traditional central-station type power generation systems. These considerations are important considerations for developing nations.

As the world's population grows from about 6 billion (in 1999) to an estimated 7 billion by 2010, most of the new energy demand will come from less-developed countries (LDCs), as these countries' living standards increase. LDC energy demand has long been answered by economic development programs generally aimed at the development of large, central-station power plants. These do not adequately address the thermal and lighting needs of the half the world's population which is poor, many of whom still use carbon fuels for these purposes. The solution for LDC's may be distributed power facilitated by BlackLight Power technology since no fuel, power plant, or transmission grid infrastructure is required.

5. BLACKLIGHT POWER TECHNOLOGY—A NEW PARADIGM IN ENERGY AND ELECTRICITY GENERATION

The products of the BlackLight Process are power, plasma, light, and novel HHCs. Using advanced catalysts in its gas power cell, the Company has sustained an energetic plasma in hydrogen at 1% of the theoretical or prior-known voltage requirement and with 1000's of times less power input in a system wherein the plasma reaction is controlled with a weak electric field. A plasma is a very hot, glowing, ionized gas. The plasma is produced from reactions which release energies over 100 times the energy of the combustion of hydrogen and correspond to an equivalent electron temperature of over 1,000,000 °C. The plasma produced in the Company's cells cannot be produced by any chemical reaction other than the Company's process.

Typically, a heat engine such as a turbine is used for converting heat into electricity. However, plasma power may be directly converted into electrical power. The technology is not based on heat. Thus, heat sinks such as a river or cooling towers as well as thermal pollution are largely eliminated. Based on research and development in this area of converters, the Company expects that routine engineering will result in devices that have

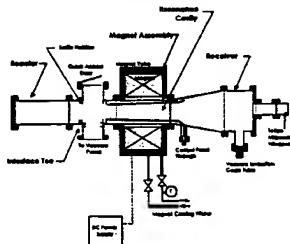Figure 1. Plasma Generated by the BlackLight Process.

Figure 2. Gyrotron Schematic.

higher conversion efficiencies than turbines. The device is linearly scaleable from the size of hand held units to large units which could replace large turbines. And, unlike turbine technology wherein the cost per unit capacity soars with miniaturization, the Company anticipates that the unit cost per capacity will be insensitive to scale. The Company anticipates applications for its technology in broad markets such as premium power, microdistributed power, motive power, consumer electronics, portable electronics, telecommunications, aerospace, and uninterruptable, remote, and satellite power supplies.

Plasma may be directly converted into electricity using a device called a gyrotron which is established technology for converting energetic electrons into microwaves. Conventionally the source of energetic electrons comprises an electron beam or a plasma formed by electrical input such as a high voltage discharge. Prior to the development of the Company's technology, it was not possible to generate a plasma in hydrogen chemically. The BlackLight Process generates an energetic plasma in hydrogen which is *a new source of energy*.

The energy released by the catalysis of hydrogen to form HHCs produces a plasma in the cell. The energetic electrons of the plasma produced by the BlackLight Process are introduced into an axial magnetic field where they undergo cyclotron motion. The force on a charged ion in a magnetic field is perpendicular to both its velocity and the direction of the applied magnetic field. The electrons of the plasma orbit in a circular path in a plane transverse to the applied magnetic field for sufficient field strength at an ion cyclotron frequency ω_c that is independent of the electron velocity. Thus, a typical case which involves a large number of electrons with a distribution of velocities will be characterized by a unique cyclotron frequency that is only dependent on the electron charge to mass ratio and the strength of the applied magnetic field. There is no dependence on their velocities. The velocity distribution will, however, be reflected by a distribution of orbital radii. The electrons emit electromagnetic radiation with a maximum intensity at the cyclotron frequency. The velocity and radius of each electron may decrease due to loss of energy and a decrease of the temperature.

The gyrotron comprises a resonator cavity which has a dominate resonator mode at the cyclotron frequency. The plasma contains electrons with a range of energies and trajectories (momenta) and randomly distributed phases initially. Electromagnetic oscillations are generated from the electrons to produced induced radiation due to the grouping of electrons under the action of the self-consistent field produced by the electrons themselves with coherent radiation of the resulting packets. In this case, the device is a feedback oscillator. The theory of induced radiation of excited classical oscillators such as electrons under the action of an external field and its use in high-frequency electronics is described by A. Gaponov et al.[24] The electromagnetic radiation emitted from the electrons excites the mode of the cavity and is received by a resonant receiving antenna.

The radiated power and the power produced by the BlackLight Process may be matched such that a steady state of power production and power flow from the cell may be achieved. The rate of the hydrogen catalysis reaction may be controlled by controlling the total pressure, the atomic hydrogen pressure, the catalyst pressure, the particular catalyst, and the cell temperature. Very fast response times may be achieved by controlling the rate of reaction and plasma formation with an applied electric or magnetic field which influences the catalysis rate. Plasma and a gyrotron can respond essentially instantaneously. Thus, unprecedented load following capability is possible.

The gyrotron relies on established microwave technology which may achieve very high efficiencies (e.g. 80%) conversion of energetic electrons into microwaves.[25] A 0.1
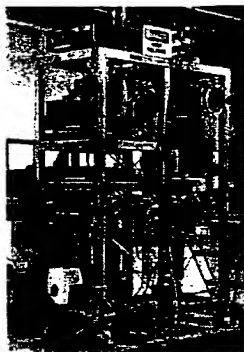
Figure 2. Gyrotron Prototype.

Table 3. Economics of International
Fuel Cells Corp.

Basis: Installed Cost < $1,000/kW DOE Credit—$3,000.kW
Capital Recovery Factor—12%
Annual Load Factor—95% (8,322 hrs of operation)
Electric Efficiency (higher heating value)—36%
Heat Rate—9,480 Btu / kWh
Waste Heat Recovery as Hot Water
(Equivalent to 875,000 Btu/hr of fuel input at 80% efficiency)
Implicit Overall Thermal Efficiency—82%
Natural Gas Cost—$3.50 / million Btu

Cents/kWh	
Capital Charges	4.3
Fuel	3.3
O&M	2.0*
Subtotal	9.6
Hot Water Credit	−1.5
Net Power Cost	8.1

* Includes $600/kW overhaul costs every six years

Tesla magnetic field will produce about 2.5 GHz microwaves. The microwaves are then rectified into DC electricity. Rectification efficiency at 2.5 GHz is about 95%.[26-29] The DC electricity may be inverted and transformed into any desired voltage and frequency with conventional power conditioning equipment.

The plasma formed by the BlackLight Process and the gyrotron have been tested independently. Current work is in progress on testing gyrotron powered by the BlackLight Process generated plasma.

5.1. Power Balance Analysis

The commercial unit would comprises a 3-stage power generator. Stage 1 would be electrolysis to provide hydrogen fuel; stage 2—production of plasma in a gas cell; and stage 3—conversion of plasma to microwaves to electricity.

Using even relatively conservative assumptions for reaction yield and power density, a competitive power generation unit appears easily possible: (1) Production of about 100 times electrical power as electrolysis power; (2) Production of *green* emission (oxygen only) *zero CO_2 emission;* (3) No fossil-fuel combustion by-products; (4) Essentially no waste heat since the gyrotron is not a heat engine; (5) Tremendously more efficient at energy conversion to electricity; and (5) Projected to dominate the home and microdistributed markets.

5.2. Comparison with Competing Microdistributed Technologies

The Company's process may start with water as the hydrogen source and convert it to HHCs; whereas, fuel cells typically require a hydrocarbon fuel and an expensive reformer to convert hydrocarbons to hydrogen and carbon dioxide. The Company's plasma to electric conversion technology with no reformer, no fuel cost, creation of a valuable chemical by-product, and significantly lower capital costs and O&M costs are anticipated to result in household units that are competitive with central power and significantly

superior to competing microdistributed power technology such as fuel cells and micro combustion turbines. With a focus on large scale production of microdistributed devices, the Company anticipates rapid penetration of the electricity energy market. In this case, the Company plans to form strategic alliances with component manufacturers, systems assemblers, and service companies to provide power for consumers with units under lease or by sale. The service companies may be utilities. Other services or utility companies such as water, gas, telephone, cable, plumbing, and HVAC companies are also potential partners. The Company may have its plasma-electric power cell manufactured under contract or license. Alternatively, the Company may manufacture the units itself.

Some of the competitive advantages of BlackLight Power generation over the competing microdistributed technologies fuel cells and micro combustion turbines are no fuel costs, no fuel handling issues nor pollution, not a heat engine and not electrochemical, no reformer, solid state device, chemically-generated plasma with proven microwave technology, linearly scalable, cost competitive (lower capital and O&M costs), long product lifetime, appliance-like, load following, no grid connection (gas or electric for fuel or load leveling), high 9's power capability, closed system, and valuable solid chemical by-product.

With strategic alliances, the Company plans to develop, manufacture, and market a unit of approximately 25 kWe which is a desirable size for a modular uninterruptable power supply for the premium power market. 25 kWe is also capable of providing for the total power requirements of a single family residence or a light commercial load. The potential advantages of the Company's power system compared to fuel cells are (1) zero fuel costs, (2) capital and O&M costs that are 10% that of fuel cells, and (3) valuable chemicals are produced rather than pollutants such as carbon dioxide. Thereby, the cost per kilowatt of electric generated by the Company's plasma-electric power cell is projected to be about 10% of that of a fuel cell. In addition, an energy consumer may also derive revenue by selling power back onto the distribution system when the full capacity of the system is not required by such consumer.

The only mass manufacturable components required to produce a gyrotron system are a magnet, a resonator cavity or waveguide, and a antenna-rectifier. For implementation in the third world and acquisition of market share in the first world, the plasma-electric cell requires essentially no fuel and fuel distribution infrastructure, no regional or on-site pipelines, no utility connection (gas or electrical), no electric lines, and no specialized or centralized manufacturing expertise. In each category, competing technologies are at a competitive disadvantage which could prevent broad adoption even if they were viable based on logistics and costs.

Fuel cells are not cost competitive with BlackLight technology. The cost of electricity with a molten carbonate fuel cell which has a much lower capital cost compared to a proton exchange membrane fuel (PEM). The projected capital cost for a BlackLight 5–25 kW plasma-electric system is as follows: rectifier—$200; inverter—$200, permanent magnet—$150, and cell—$100, totaling $650.

Also with strategic alliances, the Company further plans to develop, manufacture, and market a unit of approximately 1 MWe. One to ten of these units should provide the total power load requirements of a central power grid substation. The potential advantages of the Company's power system compared to central power are the same as with plasma-electric power cell. The cost per kilowatt of electric generated by the Company's plasma-electric power cell is projected to be about 20% of that of central power (see Table 2). With the installation of substation units, light commercial, and residential units, all

components of the present central power generation infrastructure upstream from the substation may be eliminated. Some infrastructure components that may be eliminated by the Company's technology with associated cost savings are: (1) high voltage transformers, (2) high voltage transmission lines, and (3) central power plants, including their associated turbines, fuel and pollution handling systems, ash, pollution, coal trains, coal mines, gas pipelines, gas fields, super tankers, oil fields, nuclear power plants, uranium processing plants, and uranium mines.

5.3. Motive Power—Plasma-Electric and Battery

The capital cost for BlackLight power for motive power are comparable to the cost of an automotive internal combustion engine. Whereas, fuel cells are two orders of magnitude too expensive and require trillions of dollars to be invested in a hydrocarbon to hydrogen refueling system. In contrast, a motive power plant based on BlackLight technology uses water as the fuel and requires no infrastructure. The Company is considering several promising options to commercialize its process in the motive power market. In addition to stationary power, the plasma-electric system may be used for motive power. The Company is also developing a high voltage battery which may power an electric vehicle.

5.4. Conclusion

The BlackLight Process has potentially very broad applications including: electrical power generation, space and process heating, motive power, and production of HHCs.

The technology generates plasma and heat from hydrogen, which may be obtained from ordinary water. The implications of this development could be significant. If the technology becomes proven, then the energy from this process could possibly be used to cleanly and cheaply meet the world's demand for thermal, chemical, and mechanical energy as well as electricity. Over time, it may be possible to replace or retrofit coal-fired, gas-fired, and oil-fired electric power plants. This would help to abate global warming and air and water pollution. Moreover, it may be possible to replace or retrofit some of the world's nuclear power plants. With BlackLight technology, an opportunity exists to dramatically reduce the complexity and the cost of the generation station, which includes fuel handling, thermal generation, thermal to electrical conversion, pollution abatement and spent fuel disposal or storage systems.

The Company is focusing on possible electrical and heating applications for its technology including a fit with a converter to make electricity. Electrical power generation with the Company's plasma-electric power technology may represent a major opportunity to use a microdistributed system to replace existing infrastructure at considerable savings in capital and generation costs. Residential/light commercial units, substation units, and a low voltage local distribution system could replace the central power based current system. Adaptation of the Company's technology is facilitated by the deregulation of the utility industry.

6. REFERENCES

1. R. Mills, *The Grand Unified Theory of Classical Quantum Mechanics*, January 2000 Edition, BlackLight Power, Inc., Cranbury, New Jersey, Distributed by Amazon.com.

2. R. Mills, M. Nansteel, and Y. Lu, Anomalous hydrogen/strontium discharge, *European Journal of Physics D*, submitted.

3. R. Mills, J. Dong, Y. Lu, Observation of extreme ultraviolet hydrogen emission from incandescently heated hydrogen gas with certain catalysts, *Int. J. Hydrogen Energy*, 25, 919-943 (2000).

4. R. Mills, Observation of extreme ultraviolet emission from hydrogen-KI plasmas produced by a hollow cathode discharge, *Int. J. Hydrogen Energy*, in press.

5. R. Mills, Temporal behavior of light-emission in the visible spectral range from a Ti-K_2CO_3-H-cell, *Int. J. Hydrogen Energy*, in press.

6. R. Mills, Y. Lu, and T. Onuma, Formation of a hdrogen pasma from an incandescently heated hydrogen-catalyst gas mixture with an anomalous afterglow duration, *Int. J. Hydrogen Energy*, in press.

7. R. Mills, M. Nansteel, and Y. Lu, Observation of extreme ultraviolet hydrogen emission from incandescently heated hydrogen gas with strontium that produced an anomalous optically measured power balance, *Int. J. Hydrogen Energy*, in press.

8. R. Mills, B. Dhandapani, N. Greenig, J. He, Synthesis and characterization of potassium iodo hydride, *Int. J. of Hydrogen Energy*, 25, 1185-1203 (2000).

9. R. Mills, Novel Inorganic Hydride, *Int. J. of Hydrogen Energy*, 25, 669-683 (2000).

10. R. Mills, Novel hydrogen compounds from a potassium carbonate electrolytic cell, *Fusion Technology*, 37(2) 157-182 (2000).

11. R. Mills, B. Dhandapani, M. Nansteel, J. He, T. Shannon, A. Echezuria, Synthesis and characterization of novel hydride compounds, *Int. J. of Hydrogen Energy*, in press.

12. R. Mills, Highly stable novel inorganic hydrides, *Journal of Materials Research*, submitted.

13. R. Mills, B. Dhandapani, M. Nansteel, J. He, A. Voigt, Identification of compounds containing novel hydride ions by nuclear magnetic resonance spectroscopy, *Int. J. Hydrogen Energy*, submitted.

14. R. Mills, The nature of free electrons in superfluid helium—a test of quantum mechanics and a basis to review its foundations and make a comparison to classical theory, *Int. J. Hydrogen Energy*, submitted.

15. R. Mills, N. Greenig, S. Hicks, Y. Lu, T. Onuma, Spectroscopic identification of a novel catalytic reaction of atomic hydrogen and the hydride ion product, in progress.

16. David R. Linde, *CRC Handbook of Chemistry and Physics*, 79 th Edition, CRC Press, Boca Raton, Florida, (1998-9), p. 10-175 to p. 10-177.

17. J. Phillips, J. Smith, S. Kurtz, Report On Calorimetric Investigations Of Gas-Phase Catalyzed Hydrino Formation, Final Report for Period October-December 1996, January 1, 1997, A Confidential Report submitted to BlackLight Power, Inc. provided by BlackLight Power, Inc., 493 Old Trenton Road, Cranbury, NJ, 08512.

18. USDOE 1999 Report

19. Merrill Lynch Report on Plug Power and Fuel Cell Market Size. December 6, 1999

20. S. Sanders, J. Chumbler, M. P. Zhang, Powering the Digital Economy/Digital Power Demand Meets Industrial Power Supply/Emerging Power Technologies for the Next 100 Years, Published by Stephens Inc. Investment Bankers, 111 Center Street, Little Rock, Arkansas, 72201, August, (2000).

21. T. Cooper, H. Harvey, Power Electronics, "Power Semiconductors and Power Supplies-The Building Blocks of the Digital Power Revolution, Published by Stephens Inc. Investment Bankers, 111 Center Street, Little Rock, Arkansas, 72201, (2000).

22. P. Huber, M. Mills, The Huber Mills Digital Power Report, *Powering the Telecosm*, Gilder Publishing, June 2000, Issue 3.

23. World Energy Assessment, http://services.sciencewise.com/content/index.cfm?objectid=309.

24. A. Gaponov, M. I. Petelin, V. K. Yulpatov, Izvestiya VUZ. Radiofizika, 10(9-10) 1414-1453 (1965).

25. V. A. Flyagin, A. V. Gaponov, M. I. Petelin, and V. K. Yulpatov, IEEE Transactions on Microwave Theory and Techniques, Vol. MTT-25, No. 6, June (1977), pp. 514-521.

26. R. M. Dickinson, Performance of a high-power, 2.388 GHz receiving array in wireless power transmission over 1.5 km, in 1976 IEEE MTT-S International Microwave Symposium, (1976), pp. 139-141.

27. R. M. Dickinson, *Bill Brown's Distinguished Career*, http://www.mtt.org/awards/WCB's%20distinquished %20career.htm.

28. J. O. McSpadden, Wireless power transmission demonstration, Texas A&M University, http://www.tsgc.utexas.edu/power/general/wpt.html; *History of microwave power transmission before 1980*, http://rasc5.kurasc.kyoto-u.ac.jp/docs/plasma-group/sps/history2-e.html.

29. J. O. McSpadden, R. M. Dickson, L. Fan, K. Chang, A novel oscillating rectenna for wireless microwave power transmission, Texas A&M University, Jet Propulsion Laboratory, Pasadena, CA, http://www.tamu.edu, Microwave Engineering Department.

THIS PAGE BLANK (USPTO)

The nature of free electrons in superfluid helium—a test of quantum mechanics and a basis to review its foundations and make a comparison to classical theory

Randell L. Mills *

BlackLight Power, Inc., 493 Old Trenton Road, Cranbury, NJ 08512, USA

Abstract

The Schrödinger equation was originally postulated in 1926 as having a solution of the one electron atom. It gives the principal energy levels of the hydrogen atom as eigenvalues of eigenfunction solutions of the Laguerre differential equation. But, as the principal quantum number $n \gg 1$, the eigenfunctions become nonsensical. Despite its wide acceptance, on deeper inspection, the Schrödinger solution is plagued with many failings as well as difficulties in terms of a physical interpretation that have caused it to remain controversial since its inception. Only the one electron atom may be solved without approximations, but it fails to predict electron spin and leads to models with nonsensical consequences such as negative energy states of the vacuum, infinities, and negative kinetic energy. In addition to many predictions which simply do not agree with observations, the Schrödinger equation predicts noncausality, nonlocality, spooky actions at a distance or quantum telepathy, perpetual motion, and many internal inconsistencies where contradicting statements have to be taken true simultaneously. Recently, the behavior of free electrons in superfluid helium has again forced the issue of the meaning of the wave function. Electrons form bubbles in superfluid helium which reveal that the electron is real and that a physical interpretation of the wave function is necessary. Furthermore, when irradiated with light of energy of about a 0.5 to several electron volts (H.J. Marris, J. Low Temp. Phys. 120 (2000) 173), the electrons carry current at different rates as if they exist with different sizes. It has been proposed that the behavior of free electrons in superfluid helium can be explained in terms of the electron breaking into pieces at superfluid helium temperatures (H.J. Marris, J. Low Temp. Phys. 120 (2000) 173). Yet, the electron has proven to be indivisible even under particle accelerator collisions at 90 GeV (LEPII). The nature of the wave function must now be addressed. It is time for the physical rather than the mathematical nature of the wave function to be determined. A theory of classical quantum mechanics (CQM) was derived from first principles by Mills (The grand unified theory of classical quantum mechanics. January 2000 ed; Cranbury, NJ, 2000, Blacklight Power, Inc., (Distributed by Amazon.com; Posted at www.blacklightpower.com)) that successfully applies physical laws on all scales. Using the classical wave equation with the constraint of nonradiation based on Maxwell's equations, CQM gives closed form physical solutions for the electron in atoms, the free electron, and the free electron in superfluid helium. The prediction of fractional principal quantum energy states of the electron in liquid helium match the photoconductivity and mobility observations without requiring that the electron is divisible. © 2001 International Association for Hydrogen Energy. Published by Elsevier Science Ltd. All rights reserved.

1. Divisible Electron?—is quantum mechanics fundamentally flawed?

In the 103 years since its discovery, there has been no evidence whatsoever that the electron is divisible. But, in

* Tel.: +1-609-490-1090; fax: +1-609-490-1066.
E-mail address: rmills@blacklightpower.com (R.L. Mills).

order to explain, the rise in current of free electrons in superfluid helium when irradiated with low energy light and the observation of an unexpected plethora of exotic negative charge carriers in superfluid helium with mobilities greater than that of the normal electron, Maris [1] has proposed that the electron breaks into fractional pieces. One piece acquires all of the charge and the other is neutral. Maris shows that the Schrödinger equation solution of the wave function of

the 1p state, an excited state, will break into two following the 1s to 1p transition of an electron in superfluid helium. This result is a consequence of the localization of the maximum electron density in the extremes of the dumb-bell shaped 1p orbital with the existence of a node at the center of the orbital. The large differences in time scales of the motion of the electron and the motion of the bubble wall means that the Franck–Condon principle should apply and that the wave function of the electron will deform adiabatically (Born–Oppenheimer principle) at this node to result in electron fission. Following the break, one half of the electron's wave function is trapped in each of the two daughter bubbles. As the wave function is the essence of an electron, the electron splits into two.

Electrons may be trapped in superfluid helium as autonomous electron bubbles interloped between helium atoms that have been excluded from the space occupied by the bubble. The surrounding helium atoms maintain the spherical bubble through van der Waals forces. Superfluid helium is an ideal medium to study individual trapped electrons in much the same way that individual ions may be studied in Penning traps. Both represent an ideal system to test quantum mechanics. Maris and other experimental physicists believe that the data on electrons in liquid helium reveals a fundamental flaw in quantum theory which has caused a furor [3–5]. Electron bubbles in superfluid helium reveal that the electron is real and that a physical interpretation of the wave function is necessary. Physicists have always been content to think of the wave function, the unmeasurable entity which describes quantum systems, as a mathematical device with observable consequences. The time has come for the idea to be grounded in reality. For the electron bubbles in helium, Maris's position is that the size of the bubble is determined by how much of the wave function is trapped inside the bubble. If there is no part of the wave function inside the bubble, the bubble will collapse. This makes the wave function seem to be a tangible object. Theoreticians are going to have to address the question: what is a wave function? Is it a real thing, or just a mathematical convenience? [5].

From the time of its inception, quantum mechanics (QM) has been controversial because its foundations are in conflict with physical laws and are internally inconsistent. Interpretations of quantum mechanics such as hidden variables, multiple worlds, consistency rules, and spontaneous collapse have been put forward in an attempt to base the theory in reality. Unfortunately, many theoreticians ignore the requirement that the wave function must be real and physical in order for it to be considered a valid description of reality. For example, regarding this issue Fuchs and Peres believe [6] "Contrary to those desires, quantum theory does *not* describe physical reality. What it does is provide an algorithm for computing *probabilities* for macroscopic events ("detector ticks") that are the consequences of our experimental interventions. This strict definition of the scope of quantum theory is the only

interpretation ever needed, whether by experimenters or theorists".

With Penning traps, it is possible to measure transitions including those with hyperfine levels of electrons of single ions. This case can be experimentally distinguished from statistics over equivalent transitions in many ions. Whether many or one, the transition energies are always identical within the resonant line width. So, *probabilities* have no place in describing atomic energy levels. Moreover, quantum theory is incompatible with probability theory as shown in the Appendix.

The Copenhagen interpretation provides another meaning of quantum mechanics. It asserts that what we observe is all we can know; any speculation about what an electron, photon, atom, or other atomic-sized entity really is or what it is doing when we are not looking is just that—speculation. The postulate of quantum measurement asserts that the process of measuring an observable forces it into a state of reality. In other words, reality is irrelevant until a measurement is made. In the case of electrons in helium, the fallacy with this position is that the "ticks" (migration times of electron bubbles) reveal that the electron is real before a measurement is made. Furthermore, experiments on Ba$^+$ in a Penning trap discussed in the Appendix demonstrate that the postulate of quantum measurement of quantum mechanics is experimentally disproved. These issues and other such flawed philosophies and interpretations of experiments that arise from quantum mechanics are discussed in the Appendix.

QM gives correlations with experimental data. It does not explain the mechanism for the observed data. But, it should not be surprising that it gives good correlations given that the constraints of internal consistency and conformance to physical laws are removed for a wave equation with an infinite number of solutions wherein the solutions may be formulated as an infinite series of eigenfunctions with variable parameters. There are no physical constraints on the parameters. They may even correspond to unobservables such as virtual particles, hyperdimensions, effective nuclear charge, polarization of the vacuum, worm holes, spooky action at a distance, infinities, parallel universes, faster than light travel, etc. If you invoke the constraints of internal consistency and conformance to physical laws, quantum mechanics has never successfully solved a physical problem.

Throughout the history of quantum theory; wherever there was an advance to a new application, it was necessary to repeat a trial-and-error experimentation to find which method of calculation gave the right answers. Often the textbooks present only the successful procedure as if it followed from first principles; and do not mention the actual method by which it was found. In electromagnetic theory based on Maxwell's equations, one deduces the computational algorithm from the general principles. In quantum theory, the logic is just the opposite. One chooses the principle to fit the empirically successful algorithm. For example, we know that it required a great deal of art and

tact over decades of effort to get correct predictions out of Quantum Electrodynamics (QED). For the right experimental numbers to emerge, one must do the calculation (i.e. subtract off the infinities) in one particular way and not in some other way that appears in principle equally valid. There is a corollary, noted by Kallen: from an inconsistent theory, any result may be derived.

Reanalysis of old experiments and many new experiments including electrons in superfluid helium challenge the Schrödinger equation predictions. These issues are discussed in context of a theory of classical quantum mechanics (CQM) derived from first principles by Mills [2]. Using the classical wave equation with the constraint of nonradiation based on Maxwell's equations, CQM gives closed form physical solutions for the electron in atoms, the free electron, and the free electron in superfluid helium which match the observations without requiring that the electron is divisible.

1.1. The Schrödinger theory of the hydrogen atom

In 1911, Rutherford proposed a planetary model for the atom where the electrons revolved about the nucleus (which contained the protons) in various orbits to explain the spectral lines of atomic hydrogen. There was, however, a fundamental conflict with this model and the prevailing classical physics. According to classical electromagnetic theory, an accelerated particle radiates energy (as electromagnetic waves). Thus, an electron in a Rutherford orbit, circulating at constant speed but with a continually changing direction of its velocity vector is being accelerated; thus, the electron should constantly lose energy by radiating and spiral into the nucleus.

An explanation was provided by Bohr in 1913, when he assumed that the energy levels were quantized and the electron was constrained to move in only one of a number of allowed states. Niels Bohr's theory for atomic hydrogen was based on an unprecedented postulate of stable circular orbits that do not radiate. Although no explanation was offered for the existence of stability for these orbits, the results gave energy levels in agreement with Rydberg's equation. Bohr's solution is trivial in that he specified a circular bound orbit which determined that the eccentricity was zero, and he specified the angular momentum as a integer multiple of Planck's constant bar. The solution given by Mills [7] in CGS units is

$$E = -\frac{1}{2}\frac{me^4}{n^2\hbar^2} = -\frac{e^2}{2n^2}a_0 \quad (1)$$

In 1923, de Broglie suggested that the motion of an electron has a wave aspect—$\lambda = h/p$. This was confirmed by Davisson and Germer in 1927 by observing diffraction effects when electrons were reflected from metals. Schrödinger reasoned that if electrons have wave properties, there must be a wave equation that governs their motion. And, in 1926, he proposed the time-independent Schrödinger equation

$$H\Psi = E\Psi \quad (2)$$

where Ψ is the wave function, H is the wave operator, and E is the energy of the wave. To give the sought three quantum numbers, the Schrödinger equation solutions are three-dimensional in space and four-dimensional in space-time

$$\left[\nabla^2 - \frac{1}{v^2}\frac{\delta^2}{\delta t^2}\right]\Psi(r,\theta,\phi,t) = 0, \quad (3)$$

where $\Psi(r,\theta,\phi,t)$ according to quantum theory is the probability density function of the electron as described below and the Appendix under Wave Function Solutions of Quantum Mechanics as Probability Waves are Inconsistent with Probability Theory. When the time harmonic function is eliminated [8],

$$-\frac{\hbar^2}{2\mu}\left[\frac{1}{r^2}\frac{\delta}{\delta r}\left(r^2\frac{\delta\Psi}{\delta r}\right) + \frac{1}{r^2\sin\theta}\frac{\delta}{\delta\theta}\left(\sin\theta\frac{\delta\Psi}{\delta\theta}\right)_{r,\phi}\right.$$
$$\left. + \frac{1}{r^2\sin^2\theta}\left(\frac{\delta^2\Psi}{\delta\phi^2}\right)_{r,\theta}\right] + V(r)\Psi(r,\theta,\phi) = E\Psi(r,\theta,\phi)$$
$$(4)$$

where the potential energy $V(r)$ in CGS units is

$$V(r) = -\frac{e^2}{r}. \quad (5)$$

The Schrödinger equation (Eq. (4)) can be transformed into a sum comprising a part that depends only on the radius and a part that is a function of angle only obtained by separation of variables and linear superposition in spherical coordinates. The general form of the solutions for $\psi(r,\theta,\phi)$ are

$$\psi(r,\theta,\phi) = \sum_{l,m} R_{nlm}(r)Y_{lm}(\theta,\phi) \quad (6)$$

where l and m are separation constants. The azimuthal (θ) part of Eq. (4) is the generalized Legendre equation which is derived from the Laplace equation by Jackson (Eq. (3.9) of Jackson [9]). The solutions for the full angular part of Eq. (4), $Y_{lm}(\theta,\phi)$, are the spherical harmonics

$$Y_{lm}(\theta,\phi) = \sqrt{\frac{(2l+1)(l-m)!}{4\pi(l+m)!}}P_l^m(\cos\theta)e^{im\phi}. \quad (7)$$

By substitution of the eigenvalues corresponding to the angular part [8, pp. 221–224] the Schrödinger equation becomes the radial equation, $R(r)$, given by

$$-\frac{\hbar^2}{2mr^2}\frac{d}{dr}\left(r^2\frac{dR}{dr}\right) + \left[\frac{\hbar^2 l(l+1)}{2mr^2} + V(r)\right]R(r)$$
$$= ER(r). \quad (8)$$

The time-independent Schrödinger equation is similar to Eq. (20) of Mills [7], except that the solution is for the distribution of a spatial wave function in three dimensions rather than the dynamical motion of a point particle of mass m along a one-dimensional trajectory. Electron motion is implicit in the Schrödinger equation. For wave propagation in three dimensions, the full time-dependent Schrödinger equation is required; whereas, the classical case contains time

derivatives. The kinetic energy of rotation K_{rot} is given classically by

$$K_{rot} = \tfrac{1}{2}mr^2\omega^2 \tag{9}$$

where m is the mass of the electron. In the time-independent Schrödinger equation, the kinetic energy of rotation K_{rot} is given by

$$K_{rot} = \frac{\ell(\ell+1)\hbar^2}{2mr^2} \tag{10}$$

where

$$L = \sqrt{\ell(\ell+1)\hbar^2} \tag{11}$$

is the value of the electron angular momentum L for the state $Y_{lm}(\theta,\phi)$.

In the case of the ground state of hydrogen, the Schrödinger equation solution is trivial for an implicit circular bound orbit which determines that the eccentricity is zero, and with the specification that the electron angular momentum is Planck's constant bar. With $k = e^2$, Eq. (25) of Mills [7] in CGS units becomes

$$E = -\frac{1}{2}\frac{me^4}{\hbar^2} = -\frac{e^2}{2a_0} \tag{12}$$

which corresponds to $n = 1$ in Eq. (1). Many problems in classical physics give three quantum numbers when three spatial dimensions are considered. In order to obtain three quantum numbers, the Schrödinger equation requires that the solution is for the distribution of a spatial wave function in three dimensions with implicit motion rather than a one-dimensional trajectory of a point particle as shown below. However, this approach gives rise to predictions about the angular momentum and angular energy which are not consistent with experimental observations as well as a host of other problems which are summarized below.

The radial equation may be written as [10]

$$\frac{d}{dr}\left(r^2\frac{dR}{dr}\right) + \frac{2mr^2}{\hbar^2}\left[E - V(r) - \frac{l(l+1)\hbar^2}{2mr^2}\right]R(r) = 0. \tag{13}$$

Let $U(r) = rR(r)$, then the radial equation reduces to

$$U'' + \frac{2m}{\hbar^2}\left[E - V(r) - \frac{l(l+1)\hbar^2}{2mr^2}\right]U = 0 \tag{14}$$

where

$$\psi = \frac{1}{r}U_{lm}(r)Y_{lm}(\theta,\phi). \tag{15}$$

Substitution of the potential energy given by Eq. (5) into Eq. (14) gives for sufficiently large r

$$U_\infty'' - \left(\frac{\alpha}{2}\right)^2 U = 0 \tag{16}$$

provided we define

$$\left(\frac{\alpha}{2}\right)^2 = \frac{-2mE}{\hbar^2} \tag{17}$$

where α is the eigenvalue of the eigenfunction solution of the Schrödinger equation given *infra* having units of

reciprocal length and E is the energy levels of the hydrogen atom. To arrive at the solution which represents the electron, a suitable boundary condition must be imposed. Schrödinger postulated a boundary condition: $\Psi \to 0$ as $r \to \infty$, which leads to a purely mathematical model of the electron. This equation is *not* based on first principles, has no validity as such, and should not be represented as so. The right-hand side of Eq. (17) must be *postulated* in order that the Rydberg equation is obtained as shown below. The postulate is implicit since Eq. (17) arises from the Schrödinger which is postulated. It could be defined *arbitrarily*, but is justified because it gives the Rydberg formula. That Schrödinger guessed the accepted approach is not surprising since many approaches were contemplated at this time [11], and since none of these approaches were superior, Schrödinger's approach prevailed.

The solution of Eq. (16) that is consistent with the boundary condition is

$$U_\infty = c_1 e^{(\alpha/2)r} + c_2 e^{-(\alpha/2)r}. \tag{18}$$

In the case that α is real, the energy of the particle is negative. In this case U_∞ will not have an integrable square if c_1 fails to vanish wherein the radial integral has the form

$$\int_0^\infty R^2 r^2\, dr = \int U_\infty^2\, dr. \tag{19}$$

It is shown below that the solution of the Schrödinger corresponds to the case wherein C_1 fails to vanish. Thus, the solutions with sufficiently large r are infinite. The same problem arises in the case of a free electron that is ionized from hydrogen. If α is imaginary, which means that E is positive, Eq. (16) is the equation of a linear harmonic oscillator [12]. U_∞ shows sinusoidal behavior; thus, the wave function for the free electron cannot be normalized and is infinite. In addition, the angular momentum of the free electron is infinite since it is given by $\ell(\ell+1)\hbar^2$ (Eq. (11)) where $\ell \to \infty$.

In order to solve the bound electron states, let

$$E = -W \tag{20}$$

so that W is positive. In Eq. (13), let $r = x/\alpha$ where α is given by Eq. (17).

$$x\frac{d^2R}{dx^2} + 2\frac{dR}{dx} + \left[\frac{2me^2}{\hbar^2\alpha} - \frac{x}{4} - \frac{l(l+1)}{x}\right]R = 0. \tag{21}$$

Eq. (21) is the differential equation for associated Laguerre functions given in general form by

$$xy'' + 2y' + \left[n^* - \frac{k-1}{2} - \frac{x}{4} - \frac{k^2-1}{4x}\right]y = 0 \tag{22}$$

which has a solution possessing an integrable square of the form

$$y = e^{-x/2}x^{(k-1)/2}L_{n^*}^k(x). \tag{23}$$

provided that n^* and k are positive integers. However, n^* does not have to be an integer, it may be any *arbitrary*

constant β. Then the corresponding solution is [13]

$$y = e^{-\epsilon/2} x^{(k-1)/2} \frac{d^k}{dx^k} L_\beta(x). \tag{24}$$

In the case that n^* is chosen to be an integer in order to obtain the Rydberg formula, $n^* - k \geqslant 0$ since otherwise $L_{n^*}^k(x)$ of Eq. (23) would vanish. By comparing Eqs. (21) and (22),

$$\frac{k^2 - 1}{4} = \ell(\ell + 1). \tag{25}$$

Thus,

$$k = 2\ell + 1 \tag{26}$$

and

$$n^* - \frac{k-1}{2} = n^* - \ell = \frac{me^2}{\hbar} \left(\frac{\alpha}{2}\right)^{-1}. \tag{27}$$

Substitution of the value of α and solving for W gives

$$W = \frac{1}{2} \frac{me^4}{(n^* - \ell)^2 \hbar^2}. \tag{28}$$

Because of the conditions on n^* and k, the quantity $n^* - \ell$ cannot be zero. It is usually denoted by n and called the principal quantum number. The energy states of the hydrogen atom are

$$W_n = -E_n = \frac{1}{2} \frac{me^4}{n^2 \hbar^2} \tag{29}$$

and the corresponding eigenfunctions from Eq. (23) are

$$R_{n,\ell} = c_{n,\ell} e^{-x/2} x^\ell L_{n+\ell}^{2\ell+1}(x) \tag{30}$$

where the variable x is defined by

$$x = \alpha r = \frac{\sqrt{8mW}}{\hbar} r = \frac{2me^2}{n\hbar^2} r. \tag{31}$$

In the Bohr theory of the hydrogen atom, the first orbital has a radius in CGS units given by

$$a_0 = \frac{\hbar^2}{me^2} = 0.53 \times 10^{-8} \text{ cm}. \tag{32}$$

Thus, $\alpha = 2/na_0$ and

$$x = \frac{2}{n} \frac{r}{a_0}. \tag{33}$$

The energy states of the hydrogen atom in CGS units in terms of the Bohr radius are given by Eq. (1). From Eq. (30), $R_{n,\ell}$ for the hydrogen atom ground state is

$$R_{1,0} = c_{1,0} e^{-r/a_0} L_1^1 = 2a_0^{-3/2} e^{-r/a_0}. \tag{34}$$

For this state

$$Y_{00} = \text{constant} = (4\pi)^{-1/2} \tag{35}$$

when the function is normalized. Thus, the "ground state function" *defined* by the *arbitrary* selection of n^* at Eq. (22) is

$$\psi_0 = (\pi a_0^3)^{-1/2} e^{-r/a_0}. \tag{36}$$

In fact, the Schrödinger can only yield integer eigenvalue solutions by selection from an infinite number of possibilities since the solution is over all space with no boundary (i.e. 0 to ∞). In contrast, wave equation solutions with integers are common for boundary constrained systems such as wave guides and resonators.

1.2. The postulated Schrödinger equation fails to solve the hydrogen atom correctly

The paper by Mills [7] rigorously analyzes the Schrödinger equation. One of many possible solutions of the postulated Schrödinger equation gives the Rydberg levels as does the theory of Bohr. On this basis alone, it is justified despite its inconsistency with physicals laws and numerous experimental observations such as

- The appropriate eigenvalue must be postulated and the variables of the Laguerre differential equation must be defined as integers in order to obtain the Rydberg formula.
- The Schrödinger equation is not Lorentzian invariant.
- The Schrödinger equation violates first principles including special relativity and Maxwell's equations.
- The Schrödinger equation gives no basis why excited states are radiative and the 13.6 eV state is stable. Mathematics does not determine physics. It only models physics.
- In the time-independent Schrödinger equation, the kinetic energy of rotation K_{rot} is given by Eq. (10) where the value of the electron angular momentum L for the state $Y_{lm}(\theta, \phi)$ is given by Eq. (11). The Schrödinger equation solutions, Eqs. (10) and (11), predict that the ground state electron has zero angular energy and zero angular momentum, respectively.
- The Schrödinger equation solution, Eq. (11), predicts that the ionized electron may have infinite angular momentum.
- The Schrödinger equation solutions, Eqs. (10) and (11), predict that the excited state rotational energy levels are nondegenerate as a function of the ℓ quantum number, even in the absence of an applied magnetic field, and the predicted energy is over six orders of magnitude of the observed nondegenerate energy in the presence of a magnetic field. In the absence of a magnetic field, no preferred direction exists. In this case, the ℓ quantum number is a function of the orientation of the atom with respect to an arbitrary coordinate system. Therefore, the nondegeneracy is nonsensical and violates conservation of angular momentum of the photon.
- The Schrödinger equation predicts that each of the functions that corresponds to a highly excited state electron is not integrable and can not be normalized; thus, each is infinite.
- The Schrödinger equation predicts that the ionized electron is sinusoidal over all space and cannot be normalized; thus, it is infinite.
- The Heisenberg uncertainty principle arises as the standard deviation in the electron probability wave, but experimentally it is not the basis of wave particle duality as shown in the Appendix.
- Quantum mechanical textbooks express the movement of the electron, and the Heisenberg uncertainty principle is an expression of the statistical aspects of this movement. McQuarrie [8, back cover], gives the electron speed in the

$n = 1$ state of hydrogen as 2.18764×10^6 m/s. Remarkably, the uncertainty in the electron speed according to the uncertainty principle is 1.4×10^7 m/s [8, p. 38] which is an order of magnitude larger that the speed.

- Experimentally the electron has precise velocity, kinetic energy, and angular momentum. Acquiring these exact properties instantaneously defies all known physical principles.

- The correspondence principle does not hold experimentally.

- The Schrödinger equation does not predict the electron magnetic moment and misses the spin quantum number all together.

- The Schrödinger equation is not a wave equation since it gives the velocity squared proportional to the frequency.

- The Schrödinger equation is not consistent with conservation of energy in an inverse potential field wherein the binding energy is equal to the kinetic energy and the sum of the binding energy and the kinetic energy is equal to the potential energy.

- The Schrödinger equation permits the electron to exist in the nucleus which is a state that is physically nonsensical with infinite potential energy and infinite negative kinetic energy.

- The Schrödinger equation interpreted as a probability wave of a point particle cannot explain neutral scattering of electrons from hydrogen.

- The Schrödinger equation interpreted as a probability wave of a point particle gives rise to infinite magnetic and electric energy in the corresponding fields of the electron.

- A modification of the Schrödinger equation was developed by Dirac to explain spin which relies on the unfounded notions of negative energy states of the vacuum, virtual particles, and gamma factors.

The success of quantum mechanics can be attributed to (1) the lack of rigor and unlimited tolerance to ad hoc assumptions in violation of physical laws, (2) fantastical experimentally immeasurable corrections such as virtual particles, vacuum polarizations, effective nuclear charge, shielding, ionic character, compactified dimensions, and renormalization, and (3) curve fitting parameters that are justified solely on the basis that they force the theory to match the data. Quantum mechanics is now in a state of crisis with constantly modified versions of matter represented as undetectable minuscule vibrating strings that exist in many unobservable hyperdimensions, that can travel back and forth between undetectable interconnected parallel universes. (An analysis of the many failings of quantum mechanics are given in the Appendix.) And, recent data shows that the expansion of the universe is accelerating. This observation has shattered the long held unquestionable doctrine of the origin of the universe as a big bang [14]. It may be time to reconsider the roots of quantum theory, namely the theory of the hydrogen atom. Especially in light of the observation of real electron bubbles in helium which require that the electron is divisible in order for the Schrödinger equation to explain the increase in conductivity upon irradiation with low-energy light. This argument is reinforced by the demonstration that the electron in atoms, the free electron, and the free electron in superfluid helium can be solved physically rather than mathematically in closed form equations from first principles. The predictions match the observations without requiring that the electron is a probability wave or is divisible.

2. A classical approach to quantum mechanics

2.1. Introduction

A theory of classical quantum mechanics (CQM) was derived from first principles by Mills [2] that successfully applies physical laws on all scales. The classical wave equation is solved with the constraint that a bound electron cannot radiate energy. The mathematical formulation for zero radiation based on Maxwell's equation follows from a derivation by Haus [15]. The function that describes the motion of the electron must not possess spacetime Fourier components that are synchronous with waves traveling at the speed of light. CQM gives closed form solutions for the atom including the stability of the $n = 1$ state and the instability of the excited states, the equation of the photon and electron in excited states, the equation of the free electron, and photon which predict the wave particle duality behavior of particles and light. The current and charge density functions of the electron may be directly physically interpreted. For example, spin angular momentum results from the motion of negatively charged mass moving systematically, and the equation for angular momentum, $r \times p$, can be applied directly to the wave function (a current density function) that describes the electron. The magnetic moment of a Bohr magneton, Stern Gerlach experiment, g factor, Lamb shift, resonant line width and shape, selection rules, correspondence principle, wave particle duality, excited states, reduced electron mass, rotational energies, and momenta, orbital and spin splitting, spin-orbital coupling, Knight shift, and spin-nuclear coupling are derived in closed form equations based on Maxwell's equations. The calculations agree with experimental observations.

Many great physicists rejected quantum mechanics. Feynman also attempted to use first principles including Maxwell's Equations to discover new physics to replace quantum mechanics [16]. Other great physicists of the 20th century searched. "Einstein [...] insisted [...] that a more detailed, wholly deterministic theory must underlie the vagaries of quantum mechanics [17]". He felt that scientists were misinterpreting the data.

The results of Mill's theory demonstrate that classical physical laws describe reality on all scales. Unlike quantum mechanics which postulates that different laws apply on the

atomic level, the premise of Mill's theory is that a valid theory must comply with *all* of the following:

- theory must be internally consistent even between widely different phenomena,
- Maxwell's equations,
- conservation of matter/energy,
- conservation of linear and angular momentum,
- charge conservation,
- first and second law of thermodynamics,
- Newton's law in the low speed limit; special relativity otherwise,
- general relativity (e.g. Schwarzschild metric)—no cosmological constant; and Newtonian gravitation in the weak field limit (which demands no cosmological constant),
- a vacuum is a vacuum,
- constant maximum of the speed of light in a vacuum,
- 4 dimensional spacetime,
- the only allowed parameters are the measured fundamental constants.

Quantum mechanics is based on engendering the electron with a wave nature as suggested by the Davisson–Germer experiment and fabricating a set of associated postulates and mathematical rules for wave operators. Quantum mechanics is in violation of Maxwell's equations as shown through application of Haus's condition to the Schrödinger wave functions [15]. Nonradiation based on Maxwell's equations is a necessary boundary constraint since nonradiation is observed experimentally. The shortcoming of QM regarding violation of Maxwell's equations and other first principles are further discussed in the Appendix.

2.2. Mills approach to the solution of the electron

Mills solves the electron by a different approach than that used to solve the Schrödinger wave equation. Rather than using a postulated wave equation with time eliminated in terms of the energy of the electron in a Coulomb field and solving the charge wave (Schrödinger interpretation) or the probability wave (Born interpretation), the solution for the scalar (charge) and vector potential (current) functions of the electron are sought based on first principles. Mills first assumes that the functions that physically describe the mass and charge of the electron in space and time obey the wave equation since it conserves energy and angular momentum. The solution is generalized to be three-dimensional plus time. Rather than use the postulated Schrödinger boundary condition: $\Psi \rightarrow 0$ as $r \rightarrow \infty$, which leads to a purely mathematical model of the electron, the constraint is based on experimental observation that the moving charge must not radiate. Application of the Haus condition based on Maxwell's equations to a generalized three dimension plus time wave equation requires that the functions must be solutions of Eq. (51), a two-dimensional wave equation plus time. This is consistent with first principle laws and

ultimately matches experimentation. However, it is unconventional.

The two-dimensional wave equation plus time is given by McQuarrie [8, p. 207]. The electron is confined to two dimensions (θ and ϕ) plus time. Spherical harmonic functions and time harmonic functions are well-known solutions of the angular and time components of the two-dimensional wave equation plus time, respectively. The solutions appear in McQuarrie [8, pp. 206–225]. A constant current function is also a solution of the wave equation. A constant function corresponding to the electron spin function is added to each of the spherical harmonic functions to give the charge (mass) density functions of the electron as a function of time. The integral of a spherical harmonic function over θ and ϕ is zero. The integral of the constant function over θ and ϕ is the total charge (mass) of the electron. These functions comprise the well-known s, p, d, f, etc. electrons or orbitals. In the case that such an electron state arises as an excited state by photon absorption, it is radiative due to a radial dipole term in its current density function since it possesses spacetime Fourier components synchronous with waves traveling at the speed of light.

The excited states are solved, including the radii of the orbitspheres, using Maxwell's equations with the traditional source current boundary constraints at the electron. Quantization arises from the equation of the photon and the electron—not from the solution of the electron alone. After all, each solution is for an excited state created by the absorption of a photon. The solutions are analogous to those of excited resonator modes except that the cavity is dynamic. The field lines from the proton end on the current density function of the electron, and the electric field is zero for $r > r_n$. The trapped photons are a solution of the three-dimensional wave equation plus time given by Maxwell's equations. The electrodynamic field of the photon is a constant function plus a time and spherical harmonic function that is in phase with source currents at the electron which is given by a constant plus a time and spherical harmonic function. Only particular solutions are possible as resonant photons of the electron which is a dynamic resonator cavity. The results are in agreement with first principle physics and experimental observations of the hydrogen atom, excited states, free electron, and free space photon, including the wave particle duality aspects.

2.3. Spin and orbital parameters arise from first principles

An electron is a spinning, two-dimensional spherical surface, called an *electron orbitsphere*, that can exist in a bound state only at specific radii r_n from the nucleus. (See Fig. 1 for a pictorial representation of an orbitsphere.) The result for the $n = 1$ state of hydrogen is that the charge density function remains constant with each point on the surface moving at the same angular and linear velocity. The constant function solution of the two-dimensional wave equation corresponds to the spin function which has a corresponding spin angular

The orbitsphere has zero thickness.
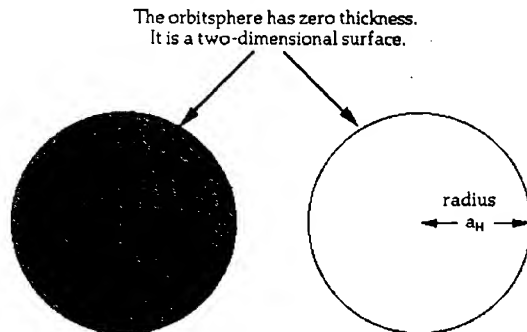It is a two-dimensional surface.

radius
← a_H →

Fig. 1. The orbitsphere is a two-dimensional spherical shell with the Bohr radius of the hydrogen atom.

momentum that may be calculated from $\mathbf{r} \times \mathbf{p}$ applied directly to the current density function that describes the electron. The radius of the nonradiative ($n = 1$) state is solved using the electromagnetic force equations of Maxwell relating the charge and mass density functions, wherein the angular momentum of the electron is given by Planck's constant bar (Eq. (1.165) of [2]). The reduced mass arises naturally from an electrodynamic interaction between the electron and the proton, rather than from a point mass revolving around a point nucleus in the case of Schrödinger wave equation solutions which presents an internal inconsistency since the wave functions are spherically symmetrical.

CQM gives closed form solutions for the resonant photons and excited state electron functions. Angular momentum of the photon given by $\mathbf{m} = (1/8\pi)\text{Re}[\mathbf{r} \times (\mathbf{E} \times \mathbf{B}^*)]\hbar$ is conserved. The change in angular velocity of the electron is equal to the angular frequency of the resonant photon. The energy is given by Planck's equation. The predicted energies, Lamb shift, hyperfine structure, resonant line shape, line width, selection rules, etc. are in agreement with observation.

The radii of excited states are solved using the electromagnetic force equations of Maxwell relating the field from the charge of the proton, the electric field of the photon, and charge and mass density functions of the electron wherein the angular momentum of the electron is given by Planck's constant bar (Eq. (1.165) of [2]).

For excited states of the hydrogen atom, the constant function solution of the two-dimensional wave equation corresponds to the spin function. Each spherical harmonic function modulates the constant spin function and corresponds to an orbital function of a specific excited state with a corresponding phased-matched-trapped photon and orbital angular momentum. Thus, the spherical harmonic function behaves as a charge density wave which travels time harmonically on the surface of the orbitsphere

about a specific axis. (See Fig. 2 for a pictorial representation.) An amplitude of the corresponding orbital energy may be calculated from Maxwell's equations. Since the constant function is modulated harmonically, the time average of the orbital energy is zero except in the presence of a magnetic field. Nondegeneracy of energy levels arises from spin, orbital, and spin-orbital coupling interactions with the applied field. The electrodynamics interaction with the magnetic field gives rise to the observed hyperfine splitting of the hydrogen spectrum.

Many inconsistencies arise in the case of the corresponding solutions of the Schrödinger wave equation. For example, where is the photon in excited states given by the Schrödinger equation? And a paradox arises for the change in angular momentum due to photon absorption. The Schrödinger equation solutions for the kinetic energy of rotation K_{rot} is given by Eq. (10) and the value of the electron angular momentum L for the state $Y_{lm}(\theta, \phi)$ given by Eq. (11) predict that the excited state rotational energy levels are nondegenerate as a function of the ℓ quantum number even in the absence of an applied magnetic field, and the predicted energy is over six orders of magnitude of the observed nondegenerate energy in the presence of a magnetic field. In the absence of a magnetic field, no preferred direction exists. In this case, ℓ the quantum number is a function of the orientation of the atom with respect to an arbitrary coordinate system. Therefore, the nondegeneracy is nonsensical and violates conservation of angular momentum of the photon.

In quantum mechanics, the spin angular momentum of the electron is called the "intrinsic angular momentum" since no physical interpretation exists. The Schrödinger equation is not Lorentzian invariant in violation of special relativity. It failed to predict the results of the Stern–Gerlach experiment which indicated the need for an additional quantum number. Quantum electrodynamics was proposed by Dirac in 1926

Modulation Function (Orbital)	Constant Function (Spin)	Spatial Charge Density Function	Orbitsphere

$\ell = 0$

$\ell = 1$

$$Re\left\{Y_1^1(\theta,\phi)\left[1 + e^{i\omega_n t}\right]\right\} = \sin\theta\cos(\phi + \omega_n t)$$

$\ell = 2$

$$Re\{Y_2^0\} = \frac{3}{2}\cos^2\theta - \frac{1}{2}$$

$\ell = 2$

$$Re\left\{Y_2^1(\theta,\phi)\left[1 + e^{i\omega_n t}\right]\right\} = \sin\theta\cos\theta\cos(\phi + \omega_n t)$$
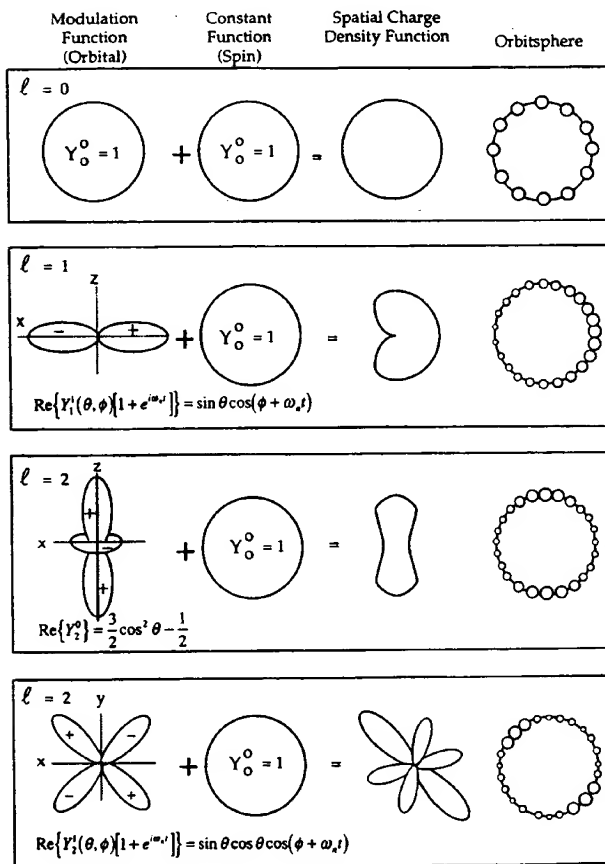
Fig. 2. The orbital function modulates the constant (spin) function (shown for $t = 0$; cross-sectional view).

to provide a generalization of quantum mechanics for high energies in conformity with the theory of special relativity and to provide a consistent treatment of the interaction of matter with radiation. It is fatally flawed. From Weisskopf [18], "Dirac's quantum electrodynamics gave a more consistent derivation of the results of the correspondence principle, but it also brought about a number of new and serious difficulties." Quantum electrodynamics: (1) *does not explain nonradiation of bound electrons*; (2) contains an internal inconsistency with special relativity regarding the classical electron radius—the electron mass corresponding

to its electric energy is infinite (the Schrödinger equation fails to predict the classical electron radius); (3) it admits solutions of negative rest mass and negative kinetic energy; (4) the interaction of the electron with the predicted zero-point field fluctuations leads to infinite kinetic energy and infinite electron mass; and (5) Dirac used the unacceptable states of negative mass for the description of the vacuum; yet, infinities still arise. Dirac's equation which was postulated to explain spin relies on the unfounded notions of negative energy states of the vacuum, virtual particles, and gamma factors. All of these features are untenable or are inconsistent

with observation. These problems regarding spin and orbital angular momentum and energies and the classical electron radius are nonexistent with CQM solutions [2].

Furthermore, Mills [2, pp. 1–21] shows that the Schrödinger equation may be transformed into a form consistent with first principles. In the case that the potential energy of the Hamiltonian, H, is a constant times the wave number, the Schrödinger equation is the well-known Bessel equation. Then with one of the solutions for the wave function Ψ (a current density function rather than a probability wave) is equivalent to an inverse Fourier transform. According to the duality and scale change properties of Fourier transforms, the energy equation of Mills theory and that of quantum mechanics are identical, the energy of a radial Dirac delta function of radius equal to an integer multiple of the radius of the hydrogen atom.

2.4. The Mills theory—a classical quantum theory

One-electron atoms include the hydrogen atom, He^+, Li^{2+}, Be^{3+}, and so on. The mass-energy and angular momentum of the electron are constant; this requires that the equation of motion of the electron be temporally and spatially harmonic. Thus, the classical wave equation applies and

$$\left[\nabla^2 - \frac{1}{v^2}\frac{\delta^2}{\delta t^2}\right]\rho(r,\theta,\phi,t) = 0 \tag{37}$$

where $\rho(r,\theta,\phi,t)$ is the charge density function of the electron in time and space. In general, the wave equation has an infinite number of solutions. To arrive at the solution which represents the electron, a suitable boundary condition must be imposed. It is well known from experiments that each single atomic electron of a given isotope radiates to the same stable state. Thus, Mills chose the physical boundary condition of nonradiation of the bound electron to be imposed on the solution of the wave equation for the charge density function of the electron. The condition for radiation by a moving point charge, given by Haus [15], is that its spacetime Fourier transform does possess components that are synchronous with waves traveling at the speed of light. Conversely, it is proposed that the condition for nonradiation by an ensemble of moving point charges that comprises a charge density function is:

For nonradiative states, the current-density function must *not* possess spacetime Fourier components that are synchronous with waves traveling at the speed of light.

The Haus derivation applies to a moving charge-density function as well, because charge obeys superposition. The Haus derivation is summarized below.

The Fourier components of the current produced by the moving charge are derived. The electric field is found from the vector equation in Fourier space (**k**, *w*-space). The inverse Fourier transform is carried over the magnitude of **k**. The resulting expression demonstrates that the radiation field is proportional to $J_\perp((\omega/c)\mathbf{n},\omega)$, where $J_\perp(\mathbf{k},\omega)$ is the spacetime Fourier transform of the current perpendicular to **k** and $\mathbf{n} \equiv \mathbf{k}/|\mathbf{k}|$. Specifically,

$$E_\perp(\mathbf{r},\omega)\frac{d\omega}{2\pi} = \frac{c}{2\pi}\int \rho(\omega,\Omega)\,d\omega\,d\Omega\sqrt{\frac{\mu_0}{\varepsilon_0}}\mathbf{n}$$
$$\times \left(\mathbf{n} \times J_\perp\left(\frac{\omega}{c}\mathbf{n},\omega\right)e^{i(\omega/c)\mathbf{n}\cdot\mathbf{r}}\right). \tag{38}$$

The field $E_\perp(\mathbf{r},\omega)d\omega/2\pi$ is proportional to $J_\perp((\omega/c)\mathbf{n},\omega)$, namely, the Fourier component for which $\mathbf{k}=\omega/c$. Factors of ω that multiply the Fourier component of the current are due to the density of modes per unit volume and unit solid angle. An unaccelerated charge does not radiate in free space, not because it experiences no acceleration, but because it has no Fourier component $J_\perp((\omega/c)\mathbf{n},\omega)$.

The time, radial, and angular solutions of the wave equation are separable. The motion is time harmonic with frequency ω_n. To be a harmonic solution of the wave equation in spherical coordinates, the angular functions must be spherical harmonic functions. A zero of the spacetime Fourier transform of the product function of two spherical harmonic angular functions, a time harmonic function, and an unknown radial function is sought. The solution for the radial function which satisfies the boundary condition is a delta function

$$f(r) = \frac{1}{r^2}\delta(r - r_n), \tag{39}$$

where $r_n = nr_1$ is an allowed radius. Thus, bound electrons are described by a charge-density (mass-density) function which is the product of a radial delta function ($f(r) = (1/r^2)\delta(r - r_n)$), two angular functions (spherical harmonic functions), and a time harmonic function. Thus, an electron is a spinning, two-dimensional spherical surface, called an *electron orbitsphere*, that can exist in a bound state at only specified distances from the nucleus as shown in Fig. 1. More explicitly, the orbitsphere comprises a two-dimensional spherical shell of moving charge.

The total function that describes the spinning motion of each electron orbitsphere is composed of two functions. One function, the spin function, is spatially uniform over the orbitsphere, spins with a quantized angular velocity, and gives rise to spin angular momentum. The other function, the modulation function, can be spatially uniform—in which case there is no orbital angular momentum and the magnetic moment of the electron orbitsphere is one Bohr magneton—or not spatially uniform—in which case there is orbital angular momentum. The modulation function also rotates with a quantized angular velocity.

The corresponding current pattern of the constant charge function of the orbitsphere corresponding to the spin function comprises an infinite series of correlated orthogonal great circle current loops. The current pattern is generated over the surface by two orthogonal sets of an infinite series of nested rotations of two orthogonal great circle current loops where the coordinate axes rotate with the two orthogonal great circles. Each infinitesimal rotation of the infinite
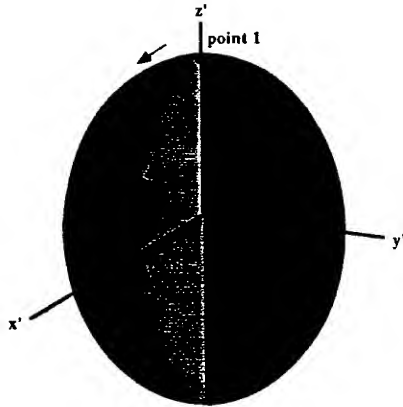
Fig. 3. Two infinitesimal point masses (charges) of two orthogonal great circle current loops in the orbitsphere frame.

series is about the new x-axis and new y-axis which results from the preceding such rotation. For each of the two sets of nested rotations, the angular sum of the rotations about each rotating x-axis and y-axis totals $\sqrt{2}\pi$ radians.

Consider the electron to be evenly distributed within two orthogonal great circle current loops. Then consider two infinitesimal point masses (charges), one and two, of two orthogonal great circle current loops. The Cartesian coordinate system wherein the first current loop lies in the yz-plane, and the second current loop lies in the xz-plane is designated the orbitsphere reference frame. Consider the two point masses, one and two, in the reference frame of the orbitsphere at time zero. Point one is at $x' = 0$, $y' = 0$, and $z' = r_n$ and point two is at $x' = r_n$, $y' = 0$, and $z' = 0$. Let point one move on a great circle toward the negative y'-axis, as shown in Fig. 3, and let point two move on a great circle toward the positive z'-axis, as shown in Fig. 3. The equations of motion, in the reference frame of the orbitsphere are given by

point one:

$$x_1' = 0, \quad y_1' = -r_n \sin(\omega_n t), \quad z_1' = r_n \cos(\omega_n t) \tag{40}$$

point two:

$$x_2' = r_n \cos(\omega_n t), \quad y_2' = 0, \quad z_2' = r_n \sin(\omega_n t). \tag{41}$$

The great circles are rotated by an infinitesimal angle $\Delta\alpha$ (a rotation around the x-axis) and then by $\Delta\alpha$ (a rotation around the new y-axis). The coordinates of each point on the rotated great circle is expressed in terms of the first (x,y,z) coordinates by the following transforms:

point one:

$$\begin{bmatrix} x_1 \\ y_1 \\ z_1 \end{bmatrix} = \begin{bmatrix} \cos(\Delta\alpha) & -\sin^2(\Delta\alpha) & -\sin(\Delta\alpha)\cos(\Delta\alpha) \\ 0 & \cos(\Delta\alpha) & -\sin(\Delta\alpha) \\ \sin(\Delta\alpha) & \cos(\Delta\alpha)\sin(\Delta\alpha) & \cos^2(\Delta\alpha) \end{bmatrix} \begin{bmatrix} x_1' \\ y_1' \\ z_1' \end{bmatrix}$$

$$\tag{42}$$

and $\Delta\alpha' = -\Delta\alpha$ replaces $\Delta\alpha$ for

$$\sum_{n=1}^{\sqrt{2}\pi/\Delta\alpha} \Delta\alpha = \sqrt{2}\pi; \qquad \sum_{n=1}^{\sqrt{2}\pi/|\Delta\alpha'|} |\Delta\alpha'| = \sqrt{2}\pi.$$

point two:

$$\begin{bmatrix} x_2 \\ y_2 \\ z_2 \end{bmatrix} = \begin{bmatrix} \cos(\Delta\alpha) & -\sin^2(\Delta\alpha) & -\sin(\Delta\alpha)\cos(\Delta\alpha) \\ 0 & \cos(\Delta\alpha) & -\sin(\Delta\alpha) \\ \sin(\Delta\alpha) & \cos(\Delta\alpha)\sin(\Delta\alpha) & \cos^2(\Delta\alpha) \end{bmatrix} \begin{bmatrix} x_2' \\ y_2' \\ z_2' \end{bmatrix}$$

$$\tag{43}$$

and $\Delta\alpha' = -\Delta\alpha$ replaces $\Delta\alpha$ for

$$\sum_{n=1}^{\sqrt{2}\pi/\Delta\alpha} \Delta\alpha = \sqrt{2}\pi; \qquad \sum_{n=1}^{\sqrt{2}\pi/|\Delta\alpha'|} |\Delta\alpha'| = \sqrt{2}\pi.$$

The total orbitsphere is given by reiterations of Eqs. (42) and (43). The output given by the nonprimed coordinates is the input of the next iteration corresponding to each successive nested rotation by the infinitesimal angle where the summation of the rotation about each of the x-axis and the y-axis is

$$\sum_{n=1}^{\sqrt{2}\pi/\Delta\alpha} \Delta\alpha = \sqrt{2}\pi \quad \text{and} \quad \sum_{n=1}^{\sqrt{2}\pi/|\Delta\alpha'|} |\Delta\alpha'| = \sqrt{2}\pi.$$

The current pattern corresponding to point one and point two shown with 8.49 degree increments of the infinitesimal angular variable $\Delta\alpha(\Delta\alpha')$ of Eqs. (42) and (43) is shown from the perspective of looking along the z-axis in Fig. 4. The complete orbitsphere current pattern corresponds to all such correlated points, point one and point two, of the orthogonal great circles shown in Fig. 3 which are rotated according to Eqs. (42) and (43) where $\Delta\alpha(\Delta\alpha')$ approaches zero and the summation of the infinitesimal angular rotations of $\Delta\alpha(\Delta\alpha')$ about the successive x-axes and y-axes is $\sqrt{2}\pi$. The current pattern gives rise to the phenomenon corresponding to the spin quantum number.

The fourth quantum number arises naturally in the Mills theory as derived in the Electron g Factor Section [2]. The Stern–Gerlach experiment implies a magnetic moment of one Bohr magneton and an associated angular momentum quantum number of 1/2. Historically, this quantum number is called the spin quantum number, s ($s = 1/2$; $m_s = \pm 1/2$). Conservation of angular momentum of the orbitsphere permits a discrete change of its "kinetic angular momentum" $(\mathbf{r} \times m\mathbf{V})$ by the field of $\hbar/2$, and concomitantly the "potential angular momentum" $(\mathbf{r} \times e\mathbf{A})$ must change by $-\hbar/2$.

Y
|
|

——————————X
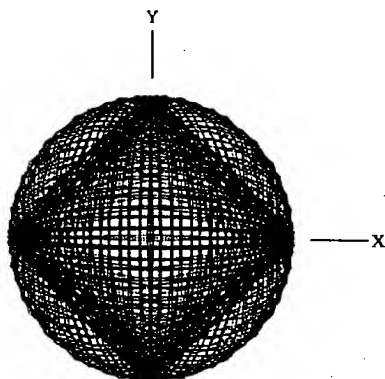
VIEW ALONG THE Z AXIS

Fig. 4. The current pattern of the orbitsphere shown with $8.49°$ increments of the infinitesimal angular variable $\Delta\alpha(\Delta\alpha')$ from the perspective of looking along the z-axis.

The flux change, ϕ, of the orbitsphere for $r < r_n$ is determined as follows:

$$\Delta\mathbf{L} = \frac{\hbar}{2} - \mathbf{r} \times e\mathbf{A}, \tag{44}$$

$$= \left(\frac{\hbar}{2} - \frac{e2\pi r A}{2\pi}\right)\hat{z}, \tag{45}$$

$$= \left(\frac{\hbar}{2} - \frac{e\phi}{2\pi}\right)\hat{z}. \tag{46}$$

In order that the change of angular momentum, $\Delta\mathbf{L}$, equals zero, ϕ must be $\Phi_0 = h/2e$, the magnetic flux quantum. Thus, to conserve angular momentum in the presence of an applied magnetic field, the orbitsphere magnetic moment can be parallel or antiparallel to an applied field as observed with the Stern–Gerlach experiment, and the flip between orientations (a rotation of $\pi/2$) is accompanied by the "capture" of the magnetic flux quantum by the orbitsphere. During the spin-flip transition, power must be conserved. Power flow is governed by the Poynting power theorem,

$$\nabla \cdot (E \times H) = -\frac{\partial}{\partial t}\left[\frac{1}{2}\mu_0 H \cdot H\right]$$
$$-\frac{\partial}{\partial t}\left[\frac{1}{2}\varepsilon_0 E \cdot E\right] - J \cdot E \tag{47}$$

Eq. (48) [2] gives the total energy of the flip transition which is the sum of the energy of reorientation of the magnetic moment (1st term), the magnetic energy (2nd term), the electric energy (3rd term), and the dissipated energy of a fluxon treading the orbitsphere (4th term), respectively.

$$\Delta E_{mag}^{spin} = 2\left(1 + \frac{\alpha}{2\pi} + \frac{2}{3}\alpha^2\left(\frac{\alpha}{2\pi}\right) - \frac{4}{3}\left(\frac{\alpha}{2\pi}\right)^2\right)\mu_B\mathbf{B} \tag{48}$$

$$\Delta E_{mag}^{spin} = g\mu_B\mathbf{B}. \tag{49}$$

The spin–flip transition can be considered as involving a magnetic moment of g times that of a Bohr magneton. The g factor is redesignated the fluxon g factor as opposed to the anomalous g factor. The calculated value of $g/2$ is 1.001 159 652 137. The experimental value of $g/2$ is 1.001 159 652 188(4).

The Mills theory solves the wave equation for the charge density function of the electron. The time, radial, and angular solutions of the wave equation are separable. Also, the radial function for the electron indicates that the electron is two-dimensional. Therefore, the angular mass-density function of the electron, $A(\theta, \phi, t)$, must be a solution of the wave equation in two dimensions (plus time),

$$\left[\nabla^2 - \frac{1}{v^2}\frac{\delta^2}{\delta t^2}\right]A(\theta, \phi, t) = 0, \tag{50}$$

where $\rho(r, \theta, \phi, t) = f(r)A(\theta, \phi, t) = (1/r^2)\delta(r - r_n)A(\theta, \phi, t)$ and $A(\theta, \phi, t) = Y(\theta, \phi)k(t)$

$$\left[\frac{1}{r^2\sin\theta}\frac{\delta}{\delta\theta}\left(\sin\theta\frac{\delta}{\delta\theta}\right)_{r,\phi} + \frac{1}{r^2\sin^2\theta}\left(\frac{\delta^2}{\delta\phi^2}\right)_{r,\theta}\right.$$
$$\left. - \frac{1}{v^2}\frac{\delta^2}{\delta t^2}\right]A(\theta, \phi, t) = 0, \tag{51}$$

where v is the linear velocity of the electron. The charge-density functions including the time-function factor are

$\ell = 0$:

$$\rho(r, \theta, \phi, t) = \frac{e}{8\pi r^2}[\delta(r - r_n)][Y_n^m(\theta, \phi) + Y_0^0(\theta, \phi)]. \tag{52}$$

$\ell \neq 0$:

$$\rho(r, \theta, \phi, t)$$
$$= \frac{e}{4\pi r^2}[\delta(r - r_n)][Y_0^0(\theta, \phi) + \text{Re}\{Y_\ell^m(\theta, \phi)[1 + e^{i\omega_n t}]\}] \tag{53}$$

where $\text{Re}\{Y_\ell^m(\theta, \phi)[1 + e^{i\omega_n t}]\} = \text{Re}[Y_\ell^m(\theta, \phi) + Y_\ell^m(\theta, \phi)e^{i\omega_n t}] = P_\ell^m(\cos\theta)\cos m\phi + P_\ell^m(\cos\theta)\cos(m\phi + \omega_n t)$ and $\omega_n = 0$ for $m = 0$.

The spin function of the electron (see Fig. 1 for the charge function and Fig. 4 for the current function) corresponds to the nonradiative $n = 1$, $\ell = 0$ state of atomic hydrogen which is well known as an s state or orbital. The constant spin function is modulated by a time and spherical harmonic function as given by Eq. (53) and shown in Fig. 2. The modulation or traveling charge density wave corresponds to an orbital angular momentum in addition to a spin angular momentum. These states are typically referred to as p, d, f, etc. orbitals and correspond to an ℓ quantum number not equal to zero. Application of Haus's [18] condition (Eqs. (54)–(56)) also predicts nonradiation for a constant spin function modulated by a time and spherically harmonic orbital function. There is acceleration without radiation. (Also see Abbott and Griffiths and Goedecke [19,20]). However, in the case that such a state arises as an excited state by photon

absorption, it is radiative due to a radial dipole term in its current density function since it possesses spacetime Fourier Transform components synchronous with waves traveling at the speed of light [2].

The Fourier transform of the electron charge density function is a solution of the four-dimensional wave equation in frequency space ($\mathbf{k}$, w-space). Then the corresponding Fourier transform of the current density function $K(s, \Theta, \Phi, \omega)$ is given by multiplying by the constant angular frequency.

$K(s, \Theta, \Phi, \omega)$

$$
= 4\pi\omega_n \frac{\sin(2s_n r_n)}{2s_n r_n} \otimes 2\pi \sum_{v=1}^{\infty} \frac{(-1)^{v-1}(\pi\sin\Theta)^{2(v-1)}}{(v-1)!(v-1)!}
$$

$$
\frac{\Gamma(\frac{1}{2})\Gamma(v+\frac{1}{2})}{(\pi\cos\Theta)^{2v+1}2^{v+1}} \frac{2v!}{(v-1)!} s^{-2v}
$$

$$
\otimes 2\pi \sum_{v=1}^{\infty} \frac{(-1)^{v-1}(\pi\sin\Phi)^{2(v-1)}}{(v-1)!(v-1)!} \frac{\Gamma(\frac{1}{2})\Gamma(v+\frac{1}{2})}{(\pi\cos\Phi)^{2v+1}2^{v+1}}
$$

$$
\frac{2v!}{(v-1)!} s^{-2v} \frac{1}{4\pi}[\delta(\omega-\omega_n) + \delta(\omega+\omega_n)]. \quad (54)
$$

The motion on the orbitsphere is angular; however, a radial component exists due to special relativistic effects. Consider the radial wave vector of the sinc function. When the radial projection of the velocity is c

$$
\mathbf{s}_n \bullet \mathbf{v}_n = \mathbf{s}_n \bullet \mathbf{c} = \omega_n \quad (55)
$$

the relativistically corrected wavelength is

$$
r_n = \lambda_n \quad (56)
$$

(i.e. the lab frame motion in the angular direction goes to zero as the velocity approaches the speed of light). Substitution of Eq. (56) into the sinc function results in the vanishing of the entire Fourier transform of the current-density function. Thus, spacetime harmonics of $\omega_n/c = k$ or $(\omega_n/c)\sqrt{\varepsilon/\varepsilon_0} = k$ for which the Fourier transform of the current-density function is nonzero do not exist. Radiation due to charge motion does not occur in any medium when this boundary condition is met.

The orbitsphere is a resonator cavity which traps photons of discrete frequencies. The radius of an orbitsphere increases with the absorption of electromagnetic energy. The solutions to Maxwell's equations for modes that can be excited in the orbitsphere resonator cavity give rise to four quantum numbers, and the energies of the modes are the experimentally known hydrogen spectrum.

The subscript n is used in Eqs. (39) and (74), the quantization condition, appears in the Excited States of the One Electron Atom (Quantization) Section of Mills [2]. Quantization arises as "allowed" solutions of the wave equation corresponding to a resonance between the electron and a photon.

More explicitly, it is well known that resonator cavities can trap electromagnetic radiation of discrete resonant frequencies. The orbitsphere is a resonator cavity which traps photons of discrete frequencies. Thus, photon absorption occurs as an excitation of a resonator mode. The "trapped photon" is a "standing electromagnetic wave" which actually is a circulating wave that propagates along with each great circle current loop of the orbitsphere. The time-function factor, $k(t)$, for the "standing wave" is identical to the time-function factor of the orbitsphere in order to satisfy the boundary (phase) condition at the orbitsphere surface. Thus, the angular frequency of the "trapped photon" has to be identical to the angular frequency of the electron orbitsphere, ω_n. Furthermore, the phase condition requires that the angular functions of the "trapped photon" have to be identical to the spherical harmonic angular functions of the electron orbitsphere. Combining $k(t)$ with the ϕ-function factor of the spherical harmonic gives $e^{i(m\phi - \omega_n t)}$ for both the electron and the "trapped photon" function. The photon is "glued" to the inner orbitsphere surface and the outer nuclear surface as photon source charge density with a radial electric field.

From the application of the nonradiative boundary condition, the instability of excited states as well as the stability of the "ground" state arise naturally in the Mills theory as derived in Stability of Atoms and Hydrinos Section [2]. In addition to the above known states of hydrogen (Eq. (1)), the theory predicts the existence of a previously unknown form of matter: hydrogen atoms and molecules having electrons of lower energy than the conventional "ground" state, called *hydrinos* and *dihydrinos*, respectively, where each energy level corresponds to a fractional quantum number.

The central field of the proton corresponds to integer one charge. Excited states comprise an electron with a trapped photon. In all energy states of hydrogen, the photon has an electric field which superposes with the field of the proton. In the $n = 1$ state, the sum is zero in the ionized state. In an excited state, the sum is a fraction of one (i.e. between zero and one). Derivations from first principles given by Mills demonstrate that each "allowed" fraction corresponding to an excited state is $1/$integer. The relationship between the electric field equation and the "trapped photon" source charge-density function is given by Maxwell's equation in two dimensions.

$$
\mathbf{n} \bullet (\mathbf{E}_1 - \mathbf{E}_2) = \sigma/\varepsilon_0 \quad (57)
$$

where $\mathbf{n}$ is the radial normal unit vector, $\mathbf{E}_1 = 0$ ($\mathbf{E}_1$ is the electric field outside of the orbitsphere), $\mathbf{E}_2$ is given by the total electric field at $r_n = na_H$, and σ is the surface charge density. The electric field of an excited state is fractional; therefore, the source charge function is fractional. It is well known that fractional charge is not "allowed". The reason is that fractional charge typically corresponds to a radiative current density function. The excited states of the hydrogen atom are examples. They are radiative; consequently, they are not stable. Thus, an excited electron decays to the first nonradiative state corresponding to an integer field, $n=1$ (i.e. a field of integer one times the central field of the proton).

Equally valid from first principles are electronic states where the magnitude of the sum of the electric field of the

photon and the proton central field are an integer greater than one times the central field of the proton. These states are nonradiative. A catalyst can effect a transition between these states via a nonradiative energy transfer. Substantial experimental evidence exists that supports the existence of this novel hydrogen chemistry and its applications [21–55] which was missed entirely due to the erroneous concept of the hydrogen atom "ground state" based on the Schrödinger equation. An analysis of the shortcomings of the Schrödinger equation are given in the Appendix and in a paper by Mills [7]. The success of the classical theory of Mills is demonstrated in a recent presentation and recent publications [53–55].

Furthermore, it is a mistake to take the position that solutions of the *Postulated* Schrödinger equation which correspond to n=integer prohibit the existence of hydrogen atoms having a binding energy corresponding to $n = 1$/integer. Specifically, it is wrong to take the position that $n=1$/integer values cannot exist according to conventional scientific theories since the Schrödinger equation may be solved for either case with equal validity. However, in neither case does the Schrödinger equation provide a physical basis for their existence or behavior with regard to radiation. For example, the Schrödinger equation does not explain the observation that spontaneous emission of radiation does not occur for the state having a binding energy of 13.6 eV. See the Appendix and Mills [7].

2.5. Schrödinger states below $n = 1$

In Eq. (22), n^* does not have to be an integer, it may be any *arbitrary* constant β. Then the corresponding solution is [13]

$$y = e^{-x/2} x^{(k-1)/2} \frac{d^k}{dx^k} L_\beta(x) \tag{58}$$

where k is a positive integer. By comparing Eqs. (21) and (22),

$$\frac{k^2 - 1}{4} = \ell(\ell + 1). \tag{59}$$

Thus,

$$k = 2\ell + 1 \tag{60}$$

and

$$n^* - \frac{k-1}{2} = n^* - \ell = \frac{me^2}{\hbar} \left(\frac{\alpha}{2}\right)^{-1}. \tag{61}$$

Substitution of the value of α and solving for W gives

$$W = \frac{1}{2} \frac{me^4}{(n^* - \ell)^2 \hbar^2}. \tag{62}$$

Because of the conditions on n^* and k, the quantity $n^* - \ell$ cannot be zero. In the case that n^* is given as $n^* = 1/p + \ell$ where p is a positive integer, the condition is satisfied. In this case, the principal quantum number is given as $1/p$ where

p is a positive integer. The energy states of the hydrogen atom are

$$W_n = -E_n = \frac{1}{2} \frac{me^4}{(\frac{1}{p})^2 \hbar^2} \tag{63}$$

and the corresponding eigenfunctions from Eq. (58) are

$$R_{p,\ell} = c_{p,\ell} e^{-x/2} x^{\ell} \frac{d^{2\ell+1}}{dx^{2\ell+1}} L_{1/p+\ell}(x) \tag{64}$$

where the variable x is defined by

$$x = \alpha r = \frac{\sqrt{8mW}}{\hbar} r = \frac{2me^2}{\frac{1}{p}\hbar^2} r. \tag{65}$$

In the Bohr theory of the hydrogen atom, the first orbital has a radius in CGS units given by

$$a_0 = \frac{\hbar^2}{me^2} = 0.53 \times 10^{-8} \text{ cm}. \tag{66}$$

Thus, $\alpha = 2p/a_0$ and

$$x = \frac{2pr}{a_0}. \tag{67}$$

The energy states of the hydrogen atom in CGS units in terms of the Bohr radius are given by

$$E = -\frac{1}{2} \frac{me^4}{(\frac{1}{p})^2 \hbar^2} = -\frac{e^2}{2(\frac{1}{p})^2 a_0}. \tag{68}$$

Eq. (68) corresponds to hydrogen atoms having a binding energy corresponding to $n = 1$/integer. It is an equally valid solution of the Schrödinger equation for the energy of the hydrogen atom as Eq. (29) corresponding to hydrogen atoms having a binding energy corresponding to $n = $ integer.

2.6. The electron of atomic hydrogen does not spontaneously emit radiation at the $n = 1$ state, but that does not preclude radiationless processes including formation of molecular hydrogen

The nonradiative state of atomic hydrogen which is historically called the "ground state" forms the basis of the boundary condition of Mills theory [2, pp. 33–109] to solve the wave equation. Mills further predicts [2, pp. 138–175] that certain atoms or ions serve as catalysts to release energy from hydrogen to produce an increased binding energy hydrogen atom called a *hydrino atom* having a binding energy of

$$\text{Binding Energy} = \frac{13.6 \text{ eV}}{n^2} \tag{69}$$

where

$$n = \frac{1}{2}, \frac{1}{3}, \frac{1}{4}, \dots, \frac{1}{p} \tag{70}$$

and p is an integer greater than 1, designated as $H[a_H/p]$ where a_H is the radius of the hydrogen atom. Hydrinos are predicted to form by reacting an ordinary hydrogen atom with a catalyst having a net enthalpy of reaction of about

$$m \times 27.2 \text{ eV} \tag{71}$$

where m is an integer. This catalysis releases energy from the hydrogen atom with a commensurate decrease in size of

the hydrogen atom, $r_n = na_H$. For example, the catalysis of $H(n = 1)$ to $H(n = 1/2)$ releases 40.8 eV, and the hydrogen radius decreases from a_H to $\frac{1}{2}a_H$.

It is taught in textbooks that atomic hydrogen cannot go below the ground state. Atomic hydrogen having an experimental ground state of 13.6 eV can only exist in a vacuum or in isolation, and atomic hydrogen cannot go below this ground state in isolation. However, there is no known composition of matter containing hydrogen in the ground state of 13.6 eV. Atomic hydrogen is a free radical and is very reactive. It may react to form a hydride ion or compositions of matter. It is a chemical intermediate which may be trapped as many chemical intermediates may be by methods such as isolation or cryogenically. A hydrino atom may be considered a chemical intermediate that may be trapped in vacuum or isolation. A hydrino atom may be very reactive to form a hydride ion or a novel composition of matter. Hydrogen at predicted lower energy levels, hydrino atoms, has been identified in the extreme ultraviolet emission spectrum from interstellar medium [7]. In addition, new compositions of matter containing hydrogen at predicted lower energy levels have recently been observed in the laboratory [32,34–52], which energy levels are achieved using the novel catalysts. Spectroscopic experiments confirm the catalysis of hydrogen [21–38].

The excited energy states of atomic hydrogen are also given by Eq. (69) except that

$$n = 1, 2, 3, \ldots . \tag{72}$$

The $n = 1$ state is the "ground" state for "pure" photon transitions (the $n = 1$ state can absorb a photon and go to an excited electronic state, but it cannot release a photon and go to a lower-energy electronic state). However, an electron transition from the ground state to a lower-energy state is possible by a nonradiative energy transfer such as multipole coupling or a resonant collision mechanism. These lower-energy states have fractional quantum numbers, $n = 1/\text{integer}$. Processes that occur without photons and that require collisions are common. For example, the exothermic chemical reaction of $H + H$ to form H_2 does not occur with the emission of a photon. Rather, the reaction requires a collision with a third body, M, to remove the bond energy—$H + H + M \rightarrow H_2 + M^*$ [56]. The third body distributes the energy from the exothermic reaction, and the end result is the H_2 molecule and an increase in the temperature of the system. Some commercial phosphors are based on nonradiative energy transfer involving multipole coupling [57]. For example, the strong absorption strength of Sb^{3+} ions along with the efficient nonradiative transfer of excitation from Sb^{3+} to Mn^{2+}, are responsible for the strong manganese luminescence from phosphors containing these ions. Similarly, the $n = 1$ state of hydrogen and the $n = 1/\text{integer}$ states of hydrogen are nonradiative, but a transition between two nonradiative states is possible via a nonradiative energy transfer, say $n = 1$ to $n = 1/2$. In these cases, during the transition the electron couples to another electron transition, electron transfer reaction, or inelastic

scattering reaction which can absorb the exact amount of energy that must be removed from the hydrogen atom. Thus, a catalyst provides a net positive enthalpy of reaction of $m \times 27.2$ eV (i.e. it absorbs $m \times 27.2$ eV where m is an integer). Certain atoms or ions serve as catalysts which resonantly accept energy from hydrogen atoms and release the energy to the surroundings to effect electronic transitions to fractional quantum energy levels.

Once formed hydrinos have a binding energy given by Eqs. (69) and (70); thus, they may serve as catalysts which provide a net enthalpy of reaction given by Eq. (71). Also, the simultaneous ionization of two hydrogen atoms may provide a net enthalpy given by Eq. (71). Since the surfaces of stars comprise significant amounts of atomic hydrogen, hydrinos may be formed as a source to interstellar space where further transitions may occur [7].

A number of experimental observations lead to the conclusion that atomic hydrogen can exist in fractional quantum states that are at lower energies than the traditional "ground" ($n = 1$) state. For example, the existence of fractional quantum states of hydrogen atoms explains the spectral observations of the extreme ultraviolet background emission from interstellar space [58], which may characterize dark matter as demonstrated in Table 2 of Mills [7].

Laboratory experiments that confirm the novel hydrogen chemistry include extreme ultraviolet (EUV) spectroscopy [21–33,36–38], plasma formation [21–33,36–38], power generation [22–24,29,55], and analysis of chemical compounds [32,36–52,55]. For example, lines observed by EUV spectroscopy could be assigned to transitions of atomic hydrogen to lower energy levels corresponding to lower energy hydrogen atoms called hydrino atoms and the emission from the excitation of the corresponding hydride ions formed from the hydrino atoms [23]. The chemical interaction of catalysts with hydrogen at temperatures below 1000 K has shown surprising results in terms of the emission of the Lyman and Balmer lines [21–38] and the formation of novel chemical compounds [32,34–52]. An energetic plasma in hydrogen was generated by a catalysis reaction at 1% of the theoretical or prior known voltage requirement and with 1000s of times less power input in a system wherein the plasma reaction is controlled with a weak electric field [23,24,29]. The optically measured output power of gas cells for power supplied to the glow discharge increased by over two orders of magnitude depending on the presence of less than 1% partial pressure of certain of catalysts in hydrogen gas or argon–hydrogen gas mixtures [22]. A hydrogen plasma formed by reacting a catalyst with hydrogen was recorded when there was no electric energy input to the reaction [27,28]. The optically measured output power of gas cells for power supplied to the glow discharge increased by over two orders of magnitude depending on the presence of less than 1% partial pressure of certain of catalysts in hydrogen gas or argon–hydrogen gas mixtures [22]. Continuum state emission of Cs^{2+} and Ar^{2+} at 53.3 nm and 45.6 nm, respectively, with

the absence of the other corresponding Rydberg series of lines from these species confirmed the resonant nonradiative energy transfer of 27.2 eV from atomic hydrogen to atomic cesium or Ar^+. The predicted hydride ion of hydrogen catalysis by either cesium atom or Ar^+ catalyst is the hydride ion $H^-(1/2)$. This ion was observed spectroscopically at 407 nm corresponding to its predicted binding energy of 3.05 eV [21].

2.7. Theory of one electron states (hydrogen atom and electron bubble in superfluid helium)

Recently a new challenge to the fundamental foundations of quantum mechanics has arisen based on experiments of free electrons injected into superfluid helium. In order to explain the increase in conductivity observed when electrons in superfluid helium are irradiated with light, British physicist Humphrey Maris has proposed that the electron breaks into equal sized fragments which he calls "electrinos". According to Maris, this process of division of the electron may continue to such that the electron breaks into two and then the 1/2 electrons may divide into two forming 1/4 electrons, and the process may repeat indefinitely.

Electrons do not break into pieces. It is shown infra that the free electron in superfluid helium is an orbitsphere which can act as a resonator cavity and absorb resonant radiation to form stable nonradiative states of radii $n = 1$/integer times that of the radius of the electron without an absorbed photon. The solutions are analogous to the solutions of lower-energy states of hydrogen called hydrinos with principal energy levels given by Eqs. (69)–(70) and radii given by a_H/p where a_H is the radius of the hydrogen atoms and p is an integer.

For the electron of the hydrogen atom which comprises a dynamic spherical resonator cavity, the relationship between an allowed radius and the "photon standing wave" wavelength is

$$2\pi r = n\lambda \tag{73}$$

where n is an integer. Now, the question arises: given that this is a resonator cavity, which nonradiative states are possible where the transition is effected by a "trapped photon"? For the electron orbitsphere, a spherical resonator cavity, the relationship between an allowed radius and the electron wavelength is

$$2\pi(nr_1) = 2\pi r_n = n\lambda_1 = \lambda_n \tag{74}$$

where

$n = 1, 2, 3, 4, \ldots,$

$n = \frac{1}{2}, \frac{1}{3}, \frac{1}{4}, \ldots, \frac{1}{p}$ where p is an integer,

λ_1 is the allowed wavelength for $n = 1$,

r_1 is the allowed radius for $n = 1$.

The nonradiative boundary condition from Haus [18] and the relationship between the electron and the photon give the "allowed" hydrogen energy states which are quantized

as a function of the parameter n. That is the nonradiative boundary condition and the relationship between an allowed radius and the photon standing wave wavelength Eq. (73) gives rise to Eq. (74), the boundary condition for allowed radii and allowed electron wavelengths as a function of the parameter n. Each value of n corresponds to an allowed transition effected by a resonant photon which excites the transition in the orbitsphere resonator cavity. In addition to the traditional integer values $(1, 2, 3, \ldots,)$ of n, values of fractions are allowed according to Eq. (74) which correspond to transitions with an increase in the central field (charge) and decrease in the radius of the orbitsphere. This occurs, for example, when the orbitsphere transfers energy nonradiatively to a catalyst which resonantly accepts the energy. The electron undergoes a transition to a lower energy nonradiative state. The "Excited states of the one electron atom (quantization)" section of Mills [2] gives the solutions of the excited states of atomic hydrogen and the "Blacklight process" section gives the solutions of lower-energy states.

The photon equation must be a solution of Laplace's equation in spherical coordinates. The "trapped photon" field comprises an electric field which provides force balance and a nonradiative orbitsphere. The solution to this boundary value problem of the radial photon electric field of hydrogen states is given by

$$\mathbf{E}_{r_{photon}n,l,m} = \frac{e(na_H)^{\ell}}{4\pi\varepsilon_0} \frac{1}{r^{(\ell+2)}} \left[- Y_0^0(\theta,\phi) + \frac{1}{n}[Y_0^0(\theta,\phi) \right.$$
$$\left. + \mathrm{Re}\{Y_\ell^m(\theta,\phi)[1 + e^{i\omega_n t}]\} \right]$$
$$\omega_n = 0 \quad \text{for } m = 0 \tag{75}$$

$\ell = 1, 2, \ldots, n - 1,$

$m_\ell = -\ell, -\ell + 1, \ldots, 0, \ldots, +\ell.$

And, the quantum numbers of the electron are n, ℓ, m_ℓ, and $m_s = \pm 1/2$ are the same as the corresponding quantum numbers for excited states. $\mathbf{E}_{r_{total}}$ is the sum of the "trapped photon" and proton electric fields,

$$\mathbf{E}_{r_{total}} = \frac{e}{4\pi\varepsilon_0 r^2} + \frac{e(na_H)^{\ell}}{4\pi\varepsilon_0} \frac{1}{r^{(\ell+2)}}$$
$$\left[- Y_0^0(\theta,\phi) + \frac{1}{n}[Y_0^0(\theta,\phi) + \mathrm{Re}\{Y_\ell^m(\theta,\phi)} \right.$$
$$\left. [1 + e^{i\omega_n t}]\} \right] \quad \omega_n = 0 \text{ for } m = 0. \tag{76}$$

For $r = na_H$ and $m = 0$, the total radial electric field is

$$\mathbf{E}_{r_{total}} = \frac{1}{n} \frac{e}{4\pi\varepsilon_0(na_H)^2}. \tag{77}$$

In Eqs. (75)–(77), the excited states of hydrogen correspond to $n = 1, 2, 3, 4, \ldots$, and the hydrino states correspond to $n = \frac{1}{2}, \frac{1}{3}, \frac{1}{4}, \ldots, \frac{1}{p}$ where p is an integer.

The "trapped photon" is a "standing electromagnetic wave" which actually is a circulating wave that propagates

along with each great circle current loop of the electron orbitsphere. The time-function factor, $k(t)$, for the "standing wave" is identical to the time-function factor of the orbitsphere in order to satisfy the boundary (phase) condition at the orbitsphere surface. Thus, the angular frequency of the "trapped photon" has to be identical to the angular frequency of the electron orbitsphere, ω_n. Furthermore, the phase condition requires that the angular functions of the "trapped photon" have to be identical to the spherical harmonic angular functions of the electron orbitsphere. Combining $k(t)$ with the ϕ-function factor of the spherical harmonic gives $e^{i(m\phi - \omega_n t)}$ for both the electron and the "trapped photon" function. The photon is "glued" to the inner orbitsphere surface and the outer nuclear surface as photon source charge density with a radial electric field. The angular functions in phase with the corresponding photon functions are given by Eqs. (52) and (53).

The solution of the "trapped photon" field of electrons in helium is analogous to those for hydrinos except that the $-Y_0^0(\theta, \phi)$ term is not present since the central field of the proton is absent and the nature of the field at the origin is equivalent to the solution of the Poisson equation with a delta function inhomogeneity at the origin [9, pp. 110–113].

$$\mathbf{E}_{r_{\text{photon}}n,l,m} = C \frac{e(na)^{l'}}{4\pi\varepsilon_0} \frac{1}{r^{(l'+2)}} \left[\frac{1}{n} [Y_0^0(\theta, \phi)] \right.$$
$$\left. + \text{Re}\{Y_l^m(\theta, \phi)[1 + e^{i\omega_n t}]\}\right]$$
$$\omega_n = 0 \quad \text{for } m = 0, \tag{78}$$

$n = 1, \frac{1}{2}, \frac{1}{3}, \frac{1}{4}, \ldots, \frac{1}{p}$,

$l = 1, 2, \ldots, n-1$,

$m = -l, -l+1, \ldots, 0, \ldots, +l$.

In Eq. (78), a is the radius of the electron in helium without an absorbed photon. C is a constant expressed in terms of an equivalent central charge. It is determined by the force balance between the centrifugal force of the electron orbitsphere and the radial force provided by the pressure from the van der Waals force of attraction between helium atoms given infra.

2.8. Stability of "ground", hydrino, and helium states

For the below "ground" (fractional quantum) energy states of the hydrogen atom, σ_{photon}, the two-dimensional surface charge due to the "trapped photon" at the electron orbitsphere, is given by Eqs. (5.13) and (2.11) of Mills [2].

$$\sigma_{\text{photon}} = \frac{e}{4\pi(r_n)^2} \left[Y_0^0(\theta, \phi) - \frac{1}{n} [Y_0^0(\theta, \phi) \right.$$
$$\left. + \text{Re}\{Y_l^m(\theta, \phi)[1 + e^{i\omega_n t}]\}\right] \delta(r - r_n),$$
$$n = 1, \frac{1}{2}, \frac{1}{3}, \frac{1}{4}, \ldots \tag{79}$$

And, σ_{electron}, the two-dimensional surface charge of the electron orbitsphere is

$$\sigma_{\text{electron}} = \frac{-e}{4\pi(r_n)^2} [Y_0^0(\theta, \phi)$$
$$+ \text{Re}\{Y_l^m(\theta, \phi)[1 + e^{i\omega_n t}]\}]\delta(r - r_n). \tag{80}$$

The superposition of σ_{photon} (Eq. (79)) and σ_{electron}, (Eq. (80)) where the spherical harmonic functions satisfy the conditions given in the "Angular Function" section of Mills [2] is a radial electric monopole represented by a delta function.

$$\sigma_{\text{photon}} + \sigma_{\text{electron}} = \frac{-e}{4\pi(r_n)^2} \left[\frac{1}{n} Y_0^0(\theta, \phi) + \left(1 + \frac{1}{n}\right) \right.$$
$$\left. \text{Re} Y_l^m(\theta, \phi)[1 + e^{i\omega_n t}] \right] \delta(r - r_n),$$
$$n = 1, \frac{1}{2}, \frac{1}{3}, \frac{1}{4}, \ldots. \tag{81}$$

As given in the "Spacetime Fourier transform of the electron function" section of Mills [2], the radial delta function does not possess spacetime Fourier components synchronous with waves traveling at the speed of light (Eqs. (54)–(56)). Thus, the below "ground" (fractional quantum) energy states of the hydrogen atom are stable. The "ground" ($n = 1$ quantum) energy state is just the first of the nonradiative states of the hydrogen atom; thus, it is the state to which excited states decay.

The speed of light in vacuum c is given by

$$c = 1/\sqrt{\mu_0 \varepsilon_0}, \tag{82}$$

where μ_0 is the permeability of free-space and ε_0 is the permittivity of free-space. The wave number is given by

$$k_{\text{vacuum}} = \frac{2\pi}{\lambda} = \omega\sqrt{\mu_0 \varepsilon_0}. \tag{83}$$

The speed of light in a medium such as superfluid helium v is given by

$$v = 1/\sqrt{\mu_0 \varepsilon}, \tag{84}$$

where μ_0 is the permeability of free space and ε is the permittivity of the medium. The wave number is given by

$$k_{\text{medium}} = \frac{2\pi}{\lambda} = \omega\sqrt{\mu_0 \varepsilon}. \tag{85}$$

The ratio of the wave number in vacuum and the wave number in superfluid helium is given by

$$\frac{k_{\text{helium}}}{k_{\text{vacuum}}} = \frac{\frac{2\pi}{\lambda_{\text{helium}}}}{\frac{2\pi}{\lambda_{\text{vacuum}}}} = \frac{\omega\sqrt{\mu_0 \varepsilon}}{\omega\sqrt{\mu_0 \varepsilon_0}}. \tag{86}$$

The frequency of the photon in free space and in helium at the electron must be the same. Thus,

$$k_{\text{helium}} = k_{\text{vacuum}} \frac{\varepsilon}{\varepsilon_0}. \tag{87}$$

Since $\varepsilon > \varepsilon_0$, the wave number in helium is greater than the wave number in vacuum. Thus, a photon traveling in liquid helium may excite a mode in an electron bubble which is nonradiative. In this case, spacetime harmonics of $\omega_n/c = k$

or $(\omega_n/c)\sqrt{\varepsilon/\varepsilon_0} = k$ for which the Fourier transform of the current-density function is nonzero do not exist. Radiation due to charge motion does not occur in any medium when this boundary condition is met.

The viscosity of superfluid helium is a function of temperature. The observation of the temperature dependence of photon absorption by electrons in superfluid helium to give rise to an increase in conductivity may be explained on this basis. That is, at 1.7 K, the viscosity is sufficiently close to zero such that the angular current of the electron may propagate without energy loss. Roton scattering dominates over phonon scattering at this temperature and below [59]. In this case, resonant absorption may occur between stable nonradiative states; wherein the forces are central. The two-dimensional surface charge due to the "trapped photon" at the electron orbitsphere of an electron in helium has the same form as that given by Eq. (81). Thus, the states of photons absorbed by electrons in helium are stable under these conditions.

2.9. Conservation of angular momentum

The field is time harmonic which is satisfied by the fields spinning around the z-axis at frequency ω_n in phase with the electron. The relationship between the electric field equation and the "trapped photon" source charge density function is given by Maxwell's equation in two dimensions.

$$\mathbf{n} \bullet (\mathbf{E}_1 - \mathbf{E}_2) = \sigma/\varepsilon_0, \tag{88}$$

where $\mathbf{n}$ is the radial normal unit vector, $\mathbf{E}_1 = 0$ ($\mathbf{E}_1$ is the electric field outside of the orbitsphere), $\mathbf{E}_2$ is given by the total electric field at $r_n = na_H$, and σ is the surface charge density. In order that the radial electric field is always positive and the surface charge density is always negative, a constant function adds to a spherical harmonic function; thus, the spherical harmonic function modulates the constant function. The surface charge density has a phase matched pattern. This provides a central force to balance the centrifugal force of the electron. The magnitude of the radial electric field is that which satisfies the boundary condition of force balance at the allowed radii of electron states.

The time harmonic condition is satisfied by the rotation of the fields in phase with the source currents. The spinning field and the corresponding source current at the electron orbitsphere conserves the angular momentum of the photon. The time-averaged angular-momentum density, $\mathbf{m}$, of the emitted photon is given by Eq. (16.61) of Jackson [9, pp. 739–779]

$$\mathbf{m} = \frac{1}{8\pi} \, \text{Re}[\mathbf{r} \times (\mathbf{E} \times \mathbf{B}^*)]. \tag{89}$$

The ratio of the square of the angular momentum, M^2, to the square of the energy, U^2, for a pure (l, m) multipole [9, pp. 739–779] is

$$M^2/U^2 = m^2/\omega^2. \tag{90}$$

Experimentally, the photon can carry $\pm\hbar$ units of angular momentum. Thus, during excitation the spin, orbital, or total angular momentum of the orbitsphere can change by zero or $\pm\hbar$. The electron transition rules arise from conservation of angular momentum. The selection rules for multipole transitions between quantum states arise from conservation of total angular momentum and component angular momentum where the photon carries $\hbar$ of angular momentum. The radiation of a multipole of order (l, m) carries $m\hbar$ units of the z component of angular momentum per photon of energy $\hbar\omega$.

Consider the angular frequency of the electron orbitsphere. Given time harmonic motion and a radial delta function, the relationship between an allowed radius and the electron wavelength is given by Eq. (74). Using the de Broglie relationship for the electron momentum where the coordinates are spherical,

$$\lambda_n = h/p_n = h/m_e v_n \tag{91}$$

and the magnitude of the velocity for *every* point on the orbitsphere is

$$v_n = \hbar/m_e r_n. \tag{92}$$

The corresponding angular frequencies are related to r_n by

$$v_n = r_n \omega_n. \tag{93}$$

Thus,

$$\omega_n = \hbar/m_e r_n^2. \tag{94}$$

The sum of the $\mathbf{L}_i$, the magnitude of the angular momentum of each infinitesimal point of the orbitsphere of mass m_i, must be constant. The constant is $\hbar$.

$$\sum |\mathbf{L}_i| = \sum |\mathbf{r} \times m_i \mathbf{v}| = m_e r_n \frac{\hbar}{m_e r_n} = \hbar, \tag{95}$$

where the velocity is given by Eq. (92). The vector projections of the orbitsphere spin angular momentum relative to the Cartesian coordinates are given in the "Spin angular momentum of the Orbitsphere with $\ell = 0$" section of Mills [2]. The result is that the electron possesses a projection of the angular momentum onto an axis S of $\pm\sqrt{\frac{1}{4}}\hbar$ which precesses about the axis of an applied magnetic field at the Larmor frequency.

2.10. Photon absorption

In order that the excitation can occur, the correspondence principle holds such that the frequency of the photon that is absorbed is equal to the change in angular frequency of the electron. The energy of the photon which excites a mode in a stationary spherical resonator cavity from radius a_H to radius na_H is

$$E_{\text{photon}} = \frac{e^2}{4\pi\varepsilon_0 a_H} \left[1 - \frac{1}{n^2} \right] = h\nu = \hbar\omega, \tag{96}$$

where n = integer. After multiplying Eq. (96) by $a_H/a_H = 4\pi\varepsilon_0\hbar^2/e^2\mu_e a_H$, where a_H is the radius of the hydrogen atom,

ω_{photon} is

$$\omega_{photon} = \frac{\hbar}{m_e a_H^2}\left[1 - \frac{1}{n^2}\right]. \tag{97}$$

In the case of an electron orbitsphere, the resonator possesses kinetic energy before and after the excitation. The kinetic energy is always one-half of the potential energy because the centripetal force is an inverse squared central force. As a result, the energy and angular frequency to excite an electron orbitsphere is only one-half of the values above, Eqs. (96) and (97). From Eq. (94), the angular velocity of an electron orbitsphere of radius na_H is

$$\omega_n = \frac{\hbar}{m_e(na_H)^2}. \tag{98}$$

The change in angular velocity of the orbitsphere for an excitation from $n = 1$ to $n = n$ is

$$\Delta\omega = \frac{\hbar}{m_e(a_H)^2} - \frac{\hbar}{m_e(na_H)^2} = \frac{\hbar}{m_e(a_H)^2}\left[1 - \frac{1}{n^2}\right]. \tag{99}$$

The kinetic energy change of the transition is

$$\frac{1}{2}m_e(\Delta v)^2 = \frac{1}{2}\frac{e^2}{4\pi\varepsilon_0 a_H}\left[1 - \frac{1}{n^2}\right] = \frac{1}{2}\hbar\omega. \tag{100}$$

The change in angular velocity of the electron orbitsphere, Eq. (99), is identical to the angular velocity of the photon necessary for the excitation, ω_{photon} (Eq. (97)). The energy of the photon necessary to excite the equivalent transition in an atomic hydrogen electron orbitsphere is one-half of the excitation energy of the stationary cavity because the change in kinetic energy of the electron orbitsphere supplies one-half of the necessary energy. The change in the angular frequency of the orbitsphere during a transition and the angular frequency of the photon corresponding to the superposition of the free space photon and the photon corresponding to the kinetic energy change of the orbitsphere during a transition are equivalent. The correspondence principle holds. It can be demonstrated that the resonance condition between these frequencies is to be satisfied in order to have a net change of the energy field [60].

3. Superfluid helium ion mobility results and discussion

Experiments to study the effect of light on ion mobility have been conducted by Northby and Sanders [61,62], Zipfel and Sanders [63,64], and Grimes and Adams [65,66]. For example, in the Northby and Sanders experiments [61,62], ions were introduced into the liquid from a radioactive source, and had to pass through two grids in order to reach the detector. The voltages on the grids were varied in time in a way such that normal negative ions could not reach the detector. It was found that when the liquid was illuminated, a small ion current reached the detector. Thus, they observed an increase in ion mobility under illumination, but recognized that the origin of the effect was unclear. It appears that

the absorption of a photon by an electron bubble or orbitsphere in superfluid helium provides a natural explanation for the majority of the photo-conductivity results.

The photon absorption is determined by the correspondence principle. Thus, the radius of the electron following the absorption of a resonant photon is given by $n = (1/\text{integer})$ times that of the original radius.

$$r = nr_1, \tag{101}$$

where $n = 1/\text{integer}$ and r_1 is the radius of the electron in superfluid helium which has not absorbed a photon. This radius is determined by a force balance between the van der Waals pressure (force per unit area) of superfluid helium and the centrifugal force of the electron. The latter is given by

$$\mathbf{F}_{centrifugal} = \frac{m_e}{4\pi r_1^2}\frac{\mathbf{v}_1^2}{r_1}, \tag{102}$$

where $m_e/4\pi r_1^2$ is the mass density of the orbitsphere and $\mathbf{v}_1$ is given by Eq. (92). The radius r_1 can be determined from the photo-conductivity experiments of Zipfel and Sanders [64]. At zero pressure a photo-conductivity peak was observed at approximately 0.5 eV. From Eq. (97), the change in the frequency of the electron which matches frequency of the exciting photon is given by

$$\omega_{photon} = \frac{\hbar}{m_e r_1^2}\left[\frac{1}{n^2} - 1\right] \tag{103}$$

where $n = 1/\text{integer}$. The radius r_1 is given by

$$r_1 = \sqrt{\frac{\hbar}{m_e\omega_{photon}}\left(\frac{1}{n^2} - 1\right)}. \tag{104}$$

The relationship between energy and angular frequency of a photon is given by Planck's equation.

$$E = \hbar\omega_{photon}. \tag{105}$$

The angular frequency corresponding to a photon of 0.5 eV is

$$\omega_{photon} = \frac{8.0 \times 10^{-20}J}{\hbar} = 7.6 \times 10^{14}\ \text{rad/s}. \tag{106}$$

In the case that 0.5 eV is the lowest energy transition for an electron in superfluid helium, the $n = 1 \rightarrow n = \frac{1}{2}$ transition corresponds to $n = \frac{1}{2}$ in Eq. (103). From Eqs. (103) and (106), the radius r_1 is

$$r_1 = \sqrt{\frac{\hbar}{m_e(7.6 \times 10^{14}\ \text{rad/s})}\left(\frac{1}{(\frac{1}{2})^2} - 1\right)}$$

$$= 6.7 \times 10^{-10}\ \text{m} = 6.7\ \text{Å} \tag{107}$$

where $n = \frac{1}{2}$. Comparing the case of the electron of a hydrogen atom to the case of an electron in helium, no initial central Coulomb field due to a proton is present, and the electron increases in kinetic energy upon photon absorption. Thus, the energy required to cause a transition in the latter case is twice that of the former. The photon stores energy

in the electric field of the resonator mode and increases the potential energy of the electron. The potential is the sum of the binding energy and the kinetic energy. The corresponding photon wavelength that will be absorbed by the electron is 2.5 μm.

The radius calculated in Eq. (107), is an approximation since the energy due to the pressure volume work and the surface energy change of the bubble were neglected. The former is given by

$$P \int dV = \frac{4}{3}\pi(r_1^3 - r_n^3)P \tag{108}$$

where P is the applied pressure, the integral is over the volume of the bubble, and r_1 and r_n are the initial and final radii of the electron bubble. The latter is given by

$$\alpha \int dA = 4\pi(r_1^2 - r_n^2)\alpha, \tag{109}$$

where α is the surface energy of helium per unit area, the integral is over the surface of the bubble, and r_1 and r_n are the initial and final radii of the electron bubble.

The contribution of these terms can be estimated by comparing the next experimental photo-conductivity peak at higher energy compared to the prediction by Eqs. (103) and (105). Northby and Sanders [61,62] found that in the range of 0.7 to 3 eV the photo-induced current had a peak when the photon energy was 1.21 eV at zero pressure. Zipfel and Sanders [63,64] confirmed the peak at 1.21 eV. In experiments similar to those of Northby and Sanders [61,62], Zipfel and Sanders [63,64] made measurements of the photo-conductivity as a function of pressure up to 16 bar. The photo-conductivity peak detected by Northby and Sanders [61,62] was found to shift to higher photon energies as the pressure increased. This is expected since the radius of the normal electron decreases and the corresponding initial angular frequency increases with increasing pressure. Thus, the transition angular frequencies and energies increase (Eq. (103)).

The next higher energy transition for an electron in superfluid helium is $n = 1 \rightarrow n = \frac{1}{3}$. The transition energy corresponds to $n = \frac{1}{3}$ in Eqs. (103) and (105). The calculated energy neglecting the energy due to the pressure volume work and the surface energy change of the bubble is

$$E = \hbar\omega_{photon} = \frac{\hbar^2}{m_e r_1^2} \left[\frac{1}{(\frac{1}{3})^2} - 1 \right]$$

$$= \frac{\hbar^2}{m_e(6.7 \times 10^{-10}\ \text{m})^2} \left[\frac{1}{(\frac{1}{3})^2} - 1 \right] = 1.3\ \text{eV}, \tag{110}$$

where r_1 is given by Eq. (107). Given the experimental uncertainty of the energy of the lowest energy transition, 1.21 eV, this result confirms that the contributions due to pressure volume work and the surface energy change of the bubble may be neglected.

In the experiments of Northby and Sanders [61,62], Zipfel and Sanders [63,64], and Grimes and Adams [65,65], it was noted that the photo-conductivity effect was absent above

a critical temperature. This temperature was approximately 1.7 K at zero pressure, and decreased to 1.2 K at 20 bar. Roton scattering dominates over phonon scattering at 1.7 K and below [59]. The photo-conductivity signal disappears because of phonon excitation of the bubble motion which causes the excited electron state to decay. As the pressure is increased, the roton energy gap goes down, and so the phonon scattering increases. Thus, it is to be expected that the critical temperature decreases with increasing pressure.

Each stable excited state electron bubble which has a radius of r_1/integer may migrate in an applied electric field. The bubble may be scattered by rotons, phonons, and He^3 impurities. At temperatures less that 1.7 K, roton scattering dominates [59]. An equation for the electron bubble mobility is derived by Baym et al. [67] in terms of the roton-bubble momentum transfer cross section by calculating the rate of roton-bubble momentum transfer using a statistical mechanical approach. In the case of an elementary excitation $\vec{k}$ scattered by the bubble with a differential cross section $\sigma(k, \theta)$ and obeying $|\vec{k}'| \cong |\vec{k}|$, their result may be written

$$\frac{e}{\mu} = -\frac{\hbar^2}{6\pi^2} \int_0^\infty k^4 \frac{\delta n}{\delta \varepsilon} v_g(k)\sigma_T(k)\,dk \tag{111}$$

where μ is the bubble mobility, n is the distribution function of the excitation, $v_g(k)$ is the group velocity of the excitation, and $\sigma_T(k)$ is the momentum-transfer cross section defined by

$$\sigma_T(k) = \int (1 - \cos\theta)\sigma(k, \theta)\,d\Omega. \tag{112}$$

Schwarz and Stark [59] made the reasonable assumption that $\sigma_T(k)$ is a weak function of $k - k_0$. Because of the strong minimum at $k_0 = 1.91\ \text{Å}^{-1}$ in the roton energy spectrum, Eq. (111) then gives to a good approximation

$$\mu = \frac{3\pi^2 e}{\hbar k_0^4 \sigma_T(k_0)} \exp(\Delta/k_B T)$$

$$= \frac{3.38 \times 10^{-25}\ \text{m}^4\ \text{V}^{-1}\ \text{s}^{-1}}{\sigma_T(k_0)} \exp(8.65\ \text{K}/T) \tag{113}$$

where $\Delta/k_B = 8.65 \pm 0.04$ K is the roton energy gap derived from neutron scattering [68]. Schwarz and Stark [59] propose that the roton de Broglie wavelength corresponding to $k_0 = 1.91\ \text{Å}^{-1}$ is $\lambda_0 = 3.3$ which is small compared with $\sqrt{\sigma_T(k_0)/\pi}$; thus, the collision cross section may be nearly geometrical. Although the roton carries a great deal of energy and momentum, its effective mass is much less than that of the ion. Assume that the scattering is elastic, then $|\vec{k}'| \cong |\vec{k}|$ is satisfied. They conclude a hard-sphere cross section given by

$$\sigma_T(k_0) \cong \pi(a_+ + a_r)^2 \tag{114}$$

where a_+ is the radius of the ion and a_r is the effective collision radius of the roton. Using experimental values for a_+ and $\sigma_T(k)$, they find that

$$a_r = 3.7 \pm 0.2\ \text{Å}. \tag{115}$$

They surmise from this that the roton is localized within a region of radius $\approx 3.7 - 4.0$ Å, and that it interacts strongly with any disturbance which penetrates this region. They point out that $\approx 3.7 - 4.0$ Å is only slightly larger than the nearest neighbor distance in liquid helium [69] and that a roton may thus be pictured as a highly correlated motion of an energetic He^4 atom and its nearest neighbors only.

The geometric cross section of the normal electron bubble σ_e is given as

$$\sigma_e = \pi r_1^2 \tag{116}$$

where r_1 is the radius of the unexcited electron bubble given by Eq. (107). From Eq. (107) and Eqs. (113)–(116), the mobility of the normal electron bubble is given by

$$\mu = \frac{3\pi^2 e}{\hbar k_0^4 \pi (a_r + r_1)^2} \exp(\Delta/k_B T)$$

$$= \frac{3.38 \times 10^{-25} \text{m}^4/\text{V s}}{\pi (3.7 \times 10^{-10}\text{m} + 6.7 \times 10^{-10} \text{ m})^2} \exp(8.65 \text{ K}/T) \tag{117}$$

At 1 K, Eq. (117) gives $\mu = 5.7$ cm^2/V s for the mobility of the normal electron bubble ($n = 1$) which is in reasonable agreement with the experimental value of 5 cm^2/V s from Fig. 6.

The normal electron bubble has a uniform constant spherical charge density. This charge density may be modulated by a time and spherically harmonic function as given by Eq. (53).[1] In the case of excited state electron bubbles, the contribution to the roton scattering cross section given by Eq. (112) is larger than the geometric cross section given in Eq. (116) where the radius is given by Eq. (101). In this case, $\sigma_T(k)$ given by Eq. (112) follows the derivation of Baym et al. [67] where the spherical harmonic angular

---

[1] It is interesting to consider that the solutions for the full angular part of the Schrödinger equation (Eq. (4)), $Y_{lm}(\theta, \phi)$, are also the spherical harmonics. McQuarrie [8, pp. 206–221] shows that the Schrödinger equation for the rigid rotor is

$$\hat{H} Y_\ell^{m_\ell}(\theta, \phi) = \frac{\hbar^2 \ell(\ell + 1)}{2I} Y_\ell^{m_\ell}(\theta, \phi) \tag{127}$$

and that $\hat{H}$ and $\hat{L}^2$ differ only by the factor $2I$ for a rigid rotor. So, Eq. (127) is equivalent to

$$\hat{L}^2 Y_\ell^{m_\ell}(\theta, \phi) = \hbar^2 \ell(\ell + 1) Y_\ell^{m_\ell}(\theta, \phi). \tag{128}$$

Thus, we see that the spherical harmonics are also eigenfunctions of $\hat{L}^2$ and that the square of the angular momentum can have values given by

$$L^2 = \hbar^2 \ell(\ell + 1) \quad \ell = 0, 1, 2, 3, \ldots . \tag{129}$$

The flaw with this result with regard to the hydrogen atom is given in the "Schrödinger Theory of the Hydrogen Atom" section. In the case of the electron in helium, the moment of inertia in Eq. (127) decreases with increasing energy states as the corresponding ℓ quantum number increases. The Schrödinger equation is flawed based on the prediction of infinite rotational energy for an electron in superfluid helium.

---

function causes a gain in the scattering cross section that may be modeled after that of a Hertzian dipole antenna. The radiation power pattern of a Hertzian dipole is given by Kong [70]. The radiation power pattern is

$$\langle S \rangle = \frac{1}{2} \text{Re}[\mathbf{E} \times \mathbf{H}] = \hat{r}\frac{\eta}{2} \left(\frac{k|I|\Delta z}{4\pi r} \right) \sin^2 \theta \tag{118}$$

where I is the current, Δz is the length of the dipole, and η is the impedance of free space. The antenna directive gain $D(\theta, \varphi)$ is defined as the radiation of the Poynting power density $\langle S_r \rangle$ over the power P, divided by the area of the sphere:

$$D(\theta, \phi) = \frac{\langle S_r \rangle}{P/4\pi r^2} = \frac{3}{2}\sin^2 \theta. \tag{119}$$

The plot of $D(\theta, \varphi)$ given by Eq. (119) is known as the gain pattern. The directivity of an antenna is defined as the value of the gain in the direction of its maximum value. For the Hertzian dipole the maximum of 1.5 occurs at $\theta = \pi/2$. Thus, the directivity of a Hertzian dipole is 1.5.

The spherical harmonic angular functions are

$$Y_{lm}(\theta, \phi) = \sqrt{\frac{(2l + 1)(l - m)!}{4\pi (l + m)!}} P_l^m(\cos\theta)e^{im\phi}$$

$$= N_{\ell, m_\ell} P_l^m(\cos\theta)e^{im\phi} \tag{120}$$

where N_{ℓ, m_ℓ} is the normalization constant given by

$$N_{\ell, m_\ell} = \sqrt{\frac{(2l + 1)(l - m)!}{4\pi (l + m)!}}. \tag{121}$$

In the case of excited states, $\sigma(k, \theta)$ of Eq. (112) is

$$\sigma(k, \theta) = k^{-2} \left| \frac{\int P_0^0(\cos\theta) e^{i0\phi} \, d\Omega}{\int P_l^m(\cos\theta) e^{im\phi} \, d\Omega} \right|^2 = k^{-2} \left(\frac{N_{\ell, m_\ell}}{N_{0,0}} \right)^2. \tag{122}$$

For excited states, the geometric cross section of the electron bubble σ_e is then given as

$$\sigma_e = \pi r_{n,\ell,m_\ell}^2 \tag{123}$$

where

$$r_{n,\ell,m_\ell} = \frac{N_{\ell, m_\ell}}{N_{0,0}} n r_1. \tag{124}$$

r_1 is the radius of the unexcited electron bubble given by Eq. (107) and $n = 1/$integer. The angular parameters $N_{\ell, m_\ell}/N_{0,0}$ are given with the first few spherical harmonics in Table 1. In this case, $\sigma_T(k)$ is given by Eq. (112) where r_1 is replaced by r_{n,ℓ,m_ℓ} (Eq. (124)). The roton scattering cross section given by the hard-sphere cross section is then

$$\sigma_T(k_0) \cong \pi(r_{n,\ell,m_\ell} + a_r)^2, \tag{125}$$

where a_r is the effective collision radius of the roton given by Eq. (115). From Eqs. (117), (124) and (125), the mobilities

Table 1

The first few spherical harmonics and $N_{\ell,m_\ell}/N_{0,0}$ of Eq. (121) as a function of ℓ, and m_ℓ

Spherical harmonics $Y_{m_\ell}^\ell$	ℓ	m_ℓ	$N_{\ell,m_\ell}/N_{0,0}$
$Y_0^0 = \frac{1}{(4\pi)^{1/2}}$	0	0	1
$Y_1^0 = (\frac{3}{4\pi})^{1/2}\cos\theta$	1	0	$\sqrt{3}$
$Y_1^1 = (\frac{3}{8\pi})^{1/2}\sin\theta\, e^{i\phi}$	1	1	$\sqrt{\frac{3}{2}}$
$Y_1^{-1} = (\frac{3}{8\pi})^{1/2}\sin\theta\, e^{-i\phi}$	1	−1	$\sqrt{\frac{3}{2}}$
$Y_2^0 = (\frac{5}{16\pi})^{1/2}(3\cos^2\theta - 1)$	2	0	$\sqrt{\frac{5}{4}}$
$Y_2^1 = (\frac{15}{8\pi})^{1/2}(\sin\theta\cos\theta\, e^{i\phi})$	2	1	$\sqrt{\frac{15}{2}}$
$Y_2^{-1} = (\frac{15}{8\pi})^{1/2}(\sin^2\theta\cos\theta\, e^{-i\phi})$	2	−1	$\sqrt{\frac{15}{2}}$
$Y_2^2 = (\frac{15}{32\pi})^{1/2}\sin^2\theta\, e^{2i\phi}$	2	2	$\sqrt{\frac{15}{8}}$
$Y_2^{-2} = (\frac{15}{32\pi})^{1/2}\sin^2\theta\, e^{-2i\phi}$	2	−2	$\sqrt{\frac{15}{8}}$

of electron bubbles are given by

$$
\begin{aligned}
\mu &= \frac{3\pi^2 e}{\hbar k_0^4 \pi (a_t + r_{n,\ell,m_\ell})^2} \exp(\Delta/k_B T) \\
&= \frac{3.38 \times 10^{-25}\, \text{m}^4/\text{V s}}{\pi(3.7 \times 10^{-10}\text{m} + n\frac{N_{\ell,m_\ell}}{N_{0,0}} 6.7 \times 10^{-10}\text{m})^2} \\
&\quad \exp(8.65\, \text{K}/T)
\end{aligned}
\tag{126}
$$

where $n = 1/\text{integer}$. The mobility of an excited state electron bubble having a fractional principal quantum number ($n = 1/\text{integer}$) relative to the normal electron bubble as a function of quantum numbers n, ℓ, and m_ℓ is given in Table 2. A plot of Eq. (126) normalized to the mobility of the normal bubble as a function of p corresponding to fractional principal quantum number $n = 1/\text{integer} = 1/p$ for given ℓ, and m_ℓ quantum numbers appears in Fig. 5.

Using time of flight, Doake and Gribbon [71] detected negatively charged ions that had a mobility substantially higher than the normal electron bubble negative ion. This ion, which has become known as the "fast ion", was next seen in another time-of-flight experiment by Ihas and Sanders in 1971 [72]. They showed that the fast ion could be produced by an α or β source, or by an electrical discharge in the helium vapor above the liquid. In addition, they reported the existence of two additional negative carriers, referred to as "exotic ions", that had mobilities larger than the mobility of the normal negative ion, but less than the mobility of the fast ion. These exotic ions were detected only when there was an electrical discharge above the liquid surface. In a paper the following year [73], Ihas and Sanders (IS) reported on further experiments in which at least 13 carriers with different mobilities were detected. The experimental details are described in the thesis of Ihas [74]. Eden and McClintock (EM) [75,76] also detected as many as 13 ions with different mobilities. Both IS and EM put forward a number of proposals to explain the exotic ions, but all of these proposals were shown to be unsatisfactory by Maris [1]. It is significant that the exotic ions appear only when an electrical discharge takes place close to the free surface of the liquid. Under these conditions, the electrons that enter the liquid and form bubbles may absorb light emitted from the discharge. Thus, it is natural to consider the possibility that the exotic ions are electron bubbles in fractional energy states.

The mobility of several electron bubbles in superfluid helium plotted versus the inverse of the temperature is shown in Fig. 6. The temperature dependence of the mobility predicted by Eq. (126) is in good agreement with the data of Ihas [74] and the plots of Maris [1]. The ion assignments given in Fig. 6 are based on their mobilities relative to the normal ion as given in Table 3.

Table 2

The mobility of an excited state electron bubble having a fraction principal quantum number ($n = 1/\text{integer}$) relative to the normal electron bubble as a function of quantum numbers n, ℓ, and m_ℓ given by Eq. (126). The peaks that appear in Fig. 7 and Table 3 are indicated

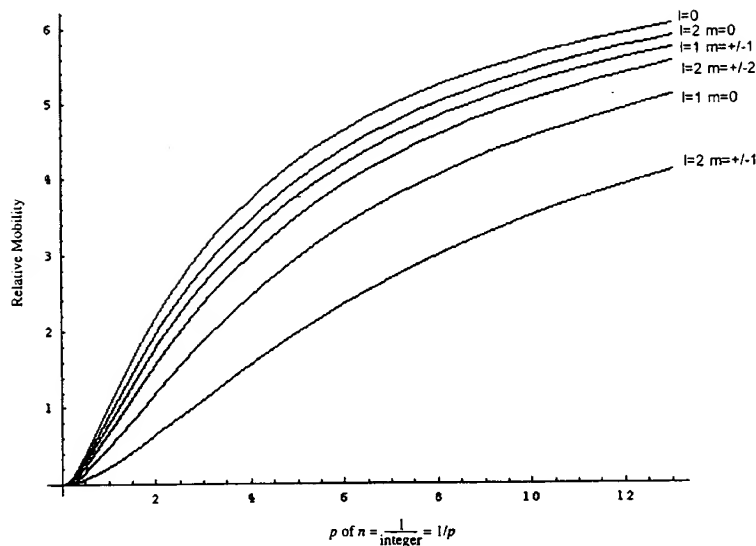| n	$\ell = 0$	$\ell = 1\ m_\ell = 0$	$\ell = 1\ m_\ell = \pm1$	$\ell = 2\ m_\ell = 0$	$\ell = 2\ m_\ell = \pm1$	$\ell = 2\ m_\ell = \pm2$
$\frac{1}{2}$	2.21 Peak # 8	1.22 Peak # 3	1.81 Peak # 5			
$\frac{1}{3}$	3.12 Peak # 10	1.92 Peak # 6	2.66	2.86	1.14 Peak # 2	2.41
$\frac{1}{4}$	3.81 Peak # 11	2.52 Peak # 9	3.33	3.54	1.60 Peak # 4	3.06
$\frac{1}{5}$	4.33 Peak # 12	3.03	3.86	4.07	2.03 Peak # 7	3.59
$\frac{1}{6}$	4.74 Peak # 13	3.47	4.28	4.49	2.41	4.02
$\frac{1}{7}$	5.07 Peak # 14	3.83	4.63	4.83	2.75	4.38
$\frac{1}{8}$	5.34 Peak # 15	4.15	4.93	5.12	3.06	4.68
$\frac{1}{9}$	5.57 Peak # 15	4.42	5.17	5.35	3.34	4.94
$\frac{1}{10}$	5.76 Peak # 15	4.66	5.38	5.56	3.59	5.16
$\frac{1}{11}$	5.92 Peak # 15	4.87	5.56	5.73	3.82	5.35
$\frac{1}{12}$	6.07 Peak # 15	5.05	5.72	5.88	4.02	5.52
$\frac{1}{100}$	7.75 Peak # 15	7.55	7.69	7.72	7.29	7.65

Fig. 5. The mobility (Eq. (126)) of an excited state electron bubble having a fraction principal quantum number ($n = 1/\text{integer} = 1/p$) relative to the normal electron bubble as a function of p for given ℓ, and m_ℓ quantum numbers.
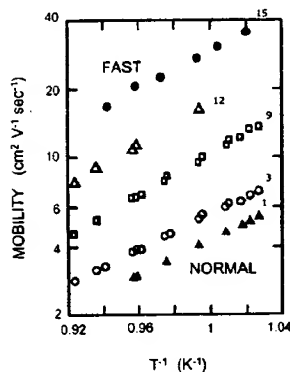

Fig. 6. The mobility from the data of Ihas [1,74] of electron bubbles in superfluid helium plotted versus the inverse of the temperature. Solid triangles are for the normal electron bubble, open squares, circles, triangles and solid circles are for the four ions of the same peak assigned in Fig. 7 and Table 3.

Following a pulse discharge with an electric field applied to superfluid helium, Ihas [74] recorded ion peaks using time of flight. Fifteen ion peaks recorded by Ihas and Sanders are identified in Fig. 7. The mobilities relative to the normal electron bubble ($n = 1$) are given in Table 3. The assignments of the mobilities of excited state electron bubbles having fraction principal quantum number ($n = 1/\text{integer}$) relative to the normal electron bubble as a function of quantum numbers n, ℓ, and m_ℓ is also given in Table 3 based on the theoretical values given in Table 2. The agreement between theory and experiment is excellent.

Peaks 14–15 of Fig. 7 and Table 3 represent a band with a cutoff at a migration velocity of about 7.5 times the velocity of the normal ion as $n = 1/\text{integer}$ approaches zero ($n = 1/100$ was used to calculate this limiting case). The electron radius is predicted to decrease such that the effective collision radius of the roton determines the maximum mobility as given by Eq. (126). The theoretically predicted maximum of electron bubble mobility of about seven times that of the normal ion is confirmed by the Ihas data [74] where the band comprising peaks 14–15 correspond to $n \leqslant \frac{1}{7}$. Furthermore, Eden and McClintock [75] and Doake and Gribbon [71] measured the drift velocity as a function of applied electric field. The fast ion showed a slope of the drift velocity versus applied electric field of about seven times

Table 3
The migration times and experimental mobilities of the 15 ion peaks shown in Fig. 7 relative to the normal ion with their assignments to excited state electron bubbles with quantum numbers n, ℓ, and m_ℓ and theoretical mobilities given in Table 2

| Peak #	Migration time (arbitrary units)	Mobility relative to peak # 1	Theoretical mobility relative to Peak # 1	Assignment n, ℓ, and m_ℓ
1	9.8	1.00	1	$n = 1 \; \ell = 0 \; m_\ell = 0$
2	8.2	1.20	1.14	$n = \frac{1}{3} \; \ell = 2 \; m_\ell = \pm 1$
3	7.6	1.29	1.22	$n = \frac{1}{2} \; \ell = 1 \; m_\ell = 0$
4	6.2	1.58	1.6	$n = \frac{1}{4} \; \ell = 2 \; m_\ell = \pm 1$
5	5.4	1.81	1.81	$n = \frac{1}{2} \; \ell = 1 \; m_\ell = \pm 1$
6	5	1.96	1.92	$n = \frac{1}{3} \; \ell = 1 \; m_\ell = 0$
7	4.85	2.02	2.03	$n = \frac{1}{5} \; \ell = 2 \; m_\ell = \pm 1$
8	4.35	2.25	2.21	$n = \frac{1}{2} \; \ell = 0 \; m_\ell = 0$
9	3.9	2.51	2.52	$n = \frac{1}{4} \; \ell = 1 \; m_\ell = 0$
10	3.3	2.97	3.12	$n = \frac{1}{3} \; \ell = 0 \; m_\ell = 0$
11	2.8	3.50	3.81	$n = \frac{1}{4} \; \ell = 0 \; m_\ell = 0$
12	2.1	4.67	4.33	$n = \frac{1}{5} \; \ell = 0 \; m_\ell = 0$
13	2	4.90	4.74	$n = \frac{1}{6} \; \ell = 0 \; m_\ell = 0$
14	1.8	5.44	5.07	$n = \frac{1}{7} \; \ell = 0 \; m_\ell = 0$
15	1.3	7.54	7.75	$n = \frac{1}{100} \; \ell = 0 \; m_\ell = 0$
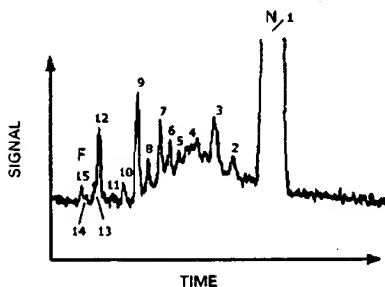
Fig. 7. Data trace from Ihas [74] showing the detected ion signal as a function of time. N and F denote the normal and fast ion peaks. The peaks labeled 1–15 are assigned in Table 3. For a description of experimental condition see Ihas [74].

Fig. 8. Data traces from Eden and McClintock [75] of the current at the collector of the velocity spectrometer (arbitrary units) as a function of the elapsed time t after a pulse was applied to release exotic ions. Signals are shown for a range of strong electric fields as indicated in units of 10^5 V/m by the number above each trace. The steep rise on the right-hand sides of the signals indicates the arrival of the normal ion current. For a description of experimental condition see Eden and McClintock [75].

that of the normal ion. Thus, these results agree with the data of Ihas and with theoretical predictions.

The small deviation of the data from the theoretical in Table 3 may be due to differences in ion production rates and mechanisms based on the spectrum of the arc. Transitions between states may also be a peak broadening factor wherein a peak undergoes a transition to a faster or slower state during migration. This may provide an explanation for the large peak width of peak #4 of Fig. 7 as well as the broad continuum background in this region. Scattering other

than roton scattering may also be involved, and these mechanisms such as phonon scattering and inter-bubble "impurity" scattering would effect larger ions more than smaller ions due to their larger geometric cross section. A preferred method to determine the migration times of each electron bubble ($n = 1/$integer) is to cause the formation of each specific state with resonant radiation (Eq. (103) and Eq. (105))

Fig. 9. The limiting electron bubble velocities shown in the data traces of Fig. 8 relative to the normal electron bubble as a function of p corresponding to principal quantum number $n = 1/\text{integer} = 1/p$ where $\ell = 0$, and $m_\ell = 0$.
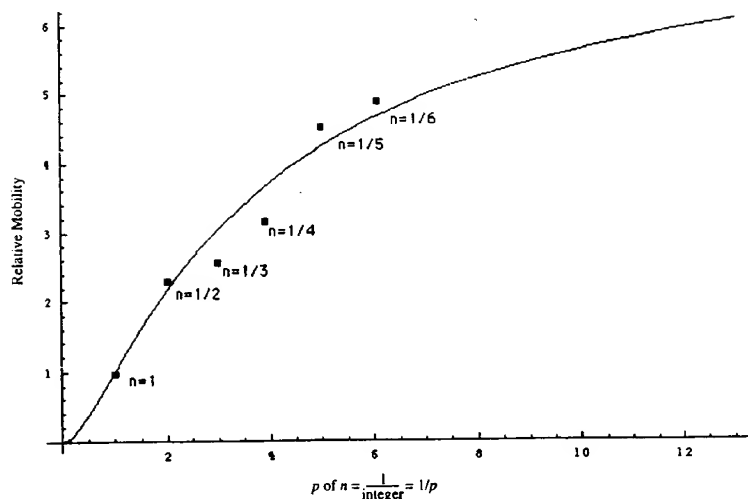
and to measure the migration time of each ion separately relative to the $n = 1$ bubble.

Using a time-of-flight method, Doake and Gribbon [71] discovered that a fast ion can exist in superfluid helium which unlike the normal ion may be accelerated to the Landau critical velocity v_L for roton creation without undergoing metamorphosis to a charged vortex ring, even under the saturated vapor pressure. As a consequence, Eden and McClintock [75] studied the behavior of the exotic ions in strong electric field and reported evidence suggesting that intermediate mobility negative ions can nucleate quantized vortex rings in superfluid helium when subject to strong electric fields. Eden and McClintock observed that the drift velocity of intermediate ions may not be linear with electric field and that this effect varies with the particular intermediate ion. Eden and McClintock [75] further observed a decrease in drift velocities of intermediate ions with inter-ion variation for increasing sufficiently strong electric fields. They attributed this to the formation of negatively charged vortex rings. However, for an appropriate electric field, the drift velocity approaches a maximum independent of the field, and formation of charged vortex rings does not explain the field independence [75]. The limiting velocities shown in the data traces of Fig. 8 may be a function of the size of the ion for all intermediate ions. In this case, the limiting velocity data of Eden and McClintock [75] are plotted in Fig. 9 with the mobility of the normal ion as a function of p corresponding to principal quantum number $n = 1/\text{integer} = 1/p$.

The agreement between the experimental data and theoretical mobilities is excellent. The existence of multiple peaks under the fast peak such as peaks #14 and #15 of Fig. 7 is also supported by the data of Eden and McClintock [75] because the peak of highest mobility split into the two peaks shown in Fig. 8 at higher fields.

4. Conclusion

Recently, the behavior of free electrons in superfluid helium has again forced the issue of the meaning of the wave function. Electrons form bubbles in superfluid helium which reveal that the electron is real and that a physical interpretation of the wave function is necessary. Furthermore, when irradiated with low energy light, the electrons carry increased current at different rates as if they exist with at least 15 different sizes. Peaks are observed in the photoconductivity absorption spectrum at 0.5 and 1.21 eV. A theory of classical quantum mechanics derived from first principles by Mills [2] gives closed form physical solutions for the electron in atoms, the free electron, and the free electron in superfluid helium. The predicted photo-conductivity absorption spectrum and the mobilities of the 15 identified ions match the experimental results. The data support the existence of fractional principal quantum energy states of free electrons in superfluid helium predicted by Mills classical theory. The results have implications that the concept

of probability waves of quantum mechanics must be abandoned and atomic theory must be based in reality.

Appendix A.

A.1. Quantum electrodynamics is purely mathematical and has no basis in reality

Quantum mechanics failed to predict the results of the Stern–Gerlach experiment which indicated the need for an additional quantum number. Quantum electrodynamics was proposed by Dirac in 1926 to provide a generalization of quantum mechanics for high energies in conformity with the theory of special relativity and to provide a consistent treatment of the interaction of matter with radiation. From Weisskopf [18], "Dirac's quantum electrodynamics gave a more consistent derivation of the results of the correspondence principle, but it also brought about a number of new and serious difficulties". Quantum electrodynamics: (1) does not explain nonradiation of bound electrons; (2) contains an internal inconsistency with special relativity regarding the classical electron radius—the electron mass corresponding to its electric energy is infinite; (3) it admits solutions of negative rest mass and negative kinetic energy; (4) the interaction of the electron with the predicted zero-point field fluctuations leads to infinite kinetic energy and infinite electron mass; (5) Dirac used the unacceptable states of negative mass for the description of the vacuum; yet, infinities still arise. In 1947, contrary to Drac's predictions Lamb discovered a 1000 MHz shift between the $^2S_{1/2}$ state and the $^2P_{1/2}$ state of the hydrogen atom [113]. This so called Lamb shift marked the beginning of modern quantum electrodynamics. In the words of Dirac [77], "No progress was made for 20 years. Then a development came initiated by Lamb's discovery and explanation of the Lamb Shift, which fundamentally changed the character of theoretical physics. It involved setting up rules for discarding . . . infinities . . .". Renormalization is presently believed to be required of any fundamental theory of physics [78].

However, dissatisfaction with renormalization has been expressed at various times by many physicists including Dirac [79] who felt that, "This is just not sensible mathematics. Sensible mathematics involves neglecting a quantity when it turns out to be small—not neglecting it just because it is infinitely great and you do not want it!"

Furthermore, Oskar Klein pointed out a glaring paradox implied by the Dirac equation which was never resolved [80]. "Electrons may penetrate an electrostatic barrier even when their kinetic energy, $E - mc^2$ is lower than the barrier. Since in Klein's example the barrier was infinitely broad this could not be associated with wave mechanical tunnel effect. It is truly a paradox: Electrons too slow to surpass the potential, may still only be partially reflected. . . . Even for an infinitely high barrier, i.e. $r_2 = 1$ and energies ≈ 1 MeV (the reflection coefficient) R is less than 75%! From (2) and (3) it appears that as soon as the barrier is sufficiently high: $V > 2mc^2$, electrons may transgress the repulsive wall—seemingly defying conservation of energy. . . . Nor is it possible by way of the positive energy spectrum of the free electron to achieve complete Einstein causality".

The Rutherford experiment demonstrated that even atoms are comprised of essentially empty space [81]. Zero-point field fluctuations, virtual particles, and states of negative energy and mass invoked to describe the vacuum are nonsensical and have no basis in reality since they have never been observed experimentally and would correspond to an essentially infinite cosmological constant throughout the entire universe including regions of no mass. As given by Waldrop [82], "What makes this problem into something more than metaphysics is that the cosmological constant is observationally zero to a very high degree of accuracy. And yet, ordinary quantum field theory predicts that it ought to be enormous, about 120 orders of magnitude larger than the best observational limit. Moreover, this prediction is almost inescapable because it is a straightforward application of the uncertainty principle, which in this case states that every quantum field contains a certain, irreducible amount of energy even in empty space. Electrons, photons, quarks—the quantum field of every particle contributes. And that energy is exactly equivalent to the kind of pressure described by the cosmological constant. The cosmological constant has accordingly been an embarrassment and a frustration to every physicist who has ever grappled with it".

The spin of the electron and the Lamb shift are calculated from first principles in closed form by Mills [2]. The spin angular momentum results from the motion of negatively charged mass moving systematically, and the equation for angular momentum, $r \times p$, can be applied directly to the wave function (a current density function) that describes the electron. The Lamb shift results from conservation of linear momentum of the photon.

A.2. The postulate of quantum measurement is experimentally disproved

Modern quantum mechanics has encountered several obstacles that have proved insurmountable as pointed out previously in the "General considerations" section and the "Classical electron radius" section of Mills [2]. And, quantum mechanics leads to certain philosophical interpretations [17, pp. 94–104] which are not sensible. Some conjure up multitudes of universes including "mind" universes; others require belief in a logic that allows two contradictory statements to be true. The question addressed is whether the

universe is determined or influenced by the possibility of our being conscious of it.

The meaning of quantum mechanics is debated, but the Copenhagen interpretation is predominant. It asserts that "what we observe is all we can know; any speculation about what a photon, an atom or even a SQUID (Superconducting Quantum Interference Device) really is or what it is doing when we are not looking is just that speculation" [17, pp. 94–104]. According to this interpretation every observable exists in a state of superposition of possible states, and observation or the potential for knowledge causes the wave function corresponding to the possibilities to collapse into a definite. As shown by Platt [83] in the case of the Stern–Gerlach experiment, "the postulate of quantum measurement [which] asserts that the process of measuring an observable forces the state vector of the system into an eigenvector of that observable, and the value measured will be the eigenvalue of that eigenvector".

According to the Zeno no-go theorem which is a consequence of the postulate of quantum measurement, observation of an atom collapses its state into a definite; thus, transitions cannot occur under continuous observation. Recently, it has become possible to test this postulate via an experiment involving transitions of a single atom, and the results are inconsistent with the predictions. Quoting from the caption of Fig. 10 of the article, by Dehmelt [84],

"Shelving" the Ba^+ optical electron in the metastable D level. Illuminating the ion with a laser tuned close to its resonance line produces strong resonance fluorescence and an easily detectable photon count of 1600 photons/s. When later an auxiliary weak Ba^+ spectral lamp is turned on, the ion is randomly transported into the metastable $D_{5/2}$ level for 30-s lifetime and becomes invisible. After dwelling in this shelving level for 30 s on average, it drops down to the S ground state spontaneously and becomes visible again. This cycle repeats randomly. According to the Zeno no-go theorem, no quantum jumps should occur under continuous observation.

In Scientific American [17, pp. 94–104] at "Superimposed philosophers"—"Pritchard says that physicists may one day be able to pass biologically significant molecules such as proteins or nucleic acids through an interferometer. In principle, one could even observe wave like behavior in a whole organism, such as an amoeba. There are some obstacles, though: the amoeba would have to travel very slowly, so slowly, in fact that it would take some three years to get through the interferometer, according to Pritchard. The experiment would also have to be conducted in an environment completely free of gravitation or other influences—that is, in outer space.

Getting a slightly larger or more intelligent organism, for instance, a philosopher, to take two paths through a two-slit apparatus would be even trickier. "It would take longer than the age of the universe," Pritchard says.".

This article is a good example of how far fetched QM has become (e.g. *parallel mind universes*).

In addition to the interpretation that photons, electrons, neutrons, and even human beings [17, pp. 94–104] have no definite form until they are measured, a more disturbing interpretation of quantum mechanics is that a measurement of a quantum entity can instantaneously influence another light years away. Einstein argued that a probabilistic versus deterministic nature of atomic particles leads to disagreement with special relativity. In fact, the nonlocality result of the Copenhagen interpretation violates causality. As a consequence of the indefinite nature of the universe according to quantum mechanics and the implied uncertainty principle, Einstein, Podolsky, and Rosen (EPR) in a classic paper [85] presented a paradox which led them to infer that quantum mechanics is not a complete theory. See the section entitled, "Heisenberg uncertainty principle predicts nonlocality, noncausality, spooky actions at a distance, and perpetual motion which can be shown to be experimentally incorrect".

Louis de Broglie, one of the founders of quantum mechanics, also condemned the probability wave approach. "But the causal link between two phenomenon implies the existence of a trajectory, and to deny this existence is to renounce causality and to deprive oneself of any understanding" [86].

A.3. Quantum mechanics based on the Schrödinger equation (SE) is an incomplete theory since it does not explain gravity or particle masses

Quantum mechanics cannot explain the existence of particles with precise masses and gives no basis of gravity. If fact, a straight forward application of the uncertainty principle predicts that particles of precise mass/energy cannot exist. These shortcomings are compounded by the prediction of zero-point field fluctuations, virtual particles, and states of negative energy and mass invoked to describe the vacuum. These consequences of the uncertainty principle are nonsensical and have no basis in reality since they have never been observed experimentally and would correspond to an essentially infinite cosmological constant throughout the entire universe including regions of no mass [87].

Mills [2] derives a theory from first principles that gives closed form solutions based on general relativity and Maxwell's equations for particle masses. It gives gravitation from the atom to the cosmos.

For any kind of wave advancing with limiting velocity and capable of transmitting signals, the equation of front propagation is the same as the equation for the front of a light wave. By applying this condition to electromagnetic and gravitational fields at particle production, the Schwarzschild metric (SM) is derived from the classical wave equation which modifies general relativity to include conservation of spacetime in addition to momentum and matter/energy. The result gives a natural relationship between Maxwell's equations, special relativity, and general relativity. It gives gravitation from the atom to the cosmos. The universe is time

harmonically oscillatory in matter energy and spacetime expansion and contraction with a minimum radius that is the gravitational radius. In closed form equations with fundamental constants only, CQM gives the deflection of light by stars, the precession of the perihelion of Mercury, the particle masses, the Hubble constant, the age of the universe, the observed acceleration of the expansion, the power of the universe, the power spectrum of the universe, the microwave background temperature, the uniformity of the microwave background radiation, the microkelvin spatial variation of the microwave background radiation, the observed violation of the GZK cutoff, the mass density, the large-scale structure of the universe, and the identity of dark matter which matches the criteria for the structure of galaxies. In a special case wherein the gravitational potential energy density of a blackhole equals that of the Plank mass, matter converts to energy and spacetime expands with the release of a gamma ray burst. The singularity in the SM is eliminated.

A.4. The wave function solutions of quantum mechanics as probability waves are inconsistent with probability theory

Wavefunction solutions of the Schrödinger equation are interpreted as probability density functions. This interpretation is fatally flawed since the use of "probability" in this instance does not conform to the mathematical rules and principles of probability theory.

Schrödinger sought a physical interpretation of his equation. He interpreted $e\Psi^*(x)\Psi(x)$ as the charge-density or the amount of charge between x and $x + dx$ (Ψ^* is the complex conjugate of Ψ). Presumably, then, he pictured the electron to be spread over large regions of space. Three years after Schrödinger's interpretation, Max Born, who was working with scattering theory, found that this interpretation led to logical difficulties, and he replaced the Schrödinger interpretation with the probability of finding the electron between r, θ, ϕ and $r + dr, \theta + d\theta, \phi + d\phi$ as

$$\int \Psi(r, \theta, \phi)\Psi^*(r, \theta, \phi)dr\, d\theta\, d\phi. \qquad (A.1)$$

Born's interpretation is generally accepted. The electron *is viewed as a discrete particle* that moves here and there (from $r = 0$ to $r = \infty$), and $\Psi\Psi^*$ gives the time average of this *motion*.

Born's interpretation is generally accepted. Nonetheless, interpretation of the wave function is a never-ending source of confusion and conflict. Many scientists have solved this problem by conveniently adopting the Schrödinger interpretation for some problems and the Born interpretation for others. This duality allows the electron to be everywhere at one time—yet have no volume. Alternatively, the electron can be viewed as a discrete particle that moves here and there (from $r = 0$ to $r = \infty$), and $\Psi\Psi^*$ gives the time average of this motion.

There is profound internal inconsistency in using probability theory as the foundation of quantum theory. In the

tradition of Einstein, a Gedanken experiment is proposed. At a given time, there exists an exact average of the amount of money in the wallets of the members of a given group such as the visitors to BLP's web site. So, I postulate some statistical test and sample 0 to all of the visitors. If I sample all of the visitors, I would know the average exactly. If I sample less than all, I could apply statistics. Using the sampling data with the assumption of a statistical distribution (e.g. *normal distribution*), I could perform a two-sided null test and determine the average within a confidence limit based on the statistical model. Probability theory permits statistical projections based on incomplete knowledge. But, according to the quantum mechanical definition of "probability", before the sampling, the number is between negative infinity and positive infinity simultaneously, and the act of sampling creates the money in the wallets of the visitors. Another example is that the capture of the numbered balls by a lottery machine creates the numbers on lottery tickets.

The basis of this paradox is that *statistical theory is based on an existing deterministic reality with incomplete information; whereas, quantum measurement acts on a "probability density function" to determine a reality that did not exist before the measurement.*

Consider the simplest of systems, the "ground state wave function of the hydrogen atom". The wave function ascribes the electron an infinite number of positions and energies simultaneously including states with infinite negative kinetic energy and infinite positive potential energy. But, experiments are consistent with 13.6 eV of kinetic energy and 27.2 eV of potential energy in every case. Atomic hydrogen has been extensively studied. For example, hydrogen has long been the focus of combustion research involving kinetic and spectroscopic studies. Neutral scattering of hydrogen atoms is always observed. How can the point electron have a statistical distribution of separate positions and energies and still always give rise to neutral scattering? If position follows a probability density function, why do all of the positions give rise to the identical scattering behavior wherein the positions of the point particles (proton and electron of the incoming hydrogen atom and the point scattered electron) are random independent variables? How do all of the electric fields always identically cancel if positions are statistical? Even one neutral scattering event violates Chebyshev's inequality.

It is also nonsense to interpret the "probability" ascribed by the wave function of the electron as equivalent to that of statistical thermodynamics. The latter corresponds to a classical statistical distribution of particles such as photons or molecules over states such as energy states for a macroscopic system. It is nonsensical to assign a single particle (e.g. an electron) to a statistical distribution over many states. It is similarly nonsensical to associate a stable property such as a thermodynamic property to a single particle based on such statistics.

Quantum mechanical textbooks express the movement of the electron, and the Heisenberg uncertainty principle is an

expression of the statistical aspects of this movement. Mc-Quarrie [8, backcover], gives the electron speed in the $n = 1$ state of hydrogen as 2.18764×10^6 m/s. Remarkably, the uncertainty in the electron speed according to the uncertainty principle is 1.4×10^7 m/s [8, p. 38] which is an order of magnitude larger than the speed. With Penning traps, it is possible to measure transitions of electrons of single ions. This case can be experimentally distinguished from statistics over equivalent transitions in many ions. Whether many or one, the transition energies are always identical within the resonant line width. So, probability has no place in describing atomic energy levels on this basis either.

According to quantum mechanics, the existence of the electron in the nucleus is the basis of spin-nuclear coupling called Fermi contact interaction [88] where $4\pi r^2 \Psi^2 \, dr$ is not zero since the Ψ^2 is not zero and the nucleus is comprised of baryons. According to the *standard model*, baryons as opposed to leptons have structure, contain more fundamental particles—namely quarks and gluons, and are not point particles. For example, the proton has an experimentally measured radius of $r_p = 1.3 \times 10^{-15}$ m. The spin-nuclear coupling energy is of the order of 10^{-24} J despite the infinite Coulombic energy of the electron when found in the nucleus (i.e. $r \rightarrow 0$ in the Schrödinger equation). This consequence of quantum mechanics is further flawed since this state is experimentally disproved. The nucleus does not contain electrons [81, p. 407]. Since the electron has no volume, based on this logic, the probability that an electron can capture a photon to form an excited state is zero. This internal inconsistency based on the description of the electron as a point particle probability wave does not arise in Mills classical theory of quantum mechanics. The spin nuclear energies are calculated by Mills in closed form based on first principles without the requirement that the electron is in the nucleus [2, pp. 98–109] and are in close agreement with the experimental results.

What does the wave function represent? It certainly does not represent the probability that a point particle will be found in a given region in space at any given instant of time if sampled. And, it has negative as well as positive values of probability which is nonsensical. This is circumvented by squaring it. But, why not take the root mean squared value or the magnitude? In the case of a wave such as an acoustic or electromagnetic wave, the energy or intensity is given as the square of the amplitude. But, when did it become correct that a probability density function (pdf) has an energy or intensity? Quantum theory confuses the concepts of a wave and a pdf that are based on totally different mathematical and physical principles. It is further meaningless to normalize such a function with the interpretation that the expectation value must be one. In addition, the postulates of the "probability" wave are internally inconsistent since negative probability density functions are often invoked to describe "antibonding orbitals" in molecules. It appears that the word "probability" as applied to quantum mechanics has nothing to do with classical probability theory.

A.5. The Schrödinger equation fails to explain scattering experiments

Scattering experiments are not consistent with an uncertainty in the radial or angular position of the electron. The Schrödinger equation interpreted as a probability wave of a point particle cannot explain that the hydrogen atom is neutral. For example, it cannot explain neutral scattering of electrons or light from hydrogen. The point particles must align perfectly; otherwise Rutherford scattering would be observed. In this case, the uncertainty principle is violated. The Born interpretation can only be valid if the speed of the electron is equal to infinity. (The electron must be in all positions weighted by the probability density function during the time of the scattering event). The correct aperture function for the Born interpretation is a Dirac delta function having a Fourier transform of a constant divided by s^2 which is equivalent to the case of the point nucleus (the Rutherford equation). The Born interpretation must be rejected because the electron velocity cannot exceed the speed of light without violating special relativity.

The elastic scattering of electrons from an atomic beam of helium atoms provides a test of the wave function solutions of the Schröinger equation. Mills [2, pp. 19–213] gives a closed form solution of the elastic scattering of 500 eV electrons from helium atoms as the Fraunhofer pattern in the far field. Mills gives a closed form equation of the free electron [2, pp. 110–120] and a closed form equation of the helium atom [2, pp. 176–191]. This is the case of $Z = 2$, in the closed form equation that Mills has solved for all two electron atoms. The calculation is a Fourier optics type which reduces to a spherical lens calculation. The math is well known. The resultant closed form equation has no adjustable parameters. The predictions identically and continuously match the experimental scattering data [89–91]. In the case of the quantum mechanical calculation, the calculation is on a point-by-point basis without regard to internal consistency or physical laws. Furthermore, it is unstable—blows up to positive or negative infinity based on roundoff error, contains adjustable parameters, and in the words of the authors, "at smaller scattering angles, however, the Born approximation calculation fails utterly, the experimental curve rising much more steeply than the theoretical" [89].

Furthermore, QM calculations are not even internally consistent. Take the inelastic scattering of electrons from He atoms as an example. Rather than using point particles which is the norm, a single plane wave is used as the equation of all of the incident electrons [92]. And, the Schrödinger equation predicts that each of the functions that corresponds to a highly excited state electron as well as the ionized electron are sinusoidal over all space which is nonsensical, are not integrable, and can not be normalized. Thus, each is infinite [7]. The SE does not give a point or a plane wave as the function of an ionized electron.

Measurements of the resistivity of hydrogen as a function of pressure provides a test of quantum mechanics which is

similar to scattering experiments. The scalar and vector potential functions of the electrons of the hydrogen molecule are given by Mills [2, pp. 234–259] as a closed form solution of the Laplacian in elliptic coordinates with the nonradiative boundary constraint. The many solutions of the hydrogen molecule based on quantum mechanics have many flaws such as internal inconsistency, violation of fundamental laws, and use of variable parameters such as "effective nuclear charge for the proton". For example, Kolos and Wolniewicz [93,94] use a 100 terms and an effective nuclear charge of 1.072. Whereas, Kolos and Roothaan [95] use an effective nuclear charge of 1.197, and their predicted bond energy is 30% less than the experimental value. The proton charge in Mills' closed form calculation is identically equal to the experimentally measured charge of the proton, and Mills' bond energy matches the experimental energy. Recent measurements of the resistivity of hydrogen as a function of pressure confirm Mills' solution rather than quantum mechanics. The finite dimensions of the hydrogen molecule are evident in the plateau of the resistivity versus pressure curve of metallic hydrogen [96]. This is in contradiction to the predictions of quantum probability functions such as an exponential distribution in space.

A.6. It has been shown experimentally that the Heisenberg uncertainty principle has nothing to do with wave-particle duality

Feynman states [97], "It is impossible to design an apparatus to determine which hole the electron passes through, that will not at the same time disturb the electrons enough to destroy the interference pattern". If an apparatus is capable of determining which hole the electron goes through, it *cannot* be so delicate that it does not disturb the pattern in an essential way. No one has ever found (or even thought of) a away around the uncertainty principle. *so we must assume that it describes a basic characteristic of nature*".

Feynman's position has recently been over turned by an experiment by Durr et al. [98]. According to Gerhard Rempe [99], who lead the Durr et al. experimental team, "The Heisenberg uncertainty principle has nothing to do with wave-particle duality". Durr et al. report, "We show that the back action onto the atomic momentum implied by Heisenberg's position-momentum uncertainty relation cannot explain the loss of interference".

A.7. Uncertainty principle

More than 60 years after the famous debate between Niels Bohr and Albert Einstein on the nature of quantum reality, a question central to their debate—the nature of quantum interference—has resurfaced. The usual textbook explanation of wave–particle duality in terms of unavoidable "measurement disturbances" is experimentally proven incorrect by an experiment reported by Durr et al. [98]. They report on the interference fringes produced when a beam of cold atoms

is diffracted by standing waves of light. Their interferometer displayed fringes of high contrast—but when they manipulated the electronic state within the atoms with a microwave field according to which path was taken, the fringes disappeared entirely. The interferometer produced a spatial distribution of electronic populations which were observed via fluorescence. The microwave field canceled the spatial distribution of electronic populations. The key to this new experiment was that although the interferences are destroyed, the initially imposed atomic momentum distribution left an envelope pattern (in which the fringes used to reside) at the detector. A careful analysis of the pattern demonstrated that it had not been measurably distorted by a momentum kick of the type invoked by Bohr, and therefore that any locally realistic momentum kicks imparted by the manipulation of the internal atomic state according to the particular path of the atom are too small to be responsible for destroying interference.

Durr et al. conclude that the "Heisenberg uncertainty relationship has nothing to do with wave–particle duality" and further conclude that the phenomenon is based on entanglement and correlation. Their interpretation of the principles of the experiment is that directional information is encoded by manipulating the internal state of an atom with a microwave field, which entangles the atom's momentum with its internal electronic state. Like all such entangled states, the constituent parts lose their separate identity. But the attachment of a distinguishable electronic label to each path means that the total electronic-plus-path wave function along one path becomes orthogonal to that along the other, and so the paths cannot interfere. By encoding information as to which path is taken within the atoms, the fringes disappear entirely. The internal labeling of paths does not even need to be read out to destroy the interferences: all you need is the option of being able to read it out.

According to Durr et al., the mere existence of information about an entity's path causes its wave nature to disappear. But, correlations are observations about relationships between quantities and do not cause physical processes to occur. The existence of information about an entity's path is a consequence of the manipulation of the momentum states of the atoms which resulted in cancellation of the interference pattern. It was not the cause of the cancellation. The cancellation is calculated by Mills [2, pp. 405–413] as the superposition of two single slit patterns as opposed to a double slit pattern which is based on determinism. In this case, an appropriate replacement terminology for "correlations are responsible for the loss of the interference pattern" is "determinism is responsible for the loss of the interference pattern".

In contrast to QM, in Mills' theory, a particle has one position and one energy in the absence of measurement. It does not have an infinite number of superimposed positions and energies simultaneously with no physical form until measurement is made. The rise-time band width relationship holds during measurement. This is a conservation statement.

Mills regards the Heisenberg uncertainty principle which is based on the probability model of fundamental particles to be wrong as well as the implicit spontaneous creation of energy and virtual particles from a perfect vacuum. The Heisenberg uncertainty principle violates first principle laws which are directly proven experimentally, and the predicted virtual particles generated from vacuum are rejected since they are not experimentally observed. Mills' theory predicts wave particle duality nature of light and particles based on first principles rather than requiring that different physics applies on the atomic scale.

A.8. The Heisenberg uncertainty principle predicts nonlocality, noncausality, spooky actions at a distance, and perpetual motion which can be shown to be experimentally incorrect

A.8.1. Flawed interpretation of the results of the Aspect experiment—there is no spooky action at a distance

Bell [100] showed that in a Gedanken experiment of Bohm [101] (a variant of that of EPR) no local hidden-variable theory can reproduce all of the statistical predictions of quantum mechanics. Thus, a paradox arises from Einstein's conviction that quantum-mechanical predictions concerning spatially separated systems are incompatible with his condition for locality unless hidden variables exist. Bell's theorem provides a decisive test of the family of local hidden-variable theories (LHVT). In a classic experiment involving measurement of coincident photons at spatially separated detectors, Aspect [102] showed that local hidden-variable theories are inconsistent with the experimental results. Although Aspect's results are touted as a triumph of the predictions of quantum mechanics, the correct coincidence rate of detection of photons emitted from a doubly excited state of calcium requires that the z component of the angular momentum is conserved on a photon pair basis. As a consequence, a paradox arises between the deterministic conservation of angular momentum and the Heisenberg uncertainty principle. The prediction derived from the quantum nature of the electromagnetic fields for a single photon is inconsistent with Aspect's results, and Bell's theorem also disproves quantum mechanics. Furthermore, the results of Aspect's experiment are predicted by Mills' theory wherein locality and causality hold. Mills derives the predicted coincidence rate based on first principles [2, pp. 511–521]. The predicted rate identically matches the observed rate.

The Aspect experiment is a test of locality and local hidden variable theories. The Aspect experiment is also a test of quantum mechanics and the HUP. In one design of the experiment, photons are incident to a beam splitter which causes each photon to be split into two that travel along opposite paths to separate detectors. The separate detectors measure the polarization of the arriving photons. By using synchronous detection, photons of a pair may be later com-

pared. The data indicate a random pattern at each detector individually; however, when photons are matched up as pairs, an essentially perfect correlation exists. The quantum mechanical explanation is that before the photon was split its state of polarization was indeterminate. It possessed an infinite number of states in superposition. Then when one element of the pair was detected information traveled instantaneously (infinitely faster than the speed of light—otherwise known as a spooky action at a distance) to cause the other photon to have a matching polarization. In quantum mechanical terms, the states were entangled, and measurement of one photon caused the other photon's wave function to collapse into the matching state.

The correct explanation is that each photon entering the beam splitter originally had a determined state, and angular momentum was conserved on a photon-by-photon basis at the splitter. Thus, each photon of a pair had a matching polarization before it hit the detector. Locality and cause and effect hold. There is no spooky action at a distance. This experiment actually disproves quantum mechanics. It also disproves local hidden variable theories. The data of the Aspect experiment matches a classical derivation, not a quantum mechanical one.

Everyday observation demonstrates that causality and locality always hold. Bell's theorem postulates that a statistical correlation of $A(a)$ and $B(b)$ is due to information carried by and localized within each photon, and that at some time in the past the photons constituting one pair were in contact and in communication regarding this information. This is the case in many everyday experiences such as transmission, processing, and reception of signals in microelectronics devices. Locality and causality always hold. They hold on the scale of the universe also. But, according to the Big-Bang theory of quantum mechanics all photons were at one time in contact; thus, no locality or causality should be observed at all. This is nonsense. The results of the Aspect experiment support the EPR paradox that QM does not describe physical reality. There is a mistake in the derivation of the analysis of the data from Aspect's experiment [103,104].

Bell's theorem is just an inequality relationship between *arbitrary* probability density functions with certain assumptions about independence, expectation value equal to one, etc. wherein an additional probability distribution function is introduced which may represent local hidden variables or something else for that matter. And, the initial functions may correspond to quantum mechanical statistics or something else for that matter. Standard probability rules are accepted such as the probability of two independent events occurring simultaneously is the product of their independent probabilities. What is calculated and plugged into the formula for the functions and whether the substitutions are valid are the issues that determine what Bell's inequality tests when compared with data. Historically, Bell's inequality is a simple proof of statistical inequalities of expectation values of observables given that quantum statistics is

correct and that the physical system possesses "hidden variables". However, if deterministic statistics are actually calculated and quantum statistics is equivalent to deterministic statistics (e.g. detection of a wave at an inefficient detector) but possesses further statistics based on the probability nature of the theory (statistical conservation of photon angular momentum), then Bell's inequality is actually testing determinism versus quantum theory when compared to the data.

Rather than demonstrating that QM does not give us all of the information about the physical world, the data is consistent with the result that QM does not describe the physical world, and that deterministic physics does. A deterministic theory is not required to posses local hidden variables. Maxwell's equations is a deterministic theory. It does not have local hidden variables (LHV). There is no corresponding statistical distribution function. Bell's theorem is a simple proof of statistical inequalities of expectation values of observables given that "*quantum*" statistics is correct and that the physical system possesses "hidden variables" corresponding to an additional statistical distribution function. What was actually derived to explain the results of the Aspect experiment [102] was a classical calculation of the detection of an extended particle, the polarized photon, at an inefficient detector wherein determinism holds with respect to conservation of angular momentum [103,104]. Thus, the statistics defined as "*quantum*" was actually deterministic. (The derivation is given by Mills [2, pp. 511–521]). Furthermore, in actuality, quantum statistics must also possess other statistical distribution functions corresponding to the probability nature of the theory such as a statistical distribution for the z component of angular momentum which is conserved statistically as the number of photons goes to infinity. Thus, the real quantum mechanics statistics corresponds to a local hidden variable theory (LHVT) with respect to the definitions of the arbitrary probability distribution functions in Bell's inequality. Aspect recorded the expectation value of the coincidence rate at separated randomly oriented inefficient polarization analyzers for pairs of photons emitted from a doubly excited state calcium atom. The data showed a violation of Bell's inequality. This proves determinism and the real QM statistics fails the test. Furthermore, the observed coincidence count rate of Aspect [102] is equal to that predicted classically from the statistics of measurement at an inefficient detector only. The additional finite distribution function required in the case of quantum mechanics and QED results in incorrect predictions. There is no spooky action at a distance.

The Aspect experiment shows that momentum in conserved on a photon-by-photon basis, not statistically as predicted by the HUP. Similar experiments regarding tests of entanglement predicted by the HUP are shown to be consistent with first principle predictions and reveal flaws in the interpretations based on the HUP. The HUP implies nonlocality, noncausality, and spooky actions at a distance which can be shown to be experimentally incorrect.

A.8.2. Flawed interpretation of the results on a single $^9Be^+$ ion in a trap in a continuous Stern–Gerlach experiment—an ion cannot be at two places at the same time

There is a mistake in the analysis of the data from Monroe et al. [105]. Their interpretation that the same beryllium ion was observed to be at widely separated points at the same time is absolute nonsense. Their experimental results show that locality and causality hold [2, pp. 521–536].

A report in New York Times [106] entitled "Physicists put atom in 2 places at once" states, "a team of physicists has proved that an entire atom can simultaneously exist in two widely separated places". The article further states, "In the quantum "microscale" world, objects can tunnel magically through impenetrable barriers. A single object can exist in a multiplicity of forms and places. In principle, two quantum-mechanically "entangled" objects can respond instantly to each other's experiences, even when the two objects are at the opposite ends of the universe". Experimentally, interference patterns were observed by Monroe et al. [105] for a single $^9Be^+$ ion in a trap in a continuous Stern–Gerlach experiment. Monroe's interpretation of the experimental observation was that the ion wave function interfered with itself wherein the ion was at two separate places at the same time corresponding to a wave function state called a "Schrödinger cat" state [105–107]. According to Monroe et al.,

> A "Schrödinger cat"-like state of matter was generated at the single atom level. A trapped $^9Be^+$ ion was laser-cooled to the zero-point energy and then prepared in a superposition of spatially separated coherent oscillator states. This state was created by application of a sequence of laser pulses, which entangles internal (electronic) and external (motional) states of the ion. The "Schrödinger cat" superposition was verified by detection of the quantum mechanical interference between the localized wave packets. This mesoscopic system may provide insight into the fuzzy boundary between the classical and quantum worlds by allowing controlled studies of quantum measurement and quantum decoherence.

The "Schrödinger cat" state analysis relies on the postulate that the *Pauli exclusion principle* applies to Rabi states wherein a rotation of the magnetic moment of the unpaired electron of an RF- trapped $^9Be^+$ ion is represented by a linear combination of spin 1/2 ($| \uparrow \rangle_i$) and spin $-1/2$ ($| \downarrow \rangle_i$) states. Three steps of rotation of the spin magnetic moment by a time harmonic field provided by pairs of copropagating off-resonant laser beams which drove two-photon-stimulated Raman magnetic resonance transitions were each separated by displacement laser pulses which excited a resonant translational harmonic oscillator level of the trapped ion by coupling only with the $| \uparrow \rangle_i$ state. According to Monroe, "this selectivity of the displacement force provides quantum entanglement of the internal state with the external motional

state. Although the motional state can be thought of as nearly classical, its entanglement with the internal atomic quantum levels precludes any type of semiclassical analysis". The interference was detected by exciting a fluorescent transition which only appreciatively coupled to the $| \downarrow \rangle_i$ state. Thus, the fluorescence reading was proportional to the probability P_1 the ion was in state $| \downarrow \rangle_i$. The "Schrödinger cat" superposition was supposedly verified by detection of the quantum mechanical interference between the localized wave packets.

However, the interference arises not from the existence of the ion at two places at once. The positively charged ion was excited to a time harmonic translational energy state, and the spin quantization axis was defined by an applied 0.20 mT magnetostatic field at an angle of $\pi/4$ with respect to the x-axis of the RF-trap. The frequency of the energy to "flip" the spin state was equivalent to the projection of that of the translational harmonic oscillator onto the spin axis

$$\frac{\omega_x}{2\pi} \cos^2 \frac{\pi}{4} = (11.2 \text{ MHz})(0.5) = 5.605 \text{ MHz} = \frac{\Delta E_{mag}^{spin}}{h} \quad (A.2)$$

given by Eqs. (37.45)–(37.48) of Mills [2, pp. 521–566]. Thus, interference occurred between the Stern–Gerlach transition and the synchrotron radiation corresponding to the charged harmonic oscillator. Since the displacement beams affected only motion correlated with the $| \uparrow \rangle_i$ state, a rotation of the magnetic moment such that $\delta \neq 0$ with application of the displacement beams gives rise to a phase shift of the interference pattern. The closed form calculation is given in Mills [2, pp. 521–536].

A.8.3. Flawed interpretation of the results of experiments on a small SQUID coupled to a biased large superconducting current loop—a superconducting current cannot flow in opposite directions at the same time

There is a mistake in the analysis of the data from Friedman et al. [108]. Their interpretation that a superconducting current loop can exist as a superposition of contradictory states at the same time is absolute nonsense. It is shown by Mills [2] that their experimental results are consistent with locality and causality.

A recent report in The New York Times [109] entitled "Here, There and Everywhere: A Quantum State of Mind" states, "Physicists at Delft University of Technology have put a 5-micrometer-wide loop of superconducting wire into a "quantum superposition" of two contradictory possibilities: in one, the current flows clockwise; in the other, current flows counterclockwise". The article further states, "In the realm of atoms and smaller particles, objects exist not so much as objects as mists of possibilities being here, there and everywhere at the same time—and then someone looks and the possibilities suddenly collapse into definite locations". The experiment was a simplified version of the concept of Schrödinger's cat. In 1935, Schrödinger [110] attempted to

demonstrate the limitations of quantum mechanics using a thought experiment in which a cat is put in a quantum superposition of alive and dead states.

Instead of a cat, Friedman et al. [108] used a small square loop of superconducting wire linked to a SQUID (Superconducting Quantum Interference Device). A SQUID comprises a superconducting loop with a Josephson junction, a weak link that causes magnetic flux to be linked in integer units of the magnetic flux quantum. When the loop is placed in an external magnetic field, the loop spontaneously sets up an electrical current to cancel the field or generate an additional magnetic field, adjusting the magnetic field to a unit of the magnetic flux quantum, one of the allowed values. In the experiment of Friedman et al., the loop was placed in a magnetic field equal to one half of the first allowed value, a magnetic flux quantum. Thus, the loop could set up either a current to raise the field strength to the first allowed value, or with equal probability, a current of equal magnitude flowing in the opposite direction to cancel out the external field. A pulse of microwaves was applied at the frequency to cause a transition of the magnetic moment of the current loop as an entirety. The absorption of microwaves caused the magnetic state of the SQUID to change and the current to reverse its direction.

Experimentally, a measurement always gave one of the two possible answers, clockwise or counterclockwise, never a zero cancellation. A difference in energy at which the flip transition occurred between the two possibilities was detected by a group led by J. Lukens and J. Friedman at the State University of New York (SUNY). A simple explanation was that the microwaves simply flipped the current direction which had an energy bias in one direction versus the opposite based on the corresponding presence or absence of a magnetic flux quantum within the SQUID. Rather, they interpreted the results as experimental evidence that a SQUID can be put into a superposition of two magnetic flux states: one corresponding to a few microamperes of current flowing clockwise and the other corresponding to the same amount of current flowing anticlockwise. "Just as the cat is neither alive nor dead but a ghostly mix of the two possibilities, the current flows neither clockwise or counterclockwise, but is a mix of the two possibilities [109]". According to Friedman, "we can have two of these macroscopically well-defined states at the same time. Which is something of an affront to our classical intuitions about the world [109]".

Current running in both directions simultaneously is nonsensical. Current is a vector and must have only one direction. The energy difference observed by Friedman et al. can be explained *classically*. The experimental apparatus comprised a small SQUID coupled to a large current loop. A second SQUID magnetometer read the flux state of the first sample SQUID. The energy difference was not due to superposition of flux states. Rather, it was due to the nature of the electron which carries the superconducting current and links flux in units of the magnetic flux quantum. Consequently, the sample SQUID linked zero or one magnetic flux

quantum. When excited by electromagnetic radiation of a resonant frequency, individual electrons undergo a spin-flip or Stern–Gerlach transition corresponding to a reversal of the electron magnetic moment, angular moment, and current. The Stern–Gerlach transition energies of electrons superimpose. The energy difference observed by Friedman et al. matches the energy corresponding to the flux linkage of the magnetic flux quantum by the ensemble of superconducting electrons in their entirety with a reversal of the corresponding macroscopic current. The linkage was caused by high power microwave excitation of a Stern–Gerlach transition of the magnetically biased loop which caused a concomitant change in the flux state of the separately magnetically biased sample SQUID. In this case, the microwave frequency was kept constant, and the bias flux of the loop was scanned at a fixed magnetic bias of the sample SQUID until the resonance with the superposition of the Stern–Gerlach transitions of the superconducting electrons in their entirety was achieved.

A.8.4. Flawed prediction of perpetual motion by the Heisenberg uncertainty principle

Another consequence of HUP wherein entanglement of states is implicit is the prediction of perpetual motion. Schewe and Stein report on the work of Allahverdyan and Nieuwenhuizen [111]:

Armen Allahverdyan of, CEA Saclay (France)/University of Amsterdam (Netherlands)/Yerevan Physics Institute (Armenia), aarmen@spht.saclay.cea.fr, and Theo Nieuwenhuizen of the University of Amsterdam (nieuwenh @wins.uva.nl, 011-31-20-525- 6332) [112] suggest that a quantum particle (such as an electron) interacting strongly with a reservoir of particles may violate the Clausius inequality—one formulation of the second law of thermodynamics, which states that it is impossible to do work without losing heat. What the researchers term "appalling behavior" can be traced to the quantum mechanical property of entanglement, in which a quantum particle (such as an electron) is so strongly interlinked with another particle or group of particles that the resulting behavior cannot be treated by standard thermodynamic approaches. In this paper, the Amsterdam scientists study the entanglement of a particle with a "quantum thermal bath", a reservoir of particles with which the first particle can exchange energy and momentum. According to the researchers, entanglement prevents the quantum bath from observing the normal requirements for a heat bath. Therefore, thermodynamics simply cannot say anything useful about the system.

Standard thermodynamics dictates that the bath be in thermal equilibrium and not interact strongly with an external object. On the contrary, the bath strongly interacts with something external to it (the entangled particle) and it cannot reach equilibrium, since it constantly exchanges energy and momentum with the particle. At low temperatures where entanglement could be easily preserved, the researchers state that this system can apparently violate the Clausius inequality—in which the heat gained by the particle must be less than or equal to the temperature multiplied by the change in its entropy (or disorder). Near absolute zero temperatures, a situation which would ordinarily require the particle to lose heat, the researchers show that the particle could gain heat, by the Clausius relation. According to this scenario, applying a cyclic parameter such a periodically varying external magnetic field can cause the entangled particle to extract work from the bath—something forbidden in a classical system. *Further, the researchers say that this phenomenon could be said to constitute a perpetual motion machine of the second kind.*

-A.9. The Postulated Schrödinger equation does not explain the stability of the hydrogen atom

QM theory does not say why an atom radiates. Quantum states of QM refer to energy levels of probability waves. From these, emission and absorption of radiation is inferred. But QM does not explain why it is emitted or absorbed or why certain states are stable. For example, the Schrödinger equation (SE) was *postulated* in 1926. It does not explain the stability of the hydrogen atom. To say that the atom obeys the SE is nonsensical. Consider the hydrogen atom without regard to the mathematical formula called the SE. Mathematics does not determine physics. It only models physics. The SE is not based on directly testable physical laws such as Maxwell's equations. It only gives correlations, and is in fact inconsistent with physical laws.

As a historical note:

[My father] said, "I understand that they say that light is emitted from an atom when it goes from one state to another, from an excited state to a state of lower energy."

I said, "That's right."

"And light is kind of a particle, a photon, I think they call it."

"Yes."

"So if the photon comes out of the atom when it goes from the excited to the lower state, the photon must have been in the atom in the excited state."

I said, "Well no."

He said, "Well, how do you look at it so you can think of a particle photon coming out without it having been there in the excited state?"

I thought a few minutes, and I said, "I'm sorry; I don't know. I can't explain it to you."

-Richard P. Feynman, The Physics Teacher (September 1969).

As shown in "Schrödinger states below $n = 1$" section, the definition of the "ground state" is mathematically purely arbitrary. It is always experimentally observed that the hydrogen atom does not spontaneously emit light once it has achieved an energy level of 13.6 eV. Thus, it is taught in textbooks that atomic hydrogen cannot go below the ground

state. But, atomic hydrogen having an experimental ground state of 13.6 eV can only exist in a vacuum or in isolation, and atomic hydrogen cannot go below this ground state only when it is in isolation. Atomic hydrogen is extremely reactive, and there is no known composition of matter containing hydrogen in the ground state of 13.6 eV.

Since the Schrödinger equation offers no foundation for the stability of isolated atomic hydrogen, Feynman attempted to find a basis for the definition of the "ground state" in the Heisenberg uncertainty principle [97, p. 2–6]. Feynman's based his derivation on the determination of the momentum as $p \approx h/a$ from the uncertainty principle wherein he argues, "We need not trust our answer to within factors like 2, π, etc. We have not even defined a very precisely". The kinetic energy follows classically from the momentum, and the electrostatic energy is given classically to give the total energy as

$$E = h^2/2ma^2 - e^2/a. \qquad (A.3)$$

Feynman determined the minimum energy in order to solve for the radius of the hydrogen atom.

$$dE/da = -h^2/ma^3 + e^2/a^2 = 0. \qquad (A.4)$$

The result is exactly the Bohr radius.

The uncertainty principle [8, pp. 135–140] is

$$\sigma_x \sigma_p \geqslant \hbar/2, \qquad (A.5)$$

where σ_x and σ_p are given by

$$\sigma_x^2 = \int \psi^*(\hat{X} - \langle x \rangle)^2 \psi \, dx, \qquad (A.6)$$

$$\sigma_p^2 = \int \psi^*(\hat{P} - \langle p \rangle)^2 \psi \, dx. \qquad (A.7)$$

The definition of the momentum operator in a *one-dimensional* system is [8, pp. 135–140]

$$\hat{P}_x = -i\hbar \frac{d}{dx} \qquad (A.8)$$

and the position operator is

$$\hat{X} = x \quad \text{(multiply by } x\text{)}. \qquad (A.9)$$

Based on the uncertainty principle, Feynman's derivation of the Bohr radius is flawed on the basis of at least five points:

(1) The uncertainty principle gives a lower limit to the product of the *uncertainty* in the momentum and the position—*not* the momentum and the position. The momentum or position could be arbitrarily larger or smaller than its uncertainty. For example, quantum mechanical textbooks express the movement of the electron, and the Heisenberg uncertainty principle is an expression of the statistical aspects of this movement. McQuarrie [15], gives the electron speed in the $n = 1$ state of hydrogen as 2.18764×10^6 m/s. Remarkably, the uncertainty in the electron speed according to the uncertainty principle is 1.4×10^7 m/s [8, p. 38] which is an order of magnitude larger than the speed.

(2) Feynman's derivation of the Bohr radius is internally inconsistent since the kinetic and electrostatic energies were derived *classically*; whereas, quantum mechanics and the uncertainty principle are not consistent with classical mechanics.

(3) Feynman's derivation of the Bohr radius is internally inconsistent since the uncertainty principle requires *uncertainty* in the position and momentum. Yet, Eqs. (2.10) and (2.11) of Feynman (Eqs. (A.2)–(A.4)) can be solved to give an *exact* rather than a most probable electron position, momentum, and energy.

(4) Feynman's derivation of the Bohr radius is flawed since Eq. (2.11) of Feynman (Eq. (A.2)) is nothing more than the Bohr force balance equation given by McQuarrie [8, pp. 22–26] and also derived by Mills [7]. Thus, this approach fails at explaining the stability of the 13.6 eV state beyond an arbitrary definition wherein "We need not trust our answer to within factors like 2, π, etc. [97, p. 2–6]".

(5) The faulty logic is compounded by the fact that the uncertainty principle is founded on the definition of the momentum operator given by Eq. (A.8) and the position operator given by Eq. (A.9). Thus, the uncertainty principle is based on the postulated Schrödinger equation and its associated postulates and descriptions of particles as probability waves. *It is not based on physics.* In fact, it is nonsensical in many physical tests such as scattering of electrons from neutral atoms, confining electrons to atoms, confining electrons to atoms in excited states wherein a photon causing a transition carries $\hbar$ of angular momentum, and the cosmological consequences of the uncertainty principle as described previously. Also, it is disproved experimentally that it provides a basis for the wave–particle duality nature of light and particles; even though, the opposite is widely touted as discussed in the "It has been shown experimentally that the Heisenberg uncertainty principle has nothing to do with wave-particle duality" section.

According to the generally accepted Born interpretation of the meaning of the wave function, the probability of finding the electron between r, θ, ϕ and $r + dr, \theta + d\theta, \phi + d\phi$ is given by Eq. (A.1). The electron *is viewed as a discrete particle* that moves here and there (from $r = 0$ to $r = \infty$), and $\Psi\Psi^*$ gives the time average of this *motion*. The Schrödinger equation possesses terms corresponding to the electron radial and angular kinetic energy which sum with the potential energy to give the total energy. These are necessary conditions for an electron bound by a central field [10]. Herman Haus derived a test of radiation based on Maxwell's equations [15]. Applying Haus's theorem to the point particle that must have radial kinetic energy demonstrates that the Schrödinger solution for the $n = 1$ state of hydrogen is radiative; thus, it violates Maxwell's equations. Since none is observed for the $n = 1$ state, QM is inconsistent with observation. The derivation is shown in the "Schrödinger wave

functions in violation of Maxwell's equations" section of Mills [2, pp. 487–489].

In contrast, the classical theory of Mills is derived from Maxwell's equation with the constraint that the $n = 1$ state is nonradiative. This approach leads to the prediction of stable states below the traditional $n = 1$ state. Corresponding states are confirmed by the data on the free electrons in superfluid helium.

References

[1] Maris HJ. J Low Temp Phys 2000;120:173.

[2] Mills R. The grand unified theory of classical quantum mechanics. January 2000 ed. Cranbury, NJ: BlackLight Power, Inc., Distributed by Amazon.com; posted at www.blacklightpower.com.

[3] Weiss P. Sci News 2000;158(14):216.

[4] Ball P. Nature, http://helix.nature.com/nsu/000921/000921-1.html.

[5] Jackson I. New Sci 2000. http://www.newscientist.com/nl/1014/double.html.

[6] Fuchs CA, Peres A. Quantum theory needs no Interpretation. Phys Today 2000;70.

[7] Mills R. The hydrogen atom revisited. Int J Hydrogen Energy 2000;25(12):1171–83.

[8] McQuarrie DA. Quantum chemistry, Mill Valley, CA: University Science Books, 1983. p. 78–9.

[9] Jackson JD. Classical electrodynamics. 2nd ed. New York: Wiley, 1962. p. 84–108.

[10] Margenau H, Murphy GM. The mathematics of chemistry and physics. 2nd ed. New York: D. Van Nostrand Company, Inc., 1956. p. 363–7.

[11] Moore W. Schrödinger life and thought. Cambridge: Cambridge University Press, 1989. p. 198.

[12] Fowles GR. Analytical mechanics. 3rd ed. New York: Holt, Rinehart, and Winston, 1977. p. 57–60.

[13] Margenau H, Murphy GM. The mathematics of chemistry and physics. New York: D. Van Nostrand Company, Inc., 1943. p. 77–8.

[14] Bahcall NA, Ostriker JP, Perlmutter S, Steinhardt PJ. Science 1999;284:1481–8.

[15] Haus HA. On the radiation from point charges. Am J Phys 1986;54:1126–9.

[16] Dyson F. Feynman's proof of Maxwell equations. Am J Phys 1990;58:209–11.

[17] Horgan J. Quantum philosophy. Sci Am 1992;96.

[18] Weisskopf VF. Rev Mod Phys 1949;21(2):305–15.

[19] Abbott TA, Griffiths DJ. Am J Phys 1985;153(12):1203–11.

[20] Goedecke G. Phys Rev B 1964;135:281.

[21] Mills R. Spectroscopic identification of a novel catalytic reaction of atomic hydrogen and the hydride ion product. Int J Hydrogen Energy, in press.

[22] Mills R, Greenig N, Hicks S. Optically measured power balances of anomalous discharges of mixtures of argon, hydrogen, and potassium, rubidium, cesium, or strontium vapor, Int J Hydrogen Energy, submitted for publication.

[23] Mills R, Nansteel M. Anomalous argon-hydrogen-strontium discharge. IEEE Trans Plasma Sci, submitted for publication.

[24] Mills R, Nansteel M, Lu Y. Anomalous hydrogen-strontium discharge, Eur J Phys D, submitted for publication.

[25] Mills R, Dong J, Lu Y. Observation of extreme ultraviolet hydrogen emission from incandescently heated hydrogen gas with certain Catalysts. Int J Hydrogen Energy, 2000;25:919–43.

[26] Mills R. Observation of extreme ultraviolet emission from hydrogen-KI plasmas produced by a hollow cathode discharge. Int J Hydrogen Energy, 2001;26(6):579–592.

[27] Mills R. Temporal behavior of light-emission in the visible spectral range from a Ti-K₂CO₃-H-cell. Int J Hydrogen Energy, 2001;26(4):327–332.

[28] Mills R, Onuma T, Lu T. Formation of a hydrogen plasma from an incandescently heated hydrogen-catalyst gas mixture with an anomalous afterglow duration. Int J Hydrogen Energy, in press.

[29] Mills R, Nansteel M, Lu Y. Observation of extreme ultraviolet hydrogen emission from incandescently heated hydrogen gas with strontium that produced an anomalous optically measured power balance. Int J Hydrogen Energy, 2001;26(4):309–326.

[30] Mills R, Dong J, Lu Y, Conrads J. Observation of extreme ultraviolet hydrogen emission from incandescently heated hydrogen gas with certain catalysts. 1999 Pacific Conference on Chemistry and Spectroscopy and the 35th ACS Western Regional Meeting, Ontario Convention Center, California, October 6–8, 1999.

[31] Mills R, Dong J, Greenig N, Lu Y. Observation of extreme ultraviolet hydrogen emission from incandescently heated hydrogen gas with certain catalysts. National Hydrogen Association, 11th Annual U.S. Hydrogen Meeting, Vienna, VA, February 29–March 2, 2000.

[32] Mills R, Dhandapani B, Greenig N, He J, Dong J, Lu Y, Conrads H. Formation of an energetic plasma and novel hydrides from incandescently heated hydrogen gas with certain catalysts. National Hydrogen Association, 11th Annual U.S. Hydrogen Meeting, Vienna, VA, February 29–March 2, 2000.

[33] Mills J. Dong, Greenig N, Lu Y. Observation of extreme ultraviolet hydrogen emission from incandescently heated hydrogen gas with certain catalysts. 219th National ACS Meeting, San Francisco, California, March 26–30, 2000.

[34] Mills R. BlackLight power technology—a new clean energy source with the potential for direct conversion to electricity. Global Foundation, Inc. Conference entitled Global Warming and Energy Policy, Fort Lauderdale, FL, November 26–28, 2000.

[35] Mills R. BlackLight power technology—a new clean energy source with the potential for direct conversion to electricity. Global Foundation International Conference on Global Warming and Energy Policy Dr. Behram N. Kursunoghu, Chairman, Fort Lauderdale, FL, November 26–28, 2000, in press.

[36] Mills R, Dhandapani B, Greenig N, He J, Dong J, Lu Y, Conrads H. Formation of an energetic plasma and novel hydrides from incandescently heated hydrogen gas with certain catalysts. 219th National ACS Meeting, San Francisco, California, March 26–30, 2000.

[37] Mills R, Dhandapani B, Greenig N, He J, Dong J, Lu Y, Conrads H. Formation of an energetic plasma and novel hydrides from incandescently heated hydrogen gas with certain catalysts. June ACS Meeting, 29th Northeast

Regional Meeting, University of Connecticut, Storrs, CT, June 18–21, 2000.

[38] Mills R, Dhandapani B, Greenig N, He J, Dong J, Lu Y, Conrads H. Formation of an energetic plasma and novel hydrides from incandescently heated hydrogen gas with certain catalysts. August National ACS Meeting 220th ACS National Meeting, Washington, DC, August 20–24, 2000.

[39] Mills R, Dhandapani B, Nansteel M, He J, Voigt A. Identification of compounds containing novel hydride ions by nuclear magnetic resonance spectroscopy. Int J Hydrogen Energy, in press.

[40] Mills R, Dhandapani B, Greenig N, He J. Synthesis and characterization of potassium iodo hydride. Int J Hydrogen Energy 2000;25(12):1185–203.

[41] Mills R. Novel inorganic hydride. Int J Hydrogen Energy 2000;25:669–83.

[42] Mills R. Novel hydrogen compounds from a potassium carbonate electrolytic cell. Fusion Technol 2000;37(2):157–82.

[43] Mills R, Dhandapani B, Nansteel M, He J, Shannon T, Echezuria A. Synthesis and characterization of novel hydride compounds. Int J Hydrogen Energy, 2001;26(4):339–367.

[44] Mills R. Highly stable novel inorganic hydrides. J Mater Res submitted.

[45] Mills R. Novel hydride compound. 1999 Pacific Conference on Chemistry and Spectroscopy and the 35th ACS Western Regional Meeting, Ontario Convention Center, California, October 6–8, 1999.

[46] Mills R, Dhandapani B, Greenig N, He J. Synthesis and characterization of potassium iodo hydride. 1999 Pacific Conference on Chemistry and Spectroscopy and the 35th ACS Western Regional Meeting, Ontario Convention Center, California, October 6–8, 1999.

[47] Mills R, He J, Dhandapani B. Novel hydrogen compounds. 1999 Pacific Conference on Chemistry and Spectroscopy and the 35th ACS Western Regional Meeting, Ontario Convention Center, California, October 6–8, 1999.

[48] Mills R. Novel hydride compound. National Hydrogen Association, 11th Annual U.S. Hydrogen Meeting, Vienna, VA, February 29–March 2, 2000.

[49] Mills R, He J, Dhandapani B. Novel alkali and alkaline earth hydrides. National Hydrogen Association, 11th Annual U.S. Hydrogen Meeting, Vienna, VA, February 29–March 2, 2000.

[50] Mills R, Novel hydride compound. 219th National ACS Meeting, San Francisco, California, March 26–30, 2000.

[51] Mills R, He J, Dhandapani B. Novel alkali and alkaline earth hydrides. 219th National ACS Meeting, San Francisco, California, March 26–30, 2000.

[52] Mills R, He J, Dhandapani B. Novel alkali and alkaline earth hydrides. August National ACS Meeting, 220th ACS National Meeting, Washington, DC, August 20–24, 2000.

[53] Mills R. The grand unified theory of classical quantum mechanics. Global Foundation, Inc. Orbis Scientiae entitled *The Role of Attractive and Repulsive Gravitational Forces in Cosmic Acceleration of Particles. The Origin of the Cosmic Gamma Ray Bursts*, 29th Conference on High Energy Physics and Cosmology Since 1964, Dr. Behram N. Kursunoglu, Chairman, December 14–17, 2000, Lago Mar Resort, Fort Lauderdale, FL.

[54] Mills R. The grand unified theory of classical quantum mechanics. Il Nuovo Cimento, submitted.

[55] Mills R, Good W, Voigt A, Jinquan Dong. Minimum heat of formation of potassium iodo hydride. Int J Hydrogen Energy, submitted.

[56] Sidgwick NV. The chemical elements and their compounds, vol. 1. Oxford, Clarendon Press, 1950. p. 17.

[57] Lamb MD. Luminescence spectroscopy. London: Academic Press, 1978. p. 68.

[58] Labov S, Bowyer S. Spectral observations of the extreme ultraviolet background. The Astrophysical Journal 1991;371:810–9.

[59] Schwarz KW, Stark RW. Phys Rev Lett 1969;22(24):1278–80.

[60] Mizushima M. Quantum mechanics of atomic spectra and atomic structure. New York: W.A. Benjamin, Inc., 1970. p. 17.

[61] Northby JA. Ph.D. thesis, University of Minnesota, 1966, unpublished.

[62] Northby JA, Sanders TM. Phys Rev Lett 1967;18:1184.

[63] Zipfel CL. Ph.D. thesis, University of Michigan, 1969, unpublished.

[64] Zipfel CL, Sanders TM. In: Allen JF, Finlayson DM, McCall DM editors. Proceedings of the 11th International Conference on Low Temperature Physics. St. Andrews, Scotland: St. Andrews University, 1969. p. 296.

[65] Grimes CC, Adams G. Phys Rev B 1990;41:6366.

[66] Grimes CC, Adams G. Phys Rev B 1990;45:2305.

[67] Baym G, Barrera RG, Pethick CJ. Phys Rev Letters 1961;22(1):20–3.

[68] Henshaw DG, Woods ADB. Phys. Rev. Letters 1961;121: p. 1266.

[69] London F. Superfluids (Dover Publications, New York, 1964), Vol. III.

[70] Shi LC, Kong JA, Applied Electromagnetism, Brooks/Cole Engineering Division, Monterey, CA, (1983), pp. 210–215.

[71] Doake CSM, Gribbon PWF. Phys Lett 1969;30A(4):251–3.

[72] Ihas GG, Sanders TM. Phys Rev Lett 1971;27:383.

[73] Ihas GG, Sanders TM. In: Timmerhaus KD, O'Sullivan WJ, Hammel EF (editors), Proceedings of the 13th International Conference on Low Temperature Physics, (Plenum, New York, 1972), Vol. 1, p. 477.

[74] Ihas G.G. Ph.D. thesis, University of Michigan, 1971.

[75] Eden VL, McClintock PVE. Phys Lett A 1984;102(4):197–200.

[76] Eden VL, M. Phil. thesis, University of Lancaster, 1986.

[77] Dirac PAM. In: Salam Aet al., editor. From a life of physics. Singapore: World Scientific, 1989.

[78] Milonni PW. The quantum vacuum. Boston: Academic Press, Inc., p. 90.

[79] Dirac PAM. In: Hora H, Shepanski JR, editors. Directions in physics, New York: Wiley, 1978. p. 36.

[80] Wergeland H. The Klein paradox revisited. In: van der Merwe A. editor. Old and new questions in physics, cosmology, philosophy, and theoretical biology. New York: Plenum Press 1983. pp. 503–15.

[81] Beiser A. Concepts of modern physics. 4th ed. New York: McGraw-Hill Book Company, 1978, pp. 119–22.

[82] Waldrop MM. Science 1988;242:1248–50.

[83] Platt DE. Am J Phys 1992;60(4):306–8.

[84] Dehmelt HJ. Am J Phys 1990;58(1):17–27.

[85] Einstein A, Podolsky B, Rosen N. Phys Rev 1935;47:777.

[86] de Broglie L. In: van der Merwe A editor. Old and new questions in physics, cosmology, philosophy, and theoretical biology. New York: Plenum Press, 1983. p. 83–6.

[87] Waldrop MM. Science 1988;242:1248–50.

[88] Karplus M, Porter RN. Atoms and molecules an introduction for students of physical chemistry. Menlo Park, CA: The Benjamin/Cummings Publishing Company, 1970. p. 567.

[89] Bromberg PJ. Absolute differential cross sections of elastically scattered electrons. I. He, N_2, and CO at 500 eV. J Chem Phys 1969;50(9):3906–21.

[90] Geiger J. Elastische und unelastische Streuung von Elektronen an Gasen. Z Phys 1963;175:530–42.

[91] Peixoto EM, Bunge CF, Bonham RA. Elastic and inelastic scattering by He and Ne atoms in their ground states. Phys Rev 1969;181:322–8.

[92] Bonham RA, Fink M. High energy electron scattering, ACS Monograph. New York: Van Nostrand Reinhold Company, 1974.

[93] Kolos W, Wolniewicz L. J Chem Phys 1964;41:3663.

[94] Kolos W, Wolniewicz L. J Chem Phys 1968;49:404.

[95] Kolos W, Roothaan CCJ. Rev Mod Phys 1960;32:219.

[96] Nellis WJ. Making metallic hydrogen. Sci. Am 2000; 84–90.

[97] Feynman RP, Leighton RB, Sands M. The Feynman lectures on physics quantum mechanics. Reading, MA: Addison-Wesley Publishing Company, p. 1–9.

[98] Durr S, Nonn T, Rempe G. Nature 1998;395:33–7.

[99] Science News. Wave or particle? Heisenberg, take a hike! 1998; 154.

[100] Bell JS. Physics 1965;1:195.

[101] Bohm D. Quantum theory, Englewood Cliffs, NJ: Prentice-Hall, Inc., 1951. p. 614.

[102] Aspect A, Grangier P, Gerard R. Phys Rev Lett 1981;47(7):460–3.

[103] Clauser JF, et al. Phys Rev Lett 1969;23(15):880–4.

[104] Horne MA. Experimental consequences of local hidden variable theories. Thesis, Boston University, 1969.

[105] Monroe C, Meekhof DM, King BE, Wineland DJ. Science 1996;272:1131–5.

[106] Browne MW. Physicist put atom in two places at once, New York Times, Tuesday, May 28, 1996. p. B5–B6.

[107] Taubes G. Science 1996;272:1134.

[108] Friedman JR, Patella V, Hen W, Tolpygo SK, Lukens JE. Quantum superposition of distinct macroscopic states. Nature 2000;406:43–5.

[109] Chang K. The New York Times, Tuesday, July 11, 2000. p. F3.

[110] E. Schrödinger, Die gegenwärtige situation in der quantenmechanik, Naturwissenschaften 1935;23:807–12, 823–8, 844–9.

[111] Schewe PF, Stein B. Physic News Update, The American Institute of Physics Bulletin of Physics News, No. 494, July 17, 2000.

[112] Allahverdyan A, Nieuwenhuizen T. Phys Rev Lett 2000;85(9):1799–802.

[113] Lamb WE, Retherford RC. Phys Rev 1947;72(3):241–3.

The hydrogen atom revisited

Randell L. Mills *

BlackLight Power, Inc., 493 Old Trenton Road, Cranbury, NJ 08512, USA

Abstract

Several myths about quantum mechanics exist due to a loss of awareness of its details since its inception in the beginning of the last century or based on recent experimental evidence. It is taught in textbooks that atomic hydrogen cannot go below the ground state. Atomic hydrogen having an experimental ground state of 13.6 eV can only exist in a vacuum or in isolation, and atomic hydrogen cannot go below this ground state in isolation. However, there is no known composition of matter containing hydrogen in the ground state of 13.6 eV. It is a myth that hydrogen has a theoretical ground state based on first principles. Historically, there were many directions in which to proceed to solve a wave equation for hydrogen. The Schrodinger equation gives the observed spontaneously radiative states and the nonradiative energy level of atomic hydrogen. On this basis alone, it is justified despite its inconsistency with physical laws as well as with many experiments. A solution compatible with first principles and having first principles as the basis of quantization was never found. Scattering results required the solution to be interpreted as probability waves that give rise to the uncertainty principle which in turn forms the basis of the wave particle duality. The correspondence principal predicts that quantum predictions must approach classical predictions on a large scale. However, recent data has shown that the Heisenberg uncertainty principle as the basis of the wave particle duality and the correspondence principle taught in textbooks are experimentally incorrect. Recently, a reconsideration of the postulates of quantum mechanics, has given rise to a closed form solution of a Schrodinger-like wave equation based on first principles. Hydrogen at predicted lower energy levels has been identified in the extreme ultraviolet emission spectrum from interstellar medium. In addition, new compositions of matter containing hydrogen at predicted lower energy levels have recently been observed in the laboratory, which energy levels are achieved using the novel catalysts. © 2000 International Association for Hydrogen Energy. Published by Elsevier Science Ltd. All rights reserved.

1. Introduction

J.J. Balmer showed, in 1885, that the frequencies for some of the lines observed in the emission spectrum of atomic hydrogen could be expressed with a completely empirical relationship. This approach was later extended by J.R. Rydberg, who showed that all of the spectral lines of atomic hydrogen were given by the equation

$$\bar{v} = R \left(\frac{1}{n_f^2} - \frac{1}{n_i^2} \right), \tag{1}$$

where $R = 109,677$ cm^{-1}, $n_f = 1, 2, 3, \ldots, n_i = 2, 3, 4, \ldots$, and $n_i > n_f$. Niels Bohr, in 1913, developed a theory for atomic hydrogen based on an unprecedented postulate of

* Tel.: 00-1-609-490-1090; fax: 00-1-609-490-1066.

E-mail address: rmills@blacklightpower.com (R.L. Mills).

stable circular orbits that do not radiate. Although no explanation was offered for the existence of stability for these orbits, the results gave energy levels in agreement with Rydberg's equation

$$E_n = -\frac{e^2}{n^2 8\pi\varepsilon_0 a_H} = -\frac{13.598 \text{ eV}}{n^2}, \tag{2}$$

$$n = 1, 2, 3, \ldots, \tag{3}$$

where a_H is the Bohr radius for the hydrogen atom (52.947 pm), e is the magnitude of the charge of the electron, and ε_0 is the vacuum permittivity. Bohr's theory was a straightforward application of Newton's laws of motion and Coulomb's law of electric force — both pillars of classical physics and is in accord with the experimental observation that atoms are stable. However, it is not in accord with electromagnetic theory — another pillar of classical physics which predicts that accelerated charges radiate energy in the form

of electromagnetic waves. An electron pursuing a curved path is accelerated and therefore should continuously lose energy, spiraling into the nucleus in a fraction of a second. The predictions of electromagnetic theory have always agreed with experiment, yet atoms do not collapse. To the early 20th century theoreticians, this contradiction could mean only one thing: The laws of physics that are valid in the macroworld do not hold true in the microworld of the atom. In 1923, de Broglie suggested that the motion of an electron has a wave aspect — $\lambda = h/p$. This concept seemed unlikely according to the familiar properties of electrons such as charge, mass and adherence to the laws of particle mechanics. But, the wave nature of the electron was confirmed by Davisson and Germer in 1927 by observing diffraction effects when electrons were reflected from metals. Schrödinger reasoned that if electrons have wave properties, there must be a wave equation that governs their motion. And in 1926, he proposed the Schrödinger equation, $H\Psi = E\Psi$, where Ψ is the wave function, H is the wave operator, and E is the energy of the wave. This equation, and its associated postulates, is now the basis of *quantum mechanics*, and it is the basis for the world view that the atomic realm including the electron and photon cannot be described in terms of "pure" wave and "pure" particle but in terms of a wave-particle duality. The wave–particle duality based on the fundamental principle that physics on an atomic scale is very different from physics on a macroscopic scale is central to present day atomic theory [1].

2. Development of atomic theory

2.1. Bohr theory

In 1911, Rutherford proposed a planetary model for the atom where the electrons revolved about the nucleus (which contained the protons) in various orbits to explain the spectral lines of atomic hydrogen. There was, however, a fundamental conflict with this model and the prevailing classical physics. According to classical electromagnetic theory, an accelerated particle radiates energy (as electromagnetic waves). Thus, an electron in a Rutherford orbit, circulating at constant speed but with a continually changing direction of its velocity vector is being accelerated; thus, the electron should constantly lose energy by radiating and spiral into the nucleus.

An explanation was provided by Bohr in 1913, when he assumed that the energy levels were quantized and the electron was constrained to move in only one of a number of allowed states. Niels Bohr's theory for atomic hydrogen was based on an unprecedented postulate of stable circular orbits that do not radiate. Although no explanation was offered for the existence of stability for these orbits, the results gave energy levels in agreement with Rydberg's equation. Bohr's theory was a straightforward application of Newton's laws

of motion and Coulomb's law of electric force. According to Bohr's model, the point particle electron was held to a circular orbit about the relatively massive point particle nucleus by the balance between the coulombic force of attraction between the proton and the electron and centrifugal force of the electron.

$$\frac{e^2}{4\pi\varepsilon_0 r^2} = \frac{m_e v^2}{r}. \tag{4}$$

Bohr postulated the existence of stable orbits in defiance of classical physics (Maxwell's equations), but he applied classical physics according to Eq. (4). Then Bohr realized that the energy formula (Eqs. (2) and (3)) was given by postulating nonradiative states with angular momentum

$$L_z = m_e v r = n\hbar, \quad n = 1, 2, 3 \dots. \tag{5}$$

and by solving the energy equation classically. The Bohr radius is given by substituting the solution of Eq. (5) for v into Eq. (4).

$$r = \frac{4\pi\varepsilon_0 \hbar^2 n^2}{m_e e^2} = n^2 a_0, \quad n = 1, 2, 3 \dots. \tag{6}$$

The total energy is the sum of the potential energy and the kinetic energy. In the present case of an inverse squared central field, the total energy (which is the negative of the binding energy) is one-half the potential energy [2]. The potential energy, $\phi(\mathbf{r})$, is given by Poisson's equation

$$\phi(\mathbf{r}) = -\int_{\mathbf{v}'} \frac{\rho(\mathbf{r}')\,\mathrm{d}v'}{4\pi\varepsilon_0 |\mathbf{r} - \mathbf{r}'|}. \tag{7}$$

For a point charge at a distance r from the nucleus the potential is

$$\phi(r) = -\frac{e^2}{4\pi\varepsilon_0 r}. \tag{8}$$

Thus, the total energy is given by

$$E = -\frac{Z^2 e^2}{8\pi\varepsilon_0 r}, \tag{9}$$

where $Z = 1$. Substitution of Eq. (6) into Eq. (9) with the replacement of the electron mass by the reduced electron mass gives Eqs. (2) and (3).

Bohr's model was in agreement with the observed hydrogen spectrum, but it failed with the helium spectrum, and it could not account for chemical bonds in molecules. The prevailing wisdom was that the Bohr model failed because it was based on the application of Newtonian mechanics for discrete particles. Its limited applicability was attributed to the unwarranted assumption that the energy levels are quantized.

Bohr's theory may also be analyzed according to the corresponding energy equation. Newton's differential equations of motion in the case of the central field such as a gravitational or electrostatic field are

$$m(\ddot{r} - r\dot{\theta}^2) = f(r), \tag{10}$$

$$m(2\dot{r}\dot{\theta} + r\ddot{\theta}) = 0, \tag{11}$$

where $f(r)$ is the central force. The second or transverse equation, Eq. (11), gives the result that the angular momentum is constant.

$$r^2\dot{\theta} = \text{constant} = L/m, \tag{12}$$

where L is the angular momentum. The central force equations can be transformed into an orbital equation by the substitution, $u = 1/r$. The differential equation of the orbit of a particle moving under a central force is

$$\frac{\delta^2 u}{\delta \theta^2} + u = \frac{-1}{mL^2 u^2/m^2} f(u^{-1}). \tag{13}$$

Because the angular momentum is constant, motion in only one plane need be considered; thus, the orbital equation is given in polar coordinates. The solution of Eq. (13) for an inverse square force

$$f(r) = -\frac{k}{r^2} \tag{14}$$

is

$$r = r_0 \frac{1 + e}{1 + e \cos \theta}, \tag{15}$$

$$e = A \frac{mL^2/m^2}{k}, \tag{16}$$

$$r_0 = \frac{mL^2/m^2}{k(1 + e)}, \tag{17}$$

where e is the eccentricity and A is a constant. The equation of motion due to a central force can also be expressed in terms of the energies of the orbit. The square of the speed in polar coordinates is

$$v^2 = (\dot{r}^2 + r^2 \dot{\theta}^2). \tag{18}$$

Since a central force is conservative, the total energy, E, is equal to the sum of the kinetic, T, and the potential, V, and is constant. The total energy is

$$\frac{1}{2}m(\dot{r}^2 + r^2\dot{\theta}^2) + V(r) = E = \text{constant}. \tag{19}$$

Substitution of the variable $u = 1/r$ and Eq. (12) into Eq. (19) gives the orbital energy equation

$$\frac{1}{2}m\frac{L^2}{m^2}\left[\left(\frac{\delta^2 u}{\delta \theta^2}\right) + u^2\right] + V(u^{-1}) = E. \tag{20}$$

Because the potential energy function $V(r)$ for an inverse square force field is

$$V(r) = -\frac{k}{r} = -ku, \tag{21}$$

the energy equation of the orbit (Eq. (20)), is

$$\frac{1}{2}m\frac{L^2}{m^2}\left[\left(\frac{\delta^2 u}{\delta \theta^2}\right) + u^2\right] - ku = E, \tag{22}$$

$$\left[\frac{\delta^2 u}{\delta \theta^2} + u^2\right] - \frac{2m}{L^2}[E + ku] = 0, \tag{23}$$

which has the solution

$$r = \frac{m(L^2/m^2)k^{-1}}{1 + [1 + 2Em(L^2/m^2)k^{-2}]^{1/2}\cos\theta}, \tag{24}$$

where the eccentricity, e is

$$e = \left[1 + 2Em\frac{L^2}{m^2}k^{-2}\right]^{1/2}. \tag{25}$$

Eq. (25) permits the classification of the orbits according to the total energy, E, as follows:

$E < 0, \quad e < 1, \quad \text{ellipse,}$

$E < 0, \quad e = 0, \quad \text{circle (special case of ellipse),}$

$E = 0, \quad e = 1, \quad \text{parabolic orbit,}$

$E > 0, \quad e > 1, \quad \text{hyperbolic orbit.} \tag{26}$

Since $E = T + V$ and is constant, the closed orbits are those for which $T < |V|$, and the open orbits are those for which $T \geqslant |V|$. It can be shown that the time average of the kinetic energy, $\langle T \rangle$, for elliptic motion in an inverse square field is $1/2$ that of the time average of the potential energy, $\langle V \rangle$. $\langle T \rangle = 1/2\langle V \rangle$.

Bohr's solution is trivial in that he specified a circular bound orbit which determined that the eccentricity was zero, and he specified the angular momentum as a integer multiple of Planck's constant bar. Eq. (25) in CGS units becomes

$$E = -\frac{1}{2}\frac{me^4}{n^2\hbar^2} = -\frac{e^2}{2n^2 a_0}. \tag{27}$$

2.2. Schrödinger theory of the hydrogen atom

In 1923, de Broglie suggested that the motion of an electron has a wave aspect — $\lambda = h/p$. This was confirmed by Davisson and Germer in 1927 by observing diffraction effects when electrons were reflected from metals. Schrödinger reasoned that if electrons have wave properties, there must be a wave equation that governs their motion. And, in 1926, he proposed the time-independent Schrödinger equation

$$H\Psi = E\Psi, \tag{28}$$

where Ψ is the wave function, H is the wave operator, and E is the energy of the wave. To give the sought three quantum numbers, the Schrödinger equation solutions are three dimensional in space and four dimensional in spacetime

$$\left[\nabla^2 - \frac{1}{v^2} \frac{\delta^2}{\delta t^2} \right] \Psi(r, \theta, \phi, t) = 0, \tag{29}$$

where $\Psi(r, \theta, \phi, t)$ according to quantum theory is the probability density function of the electron as described below. When the time harmonic function is eliminated [3]

$$-\frac{\hbar^2}{2\mu} \left[\frac{1}{r^2} \frac{\delta}{\delta r} \left(r^2 \frac{\delta \Psi}{\delta r} \right) + \frac{1}{r^2 \sin \theta} \frac{\delta}{\delta \theta} \left(\sin \theta \frac{\delta \Psi}{\delta \theta} \right)_{r, \phi} \right.$$
$$\left. + \frac{1}{r^2 \sin^2 \theta} \left(\frac{\delta^2 \Psi}{\delta \phi^2} \right)_{r, \theta} \right] + V(r) \Psi(r, \theta, \phi) = E \Psi(r, \theta, \phi), \tag{30}$$

where the potential energy $V(r)$ in CGS units is

$$V(r) = -\frac{e^2}{r}. \tag{31}$$

The Schrödinger equation (Eq. (30)) can be transformed into a sum comprising a part that depends only on the radius and a part that is a function of angle only obtained by separation of variables and linear superposition in spherical coordinates. The general form of the solutions for $\psi(r, \theta, \phi)$ are

$$\psi(r, \theta, \phi) = \sum_{l, m} R_{nlm}(r) Y_{lm}(\theta, \phi), \tag{32}$$

where l and m are separation constants. The azimuthal (θ) part of Eq. (30) is the generalized Legendre equation which is derived from the Laplace equation by Jackson (Eq. (3.9) of Jackson [4]). The solutions for the full angular part of Eq. (30), $Y_{lm}(\theta, \phi)$, are the spherical harmonics

$$Y_{lm}(\theta, \phi) = \sqrt{\frac{(2l+1)(l-m)!}{4\pi(l+m)!}} P_l^m(\cos \theta) e^{im\phi}. \tag{33}$$

By substitution of the eigenvalues corresponding to the angular part [5], the Schrödinger equation becomes the radial equation, $R(r)$, given by

$$-\frac{\hbar^2}{2mr^2} \frac{d}{dr} \left(r^2 \frac{dR}{dr} \right) + \left[\frac{\hbar^2 l(l+1)}{2mr^2} + V(r) \right] R(r) = ER(r). \tag{34}$$

The time-independent Schrödinger equation is similar to Eq. (20) except that the solution is for the distribution of a spatial wavefunction in three dimensions rather than the dynamical motion of a point particle of mass m along a one-dimensional trajectory. Electron motion is implicit in the Schrödinger equation. For wave propagation in three dimensions, the full time-dependent Schrödinger equation is required, whereas the classical case contains time

derivatives. The kinetic energy of rotation is K_{rot} is given classically by

$$K_{rot} = \tfrac{1}{2} m r^2 \omega^2, \tag{35}$$

where m is the mass of the electron. In the time-independent Schrödinger equation, the kinetic energy of rotation K_{rot} is given by

$$K_{rot} = \frac{\ell(\ell+1)\hbar^2}{2mr^2}, \tag{36}$$

where

$$L = \sqrt{\ell(\ell+1)\hbar^2} \tag{37}$$

is the magnitude of the electron angular momentum L for the state $Y_{lm}(\theta, \phi)$.

In the case of the ground state of hydrogen, the Schrödinger equation solution is trivial for an implicit circular bound orbit which determines that the eccentricity is zero, and with the specification that the electron angular momentum is Planck's constant bar. With $k = e^2$, Eq. (25) in CGS units becomes

$$E = -\frac{1}{2} \frac{me^4}{\hbar^2} = -\frac{e^2}{2a_0}, \tag{38}$$

which corresponds to $n = 1$ in Eq. (27). Many problems in classical physics give three quantum numbers when three spatial dimensions are considered. In order to obtain three quantum numbers, the Schrödinger equation requires that the solution is for the distribution of a spatial wavefunction in three dimensions with implicit motion rather than a one dimensional trajectory of a point particle as shown below. However, this approach gives rise to predictions about the angular momentum and angular energy which are not consistent with experimental observations as well as a host of other problems which are summarized in Section 10.

The radial equation may be written as

$$\frac{d}{dr} \left(r^2 \frac{dR}{dr} \right) + \frac{2mr^2}{\hbar^2} \left[E - V(r) - \frac{l(l+1)\hbar^2}{2mr^2} \right] R(r) = 0. \tag{39}$$

Let $U(r) = rR(r)$, then the radial equation reduces to

$$U'' + \frac{2m}{\hbar^2} \left[E - V(r) - \frac{l(l+1)\hbar^2}{2mr^2} \right] U = 0, \tag{40}$$

where

$$\psi = \frac{1}{r} U_{lm}(r) Y_{lm}(\theta, \phi). \tag{41}$$

Substitution of the potential energy given by Eq. (31) into Eq. (40) gives for sufficiently large r

$$U''_\infty - \left(\frac{\alpha}{2} \right)^2 U = 0 \tag{42}$$

provided we define

$$\left(\frac{\alpha}{2} \right)^2 = \frac{-2mE}{\hbar^2}, \tag{43}$$

where α is the eigenvalue of the eigenfunction solution of the Schrödinger equation given *infra* having units of reciprocal length and E is the energy levels of the hydrogen atom. To arrive at the solution which represents the electron, a suitable boundary condition must be imposed. Schrödinger postulated a boundary condition: $\Psi \to 0$ as $r \to \infty$, which leads to a purely mathematical model of the electron. This equation is not based on first principles, has no validity as such, and should not be represented as so. The right-hand side of Eq. (43) must be *postulated* in order that the Rydberg equation is obtained as shown below. The postulate is implicit since Eq. (43) arises from the Schrödinger equation which is postulated. It could be defined *arbitrarily*, but is justified because it gives the Rydberg formula. That Schrödinger guessed the accepted approach is not surprising since many approaches were contemplated at this time [6], and since none of these approaches were superior, Schrödinger's approach prevailed.

The solution of Eq. (42) that is consistent with the boundary condition is

$$U_\infty = c_1 e^{(\alpha/2)r} + c_2 e^{-(\alpha/2)r}. \tag{44}$$

In the case that α is real, the energy of the particle is negative. In this case U_∞ will not have an integrable square if c_1 fails to vanish wherein the radial integral has the form

$$\int_0^\infty R^2 r^2 \, dr = \int U_\infty^2 \, dr. \tag{45}$$

It is shown below that the solution of the Schrödinger corresponds to the case wherein c_1 fails to vanish. Thus, the solutions with sufficiently large r are infinite. The same problem arises in the case of a free electron that is ionized from hydrogen. If α is imaginary, which means that E is positive, Eq. (42) is the equation of a linear harmonic oscillator [7]. U_∞ shows sinusoidal behavior; thus, the wavefunction for the free electron cannot be normalized and is infinite. In addition, the angular momentum of the free electron is infinite since it is given by $\ell(\ell + 1)\hbar^2$ (Eq. (37)) where $\ell \to \infty$.

In order to solve the bound electron states, let

$$E = -W \tag{46}$$

so that W is positive. In Eq. (39), let $r = x/\alpha$ where α is given by Eq. (43)

$$x \frac{d^2R}{dx^2} + 2 \frac{dR}{dx} + \left[\frac{2me^2}{\hbar^2\alpha} - \frac{x}{4} - \frac{l(l+1)}{x} \right] R = 0. \tag{47}$$

Eq. (47) is the differential equation for associated Laguerre functions given in general form by

$$xy'' + 2y' + \left[n^* - \frac{k-1}{2} - \frac{x}{4} - \frac{k^2-1}{4x} \right] y = 0, \tag{48}$$

which has a solution possessing an integrable square of the form

$$y = e^{-x/2} x^{(k-1)/2} \frac{d^k}{dx^k} L_{n^*}(x), \tag{49}$$

provided that n^* and k are positive integers. However, n^* does not have to be an integer, it may be any *arbitrary* constant β. Then the corresponding solution is [8]

$$y = e^{-x/2} x^{(k-1)/2} \frac{d^k}{dx^k} L_\beta(x). \tag{50}$$

In the case that n^* is chosen to be an integer in order to obtain the Rydberg formula, $n^* - k \geqslant 0$ since otherwise $L_{n^*}^k(x)$ of Eq. (49) would vanish. By comparing Eqs. (47) and (48),

$$\frac{k^2-1}{4} = \ell(\ell + 1). \tag{51}$$

Thus,

$$k = 2\ell + 1 \tag{52}$$

and

$$n^* - \frac{k-1}{2} = n^* - \ell = \frac{me^2}{\hbar} \left(\frac{\alpha}{2} \right)^{-1}. \tag{53}$$

Substitution of the value of α and solving for W gives

$$W = \frac{1}{2} \frac{me^4}{(n^* - \ell)^2 \hbar^2}. \tag{54}$$

Because of the conditions on n^* and k, the quantity $n^* - \ell$ cannot be zero. It is usually denoted by n and called the principal quantum number. The energy states of the hydrogen atom are

$$W_n = -E_n = \frac{1}{2} \frac{me^4}{n^2 \hbar^2} \tag{55}$$

and the corresponding eigenfunctions from Eq. (49) are

$$R_{n,\ell} = c_{n,\ell} \, e^{-x/2} x^\ell L_{n+\ell}^{2\ell+1}(x), \tag{56}$$

where the variable x is defined by

$$x = \alpha r = \frac{\sqrt{8mW}}{\hbar} r = \frac{2me^2}{n\hbar^2} r. \tag{57}$$

In the Bohr theory of the hydrogen atom, the first orbital has a radius in CGS units given by

$$a_0 = \frac{\hbar^2}{me^2} = 0.53 \times 10^{-8} \text{ cm}. \tag{58}$$

Thus, $\alpha = 2/na_0$ and

$$x = \frac{2}{n} \frac{r}{a_0}. \tag{59}$$

The energy states of the hydrogen atom in CGS units in terms of the Bohr radius are given by Eq. (27). From

Eq. (56), $R_{n,\ell}$ for the hydrogen atom ground state is

$$R_{1,0} = c_{1,0}e^{-r/a_0}L_1^1 = 2a_0^{-3/2}e^{-r/a_0}. \tag{60}$$

For this state

$$Y_{00} = const \tan t = (4\pi)^{-1/2}, \tag{61}$$

when the function is normalized. Thus, the ground state function is

$$\psi_0 = (\pi a_0^3)^{-1/2}e^{-r/a_0}. \tag{62}$$

Immediately further problems arise. Since ℓ must equal zero in the ground state, the predicted angular energy and angular momentum given by Eqs. (36) and (37), respectively, are zero which are experimentally incorrect. In addition, different integer values of ℓ exist in the case of excited electron states. In these cases, the Schrödinger equation solutions (Eqs. (36) and (37)), predict that the excited state rotational energy levels are nondegenerate as a function of the ℓ quantum number even in the absence of an applied magnetic field. Consider the case of the excited state with $n = 2$; $\ell = 1$ compared to the experimentally degenerate state $n = 2$; $\ell = 0$. According to Eq. (37) the difference in angular energy of these two states is 3.4 eV where the expectation radius, $4a_0$, is given by the squared integral of Eq. (70) over space. Thus, the predicted rotational energy in the absence of a magnetic field is over six orders of magnitude of the observed nondegenerate energy (10^{-7}–10^{-6} eV) in the presence of a magnetic field.

Schrödinger realized that his equation was limited. It is not Lorentzian invariant; thus, it violates special relativity. It also does not comply with Maxwell's equations and other first principle laws. Schrödinger sought a resolution of the incompatibility with special relativity for the rest of his life. He was deeply troubled by the physical consequences of his equation and its solutions. His hope was that the resolution would make his equation fully compatible with classical physics and the quantization would arise from first principles.

Quantum mechanics failed to predict the results of the Stern–Gerlach experiment which indicated the need for an additional quantum number. Quantum electrodynamics was proposed by Dirac in 1926 to provide a generalization of quantum mechanics for high energies in conformity with the theory of special relativity and to provide a consistent treatment of the interaction of matter with radiation. From Weisskopf [9], "Dirac's quantum electrodynamics gave a more consistent derivation of the results of the correspondence principle, but it also brought about a number of new and serious difficulties". Quantum electrodynamics: (1) does not explain nonradiation of bound electrons; (2) contains an internal inconsistency with special relativity regarding the classical electron radius — the electron mass corresponding to its electric energy is infinite; (3) it admits solutions of negative rest mass and negative kinetic energy; (4) the interaction of the electron with the predicted zero-point field

fluctuations leads to infinite kinetic energy and infinite electron mass; and (5) Dirac used the unacceptable states of negative mass for the description of the vacuum; yet, infinities still arise.

A physical interpretation of Eq. (28) was sought. Schrödinger interpreted $e\Psi^*(x)\Psi(x)$ as the charge-density or the amount of charge between x and $x + dx$ (Ψ^* is the complex conjugate of Ψ). Presumably, then, he pictured the electron to be spread over large regions of space. Three years after Schrödinger's interpretation, Max Born, who was working with scattering theory, found that this interpretation led to logical difficulties, and he replaced the Schrödinger interpretation with the probability of finding the electron between r, θ, ϕ and $r + dr, \theta + d\theta, \phi + d\phi$ as

$$\int \Psi(r,\theta,\phi)\Psi^*(r,\theta,\phi)\,dr\,d\theta\,d\phi. \tag{63}$$

Born's interpretation is generally accepted. Nonetheless, interpretation of the wave function is a never-ending source of confusion and conflict. Many scientists have solved this problem by conveniently adopting the Schrödinger interpretation for some problems and the Born interpretation for others. This duality allows the electron to be everywhere at one time — yet have no volume. Alternatively, the electron can be viewed as a discrete particle that moves here and there (from $r = 0$ to ∞), and $\Psi\Psi^*$ gives the time average of this motion.

Schrödinger was also troubled by the philosophical consequences of his theory since quantum mechanics leads to certain philosophical interpretations [10] which are not sensible. Some conjure up multitudes of universes including "mind" universes; others require belief in a logic that allows two contradictory statements to be true. The question addressed is whether the universe is determined or influenced by the possibility of our being conscious of it. The meaning of quantum mechanics is debated, but the Copenhagen interpretation is predominant. It asserts that "what we observe is all we can know; any speculation about what a photon, an atom, or even a superconducting quantum interference device (SQUID) really is or what it is doing when we are not looking is just that — speculation" [10]. As shown by Platt [11] in the case of the Stern–Gerlach experiment, "the postulate of quantum measurement (which) asserts that the process of measuring an observable forces the state vector of the system into an eigenvector of that observable, and the value measured will be the eigenvalue of that eigenvector". According to this interpretation every observable exists in a state of superposition of possible states, and observation or the potential for knowledge causes the wavefunction corresponding to the possibilities to collapse into a definite.

According to the quantum mechanical view, a moving particle is regarded as a wave group. To regard a moving particle as a wave group implies that there are fundamental limits to the accuracy with which such "particle" properties as position and momentum can be measured. Quantum predicts that the particle may be located anywhere within its

wave group with a probability $|\Psi|^2$. An isolated wave group is the result of superposing an infinite number of waves with different wavelengths. The narrower the wave group, the greater range of wavelengths involved. A narrow de Broglie wave group thus means a well-defined position (Δx smaller) but a poorly defined wavelength and a large uncertainty Δp in the momentum of the particle the group represents. A wide wave group means a more precise momentum but a less precise position. The infamous Heisenberg uncertainty principle is a formal statement of the standard deviations of properties implicit in the probability model of fundamental particles.

$$\Delta x \, \Delta p \geqslant \frac{\hbar}{2}. \tag{64}$$

According to the standard interpretation of quantum mechanics, the act of measuring the position or momentum of a quantum mechanical entity collapses the wave–particle duality because the principle forbids both quantities to be simultaneously known with precision.

3. The wave–particle duality is not due to the uncertainty principle

Quantum entities can behave like particles or waves, depending on how they are observed. They can be diffracted and produce interference patterns (wave behavior) when they are allowed to take different paths from some source to a detector — in the usual example, electrons or photons go through two slits and form an interference pattern on the screen behind. On the other hand, with an appropriate detector put along one of the paths (at a slit, say), the quantum entities can be detected at a particular place and time, as if they are point-like particles. But any attempt to determine which path is taken by a quantum object destroys the interference pattern. Richard Feynman described this as the central mystery of quantum physics.

Bohr called this vague principle 'complementary', and explained it in terms of the uncertainty principle, put forward by Werner Heisenberg, his postdoc at the time. In an attempt to persuade Einstein that wave–particle duality is an essential part of quantum mechanics, Bohr constructed models of quantum measurements that showed the futility of trying to determine which path was taken by a quantum object in an interference experiment. As soon as enough information is acquired for this determination, the quantum interferences must vanish, said Bohr, because any act of observing will impart uncontrollable momentum kicks to the quantum object. This is quantified by Heisenberg's uncertainty principle, which relates uncertainty in positional information to uncertainty in momentum — when the position of an entity is constrained, the momentum must be randomized to a certain degree.

More than 60 years after the famous debate between Niels Bohr and Albert Einstein on the nature of quantum

reality, a question central to their debate — the nature of quantum interference — has resurfaced. The usual textbook explanation of wave–particle duality in terms of unavoidable 'measurement disturbances' is experimentally proven incorrect by an experiment reported by Durr et al. [12]. Durr et al. report on the interference fringes produced when a beam of cold atoms is diffracted by standing waves of light. Their interferometer displayed fringes of high contrast — but when they manipulated the electronic state within the atoms with a microwave field according to which path was taken, the fringes disappeared entirely. The interferometer produced a spatial distribution of electronic populations which were observed via fluorescence. The microwave field canceled the spatial distribution of electronic populations. The key to this new experiment was that although the interferences are destroyed, the initially imposed atomic momentum distribution left an envelope pattern (in which the fringes used to reside) at the detector. A careful analysis of the pattern demonstrated that it had not been measurably distorted by a momentum kick of the type invoked by Bohr, and therefore that any locally realistic momentum kicks imparted by the manipulation of the internal atomic state according to the particular path of the atom are too small to be responsible for destroying interference.

4. The correspondence principle does not hold

Recent experimental results also dispel another doctrine of quantum mechanics [13,14]. Bohr proposed a rule of thumb called the correspondence principle [15]. A form of the principle widely repeated in textbooks and lecture halls states that predictions of quantum mechanics and classical physics should match for the most energetic cases.

Bo Gao [13] calculates possible energy states of any chilled, two-atom molecule, such as sodium, that's vibrating and rotating almost to the breaking point. He performs the calculations via quantum mechanical and the so-called semi-classical methods and compares the results. Instead of the results agreeing better for increasingly energetic states, the opposite happens.

5. Classical solution of the Schrodinger equation

Mills has solved and published a solution of a Schrödinger type equation based on first principles [16]. The central feature of this theory is that all particles (atomic-size and macroscopic particles) obey the same physical laws. Whereas Schrödinger postulated a boundary condition: $\Psi \rightarrow 0$ as $r \rightarrow \infty$, the boundary condition in Mills' theory was derived from Maxwell's equations [17].

For non-radiative states, the current–density function must not possess space-time Fourier components that

are synchronous with waves traveling at the speed of light.

Application of this boundary condition leads to a physical model of particles, atoms, molecules, and, in the final analysis, cosmology. The closed-form mathematical solutions contain fundamental constants *only*, and the calculated values for physical quantities agree with experimental observations. In addition, the theory predicts that Eq. (3), should be replaced by Eq. (65).

$$n = 1, 2, 3, \ldots \quad \text{and} \quad n = \tfrac{1}{2}, \tfrac{1}{3}, \tfrac{1}{4}, \ldots . \quad (65)$$

Some revisions to standard quantum theory are implied. Quantum mechanics becomes a real physical description as opposed to a purely mathematical model where the old and the revised versions are interchangeable by a Fourier transform operation [16].

The theories of Bohr, Schrödinger, and presently Mills all give the identical equation for the principal energy levels of the one-electron atom.

$$E_{ele} = -\frac{Z^2 e^2}{8\pi\varepsilon_0 n^2 a_H} = -\frac{Z^2}{n^2} 2.1786 \times 10^{-18},$$

$$J = -Z^2 \frac{13.598}{n^2} \text{ eV}. \quad (66)$$

The Mills theory solves the two-dimensional wave equation for the charge–density function of the electron. And, the Fourier transform of the charge–density function is a solution of the three-dimensional wave equation in frequency (k, ω) space. Whereas, the Schrödinger equation solutions are three dimensional in spacetime. The energy is given by

$$\int_{-\infty}^{\infty} \psi H \psi \, dv = E \int_{-\infty}^{\infty} \psi^2 \, dv, \quad (67)$$

$$\int_{-\infty}^{\infty} \psi^2 \, dv = 1. \quad (68)$$

Thus,

$$\int_{-\infty}^{\infty} \psi H \psi \, dv = E. \quad (69)$$

In the case that the potential energy of the Hamiltonian, H, is a constant times the wavenumber, the Schrödinger equation is the well-known Bessel equation. Then with one of the solutions for ψ, Eq. (69) is equivalent to an inverse Fourier transform. According to the duality and scale change properties of Fourier transforms, the energy equation of the present theory and that of quantum mechanics are identical, the energy of a radial Dirac delta function of radius equal to an integer multiple of the radius of the hydrogen atom (Eq. (66)). Bohr obtained the same energy formula by postulating nonradiative states with angular momentum

$$L_z = m\hbar \quad (70)$$

and solving the energy equation classically.

The mathematics for all three theories converge to Eq. (66). However, the physics is quite different. Only the Mills theory is derived from first principles and holds over a scale of spacetime of 45 orders of magnitude: it correctly predicts the nature of the universe from the scale of the quarks to that of the cosmos.

Mills' revisions transform Schrödinger's and Heisenberg's quantum theory into what may be termed a *classical quantum theory*. Physical descriptions flow readily from the theory. For example, in the old quantum theory the spin angular momentum of the electron is called the "intrinsic angular momentum". This term arises because it is difficult to provide a physical interpretation for the electron's spin angular momentum. Quantum Electrodynamics provides somewhat of a physical interpretation by proposing that the "vacuum" contains fluctuating electric and magnetic fields. In contrast, in Mills' theory, spin angular momentum results from the motion of negatively charged mass moving systematically, and the equation for angular momentum, $\mathbf{r} \times \mathbf{p}$, can be applied directly to the wave function (a current–density function) that describes the electron, and quantization is carried by the photon, rather than probability waves of the electron.

6. Fractional quantum energy levels of hydrogen

The nonradiative state of atomic hydrogen which is historically called the "ground state" forms the basis of the boundary condition of Mills' theory to solve the wave equation. Mills further predicts [16] that certain atoms or ions serve as catalysts to release energy from hydrogen to produce an increased binding energy hydrogen atom called a *hydrino atom* having a binding energy of

$$\text{Binding energy} = \frac{13.6 \, \text{eV}}{n^2}, \quad (71)$$

where

$$n = \frac{1}{2}, \frac{1}{3}, \frac{1}{4}, \ldots, \frac{1}{p} \quad (72)$$

and p is an integer greater than 1, designated as $H[a_H/p]$ where a_H is the radius of the hydrogen atom. (Although it is purely mathematical, these stable energy levels are also given by both Bohr's and Schrödinger's theories by postulating integer values of the central charge. Justification may be based on notions such virtual particles which are acceptable in other applications of Schrödinger's equation.) Hydrinos are predicted to form by reacting an ordinary hydrogen atom with a catalyst having a net enthalpy of reaction of about

$$m \cdot 27.2 \text{ eV}, \quad (73)$$

where m is an integer. This catalysis releases energy from the hydrogen atom with a commensurate decrease in size of the hydrogen atom, $r_n = n a_H$. For example, the catalysis of $H(n=1)$ to $H(n=1/2)$ releases 40.8 eV, and the hydrogen radius decreases from a_H to $(1/2)a_H$.

It is taught in textbooks that atomic hydrogen cannot go below the ground state. Atomic hydrogen having an experimental ground state of 13.6 eV can only exist in a vacuum or in isolation, and atomic hydrogen cannot go below this ground state in isolation. However, there is no known composition of matter containing hydrogen in the ground state of 13.6 eV. Atomic hydrogen is radical and is very reactive. It may react to form a hydride ion or compositions of matter. It is a chemical intermediate which may be trapped as many chemical intermediates may be by methods such as isolation or cryogenically. A hydrino atom may be considered a chemical intermediate that may be trapped in vacuum or isolation. A hydrino atom may be very reactive to form a hydride ion or a novel composition of matter. Hydrogen at predicted lower energy levels, hydrino atoms, has been identified in the extreme ultraviolet emission spectrum from interstellar medium. In addition, new compositions of matter containing hydrogen at predicted lower energy levels have recently been observed in the laboratory, which energy levels are achieved using the novel catalysts.

The excited energy states of atomic hydrogen are also given by Eq. (71) except that

$$n = 1, 2, 3, \ldots . \tag{74}$$

The $n = 1$ state is the "ground" state for "pure" photon transitions (the $n = 1$ state can absorb a photon and go to an excited electronic state, but it cannot release a photon and go to a lower energy electronic state). However, an electron transition from the ground state to a lower energy state is possible by a nonradiative energy transfer such as multipole coupling or a resonant collision mechanism. These lower energy states have fractional quantum numbers, $n = 1/\text{integer}$. Processes that occur without photons and that require collisions are common. For example, the exothermic chemical reaction of $H + H$ to form H_2 does not occur with the emission of a photon. Rather, the reaction requires a collision with a third body, M, to remove the bond energy — $H + H + M \rightarrow H_2 + M^*$ [18]. The third body distributes the energy from the exothermic reaction, and the end result is the H_2 molecule and an increase in the temperature of the system. Some commercial phosphors are based on nonradiative energy transfer involving multipole coupling [19]. For example, the strong absorption strength of Sb^{3+} ions along with the efficient nonradiative transfer of excitation from Sb^{3+} to Mn^{2+}, are responsible for the strong manganese luminescence from phosphors containing these ions. Similarly, the $n = 1$ state of hydrogen and the $n = 1/\text{integer}$ states of hydrogen are nonradiative, but a transition between two nonradiative states is possible via a nonradiative energy transfer, say $n = 1$ to $1/2$. In these cases, during the transition the electron couples to another electron transition, electron transfer reaction, or inelastic scattering reaction which can absorb the exact amount of energy that must be removed from the hydrogen atom. Thus, a catalyst provides a net positive enthalpy of reaction of $m \cdot 27.2$ eV (i.e. it absorbs $m \cdot 27.2$ eV where m is an integer). Certain atoms or ions serve as catalysts which resonantly accept energy from hydrogen atoms and release the energy to the surroundings to effect electronic transitions to fractional quantum energy levels.

Once formed hydrinos have a binding energy given by Eqs. (71) and (72); thus, they may serve as catalysts which provide a net enthalpy of reaction given by Eq. (73). Also, the simultaneous ionization of two hydrogen atoms may provide a net enthalpy given by Eq. (73). Since the surfaces of stars comprise significant amounts of atomic hydrogen, hydrinos may be formed as a source to interstellar space where further transitions may occur.

A number of experimental observations lead to the conclusion that atomic hydrogen can exist in fractional quantum states that are at lower energies than the traditional "ground" ($n = 1$) state. For example, the existence of fractional quantum states of hydrogen atoms explains the spectral observations of the extreme ultraviolet background emission from interstellar space [20], which may characterize dark matter as demonstrated in Table 2. (In these cases, a hydrogen atom in a fractional quantum state, $H(n_i)$, collides, for example, with a $n = 1/2$ hydrogen atom, $H(1/2)$, and the result is an even lower energy hydrogen atom, $H(n_f)$, and $H(1/2)$ is ionized.

$$H(n_i) + H(\tfrac{1}{2}) \rightarrow H(n_f) + H^+ + e^- + \text{photon}. \tag{75}$$
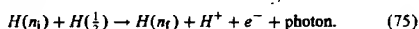
The energy released, as a photon, is the difference between the energies of the initial and final states given by Eqs. (71) and (72) minus the ionization energy of $H(1/2)$, 54.4 eV. The catalysis of an energy state of hydrogen to a lower energy state wherein a different lower energy state atom of hydrogen serves as the catalyst is called disproportionation by Mills [16].

7. Identification of lower energy hydrogen by soft X-rays from dark interstellar medium

The first soft X-ray background was detected and reported [21] about 25 years ago. Quite naturally, it was assumed that these soft X-ray emissions were from ionized atoms within hot gases. In a more recent paper, a grazing incidence spectrometer was designed to measure and record the diffuse extreme ultraviolet background [20]. The instrument was carried aboard a sounding rocket and data were obtained between 80 and 650 Å (data points approximately every 1.5 Å). Here again, the data were interpreted as emissions from hot gases. However, the authors left the door open for some other interpretation with the following statement from their introduction:

It is now generally believed that this diffuse soft X-ray background is produced by a high-temperature component of the interstellar medium. However, evidence of the thermal nature of this emission is indirect in that it is based not on observations of line emission, but on

Table 1
Energies (Eq. (76)) of several fractional-state transitions catalyzed by H[a_H/2]

n_i	n_f	ΔE (eV)	λ (Å)
1/2	1/3	13.6	912
1/3	1/4	40.80	303.9
1/4	1/5	68.00	182.4
1/5	1/6	95.20	130.2
1/6	1/7	122.4	101.3
1/7	1/8	149.6	82.9

indirect evidence that no plausible non-thermal mechanism has been suggested which does not conflict with some component of the observational evidence.

The authors also state that "if this interpretation is correct, gas at several temperatures is present". Specifically, emissions were attributed to gases in three ranges: $5.5 < \log T < 5.7; \log T = 6; 6.6 < \log T < 6.8$.

The explanation proposed herein of the observed dark interstellar medium spectrum hinges on the possibility of energy states below the $n = 1$ state, as given by Eqs. (71) and (72). Thus, lower energy transitions of the type

$$\Delta E = \left(\frac{1}{n_f^2} - \frac{1}{n_i^2}\right) \times 13.6 \text{ eV} - 54.4 \text{ eV}$$

$$n = 1, \tfrac{1}{2}, \tfrac{1}{3}, \tfrac{1}{4}, \dots \quad \text{and} \quad n_i > n_f. \quad (76)$$

induced by a disproportionation reaction with $H[a_H/2]$ ought to occur. The wavelength is related to ΔE by

$$\lambda \text{ (Å)} = \frac{1.240 \times 10^4}{\Delta E(\text{eV})}. \quad (77)$$

The energies and wavelengths of several of these proposed transitions are shown in Table 1. Note that the lower energy transitions are in the soft X-ray region.

8. The data and its interpretation

In their analysis of the data, Labov and Bowyer [20] established several tests to separate emission features from the background. There were seven features (peaks) that passed their criteria. The wavelengths and other aspects of these peaks are shown in Table 2. Peaks 2 and 5 were interpreted by Labov and Bowyer as instrumental second-order images of peaks 4 and 7, respectively. Peak 3, the strongest feature, is clearly a helium resonance line: He($1s^1 2p^1 \to 1s^2$). At issue here, is the interpretation of peaks 1, 4, 6, and 7. It is proposed that peaks 4, 6, and 7 arise from the $1/3 \to 1/4$, $1/4 \to 1/5$, and $1/6 \to 1/7$ hydrogen atoms transitions given by Eq. (76). It is also proposed that peak 1 arises from inelastic helium scattering of peak 4. That is, the $1/3 \to 1/4$ transition yields a 40.8 eV photon (303.9 Å).

When this photon strikes He($1s^2$), 21.2 eV is absorbed in the excitation to He($1s^1 2p^1$). This leaves a 19.6 eV photon (632.6 Å), peak 1. For these four peaks, the agreement between the predicted values (Table 1) and the experimental values (Table 2) is remarkable.

One argument against this new interpretation of the data is that the transition $1/5 \to 1/6$ is missing — predicted at 130.2 Å by Eqs. (76) and (77). This missing peak cannot be explained into existence, but a reasonable rationale can be provided for why it might be missing from these data. The data obtained by Labov and Bowyer are outstanding when the region of the spectrum, the time allotted for data collection, and the logistics are considered. Nonetheless, it is clear that the signal-to-noise ratio is low and that considerable effort had to be expended to differentiate emission features from the background. This particular peak, $1/5 \to 1/6$, is likely to be only slightly stronger than the $1/6 \to 1/7$ peak (the intensities, Table 2, appear to decrease as n decreases), which has low intensity. Labov and Bowyer provided their data (wavelength, count, count error, background, and background error). The counts minus background values for the region of interest, 130.2 ± 5 Å, are shown in Table 3 (the confidence limits for the wavelength of about ± 5 Å are the single-side 1 confidence levels and include both the uncertainties in the fitting procedure and uncertainties in the wavelength calibration). Note that the largest peak (count − background) is at 129.64 Å and has a counts − background = 8.72. The counts − background for the strongest signal of the other hydrino transitions are: $n = 1/3 - 1/4$, 20.05; $n = 1/4 - 1/5$, 11.36; $n = 1/6 - 1/7$, 10.40. Thus, there is fair agreement with the wavelength and the strength of the signal. This, of course, does not mean that there is a peak at 130.2 Å. However, it is not unreasonable to conclude that a spectrum with a better signal-to-noise ratio might uncover the missing peak.

Another, and more important, argument against this new interpretation is the fact that the proposed fractional-quantum-state hydrogen atoms have not been detected before. There are several explanations. Firstly, the transitions to these fractional states must be forbidden or must have very high activation energies — otherwise, all hydrogen atoms would quickly go to these lower energy states (an estimated transition probability, based on the Labov and Bowyer data, is between 10^{-15} and 10^{-17} s^{-1}). In actuality, a catalyst is required in order to obtain emission. Secondly, the number of hydrogen *atoms* ($n = 1$), the hydrogen-*atom* density, and the presence of an active catalyst under any conditions on Earth is exceeding low. The combination of extremely low population and extremely low transition probability makes the detection of these transitions especially difficult. Thirdly, this is a very troublesome region of the electromagnetic spectrum for detection because these wavelengths do not penetrate even millimeters of the atmosphere (i.e. this region is the vacuum ultraviolet which requires windowless spectroscopy at vacuum for detection). Lastly, no one previously has been

Table 2
Emission features of the LaBov and Bowyer spectrum and their interpretation

Peak	λ (Å)	Confidence limit (Å)	Intensity (photons cm^{-2} s^{-1} sr^{-1})	Assignment [20]	Assignment [33]	Predicted λ (Eqs. (76) and (77)) (Å)
1	633.0	−4.7 to +4.7	19,000	O^{4+}; log $T = 5.5$	He scattering of 303.9 line (peak 4)	633.0
2	607.5	−4.9 to +4.9	Second order	Second order of 302.5 line	Second order of 303.9 line	607.8
3	584	−4.5 to +4.5	70,400	He resonance ($1s^12p^1 \rightarrow 1s^2$)	He resonance ($1s^12p^1 \rightarrow 1s^2$)	584
4	302.5	−6.0 to +5.9	2,080	He^+; ($2p^1 \rightarrow 1s^1$)	$n = 1/3–1/4$	303.9
5	200.6	−4.4 to +5.3	Second order	Second order of 101.5 line	Second order of 101.3 line	202.6
6	181.7	−4.6 to +5.1	1030	Fe^{9+} and Fe^{10+}; log $T = 6$	$n = 1/4–1/5$	182.3
7	101.5	−5.3 to +4.2	790	Fe^{17+} and Fe^{18+}; log $T = 6.6 – 6.8$	$n = 1/6–1/7$	101.3

Table 3
Data (Labov and Bowyer) near the predicted $1/5 \rightarrow 1/6$ transition (130.2 Å)

l (Å)	Counts	Background	Counts−background
125.82	26	21.58	4.42
127.10	22	21.32	0.68
128.37	18	19.50	−1.50
129.64	29	20.28	8.72
130.90	18	19.76	−1.76
132.15	20	19.50	0.50
133.41	19	19.50	−0.50
134.65	19	20.80	−1.80

actively searching for these transitions. The Chandra X-ray Observatory is scheduled to perform similar experiments with detection at much better signal to noise than obtained by Labov and Bowyer.

9. Novel energy states of hydrogen formed by a catalytic reaction

The catalysis of hydrogen involves the nonradiative transfer of energy from atomic hydrogen to a catalyst which may then release the transferred energy by radiative and nonradiative mechanisms. As a consequence of the nonradiative energy transfer, the hydrogen atom becomes unstable and emits further energy until it achieves a lower energy nonradiative state having a principal energy level given by Eqs. (71) and (72).

Potassium ions can also provide a net enthalpy of a multiple of that of the potential energy of the hydrogen atom. The second ionization energy of potassium is 31.63 eV; and K^+ releases 4.34 eV when it is reduced to K. The combination of reactions K^+ to K^{2+} and K^+ to K, then, has a net enthalpy of reaction of 27.28 eV, which is equivalent to

$m = 1$ in Eq. (73).

$$27.28 \text{ eV} + K^+ + K^+ + H\left[\frac{a_H}{p}\right] \rightarrow K + K^{2+} + H\left[\frac{a_H}{(p+1)}\right] + [(p+1)^2 - p^2]13.6 \text{ eV}, \tag{78}$$

$$K + K^{2+} \rightarrow K^+ + K^+ + 27.28 \text{ eV}. \tag{79}$$

The overall reaction is

$$H\left[\frac{a_H}{p}\right] \rightarrow H\left[\frac{a_H}{(p+1)}\right] + [(p+1)^2 - p^2]13.6 \text{ eV}. \tag{80}$$

Typically, the emission of extreme ultraviolet light from hydrogen gas is achieved via a discharge at high voltage, a high-power inductively coupled plasma, or a plasma created and heated to extreme temperatures by RF coupling (e.g. $> 10^6$ K) with confinement provided by a toroidal magnetic field. Intense EUV emission was observed by Mills et al. [22–27] at low temperatures (e.g. $< 10^3$ K) from atomic hydrogen and certain atomized pure elements or certain gaseous ions which ionize at integer multiples of the potential energy of atomic hydrogen. The release of energy from hydrogen as evidenced by the EUV emission must result in a lower energy state of hydrogen. The lower energy hydrogen atom called a hydrino atom by Mills [16] would be expected to demonstrate novel chemistry. The formation of novel compounds based on hydrino atoms would be substantial evidence supporting catalysis of hydrogen as the mechanism of the observed EUV emission. A novel hydride ion called a hydrino hydride ion having extraordinary chemical properties given by Mills [16] is predicted to form by the reaction of an electron with a hydrino atom. Compounds containing hydrino hydride ions have been isolated as products of the reaction of atomic hydrogen with atoms and ions identified as catalysts in the Mills et al. EUV study [16,22–33]. The novel hydride compounds were identified

analytically by techniques such as time of flight secondary ion mass spectroscopy, X-ray photoelectron spectroscopy, and proton nuclear magnetic resonance spectroscopy. For example, the time of flight secondary ion mass spectroscopy showed a large hydride peak in the negative spectrum. The X-ray photoelectron spectrum showed large metal core level shifts due to binding with the hydride as well as novel hydride peaks. The proton nuclear magnetic resonance spectrum showed significantly upfield shifted peaks which corresponded to and identified novel hydride ions.

10. Discussion

The Schrödinger equation gives the observed spontaneously radiative energy levels and the nonradiative state of hydrogen. On this basis alone, it is justified despite its inconsistency with physicals laws and numerous experimental observations such as

- The appropriate eigenvalue must be postulated and the variables of the Laguerre differential equation must be defined as integers in order to obtain the Rydberg formula.
- The Schrödinger equation is not Lorentzian invariant.
- The Schrödinger equation violates first principles including special relativity and Maxwell's equations [16,34].
- The Schrödinger equation gives no basis why excited states are radiative and the 13.6 eV state is stable [16].
- The Schrödinger equation solutions (Eqs. (36) and (37)), predict that the ground state electron has zero angular energy and zero angular momentum, respectively.
- The Schrödinger equation solution (Eq. (37)) predicts that the ionized electron may have infinite angular momentum.
- The Schrödinger equation solutions (Eqs. (36) and (37)), predict that the excited state rotational energy levels are nondegenerate as a function of the ℓ quantum number even in the absence of an applied magnetic field, and the predicted energy is over six orders of magnitude of the observed nondegenerate energy in the presence of a magnetic field. In the absence of a magnetic field, no preferred direction exists. In this case, the ℓ quantum number is a function of the orientation of the atom with respect to an arbitrary coordinate system. Therefore, the nondegeneracy is nonsensical and violates conservation of angular momentum of the photon.
- The Schrödinger equation predicts that each of the functions that corresponds to a highly excited state electron is not integrable and cannot be normalized; thus, each is infinite.
- The Schrödinger equation predicts that the ionized electron is sinusoidal over all space and cannot be normalized; thus, it is infinite.
- The Heisenberg uncertainty principle arises as the standard deviation in the electron probability wave, but experimentally it is not the basis of wave–particle duality.

- The correspondence principle does not hold experimentally.
- The Schrödinger equation does not predict the electron magnetic moment and misses the spin quantum number all together.
- The Schrödinger equation is not a wave equation since it gives the velocity squared proportional to the frequency.
- The Schrödinger equation is not consistent with conservation of energy in an inverse potential field wherein the binding energy is equal to the kinetic energy and the sum of the binding energy and the kinetic energy is equal to the potential energy [2].
- The Schrödinger equation permits the electron to exist in the nucleus which is a state that is physically nonsensical with infinite potential energy and infinite negative kinetic energy.
- The Schrödinger equation interpreted as a probability wave of a point particle cannot explain neutral scattering of electrons from hydrogen [16].
- The Schrödinger equation interpreted as a probability wave of a point particle gives rise to infinite magnetic and electric energy in the corresponding fields of the electron.
- A modification of the Schrödinger equation was developed by Dirac to explain spin which relies on the unfounded notions of negative energy states of the vacuum, virtual particles, and gamma factors.

The success of quantum mechanics can be attributed to (1) the lack of rigor and unlimited tolerance to ad hoc assumptions in violation of physical laws, (2) fantastical experimentally immeasurable corrections such as virtual particles, vacuum polarizations, effective nuclear charge, shielding, ionic character, compactified dimensions, and renormalization, and (3) curve fitting parameters that are justified solely on the basis that they force the theory to match the data. Quantum mechanics is now in a state of crisis with constantly modified versions of matter represented as undetectable minuscule vibrating strings that exist in many unobservable hyperdimensions, that can travel back and forth between undetectable interconnected parallel universes. And, recent data shows that the expansion of the universe is accelerating. This observation has shattered the long held unquestionable doctrine of the origin of the universe as a big bang [35]. It may be time to reconsider the roots of quantum theory, namely the theory of the hydrogen atom. Especially in light of the demonstration that the hydrogen atom can be solved in closed form from first principles, that new chemistry is predicted, and that the predictions have substantial experimental support.

Billions of dollars have been spent to harness the energy of hydrogen through fusion using plasmas created and heated to extreme temperatures by RF coupling (e.g. $> 10^6$ K) with confinement provided by a toroidal magnetic field. Mills et al. [22–27] have demonstrated that energy may be released from hydrogen *using a chemical catalyst* at relatively low temperatures with an apparatus which is of trivial technological complexity compared to a tokamak. And, rather

than producing radioactive waste, the reaction has the potential to *produce compounds* having extraordinary properties [28–33]. The implications are that a vast new energy source and a new field of hydrogen chemistry have been discovered.

References

[1] Beiser A. Concepts of modern physics, 4th ed. New York: McGraw-Hill, 1987. p. 87–117.

[2] Fowles GR. Analytical mechanics, 3rd ed. New York: Holt, Rinehart, and Winston, 1977. p. 154–6.

[3] McQuarrie DA. Quantum chemistry. Mill Valley, CA: University Science Books, 1983. p. 78–9.

[4] Jackson JD. Classical electrodynamics, 2nd ed. New York: Wiley, 1962. p. 84–108.

[5] McQuarrie DA. Quantum chemistry. Mill Valley, CA: University Science Books, 1983. p. 221–4.

[6] Moore W. Schrödinger life and thought. Cambridge: Cambridge University Press, 1989. p. 198.

[7] Fowles GR. Analytical mechanics, 3rd ed. New York: Holt, Rinehart, and Winston, 1977. p. 57–60.

[8] Margenau H, Murphy GM. The mathematics of chemistry and physics. New York: D. Van Nostrand Company, Inc. 1943. p. 77–8.

[9] Weisskopf VF. Rev Mod Phys 1949;21(2):305–15.

[10] Horgan J. Quantum philosophy. Sci Am 1992;267:94–104.

[11] Platt DE. Am J Phys 1992;60(4):306–8.

[12] Durr S, Nonn T, Rempe G. Nature 1998;395:33–7.

[13] Gao B. Phys Rev Lett 1999;83(21):4225–8.

[14] Weiss P. Physics rule of thumb gets thumbs down: Sci News 1999;156:342.

[15] Thomsen DE. Going Bohr's way in physics. Sci News 1/11/86. p. 26.

[16] Mills R. The grand unified theory of classical quantum mechanics, January 1999 ed. Cranbury, NJ: BlackLight Power, Inc. Distributed by Amazon.com.

[17] Haus HA. On the radiation from point charges. Am J Phys 1986;54:1126–9.

[18] Sidgwick NV. The chemical elements and their compounds, vol. 1. Oxford: Clarendon Press, 1950. p. 17.

[19] Lamb MD. Luminescence spectroscopy. London: Academic Press, 1978, p. 68.

[20] Labov S, Bowyer S. Spectral observations of the extreme ultraviolet background. Astrophys J 1991;371:810–9.

[21] Bower S, Field G, Mack J. Detection of an anisotrophic soft X-ray background flux. Nature 1968;217:32.

[22] Mills R, Dong J, Lu Y. Observation of extreme ultraviolet hydrogen emission from incandescently heated hydrogen gas with certain catalysts. 1999 Pacific Conference on Chemistry and Spectroscopy and the 35th ACS Western Regional Meeting, Ontario Convention Center, CA, October 6–8, 1999.

[23] Mills R, Dong J, Lu Y. Observation of extreme ultraviolet hydrogen emission from incandescently heated hydrogen gas with certain catalysts. Int J Hydrogen Energy, 2000;25: 919–43.

[24] Mills R. Observation of extreme ultraviolet hydrogen and hydrino emission from hydrogen-KI plasmas produced by a hollow cathode discharge. Int J Hydrogen Energy, submitted.

[25] Mills R. Temporal behavior of light-emission in the visible spectral range from a Ti-K2CO3-H-Cell. Int J Hydrogen Energy, in press.

[26] Mills R, Lu Y, Onuma T. Formation of a hydrogen plasma from an incandescently heated hydrogen-potassium gas mixture and plasma decay upon removal of heater power. Int J Hydrogen Energy, submitted.

[27] Mills R, Nansteel M, Lu Y. Observation of extreme ultraviolet hydrogen emission from incandescently heated hydrogen gas with strontium that produced an optically measured power balance that was 4000 times the control. Int J Hydrogen Energy, in press.

[28] Mills R, Dhandapani B, Greenig N, He J. Synthesis and characterization of potassium iodo hydride. Int J Hydrogen Energy, 2000;25:1185–1203.

[29] Mills R. Novel hydride compound. Int J Hydrogen Energy, in press.

[30] Mills R. Novel hydrogen compounds from a potassium carbonate electrolytic cell. Fusion Technol 2000;37(2): 157–82.

[31] Mills R, He J, Dhandapani B. Novel hydrogen compounds. 1999 Pacific Conference on Chemistry and Spectroscopy and the 35th ACS Western Regional Meeting, Ontario Convention Center, CA, October 6–8, 1999.

[32] Mills R, Dhandapani B, Nansteel M, He J. Synthesis and characterization of novel hydride compounds. Int J Hydrogen Energy, in press.

[33] Mills R. Highly stable novel inorganic hydrides. Int J Inorganic Mater, submitted.

[34] Fuchs CA, Peres A. Quantum theory needs no 'interpretation'. Phys Today 2000;53(3):70–1.

[35] Bahcall NA, Ostriker JP, Perlmutter S, Steinhardt PJ. Science 1999;284:1481–8.

THIS PAGE BLANK (USPTO)

Report on BlackLight Power Technology: Its Apparent Scientific Basis, State of Development and Suitability for Commercialization by Liebert Corporation

Prepared under a Consulting Agreement with Liebert Corporation (hereinafter "my client") effective 11/1/00 and submitted in final form on 1/31/01.

Keith Keefer, Ph. D.
Keith Keefer Consulting
208 Hartwood Street
Richland, WA 99352

Foreword

I have observed demonstrations of the BlackLight Power (BLP) process and have reached the inescapable conclusion that it is based on extraordinary chemical reactions that seem to release extraordinary amounts of energy. The explanation provided by Randell Mills, M. D., president and chief scientist of BLP is that, in the presence of certain catalysts, atomic hydrogen undergoes a quantum transition to a lower energy state, releasing energy. Mills has published details of his theory in the open scientific literature, but it is wholly unlike anything that neither I, nor any of my colleagues has previously encountered. It is not widely accepted by the scientific community at large.

Although I am personally rather skeptical of Mills explanation, I did observe phenomena, such as plasmas apparently driven by chemical reactions rather than electric fields, that emitted ultraviolet light. I can offer no alternative explanation of my observations.

The BLP scientists who performed these demonstrations were open and honest in their descriptions of the apparatus. For each demonstration of energy output, a control experiment, identical in all respects except that a chemically similar, but non-catalytic substance, was substituted for the catalyst. The control experiments never exhibited any unusual phenomena, including plasmas or other evidence of energy production.

These demonstrations were not designed to generate power in a fashion that could be accurately measured. However, my observations were consistent with the hypothesis that the BLP process does generate energy and does so with an apparent fuel efficiency 10-100 times that of simple combustion of hydrogen gas.

Preface

BlackLight Power (BLP) claims to have discovered a process in which ordinary atomic hydrogen (H) is converted to lower energy quantum states, called "hydrinos" (Hy, my nomenclature) by contact with a suitable catalyst, resulting in an extraordinary release of energy. Dr. Randell Mills, the founder of BLP, developed the theory underlying this process. It is novel and therefore somewhat controversial and not yet broadly accepted. The theory's existence is important because it guides the development effort. Its acceptance by certain parts of the scientific community, however, does not affect whether or not the BLP process will provide an energy source with which Liebert can successfully develop a product. This product has the potential to be technologically superior to other relatively small-scale electrical energy generation devices, such as fuel cells.

My objective in this Interim Report is to assess the apparent validity of BLP's claims, the current stage of development of this process and to address, insofar as is practical, the engineering issues that would be important to commercialization of this process.

It is my professional opinion that the BLP process represents a chemical conversion of atomic hydrogen unlike any previously reported the archival scientific literature. Furthermore, this process appears to me to result in an energy release that is at least 10 times greater than the combustion of an equivalent amount of hydrogen gas and there is evidence that I find credible that this factor could be closer to 100 times the combustion of hydrogen.

The contents of this report is based on a visit to BLP's Cranbury, NJ laboratory from 1/8/01 to 1/15/01 and on study and analysis of BLP documents provided by Randell Mills of BLP prior to the visit. During the visit, I observed several demonstrations of the process and had lengthy and candid discussions with BLP personnel, ranging from Mill's, BLP's president, to the scientists and engineers working on the development, to the technicians who set up some of the experiments. I believe that I had free and open access to all aspects of the technology covered by the confidentiality agreement between BLP and me (Keith D. Keefer), although I report only those covered by the confidentiality agreement between BLP and my client.

This report is comprised of two sections and a series of Appendices. Section 1 is my assessment, analysis and opinions of BLP's technology at its current state of development in the context of proposed development and marketing plans. I regard this as my client's intellectual property, to be conveyed to BLP only at my client's discretion. Section 2 describes in more detail the observations I made at BLP and data provided to me by BLP. The Appendices contain technical details of the experiments I observed and figures of some of the apparatus and graphs from which the data were derived and were generously provided by BLP. These data and my observations are BLP's intellectual property and Section 2 will be provided to BLP before release to my client, so that BLP may review them for technical accuracy and protection of proprietary information, as provided for in my confidentiality agreement with BLP. This section will also cover the general nature of any BLP redactions, as provided for in my agreement with BLP. Although the technical content is BLP's property, the actual report itself belongs to my client and BLP should not release it to third parties without express consent.

2

Section 1.

Assessment, Analysis and Opinions Regarding the BlackLight Power Process

Introduction

This report is based on both my visit to BlackLight Power's (BLP) Cranbury, NJ laboratory and my study of BLP manuscripts submitted for publication in the scientific literature and reports commissioned by BLP from other institutions.

I found the personnel at BLP to be open, candid and enthusiastic about their results. I observed first hand many of the experiments that BLP has reported. The data that I observed were consistent with those I had read prior to my visit and appear to be completely factual. Although I was often accompanied by my host, William Good, V.P. of BLP, I was in no way escorted and was free to observe in the laboratory and to talk with any BLP researchers at any time, sometimes behind closed doors. All of my questions were answered, even when the answer was "We just don't know yet". I was never given the reply "We are not able to discuss that". These areas are discussed under Redactions in Section 2 and do not, in my opinion, have any impact on the commercialization of the technology. I kept two separate notebooks, one the property of BLP, the other notes upon which this report is based. The latter were copied by BLP prior to my departure, but were not censored, although they were discussed with William Good.

In deference to my audience, I will depart from the usual format of a scientific report and present my conclusions first, at the expense of a more coherent narrative. Although you may have simply asked me the time, ultimately you will need to build the watch, hence the detail provided.

Energy Generated by the BLP Process

It is my opinion, based upon my observations, discussions with BLP personnel and reports generated by BLP and others, that the BLP process is based on an extraordinary chemical reaction that generates an extraordinary amount of energy compared to the combustion of hydrogen gas by oxygen, i.e. a factor of 10 to over 100. I am unable to conceive of any other explanation for the results of BLP's experiments. There are two distinct classes of experiments, one comprised of strictly chemical reactions and the other based on observations of plasma reactors.

I regard chemical evidence as the most concrete and important. Chemical reactions generate chemical products. Methods of characterizing chemical compounds are well established. If no extraordinary chemical products are produced, the claim of extraordinary energy production by BLP's process is almost fatally weakened. (The lack of evidence of products of a nuclear reaction, neutrons, was the most damning to cold fusion, not the calorimetric results.) There is, however, substantial, although not, in my opinion, incontrovertible, evidence for extremely unusual chemical products.

The mere presence of hydrogen itself in these products, as demonstrated by mass spectroscopy (TOF-SIMS, in BLP jargon) provides good evidence of unusual compounds. The X-ray Photoelectron Spectroscopy (XPS) results show clear

3

differences in the energy of the chemical bonds in the products from those of the reactants. The Nuclear Magnetic Resonance (NMR) results also indicate that hydrogen present in the products is in a very unusual chemical environment. The First Law of Thermodynamics demands that the difference in free energy between the reactants and the products equals the amount of energy released in a reaction. The existence of reaction products allows, in principle, confirmation of adherence to the First Law by thermochemical measurements. As described in Section 2, I observed a Differential Scanning Calorimetric (DSC) experiment, the results of which, by any standard interpretation, showed an enthalpy of reaction in excess of 7 times that of the enthalpy of combustion of hydrogen.[1] As BLP's synthesis techniques become more refined and reproducible, calorimetric results should become even more compelling.

Obviously, it is the energy generated in the plasma reactors that is of most immediate and practical importance. While the plasma reactions are certainly much more dramatic than those conducted in a DSC, they are also more difficult to quantify. Part of this is due to the rather fickle nature of plasmas themselves. The other part is that the catalysts currently used by BLP need to be heated to produce the vapor necessary for reaction with hydrogen and need an incandescent filament for the dissociation of H_2 gas to atomic hydrogen, necessitating the separation of the contribution from the two energy sources. Qualitatively, the presence of catalyst vapor in the presence of hydrogen (compared to a chemically similar, but non-catalytic control substance used as a reference) makes an enormous difference in the amount of light (in the infra-red (IR), visible and ultraviolet (UV)) produced in these reactions. I find it difficult to believe that these plasmas do not release copious amounts of energy compared with that which would have been produced by a more conventional reaction with the same amount of hydrogen. (There is no air in the reactor and almost any other postulated reaction would generate far less energy than the direct combustion of hydrogen). A calculation presented in Section 2, based on the thermal data reported in Appendix B, yields a heat of conversion index of H to Hy in the plasma reactor 445X (i.e. 445 times that that would result from the combustion of a comparable amount of H_2). This figure is not regarded as accurate, both in my opinion and that of BLP; an estimate of 70-100X is much more plausible. The discrepancy is probably due to the conversion of H2 already present in the reactor in the form of metal hydrides.

The observations of the plasma reactors also provide qualitative estimates of the free energy of the reaction, which, as noted above, is the quantity of interest. A rough conversion of qualitative light output to energy can made. The free energy is the sum of the enthalpy (heat energy) produced by the reaction and the amount work that can be extracted in forms other than heat. The latter quantity is the product of the potential (e.g. voltage, temperature or pressure) at which the energy is provided and the amount of matter (e.g. electrons or gas molecules) that moves through the potential. The energy of a photon of visible light is about 1 eV and therefore corresponds to an electrical potential of about one volt. The temperature at which a blackbody starts to emit visible light is about 2000°C (c.f. a tungsten incandescent light bulb at ca. 2880K) One eV is roughly the energy of a single chemical bond. Thus, visible light can bleach organic dyes by breaking chemical bonds and few substances are solid at 2000°C. The plasmas in a BLP reactor radiate well into the ultraviolet, photons having energies roughly in the

---

[1]. Strictly speaking, calorimetry measures only the enthalpy [heat] of formation and not the free energy, the actual quantity of importance. They differ by the amount of work done by the reaction, but the latter is difficult to measure and is usually small compared to the enthalpy.

range of 10's to 100's of eV. This means that not only do the plasma reactors generate energy, but they do so under conditions corresponding to a large ΔT which, according to the Second Law of Thermodynamics, is very favorable to the efficient conversion of that energy to work, electrical or otherwise.

Engineering Considerations

Sustainability and Stability of the Plasma Reactions

The factor that currently limits the duration of a plasma in BLP reactors is the condensation of the relatively non-volatile catalysts in cooler parts of the reactor, particularly the vacuum outlet tube. At this stage, this is primarily an issue of the design and thermal management of the reactor, engineering issues. Until these are resolved, subtler issues such as filament life and reactor vessel corrosion will remain unknown. The development of more volatile catalysts, currently underway by BLP, will mitigate this problem.

The stability of the plasma and its energy output can presumably be controlled by feedback to the filament and electric fields in the reactor. "Presumably" is used because the role of electric fields to generate or sustain the plasma is not yet well understood. (It appears to be larger a chemical process). A small UPS in the system could function long time constant filter may also facilitate the necessary periodic maintenance of the system without disrupting power to the customer.

Construction Materials

The most expensive materials I saw employed in BLP reactors were stainless steel and fused silica (a.k.a. fused quartz, quartz glass) reaction vessels and nickel metal hydrogen gas dissociators. Again, the use of these materials is primarily one of product design and cost. The stainless steel is used because of the high temperature required to generate the vapor pressure of strontium (Sr) metal catalyst at which the BLP process occurs, but it is also the least volatile of the catalysts under consideration. BLP uses 316 stainless, probably because of its superior corrosion resistance and high temperature performance. A commercial reactor could probably use a more generic steel, such as"18-8", of which the 300 series stainless is a more refined subset. Fused silica is obviously more fragile and is more subject to corrosion by the catalyst materials than is stainless steel. It is, however widely used commercially in halogen cycle lamps. The use of the more volatile and less corrosive catalysts currently being studied by BLP should, again mitigate this problem. The nickel dissociators seem not to degrade under present use conditions. No precious metals or radioactive materials were used in any of the reactors I observed.

Scale Up

The plasma reactors use gas phase reactions so their power output should scale with the reactor volume. Depending on the geometry of the reactor (e.g. the diameter to length ratio of a cylindrical design) a potential decrease in the surface to volume ratio of the scaled up reactor would reduce both the cost of construction materials and the difficulty of thermal management. Mills has provided estimates of power densities of $1W/cm^3$, which I regard as rather optimistic in the short term.

"Open system" Issues

My questions in this area were readily dismissed as, "We don't know enough, yet". At the current state of the BLP effort, which is still essentially pure research, this response is justified. Technological development is performed as necessary to support their research effort. However, "open system issues present, in my opinion, a significant engineering challenge to the development of any device lacking moving parts. Obviously, for any technology based upon heat engines, this may not be an issue.

By "open system" I mean that BLP's devices, in their current state of development, are not hermetically sealed. This has the greatest impact on gyrotron-based devices. Hermeticity, in my experience at Sandia, requires that components are connected by "fused" joints, e.g. welds, glass or ceramic seals, solder joints or brazes, and is necessary to maintain even a low vacuum without active pumping. No gasket or swage connection will suffice. It is difficult for me to see how hermeticity can be maintained in a system into which gas must be introduced. However, high vacuum pumping systems are highly engineered and are extremely reliable, operating for months or years, with usually only annual oil changes. A hydrogen consumption of less than 100% would require that H_2 be recycled in the system or exhausted by the vacuum system. Examples of other related issues are cooling water, hydrogen generation by electrolysis, etc. These tend to be relatively high maintenance items that are less controllable by a supplier or lessor.

At a BLP process conversion efficiency of 100x the heat of formation of water, the use of metal hydrides as the hydrogen supply becomes plausible and a sealed system, although one probably requiring active pumping within the sealed system, becomes conceivable, as discussed below.

Comments on Mills' Theory

While not of direct engineering importance, Mills' theory does have an impact on the credibility of the BLP process and hence on the credibility of Liebert's commercialization plans. This is by no means a defense of Mill's theory; that he will have to provide for himself. It is just an attempt to put it in the context of other attempts to incorporate Einstein's General Theory of Relativity and gravity into quantum mechanics and some of the general conundrums posed by quantum mechanics itself.

Quantum mechanics has many unexplained and unsettling mysteries, e.g. the Heisenberg Uncertainty Principle, wave particle duality. Resolving some of these requires concepts that generate their own problems. For instance, consider superposition of states. According to this principle, a coin tossed in a dark room can exist in both states, heads and tails but its observed state is only resolved when the lights are turned on. Attempts to incorporate General Relativity lead to "vacuum states" in which electric fields are spontaneously created and then annihilated, which to me hearkens back to the theory of ether. These issues are the subject of popular scientific articles in respected periodicals such as "Scientific American" and "Science News". Attempts at "Grand Unified Theories" and theories of the cosmos result in more bizarre phenomena, such as eleven dimensional "superstrings", "dark matter" (which certainly would encompass Mills' hydrinos) and even antigravity.

I believe that some of the derision accorded Mills by some of his colleagues arises from his style of presentation of his theory and not BLP's experimental results. While very reasonable and affable in person, his writing style is somewhat confrontational. Solid scientific evidence (assuming it is forthcoming) will eventually generate converts.

6

Caveats About Thermochemical Calculations

There are two. One concerns the normalization of energy to a unit of matter, the other the thermodynamic reference states upon which tabulated values of energy differences are based. At this stage of knowledge, these *caveats* are more important to understanding the consistency (or apparent lack thereof) of some of the calculated values, rather than the values themselves.

First, the reaction for the enthalpy of oxidization of hydrogen for which values are tabulated is $H_2 + \frac{1}{2} O_2 \rightarrow H_2O$, that is enthalpy per mole of hydrogen gas. BLP typically reports enthalpies of reaction per mole of hydrogen atoms, so they must be compared to ½ of any quantity referred to moles of hydrogen gas.

Second, only differences in energy between two thermodynamic states can be measured. The reference point for so-called Standard Enthalpies and Free Energies is generally reactants and products at a temperature of 25°C. However, values are often tabulated for two different states of the products. For example, the enthalpy of formation of $H_2 + 1/2 O_2 \rightarrow H_2O$ liquid is 285 kJ/mole, whereas that for the same reaction in which the product is H_2O gas, a different reference state, is 241 kJ/mole. The difference is due to the latent heat of vaporization of water and the difference in the heat capacities of liquid water, water vapor and H_2 and O_2 gas.

Mass and Energy Balance Calculations

I am providing some crude mass and energy balance calculations that affect some of the engineering estimates. BLP tends to provide energy balance calculations that are more applicable to their device than to an entire engineered system.

The base assumption for these calculations is an average power output of 1 kW for one year. This gives a total energy output of 3.14×10^7 kJ/year. The "unit" of energy I will use is the heat of formation of water vapor from hydrogen and oxygen, 241 kJ/mole of water vapor. At 100% combustion efficiency, this is the energy supplied by 130×10^3 moles of H_2 gas, which has a volume of 2.92×10^6 liters or 103×10^3 cu ft. This amount of hydrogen is generated by the complete hydrolysis of 2.34×10^3 liters of water.

At a baseline of BLP conversion efficiency of 10x the heat of formation of water vapor, this generating capacity requires 0.64 liter of water/ day. Such a system would be "open" as discussed above.

A sealed system using titanium hydride (TiH_2) as a replenishable hydrogen reservoir becomes plausible at conversion efficiencies of 100x. The volume of Titanium (Ti) required to store a year's supply of H_2 gas would be around 20 liters.

Section 2.

Technical Observations of the BLP process

Redactions

There are three technical areas that BLP considers sensitive and proprietary and not covered by the current confidentiality agreement with my (Keith D. Keefer) client. I will discuss them, with BLP's permission, only to the level of detail that I believe might have an impact on my client's engineering efforts.

1. Specific catalysts and catalyst systems not yet reported in the literature.

   These catalysts tend to be more volatile than those previously reported and their development will only make the engineering of a commercial product easier. Complete peak assignments in the spectra were omitted to preserve confidentiality.

2. Specific operating parameters of BLP reactors.

   These obviously do affect engineering. I report an engineering envelope that I devised based on my own judgment and experience that encompasses the BLP process and was agreed to by BLP, but is not based directly on any BLP information, again to provide confidentiality.

   A. Operating temperatures.

      The maximum operating temperatures are within the range in which stainless steel could be used, roughly 600°-650° C. The minimum, which depends on item 1 above, could be as low as ambient.

   B. Operating pressures

      These range from low vacuum (i. e. less stringent) as defined by the vacuum sustainable, with modest active pumping, with standard Buna-N O-rings. The upper range is 100 psi, a pressure readily achieved by "hardware store" air compressors and contained by standard, non-armored, pressure hose. The suitability of elastomeric materials is subject to item A.

   C. Operating voltages

      Less than 600V, the (hardware store) rating of ordinary house wiring.

3. The engineering details of the BLP gyrotron

   These primarily affect the scale up and efficiency of the gyrotron. I will report, because it has a bearing on engineering design, with BLP's permission, that the microwave cavity of the test device that I saw was roughly 4 inches in diameter and 4 inches long. The details of the dimensions and design are proprietary to BLP.

Observation of Plasma Monitored by Vacuum-Ultraviolet (VUV)-Visible Spectroscopy

The reactor in these demonstrations was a closed end fused silica tube about 2 inches in diameter. Placed in this tube was a mixture of strontium (Sr) metal catalyst and a proprietary activatable catalyst or a magnesium (Mg) non-catalytic control with the activatable catalyst. Also in the tube was a tungsten filament wrapped around a ceramic tube. This filament both heated the metal catalysts to provide metal vapor and to provide a means of dissociating H_2 gas to atomic H. It also provided the weak (1-10 V/cm) electrical field necessary to initiate a plasma with Sr vapor. A band heater was placed around the tube near the closed end to prevent condensation of metal vapor in this cooler zone. The entire tube, except for the opening, was contained in an insulated box. The open end of the tube was sealed with a Viton O-ring and a Pyrex cap with 5 tubulations: two were electrical feedthroughs for the filament, one for the admission of H_2 gas, one for a vacuum connection and the fifth was connected to the VUV-Visible spectrometer, which used a normal incidence monochromator. (A schematic of the apparatus, without the VUV observation port, is shown in Appendix B., Fig.1)

I observed three demonstrations of this apparatus. In the first a mixture of Sr catalyst and a proprietary catalyst that had a vapor pressure higher than that of Sr, hence heating requirements were dictated solely by the Sr. Initially only a reddish glow from the tungsten filament was observed. After several hours, the apparatus had reached a temperature at which the Sr vapor pressure was high enough for the reaction to occur at a significant rate. Bright white light was observed through the Pyrex cap and the spectrum in the range from VUV to UV, 40-170nm, was recorded by the spectrometer (Appendix A, Fig. 1). The plasma was most intense inside the cap itself, where the electric field from the leads to the filament was highest. The leads themselves glowed at red heat. The second demonstration used Mg metal, a non-catalyst control, with the activatable catalyst. The operating conditions were identical and the same reactor vessel was used. Only the reddish glow from the filament was observed even after several hours of operation and there was no light emitted from the leads. The spectrum recorded is shown in Fig. 2. The salient feature in these spectra is magnitude of the hydrogen Lyman emission line at about 121nm. About 200,000 photons per second were recorded from the reactor containing Sr while only 1,800 were recorded from the reactor when it contained Mg. The latter value is larger than typically measured by BLP and may be due to some activation by the proprietary catalyst referred to above. In the third experiment, Sr and the activatable catalyst were used again, but the transparent Pyrex cap was surrounded by Al foil to raise its temperature and therefore the vapor pressure of Sr in the cap. Two thermocouples were placed on each side of the cap, to provide a rough estimate the of heat flux. The analysis of the thermocouple measurements is described below. Again, a brilliant white light was visible through an observation hole in the Al foil shroud.

Heat Flux Measurements of the VUV Reactor

The thermal power generated in the VUV style reactor described above was estimated from thermocouple measurements. The energy generated by the reactor is calculated from the heat flux and the flow rate of the H_2 fuel.

Appendix B details the measurements and calibration of the heat flux. Fig. 1 shows the placement of the thermocouples (circled numbers). Only readings from thermocouple 9 are used in the power calculation. Unlike some of the other catalysts used in the BLP process, strontium (Sr) requires a small (1-10V/cm) electric field to raise its electron

binding energy to that of atomic H, in accord with Mills' theory. This permits the plasma in an Sr catalyzed reaction to be turned on and off by adjusting the power supplied to the filament, which also provides the electric field. (More detail is provided below.) Figure 2 shows the results of temperature readings of an experiment in which thermal spikes were generated by the adjustment of the filament power, in a reactor configuration the same as the third one described above. Figure 3. is the result of a similarly instrumented reactor with a 300W halogen light bulb as the heat source instead of the Sr catalyzed plasma. The power supplied to the two heaters, filament and band was the same in both cases. Figures 3.1 and 3.2 are expanded scales of the temperature spikes recorded from two different light bulb power settings. Figure 4 is the calibration curve derived from the light bulb, relating the observed temperature rise to the bulb power. Figure 5 is an expanded scale of the thermal spike used for the power estimation. The power observed from the reactor is 163W, a figure arrived at by normalizing the observation time to that used for the calibration curves. A similar figure, 139W, was obtained from the same calibration curve from the temperature readings from the experiment that I observed. Although a molar conversion energy of H to Hy may be calculated from these data, the figure (445x the combustion of H_2) is regarded as exaggerated, by both BLP and I. The most likely reason is that H_2 can be retained in the metal catalysts as hydrides, and so the reaction of H_2 already present in the vessel may have contributed to the observed energy output.

Observation of Plasma Monitored by a Visible Light Spectrometer

The configuration of this reactor was the same as that described above, except that potassium (K) metal was used as the catalyst. Because K is much more volatile than Sr, the closed end of the reactor vessel protruded from the insulated box. Unlike the previous experiments in which the Sr was placed in proximity to the tungsten filament, the K metal was placed at the closed end of the tube outside the insulated box and was heated with a separately powered heat tape. Again, after an equilibration period, a white light was observed in the apparatus. At my request, the heat tape surrounding the closed end of the tube was removed so that K metal vapor would condense there and not be present in the vicinity of the dissociating filament. In a few minutes, the bright white light disappeared, demonstrating that K metal vapor was essential to the reaction generating the plasma. A control experiment with a non-catalyst was run in the same reactor the next day and showed no unusual emission of light.

Observation of Plasma Generated by Electric Discharge

In this demonstration, the reactor was a stainless steel vessel heated externally in a furnace. Instead of a filament, a nickel (Ni) mesh was used as the hydrogen dissociator. (See Appendix C for more detailed reaction conditions and a diagram of the apparatus, Fig. 1). The Ni mesh also served as one electrode for the electrical discharge and the stainless steel vessel as the other. A port with a sapphire window allowed observation of the discharge and a fused silica rod was used as a light conduit to couple visible light to the spectrometer. Two experiments were performed, one with Sr metal catalyst, the other with sodium (Na) metal as a control. The reaction conditions used for the control were optimized for discharge from Na using data from A. von Engle, Ionized Gasses, American Institute of Physics, p. 196. Unlike the fused silica reactors, the applied electric filed was AC rather than DC, so the peak voltages were about 40% higher than those reported. However, electric power input was monitored with true RMS instrumentation.

The electric discharge phenomenon was only recently discovered and the nature of all of the plasma experiments is such that the principal physical observable is the ratio of the power input to the power output. Certain assumptions must be made to extract a measure of the actual energy generated by the reaction. The experimental data are reported in Figs. 2 and 3 of Appendix C. The key result is that with the Sr catalyst, the operating parameters could be tuned such that a plasma was sustained at a voltage of 16.7V RMS (the electrode gap being about 1.75 cm) and an input current of 0.5mA, an input electrical power of 7.2mW. The spectrally integrated visible light output was 0.74 microwatts per cm2 at the detector face. The maximum measured visible light output from the reactor containing Na control (reference material)was less than 0.1 microwatt at an applied voltage of 327V and an electrical power input of 162W. Thus the ratio of the power required by the Na containing reactor to produce less than one seventh the optical power of the Sr reactor is 22,500. The observable spectral response in this apparatus is limited by the transmission of the windows. The significant contributions in the IR and UV are not measurable and so even a qualitative estimate of the energy generated by the reaction in this apparatus is not possible.

Differential Scanning Calorimetry of Hydrino Generating Reactions

Because of the power input required to sustain a plasma in BLP reactors, direct calorimetric measurements are difficult and somewhat tricky. Calorimetric measurements of chemical reactions, while still tricky, probably provide the most accurate measurement of the enthalpy generated in the BLP process. I observed two such measurements, one on a catalytic system and one on a control. My interpretation of the data is in agreement with that of BLP: the reactions I observed generated an enthalpy of reaction at least a factor of seven larger than the enthalpy of combustion of H_2 gas with oxygen.

The technique that BLP uses, Differential Scanning Calorimetry (DSC), is widely used in Materials Science, but differs from many of the methods more familiar to chemists and engineers. Since the results of these measurements are important and data are presented here, I believe that a brief explanation of the measurement and why it is used by BLP is in order.

Many calorimetric measurements are conducted at near ambient temperatures, where heat transfer occurs primarily by conduction and convection. At higher temperatures, e.g. greater than 250°C, radiant heat transfer dominates and optical properties of the apparatus, such as emissivity and reflectivity must be accounted for. In DSC, a reference material, almost invariably aluminum oxide, is heated in a reference cell identical to that of the sample cell, in close proximity, in the same insulated furnace. Heat output is derived from the difference in temperature between the two cells, hence almost all of the influence of heat transfer cancels out. Although the actual physical observable is temperature, the instrument can be accurately calibrated from the well-known thermal properties of aluminum oxide and from heats of fusion of standard reference materials known well from other measurements. Unlike many other techniques, DSC is not isothermal: the temperature of the furnace is slowly ramped up and down so the temperature of the reaction is also measured and the heat consumed or generated is derived from the integral of the temperature difference, time and the calibration factors. There is a baseline that is a function of temperature that reflects the heat capacity of the cells. Deviations from this baseline are due to heat generated or consumed in the sample, but not in the chemically inert reference material. I should note that the instrument that BLP uses, a SETARM 1000 II, is not an ordinary DSC. Its

insulating blanket is at least 5 times thicker than others I have used and the maximum temperature ramp rate is 0.1 /min compared to 10 /min. The slow ramp rate minimizes distortions due to reaction rates and is dictated in part by the thickness of the thermal insulation, which slows the rate at which an approximately steady-state thermal gradient can be maintained.

I observed two DSC measurements, one, the reaction of potassium hydride (KH) with potassium iodide (KI) and the other a control of magnesium hydride (MgH_2). Potassium hydride is comprised of both a catalyst (K) and the fuel (H). The results are shown in Appendix D., Fig. 1. Downward peaks are endothermic. The ones observed between 350° and 400°C are due to the decomposition of KH and the one at about 660° is due to the melting of KI. The former are broader than the latter because a decomposition reaction is generally slower than melting and the temperature is a function of time. The huge, broad positive (exothermic) peak is ascribed to the formation of hydrino hydrogen and its reaction to form KHyI. The enthalpy derived from the integration of this very broad peak is equivalent to 7.0 times the molar heat of formation of H2O from H2 and ½ O2. The control, MgH_2 shows only two endotherms, one at 350°C from the decomposition of MgH_2 to Mg metal and H_2 and one at 650° from the melting of Mg metal (Fig. 2). Fig. 3 shows the reaction of KH alone the results of which I requested from BLP's archives. The observed enthalpies represent lower limits of the molar enthalpy of reaction, since the H to Hy conversion efficiency is not known with great accuracy and the reported number is based upon 100% conversion. The substantial observed enthalpy difference between the reaction of KH+KI and KH alone is not necessarily due the enthalpy of formation of KHyI as opposed to the reaction of H to form Hy, since the presence of KI could substantially change the conversion efficiency of H to Hy. Although the exotherms are very broad, and by DSC standards unusually shaped, the two presented here and others I saw in the BLP archives are strikingly similar. For example, there is a change in slope from the baseline at 300°C, a double endotherm between 350° and 400°C, the onset of the exotherm at 400°C (the sharp spikes are noise), the plateau at around 450°, the broad peak at 500° and the long tail out to about 650°. In my experience, these attest to a well-defined and reproducible chemical reaction. The differences in enthalpy arise from the magnitude and breadth of the exotherm, which are the result of the rate and duration of the reaction, variations to be expected in gas phase reactions under non-isothermal conditions.

Synthesis Reactions

The difference in the enthalpy of formation of the reactants and the products is the most accurate and incontrovertible evidence of the efficacy of energy production. The products of these reactions may, themselves, be commercially valuable.

I observed four synthesis reactions of H_2 and KCl to form KHyCl, catalyzed by K metal. These reactions were conducted in stainless steel vessels under conditions similar to those used in the electrical discharge experiments described above, except the vessels lacked electrical feed-throughs and an observation port. The experimental conditions are reported in the Appendix. Hydrogen uptake in excess of that of the Ni dissociator was monitored by the periodic addition of H_2 gas to maintain a constant internal pressure.

The most significant analytical results from these products are the Nuclear Magnetic Resonance spectra shown in Figs 1-5. Briefly and crudely, NMR signals arise from nuclei with an odd atomic weight such as a proton (^1H). When a magnetic field is

applied to such nuclei, their magnetic moment tends to align with the field, and the nuclei's angular momentum causes it to precess. In a radio-frequency (RF) field tuned to this precession frequency, the resonance causes the magnetic moment of the nucleus to "flip" and absorb RF energy. The magnetic field experienced by the nucleus is the sum of the contributions from both the applied and RF fields. Electrons in the chemical bonds to the atom containing the nucleus "shield" it from the applied RF field and result in the resonance appearing to occur at a magnetic field different from that applied. This difference is called a "chemical shift" and is usually reported in parts per million of the applied field, referred to a standard (which for protons, is typically tetramethylsilane (TMS)). This shift varies with the electron density in the chemical bonds of the atom containing the nucleus, which controls the degree of screening. The large "upfield" shift of the resonance at -4.4 to −4.5 in these spectra (Appendix E, Figs 1-4) is interpreted as arising from hydrino hydride and means that a higher external magnetic field would need to be applied for the nucleus to precess at the same RF. This higher field is required because the electrons shield the nucleus from it, the higher the shift, the greater the electron density around the nucleus. Fractional quantum states for the electron in the hydrino atom would increase the shielding and could account for the extremely large observed shifts. Also, the NMR peak intensity is directly proportional to the number of resonating nuclei and so is a measure of their concentration. These NMR spectra provide compelling, although not conclusive, evidence that hydrino hydride is present in the reaction products.

(Other experiments were in preparation during my first visit and will be described in the final report. These include, but are not limited to, the following:)

Gyrotron

I observed the gyrotron under development by BLP. It is comprised of a vacuum system incorporating a diffusion pump, a tunable microwave cavity and an electron source. The system had recently undergone some modifications and was not operating at the time of my visit. A tungsten filament was in place as the electron source for tuning and calibration purposes and will be replaced by a BLP reactor when these activities are completed.

Calorimeters

A heat flux calorimeter for more accurate measurements of the fused silica plasma reactor was near completion at the time of my visit. Calvet calorimeters for measurements of the stainless steel discharge reactors were in the process of being set up.

THIS PAGE BLANK (USPTO)